PB92-192954

REPORT NO.
UCB/EERC-90/09
JULY 1990

EARTHQUAKE ENGINEERING RESEARCH CENTER

INFLUENCE OF THE EARTHQUAKE GROUND MOTION PROCESS AND STRUCTURAL PROPERTIES ON RESPONSE CHARACTERISTICS OF SIMPLE STRUCTURES

by

JOEL P. CONTE
KARL S. PISTER
STEPHEN A. MAHIN

Report to the National Science Foundation

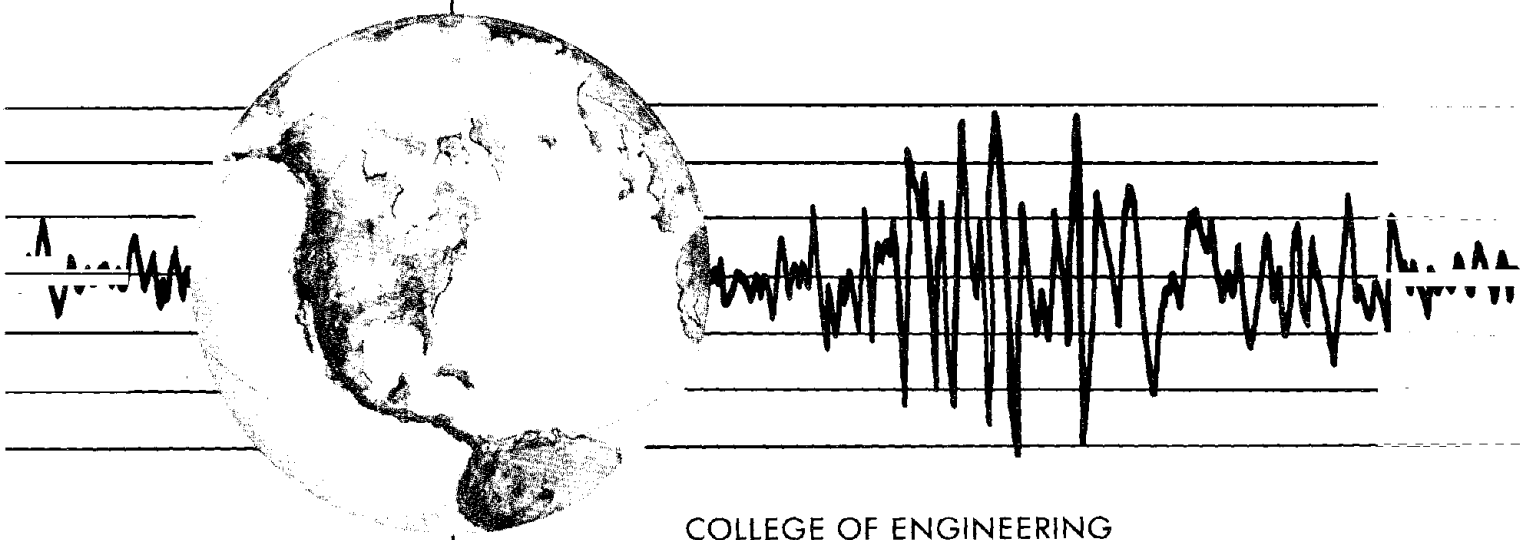

COLLEGE OF ENGINEERING

UNIVERSITY OF CALIFORNIA AT BERKELEY

REPRODUCED BY
U.S. DEPARTMENT OF COMMERCE
NATIONAL TECHNICAL INFORMATION SERVICE
SPRINGFIELD, VA. 22161

For sale by the National Technical Information Service, U.S. Department of Commerce, Springfield, Virginia 22161

See back of report for up to date listing of EERC reports.

DISCLAIMER

Any opinions, findings, and conclusions or recommendations expressed in this publication are those of the authors and do not necessarily reflect the views of the National Science Foundation or the Earthquake Engineering Research Center, University of California at Berkeley.

REPORT DOCUMENTATION PAGE	1. REPORT NO. NSF/ENG-90004	2.	3. PB92-192954

4. Title and Subtitle
Influence of the Earthquake Ground Motion Process and Structural Properties on Response Characteristics of Simple Structures

5. Report Date
July 1990

6.

7. Author(s)
J.P. Conte, K.S. Pister, and S.A. Mahin

8. Performing Organization Rept. No.
UCB/EERC-90/09

9. Performing Organization Name and Address
Earthquake Engineering Research Center
University of California, Berkeley
1301 So. 46th Street
Richmond, Calif. 94804

10. Project/Task/Work Unit No.

11. Contract(C) or Grant(G) No.
(C)
(G) ENG-7810992

12. Sponsoring Organization Name and Address
National Science Foundation
1800 G Street, N.W.
Washington, D.C. 20550

13. Type of Report & Period Covered

14.

15. Supplementary Notes

16. Abstract (Limit: 200 words) In this study, a quantitative description of the uncertainty or inherent variability of earthquake ground motion input into structures is proposed. It utilizes a time-varying discrete ARMA stochastic process able to reliably capture the amplitude and frequency nonstationarities typical of real earthquake records. The ARMA earthquake models are estimated using (i) Kalman filtering with a state-space formulation of the ARMA model and (ii) a more traditional nonstationary estimation technique based on the concept of a stationary moving time window. Two real very different earthquake records are analyzed and simulated using the proposed ARMA modeling procedure. The fitted earthquake models are used as seismic input into simple elastic and inelastic structural models. A comprehensive parametric study using ARMA Monte Carlo simulation is undertaken to gain insight into the stochastic nature of the seismic response of structures. The results of this study can be directly used for seismic reliability assessment of simple structures using formal reliability theory.

17. Document Analysis a. Descriptors

b. Identifiers/Open-Ended Terms

c. COSATI Field/Group

18. Availability Statement	19. Security Class (This Report)	21. No. of Pages
Release Unlimited	unclassified	360
	20. Security Class (This Page) unclassified	22. Price

(See ANSI-Z39.18) See Instructions on Reverse OPTIONAL FORM 272 (4-77) (Formerly NTIS-35) Department of Commerce

INFLUENCE OF THE EARTHQUAKE GROUND MOTION PROCESS AND STRUCTURAL PROPERTIES ON RESPONSE CHARACTERISTICS OF SIMPLE STRUCTURES

by

Joël P. Conte

Karl S. Pister

and

Stephen A. Mahin

Report to the National Science Foundation

Report No. UCB/EERC-90/09
Earthquake Engineering Research Center
College of Engineering
University of California at Berkeley

July 1990

ABSTRACT

The earthquake engineer is faced with the complicated problem of designing safe and economical structures in a highly uncertain seismic environment. In conventional seismic design, a design philosophy which relies on inelastic ductile behavior of structures to withstand rare, severe earthquakes has been widely accepted. However, the complex interaction between ground motion features, structural properties and structural response parameters is not well understood, nor are the corresponding levels of variability.

In this study, a quantitative description of the uncertainty or inherent variability of earthquake ground motion input into structures is proposed. It utilizes a time-varying discrete ARMA stochastic process able to reliably capture the amplitude and frequency nonstationarities typical of real earthquake records. The ARMA earthquake models are estimated using (i) Kalman filtering with a state-space formulation of the ARMA model and (ii) a more traditional nonstationary estimation technique based on the concept of a stationary moving time window.

Two real earthquake records, very different in nature, are analyzed and simulated using the proposed ARMA modeling procedure. The fitted earthquake models are used as seismic input into simple elastic and inelastic structural models. The resulting stochastic response processes are characterized using various elastic and inelastic response parameters. Some of the inelastic response parameters used are indicative of the degree of damage corresponding to damage mechanisms most commonly observed in steel and reinforced concrete structures subjected to strong dynamic cyclic loading.

The fitted earthquake models are checked thoroughly at three different levels: (i) "whiteness" and normality of residuals, (ii) simulation of stochastic elastic response, and (iii) simulation of stochastic inelastic response.

Probabilistic elastic and inelastic (or damage) response spectra corresponding to a given source-site pair can be easily generated using ARMA Monte Carlo simulation. Such probabilistic spectra provide necessary tools for probabilistic seimic design and seismic safety analysis.

A comprehensive parametric study using ARMA Monte Carlo simulation is undertaken to

gain insight into the stochastic nature of the seismic response of structures. The sensitivities of the probability distributions of the various response parameters with respect to the earthquake process, the type of structural behavior and the structural properties are obtained. The absolute and relative levels of variability of the traditional ground motion parameters, the elastic response parameters and the inelastic response parameters are also investigated using the fitted ARMA earthquake models.

The results of this study can be directly used for seismic reliability assessment of simple structures using formal reliability theory. The ARMA Monte Carlo simulation methodology can be integrated into the formulation of reliability-based seismic design procedures that can admit some tolerable degree of damage while minimizing the risk of collapse.

ACKNOWLEDGEMENTS

The research described in this report was supported by the National Science Foundation under grant ENG-7810992 and by Dean Karl Pister through his Roy W. Carlson professorship. This financial support is gratefully acknowledged.

Sincere thanks are also due to the following for their help in the course of the study:

Professor Robert Oliver for his helpful suggestions in ARMA modeling

Professor David Brillinger for several fruitful interactions in the field of statistics and time series analysis

Dr. James Hart for a thorough review of the manuscript

Dr. Mark Austin for initial cooperation on the research project and Izuru Takewaki for ongoing cooperation

"Nothing in Nature is random ... A thing appears random only through the incompleteness of our knowledge." - Spinoza, Ethics I

"I do not believe that God rolls dice" - Einstein

"In the case of Earthquakes (as in other physical processes), we consider two kinds of representations: dynamic models, and stochastic models. These two categories of theoretical constructs are complementary: the more we know about the dynamics of a process, the less we need to know about its statistics." - Lomnitz

TABLE OF CONTENTS

ABSTRACT i

ACKNOWLEDGEMENTS iii

TABLE OF CONTENTS v

LIST OF TABLES ix

LIST OF FIGURES x

CHAPTER 1 : INTRODUCTION

1.1 Background and Motivation 1

1.2 Probability Bases for Earthquake Resistant Design 4

1.3 Seismic Hazard Analysis 4

1.4 Objectives and Scope 6

1.5 Organization of Text 8

CHAPTER 2 : EARTHQUAKE GROUND MOTION CHARACTERIZATION

2.1 Uncertainties in Earthquake Engineering 10

2.2 Predictive Physical Earthquake Models 12

2.3 Continuous-Time Stochastic Earthquake Models: A Review 14

CHAPTER 3 : ARMA MODELS FOR EARTHQUAKE GROUND MOTION MODELING

3.1 Introduction 26

3.2 Stationary ARMA(p,q) Models 26

3.3 Nonstationary ARMA Models 30

3.4 Time-Varying ARMA Model Estimation Using Moving Window Technique 32

3.5 Time-Varying ARMA Model Estimation Using Kalman Filtering 35

3.6 ARMA Simulation of Original Records 39

3.7 ARMA Model Diagnostic Checking 42

3.8 Advantages of ARMA Models 47

CHAPTER 4 : PHYSICAL INTERPRETATION OF ARMA MODELS

4.1 Introduction 50

4.2 The ARMA(2,1) Model 50

4.3 Higher Order ARMA Models 59

4.3.1 Multiple Cascading of Low Order ARMA Models 59

4.3.2 Multiple-Degree-of-Freedom Dynamical Systems 63

CHAPTER 5 : APPLICATIONS OF STOCHASTIC GROUND MOTION MODELING

5.1 Introduction 65

5.2 Earthquake Analysis 66

5.3 Earthquake Simulation 70

5.4 Model Checking 71

5.5 Probability Distribution of Ground Motion Parameters 78

CHAPTER 6 : STRUCTURAL SYSTEMS, RESPONSE PARAMETERS AND DAMAGE MODELS

6.1 Structural Systems 80

6.2 Structural Damage Characterization 82

6.3 Response Computation and Response (Damage) Parameters 89

6.4 Earthquake Response Simulation 94

6.5 Comprehensive Parametric Study 97

CHAPTER 7 : STATISTICAL RESPONSE OF LINEAR ELASTIC STRUCTURES

7.1 Introduction 99

7.2 Probabilistic Response Spectra 100

7.3 Probabilistic Seismic Design and Seismic Safety Analysis of Elastic Structures 104

CHAPTER 8 : STATISTICAL RESPONSE OF INELASTIC SDOF STRUCTURES

8.1 Introduction 110

8.2 Presentation of Simulation Results 110

8.3 Earthquake Model Checking Based on Inelastic Response Parameters 112

8.4 Influence of Earthquake Model and Structural Parameters on Stochastic Response Parameters 114

8.4.1 Type of Probability Distributions 114

8.4.2 Influence of Target Earthquake 115

8.4.3 Influence of ARMA Model Order 117

8.4.4 Influence of Hysteretic Model 118

8.4.5 Influence of Structural Parameters 123

8.5 Probability Distribution of Plastic Deformation Ranges 130

8.6 Variability of Structural Response Parameters vs. Variability of Ground Motion Parameters 134

CHAPTER 9 : CONCLUDING REMARKS

9.1 Summary of Work 136

9.2 Summary of Findings 140

9.3 Recommendations for Future Research 146

REFERENCES 148

TABLES 153

FIGURES 164

APPENDIX A : BI-LATERAL BUTTERWORTH FILTER 319

APPENDIX B : ANALYTICAL INTEGRATION OF EQUATION OF MOTION 321

LIST OF TABLES

Table	Description	Page
4.1	Roots of Characteristic Equation: $r^2 - \phi_1 r - \phi_2 = 0$	153
4.2	Discrete Autocorrelation Function ρ_n	154
4.3	Discrete/Continuous Parameter Relationships for Zone 1 (Underdamped Case)	155
4.4	Discrete/Continuous Parameter relationships for Zone 2 (Overdamped Case)	156
5.1	Summary of Earthquake Data	157
5.2	Characteristics of Target Earthquake Records	158
5.3	High-Pass Filters	159
5.4	Statistical Tests for the ARMA Models Fitted to the E02NS Record	159
5.5	Statistical Tests for the ARMA(2,1) Model Fitted to El Centro 1940	160
5.6	Ground Motion Parameters of E02NS and Statistics from ARMA(2,1) and ARMA(4,2) Earthquake Models	161
5.7	Ground Motion Parameters of El Centro 1940 and Statistics from ARMA(2,1) Earthquake Model	162
8.1	Lower and Upper Bounds on Coefficients-of-Variation of Elastic and Inelastic Response Parameters in Period Range $[0.10 \leq T_0 \leq 3.0 \text{ seconds}]$	163
B.1	Characteristic Roots of Homogeneous Equation of Motion	328
B.2a	Complete Solution of Equation of Motion (Part A)	329
B.2b	Complete Solution of Equation of Motion (Part B)	330

LIST OF FIGURES

Figure	Description	Page
1.1	Probabilistic Seismic Hazard Analysis Procedure	164
2.1	Schematic Representation of a Random Process X(t)	165
3.1	Time Windowing of an Accelerogram	165
3.2	Kalman Filter Loop	166
3.3	Starting Conditions for Kalman Filtering	166
4.1	Stability Region for the ARMA(2,1) Model	167
4.2	Definitions of Zones 1 to 5	167
4.3	Underlying Physical System	168
4.4	Reduced Mapping $(\phi_1, \phi_2) \longleftrightarrow (\omega_g, \xi_g)$ for Underdamped Case	168
4.5	Reduced Mapping $(\phi_1, \phi_2) \longleftrightarrow (\omega_g, \xi_g)$ for Overdamped Case	169
4.6	Kanai-Tajimi and Corresponding ARMA(2,1) PSD	169
4.7	Multiple Cascading of Low Order ARMA Models	170
4.8	Tri-Modal PSD Corresponding to an ARMA(6,3) Model	170
5.1	Ground Acceleration (a), Velocity (b) and Displacement (c) Time Histories of the E02NS Record	171
5.2	Ground Acceleration (a), Velocity (b) and Displacement (c) Fourier Amplitude Spectra of the E02NS Record	172
5.3	Ground Acceleration (a), Velocity (b) and Displacement (c) Time Histories of the El Centro 1940 Record	173
5.4	Ground Acceleration (a), Velocity (b) and Displacement (c) Fourier Amplitude Spectra of the El Centro 1940 Record	174
5.5	Standard Deviation Envelope of the E02NS Record	175
5.6	Amplitude Demodulated E02NS Record	175
5.7	ARMA(2,1) Model Parameter Estimates for the E02NS Record	176
5.8	Time Histories of Physical Parameters for the E02NS Record	177
5.9	Normalized ARMA(2,1) Evolutionary Power Spectral Density Estimate of the E02NS Record	178

5.10	Normalized ARMA(4,2) Evolutionary Power Spectral Density Estimate of the E02NS Record	178
5.11	ARMA(4,2) Model Parameter Estimates for the E02NS Record	179
5.12	Convergence of the Iterative Kalman Filtering Scheme	180
5.13	Standard Deviation Envelope of the El Centro 1940 Record	181
5.14	Amplitude-Demodulated El Centro Record	181
5.15	ARMA(2,1) Model Parameter Estimates for El Centro 1940	182
5.16	Time Histories of Physical Parameters for El Centro 1940	183
5.17	Normalized ARMA(2,1) Evolutionary Power Spectral Density Estimate of the El Centro record	184
5.18	Four Different High-Pass Filters	184
5.19	Single ARMA(2,1) Artificial Earthquake Ground Acceleration for the E02NS Target Record Using Four Different High-Pass Filters: (a) Filter I, (b) Filter II, (c) Filter III, and (d) Filter IV	185
5.20	Single ARMA(2,1) Artificial Earthquake Ground Velocity for the E02NS Target Record Using Four Different High-Pass Filters: (a) Filter I, (b) Filter II, (c) Filter III, and (d) Filter IV	186
5.21	Single ARMA(2,1) Artificial Earthquake Ground Displacement for the E02NS Target Record Using Four Different High-Pass Filters: (a) Filter I, (b) Filter II, (c) Filter III, and (d) Filter IV	187
5.22	Single ARMA(4,2) Artificial Earthquake Ground Acceleration for the E02NS Target Record Using Four Different High-Pass Filters: (a) Filter I, (b) Filter II, (c) Filter III, and (d) Filter IV	188
5.23	Single ARMA(4,2) Artificial Earthquake Ground Velocity for the E02NS Target Record Using Four Different High-Pass Filters: (a) Filter I, (b) Filter II, (c) Filter III, and (d) Filter IV	189
5.24	Single ARMA(4,2) Artificial Earthquake Ground Displacement for the E02NS Target Record Using Four Different High-Pass Filters: (a) Filter I, (b) Filter II, (c) Filter III, and (d) Filter IV	190
5.25	Single ARMA(2,1) Artificial Earthquake for El Centro 1940 Ground (a) Acceleration, (b) Velocity and (c) Displacement	191
5.26	Single ARMA(2,1) Artificial Earthquake for El Centro 1940 Ground (a) Acceleration, (b) Velocity and (c) Displacement	192
5.27	Butterworth High-Pass Filter for the ARMA(2,1) El Centro 1940 Earthquake Process	192

5.28 Residuals from the ARMA(2,1) Model Fitted to the E02NS Record (a) Time History, (b) Sample Autocorrelation Function, Periodogram in (c) Decimal Scale, and (d) Logarithmic Scale 193

5.29 Residuals from the ARMA(4,2) Model Fitted to the E02NS Record (a) Time History, (b) Sample Autocorrelation Function, Periodogram in (c) Decimal Scale, and (d) Logarithmic Scale 194

5.30 Computer Generated Discrete White-Noise (a) Time History, (b) Sample Autocorrelation Function, Periodogram in (c) Decimal Scale, and (d) Logarithmic Scale 195

5.31 Sample Autocorrelation Function and Periodogram of the Amplitude-Demodulated E02NS Record 196

5.32 Normality Test of the Residuals from the ARMA(2,1) Model Fitted to the E02NS Record 197

5.33 Normality Test of the Residuals from the ARMA(4,2) Model Fitted to the E02NS Record 197

5.34 Residuals from the ARMA(2,1) Model Fitted to the El Centro 1940 Record: (a) Time History, (b) Sample Autocorrelation Function, Periodogram in (c) Decimal Scale, and (d) Logarithmic Scale 198

5.35 Sample Autocorrelation Function and Periodogram of the Amplitude-Demodulated El Centro 1940 Record 199

5.36 Normality Test of the Residuals from the ARMA(2,1) Model Fitted to the El Centro 1940 Record 199

5.37 Fourier Amplitude Spectra of an Artificial Ground Motion (acceleration, velocity, and displacement) Generated from the ARMA(2,1) Model Fitted to the E02NS Record 200

5.38 Fourier Amplitude Spectra of an Artificial Ground Motion (acceleration, velocity, and displacement) Generated from the ARMA(4,2) Model Fitted to the E02NS Record 201

5.39 ARMA(2,1) Model Parameter Estimates for an ARMA(2,1) Artificial Realization of the E02NS Earthquake Process 202

5.40 ARMA(4,2) Model Parameter Estimates for an ARMA(4,2) Artificial Realization of the E02NS Earthquake Process 203

5.41 Comparison Between the Normalized ARMA EPSD Estimate and the Normalized Moving Periodogram Estimate of the EPSD of the E02NS Earthquake Process 204

5.42 Fourier Amplitude Spectra of an Artificial Ground Motion (acceleration, velocity, and displacement) Generated from the ARMA(2,1) Model Fitted to the El Centro 1940 Record 205

5.43 ARMA(2,1) Model Parameter Estimates for an ARMA(2,1) Artificial Realization of the El Centro Earthquake Process 206

5.44	Comparison Between the Normalized ARMA EPSD Estimate and the Normalized Moving Periodogram Estimate of the EPSD of the El Centro Record	207
5.45	Statistical Convergence of the Ground Motion Parameters Simulated from the ARMA(2,1) Model of El Centro 1940	208
5.46	Histograms of the Ground Motion Parameters Simulated from the ARMA(2,1) Model of E02NS	209
5.47	Histograms of the Ground Motion Parameters Simulated from the ARMA(4,2) Model of E02NS	210
5.48	Histograms of the Ground Motion Parameters Simulated from the ARMA(2,1) Model of El Centro 1940	211
5.49	Lognormal Distribution Fit of Ground Motion Parameters on Probability Paper (El Centro 1940, ARMA(2,1))	212
6.1	Cyclic Load-Deflection Diagram for constant amplitude cycling of a Wide-Flange Component of Steel Structure ("crack propagation at weldment" damage mode)	213
6.2	Cyclic Load-Deflection Diagram for variable amplitude cycling of a Wide-Flange Component of Steel Structure ("crack propagation at weldment" damage mode)	213
6.3	Cyclic Load-Deflection Diagram for constant amplitude cycling of a Wide-Flange Component of Steel Structure ("flange local buckling" damage mode)	214
6.4	Damage Index D_1 plotted on Lognormal Probability Paper	214
6.5	Definition of Plastic Deformation Ranges for Different Hysteretic Models	215
6.6	Centroid of Plastic Deformation Range, $\overline{\Delta u_{p,i}}$	216
6.7	Hysteretic Behavior of Four Different Systems in Response to the Same Artificial Earthquake Derived From El Centro 1940	217
6.8	Energy Response Time Histories of Four Different Systems to the Same Artificial Earthquake Derived From El Centro 1940	218
6.9	Rate of Hysteretic Energy Response Time Histories of Four Different Systems to the Same Artificial Earthquake Derived from El Centro 1940	219
6.10	Convergence of the Second Order Statistics of Two Response Parameters to the number of Artificial Earthquakes from the ARMA(2,1) El Centro Process	220
6.11	Histogram and Lognormal Probability Model Fit of the Plastic Deformation Ranges Generated by the ARMA(2,1) El Centro Process	220

6.12	Flow Chart of Statistical Parametric (Sensitivity) Study	221
7.1	Statistical Convergence of the Pseudo-Acceleration Response	222
7.2	Probabilistic and Target Elastic Response Spectra for E02NS (Statistical "Fractile Method")	223
7.3	Probabilistic and Target Elastic Response Spectra for El Centro 1940	224
7.4	Histograms of the Peak Responses of Linear SDOF Oscillators	225
7.5	Probability Model Fit of Peak Elastic Responses Simulated from the ARMA(2,1) Model of El Centro 1940	226
7.6	Risk-Inconsistence of Elastic Response Spectra Derived from Single Earthquake Realizations	227
8.1	Flow Chart of Parametric Study	228
8.2	Probabilistic Inelastic Response Spectra for the E02NS Target Record (ARMA(2,1) Earthquake Model and Bilinear Inelastic Structural Model)	229
8.3	Probabilistic Inelastic Response Spectra for the E02NS Target Record (ARMA(4,2) Earthquake Model and Bilinear Inelastic Structural Model)	232
8.4	Probabilistic Inelastic Response Spectra for the E02NS Target Record (ARMA(4,2) Earthquake Model and Modified Clough's Structural Model)	235
8.5	Probabilistic Inelastic Response Spectra for the E02NS Target Record (ARMA(4,2) Earthquake Model and Slip Structural Model)	238
8.6	Probabilistic Inelastic Response Spectra for the E02NS Target Record (ARMA(4,2) Earthquake Model and Bilinear Elastic Structural Model)	241
8.7-8.9	Probabilistic Inelastic Response Spectra for the E02NS Target Record (ARMA(4,2) Earthquake Model and Bilinear Inelastic Structural Model)	244
8.10	Probabilistic Inelastic Response Spectra for the E02NS Target Record (ARMA(4,2) Earthquake Model and Modified Clough's Structural Model)	253
8.11	Probabilistic Inelastic Response Spectra for the E02NS Target Record (ARMA(4,2) Earthquake Model and Bilinear Inelastic Structural Model)	255
8.12	Probabilistic Inelastic Response Spectra for the El Centro Target Record (ARMA(2,1) Earthquake Model and Bilinear Inelastic Structural Model)	258

8.13	Probabilistic Inelastic Response Spectra for the El Centro Target Record (ARMA(2,1) Earthquake Model and Modified Clough's Structural Model)	261
8.14	Probabilistic Inelastic Response Spectra for the El Centro Target Record (ARMA(2,1) Earthquake Model and Slip Structural Model)	264
8.15	Probabilistic Inelastic Response Spectra for the El Centro Target Record (ARMA(2,1) Earthquake Model and Bilinear Elastic Structural Model)	267
8.16-8.18	Probabilistic Inelastic Response Spectra for the El Centro Target Record (ARMA(2,1) Earthquake Model and Bilinear Inelastic Structural Model)	270
8.19	Probabilistic Inelastic Response Spectra for the El Centro Target Record (ARMA(2,1) Earthquake Model and Modified Clough's Structural Model)	279
8.20	Probabilistic Inelastic Response Spectra for the El Centro Target Record (ARMA(2,1) Earthquake Model and Bilinear Inelastic Structural Model)	282
8.21	Comparison Between Probabilistic Inelastic Response Spectra and Deterministic Inelastic Response Spectra Derived from Single Earthquake Realizations (ARMA(4,2) Model of E02NS)	285
8.22	C.O.V. of Inelastic Response Parameters for Different Hysteretic Models (ARMA(4,2) Simulation of E02NS)	288
8.23	C.O.V. of Inelastic Response Parameters for Different Hysteretic Models (ARMA(2,1) Simulation of El Centro 1940)	290
8.24	C.O.V. of Inelastic Response Parameters for Different Values of Strain-Hardening Ratio (ARMA(4,2) Simulation of E02NS and Bilinear Inelastic Structural Model)	292
8.25	C.O.V. of Inelastic Response Parameters for Different Values of Strain-Hardening Ratio (ARMA(2,1) Simulation of El Centro and Bilinear Inelastic Structural Model)	294
8.26	C.O.V. of Inelastic Response Parameters for Different Strength Levels (ARMA(4,2) Simulation of E02NS and Bilinear Inelastic Structural Model)	296
8.27	C.O.V. of Inelastic Response Parameters for Different Strength Levels (ARMA(4,2) Simulation of E02NS and Modified Clough's Structural Model)	298
8.28	C.O.V. of Inelastic Response Parameters for Different Strength Levels (ARMA(2,1) Simulation of El Centro and Bilinear Inelastic Structural Model)	300

8.29 C.O.V. of Inelastic Response Parameters for Different Strength Levels (ARMA(2,1) Simulation of El Centro and Modified Clough's Structural Model) 302

8.30 Probability Distribution of Normalized Plastic Deformation Ranges (ARMA(4,2) Simulation of E02NS and Bilinear Inelastic Structural Model with $\xi = 0.05$, $\eta = 0.05$ and $\alpha = 0.00$) 304

8.31 Comparison of Lognormal and Shifted Exponential Probability Distribution Fits (ARMA(4,2) Simulation of E02NS and Bilinear Inelastic Structural Model with $\xi = 0.05$, $\eta = 0.05$ and $\alpha = 0.00$) 305

8.32 Probability Distribution of Normalized Plastic Deformation Ranges (ARMA(4,2) Simulation of E02NS and Bilinear Inelastic Structural Model with $\xi = 0.05$, $\eta = 0.05$ and $\alpha = 0.05$) 306

8.33 Probability Distribution of Normalized Plastic Deformation Ranges (ARMA(4,2) Simulation of E02NS and Bilinear Inelastic Structural Model with $\xi = 0.05$, $\eta = 0.10$ and $\alpha = 0.00$) 307

8.34 Probability Distribution of Normalized Plastic Deformation Ranges (ARMA(4,2) Simulation of E02NS and Modified Clough's Structural Model with $\xi = 0.05$, $\eta = 0.05$ and $\alpha = 0.00$) 308

8.35 Probability Distribution of Normalized Plastic Deformation Ranges (ARMA(4,2) Simulation of E02NS and Slip Structural Model with $\xi = 0.05$, $\eta = 0.05$ and $\alpha = 0.00$) 309

8.36 Probability Distribution of Normalized Plastic Deformation Ranges (ARMA(4,2) Simulation of E02NS and Bilinear Elastic Structural Model with $\xi = 0.05$, $\eta = 0.05$ and $\alpha = 0.00$) 310

8.37 Probability Distribution of Normalized Plastic Deformation Ranges (ARMA(2,1) Simulation of El Centro 1940 and Bilinear Inelastic Structural Model with $\xi = 0.05$, $\eta = 0.10$ and $\alpha = 0.00$) 311

8.38 Comparison of Lognormal and Shifted Exponential Probability Distribution Fits (ARMA(2,1) Simulation of El Centro 1940 and Bilinear Inelastic Structural Model with $\xi = 0.05$, $\eta = 0.10$ and $\alpha = 0.00$) 312

8.39 Probability Distribution of Normalized Plastic Deformation Ranges (ARMA(2,1) Simulation of El Centro 1940 and Bilinear Inelastic Structural Model with $\xi = 0.05$, $\eta = 0.10$ and $\alpha = 0.05$) 313

8.40 Probability Distribution of Normalized Plastic Deformation Ranges (ARMA(2,1) Simulation of El Centro and Bilinear Inelastic Structural Model with $\xi = 0.05$, $\eta = 0.20$ and $\alpha = 0.00$) 314

8.41 Probability Distribution of normalized Plastic Deformation Ranges (ARMA(2,1) Simulation of El Centro and Modified Clough's Structural Model with $\xi = 0.05$, $\eta = 0.10$ and $\alpha = 0.00$) 315

8.42	Probability Distribution of Normalized Plastic Deformation Ranges (ARMA(2,1) Simulation of El Centro and Slip Structural Model with $\xi = 0.05$, $\eta = 0.10$ and $\alpha = 0.00$)	316
8.43	Probability Distribution of Normalized Plastic Deformation Ranges (ARMA(2,1) Simulation of El Centro and Bilinear Elastic Structural Model with $\xi = 0.05$, $\eta = 0.10$ and $\alpha = 0.00$)	317
8.44	C.O.V. of Linear Elastic Response Spectra for E02NS	318
8.45	C.O.V. of Linear Elastic Response Spectra for El Centro 1940	318
A.1	Butterworth Filter	319
B.1	Nonlinear SDOF System	331
B.2	Examples of Piecewise Linear Force-Deformation Behavior	332
B.3	Piecewise Linear Restoring Force	333
B.4	Piecewise Linear Forcing Function	333
B.5	Total Spring Energy $E_s(t)$	331

CHAPTER 1

INTRODUCTION

1.1 Background and Motivation

In the case of a "plate boundary" type of earthquake, strains and stresses build up along a geological fault due to tectonic forces. When these stresses overcome the frictional resistance of the rock, the lips of the fault suddenly slip on each other; this phenomenon is called a fault rupture, which results in a sudden release of strain energy. Part of this energy is dissipated through frictional heating in the rock material and the remaining part, called seismic energy, is manifested as seismic waves. Along their propagation path, the seismic waves undergo reflections, refractions, attenuation with distance, scattering, dispersion, and site amplification before they finally reach the support points of various structures such as buildings, bridges, dams, nuclear power plants, etc. Under the imposed excitation of their foundations, these structures respond dynamically and can remain elastic or suffer various degrees of damage and collapse depending on the relative strength of the earthquake and the structures.

When designing earthquake-resistant structures, the ultimate goal of the earthquake engineer is to save human lives and reduce damage. However, the challenge is to provide structural safety under economic constraints, which dictate a tolerance for some degree of structural damage under a severe earthquake motion. If one accepts that part of the seismic input energy in the structure is dissipated by means of ductile, inelastic deformations, the seismic loads to which the structure is subjected are reduced (from the elastic condition). The task of the earthquake engineer is further complicated by two important facts: i) the considerable uncertainty associated with seismic excitation, and ii) the possibility of high sensitivity of inelastic structural behavior with respect to ground motion details [3,43].

The first step in earthquake-resistant design is to define the design earthquake in terms of global ground motion parameters or ground motion time histories. Both engineers and seismologists are currently working on the problem of strong ground motion prediction but from rather different perspectives. Engineers often use an expedient approach in which earthquake motions are simulated so as to agree in essential ways (such as amplitude, frequency content and duration) with existing data. The intent of this approach is to capture the essential characteristics of earthquake ground motion at an average site from an average earthquake of a specified size, and to perform accurate response, damage estimation and risk calculations. These techniques are called replicative or empirical models. On the other hand, seismologists try to understand the fault rupture process and the subsequent propagation of waves within and on the surface of the earth. The ultimate goal of seismologists in earthquake source modeling is so-called "dynamic modeling". In this approach, strong ground motion is quantitatively predicted for a given potential earthquake fault at a specific site of an engineering structure using the laws of physics of rock failure (dynamic fracture mechanics) and seismic wave propagation under a given tectonic stress condition. At the present stage, only long period (longer than 5 seconds) components of near fault ground motion can be simulated deterministically with an accuracy meaningful for engineering purposes. Any practical simulation of high frequency acceleration requires a stochastic model due to our ignorance of the details of the fault zone (asperities and barriers) and the rupture process. Therefore, to model the frequency band required for structural response analysis (0-15 Hz), a hybrid of deterministic and stochastic models is needed.

There is considerable uncertainty at all levels of the ground motion and structural response prediction problem. The precise nature of the rupture process, the characteristics of the wave propagation path and local site conditions, and the characteristics of the structural system are all, to some extent, uncertain. This uncertainty must be quantified and used in analysis, design and risk assessment.

Since most seismic design codes rely on inelastic response of structures to resist strong ground motions, nonlinear constitutive models must be used for mathematical structural modeling. Many nonlinear hysteretic models, covering a wide spectrum of sophistication, have been developed in the literature [30,79,80]. For structural damage assessment purposes, damage needs to be characterized and quantified through the use of realistic damage models. Such models provide a measure of the degree of damage sustained by a structure during an earthquake and are intended to cover the whole range of structural damage from the point of incipient damage to the point of incipient collapse. To this end, various global or local damage indices have been proposed and used in the literature [30,31,74]. However, there is not yet a consensus on the mathematical definition of structural damage and the ability to model structural behavior in the collapse range is very limited. The damage path and failure behavior of most large structures remain unknown because few experimental studies of full scale structures have been conducted to date.

The seismic safety of a structure must be evaluated as the combination of the calculated conditional structural reliability (assuming a level of earthquake intensity at a given source) with the probabilities attached to all the significant levels of seismic intensity. The latter information requires a seismic hazard analysis. The risk contributions associated with several potential seismic sources are additive, provided that these seismic sources are of independent activities.

Over the years, stochastic input models and nonlinear structural models have become increasingly sophisticated. Unfortunately, little attention has been directed towards answering the question of what level of modeling refinement is necessary to achieve meaningful response assessment results. Neither has the complex interaction between ground motion characteristics, structural properties, and structural response parameters been well understood. A clear understanding of the cause of structural damage would facilitate the specification of ground motions in terms of their damage potential. Developing such a measure of ground motion would be a laudable goal for both seismologists and engineers. Finally,

the integration of seismic hazard analysis, ground motion modeling and structural damage characterization could result in the formulation of reliability-based design procedures that can admit some tolerable degree of damage while minimizing the risk of collapse.

1.2 Probability Bases for Earthquake-Resistant Design

The occurrence of strong motion earthquakes is unpredictable in time and in space. The earthquake-induced ground shaking of a structure is uncertain in intensity, frequency content, and duration. With this in mind, the evaluation of safety and the design of earthquake-resistant structures should be done in a probabilistic setting. Therefore, probabilistic methods should be used for evaluating potential structural damage due to future earthquakes. A probability-based earthquake-resistant design procedure contains the following steps:

(1) assess the seismic hazard at a given site for the lifetime of the structure;

(2) model the frequency distribution of the seismic energy (earthquake signal modeling);

(3) model the hysteretic degrading behavior of structures subject to random cyclic dynamic loading;

(4) simulate the structural response process produced by earthquake loading;

(5) assess the structural damage in terms of structural response characteristics in a statistical sense;

(6) combine the damage probabilities with all possible hazard levels to obtain the lifetime damage probabilities.

This dissertation is limited to steps (2) to (5), but the overall picture would be incomplete without the steps (1) and (6). The next Section will define the important topic of seismic hazard analysis.

1.3 Seismic Hazard Analysis

The objective of Probabilistic Seismic Hazard Analysis (PSHA) is to assess the probability of exceedence of a specified ground motion intensity level at a given site and during

a specified time interval [6]. As specified in Fig. 1.1, the PSHA procedure involves the following elements:

(1) Probabilistic modeling of earthquake occurrences in time and space, including descriptions of the sources of future earthquakes and estimates of their activity rates;

(2) Description of the recurrence relationship that provides information on the relative frequency of occurrence of earthquakes of different magnitudes, and determination of the probability distribution of earthquake parameters, such as seismic moment, fault rupture length, slip rate, duration, etc;

(3) Description of the attenuation of ground motion with distance from the earthquake source, as a function of the earthquake magnitude and other parameters that characterize the energy release at the source and the propagation of seismic waves to the site;

(4) Evaluation of the probability of exceedence for various levels of the intensity of shaking measured by various ground motion parameters, not limited to the traditional "Peak Ground Acceleration" which has been recognized as being an inadequate index of earthquake damage potential.

Each of the above elements involves uncertainties that should be modeled and analyzed using probabilistic methods. The probability of exceedence of a ground motion intensity level for a given earthquake occurrence is computed by use of the total probability theorem:

$$P(Y > y) = \int P(Y > y \mid \underline{x})\, f_{\underline{X}}(\underline{x})\, d\underline{x} \tag{1.1}$$

where P indicates probability, Y is the earthquake intensity, y is the intensity level for which the exceedence probability is sought, $\underline{X}$ is a vector of random variables that influence the outcome of Y, and the integration is performed over all possible outcomes of $\underline{X}$. To determine the probability of exceedence of the specified intensity level during a given interval of time, the above probability should be combined with a model of earthquake occurrences in time. The resulting estimate can be plotted as an annual probability of

exceedence versus the intensity level for instance, as depicted in step 4 of Fig. 1.1.

The overall intensity level of a future earthquake still does not define the earthquake motions actually felt by the structure, i.e., ground motion time histories of the support points of the structure. To generate an earthquake motion time history, the time-varying amplitude and spectral distribution of the seismic energy have to be specified. Since the details of an earthquake accelerogram cannot be described deterministically, a stochastic model is needed to represent the uncertainty of the motions.

1.4 Objectives and Scope

Objectives:

The primary objectives of the present study are to:

(1) Model the inherent uncertainty contained in earthquake ground motion time histories for a given source-site pair using stochastic processes. These stochastic earthquake models should be able to represent the amplitude and frequency nonstationarities typical of real earthquake records.

(2) Verify thoroughly the adequacy of the proposed earthquake model, especially in regard to its application as seismic input into structural models.

(3) Simulate, characterize and represent the stochastic response process of simple elastic and inelastic and nondegrading and degrading structural models using the proposed stochastic input model.

(4) Perform a comprehensive parametric (sensitivity) study of the stochastic seismic response of simple structures. Such a study provides a tool to investigate the complex cause-and-effect relationships existing among the earthquake process, the type of structural behavior and the structural properties such as stiffness and strength. The stochastic approach of this parametric study provides a useful insight into the probabilistic nature of the seismic response of structures.

Scope:

The above objectives are achieved by:

(1) Using a nonstationary discrete-time ARMA model. The amplitude nonstationarity is represented by a variance envelope. The latter is directly estimated from a real earthquake record using a non-parametric, two-stage weighted moving average scheme operating on the squared ground acceleration time history. The frequency nonstationarity is modeled by the time-varying property of the ARMA model. The time histories of the ARMA parameters are estimated using Kalman (time adaptive) filtering and a more traditional nonstationary estimation technique based on the concept of a stationary moving time window.

(2) Checking the estimated earthquake models at three different levels:

(i) check of the residuals (generated by the model estimation procedure) for uncorrelation in the time and frequency domains and for normality;

(ii) check the individual and statistical properties of the ARMA-simulated ground motions compared to the ground motion properties of the target earthquake record;

(iii) check the statistics of various elastic and inelastic response parameters (damage parameters) of the simple structural models analyzed and subjected to a family of artificial earthquakes generated from the estimated earthquake model. As third level of model checking, these response statistics are compared to the corresponding deterministic response parameter values produced by the target earthquake motion.

(3) Selecting response parameters to characterize the seismic response of the elastic and inelastic structural models utilized. The response parameters associated with the inelastic structural models are correlated to real damage mechanisms of structures subjected to dynamic cyclic loading such as earthquakes. In other words, they are indicative of the extent of damage imparted to the structure to be modeled. The probabilistic structure of these response parameters is obtained by ARMA Monte Carlo simulation and represented in terms of (i) histograms to identify the type of the underlying

probability distributions, (ii) probabilistic elastic and inelastic response spectra, useful for probabilistic seismic design and seismic safety analysis, and (iii) "coefficient-of-variation versus initial structural period" curves.

(4) By systematically varying (i) the target earthquake record, (ii) the ARMA model order, (iii) the type of structural behavior, and (iv) the structural properties in the basic ARMA Monte Carlo simulation scheme. The resulting sensitivities of the various probabilistic representations of the response parameters are obtained.

1.5 Organization of Text

The presentation of this study has been divided into nine chapters, the contents of which are outlined below:

Chapter 1 serves as an introduction by defining the general problem facing earthquake engineers anxious to design safe structures. It gives the motivation for a probabilistic approach to the problem of earthquake-resistant design. The research objectives of this work are also outlined.

Chapter 2 defines and classifies the various sources of uncertainty present in earthquake engineering. The seismological approach to earthquake strong motion modeling is briefly presented. The topic of stochastic ground motion modeling is introduced by a review of the state-of-the-art, continuous-time stochastic models used.

In Chapter 3, the nonstationary, discrete-time stochastic ARMA model used in this study is thoroughly described. The model estimation and model checking procedures are defined. In conclusion, the advantages of the ARMA model motivating its choice over the other models available for this study are outlined.

Chapter 4 contains a thorough physical interpretation of the low order ARMA(2,1) model and discusses the physical interpretation of higher order ARMA models in terms of dynamic systems.

In Chapter 5, two real earthquake records are analyzed and simulated using the nons-

tationary ARMA modeling procedure developed. The resulting simulated probability distributions of the traditional ground motion parameters are presented.

In Chapter 6, the structural models used in this study are presented in the context of a discussion on the difficult problem of structural damage characterization. The structural response calculation algorithm is presented and the selected structural response parameters are defined. The comprehensive response parametric study using ARMA simulation is outlined.

Chapter 7 presents the response simulation results for linear elastic SDOF systems. Probabilistic elastic response spectra corresponding to a given source-site pair are defined. A methodology using them to derive uniform hazard elastic response spectra is presented.

Chapter 8 contains the response simulation results for nonlinear elastic and inelastic SDOF systems. Probabilistic inelastic response spectra are defined. The results of the comprehensive probabilistic parametric study are presented. The results related to the probability distribution of the plastic deformation ranges response quantities are given special attention. Based on the present study, the relative levels of variability of the ground motion parameters and of the elastic and inelastic structural response parameters are presented.

Chapter 9 provides a summary of the work completed, a summary of findings from previous chapters and presents recommendations for future research based on these findings.

CHAPTER 2

EARTHQUAKE GROUND MOTION CHARACTERIZATION

2.1 Uncertainties in Earthquake Engineering

In recent years, an increasing research interest has focused on the problem of the stochastic response and reliability analyses of hysteretic structural systems subjected to severe earthquakes, since there are many uncertainties in defining seismic excitation at the site, in modeling the dynamic characteristics of structural systems and their performance criteria. The various sources of uncertainty in earthquake engineering can be listed as follows:

(a) uncertainty of seismic excitation (seismic input);

(b) uncertainty of structural properties (mechanical and geometrical);

(c) uncertainty of structural mathematical model;

(d) uncertainty of computational algorithm for dynamic response calculations;

(e) uncertainty of structural evaluation based on some selected response parameters (damage indices).

The earthquake phenomenon is so complex and poorly understood that the resulting ground motion signal at a given site appears to be random, i.e., earthquake accelerograms have erratic appearances. The uncertainty of the seismic excitation will decrease slowly in the future with the growing library of earthquake data and the development of seismological prediction techniques (physical earthquake models). However, the seismic excitation contains an inherent type of uncertainty, which cannot be reduced and has to be accepted as such. The overall earthquake phenomenon can be split into several components, each with its respective uncertainty:

(i) earthquake occurrence in space and time;

(ii) earthquake magnitude (amount of energy released);

(iii) earthquake source mechanism;

(iv) seismic wave propagation along transmission path;

(v) local site geology (site amplification/attenuation properties).

The uncertainties characterizing parts (i) and (ii) can be quantified by using the well-known Richter law of magnitudes [78]. Richter's law says that in a certain zone of the earth crust and during a given period of time, the occurrence of earthquakes can be approximated by the frequency-magnitude relationship:

$$N(m) = e^{\alpha - \beta m} \tag{2.1}$$

where N(m) is the number of earthquakes with magnitude greater than or equal to m, and α and β are empirical constants. From the information contained in Eq. (2.1), the probability density function of magnitudes given an earthquake occurrence and the average rate of earthquake occurrences $\nu_a(m)$ corresponding to a magnitude $\geq$ m can be derived [27]. As a first step, a Poisson model with parameter $\nu_a(m)$ can be used to simulate earthquake occurrences in time. To correct for the absence of memory in the Poisson model, more sophisticated models such as Markov processes [48] can be used, but often there is not enough historical data to properly calibrate these models for a given application.

Considerable uncertainty is associated with the earthquake source mechanism and the subsequent seismic wave propagation. The topology of the causative fault, the material properties and geometrical configuration of the geological medium along the transmission path are largely unknown. They are inferred from surface measurement using the indirect method.

In past years, the importance of local site conditions in earthquake engineering has been revealed. A good illustration has been the amplification effect of the deep layer of soft clay underlying Mexico City during the September 1985 earthquake. The present state-of-the-art enables propagating an incoming motion at bedrock level through the elastic or inelastic surficial soil layers given their mechanical (stiffness, damping, hysteretic characteristics) and geometrical properties. No general conclusions can be drawn about the

overall amplification/attenuation characteristics of a soil layered system since they depend on the relative properties of the incoming motion at bedrock level and the properties of the soil layers.

Structural material properties and structure geometrical properties show some inherent variability. The mathematical idealization of a real structure for analysis purposes simplifies reality and the computational algorithm approximates the exact behavior of the structural model. The uncertainties associated with the structural mathematical modeling and the computational algorithm can be reduced by improving the model and algorithm, respectively.

For a given structural model, one has to identify pertinent model response parameters which measure the damage state or functional disorder of the real structure. Many such damage indices (or damage models) have been proposed in the literature, but they are all imperfect and none has been universally accepted. Each of them correlates well with actual physical damage observed during experimentation performed on a given structure or substructure subjected to a particular loading. Their extensions to different types of loadings and structures are uncertain.

The uncertainty of the seismic response of structures is predominantly driven by the uncertainty of the seismic input [7,20,73,81]. Chopra and Kan [20] and Powell and Row [73] studied the effects of varying the ground motion and modeling assumptions for analysis, and both concluded that uncertainties in the ground motion are critical. Accordingly, this study will consider only the seismic input uncertainty and the structural mathematical model, computational algorithm and damage indicators will be assumed to be unbiased.

2.2 Predictive Physical Earthquake Models

A portion of earthquake engineering, called strong motion seismology, is research devoted to understanding the physical nature of strong ground motions. Seismologists study records of earthquake-induced motions for several reasons: (1) to learn the details of

earthquake sources, (2) to determine the earth structure, (3) from the knowledge of sources and structures, to predict the shaking at the surface of the earth from earthquakes. Strong motion seismology has made considerable progress in the last decade. However, the state-of-the-art physical earthquake models are still not able to adequately explain observed strong motion data in the frequency range of concern for structural engineering. Observed recordings can be modeled in a realistic way provided the maximum frequency does not exceed ~ 1 Hz, which is too low for structural engineering purposes. Nevertheless, it is important for the earthquake engineer to have an overall understanding of the state-of-the-art strong motion prediction methods. An exhaustive and well referenced review on this topic is available in Ref. [15]. A very brief outline of these predictive methods is given below.

The surface ground shaking resulting from an earthquake is the result of a complex, dynamical rupture process followed by propagation in the earth of the generated seismic waves. Near-field earthquake records are dominated by source effects, whereas far-field records are dominated by surface waves "shaped" by the earth structure along the propagation path. Two main approaches for modeling mathematically the earthquake strong motion seismic waves have been used. The first approach uses a so-called kinematic dislocation model in which the time history of the slip on the generating fault is known a priori. In this approach, the slip function defines the source model and the source parameters are shape, rise time and amplitude of the slip function, the velocity of the slip over the fault, and the final area over which the slip occurred. The propagation effect is quantitatively expressed by theoretical or semi- empirical Green's functions which represent the response of the earth when an impulsive double-couple (point-force equivalent to a fault slip) is applied at a point on the fault. Records of small earthquakes are used as semi-empirical Green's functions. Finally, a seismogram is synthesized by a space-time convolution of the slip function and Green's functions. This earthquake modeling technique does not incorporate rupture initiation, spreading and stopping on the fault. It is useful for obtaining a first-order understanding of the earthquake rupture process.

The second approach, called dynamic modeling, is to solve the wave equations for the two- or three-dimensional space, under appropriate boundary conditions and a fracture criterion. This approach makes use of results from theoretical fracture mechanics as well as laboratory results on rock failure. The wave equations are solved numerically using (1) the finite-difference method, (2) the finite element method or (3) boundary value integral methods. Using this dynamic approach, two- and three-dimensional shear crack models have been developed to synthesize strong motion records.

It has been found that most of the high-frequency emissions come from the rupture front when it changes its speed of advance. Therefore, the presence of "asperities" or unbroken "barriers" on the fault surface has a strong influence on the generation of high-frequency seismic waves. Since no reliable techniques are available at this time to identify the details of a fault surface and of the geological structure of the surrounding medium, stochastic fault models have been developed involving random distributions of source parameters.

In the future, the physical explanation of observed strong motion data will be improved by: (i) using more realistic, less restrictive, seismic source and wave propagation models, and (ii) obtaining more accurate geological structures and source topography.

The stochastic earthquake model used in this study does not depend directly on source and path parameters. It is fitted from an observed earthquake record and is required to reliably reproduce the observed waveforms in the frequency range of interest for structural engineering.

2.3 Continuous-Time Stochastic Earthquake Models: A Review

To quantify the uncertainty of earthquake loading, the overall problem is split into two sub-problems. In the first sub-problem, the probability of exceedence of a specified ground motion intensity level is considered. This part is solved using probabilistic seismic hazard analysis techniques. Given an overall intensity level and a representative set of global ground motion parameters characterizing amplitude, frequency content and duration,

the second sub-problem is involved with the definition and fitting of a stochastic process. The latter must be able to generate artificial earthquake signals consistent with the source-site pair and the seismic risk level under consideration.

In earthquake engineering, the ground motion is commonly represented in terms of an earthquake ground acceleration history, called an accelerogram or an acceleration record. By visual inspection, earthquake ground acceleration records have the following common characteristics:

(1) They are causal and transient events, that start at a certain time with zero acceleration, exhibit strong and chaotic oscillations about the zero acceleration line (erratic behavior), and after a sufficiently long time tend to zero acceleration. They represent finite energy events.

(2) They show a strong non-stationarity in both intensity and frequency content.

(3) Acceleration records are vastly different from event to event. Even for the same earthquake, two accelerograms recorded at closely spaced stations may differ substantially.

In this Section, continuous-time stochastic earthquake models will be reviewed. This review is not intended to be exhaustive, but representative.

The first engineering interpretation of strong motion accelerograms was made by Housner [38,39] who explained their appearance by reasoning that high-frequency seismic waves are generated by irregular slippage along faults. The seismic waves are subsequently subjected to numerous random reflections, refractions and attenuations as they propagate through the heterogeneous crustal structure of the earth. Subsequently, many researchers followed Housner's paradigm in interpreting and modeling strong motion accelerograms as random processes for seismic-resistant design. Over the years, stochastic earthquake models have become increasingly sophisticated: shot noise and white-noise, filtered white-noise and filtered Poisson processes, and random processes with an evolutionary power spectral density are examples.

Theory of Random Processes

The central notion involved in the concept of a random process or stochastic process X(t) is that not just one time history is described, but the whole family or ensemble of possible time histories which might have been the outcome of the same experiment are described [25]. Any single individual time history belonging to the ensemble is called a sample function or a realization. A random process can be portrayed schematically as in Fig. 2.1. Each sample function $x^{(j)}(t)$ is sketched as a function of time.

A random process is a parameterized family of random variables. In the literature, random processes are also called random functions or stochastic processes if the indexing parameter is continuous time, or time series if the indexing parameter is discrete time. At fixed times $t = t_1$ and $t = t_2$, $X(t_1)$ and $X(t_2)$ are random variables and $x^{(j)}(t_1)$ and $x^{(j)}(t_2)$ their j^{th} realizations. Visually, realizations of a given stochastic process look different, but they are governed by a common underlying probability structure. The latter can be defined by the whole hierarchy of joint probability density functions, but the most common and easiest way is to use statistical moments.

A general stochastic process X(t) with time-varying statistical properties is called nonstationary. The second-order statistics of such a process are:

Ensemble mean: $$E[X(t)] = \mu(t) \tag{2.2}$$

Autocorrelation function: $$R_{XX}(t_1, t_2) = E[X(t_1)X(t_2)] \tag{2.3}$$

Autocovariance function: $$K_{XX}(t_1,t_2) = E[(X(t_1) - \mu(t_1))(X(t_2) - \mu(t_2))] \tag{2.4}$$

$$= R_{XX}(t_1,t_2) - \mu(t_1)\mu(t_2) \tag{2.5}$$

Variance of the process: $$\mathrm{Var}[X(t)] = \sigma_X^2(t) = K_{XX}(t,t) \tag{2.6}$$

A normalized form of the autocovariance function is called the autocorrelation coefficient function:

$$\rho_{XX}(t_1,t_2) = \frac{K_{XX}(t_1,t_2)}{\sigma_X(t_1)\,\sigma_X(t_2)} \tag{2.7}$$

A random process X(t) whose probability structure is invariant under arbitrary translations of the indexing parameter t is called stationary. A process is strongly stationary (or stationary in the strict sense) if all orders of its probability density functions are stationary and weakly stationary (or stationary in the wide sense) if its probability structure is time invariant up to the second order only. In the case of a Gaussian process, weak stationarity and strong stationarity coincide, since a Gaussian process is completely defined by its second order statistics. In the case of stationary processes, the above definitions can be reduced to:

Ensemble mean: $$E[X(t)] = \mu = \text{constant} \tag{2.8}$$

Autocorrelation function: $$R_{XX}(\tau) = E[X(t)X(t+\tau)] \tag{2.9}$$

Autocovariance function: $$\begin{aligned}\Sigma_{XX}(\tau) &= E[(X(t)-\mu)(X(t+\tau)-\mu)] \\ &= R_{XX}(\tau) - \mu^2\end{aligned} \tag{2.10}$$

Variance: $$\mathrm{Var}[X(t)] = \sigma_X^2(t) = R_{XX}(0) - \mu^2 = \sigma_X^2 \tag{2.11}$$

Autocorrelation coefficient function: $$\rho_{XX}(\tau) = \frac{\Sigma_{XX}(\tau)}{\sigma_X^2} \tag{2.12}$$

Note that zero mean random processes ($\mu(t) = 0$) are needed for stochastic modeling of earthquake digitized accelerograms. Therefore, autocorrelation and autocovariance functions are identical and the distinction between them can be dropped.

A zero mean stationary process X(t) can be represented in its spectral form by the Fourier-Stieltjes integral [76]:

$$X(t) = \int_{-\infty}^{\infty} e^{i\omega t} dZ(\omega) \tag{2.13}$$

where $Z(\omega)$ is a complex valued orthogonal stochastic process such that:

$$E[dZ(\omega)] = 0 \quad \text{and} \quad E[dZ^*(\omega)\,dZ(\omega')] = 0 \quad \text{for } \omega \neq \omega' \tag{2.14a}$$

$dZ^*(\omega)$ being the complex conjugate of $dZ(\omega)$ and

$$E[\,|dZ(\omega)|^2] = dH(\omega) \tag{2.14b}$$

In essence, Eq. (2.13) states that any stationary process can be represented as a sum of sine and cosine functions with random uncorrelated coefficients $dZ(\omega)$. From Eqs. (2.13) and (2.14b), the autocorrelation function $R_{XX}(\tau)$ can be derived:

$$R_{XX}(\tau) = \int_{-\infty}^{\infty} e^{i\omega\tau}\, dH(\omega) \tag{2.15}$$

If $H(\omega)$ is differentiable, i.e., $dH(\omega) = \Phi(\omega)\, d\omega$, Eq. (2.15) reduces to:

$$R_{XX}(\tau) = \int_{-\infty}^{\infty} e^{i\omega\tau}\, \Phi(\omega)\, d\omega \tag{2.16}$$

which is one member of the Fourier transform pair, called the Wiener-Khinchine relation, which relates the autocorrelation function $R(\tau)$ and the power spectral density (PSD) function $\Phi_{XX}(\omega)$. The other member of the Wiener-Khinchine relation is:

$$\Phi_{XX}(\omega) = \frac{1}{2\pi} \int_{-\infty}^{\infty} e^{-i\omega\tau}\, R_{XX}(\tau)\, d\tau \tag{2.17}$$

The definition of the PSD function of a stationary process X(t) given by Eq. (2.17) is equivalent to the following definition [76]:

$$\Phi_{XX}(\omega) = \lim_{T\to\infty} [\, E\left\{ \frac{|G_T(\omega)|^2}{2T} \right\}] \tag{2.18}$$

where

$$G_T(\omega) = \frac{1}{\sqrt{2\pi}} \int_{-T}^{T} X(t)\, e^{-i\omega t} dt \tag{2.19}$$

The variance, also called average energy, of a zero mean stationary process X(t) can be expressed in terms of the PSD function by using Eq. (2.16):

$$\mathrm{Var}[X(t)] = E[X(t)\,X(t)] = R_{XX}(0) = \int_{-\infty}^{\infty} \Phi_{XX}(\omega)\, d\omega \tag{2.20}$$

From Eq. (2.20), the spectrum has an immediate physical interpretation as the distribution of energy over a continuous range of frequencies.

A class of nonstationary processes, called an "evolutionary process", can be represented using the concept of a time-dependent spectrum (or evolutionary power spectrum) which possesses a physical interpretation as a "local" power-frequency distribution. The concept of evolutionary PSD function is a natural extension of the PSD function for stationary processes. A time evolutionary random process X(t) can be represented by the following Fourier - Stieltjes integral:

$$X(t) = \int_{-\infty}^{\infty} A(t,\omega)\, e^{i\omega t} dZ(\omega) \tag{2.21}$$

instead of Eq. (2.13). The deterministic function $A(t,\omega)$ is called a modulating function. The special case of a stationary process corresponds to $A(t,\omega) = 1$. Using the orthogonality properties of $Z(\omega)$, the time dependent mean square, or variance, of the random process X(t) defined in Eq. (2.21) can be derived:

$$\mathrm{Var}[X(t)] = E[X^2(t)] = \int_{-\infty}^{\infty} |A(t,\omega)|^2 dH(\omega) \tag{2.22}$$

where $dH(\omega)$ has been defined in Eq. (2.14b). If $H(\omega)$ is a differentiable function, then Eq. (2.22) can be written as a Riemman integral:

$$E[X^2(t)] = \int_{-\infty}^{\infty} |A(t,\omega)|^2 \Phi_{XX}(\omega)\, d\omega \tag{2.23}$$

and the evolutionary PSD is defined as:

$$\Phi_{XX}(t,\omega) = |A(t,\omega)|^2 \Phi_{XX}(\omega) \tag{2.24}$$

A time evolutionary random process can then be interpreted as a sum of sine waves with different frequencies and time varying random amplitudes $\{A(t,\omega)\, dZ(\omega)\}$. The autocorrelation function of the nonstationary process is a function of both t and τ:

$$R_{XX}(t,\tau) = \int_{-\infty}^{\infty} \Phi_{XX}(t,\omega)\, e^{i\omega\tau} d\omega \tag{2.25}$$

There is an interesting alternative interpretation of time evolutionary random processes in

terms of time varying filters. If the modulating function $A(t,\omega)$ is written as:

$$A(t,\omega) = \int_{-\infty}^{\infty} h(t,u)\, e^{i\omega u}\, du \tag{2.26}$$

then Eq. (2.21) can be converted to:

$$X(t) = \int_{-\infty}^{\infty} S(t-u)\, h(t,u)\, du \tag{2.27}$$

where $S(t)$ is a stationary process. Thus, $X(t)$ may be interpreted as the result of passing a stationary process through a time varying filter $\{h(t,u)\}$.

The kind of nonstationary process obtained by using a frequency independent modulation function $A(t,\omega) = \Psi(t)$ in Eq. (2.21) is called a uniformly modulated process or separable process, since such a process can be factored as:

$$X(t) = \Psi(t)\, S(t) \tag{2.28}$$

where $\Psi(t)$ is a deterministic envelope function and $S(t)$ is a unit variance stationary process. Often, in the literature, $I(t) = \Psi^2(t)$ is referred as an intensity function, strength function or variance envelope. The relative amplitude of the various frequency components of a uniformly modulated random process do not change with time; only their absolute magnitude changes.

White-Noise Process

A mathematical idealization of a stationary random process $W(t)$ in which all frequencies contribute with equal intensity to the mean square value of the process is called white-noise or a purely random process and consists of a sequence of uncorrelated random variables. It has an infinite variance, due to the contribution of all frequencies, and is therefore not physically realizable, but it provides a basic "building block" from which more complicated finite variance models can be constructed. The correlation and spectral properties of white-noise are:

Autocorrelation function: $$R_{WW}(\tau) = 2\pi\, \phi_0\, \delta(\tau) \tag{2.29}$$

PSD function: $\Phi_{WW}(\omega) = \phi_0$ (2.30)

where $\delta(\tau)$ is the Dirac delta function. The statement of white-noise does not imply any probability distribution. If, at any time t, a white-noise process has a Gaussian distribution, then it is called a Gaussian white-noise.

Shot Noise Process

A sequence of independent, identically distributed (i.i.d) zero mean random impulses A_n occurring at random uncorrelated times τ_n is called a stationary shot noise [55,57]. A simple mathematical representation of this idea is given by the following expressions:

$$S(t) = \sum_{n=1}^{N(t)} A_j \delta(t-\tau_n) \tag{2.31}$$

$$E[A_n] = 0 , \qquad E[A_n^2] = \sigma^2 \tag{2.32}$$

where $\delta(.)$ stands for the Dirac delta function and N(t) for a random number of counts in the time interval (0,t]. An interesting case of shot noise is obtained when the counting process N(t) is a homogeneous Poisson random process with constant mean impulse occurrence rate λ. In this case, the sequence of time instants $\{\tau_1, \tau_2, \tau_3, \cdots\}$ indicates Poisson arrival times. This superposition of random impulses is suggested by the concept of a train of seismic waves. It can be shown that a shot noise process with Poisson arrival times tends to a Gaussian white-noise process as λ tends to infinity and σ^2 tends to zero in such a way that $\lambda\sigma^2$ is constant [41]. Hence, for large λ, S(t) can be regarded as a good approximation to a white-noise process. Finally, if the random impulses are Gaussian distributed, the process is called a Gaussian shot noise.

Filtered white-noise Process

To shape the PSD function of a white-noise process W(t), a time-invariant linear filter can be used to generate a filtered white-noise random process:

$$X_{FWN}(t) = \int_{-\infty}^{\infty} h(t-\tau)\, W(\tau)\, d\tau \tag{2.33}$$

where h(.) corresponds to the filter impulse response function. The PSD function of a filtered white-noise process is given by [56]:

$$\Phi_{X_{FWN}}(\omega) = |H(\omega)|^2 \Phi_{WW} \tag{2.34}$$

where $\Phi_{WW} = \phi_0$ = constant white-noise PSD and $H(\omega)$ = Fourier transform of the filter impulse response function h(t), also called the filter transfer function. The variance of the process X_{FWN} is given by Eq. (2.20):

$$\mathrm{Var}[X_{FWN}(t)] = \int_{-\infty}^{\infty} |H(\omega)|^2 \Phi_{WW}\, d\omega = \phi_0 \int_{-\infty}^{\infty} |H(\omega)|^2 d\omega \tag{2.35}$$

Filtered Poisson Process

A filtered Poisson Process is obtained by filtering the stationary shot noise process with Poisson arrival times t_n described in Eq. (2.31):

$$X_{FP}(t) = \sum_{n=-\infty}^{\infty} A_n h(t-t_n) \tag{2.36}$$

Non-Stationarity Modeling

Nonstationary random processes can be represented by either (i) uniform modulation of a filtered white-noise process or Poisson process:

$$X_{MFWN}(t) = \int_{-\infty}^{\infty} h(t-\tau)\, \Psi(t)\, W(\tau)\, d\tau = \Psi(t)\, X_{FWN}(t) \tag{2.37}$$

$$X_{MFP}(t) = \sum_{n=-\infty}^{\infty} A_n \Psi(t)\, h(t-t_n) = \Psi(t)\, X_{FP}(t) \tag{2.38}$$

or (ii) filtering of a uniformly modulated white-noise process or Poisson process:

$$X_{FMWN}(t) = \int_{-\infty}^{\infty} h(t-\tau)\, \Psi(\tau)\, W(\tau)\, d\tau \tag{2.39}$$

$$X_{FMP}(t) = \sum_{n=-\infty}^{\infty} A_n \Psi(t_n)\, h(t-t_n) \tag{2.40}$$

The processes $X_{MFWN}(t)$ and $X_{MFP}(t)$ are separable processes and therefore are

nonstationary in amplitude only. On the other hand, the processes $X_{FMWN}(t)$ and $X_{FMP}(t)$ are not exactly separable, but they approximately retain the shape of the PSD function of the underlying stationary process if the deterministic envelope function $\Psi(t)$ is chosen to be a slowly varying function of time. It can be shown [57,83] that $X_{FMP}(t)$ in Eq. (2.40) is equivalent to:

$$X(t) = \sum_{n=-\infty}^{\infty} A_n h(t-t_n) \tag{2.41}$$

if the underlying Poisson process has the nonstationary arrival rate $\lambda \Psi^2(t)$ (nonhomogeneous Poisson process). The two assumptions of time-dependent average impulse occurrence rate λ with time-independent statistics of A_n and constant λ with time-dependent statistics of A_n can be shown to be statistically equivalent [57]. The random pulse train represented in Eq. (2.41) can be shown [58] to be an evolutionary process of evolutionary spectral density:

$$\Phi_{XX}(t,\omega) = \frac{1}{2\pi} E[A_n^2] \left| \int_{-\infty}^{\infty} h(u) \sqrt{\lambda(t-u)}\, e^{-i\omega u}\, du \right|^2 \tag{2.42}$$

where $\lambda(t)$ is the time-dependent average pulse arrival rate.

It can be shown [83] that the filtered white-noise processes and filtered Poisson processes as defined above can be made identical up to the second moment by imposing the condition $\lambda \sigma^2 = 2\pi \phi_0$.

Green's Functions

The existence of high-frequency components in a typical earthquake record suggests that slips in a fault zone occur intermittently rather than smoothly [70]. In a first modeling approach, slippings can be assumed to occur in independent short spurts, almost impulsively. The impulse response function $h(t-\tau)$ of the linear filter used in Eqs. (2.33) to (2.40) can be viewed as a Green's function that describes the ground acceleration at time t at a given site, due to a fault slip impulse at time τ. Various physical features of the seismic wave propagation path can be incorporated by using the appropriate Green's

functions. For example, the Kanai-Tajimi model is a simplified representation of the behavior of the uppermost layer between the ground surface and the nearest bedrock, obtained by lumping the stiffness, inertia and dissipative properties of the medium [24,47,88]. The uppermost soil layer is viewed as a one-story shear building and the Kanai-Tajimi model represents the transfer function between the ground acceleration and the absolute acceleration of the roof of the shear building:

$$H(\omega) = \frac{\omega_g^2 + i\,2\xi_g\omega_g\omega}{\omega_g^2 - \omega^2 + i\,2\xi_g\omega_g\omega} \tag{2.43}$$

The corresponding impulse response function is:

$$h(t-\tau) = H(t)\,(\,\omega_g\, e^{-\xi_g\omega_g(t-\tau)}\,[\frac{1-2\xi_g^2}{\sqrt{1-\xi_g^2}}\sin\omega_{gd}(t-\tau) + 2\xi_g\cos\omega_{gd}(t-\tau)\,]\,) \tag{2.44}$$

where $H(t)$ = Heaviside step function, ω_g = ground predominant frequency, ξ_g = ground damping characterizing the frequency bandwidth, $\omega_{gd} = \sqrt{1-\xi_g^2} =$ damped ground predominant frequency. If the Kanai-Tajimi impulse response function is used in the random pulse train of Eq. (2.41) with a time-dependent average pulse arrival rate $\lambda(t)$, an evolutionary (Priestley) Kanai-Tajimi earthquake model is obtained. Other types of Green's functions have been defined in the literature, such as the one corresponding to the one-dimensional wave propagation in a linear elastic medium or a linear Maxwell medium [58].

Digital Simulation of Seismic Ground Motion

Even though the filtered Poisson process model, Eqs. (2.38) and (2.40), appears preferable in terms of physical interpretation, sample functions of the stochastic process simulating the ground acceleration are usually generated with the aid of the filtered white-noise model of Eqs. (2.37) and (2.39), due to simulation efficiency. The generation of a Gaussian discrete white-noise is the starting point of the simulation procedure. This is done by computer generation of a sequence of uncorrelated Gaussian numbers with zero

mean and unit variance. By spacing these numbers at time interval Δt and joining them by straight lines, a piecewise linear function is obtained that approximates a realization of Gaussian white-noise. The next phase of the simulation procedure consists in linear filtering the time modulated discrete white-noise or, alternatively, time modulating the linear filtered white-noise. The linear filtering can be performed either in the time domain or in the frequency domain. In the time domain, the linear differential equation corresponding to the filter has to be integrated numerically for a piecewise linear forcing function. Hence, the filter differential equation is approximated by a difference equation. The alternative procedure is to use the spectral representation method in the frequency domain according to which a stationary process of PSD $\Phi_{XX}(\omega)$ can be simulated by the following series, as N tends to infinity [85]:

$$X(t) = \sqrt{2} \sum_{j=1}^{N} \sqrt{2\,\Phi_{XX}(\omega_j)\,\Delta\omega}\,\cos(\omega_j t + \theta_j) \tag{2.45}$$

where $\omega_j = j\Delta\omega$, $j=1, \cdots ,N$. In Eq. (2.45), θ_j are independent random phase angles uniformly distributed over the range $(0,2\pi)$. The spectral representation method of stationary random processes can be directly generalized to a nonstationary process characterized by an evolutionary power spectrum $|A(t,\omega)|^2 \Phi_{XX}(\omega)$ [84] :

$$X(t) = \sqrt{2} \sum_{j=1}^{N} \sqrt{2\,A^2(t,\omega_j)\,\Phi_{XX}(\omega_j)\,\Delta\omega}\,\cos(\omega_j t + \theta_j) \tag{2.46}$$

As presented above, continuous-time, stochastic models for earthquake ground motions have to eventually be discretized for simulation purposes. Therefore, in this study, a more direct and versatile approach is adopted which consists in using, from start, discrete stochastic models in the form of stochastic linear difference equations. Two other advantages of such models are: (i) their computational efficiency, since they require only additions and multiplications in comparison with the computationally very expensive evaluation of trigonometric functions needed in the spectral representation method (Eqs. (2.44) and (2.45)); (ii) their statistical estimation from observed records is easier and they provide more flexibility to fit the local properties of real strong motion data than continuous models.

CHAPTER 3

ARMA MODELS FOR EARTHQUAKE GROUND MOTION MODELING

3.1 Introduction

In this study, models explicitly formulated in discrete time are used for the analysis and simulation of earthquake ground motion records. An important class of discrete models is the class of autoregressive moving-average models, abbreviated ARMA, which represents the cornerstone of time series analysis [16]. ARMA models are of equal generality with linear continuous-time models (differential equations), but they have a number of significant advantages for digital analysis and simulation purposes. In other words, these discrete models provide a useful class of transfer functions and need not be justified by continuous models. However, in some cases, the discrete model can be used to reveal some of the characteristics of the underlying continuous model.

3.2 Stationary ARMA(p,q) Model

The general ARMA model of order (p,q), abbreviated ARMA(p,q), is represented by the following stochastic linear difference equation:

$$a_k - \phi_1 a_{k-1} - \cdots - \phi_p a_{k-p} = e_k - \theta_1 e_{k-1} - \cdots - \theta_q e_{k-q} \tag{3.1}$$

where $\{a_k = a(k\Delta t)\ ,\ k = 0, 1, 2, \cdots\}$ represents the discrete stationary correlated process; $\{e_k = e(k\Delta t)\}$ is a stationary discrete white-noise process, assumed to be Gaussian, i.e., $e_k \sim N(0, \sigma_e^2)$; $(\phi_i, i = 1, \cdots, p)$ are the autoregressive parameters; and $(\theta_i, i = 1, \cdots, q)$ are the moving-average parameters. In terms of the backward shift operator B (defined by $B^n x_k = x_{k-n}$), Eq. (3.1) can be rewritten more concisely:

$$(1 - \phi_1 B - \cdots - \phi_p B^p) a_k = (1 - \theta_1 B - \cdots - \theta_q B^q) e_k \tag{3.2}$$

or

$$\Phi(B) a_k = \Theta(B) e_k \tag{3.3}$$

where $\Phi(B)$ and $\Theta(B)$ are polynomials of finite degree p and q.

Stationarity

The stationarity conditions ensure that the process $\{a_k\}$ has a finite variance σ_a^2. The stationarity of a mixed autoregressive moving-average process is controlled by the autoregressive part only. The ARMA(p,q) model, represented by Eq. (3.1), is stationary if the roots of the characteristic equation

$$x^p - \phi_1 x^{p-1} - \cdots - \phi_p = 0 \tag{3.4}$$

lie within the unit circle, i.e., are less than one in absolute value. An alternative way of expressing this condition is in terms of the associated autoregressive polynomial $\Phi(B)$. The polynomial equation,

$$1 - \phi_1 B - \cdots - \phi_p B^p = 0, \tag{3.5}$$

is similar in form to Eq. (3.4) except that x is replaced by 1/B and the whole equation is multiplied through by B^p. In this case, the stationarity condition requires that the roots of the autoregressive polynomial equation lie outside the unit circle.

Invertibility

To illustrate the basic idea of invertibility, consider the very simple first order moving-average MA(1) process:

$$a_k = e_k - \theta_1 e_{k-1} \tag{3.6}$$

This process can be expressed in terms of lagged values of a_k by substituting repeatedly for lagged values of e_k. This yields

$$a_k = e_k - \theta_1 a_{k-1} - \theta_1^2 a_{k-2} - \cdots - \theta_1^n a_{k-n} - \theta_1^{n+1} e_{k-n-1} \tag{3.7}$$

If a_k is not to depend on a shock to the system arising at some point in the remote past, θ_1 must be less than one in absolute value. If n is allowed to go to infinity, the last term in Eq. (3.7) disappears and a_k may be written as an infinite autoregressive process with dec-

lining weights, i.e.,

$$a_k = \sum_{n=1}^{\infty} -\theta_1^n a_{k-n} + e_k \tag{3.8}$$

The MA(1) model with $|\theta_1| > 1$ is not invertible, but it is still stationary. Restricting attention to invertible processes resolves the problem of identifiability, since a particular autocorrelation function will be compatible with two processes, only one of which is invertible. However, the fundamental reason for excluding stationary non-invertible processes is that they are not physically realizable, i.e., a small perturbation in the distant past can have an explosive effect on the present noise e_k. For finite nonstationary processes, non-invertibility may be realistic and very useful. The invertibility conditions for a general ARMA(p,q) model may be expressed in terms of the associated MA polynomial, $\Theta(B)$ in Eq. (3.3), by requiring that the roots of $\Theta(B) = 0$ lie outside the unit circle.

Statistical Properties in the Time Domain

The second order statistics for zero mean, discrete, stationary, stochastic processes are analogous to those belonging to continuous processes and presented in Section 2.3, i.e.,

Autocovariance function: $$\Sigma_{aa}(n) = \gamma_n = E[a_k a_{k+n}] = E[a_{k-n} a_k] \tag{3.9}$$

Variance: $$\mathrm{Var}[a_k] = \sigma_a^2 = E[a_k^2] = \gamma_0 \tag{3.10}$$

Autocorrelation coefficient function: $$\rho_n = \frac{\Sigma_{aa}(n)}{\mathrm{Var}[a_k]} = \frac{E[a_k a_{k+n}]}{E[a_k^2]} \tag{3.11}$$

The variance σ_a^2 of an ARMA process $\{a_k\}$ is proportional to the variance σ_e^2 of the random forcing function $\{e_k\}$. In the sequel, the ratio of the observed process variance to the noise variance σ_a^2/σ_e^2 will be called the variance gain, abbreviated $G_v(\underline{\phi}, \underline{\theta})$, of an ARMA model.

The knowledge of the autocorrelation coefficient function γ_n alone is equivalent to the knowledge of both variance and autocorrelation function ρ_n. It is shown [16] that, at higher lags, the autocorrelation coefficient function of the ARMA(p,q) process is entirely

determined by the difference equation corresponding to its autoregressive part:

$$\Phi(B)\rho_n = 0, \qquad n \geq q + 1 \tag{3.12}$$

At lower lags, there will be q autocorrelation coefficients $\rho_q, \rho_{q-1}, \cdots, \rho_1$ whose values depend directly on the q moving-average parameters $\underline{\theta}$, as well as on the p autoregressive parameters $\underline{\phi}$. Also, the p values $\rho_q, \rho_{q-1}, \cdots, \rho_{q-p+1}$ provide the necessary starting values for the difference equation, Eq. (3.12). If $q-p < 0$, the whole autocorrelation function ρ_n, for $n = 0, 1, 2, \cdots$, will consist of a mixture of damped exponentials and/or damped sine waves, whose nature is dictated by the polynomial $\Phi(B)$ and the starting values. If, however, $q-p \geq 0$, there will be $q-p+1$ initial values $\rho_0, \rho_1, \cdots, \rho_{q-p}$, which do not follow this general pattern.

Statistical Properties in the Frequency Domain

The frequency distribution of the variance of a stationary ARMA(p,q) process is described by its one-sided spectrum:

$$\begin{aligned} p(f) &= 2\sigma_e^2 \frac{|\Theta(e^{-i2\pi f\Delta t})|^2}{|\Phi(e^{-i2\pi f\Delta t})|^2}\Delta t \\ &= 2\sigma_e^2 \frac{|1 - \theta_1 e^{-i2\pi f\Delta t} - \cdots - \theta_q e^{-i2\pi q f\Delta t}|^2}{|1 - \phi_1 e^{-i2\pi f\Delta t} - \cdots - \phi_p e^{-i2\pi p f\Delta t}|^2}\Delta t, \qquad 0 \leq f \leq f_{Nyq} \end{aligned} \tag{3.13}$$

where $f_{Nyq} = 1/(2\Delta t)$ denotes the Nyquist frequency. The spectrum defined above is the discrete counterpart of the power spectral density function, Eq. (2.17), defined for a continuous process. The variance of an ARMA process can be obtained from its spectrum by the following relation:

$$\mathrm{Var}[a_k] = \sigma_a^2 = \int_0^{f_{Nyq}} p(f)\,df \tag{3.14}$$

Stochastic Model Building

According to the classical Box-Jenkins method, the fitting of an ARMA model to a set of data is usually best achieved by a three stage iterative procedure based on identifica-

tion, estimation, and diagnostic checking. The specific aim of model identification is to obtain some idea of the values for the model order (p,q) and to obtain initial guesses for the ARMA parameters. After the identification process has established a tentative model, model estimation uses the data to make inferences about the model parameters, $\underline{\phi}$, $\underline{\theta}$ and σ_e, conditional on the adequacy of the selected model. Likelihood and Bayesian methods are commonly applied for this purpose [16]. Finally, diagnostic checks of the fitted model in its relation to the data are applied in an effort to reveal model inadequacies and to provide a basis for model improvement.

3.3 Nonstationary ARMA Models

The traditional approach for dealing with nonstationary processes has been to try to transform the process into a stationary form. For example, the autoregressive integrated moving-average model, abbreviated ARIMA, is a suitable nonstationary model if the dth difference of the time series $\{a_k\}$ can be represented by a stationary, invertible ARMA process [16]. The general ARIMA(p,q,d) model is defined by the following difference equation:

$$\Phi(B)\nabla^d a_k = \Theta(B)\, e_k \tag{3.15}$$

where $\Phi(B)$ and $\Theta(B)$ represent the autoregressive and moving-average operators and ∇ denotes the difference operator, defined by $\nabla a_k = a_k - a_{k-1}$. Nevertheless, there are many processes, such as earthquake accelerograms, which possess nonstationary characteristics of a much more complex nature, and for which the above technique is quite inadequate. The nonstationary properties of earthquake signals are separated into two types. The first type of nonstationarity characterizes the time variation of the overall amplitude or intensity of the ground oscillations. Typically, the amplitude starts at zero, increases to a level of strong motion, stays at that level for a while, and then decays to zero. Mathematically, the amplitude nonstationarity is best represented by a variance, or root mean square, envelope $\sigma^2(t)$. It can be integrated easily in the ARMA model of Eq. (3.3) in two different ways, as for the continuous models of Eqs. (2.37-40). The first way is to modulate

the unit-variance driving white-noise $\{e_k\}$ using the envelope function $\sigma(t)$ and then use the ARMA filter:

$$\Phi(B)\, a_k = \Theta(B)\,(\sigma_k e_k) \tag{3.16}$$

The second way is to reverse the time-modulation and filtering operations as follows:

$$\Phi(B)\, a'_k = \Theta(B)\,(e_k) \tag{3.17a}$$

$$a_k = \sigma_k a'_k \tag{3.17b}$$

The second type of nonstationarity describes the change in time of the frequency content of the earthquake motion. The autoregressive and moving-average parameters of the ARMA model control the spectral content of the ARMA process. It follows that a nonstationarity in frequency content can be modeled using an ARMA model with time-varying parameters (dynamic ARMA model). The two types of nonstationarity can both be integrated in the same ARMA model resulting in the following stochastic earthquake model:

$$\begin{aligned} a_k - \phi_{1,k} a_{k-1} - \cdots - \phi_{p,k} a_{k-p} = \sigma_k e_k &- \theta_{1,k}(\sigma_{k-1} e_{k-1}) - \cdots \\ &- \theta_{q,k}(\sigma_{k-q} e_{k-q}) \end{aligned} \tag{3.18}$$

or, more succinctly:

$$\Phi_k(B)\, a_k = \Theta_k(B)\,(\sigma_k e_k) \tag{3.19}$$

At this point, it is important to realize that the uncoupling of the types of nonstationarity defined above is possible as long as the envelope $\sigma(t)$ is slowly varying in time compared to the periods of the process oscillations(1). In the present research, two methods have been considered to capture the time-histories of ARMA parameters in real accelerograms. The first method uses a sliding stationary ARMA model window while the second method uses a time adaptive filter. These two methods are described in detail in the next two Sections.

(1) The nonstationary time series represented by an earthquake accelerogram is characterized by relatively fast wiggles modulated by a relatively slowly changing envelope function.

ARMA Evolutionary Spectral Estimate

For a stationary ARMA process, the theoretical spectrum of the process is obtained from Eq. (3.13). Motivated by this relation, the instantaneous spectrum of a time-varying coefficient ARMA process can be defined by:

$$p(f,k) = 2\sigma_{e,k}^2 \frac{\left|1 - \sum_{j=1}^{q} \theta_j e^{-i2\pi jf\Delta t}\right|^2}{\left|1 - \sum_{j=1}^{p} \phi_j e^{-i2\pi jf\Delta t}\right|^2}, \qquad 0 \le f \le f_{Nyq} \tag{3.20}$$

The estimate of the instantaneous spectrum is computed by substituting the estimates of the time-varying ARMA parameters $\hat{\underline{\phi}}_k$ and $\hat{\underline{\theta}}_k$ and the smoothed estimate of the driving noise variance $\hat{\sigma}_{e,k}^2$ into Eq. (3.20). Kitagawa and Gersch [49,50] were the first researchers to have introduced the definition of instantaneous power spectral density represented by Eq. (3.20). The term instantaneous power spectra was first defined by Page in a pioneering paper [67], in which the estimation of instantaneous power spectral density was not considered. The computational form of Priestley's evolutionary spectral estimate is quite similar to the windowed periodogram method of estimating spectra of stationary processes.

The instantaneous spectral density can be used as a "diagnostic" to more fully express what the eye can only superficially discern in a visual examination of the earthquake signal. It reveals the instantaneously changing distribution and complexity of the distribution of energy as function of frequency in the earthquake signal.

3.4 Time-Varying ARMA Model Estimation Using Moving Window Technique

One way to estimate the time-histories of the ARMA parameters for a real accelerogram is to assume that this accelerogram is stationary within a time window of size ($n_{wd}\Delta t$) and given position (see Fig. 3.1). Standard statistical methods from time series analysis can then be used to estimate the ARMA parameters characterizing this segment of accelerogram. The parameter estimates corresponding to a certain window position are assumed to be representative of the center point of the window. This stationary parameter

estimation is repeated for successive equidistant window positions, the equidistance being $(n_{slid}\Delta t)$.

In this study, the subroutine FTML from the IMSL library [45] has been used to perform the maximum likelihood estimation of the ARMA parameters and driving white-noise variance, given a stationary time series. The subroutine FTML uses a modified steepest descent algorithm to find the ARMA parameters which minimize the sum of squares of the residuals, or one-step forecasting errors $\hat{e}_k$ defined as:

$$\hat{e}_k = a_k - [\hat{\phi}_1 a_{k-1} + \cdots + \hat{\phi}_p a_{k-p} - \hat{\theta}_1 \hat{e}_{k-1} - \cdots - \hat{\theta}_q \hat{e}_{k-q}] \qquad (3.21)$$

where $\{a_k\}$ is the measured ground acceleration and $\hat{e}_k = 0$ for $k = 1, \cdots, \max(p,q)$ and the "hat" symbol denotes an estimated quantity. This method, referred to as Method I, produces the time-varying variance $\hat{\sigma}_k^2$ of the driving white-noise.

A slightly different method, referred to as Method II, consists of first demodulating the amplitude of the target earthquake record to a unit-variance and then running the stationary ARMA window described above. A variance envelope estimate $\hat{\Psi}^2(t)$ is needed for the amplitude demodulation phase. The variance envelope estimation scheme used here is described at the end of this Section.

Based on the applications of this study, it was found that the amplitude demodulation only slightly influences the results of the ARMA estimation procedure. In Method II, the variance gain $G_v(\underline{\phi}(t), \underline{\theta}(t))$ is needed to deduce the time-varying variance $\hat{\sigma}_e^2(k)$ of the driving noise from the variance estimate of the target earthquake signal $\hat{\Psi}^2(t)$ as follows:

$$\hat{\sigma}_e^2(k) = \hat{\Psi}^2(k\Delta t) \,/\, G_v(\underline{\hat{\phi}}_k, \underline{\hat{\theta}}_k) \qquad (3.22)$$

Method I provides directly an estimate of $\hat{\sigma}_e^2(k)$.

The time window used in Methods I and II should be short enough to follow important spectral nonstationarities and long enough to provide for stability of parameter estimation and ability to capture low frequency spectral components. From experience gained in this research, it seems that a typical window size of 5.00 seconds(1) is a good compromise.

(1) This corresponds to a time window of 251 ground acceleration values digitized with a sampling

Variance-Envelope Estimation

The non-parametric variance-envelope estimation scheme developed by Nau et. al. [64], called the "two-stage weighted moving average estimate", is used in this study. The first stage of the technique consists in applying a weighted moving average to the squared sequence of the discrete ground acceleration values $\{a_k^2\}$, i. e.,

$$\bar{\sigma}_k^2 = \sum_{j=-n}^{n} w_j a_{k+j}^2 \qquad k = 1, 2, \cdots, N \tag{3.23}$$

where n is the half-width of the window, and $\{w_j, j \in [-n,n]\}$ is a weighting function satisfying:

$$\sum_{j=-n}^{n} w_j = 1, \qquad w_j \geq 0 \text{ for all } j \in [-n, n] \tag{3.24}$$

The truncated cosine bell defined in the next equation has been used in this study:

$$w_j = \frac{1 + \cos\left(\frac{j}{2\pi(n+1)}\right)}{\sum_{i=-n}^{n} \left\{1 + \cos\left(\frac{i}{2\pi(n+1)}\right)\right\}}, \qquad j = -n, \cdots, n \tag{3.25}$$

This "single stage weighted moving average" yields a smooth variance envelope estimate $\{\bar{\sigma}_k^2\}$ which tends to be biased or distorted in certain systematic ways, namely that the estimated peaks of the envelope are usually not quite as high as the true peaks and the estimated troughs are not quite as low as the true troughs. In order to reduce this bias, a multiplicative correction $\hat{\gamma}_k$ is applied to the single stage estimate $\bar{\sigma}_k^2$:

$$\hat{\sigma}_k^2 = \hat{\gamma}_k \bar{\sigma}_k^2 \tag{3.26}$$

where $\hat{\gamma}_k$ is obtained by re-applying the weighted moving average to the sequence $\{a_k/\bar{\sigma}_k\}$, i. e.,

$$\hat{\gamma}_k = \sum_{j=-n}^{n} w_j \frac{a_{k+j}^2}{\bar{\sigma}_{k+j}^2} \tag{3.27}$$

---

time interval of 0.02 second.

In general, it can be shown [64] that the two-stage estimate $\hat{\sigma}_k^2$ will generally be much less biased than the single stage estimate.

3.5 Time-Varying ARMA Model Estimation Using Kalman Filtering

The basic idea of a time adaptive algorithm is to optimally update the system parameters at each time step, using the observation at this time step. In this manner, a continuous description of the time-varying properties of the input data is obtained. A technique of adaptive estimation based on Kalman filtering theory can be used for the identification of the time-dependent ARMA coefficients of the earthquake model represented by Eq. (3.18). This technique is primarily based on the work done by Nau and Oliver [64] with an extension providing for iterative Kalman filtering.

The general dynamic ARMA(p,q) model shown in Eq. (3.18) can be recast in the following discrete state-space model:

$$\underline{\xi}_{k+1} = \underline{\xi}_k + \underline{\delta}_k \tag{3.28a}$$

$$a_{k+1} = \underline{H}_{k+1}^T \underline{\xi}_{k+1} + e_{k+1} \tag{3.28b}$$

where

$$\underline{\xi}_k = [\phi_{1,k}, \cdots, \phi_{p,k}, -\theta_{1,k}, \cdots, -\theta_{q,k}]^T \tag{3.29}$$

$$\underline{\delta}_k = [\delta_{1,k}, \cdots, \delta_{p+q,k}]^T \tag{3.30}$$

$$\underline{H}_k = [a_{k-1}, \cdots, a_{k-p}, e_{k-1}, \cdots, e_{k-q}]^T \tag{3.31}$$

The underlying equation of motion for the time-dependent parameters, Eq. (3.28a), also called the transition (or state) equation, and the measurement (or observation) equation, Eq. (3.28b), completely define the earthquake signal model. The state vector $\underline{\xi}_k$ is partitioned in such a way that the first p terms are the autoregressive parameters, the remaining elements being the moving average parameters. The true noise of the motion, also called "plant" noise in the literature of control theory, is represented by the random vector $\underline{\delta}_k$. The ground acceleration measurement at time $t_k = k\Delta t$ ($k = 0, 1, 2, \cdots$) is represented

by a_k. The vector $\underline{H}_k$ is called the "history" vector and gives the ideal (noiseless) connection between the measurement and the state vector at time t_k. Finally, $\{e_k\}$ represents the true measurement noise, also called driving noise of the ARMA model. The following assumptions are made:

$$E[\underline{\delta}_k] = \underline{0}, \qquad \mathrm{Cov}[\underline{\delta}_k, \underline{\delta}_k^T] = \underline{\Sigma}_\delta \tag{3.32}$$

$$E[e_k] = 0, \qquad \mathrm{Var}[e_k] = \sigma_{e,k}^2 \tag{3.33}$$

$$\mathrm{Cov}[\underline{\delta}_k, e_k] = \underline{0} \tag{3.34}$$

The random walk model for the parameters, Eq. (3.28a), may not appear physically reasonable. However, it is the simplest equation of motion that can be assumed in the absence of detailed prior information about parameter behavior. In this context, it is merely a device for ensuring that the Kalman filter will remain continually adaptive to any changes in the parameters that may occur. The covariance matrix $\underline{\Sigma}_\delta$ governs the average step size of the random walk assumed for the parameters and it therefore determines the long-run sensitivity of the filter to changes in the parameter. The problem of "tuning" the filter to obtain parameter estimates, which on one hand respond quickly to nonstationarities in the data, but on the other hand are not unstable, is a difficult problem and will be discussed in Section 5.2. It is generally convenient to assume $\underline{\Sigma}_\delta = \sigma_\delta^2 \underline{I}$, where σ_δ is a small number compared to average values of the parameters (e.g., $\sigma_\delta \leq 0.01$). The notation

$$\bar{\underline{\xi}}_k = E^*[\underline{\xi}_k \mid a_{k-1}, a_{k-2}, \cdots, a_0]^{(1)} : \quad \text{prior mean estimate} \tag{3.35a}$$

$$\hat{\underline{\xi}}_k = E^*[\underline{\xi}_k \mid a_k, a_{k-1}, \cdots, a_0] : \quad \text{posterior mean estimate} \tag{3.35b}$$

is used to denote the expected values of $\underline{\xi}_k$ conditional on the observations up to $k-1$ and k, respectively. Also,

$$\bar{\underline{P}}_k = E^*[(\underline{\xi}_k - \bar{\underline{\xi}}_k)(\underline{\xi}_k - \bar{\underline{\xi}}_k)^T] = \mathrm{Cov}^*[\underline{\xi}_k, \underline{\xi}_k^T \mid a_{k-1}, \cdots, a_0] \tag{3.36a}$$

$$\hat{\underline{P}}_k = E^*[(\underline{\xi}_k - \hat{\underline{\xi}}_k)(\underline{\xi}_k - \hat{\underline{\xi}}_k)^T] = Cov^*[\underline{\xi}_k, \underline{\xi}_k^T \mid a_k, \cdots, a_0] \tag{3.36b}$$

denote the prior and posterior error covariance matrices, respectively. The discrete-time Kalman filter [2] provides a set of recursive equations to update the conditional expected values and covariances of the parameters as follows:

$$\bar{\underline{\xi}}_{k+1} = \hat{\underline{\xi}}_k \quad \text{(prior expected value)} \tag{3.37a}$$

$$\bar{\underline{P}}_{k+1} = \hat{\underline{P}}_k + \underline{\Sigma}_\delta \quad \text{(prior error covariance)} \tag{3.37b}$$

$$\underline{K}_{k+1} = \bar{\underline{P}}_{k+1}\underline{H}_{k+1}(\underline{H}_{k+1}^T\bar{\underline{P}}_{k+1}\underline{H}_{k+1} + \sigma_{e,k+1}^2)^{-1} \quad \text{(Kalman gain}^{(2)}\text{)} \tag{3.37c}$$

$$\hat{\underline{\xi}}_{k+1} = \bar{\underline{\xi}}_{k+1} + \underline{K}_{k+1}(a_{k+1} - \underline{H}_{k+1}^T\bar{\underline{\xi}}_{k+1}) \quad \text{(posterior expected value)} \tag{3.37d}$$

$$\hat{\underline{P}}_{k+1} = (\underline{I} - \underline{K}_{k+1}\underline{H}_{k+1}^T)\bar{\underline{P}}_{k+1} \quad \text{(posterior error covariance)} \tag{3.37e}$$

The Kalman filter equations and the sequence of computational steps are shown in Fig. 3.2. The equations yielding $\bar{\underline{\xi}}_{k+1}$ and $\bar{\underline{P}}_{k+1}$ from $\hat{\underline{\xi}}_k$ and $\hat{\underline{P}}_k$, Eqs. (3.37a-b), are termed the time-update equations (or prediction equations), while the equations yielding $\hat{\underline{\xi}}_{k+1}$ and $\hat{\underline{P}}_{k+1}$ from $\bar{\underline{\xi}}_{k+1}$ and $\bar{\underline{P}}_{k+1}$, Eqs. (3.37d-e), are known as the measurement-update equations (or updating equations). The quantity $\bar{e}_{k+1} = (a_{k+1} - H_{k+1}^T\bar{\underline{\xi}}_{k+1})$ in Eq. (3.37d) is called the forecast error (or innovation) and corresponds to the difference between the measurement value a_{k+1} and the one-step-ahead forecast of the measurement ($\underline{H}_{k+1}^T\bar{\underline{\xi}}_{k+1}$). The residual at period $(k+1)$ is defined as $\hat{e}_{k+1} = a_{k+1} - \underline{H}_{k+1}^T\hat{\underline{\xi}}_{k+1}$ and is therefore based on the estimate of $\underline{\xi}_{k+1}$ posterior to a_{k+1}, whereas the innovation $\bar{e}_{k+1}$ defined previously is based on the estimate of $\underline{\xi}_{k+1}$ prior to a_{k+1}.

---

(1) The "star" notation (i.e., $E^*(.)$ and $Cov^*(.)$) indicates that the quantities defined are not exact conditional expectations and covariances of random variables. This inexactness is due to the linearization required to include moving-average parameters, the data dependence of the term $\underline{H}_k$, and the uncertainty in the underlying model.

(2) The following alternative form, algebraically equivalent, of the Kalman gain $\underline{K}_{k+1}$ is sometimes found in the literature [63]:

$$\underline{K}_{k+1} = \frac{1}{\sigma_{e,k+1}^2}\left(\bar{\underline{P}}_{k+1}^{-1} + \frac{1}{\sigma_{e,k+1}^2}\underline{H}_{k+1}H_{k+1}^T\right)^{-1}\underline{H}_{k+1}$$

If $\{\xi_k\}$ and $\{a_k\}$ are jointly distributed Gaussian processes, the Kalman filter equations define the evolution of the Gaussian conditional probability density of the state. Among the set of filters of a restricted class, the Kalman filter is optimal in the sense that it is a minimum error variance estimator, whether or not Gaussian assumptions are made.

Nonlinear Aspect of the Filtering Problem

The presence of moving-average terms in the selected earthquake model introduces a nonlinear aspect to the filtering problem, since products of unknown parameters and noise values appear in the system equations, and require some form of "extension" of the basic Kalman filtering algorithm. Note that, in practice, the true measurement noise $\{e_k\}$ is never observed directly. Hence, when implementing the Kalman filter, estimates of the true noise terms $(e_k, \cdots, e_{k-q+1})$ must be substituted in the "history" vector $\underline{H}_{k+1}$. The residual estimates $(\hat{e}_k, \cdots, \hat{e}_{k-q+1})$, defined above, are used for this purpose. This constitutes the linearization needed to extend the Kalman filter to cover the inherently nonlinear problem of estimating moving average parameters.

Iterative Kalman Filtering

The true noise variance envelope $\{\sigma^2_{e,k}\}$ is required as an input to the Kalman filter at each time step. Because $\{\sigma^2_{e,k}\}$ is a priori unknown, the Kalman filter is applied iteratively using improved estimates of the true noise variance envelope. For the first iteration, a rough estimate of $\{\sigma^2_{e,k}\}$ is obtained by estimating the observed process (earthquake record) variance envelope $\Psi(t_k)$, and then dividing it by an assumed temporal average value $\overline{G}_v$ of the variance gain G_v defined in Section 3.2. Therefore, the estimate of $\{\sigma^2_{e,k}\}$ for the first iteration is a scaled version of the variance envelope estimate, $\hat{\Psi}(t_k)$, of the observed process:

$$\left\{\hat{\sigma}^{2}_{e,k}{}^{(1)}\right\} = \frac{\hat{\Psi}(t_k)}{\overline{G}_v} \tag{3.38}$$

The variance envelope estimate of the residuals $\{\hat{e}_k^{(1)}\}$, computed during the first applica-

tion of the Kalman filter, is used as true noise variance envelope estimate , $\{\hat{\sigma}^2_{e,k}{}^{(2)}\}$, for the second application of the Kalman filter. The Kalman filter is applied iteratively until the difference between $\{\hat{\sigma}^2_{e,k}{}^{(i)}\}$ and $\{\hat{\sigma}^2_{e,k}{}^{i-1}\}$ is below a pre-specified tolerance.

Starting Procedure of Kalman Filtering

The Kalman filtering starting procedure is illustrated in Fig. 3.3. The p first discrete ground acceleration values of the target earthquake record are used to build the initial "history" vector $\underline{H}_1$:

$$\underline{H}_1 = [a_0, \cdots, a_{-p+1}; 0, \cdots, 0]^T \tag{3.39}$$

in which the estimates of the initial true noise terms $(e_0, \cdots, e_{1-q})$ have been taken equal to zero. Initial estimates for $\underline{\xi}_0$ and $\underline{P}_0$ have to be entered. An initial estimate $\hat{\underline{\xi}}_0$ can be obtained by performing a maximum likelihood estimation within a time window positioned at the beginning of the earthquake record. The initial error covariance matrix $\hat{\underline{P}}_0$ is selected to be equal to the covariance matrix $\underline{\Sigma}_\delta$ of the random walk of the ARMA parameters. The first data used by the Kalman filter is a_1. From these initial conditions, the Kalman filter can be run recursively until the end of the data set $\{a_k\}$.

3.6 ARMA Simulation of Original Records

Two different cases of earthquake ground motion simulation are considered in this study. In the first case, an ensemble of artificial ground motions statistically similar to a "target" real accelerogram, is generated. In the second case, a set of artificial motions satisfying a set of ground motion features corresponding to a particular continuous-time model and source-site condition is generated. In the latter case, the continuous model parameters must first be converted into discrete ARMA model parameters, using the discrete-continuous relationships developed in Chapter 4. Then, for both cases, the analysis procedures described in the previous Sections are simply reversed for simulation purposes. The sequence of operations to perform are:

(1) Computer generation of a stationary Gaussian discrete white-noise $\{e_k, k = 1, \cdots, N\}$ having zero mean and unit variance. The subroutine GGNML of the IMSL library [45] is used for this task. It generates pseudo-random standard normal numbers by first generating uniform random numbers in the exclusive range (0,1) and then transforming these to normal numbers using the inverse normal function.

(2) Uniform time modulation of the stationary white-noise:

$$w_k = \Psi(t_k)\, e_k, \qquad k = 1, \cdots, N \tag{3.40}$$

(3) ARMA filtering of the nonstationary white-noise:

$$a_k = \Phi_k^{-1}(B)\, \Theta_k(B)\, w_k, \qquad k = 1, \cdots, N \tag{3.41}$$

(4) Baseline correction using a time invariant high-pass filter to remove the low frequency components responsible for baseline effects.

Baseline Correction

According to Eq. (3.13), the power spectrum of a pure AR(p) model ($\theta_i = 0, i = 1, \cdots, q$) has only poles. A pure AR(p) transfer function is, therefore, unable to model the zeros in the earthquake spectrum. This results in a spectrum that is greater than zero for all frequencies. This can result in large baseline errors in the integrated velocity and displacement of the artificial records, because of the presence of spurious low frequency components. The transfer function of the ARMA(p,q) model of Eq. (3.13) contains both poles and zeros. The ARMA model is therefore able to model zeros in the spectrum, which offers the possibility of a built-in baseline correction type of filter. However, the numerical experimentation performed during this study has shown that even for the ARMA models, the simulated acceleration histories exhibit a deficiency at the very low frequencies.

In an effort to improve the incorrect spectral amplitudes at low frequencies for the AR(p) model, Papadimitriou and Beck [69] have incorporated Brune's earthquake source

model [18], which appears adequate for deterministic predictions at very low frequencies. Brune's source model corresponds to the relative acceleration response of a critically damped oscillator with corner frequency f_c, and accounts for the form of the spectral amplitude near the source. According to Brune, the source Fourier spectral acceleration for shear waves has the shape:

$$S(f, f_c) = \frac{f^2}{f^2 + f_c^2} \tag{3.42}$$

Typically, the value of the corner frequency is $f_c = 0.1$ Hz. Papadimitriou and Beck perform the low frequency shaping in the time domain, using the following ARMA(2,2) filter whose transfer function coincides with Brune's model of Eq. (3.42):

$$a'_k - 2\alpha a'_{k-1} + \alpha^2 a'_{k-2} = a_k - 2a_{k-1} + a_{k-2} \tag{3.43}$$

where $\{a'_k\}$ = corrected accelerogram, $\{a_k\}$ = uncorrected accelerogram and $\alpha = e^{-\omega_c \Delta t}$ with $\omega_c = 2\pi f_c$.

In this study, the simulated records are baseline corrected and integrated to velocity and displacement in the frequency domain. Both the two-way Butterworth filter and the filter defined by Brune's model have been used.

The uni-directional Butterworth filter has a phase relation between the input and output signals that is not the same for all frequencies (nonlinear phase spectrum). Therefore, it has to be applied successively in both forward and backward directions to eliminate the phase shift. As a result, the bi-lateral Butterworth filter is a pure amplitude filter (zero phase filter). For more details about the filter design, the interested reader is referred to Appendix A. The high-pass Butterworth filter is one of the most commonly used filters for processing of real seismic strong motion records [77]. The processing procedure utilized here involves the following steps:

1. Compute discrete Fourier transform of the simulated acceleration record using an FFT subroutine.

2. High-pass filter the acceleration in frequency domain.
3. Integrate the corrected acceleration in frequency domain to obtain the velocity assuming zero initial velocity.
4. Doubly integrate the corrected acceleration in frequency domain to obtain the displacement assuming zero initial velocity and displacement.
5. Least square fit a straight line to the displacement to obtain the corrected displacement.
6. Add the slope of the straight line of previous step to the velocity of step 3 to obtain the corrected velocity.

3.7 ARMA Model Diagnostic Checking

If an ARMA model fitted to a real accelerogram were perfect, it would map the highly correlated time series represented by the real accelerogram into a realization of a perfectly uncorrelated stationary Gaussian white-noise. Therefore, the first level of model checking is applied to the final (converged) sequence of normalized residuals $\{\hat{e}_k/\hat{\sigma}_{e,k}\}$ given by the model estimation procedure. These normalized residuals are checked for "whiteness" (uncorrelation) and normality. However, a model is never perfect and in the present case, the imperfection is a result of one or more of the following causes:

- The model estimation is not accurate enough or incorrect due to a bad choice of estimation algorithm;
- The selected model order (p,q) is not adequate for the nature of the particular earthquake process under consideration;
- The assumption of a linear earthquake model is too restrictive given the high nonlinearity of the particular earthquake process under consideration.

The next question to be addressed is whether the imperfect estimated earthquake model is sufficient for the present research objectives, which are ground motion variability and structural response variability modeling for a given earthquake process. To answer this

question, the estimated earthquake model is used further for ground motion and structural response simulation.

The second level of model diagnostic checking is applied to simulated accelerograms (individual or ensemble) to verify the extent to which they resemble the actual "target" accelerogram. For this purpose, the following checking operations are made:

- Analyze ARMA-model-simulated accelerograms, utilizing the analysis and estimation techniques used on the "target" accelerogram. The objective of this analysis is to verify the accuracy with which the estimation techniques can recover the "true" parameters of the earthquake process when they are known.
- Compare ground velocity and displacement from simulated and "target" motions. This test is used to insure that not only the simulated acceleration, but also the corresponding ground velocity and displacement time histories are realistic, since the latter two can control the earthquake response of certain structures.
- Compare the Fourier amplitude spectra of the simulated and "target" ground motions (acceleration, velocity and displacement). The Fourier amplitude spectra give an indication of the global frequency content over the whole duration of the earthquake.
- Compare the evolutionary power spectral density of the fitted ARMA model to the moving periodogram estimate of the evolutionary PSD of the "target" accelerogram.
- Compare the traditional ground motion parameter values of the "target" earthquake to the statistics of these parameters for an ensemble of simulated earthquakes. The ground motion parameters include: peak ground acceleration (PGA), velocity (PGV) and displacement (PGD), the ratios PGV/PGA and PGD/PGA, root-mean-square acceleration (RMSA), velocity (RMSV) and displacement (RMSD), Arias intensity (AI) and Housner's spectral intensity (SI).

The third level of model diagnostic checking consists in comparing the response of a structure to the "target" earthquake motion with the statistical structural response to an ensemble of simulated earthquake motions. The earthquake structural response can be

characterized by various response parameters. For a linear SDOF structure, these parameters are the traditional response spectrum quantities (max. absolute acceleration, relative velocity and relative displacement responses). For nonlinear SDOF structures, the response parameters may depend on the force-deformation relationship and will be defined in Chapter 6.

Residuals Check

As mentioned above, the diagnostic checking (or goodness of fit) of the model may be carried out by examining the normalized residuals $\{w_k = \hat{e}_k/\hat{\sigma}_{e,k}, k = ,1, \cdots, N\}$ for departures from randomness. Formal tests can be performed in the time domain, based on the sample autocorrelation coefficient function $\{\hat{\rho}_k, k = 0,,1,2, \cdots\}$ and, in the frequency domain, based on the periodogram. However, neither of these should be seen as a substitute for a direct plot of the residuals. In this matter, Box and Jenkins [16,p.289] say: "It cannot be too strongly emphasized that visual inspection of a plot of the residuals themselves is an indispensable first step in the checking process." In the time domain, the sample autocorrelation coefficient function at lag $(k\Delta t)$, $\hat{\rho}_k$, is defined as:

$$\hat{\rho}_k = \hat{R}_k/\hat{R}_0 \tag{3.44}$$

where

$$\hat{R}_k = \frac{1}{N}\sum_{i=1}^{N-k}(w_i - \overline{w})(w_{i+k} - \overline{w}) \tag{3.45}$$

and $\overline{w} = \frac{1}{N}\sum_{i=1}^{N} w_k$. If $\{w_k\}$ is a purely random (uncorrelated) process, it can be shown [76] that:

$$E[\hat{\rho}_k] \sim 0 \quad \text{and} \quad Var[\hat{\rho}_k] \sim \frac{1}{N}, \quad \text{all } k \neq 0 \tag{3.46}$$

Hence, on the basis of the asymptotic normal distribution, an approximate 95% of confidence interval for $\hat{\rho}_k$ is $\{\rho_k \pm 2\sqrt{1/N}\}$. Even if the hypothesis that $\{w_k\}$ is a purely random process is true, about 5% of the $\hat{\rho}_k$ are expected to lie outside the critical values. This feature must be allowed for in assessing the "significance" of departures of $\hat{\rho}_k$ from its

predicted form.

Another time domain test for goodness of fit is provided by the so-called "portmanteau" statistic:

$$Q = N \sum_{k=1}^{n} \hat{\rho}_k \tag{3.47}$$

where N is the number of data points, and $n \sim N/5$. Under the hypothesis that the residuals are completely uncorrelated (white-noise), Q is approximately chi-square distributed with the number of degrees of freedom equal to n minus the number of parameters estimated $(p+q)$. Therefore, an approximate "portmanteau" test of the hypothesis of model adequacy may be made by referring an observed value of Q to a table of the percentage points of χ^2. However, as a general rule, a value of Q not much larger than the number of d.o.f's is considered to indicate a good fit.

In the frequency domain, the periodogram of a stationary time series $\{a_k, k = 1, \cdots, N\}$ is defined as:

$$P_k = P(\omega_k) = \frac{\Delta t}{2\pi N} |A(\omega_k)|^2 \tag{3.48}$$

where $A(\omega_k)$ is the discrete Fourier transform of $\{a_k\}$:

$$A_k = A(\omega_k) = \sum_{n=0}^{N-1} a_n e^{-i2\pi nk/N}, \qquad k = 0, \cdots, N-1 \tag{3.49}$$

and $\omega_k = k\Delta\omega$, $\Delta\omega = 2\pi\Delta f$, $\Delta f = 1/N\Delta t$. It can be shown [17] that the periodogram $P(\omega_k)$ is an unbiased estimate of the PSD $\Phi(\omega)$ of the underlying stationary process and that $\mathrm{Var}[P(\omega_k)] = \Phi^2(\omega_k)$ no matter how large N is. The periodogram ordinates at different frequencies $(P(\omega_k), k = 0, \cdots, N-1)$ are also shown to be asymptotically independent $\Phi(\omega_k)\chi_2^2/2$ variates. Thus, due to a large variance and statistical independence at neighboring frequencies, the periodogram $P(\omega_k)$ is a very irregular function of ω_k even if $\Phi(\omega)$ is a regular function of ω.

The total power in a signal is the same whether it is computed in the time domain or

in the frequency domain. This result is known as the Parseval's theorem:

$$\text{Total Power} \equiv \int_{-\infty}^{\infty} |a(t)|^2 dt = \int_{-\infty}^{\infty} |A(f)|^2 df \tag{3.50}$$

From the discrete form of Parseval's theorem, it follows that

$$\sum_{k=0}^{N-1} P(\omega_k)\,\Delta\omega = 2\pi \sum_{k=0}^{N-1} P(f_k)\,\Delta f = \frac{1}{N}\sum_{k=0}^{N-1} |a_k|^2 \tag{3.51}$$

For a zero-mean time series $\{a_k\}$, the right-hand-side of Eq. (3.51) represents the sample variance. Hence, Eq. (3.51) expresses that the area under the periodogram is equal to the variance of the time series and gives an indication of the distribution of energy over a discrete range of frequencies (see Eqs. (2.20) and (3.14) for analogies).

To reduce the "leakage" between neighboring discrete frequencies, a taper w_j (or data windowing) [75] is applied to the data $\{a_k\}$ prior to computing their Fourier transform. The Parzen window provides a good compromise between main lobe's width and sidelobes' size of the leakage function. The Parzen window is defined as follows:

$$w_j = 1 - \left| \frac{j-(N-1)/2}{(N+1)/2} \right|, \qquad j = 0, \cdots, N-1 \tag{3.52}$$

To reduce the large variance of the periodogram defined in Eq. (3.48), smoothing using uniform or differential weighting can be applied

$$P_s(\omega_k) = \sum_{j=-m}^{m} W_j\, P(2\pi\,(k+j)\,\Delta f) \tag{3.53}$$

where W_j, $j = 0, \pm 1, \cdots, \pm m$ are weighting coefficients satisfying

$$\sum_{j=-m}^{m} W_j = 1 \tag{3.54}$$

The effect of averaging $2m+1$ adjacent periodogram ordinates is to produce an estimate $P_s(\omega_k)$ whose asymptotic variance is $(\sum_{j=-m}^{m} W_j^2)$ times that of the unsmoothed periodogram $P(\omega_k)$. However, smoothing introduces some bias into the estimate $P_s(\omega_k)$ which increases

with m. Therefore, some compromise value for m has to be selected. In this study, m = 3 and W_j = [¼ ½ ¼] provided good results.

The periodogram estimate, applied to the sequence of normalized residuals produced by the ARMA model fitting, is very useful. Its visual inspection can reveal the presence of some periodic randomness causing "bump(s)" in the periodogram.

The normality test of the normalized residuals is done by visual inspection of data plotted on normal probability paper [4]. For this purpose, the mth value among the N residuals (arranged in increasing order) is plotted (in arithmetic scale) versus the standard normal value (plotted in arithmetic scale) corresponding to the cumulative probability $n/(N+1)$. A lack of linearity in the resulting graph of data points suggests that the underlying population is not Gaussian.

Moving Periodogram Estimate of the EPSD of a Target Accelerogram

An estimate of the evolutionary power spectral density (EPSD) of a target accelerogram can be obtained by sliding, along the time axis, the aforementioned periodogram estimate taken over a time segment of the accelerogram. This EPSD estimate can be compared to the theoretical ARMA EPSD estimate. This comparison could reveal a deficiency of the identified ARMA model and help to suggest an improved model.

3.8 Advantages of ARMA Models

The ARMA models and their identification procedures have been defined in previous Sections. In this Section, the relative advantages of ARMA models with respect to other ground motion modeling procedures are discussed. ARMA models are of equal generality with linear continuous-time analytical models, but have a number of significant advantages for digital analysis and simulation purposes.

(i) The statistical model building procedure from recorded accelerograms includes systematic model-identification techniques which do not require any a priori assumptions on the order of the model. This feature is one of the principal advantages of

ARMA models relative to other model-fitting procedures commonly applied to earthquake data.

(ii) ARMA models furnish a characterization of recorded earthquakes using linear models with a small number of parameters. Thus, they satisfy the desirable condition of model parsimony. Controlled by only a few parameters, these linear processes provide a wide variety of correlation functions.

(iii) Because ARMA models are identified and their parameters are estimated directly from data in the time domain, they provide an extremely direct method of proceeding from the analysis of actual accelerograms to the generation of artificial accelerograms with the same characteristics. Earthquake ground motions are generated by simple iteration of a linear difference equation. The number of steps from analysis to simulation is reduced since it is not necessary to convert back and forth between discrete and continuous models, or between time domain and frequency domain characterizations. Therefore, ARMA models for earthquake ground motions are computationally very efficient.

(iv) ARMA discrete-time simulation models for earthquake ground motion provide acceleration data outputs directly suited for use as input data to linear and nonlinear structural models.

(v) ARMA models can be related to equivalent continuous dynamic models, which enable their interpretation as a physical process. These physical interpretations constitute a strong potential link between seismology and ground motion time history modeling.

(vi) Time domain identification techniques are somewhat less sensitive than frequency domain techniques to certain violations of stationarity assumptions and to the effects of digitizing a continuous record.

(vii) The use of time-varying parameters, necessary to represent the spectral nonstationarity of most earthquake records, is not problematic with the time-domain framework

of the ARMA model simulation method.

CHAPTER 4

PHYSICAL INTERPRETATION OF ARMA MODELS

4.1 Introduction

As previously mentioned in Chapter 2, earthquake ground motions are the output of a very complex physical process. A macroscopic dynamic model able to "explain" an earthquake accelerogram should reveal something about the underlying physical system generating the earthquake ground motion. ARMA models can be interpreted as discrete dynamic models. The relationship or mapping between the ARMA coefficients and the physical parameters of the corresponding continuous dynamic model is attractive because (i) it offers a physical interpretation of the ARMA parameters and (ii) it provides a potential link between ARMA modeling of earthquake ground motions and seismology, needed for seismic risk studies.

In Ref. [19], several California earthquake digitized accelerograms have been best fitted by low order ARMA models, particularly the ARMA(2,1) and ARMA(4,1) models. With only three parameters, the ARMA(2,1) model satisfies the desirable feature of model parsimony and hence is very appealing for stochastic earthquake modeling. In the next Section, the detailed physical interpretation of the ARMA(2,1) model will be presented. It will be seen that the well-known Kanai-Tajimi earthquake model [47,88] is a subcase of the continuous version of the discrete ARMA(2,1) model. The ARMA(2,1) model can be used as a "building block" to build or interpret higher order ARMA models.

4.2 The ARMA(2,1) Model

The stationary ARMA(2,1) model is defined by the difference equation

$$a_k - \phi_1 a_{k-1} - \phi_2 a_{k-2} = e_k - \theta_1 e_{k-1} \tag{4.1}$$

or, in the backshift operator notation

$$[1 - \phi_1 B - \phi_2 B^2]\, a_k = [1 - \theta_1 B]\, e_k \tag{4.2}$$

The stationarity conditions are achieved if the roots of $1 - \phi_1 B - \phi_2 B^2 = 0$ lie outside the unit circle, that is if the parameters ϕ_1 and ϕ_2 lie in the triangular region shown in Fig. 4.1, i.e.,

$$\phi_1 + \phi_2 < 1 \tag{4.3a}$$

$$\phi_2 - \phi_1 < 1 \tag{4.3b}$$

$$|\phi_2| < 1 \tag{4.3c}$$

The invertibility condition is satisfied if the root of $1 - \theta_1 B = 0$ lies outside the unit circle, that is if

$$|\theta_1| < 1 \tag{4.4}$$

Discrete Autocovariance Function

It can be shown [16,24] that the autocovariance function γ_n of the output process $\{a_k\}$ is given by

$$\gamma_0 = E[a_k^2] = \sigma_a^2 = \frac{1 - \phi_2}{1 + \phi_2} \frac{1 + \theta_1^2 - 2\,\phi_1\,\theta_1}{(1 - \phi_2)^2 - \phi_1^2}\, \sigma_e^2 , \tag{4.5a}$$

$$\gamma_1 = E[a_k a_{k+1}] = \frac{\phi_1\,(1 + \theta_1^2 - \theta_1\,\phi_1) - \theta_1\,(1 - \phi_2^2)}{(1 - \phi_2)\,(1 + \theta_1^2 - \theta_1\,\phi_1) - \theta_1\,\phi_1\,(1 + \phi_2)}\, \gamma_0 , \tag{4.5b}$$

$$\Phi(B)\,\gamma_n = \Phi(B)\,E[a_k a_{k+n}] = 0, \qquad n > 1 . \tag{4.5c}$$

Discrete Autocorrelation Coefficient Function (ACCF)

According to Eq. (3.11), the ACCF ρ_n of the output process $\{a_k\}$ is a normalized form of the autocovariance function γ_n :

$$\rho_0 = 1 \tag{4.6a}$$

$$\rho_1 = \frac{\phi_1 (1 + \theta_1^2 - \theta_1 \phi_1) - \theta_1 (1 - \phi_2^2)}{(1 - \phi_2)(1 + \theta_1^2 - \theta_1 \phi_1) - \theta_1 \phi_1 (1 + \phi_2)} \tag{4.6b}$$

$$\Phi(B)\, \rho_n = 0\,, \quad n > 1 \tag{4.6c}$$

Depending on the nature (real or complex) of the roots of the difference equation $\Phi(B) = 0$, the ACCF ρ_n is either the superposition of two exponentials or follows a damped sine wave. In Fig. 4.2, the stationary triangular region in coordinates ϕ_1 and ϕ_2 has been subdivided in five zones. Each of these five zones possesses its own set of properties for the roots r_1 and r_2 of the characteristic equation

$$r^2 - \phi_1 r - \phi_2 = 0 \tag{4.7}$$

Table 4.1 summarizes the roots of the above characteristic equation for the five zones. For example, in Zone 1, r_1 and r_2 are complex conjugate, which is not the case in any other zone. From Eq. (4.6c), the ACCF at higher lags ($n \geq 2$) is given by

$$\rho_n = \rho(n\,\Delta t) = C_1 r_1^n + C_2 r_2^n \tag{4.8}$$

where the constants C_1 and C_2 depend on the initial conditions ρ_0 and ρ_1. Table 4.2 summarizes the discrete ACCF represented by Eq. (4.8) for each of the five zones [24].

Underlying Physical System

The underlying physical system corresponding to the ARMA(2,1) model is the linear viscously damped single-degree-of-freedom (SDOF) oscillator represented in Fig. 4.3 [19] where m = mass of SDOF oscillator, k = spring stiffness, c = dashpot damping coefficient, X(t) = input displacement applied separately to the spring and the dashpot in proportions C_s and C_d respectively, Z(t) = SDOF absolute displacement (measured with respect to a fixed reference). According to Newton's second law, the equation of motion of the SDOF is :

$$-c\,[\dot{Z}(t) - C_d\,\dot{X}(t)] - k\,[Z(t) - C_s\,X(t)] = m\,\ddot{Z}(t) \tag{4.9}$$

By defining $\omega_g^2 = k/m$ and $c/m = 2\,\xi_g\,\omega_g$, the above equation can be rewritten as

$$\ddot{Z}(t) + 2\xi_g\omega_g\dot{Z}(t) + \omega_g^2 Z(t) = C_s\omega_g^2 X(t) + 2C_d\xi_g\omega_g\dot{X}(t) \tag{4.10}$$

In the following, it will be shown that if the input acceleration process $\ddot{X}(t)$ is a continuous white-noise of constant PSD ϕ_0, then the continuous output process $a(t) \equiv \ddot{Z}(t)$ is discretely coincident with the discrete output process of an ARMA(2,1) model.

Continuous Autocorrelation Function

The system transfer function between the input acceleration $\ddot{X}(t)$ and the output absolute acceleration $\ddot{Z}(t)$ is

$$H(\omega) = \frac{C_s\omega_g^2 + i\,2C_d\xi_g\omega_g\omega}{\omega_g^2 - \omega^2 + i\,2\xi_g\omega_g\omega} \tag{4.11}$$

From linear random vibration theory [56], the power spectral density of the stationary output process $a(t) \equiv \ddot{Z}(t)$ is obtained by multiplying the PSD of the input process by the square of the transfer function $|H(\omega)|^2$:

$$\Phi_{\ddot{Z}\ddot{Z}}(\omega) = \phi_0 \frac{C_s^2\,\omega_g^4 + 4\,C_d^2\,\xi_g^2\,\omega_g^2\,\omega^2}{(\omega_g^2 - \omega^2)^2 + 4\,\xi_g^2\,\omega_g^2\,\omega^2} \tag{4.12}$$

The autocorrelation function $R_{aa}(\tau) = E[a(t)\,a(t+\tau)]$ of the continuous process $a(t)$ can be obtained from the PSD of Eq. (4.12) by using the Wiener-Khinchine relation [56], i.e.,

$$R_{aa}(\tau) = \int_{-\infty}^{\infty} \phi_0 \frac{C_s^2\,\omega_g^4 + 4\,C_d^2\,\xi_g^2\,\omega_g^2\,\omega^2}{(\omega_g^2 - \omega^2)^2 + 4\,\xi_g^2\,\omega_g^2\,\omega^2}\, e^{i\omega\tau}\, d\omega \tag{4.13}$$

Using contour integration in the complex plane, the final results are:

Underdamped Case : $\xi_g < 1$

$$R_{aa}(\tau) = \frac{\pi\,\phi_0}{2}\, e^{-\xi_g\omega_g|\tau|}\, [\frac{\omega_g}{\xi_g}\,(C_s^2 + 4\,C_d^2\,\xi_g^2)\cos\omega_{gd}|\tau| + \frac{\omega_g}{\sqrt{1-\xi_g^2}}\,(C_s^2 - 4\,C_d^2\,\xi_g^2)\sin\omega_{gd}|\tau|] \tag{4.14}$$

where $\omega_{gd} = \omega_g\sqrt{1-\xi_g^2}$.

Overdamped Case : $\xi_g > 1$

$$R_{aa}(\tau) = \frac{\pi\,\phi_0}{2}\,\omega_g\,e^{-\xi_g\omega_g|\tau|}\,[\alpha\,(\frac{C_s^2}{\xi_g} - 4\,C_d^2\,\xi_g\,(\xi_g - \sqrt{\xi_g^2 - 1})^2)\,e^{\omega_g\sqrt{\xi_g^2-1}\,|\tau|}$$
$$- \beta\,(\frac{C_s^2}{\xi_g} - 4\,C_d^2\,\xi_g\,(\xi_g + \sqrt{\xi_g^2 - 1})^2)\,e^{-\omega_g\sqrt{\xi_g^2-1}\,|\tau|}] \tag{4.15}$$

where

$$\alpha \equiv \frac{1}{2\,[\xi_g\sqrt{\xi_g^2 - 1} - (\xi_g^2 - 1)]} \quad ; \quad \beta = \frac{1}{2\,[\xi_g\sqrt{\xi_g^2 - 1} + (\xi_g^2 - 1)]} \tag{4.16}$$

Since $a(t) \equiv \ddot{Z}(t)$ is a zero mean process, its autocorrelation coefficient function is given by

$$\rho_{aa}(\tau) = \frac{R_{aa}(\tau)}{R_{aa}(0)} \tag{4.17}$$

where $R_{aa}(0)$ is the variance of the process a(t). For both under- and overdamped cases, the variance can be expressed as

$$R_{aa}(0) = \mathrm{Var}[a(t)] = \frac{\pi\,\phi_0}{2}\,\frac{\omega_g}{\xi_g}\,(C_s^2 + 4\,C_d^2\,\xi_g^2) \tag{4.18}$$

Normalizing the continuous autocorrelation functions (4.14) and (4.15) by the variance of the process (Eq. (4.18)), the continuous autocorrelation coefficient functions are obtained.

Underdamped Case : $\xi_g < 1$

$$\rho_{aa}(\tau) = e^{-\xi_g\omega_g|\tau|}\,[\cos\omega_{gd}|\tau| + \frac{\xi_g}{\sqrt{1 - \xi_g^2}}\,\frac{(C_s^2 - 4\,C_d^2\,\xi_g^2)}{(C_s^2 + 4\,C_d^2\,\xi_g^2)}\,\sin\omega_{gd}|\tau|] \tag{4.19}$$

which can be converted into a more appropriate form for direct comparison with the discrete case (see Table 4.2):

$$\rho_{aa}(\tau) = e^{-\xi_g\,\omega_g\,|\tau|}\,[\frac{\cos(\omega_{gd}\,|\tau| - \mu_c)}{\cos(-\mu_c)}] \tag{4.20}$$

where

$$\mu_c = \tan^{-1}[\frac{(C_s^2 - 4\,C_d^2\,\xi_g^2)}{(C_s^2 + 4\,C_d^2\,\xi_g^2)}\,\frac{\xi_g}{\sqrt{1 - \xi_g^2}}]\,, \qquad -\frac{\pi}{2} < \mu_c < \frac{\pi}{2} \tag{4.21}$$

Overdamped Case : $\xi_g > 1$

$$\rho_{aa}(\tau) = e^{-\xi_g \omega_g |\tau|} \left[\alpha \frac{C_s^2 - 4\, C_d^2\, \xi_g^2\, (\xi_g - \sqrt{\xi_g^2 - 1})^2}{C_s^2 + 4\, C_d^2\, \xi_g^2} e^{\omega_g \sqrt{\xi_g^2 - 1}\, |\tau|} - \beta \frac{C_s^2 - 4\, C_d^2\, \xi_g^2\, (\xi_g + \sqrt{\xi_g^2 - 1})^2}{C_s^2 + 4\, C_d^2\, \xi_g^2} e^{-\omega_g \sqrt{\xi_g^2 - 1}\, |\tau|}\right] \tag{4.22}$$

where α and β are defined in Eq. (4.16). The above expression is also converted into a more appropriate form for direct comparison with the discrete case (Table 4.2) using the hyperbolic functions:

$$\rho_{aa}(\tau) = e^{-\xi_g \omega_g |\tau|} \left[\cosh\left(\omega_g \sqrt{\xi_g^2 - 1}\, |\tau|\right) + \frac{C_s^2 - 4\, C_d^2\, \xi_g^2}{C_s^2 + 4\, C_d^2\, \xi_g^2} \frac{\xi_g}{\sqrt{\xi_g^2 - 1}} \sinh\left(\omega_g \sqrt{\xi_g^2 - 1}\, |\tau|\right)\right] \tag{4.23}$$

Discrete / Continuous Model Relationship

The discrete-to-continuous and continuous-to-discrete parameter conversions can be established by comparison of the ACCF's of the discrete and continuous processes, a_t and $a(t)$, (see Table 4.2 and Eqs. (4.19) and (4.22)). Again, Zones 1 to 5 need separate considerations. The indexing parameter n for the discrete ACCF and the time lag τ of the continuous ACCF are related as follows:

$$\tau = n\,\Delta t \quad \rightarrow \quad n = \frac{\tau}{\Delta t} \tag{4.24}$$

where Δt is the sampling time interval.

Zone 1 :

By comparing the discrete ACCF for Zone 1 in Table 4.2 to the continuous ACCF for the underdamped case represented in Eqs. (4.19) and (4.20), the discrete and continuous parameter relationships are identified. They are summarized in Table 4.3. If both conditions

$$\omega_{gd} = \omega_g \sqrt{1 - \xi_g^2} \leq \frac{2\pi}{T_{g,min}} = \frac{\pi}{\Delta t} \tag{4.25}$$

$$0 \leq \lambda_d \leq \pi \tag{4.26}$$

are satisfied, the parameter relationships of Table 4.3 define a one-to-one mapping between the "ARMA space" $(\phi_1 , \phi_2 , \theta_1)$ and the "physical space" $(\omega_g , \xi_g , C_s/C_d)$. A (2x2) one-to-one mapping $(\phi_1 , \phi_2) \longleftrightarrow (\omega_g , \xi_g)$ is contained in the (3x3) one-to-one mapping $(\phi_1 , \phi_2 , \theta_1) \longleftrightarrow (\omega_g , \xi_g , C_s/C_d)$. This reduced mapping is illustrated in Fig. 4.4.

Zone 2 :

By comparing the discrete ACCF for Zone 2 (see Table 4.2) to the continuous ACCF for the overdamped case represented in Eq. 4.22, the discrete and continuous parameter relationships are established. This mapping is summarized in Table 4.4. The two-way conversion rules defined in Table 4.4 define a one-to-one mapping between the "ARMA space" $(\phi_1 , \phi_2 , \theta_1)$ and the "physical space" $(\omega_g , \xi_g , C_s/C_d)$. As for Zone 1, a reduced (2x2) mapping can be extracted from the (3x3) mapping. This reduced mapping is illustrated in Fig. 4.5.

Zone 3 :

The discrete ACCF corresponding to Zone 3 (see Table 4.2) cannot be discretely coincident with the continuous ACCF of Eq. (4.23) due to the simultaneous presence of the factors $(-1)^n$ and $(-1)^{n+1}$ in the discrete ACCF. Therefore, an ARMA(2,1) process defined in Zone 3 is not discretely coincident with a physical process generated by the SDOF oscillator shown in Fig. 4.3.

Zones 4 and 5 :

In Zones 4 and 5, the discrete (Table 4.2) and continuous (Eq. 4.23) ACCF's can be discretely coincident only for odd indexing parameter n $(\tau_n = n\Delta t$, n odd). The

corresponding parameter relationships are the same as for Zone 2 (Table 4:4), except for the following changes:

$$\sqrt{-\phi_2} \text{ and } \ln(-\phi_2) \text{ are replaced by } \sqrt{\phi_2} \text{ and } \ln(\phi_2) ,$$

$$\phi_2 = e^{-2\xi_s \omega_s \Delta t} ,$$

$$d = \frac{1}{2} \ln\left[- \frac{\phi_1 + \sqrt{\phi_1^2 + 4\,\phi_2}}{\phi_1 - \sqrt{\phi_1^2 + 4\,\phi_2}} \right] .$$

Notes :

1) It can be shown that the quantity $\sqrt{2K - K^2}$ appearing in the calculation of the damping ratio ξ_g in Zones 2, 4 and 5 is real-valued.

2) For all zones, the input displacement ratio C_s/C_d is not necessarily real-valued. Depending on the values of ϕ_1, ϕ_2 and θ_1, it can be complex-valued in which case the displacement loading of the underlying SDOF oscillator is imaginary and hence does not correspond to a physical process.

3) Discrete ARMA stochastic processes generated in Zones 3, 4 and 5 are not completely physically realizable, since the discrete coincidence, at all time-lags, of their ACCF with the ACCF of the continuous physical case is not possible. On the other hand, the processes generated in Zones 1 and 2 are physically realizable (except when $(C_s/C_d)^2 < 0$) and, conversely, all the physically realizable processes generated by the SDOF of Fig. 4.3 are mapped into Zones 1 (underdamped case) and 2 (overdamped case).

4) The reduced mapping between (ϕ_1 , ϕ_2) and (ω_g , ξ_g) for both the underdamped and overdamped cases can also be obtained by enforcing discrete coincidence between the homogeneous solutions of the ARMA difference equation (Eq. (4.1) with $e_k \equiv 0$) and the differential equation of motion (Eq. (4.10) with $X(t) \equiv 0$) [69].

5) The physical parameter ω_g can be interpreted as the ground predominant frequency at a given site. The parameter ξ_g gives an indication of the bandwidth of the frequency content of the earthquake model.

Equivalence Between Kanai-Tajimi and ARMA(2,1) Models

The well-known Kanai-Tajimi uni-modal stochastic earthquake model [47,88] corresponds to the subcase of the ARMA(2,1) model for which $C_s = C_d = 1.0$ (or $C_s/C_d = 1.0$). For firm ground conditions at moderate epicentral distance, Kanai and Tajimi have suggested the following parameter values: $\omega_g = 5\pi$ (or $T_g = 0.4$ sec) and $\xi_g = 0.60$. The parameters of the corresponding ARMA(2,1) model are computed as follows:

Physical parameters :

$$\omega_g = 5\pi$$
$$\xi_g = 0.60$$
$$C_s = C_d = 1.0$$
$$\phi_0 = 1.0 \quad \text{(input continuous white noise PSD)}$$

Using the continuous-to-discrete conversion rules of Table 4.3 for Zone 1, the following ARMA parameters are obtained:

$$\phi_1 = 1.604$$
$$\phi_2 = -0.686$$
$$\theta_1 = 0.767 \quad (\rho_1 = 0.774)$$

The input discrete white-noise variance σ_e^2 is obtained by equating the variances of the discrete and continuous processes (Eqs. (4.5a) and (4.18)):

$$\frac{1-\phi_2}{1+\phi_2}\,\frac{1+\theta_1^2-2\,\phi_1\,\theta_1}{(1-\phi_2)^2-\phi_1^2}\,\sigma_e^2 = \frac{\pi\,\phi_0}{2}\,\frac{\omega_g}{\xi_g}\,(C_s^2 + 4\,C_d^2\,\xi_g^2)$$

By substituting the above numerical values for the ARMA and physical parameters, the following discrete white-noise variance is obtained:

$$\sigma_e^2 = 39.08$$

The Kanai-Tajimi and ARMA(2,1) PSD's corresponding to the previous numerical values are shown in Fig. 4.6. The Kanai-Tajimi spectrum is defined for all frequencies ($0 \leq f < \infty$), whereas the ARMA(2,1) spectrum is defined for all frequencies smaller or equal to the Nyquist frequency ($0 \leq f \leq f_{Nyq} = 1/2\Delta t$). Therefore, if the value of the Kanai-Tajimi PSD at the Nyquist frequency is small, the Kanai-Tajimi and ARMA(2,1) PSD's practically coincide. Otherwise, the ARMA model reproduces the spectral density of the SDOF structural system up to the point where the influence of the aliasing phenomenon becomes apparent [34].

4.3 Higher Order ARMA Models

In the next two Sections, two different physical interpretations of higher order ARMA models will be presented: (i) the series-action (multiple-cascading) of uncoupled SDOF systems and (ii) the interpretation in terms of truly multi-degree-of-freedom systems.

4.3.1 Multiple Cascading of Low Order ARMA Models

As illustrated in Fig. 4.7, a discrete ARMA stochastic process $\{a_k\}$ generated by the multiple cascading-action of N SDOF oscillators is defined as follows:

$$\Phi_j(B)\, a_{j,k} = \Theta_j(B)\, a_{j-1,k}\,, \qquad j = 1\,,\ \cdots\ ,N \tag{4.27a}$$

$$a_{0,k} = e_k \tag{4.27b}$$

where $\{a_k\} \equiv \{a_{N,k}\}$, $\Phi_j(B)$ and $\Theta_j(B)$ are the autoregressive and moving-average polynomials of some low order ARMA models discretely coincident with SDOF linear oscillators, for example such as the one shown in Fig. 4.3, and $\{e_k\}$ is a discrete Gaussian white-noise with zero mean and constant PSD. Eqs. (4.27) can be developed recursively to obtain the resulting higher order ARMA operators:

$$a_{0,k} = e_k \tag{4.28a}$$

$$\begin{aligned} \Phi_1(B)\, a_{1,k} &= \Theta_1(B)\, a_{0,k} \\ &= \Theta_1(B)\, e_k \end{aligned} \tag{4.28b}$$

$$\begin{aligned}\Phi_2(B)\,a_{2,k} &= \Theta_2(B)\,a_{1,k}\\ &= \Theta_2(B)\,\Phi_1^{-1}(B)\,\Theta_1(B)\,e_k\\ \Phi_1(B)\,\Phi_2(B)\,a_{2,k} &= \Theta_1(B)\,\Theta_2(B)\,e_k \qquad (4.28c)\end{aligned}$$

.

.

.

$$\left\{\prod_{j=1}^{N}\Phi_j(B)\right\}a_k = \left\{\prod_{j=1}^{N}\Theta_j(B)\right\}e_k \qquad (4.28d)$$

The autoregressive (moving-average) polynomial of the resulting higher order ARMA model is the product of the autoregressive (moving average) polynomials of the low order ARMA models building the cascade. According to Eq. (3.13), the power spectral density of the higher order ARMA model of Eq. (4.28d) can be expressed as:

$$p(f) = 2\sigma_e^2 \frac{\left|\prod_{j=1}^{N}\Theta_j(e^{-i2\pi f})\right|^2}{\left|\prod_{j=1}^{N}\Phi_j(e^{-i2\pi f})\right|^2}$$

$$= 2\sigma_e^2\left\{\prod_{j=1}^{N}\frac{|\Theta_j(e^{-i2\pi f})|^2}{|\Phi_j(e^{-i2\pi f})|^2}\right\}, \qquad 0 \le f \le f_{Nyq} \qquad (4.29)$$

which is the product of the PSD functions of the low order ARMA models building the cascade.

Example :

Using the physically interpretable uni-modal ARMA(2,1) model as a "building block", a tri-modal ARMA(6,3) model is constructed by specifying the three physical parameters (ω_g , ξ_g , C_s/C_d) for each "mode". Using the continuous-to-discrete conversion relationships of Tables 4.3 or 4.4, the corresponding ARMA parameters (ϕ_1 , ϕ_2 , θ_1) are computed ($\Delta t = 0.02\,\text{sec}$).

$F_{g,1} = 2.0\text{Hz}$ (or $\omega_{g,1} = 4\pi$ rad/sec) $\qquad \phi_{1,1} = 1.722$

$\xi_{g,1} = 0.50 \qquad \phi_{2,1} = -0.778$

$(C_s/C_d)_{,1} = 1.0 \qquad \theta_{1,1} = 0.776$

$F_{g,2} = 5.0\text{Hz}$ (or $\omega_{g,2} = 10\pi$ rad/sec) $\qquad \phi_{1,2} = 1.440$

$\xi_{g,2} = 0.20 \qquad \phi_{2,2} = -0.778$

$(C_s/C_d)_{,2} = 1.0 \qquad \theta_{1,2} = 0.150$

$F_{g,3} = 7.0\text{Hz}$ (or $\omega_{g,3} = 14\pi$ rad/sec) $\qquad \phi_{1,3} = 1.174$

$\xi_{g,3} = 0.10 \qquad \phi_{2,3} = -0.839$

$(C_s/C_d)_{,3} = 1.0 \qquad \theta_{1,3} = 0.182$

The cascading of these three ARMA(2,1) models produce the following ARMA(6,3) model:

$$(1 - \phi_{1,1}B - \phi_{2,1}B^2)(1 - \phi_{1,2}B - \phi_{2,2}B^2)(1 - \phi_{1,3}B - \phi_{2,3}B^2)\,a_k =$$

$$(1 - \theta_{1,1}B)(1 - \theta_{1,2}B)(1 - \theta_{1,3}B)\,e_k$$

By substituting the above numerical values, the parameters of the ARMA(6,3) model become:

$$[1 - 4.336B + 8.587B^2 - 9.851B^3 + 6.879B^4 - 2.775B^5 + 0.508B^6]\,a_k =$$

$$[1 - 1.108B + 0.285B^2 - 0.021B^3]\,e_k$$

The tri-modal power spectral density of this ARMA(6,3) model is represented in Fig. 4.8 ($\sigma_e^2 = 1.0$ is assumed). It is important to notice that the (9x9) mapping between the physical modal parameters $[(\omega_{g,i}, \xi_{g,i}, (C_s/C_d)_{,i}), \quad i = 1,2,3]$ and the ARMA parameters $[\phi_1, \phi_2, \phi_3, \phi_4, \phi_5, \phi_6, \theta_1, \theta_2, \theta_3]$ is not one-to-one. Indeed, given a set of nine physical parameters, there is only one set of corresponding ARMA parameters. But, by changing the associations between the second order autoregressive polynomials and the first

order moving-average polynomials, different physical parameters are obtained for the same ARMA(6,3) model. For example, the above ARMA(6,3) model can be decomposed as follows:

$$(1 - \phi_{1,1} B - \phi_{2,1} B^2)\, a_{k,1} = (1 - \theta_{1,3} B)\, e_k$$

$$(1 - \phi_{1,2} B - \phi_{2,2} B^2)\, a_{k,2} = (1 - \theta_{1,2} B)\, a_{k,1}$$

$$(1 - \phi_{1,3} B - \phi_{2,3} B^2)\, a_{k,3} = (1 - \theta_{1,1} B)\, a_{k,2}$$

which results in the following physical modal parameters (using the discrete-to-continuous conversion relationships of Table 4.3):

$F_{g,1} = 2.0\text{Hz}$	$F_{g,2} = 5.0\text{Hz}$	$F_{g,3} = 7.0\text{Hz}$
$\xi_{g,1} = 0.50$	$\xi_{g,2} = 0.20$	$\xi_{g,3} = 0.10$
$(C_s/C_d)_{,1} = 5.94$	$(C_s/C_d)_{,2} = 1.0$	$(C_s/C_d)_{,3} = 0.0$

The frequency and damping parameters F_g and ξ_g which do not depend on the moving-average parameter θ_1 of the ARMA(2,1) model (see Table 4.3) are conserved, but the modal "input ratio" parameters C_s/C_d are different. Therefore, the decomposition of the above ARMA(6,3) model into three ARMA(2,1) models acting in cascade is not unique and this is a simple illustration of the general situation.

Nonstationary Case

The stochastic model represented by Eqs. (4.27) is stationary. However, it can be generalized to the nonstationary case without further complication as follows:

$$\Phi_{j,k}(B)\, a_{j,k} = \Theta_{j,k}(B)\, a_{j-1,k}\,, \qquad j = 1\,, \cdots\,, N \tag{4.30a}$$

$$a_{0,k} = \sigma_{e,k}\, e_k \tag{4.30b}$$

where $\Phi_{j,k}(B)$ and $\Theta_{j,k}(B)$ represent the time-varying autoregressive and moving-average discrete operators and $\sigma_{e,k}$ the standard deviation envelope of the driving noise process $\{e_k\}$. The model represented by Eqs. (4.30) includes both nonstationarity in intensity and

frequency content, and allows for multi-modal frequency content. A more general model than the one described in Eqs. (4.30) would consider several variance envelopes, one for each uni-modal component:

$$\Phi_{j,k}(B)\, a_{j,k} = \Theta_{j,k}(B)\, \sigma_{j,k}\, a_{j-1,k}\,, \qquad j = 1\,,\ \cdots\ ,N \tag{4.31a}$$

$$a_{0,k} = e_k \tag{4.31b}$$

The multiple cascading approach described in this Section is very useful for parametric modeling of earthquake motions in the context of analytical random vibration studies. It has the advantage of being intuitive for the "dynamicist" because of its interpretation in terms of natural frequencies and damping ratios. The time-varying discrete ARMA operators can be transformed into time-varying continuous differential operators [69].

4.3.2 Multi-Degree-of-Freedom (MDOF) Dynamic Systems

The result that the uniform samples of a one DOF system excited by white-noise is an ARMA model is due to Bartlett, 1940 [9]. Walker, 1950 [96], extended that result so that it is applicable to a general N degrees-of-freedom (N DOF) system. Therefore, ARMA processes can be interpreted as sampled outputs from randomly excited MDOF linear systems. Gersch and Liu [34] have shown that a scalar input-scalar output ARMA model duplicates the scalar output autocorrelation function of a uniformly sampled linear structural system with a multivariate white-noise input. More precisely, the scalar vibration response plus additive noise of a randomly excited N DOF structural system has an exact ARMA(2N,2N) representation. The same authors propose a computationally efficient method for computing the autocorrelation function of a randomly excited structural system and a procedure for the computation of the ARMA parameters from the output autocorrelation function. For example, in [34] it is shown that an ARMA(2,2) model duplicates the autocorrelation function of the uniformly sampled relative acceleration response of a SDOF linear oscillator excited by a zero mean white noise ground acceleration. The synthesized random vibration records using ARMA time series are valuable to develop procedures for

estimating the natural frequency and damping parameters of randomly excited linear structural systems (system identification techniques).

Gawronski and Natke [33] describe the possible ARMA models, which can be derived for linear vibrating systems. They show the almost certain existence of the minimal parameter ARMA model and present the classification of ARMA models for vibrating systems of which the Gersch model [34] is a subcase.

The stationary spectral input-output relationship of a cascading (or series) system of ARMA filters is multiplicative as shown by Eq. (4.29). On the other hand, the PSD function of the scalar response of a N DOF linear structure excited by a scalar white-noise (of constant PSD ϕ_0) takes the general form:

$$S(\omega) = \left|\sum_{i=1}^{N} \alpha_i H_i(\omega)\right|^2 \phi_0 \tag{4.32}$$

in which the coefficients α_i represent effective modal participation factors and the functions $H_i(\omega)$ are modal complex frequency response functions. The form of Eq. (4.32) shows that the ARMA model built from the cascading-action of N SDOF type ARMA models does not represent the single input-single output relationship of a randomly excited N DOF system whose modal properties are given by the N SDOF systems. Compared to the difficulty of the N DOF interpretation of a higher order ARMA model, it appears that the multiple-cascading approach, which corresponds to the series-action of uncoupled SDOF systems, furnishes a much easier and faster physical interpretation of a higher order ARMA model.

CHAPTER 5

APPLICATIONS OF STOCHASTIC GROUND MOTION MODELING

5.1 Introduction

The stochastic model identification procedures presented in Chapter 3 have been applied to two real earthquake records which are very different in nature. The first record corresponds to the North-South component of the moderate magnitude earthquake (M_L = 6.5), referred to as Event 39, recorded at the station E-02 of the SMART 1 accelerograph array in Taiwan [1]. Hereafter, this record will be referred to as E02NS. The epicentral distance of the recording site is 22 km. Station E-02 is classified as a rock site, which explains the high frequency content of the ground shaking (see Fig. 5.2(a)). The peak ground acceleration (PGA) is 0.20g and the strong motion duration is short (about 5 seconds). The ground acceleration, velocity and displacement time histories and their corresponding Fourier amplitude spectra are shown in Figs. 5.1 and 5.2, respectively. As can be seen from Fig. 5.2(a), most of the energy of the ground acceleration is contained in the wide frequency band [2-11 Hz] with an overall predominant frequency of approximately 9 Hz. A gradual change in instantaneous frequency content can be observed in Figs. 5.1(a) and (b). The various properties of this record and of the underlying earthquake are summarized in Tables 5.1 and 5.2. This earthquake signal has been digitally recorded with a time sampling interval of 0.01 second. A baseline correction has been applied to it by using a high-pass, two-way Butterworth filter set at approximately 0.10 Hz (see Section 5.3).

The second record is the North-South component of the 1940 Imperial Valley earthquake recorded at El Centro, California. The source mechanism of this earthquake was a strike lateral slip on the Imperial Valley fault. The corresponding epicentral distance is 12 km for a moderate earthquake magnitude of 6.4. The soil site condition at the recording

station is classified as a deep firm alluvium deposit. The PGA of this record is 0.348g. Only the first 35 seconds of the original record are considered in this study. The ground acceleration, velocity and displacement time histories and their corresponding Fourier amplitude spectra are shown in Figs. 5.3 and 5.4, respectively. Most of the energy of the ground acceleration is contained in the frequency band [0-5 Hz] with an overall predominant frequency of about 2.0 Hz (see Fig. 5.4(a)). The fault rupture process of the Imperial Valley earthquake has been studied [89,90] and appears to be a very complex superposition of several subevents (see Fig. 5.3(a)). As can be seen from Fig. 5.3(a), the instantaneous frequency content of the ground acceleration changes very rapidly from low frequencies to high frequencies or vice-versa. The characteristics of this record and of the causative earthquake are summarized in Tables 5.1 and 5.2. This record is digitized with a time sampling interval of 0.02 second. For the baseline correction, it has been band-pass filtered between 0.070 Hz and 25 Hz according to the standard CALTECH procedure [44].

5.2 Earthquake Analysis

E02NS record

Two low order time-varying ARMA models, namely an ARMA(2,1) and an ARMA(4,2), have been fitted to the E02NS record using the Kalman filtering technique described in Section 3.5. The moving window estimation technique (see Section 3.4) has also been applied for the estimation of the ARMA(2,1) model for the purpose of comparison with the Kalman filter solution. These two models have been estimated by implementing the Kalman filter in the reverse direction, from the end to the beginning of the earthquake record. Since the strong shaking portion of the E02NS record is closer to the beginning than the end of the record, the Kalman filter applied in the reverse direction has more time to tune itself with the data prior to reaching the most important segment of the record.

ARMA(2,1) Model:

To obtain an estimate for the initial values[1] of the ARMA parameters, a maximum likelihood estimation has been performed on the last 100 points of the amplitude-demodulated record shown in Fig. 5.6. The standard-deviation envelope of the E02NS record, used for amplitude-demodulation, has been computed as the "two-stage weighted moving average estimate" (using n = 30) described in Section 3.4 and is shown in Fig. 5.5. For the Kalman filtering, a trade-off value of $\sigma_\delta = 0.008$ was selected after several trials. A σ_δ which is too small produces a stable but slow learning rate of the Kalman filter, which is unable to capture sharp changes in the structure of the earthquake signal. On the other hand, a σ_δ which is too large yields a fast learning rate, which results in very irregular and unrealistic model parameter time histories. For application of the moving window technique, the following parameters have been used (see Section 3.4): $n_{wd}\Delta t = 1.0$ sec, $n_{slid}\Delta t = 0.25$ sec. The time histories of the ARMA(2,1) parameter estimates ($\hat{\phi}_1$, $\hat{\phi}_2$ and $\hat{\theta}_1$) and the standard-deviation envelope estimate $\hat{\sigma}_e$ of the driving noise are displayed in Fig. 5.7 for the Kalman algorithm (solid line) and the moving window technique (dashed line). The results obtained using the two different methods have the same general trends.

By using the discrete-to-continuous conversion relationship presented in Section 4.2, the time histories of the physical parameters corresponding to the ARMA(2,1) model parameters of Fig. 5.7 have been computed and are shown in Fig. 5.8. From Fig. 5.8(a), it can be seen that the predominant frequency, F_g, of the ground acceleration drops from 14 Hz to 7 Hz in the first 4 seconds of the earthquake, then varies between an average of 8 Hz and 6 Hz in the middle portion of the earthquake, and finally drops to an average of 4 Hz at the end of the earthquake. In Fig. 5.8(b), the time history of the damping ratio parameter ξ_g indicates that the frequency bandwidth of the ground acceleration decreases for the first 3 seconds of the earthquake and then increases almost monotonically until the end of the record. The underlying SDOF model becomes overdamped ($\xi_g > 1$) only in the

(1) At the end of the record, since the filter is run in the reverse direction.

last few seconds of the record. Fig. 5.8(c) displays the evolution in time of the input ratio parameter " $\mathrm{sign}((C_s/C_d)^2)((C_s/C_d)^2)^{1/2}$ ". It is observed that the input of the underlying SDOF model is imaginary ($(C_s/C_d)^2 < 0$) until 8 seconds into the earthquake and then becomes real with a large average C_s/C_d ratio, which means physically that the dashpot support of the SDOF model shown in Fig. 4.3 is almost fixed.

Using the time histories of the ARMA parameters obtained with the Kalman filter, the normalized ARMA(2,1) evolutionary power spectral density (EPSD) estimate (see Eq. (3.20)) corresponding to the amplitude-demodulated record of Fig. 5.6 can be evaluated and is presented in Fig. 5.9. This illustrates the change of the frequency content of the earthquake in time, referred to as "spectral nonstationarity".

ARMA(4,2) Model:

For the estimation of the ARMA(4,2) model using Kalman filtering, the following parameters have been selected: $n=50$ for the variance envelope estimation and $\sigma_\delta = 0.012$ for the "random walk" of the model parameters. The time histories of the ARMA(4,2) parameter estimates ($\hat{\phi}_1$, $\hat{\phi}_2$, $\hat{\phi}_3$, $\hat{\phi}_4$, $\hat{\theta}_1$ and $\hat{\theta}_2$) are shown in Fig. 5.11. From this figure, it can be concluded that after 8 seconds of ground shaking, an ARMA(1,2) model would be sufficient, since $\hat{\phi}_2$, $\hat{\phi}_3$ and $\hat{\phi}_4$ are very small. The convergence of the iterative Kalman filtering scheme is illustrated in Fig. 5.12 via the convergence of the standard deviation envelope estimate $\hat{\sigma}_e$ of the driving noise. Typically, convergence is obtained in only a few iterations provided the amplitude of the scaled standard deviation envelope of the original record used in the first iteration is reasonable. The normalized ARMA(4,2) EPSD estimate of the E02NS earthquake record (presented in Fig. 5.10) shows the same trend as the ARMA(2,1) EPSD estimate (see Fig. 5.9) with more low frequency energy in the second half of the record.

El Centro 1940, N-S Component

In Ref. [19], the East-West component of the El Centro 1940 record was satisfactorily

fitted to a piecewise stationary ARMA(2,1) model. In the present study, an ARMA(2,1) model has also been chosen to represent the North-South component of the same earthquake. A sliding time window of 3.20 seconds (n=80) was used to estimate the record's standard-deviation envelope shown in Fig. 5.13 and to amplitude-demodulate the original earthquake record (see Fig. 5.14). For the "random walks" of the model parameters, a standard deviation $\sigma_\delta = 0.005$ was chosen. For application of the moving window technique, the following parameters were used:

$n_{wd}\Delta t = 5.0$ seconds, $n_{slid}\Delta t = 0.50$ second.

The time histories of the ARMA(2,1) parameter estimates and the standard-deviation envelope estimate of the driving noise are shown in Fig. 5.15 for both the Kalman filter (solid line) and the moving window technique (dashed line). The results obtained using the two methods exhibit the same overall trends, except within the time segments [8-12 seconds] where there is a significant difference. The parameters of the underlying physical model are presented in Fig. 5.16. The predominant frequency of the ground acceleration is contained in the range 2.0-2.5 Hz without large overall changes, but several sharp local changes such as those at t=1.50, 6.50, 8.50, 11.50 and 13.50 seconds. These sharp local changes of model parameters coincide with sharp changes in the instantaneous frequency content visible in the accelerogram of Fig. 5.3(a).

From Fig. 5.16(b), it is apparent that the bandwidth of the frequency content of the ground acceleration is larger in the first half of the record (larger ξ_g values). The underlying SDOF model is underdamped ($\xi_g < 1$), except at around 2 and 12 seconds where the ground acceleration (Fig. 5.3(a)) exhibits relatively long period pulses. Fig. 5.16(c) indicates that the input of the underlying SDOF model is real ($(C_s/C_d)^2 > 0$) at all times and that the input ratio parameter $C_s/C_d \simeq 4$ on average. The ARMA(2,1) EPSD estimate of the amplitude-demodulated record of Fig. 5.14 is illustrated in Fig. 5.17.

5.3 Earthquake Simulation

To study the probabilistic structure of both ground motion and structural response parameters associated with a given target earthquake process, a family of artificial earthquake ground motions must be generated. For statistical convergence requirements, a sample size of 100 artificial earthquakes has been selected. Each artificial earthquake is constructed from a discrete, zero mean, unit variance, Gaussian white-noise. Each sequence of computer generated uncorrelated pseudo-random numbers corresponds to a seed number. Each call to the IMSL subroutine GGNML requires a seed number and returns the desired discrete white-noise with a seed number to be used for the next call to the subroutine. The use of the seed numbers returned by GGNML ensures statistical uncorrelation across the different white sequences. A set of 100 seed numbers to be used for all target earthquakes was obtained by calling the subroutine GGNML 100 times consecutively and storing the returned seed numbers in the vector seed(100), starting with seed(1)=1.0.

The artificial ground acceleration records shown in Fig. 5.19 represent the same realization from the ARMA(2,1) model fitted to the E02NS record, but correspond to different high-pass filters. The four filters used are summarized in Table 5.3 and shown in Fig. 5.18. The solid lines represent the discrete filters actually implemented digitally (frequency resolution = Δf = 1/1850(0.01 sec) = 0.054 Hz) whereas the dashed lines represent the corresponding theoretical continuous filters. Notice that the Butterworth Filters I, II and III correspond to an increasing cut-off frequency (from about 0.09 Hz to about 0.14 Hz). It should be noted that the Brune's model (Filter IV) has a wider range of action than the Butterworth filters; it still reduces the 0.3 Hz frequency component by 10%. Figs. 5.20 and 5.21 show the relative influence of these four high-pass filters and the baseline correction algorithm described in Section 3.6 on the resulting artificial ground velocity and displacement, respectively. By comparing this artificial ground motion (acceleration, velocity and displacement) with the target record shown in Fig. 5.1, the following observations can be

made: (i) these high-pass filters have a very small influence on the ground acceleration time history, (ii) they have a small, but observable influence on the ground velocity time history and (iii) they have a large influence on the ground displacement time history. The magnitude of the ground displacement time history obtained using Filter III is close to the magnitude of the target ground displacement (Fig. 5.1(c)). Filter III acts on frequency components up to 0.17 Hz, which corresponds to the critical excitation range of structures having a fundamental natural period of about 6.0 seconds. Therefore, this particular ARMA(2,1) model covers a meaningful range of excitation periods up to about 6.0 seconds. This illustrates the known defect [69,82] of the low order ARMA models, namely a low frequency error. Figs. 5.22-24 are analogous to Figs. 5.19-21, but for a single realization from the ARMA(4,2) model fitted to the E02NS record and using the same initial discrete white-noise. Based on this particular realization, it can be concluded that the low frequency error is larger for the fitted ARMA(4,2) model than for the ARMA(2,1) model.

Figs. 5.25-26 present two single realizations of ground acceleration, velocity and displacement from the ARMA(2,1) model fitted to El Centro 1940 using the Butterworth filter shown in Fig. 5.27. Again, in this case, the low frequency error of low order ARMA models appears in the artificial ground velocities and displacements.

5.4 Model Checking

First Level of Model Checking

The first level of model checking is performed on the converged sequence of normalized residuals given by the iterative Kalman filtering algorithm. Two tests for uncorrelation (or tests of randomness) are accomplished, one in the time domain by means of the sample autocorrelation coefficient function (ACCF) defined in Eq. (3.44) and the other in the frequency domain using the periodogram estimate of the PSD of the residual process.

E02NS record

The time history of the residuals produced by the fitting of the ARMA(2,1) model is shown in Fig. 5.28(a). The residuals sample ACCF $\hat{\rho}(k\Delta t)$ calculated up to a lag-time equal to one-fifth of the E02NS record duration is plotted in Fig. 5.28(b). Figs. 5.28(c) and (d) display, in decimal and logarithmic scales, the unsmoothed residuals periodogram using a Parzen taper (Eq. (3.52)). Fig. 5.29 is similar to Fig. 5.28, but corresponds to the fitted ARMA(4,2) model. For comparison with Figs. 5.28 and 5.29, the time history, sample ACCF and periodogram of a computer generated discrete white-noise sequence with the same duration and time sampling interval as the E02NS record have been plotted in Fig. 5.30. The two parallel dashed lines of Figs. 5.28(b), 5.29(b) and 5.30(b) define the approximate 95% confidence interval for the sample ACCF $\hat{\rho}(k\Delta t)$ under the hypothesis that the residual process is purely random (see Eq. (3.46)). The residuals associated with the ARMA(2,1) model fitted to the E02NS record show some correlation structure for small time-lags ($\tau < 0.20$ seconds) apparent in Fig. 5.28(b). By comparing with Fig. 5.30(b), it is observed that the overall magnitude of the residuals sample ACCF is larger than in the case of a true discrete white-noise. Figs. 5.28(c) and (d) also reveal a non-uniformity of the PSD of the underlying residual process, a partial spectral gap (or spectral lack) between 25 and 40 Hz. Figs. 5.30(c) and (d) show the uniform frequency distribution of the variance in the case of an underlying "true" white-noise process. By comparing Figs. 5.28 and 5.29, it can be concluded that based on the analysis of the residuals, the fitted ARMA(4,2) model is better than the ARMA(2,1) model, but still is not a perfect model.

In the case of the E02NS record, the 95% confidence interval for the sample ACCF $\hat{\rho}(k\Delta t)$ is (Eq. (3.46)): $\pm 2\sqrt{1/N} = \pm 2\sqrt{1/1850} = \pm 0.0465$. The results of the Portmanteau and "95% confidence interval" tests are summarized in Table 5.4 for the residuals of the ARMA(2,1) and ARMA(4,2) models as well as for three computer generated discrete Gaussian white-noises of the same duration. The discrete white-noise #1 is shown

in Fig. 5.30. The results of these statistical tests confirm the superiority of the ARMA(4,2) model over the ARMA(2,1) model since the ARMA(4,2) model has a smaller Portmanteau statistic value and a smaller percentage of $\hat{\rho}(k\Delta t)$ outside the 95% confidence interval. To visualize the uncorrelation or whitening effect of the ARMA filters, the sample ACCF and the unsmoothed periodogram of the amplitude-demodulated E02NS record (Fig. 5.6) have been plotted in Fig. 5.31.

Finally, Figs. 5.32 and 5.33 show the results of the normality tests on normal probability paper for the residuals produced by the fitting of the ARMA(2,1) and ARMA(4,2) models. For both cases, the linearity of the cumulative distribution of the residuals indicates that the underlying populations of residuals are well represented by the Gaussian distribution. Therefore, the assumption of the ARMA model of the earthquake is verified.

El Centro 1940, N-S Component

The results concerning the residuals check are presented for the ARMA(2,1) model fitted to the El Centro 1940 record. Fig. 5.34 displays the time history of the residuals, their sample ACCF and their unsmoothed periodogram computed using a Parzen taper. Here again, the two dashed lines of Fig. 5.34(b) define the approximate 95% confidence interval for the sample ACCF $\hat{\rho}(k\Delta t)$, which in this case is: $\pm 2\sqrt{1/N} = \pm\sqrt{1/1750} = \pm 0.0478$. The results of the Portmanteau and "95% confidence interval" tests evaluated from the sample ACCF $\hat{\rho}(k\Delta t)$ of Fig. 5.34(b) are summarized in Table 5.5, together with the test values corresponding to three computer generated discrete white-noise records of the same duration. These statistical test results show that the residuals obtained by fitting the ARMA(2,1) model are fairly uncorrelated, which is also visible on the periodogram of Figs. 5.34(c) and (d). To illustrate the uncorrelation effect of the fitted ARMA(2,1) model, the sample ACCF and periodogram of the amplitude-demodulated El Centro record of Fig. 5.3(a) are presented in Fig. 5.35.

From the results of the normality test presented in Fig. 5.36, it is seen that the underlying population of residuals is not Gaussian. The results presented in Chapters 7 and 8

will indicate if the lack of the Gaussian property of the driving noise has some influence on the distribution of the structural response parameters.

Second Level of Model Checking

The second level of model checking is performed on simulated earthquake ground motions (single or ensemble) to verify the extent to which they resemble the target real earthquake ground motion.

E02NS record

A single realization (acceleration, velocity and displacement) from the fitted ARMA(2,1) and ARMA(4,2) models has been presented in Figs. 5.19-24. The Fourier amplitude spectra (acceleration, velocity and displacement) of the same artificial earthquake baseline-corrected using Filter I are plotted in Figs. 5.37 and 5.38 for the ARMA(2,1) and ARMA(4,2) models, respectively. By comparing Figs. 5.37(a) and 5.38(a) with Fig. 5.3(a), it can be concluded that the overall frequency content of the ground acceleration over the entire duration of the record is well reproduced. By comparing Figs. 5.37(b-c) and Figs. 5.38(b-c) with Figs. 5.3(b-c), the aforementioned low frequency error of the ARMA models can be observed. The artificial motions are too rich in very low frequency components which increase in amplitude by $1/f$ at every time integration. These two ARMA-simulated accelerograms have been analyzed, utilizing the estimation algorithm used for the target real earthquake from which they are derived. The results are presented in Figs. 5.39 and 5.40 for the ARMA(2,1) and ARMA(4,2) models, respectively. It appears that the "true" model parameters can be recovered from the artificial realizations with a relatively high degree of accuracy and stability.

The normalized ARMA evolutionary power spectral density (EPSD) estimates derived from the Kalman filter results are compared to the normalized moving periodogram estimate (see Section 3.7) of the EPSD of the E02NS record. This comparison is shown in Fig. 5.41. It is observed that when a single predominant peak is present in the periodo-

gram estimate, it is captured accurately by both the ARMA(2,1) and ARMA(4,2) models (see Figs. 5.41(a),(b) and (c)). On the other hand, when several spectral peaks of the same magnitude are present in the periodogram estimate, both the ARMA(2,1) and ARMA(4,2) EPSD estimates exhibit a single peak whose position and shape can be interpreted as some weighted average of the positions and shapes of the spectral peaks of the periodogram (see Figs. 5.41(d), (e) and (f)). Even though the ARMA(4,2) model is bi-modal (can develop two spectral peaks), its Kalman filter estimate, in this particular example, appears to be uni-modal at all times.

Using a sample of 100 artificial earthquake ground motions, the second order statistics (mean and standard-deviation) of 10 traditional ground motion parameters used to characterize earthquake ground motions are computed. These ground motion parameters are:

- Peak ground acceleration (PGA), velocity (PGV) and displacement (PGD);
- the peak motion ratios: PGV/PGA and PGD/PGA;
- root-mean-square acceleration (RMSA), velocity (RMSV) and displacement (RMSD) defined as:

$$\mathrm{RMSX} = \left[\frac{1}{t_d} \int_0^{t_d} x_g^2(t)\, dt \right]^{\frac{1}{2}} \tag{5.1}$$

  where $x_g(t)$ is either the ground acceleration, velocity or displacement and t_d represents the duration of the earthquake record;
- Arias intensity(1) (AI) defined as:

(1) The Arias intensity is directly related to the root-mean-square acceleration as follows:

$$\mathrm{AI} = \frac{\pi}{2g} t_d (\mathrm{RMSA})^2 .$$

However, the Arias intensity parameter carries some insight to the effect of earthquake ground motions on structural response. Housner and Jennings [42] have shown that for a given earthquake and critical damping ratio ξ, the earthquake input energy dissipated by a series of elastic single-degree-of-freedom oscillators with fundamental frequencies uniformly distributed between zero and infinity can be expressed as :

$$W_F = \frac{\cos^{-1} \xi}{\sqrt{1 - \xi^2}} \int_0^{\infty} a_g^2(t)\, dt$$

$$AI = \frac{\pi}{2g} \int_0^{t_d} a_g^2(t)\, dt \tag{5.2}$$

where $a_g(t)$ is the ground acceleration time history.

- Housner spectral intensity (SI) defined as:

$$SI_\xi = \int_{0.10}^{2.50} PSV(\xi, T)\, dT \tag{5.3}$$

where $PSV(\xi, T)$ represents the pseudo-spectral velocity for the earthquake record under consideration and for a SDOF oscillator of damping ratio ξ and undamped natural period T.

For both the ARMA(2,1) and ARMA(4,2) earthquake models, the statistics of the above ground motion parameters are presented in Table 5.6, where they can be directly compared to the corresponding values of the target E02NS record. It is found that:

- For both ARMA models, the statistical interval represented by the "mean ± standard deviation" contains the target parameter in the case of only four ground motion parameters which are: PGA, PGV, PGV/PGA and SI.

---

where W_F is referred to as "frequency ensemble work". The special case of zero damping gives the Arias intensity (except for the factor 1/g) obtained by Arias in developing a measure of seismic intensity :

$$AI = \frac{\pi}{2g} \int_0^{\infty} a_g^2(t)\, dt$$

Because the frequency ensemble work is almost unaffected by large changes in the amount of damping for linear structures, it seems probable that W_F may be relatively insensitive to the mechanism by which energy is dissipated. It implies that the previous result on input energy could apply to the case of an hysteretic energy dissipation mechanism modeled as equivalent viscous damping. If the earthquake energy input is integrated with respect to period, T, of the SDOF oscillators instead of the frequency, ω, for an undamped system, the "period ensemble work", W_T, is defined :

$$W_T = \pi^2 \int_0^{\infty} v_g^2(t)\, dt$$

The integral of the squared ground acceleration and the integral of the squared ground velocity are broadband measures of the energy input capability of the ground motions, the former giving more weight to higher frequencies than the latter. Since they are energy inputs integrated over all frequencies or all periods, they cannot be related directly to damage observed in a single structure.

- If the target values of the ground motion parameters are compared to the corresponding values generated by the ARMA models, it is concluded that the PGA, RMSA and AI parameters are underestimated by both ARMA models, whereas the other parameters are overestimated by both ARMA models.
- The ground displacement related parameters (PGD, PGD/PGA, RMSD) are largely overestimated by the ARMA models due to their low frequency error.
- Some ground motion parameters are better represented statistically by the ARMA(2,1) model (PGV/PGA, PGD/PGA, RMSA), whereas some others are better represented by the ARMA(4,2) model (PGA, PGD, AI and SI).
- The coefficients of variation of the ground motion parameters generated by the ARMA(4,2) model are systematically larger or equal to their ARMA(2,1) counterparts.

El Centro 1940, N-S Component

A single realization (acceleration, velocity and displacement) from the fitted ARMA(2,1) model has been presented in Fig. 5.25 (Section 5.3). The ground acceleration, velocity and displacement Fourier amplitude spectra of this artificial earthquake are shown in Fig. 5.42. By comparing these Fourier amplitude spectra with those of the target record plotted in Fig. 5.4, a low frequency error appears. This low frequency error is responsible for the excess in amplitude of the artificial ground velocity and displacement. However, the overall frequency content of the ground acceleration is well duplicated. As shown in Fig. 5.43, the analysis of this artificial record is able to reproduce the general trends of the "true" parameters used for its simulation.

The comparison between the normalized ARMA(2,1) EPSD estimate and the normalized periodogram estimate of the EPSD of El Centro 1940 is displayed in Fig. 5.44. It is observed that the ARMA(2,1) model is able to capture the spectral nonstationarity fairly well.

The ground motion parameters of the El Centro 1940 target record and the second order statistics obtained by simulation of 100 artificial earthquakes are contained in Table 5.7. By comparing the target values and the statistics of the ground motion parameters, it is found that:

- The PGA, RMSA, AI and SI parameters are very well described statistically by the ARMA(2,1) representation of the El Centro record. All the other ground motion parameters are well overestimated by the ARMA(2,1) model due to its low frequency error.

5.5 Probability Distribution of Ground Motion Parameters

In this Section, the previously fitted stochastic earthquake models are used to simulate the target earthquake processes and to investigate the statistical distribution of the ground motion parameters defined in Section 5.4. The sample size of artificial earthquakes used for simulation depends on the statistical convergence characteristics. As a preliminary task, the convergence of the second order statistics of the ground motion parameters versus the number of artificial earthquakes used is examined. As an illustration, Figs. 5.45(a), (b) and (c) show the convergence of the statistical mean and standard-deviation of three ground motion parameters, namely PGA, RMSA and SI, in the case of the ARMA(2,1) simulation of the El Centro 1940 record. The solid lines correspond to the set of seed numbers used throughout this study, whereas the dashed lines correspond to a different set of seed numbers. The second set of seed numbers was used to check that the second order statistics converge to the same values for two sets of seed numbers, i.e., the asymptotic behavior of the second order statistics is independent of the set of seed numbers. In the examples of Fig. 5.45, it is observed that (i) the statistics of the RMSA parameter converge relatively rapidly (at a sample size of about 50), (ii) the statistics of the PGA and SI parameters oscillate slightly for a large sample size and converge within a few percent (3-4%) at 100 artificial earthquakes.

The probability distributions of the ground motion parameters are plotted as histograms[1] in Figs. 5.46-48 for the ARMA(2,1) and ARMA(4,2) simulations of E02NS and for the ARMA(2,1) simulation of El Centro 1940, respectively. Several probability distribution functions, namely Rayleigh, Exponential, Normal and Gumbel type I, have been fitted to the simulated data, but the lognormal distribution proved to be the most satisfactory. Fig. 5.49 shows the lognormal distribution fits of the data on probability paper in the case of the ARMA(2,1) simulation of El Centro. By comparing Figs. 5.46 and 5.47, it appears that the detailed shape of the histograms depend on the order of the ARMA model fitted to a given target earthquake record. However, the overall shape and bounds of the distributions are relatively independent of the model order.

For a given earthquake process, the RMSA is much less variable (much lower coefficient of variation) than the PGA, which has been used extensively in the past to characterize the damage potential of earthquake ground motions. This statement can be verified in Figs. 5.46(a) and (d), 5.47(a) and (d), 5.48(a) and (d) and also on Fig. 5.45(a) and (b). The second order statistics of the ground motion parameters (mean, standard deviation, coefficient of variation) for the three earthquake processes considered in this study are summarized in Tables 5.6 and 5.7.

---

(1) In the figures representing histograms, the ordinate "freq" means the frequency of occurrence in a given interval of the quantity represented along the abscissa.

CHAPTER 6

STRUCTURAL SYSTEMS, RESPONSE PARAMETERS AND DAMAGE MODELS

6.1 Structural Systems

World-wide seismic design procedures rely implicitly or explicitly on ductile inelastic behavior of structures to withstand severe earthquake motions. This ductile hysteretic behavior can provide an economical way to dissipate the earthquake input energy in the structure without causing structural failure or collapse. In order to understand the nature of the inelastic seismic behavior of structures, comprehensive nonlinear mathematical models of real structures are needed. These inelastic structural models are also useful to design new structures and assess the safety of existing structures.

In general, the restoring forces of a complex structure, modeled as a multi-degree-of-freedom system, depend on the deformation time histories of all its structural components in a very complicated way. In this research, the approach has been to use, as a first step, idealized nonlinear single-degree-of-freedom representations of structures (Fig. B.1). The SDOF idealization was used to:

1) identify the effects and relative importance of the various factors which influence the stochastic response of these simple systems;
2) identify general patterns and trends in stochastic inelastic seismic response behavior of structures;
3) provide foundation and guidance for the study of more complex structures.

Although the concepts of coordinate reduction from MDOF to SDOF systems are usually applied to linear elastic systems, a good deal of research has been conducted on SDOF representations of MDOF systems for use in nonlinear response analysis [11,37,79,80]. Such SDOF representations are able to capture the overall inelastic behavior of a complex structure.

The structural damping characteristics are modeled by the viscous dashpot of the SDOF structural model. The amount of viscous damping is controlled by the damping ratio ξ (see Appendix B and Table B.1). Four simplified piecewise linear resistance-deformation relationships have been used to characterize the nonlinear spring of the SDOF systems, namely : the popular bilinear hysteretic model of the softening type (Fig. B.2a), Clough's stiffness degrading model(1) (Fig. B.2b), the slip model (Fig. B.2c) and the bilinear elastic model (Fig. B.2d). A possible cycle of deformation for each diagram is shown by arrows or by consecutively numbered points. The four hysteretic models considered have a bilinear skeleton curve characterized by a pre-yield stiffness k_0, a post-yield stiffness αk_0 and a yield force R_y or yield displacement U_y. The ratio of the post-yield stiffness to the pre-yield stiffness, α, is called the strain hardening (or softening) ratio. The post-yield stiffness of the bilinear model, αk_0, can be positive (positive bilinear model), negative (negative bilinear model) or null. A null post-yield stiffness corresponds to the classic elastoplastic restoring force model.

A stable non-degrading elastoplastic or positive bilinear model is often used to represent the restoring force characteristics of a steel moment-resisting frame in the absence of local buckling. When the frame is subjected to high axial force, a negative bilinear model is sometimes useful to account for the P-Δ effect (negative first order geometric stiffness). For simplicity, this bilinear model is sometimes used for a reinforced-concrete (R/C) frame. Clough's stiffness degrading model allows for the effect of stiffness degradation caused by load reversals in inelastic ranges in an R/C moment-resisting frame (that yields by flexure). This model is also representative of R/C shear wall behavior dominated by flexural deformations [95]. The slip model approximates the behavior of steel-braced frames (with a significant brace buckling effect) and also the behavior of R/C members in which shear distortion or bond-slip action dominates overall behavior (e.g., short shear walls). The bilinear elastic resistance-deformation relationship is representative of

(1) In fact, this is a modified version of the original Clough's stiffness degrading model which is defined in [21].

unbonded R/C behavior, uplifting behavior of the foundation of a structure (e.g., multi-story shear wall) and the moment-curvature relationship for a prestressed concrete beam [95]. The bilinear elastic model has been included in this study mainly to identify, by comparison with the bilinear hysteretic case, the influence of the hysteretic energy dissipation mechanism on the structural response statistics (response amplitude and distribution).

6.2 Structural Damage Characterization

During a major earthquake, disregarding instability, failure of a steel structure may be characterized by one of three mechanisms [52]. The first and most commonly recognized is the largest excursion failure where failure is due to the exceedence of a strength or deformation capacity level in a single excursion. This failure mechanism is at the origin of the first passage problem handled by time-varying reliability theory [25,56,65]. The second mechanism is fatigue failure which happens upon the exceedence of a deterioration level of a structural member caused by several excursions into the plastic range. Therefore, this failure mechanism is associated with a cumulative type of damage. The third failure mechanism, incremental collapse, comes about when resistance is lost due to the incremental drifting of the response in one direction.

Under earthquake loadings, R/C structures are generally damaged by a combination of repeated stress reversals and high stress excursions [72]. These two sources of damage correspond to the first and second failure mechanisms described above for seismic loading of steel structures.

Within the scope of structural damage characterization and assessment, several definitions need to be identified and are borrowed from Ref. [51].

Failure: In the context of this study, failure may be defined as the inability of a structure to provide its intended resistance function. Thus, failure presumes a severe deterioration in strength or unacceptable loss of resistance.

Deterioration: This term refers to a gradual loss of strength or stiffness under cyclic load (or deformation) reversals. Since deterioration often occurs at a slow rate, it may be

acceptable until a limit value of acceptable deterioration is reached. The limit value which identifies failure could be defined as a certain percentage of the undeteriorated strength (or stiffness) of a structure or structural component.

Damage: Within the context of this study, damage is defined as a cumulative parameter which measures the "closeness to failure". Every inelastic excursion is presumed to cause damage in a component, since it accentuates a local failure mechanism (e.g. crack propagation, local instability) and decreases the safety against failure. Failure is presumed to take place when the cumulative damage caused by a series of inelastic excursions reaches a target value depending on the calibration of the damage model.

In earthquake engineering, damage prediction has become an important problem. A damage theory and damage models for rational quantification of the seismic damage imparted to structures are needed. Such tools are necessary (i) to evaluate the seismic safety of new and existing structures against future potential earthquakes or alternatively the potential destructiveness of future earthquakes and (ii) to develop damage-limiting or damage-control procedures for earthquake-resistant design. For example, past seismic damage of R/C structures has shown that (i) building collapse is caused mainly by damage concentration, especially in the first story and (ii) buildings sustaining only minor damage are characterized by a more uniform spatial distribution of damage over the structure. This implies that the seismic performance of buildings can be improved if uniform potential damage distribution can be guaranteed in the design stage by using damage-control earthquake-resistant design procedures. These procedures would help in the proper selection of strength and ductility of the structural members.

The techniques which have been used in damage prediction can be subdivided in two types [74]. The first type is based on the balance between some demand on the structure and its corresponding capacity, and the second on the degradation of some structural property. For each type of technique, several damage parameters representative of the damage state can be computed. Damage parameters must be response quantities which can be

calculated from the results of a dynamic structural analysis. The challenge is to find some which correlate well with actual physical damage observed in structures. In the "demand vs. capacity" procedure, possible choices for the demand and capacity include strength, displacement, deformation and energy dissipation. In the "degradation procedure", possible choices for the structural property include stiffness, strength and energy dissipation capacity. In each case, the damage parameter may be based on a single maximum value, a maximum range, or some cumulative value. In the "demand vs. capacity" approach, it is relatively easy to compute the demand, but more difficult to estimate the capacity. In the "degradation approach", the reverse tends to be the case. A typical example of the "degradation procedure" is the damage index based on the lengthening of the fundamental period of a structure identified from a strong motion record and reflecting overall stiffness degradation [30,31]. Exhaustive reviews of damage parameters and indices used in the past can be found in [30,74].

Besides the structural engineering approach to damage modeling and analysis, there is also a continuum mechanics approach called "Continuum Damage Mechanics" (CDM) [53]. CDM studies the local distribution of damage in engineering materials by postulating smeared damage models, unlike fracture mechanics which studies the propagation of individual cracks. In other words, CDM assumes statistical homogeneity of the material microstructure and of the developed microcracks and microvoids which physically define the material damage. Damage mechanics has been applied to model fatigue, creep, creep-fatigue, ductile plastic and brittle damage [53,54,46,86,87]. The thermodynamics of irreversible processes is used as framework to derive the coupled elastoplastic-damage constitutive equations describing the damage model mathematically in the case of ductile plastic damage, for example. Depending upon whether anisotropic or isotropic damage is assumed, the local damage variable or internal variable is of tensorial or scalar nature, respectively. However, the assumption of isotropic damage is often sufficient [53].

As implied by the aforementioned coupling between the damage variable and the

elastoplastic constitutive behavior, the progressive degradation of the material mechanical properties such as strength, stiffness, etc. is controlled by a damage variable governed by an evolution equation. Typically, the numerical integration of the elastoplastic-damage evolution equations is performed in the context of the finite element method [46,86,87].

Recently, the relationship between parameter-based global damage indices of the empirical structural engineering approach and local damage variables of the continuum approach has been established in the case of elastic damage [32]. This gives a theoretical (thermodynamic) foundation to global damage indices, and opens new areas of research.

In the present research, various inelastic response parameters indicative of damage (see Section 6.3) and two damage functions describing both the largest excursion and the cumulative low-cycle fatigue type of damage mechanisms are considered. The damage parameters and damage functions are used in conjunction with the four resistance-deformation models presented in the previous Section, but are not directly coupled to the mechanical properties (strength and stiffness) of these restoring force models. The non-deteriorating bilinear inelastic model together with a damage parameter or damage function is able to model a structural damage process characterized by a long deterioration threshold and a relatively short range of rapid deterioration. Such a damage mechanism is characteristic of the "crack propagation at weldment" mode of failure in wide-flange components of steel structures. Two experimental load-deformation diagrams from [51] are shown in Figs. 6.1 and 6.2 for constant and variable amplitude cycling. Ignoring the deterioration range, failure can be defined as the onset of noticeable deterioration which is associated with the occurrence of a through crack in the flange. On the other hand, the same experimental study [51] has shown that in the flange local buckling mode of failure under cyclic loading, deterioration in strength, stiffness, and hysteretic energy occurs after a period of deterioration threshold. Three different ranges with almost constant deterioration rates (relatively high rate first, then decrease in deterioration rate and rapid deterioration at the end) can be distinguished in the deterioration stage. A typical load-deflection

diagram from [51] is shown in Fig. 6.3 for the flange local buckling damage mode under constant amplitude cyclic loading. A comprehensive model representative of this damage behavior would require the coupling between a cumulative (or evolutive) damage variable characterizing the past deformation time history and the deteriorated elastoplastic mechanical properties. In other words, the formal concepts from continuum damage mechanics should be applied to structural engineering damage modeling. Clough's stiffness degrading model and the slip model are closer to the continuum damage mechanics approach, since they couple the largest past excursion to the stiffness property. In this case, the largest past excursion is a single response quantity, not of the cumulative type, and strength degradation is not modeled.

The first of the damage functions considered in the present study has been developed by Park, Ang and Wen and is described in [71,72]. In their approach, consistent with the behavior of R/C components under severe seismic loading, seismic structural damage is expressed as a linear combination of the damage caused by excessive deformation and that contributed by repeated cyclic loading effect. Therefore, they define the following damage index:

$$D_1 = \frac{\delta_M}{\delta_u} + \frac{\beta}{Q_y \delta_u} \int dE \tag{6.1}$$

where,

δ_M = maximum response deformation under an earthquake ;
δ_u = ultimate deformation capacity under monotonic loading ;
Q_y = calculated yield strength ;
β = non−negative parameter ;
dE = incremental absorbed hysteretic energy.

Values of the damage index, D_1, are such that $D_1 \geq 1.0$ signifies collapse or total damage. Structural damage, therefore, is a function of both the maximum response (maximum yield excursion) δ_M and the hysteretic energy dissipated $\int dE$, both of which depend on the loading history and the hysteretic behavior and the parameters δ_u, Q_y and β, which specify

the structural capacity. The damage index given by Eq. (6.1) is an indicator of closeness to failure for R/C components under repeated cyclic loading and the condition $D_1 \geq 1.0$ is a criteria for structural failure. Park and Ang [72] analyzed available monotonic and cyclic test data of R/C beams and columns to evaluate the statistics of the parameters of their proposed damage model. They found the lognormal distribution to be appropriate for describing the capacity (in terms of D_1) of R/C components (see Fig. 6.4). The statistics of the damage index D_1 are characterized by a large coefficient of variation (c.o.v. $\simeq$ 0.5) which indicates a high degree of uncertainty in the damage capacity of R/C components under inelastic repeated cyclic loading.

The second damage function (model) considered in this study is a low-cycle fatigue damage model used, verified and calibrated by Krawinkler et al. [51] in the context of an extensive experimental study on steel structural component performance. This experiment considered the deterioration and failure modes of local buckling in beam flanges and of crack propagation at weldments [51,99]. The conclusion drawn from this study was that simple cumulative damage models can be utilized to assess deterioration and failure in structural components.

The low-cycle fatigue (LCF) damage process is caused by a relatively small number of plastic strain reversals, characteristic of earthquake loading. LCF damage does not accumulate if the applied force is below a certain level. Therefore the contribution of the elastic strain components to the low-cycle fatigue life can be disregarded.

An empirical model for representing low-cycle fatigue data in the case of constant amplitude cycling was found independently by Manson [60] and Coffin [23] and is customarily referred to as the Coffin-Manson model. It relates the plastic strain amplitude, $\Delta\epsilon_p$, to the number of cycles to failure, N_f, by the equation

$$N_f = C^{-1} \Delta\epsilon_p^{-c} \tag{6.2}$$

in which C and c are material parameters or structural performance parameters in the case of structural components. To evaluate the low-cycle fatigue damage caused by complicated

loading histories (e.g. earthquake loading), a damage accumulation law is needed in conjunction with the empirical Coffin-Manson relationship describing constant amplitude fatigue test data. The simplest and most commonly employed damage accumulation law is the one propounded by Miner [62] and proposed earlier by Palmgren [68]. This theory is based on a linear damage accumulation assumption throughout the fatigue life, and hypothesizes that the damage due to a set of different stress (strain) amplitudes is equal to the sum of damages at each amplitude:

$$D_2 = \sum_{i=1}^{N} \frac{1}{N_{f,i}} = C \sum_{i=1}^{N} (\Delta\epsilon_{p,i})^c \tag{6.3}$$

where $1/N_{f,i}$ represents the damage contribution of the ith plastic strain cycle of amplitude $\Delta\epsilon_{p,i}$. Miner-Palmgren's rule requires that the amount of damage at failure be equal to unity:

$$D_2 = C \sum_{i=1}^{N} (\Delta\epsilon_{p,i})^c = 1 \tag{6.4}$$

Miner-Palmgren's rule has shortcomings, namely, it ignores both the sequence effect of the damaging plastic cycles as well as the mean deformation effect. The sequence effect has been verified by experimental observation. However, it is difficult to account for, since seismic response cycles do not follow recognizable sequence patterns. Modifications of the Palmgren-Miner linear cumulative damage theory exist, such as the nonlinear damage accumulation model proposed by Marco & Starkey [61] or the history-dependent phenomenological stochastic model of cumulative damage proposed by Bogdanoff, Krieger and Kozin [12,13,14]. Nevertheless, Minor-Palmgren's rule remains the most widely used hypothesis.

In order to utilize cumulative damage models in the case of complicated deformation histories, the history has to be converted into a series of cycles or half cycles (reversals). This is the task of cycle counting methods such as the rain-flow counting method described in [99]. However, in the present study, the amplitudes of the plastic deformation ranges or

plastic half cycles have been obtained directly from the simulated deformation response time histories as explained in the next Section.

A cumulative damage model can also be formulated using a fracture mechanics (FM) approach. For example, utilizing a crack growth rate model and information on initial and critical crack sizes a_0 and a_c, it has been shown [51] that failure is expected to occur under the condition:

$$D_3 = \alpha \left(\ln \frac{a_c}{a_0}\right)^{-1} \sum_{i=1}^{N} (\Delta\epsilon_{p,i})^{\beta} = 1 \tag{6.5}$$

where the parameters α and β depend on the material properties, the geometry of the specimen and the shape of the crack. A comparison of this equation with the empirical cumulative damage model presented in the low-cycle fatigue approach (see Eg. (6.4)) shows that both approaches result in identical failure definitions provided that the following equivalence in parameters is established:

$$C = \alpha \left(\ln \frac{a_c}{a_0}\right)^{-1} \tag{6.6a}$$

$$c = \beta \tag{6.6b}$$

The experimentally observed large uncertainty of the low-cycle fatigue cumulative damage model (Eg. (6.4)) can be explained by differences in initial imperfections (initial crack size a_0). Thus the most critical parameter in life prediction is the equivalent initial crack size a_0, which is a random variable with large scatter. Using the equivalence between the LCF and FM approaches, it can be concluded that the structural performance parameter C should be treated as a random variable for structural reliability calculations.

6.3 Response Computation and Response (Damage) Parameters

In this study, the equation of motion of the various inelastic SDOF systems is integrated analytically, taking advantage of the piecewise linearity of the force-deformation relationships and assuming piecewise linear ground acceleration time histories. The deriva-

tion and implementation of this piecewise exact method are explained in detail in Appendix B.

The equation of motion for a SDOF structure (see Eq. (B.1) of Appendix B)

$$m\ddot{u}(t) + c\dot{u}(t) + R(t) = -m\ddot{u}_g(t) \tag{6.7}$$

can be solved for the response of a particular system. However, it is desirable to express the basic equation of motion in a normalized form. In this manner, the specific parameters that influence the response can be more readily identified. In addition, the computed responses can be applied to a family of related systems thereby facilitating the development of design aids [59]. It is convenient to write Eq. (6.7) as :

$$\ddot{u}(t) + 2\xi_0\,\omega_0\dot{u}(t) + \frac{1}{m}R(t) = -\ddot{u}_g(t) \tag{6.8}$$

where $\omega_0 = \left(\frac{k_0}{m}\right)^{\frac{1}{2}}$

and $\xi_0 = \frac{c}{2m\omega_0}$

are the initial natural circular frequency and damping ratio corresponding to the unyielded system. Eq. (6.8) can be rewritten in terms of the displacement ductility

$$\mu(t) = \frac{u(t)}{U_y} \tag{6.9}$$

as

$$\ddot{\mu}(t) + 2\xi_0\,\omega_0\dot{\mu}(t) + \frac{1}{m\,U_y}R(t) = -\frac{1}{U_y}\ddot{u}_g(t) \tag{6.10}$$

The last two terms of Eq. (6.10) can be reworked as follows:

$$\frac{1}{m\,U_y}R(t) = \frac{k_0}{m}\frac{R(t)}{k_0\,U_y} = \omega_0^2\frac{R(t)}{R_y} = \omega_0^2\,\rho(t) \tag{6.11}$$

$$\frac{1}{U_y}\ddot{u}_g(t) = \frac{k_0}{k_0}\frac{\ddot{u}_g(t)}{U_y} = \frac{\omega_0^2\,m\,\ddot{u}_g(t)}{R_y} \tag{6.12}$$

By defining the nondimensional strength coefficient(1)

(1) In seismic design, this strength coefficient is referred to as the structure's yielding seismic resis-

$$\eta = \frac{R_y}{m\,g} \tag{6.13}$$

which expresses a system's yield strength as a fraction of its weight. Eq. (6.12) can be further reduced as

$$\frac{1}{U_y}\,\ddot{u}_g(t) = \frac{\omega_0^2}{\eta}\,\frac{\ddot{u}_g(t)}{g} \tag{6.14}$$

Eqs. (6.11) and (6.14) can be substituted in Eq. (6.10) which gives the final form of the normalized equation of motion:

$$\ddot{\mu}(t) + 2\,\xi_0\,\omega_0\,\dot{\mu}(t) + \omega_0^2\,\rho(t) = -\frac{\omega_0^2}{\eta}\,\frac{\ddot{u}_g(t)}{g} \tag{6.15}$$

In this form, the displacement ductility responses of all systems having the same initial natural frequency ω_0 and damping ratio ξ_0, the same normalized hysteretic characteristics(2) and the same strength coefficient η, subjected to the same ground motion can be determined from a single analysis. According to the dimensionless equation of motion described above, each of the inelastic SDOF systems defined in Section 6.1 is completely defined by the following structural parameters:

Initial natural period: T_0 [sec] , $(T_0 = 2\pi/\omega_0)$ (6.16a)

Initial damping ratio: ξ_0 [−] (6.16b)

Strength coefficient: $\eta = \dfrac{R_y}{mg}$ [−] (6.16c)

Strain hardening (or softening) ratio: $\alpha = \dfrac{\text{post-yield stiffness}}{\text{pre-yield stiffness}}$ (6.16d)

In the numerical implementation of the exact piecewise integration described in Appendix B, the following initialization is made:

Mass of the system: $m = 1/g$ (arbitrary choice) (6.17a)

where g is the acceleration of gravity

---

tant coefficient (e.g., UBC Code).

(2) The same normalized hysteretic characteristics (R/R_y vs. u/U_y) imply the same strain-hardening (or softening) ratio α in the case of hysteretic models defined by a bilinear skeleton curve.

Initial stiffness: $k_0 = \dfrac{4\pi^2 m}{T_0^2}$ (6.17b)

Below are presented the various structural response parameters whose statistical distributions within or across real earthquake processes are investigated in the present study. The damage parameters used in the definition of the two damage indices D_1 and D_2 defined in the last Section (Eqs. (6.1) and (6.3)) are of primary concern here:

- Maximum displacement ductility(1) : $\mu_d = \underset{0 \le t \le t_d}{\text{Max}} |u(t)/U_y|$;
- Normalized total hysteretic energy dissipated : $E_H^* = (\int_0^{t_d} dE_H)/(R_y U_y)$;
- Number of inelastic excursions (positive and negative) : $n^{(+)}$ and $n^{(-)}$ where $N = n^{(+)} + n^{(-)}$;
- Number of yield reversals : n_{rev};
- Ensemble of normalized plastic deformation ranges(2) (see Fig. 6.5) : $|\Delta u_{p,i}|/U_y$;
- Maximum normalized plastic deformation range : $\underset{0 \le t \le t_d}{\text{Max}} \left\{ |\Delta u_{p,i}|/U_y \right\}$;

In addition to these basic damage parameters, several others have been considered. They can be subdivided in three classes. The response parameters of the first class are directly derived from the force-deformation response:

- Normalized cumulative displacement ductility: $\mu_{acc} = (\sum_{i=1}^{N} |\Delta u_{p,i}|/U_y) + 1$;
- Normalized residual displacement ductility : $\mu_{res} = |u_{res}|/U_y$ where u_{res} represents the permanent displacement shift at the end of the earthquake record;

(1) t_d represents the earthquake record duration.

(2) The definition of the plastic deformation range used in this study is the material science definition [52]. The quantity Δu_p used here is equivalent to the plastic strain amplitude $\Delta \epsilon_p$ used in Eqs. (6.2) through (6.5).

- Normalized mean deformation with respect to the undeformed configuration:

$$\overline{\Delta u}_p / U_y = \frac{\left| \sum_{i=1}^{N} (|\Delta u_{p,i}| / U_y)\, (\bar{u}_{p,i} / U_y) \right|}{(\sum_{i=1}^{N} (|\Delta u_{p,i}| / U_y)} \tag{6.18}$$

where $\bar{u}_{p,i}$ is illustrated in Fig. 6.6. This response quantity can be interpreted as the abscissa of the centroid of the plastic deformation ranges. It indicates how symmetric the response is with respect to the undeformed configuration and is of possible use to incorporate the mean effect (which is not contained in the cumulative damage model of Eq. (6.3)) in seismic damage studies [35].

The second class of response parameters is based on the energy responses (see Appendix B, Eq. (B.14)):

$$E_K(t) + E_D(t) + E_E(t) + E_H(t) = E_I(t) \tag{6.19}$$

where $E_K(t)$, $E_D(t)$, $E_E(t)$, $E_H(t)$ and $E_I(t)$ are the kinetic energy, the energy dissipated by linear viscous damping, the recoverable elastic strain energy, the hysteretic energy dissipated and the earthquake input energy at time t, respectively. The following response parameters are considered:

- Normalized maximum input energy during the earthquake:

$$E^*_{I,max} = \underset{0 \le t \le t_d}{\text{Max}} (E_I(t) / R_y U_y) \; ;$$

- Normalized input energy at the end of the earthquake record:

$$E^*_{I,end} = E_I(t_d) / (R_y U_y) \; ;$$

- Normalized hysteretic energy ductility: $\mu_E = (E_H(t_d) / (R_y U_y)) + 1$;

- Ratio of the total hysteretic energy dissipated to the total dissipated energy:

$$E_H / TDE = E_H(t_d) / (E_D(t_d) + E_H(t_d)) \; ;$$

The response parameters of the third class are related to the various rate of energy (power) responses. These rate quantities are indicative of how fast the earthquake input

energy is imparted to, stored in, and dissipated by the structure. Although not much research work has been done in this area, these power responses must be correlated to the amount and type of damage imparted to a structure. For example, a low and uniform rate of hysteretic energy dissipation or a highly variable, spiky, rate of hysteretic energy dissipation through a structure must correspond to different levels and types of damage. In [66], Ohi et al. have defined the energy input rate (EIR) spectrum for viscously damped linear oscillators or nonlinear oscillators with hysteresis. Then they have used the EIR spectrum to explain the considerable difference in damage potential observed on a real structure and caused by two earthquakes of the same apparent overall intensity (very similar variance envelope and duration). The rates of energy response considered here are:

- Maximum positive rate of normalized earthquake input energy:

$$P^*_{I,max} = \underset{0 \le t \le t_d}{\text{Max}} \left(\frac{1}{R_y U_y} \frac{dE_I(t)}{dt} \right)$$

- Maximum rate of normalized hysteretic energy dissipated:

$$P^*_{H,max} = \underset{0 \le t \le t_d}{\text{Max}} \left(\frac{1}{R_y U_y} \frac{dE_H(t)}{dt} \right)$$

- Maximum rate of normalized viscous damping energy:

$$P^*_{D,max} = \underset{0 \le t \le t_d}{\text{Max}} \left(\frac{1}{R_y U_y} \frac{dE_D(t)}{dt} \right)$$

6.4 Earthquake Response Simulation

The second part of this study is concerned with characterizing the inelastic stochastic response process of SDOF structures given the input stochastic earthquake process. For this purpose, two general classes of methods are available: (i) formal probability theory of nonlinear random vibration and (ii) statistical analysis on a population of deterministically simulated nonlinear responses corresponding to an ensemble of realizations of the earthquake process under consideration. The results derived from a random vibration approach are only applicable in idealized restrictive circumstances. An exact random vibration analysis of inelastic systems subjected to a nonstationary excitation does not exist.

Therefore, a number of approximate techniques such as perturbation techniques or equivalent linearization [8,97] have been developed to obtain approximate solutions. Most of these methods are limited to small or moderate nonlinearities. In this research, to allow for a general and realistic nonstationary earthquake model and inelastic structural model, the statistical analysis approach using ARMA Monte Carlo Simulation has been chosen.

In the simulation procedure, a population of artificial ground motions from an original earthquake process is generated. The corresponding population of structural responses for a given structural system is computed deterministically using the analytical integration scheme described in Appendix B. Since each artificial ground motion belongs to the same underlying earthquake process, no ground motion scaling is needed and the variability of the corresponding ground motion and structural response parameters is an intrinsic type of variability related to the earthquake process under consideration. This is the response variability which is characteristic of the seismic loading and for which an appropriate design must be furnished.

Simulated Data Acquisition and Presentation

For each structural system, the response parameters defined in Section 6.3 for 100 artificial earthquakes are stored and constitute the simulated raw data. A family of post-processing routines has been developed to perform a statistical study on seismic response parameters of inelastic SDOF structures for damage evaluation. The various possible outputs of this statistical analysis are:

- The "evolutionary" second order statistics (mean and standard deviation) of any response quantity. The term "evolutionary statistics" means the evolution of the statistical estimates as a function of the number of artificial earthquakes used. This result is necessary to examine the statistical convergence. The evolutionary statistical mean and standard deviation estimates, $\bar{R}(n)$ and $\bar{\sigma}_R(n)$ of any response quantity R are computed as:

$$\bar{R}(n) = \left(\sum_{i=1}^{n} r_i \right) / n \,, \quad n = 1, \cdots, N \tag{6.20}$$

$$\bar{\sigma}_R^2(n) = \left(\sum_{i=1}^{n} (r_i - \bar{R}(n))^2 \right) / n \,, \quad n = 1, \cdots, N \tag{6.21}$$

where N is the total number of artificial earthquakes used, chosen to be 100 in this study.

- The histogram of any response quantity of a given system. The "distance" between the minimum and maximum response parameter values is divided in N intervals (N=50 for response parameters and N=100 for plastic deformation ranges) and the frequency of occurrence of the response parameter under consideration within each interval is counted. Histograms are used to visualize the form of the distribution and to suggest an underlying theoretical probability distribution.
- Probabilistic model fitting of any response quantity of a given system. Attempts to fit probability models have been made using the visual method of probability paper [4,5], according to which the sample points plotted should be on a straight line if the fitted model is correct. The typical probabilistic models considered are the lognormal, Rayleigh, Gumbel type I and exponential distributions.
- Probability distribution of any response parameter of a given system using the fractile method of order statistics. The 5, 10, 30, 50, 70, 90 and 95 percentile values of the random response variable are estimated by the 5th, 10th, 30th, 50th, 70th, 90th and 95th largest response values from the 100 simulated response values.

In this study, special attention has been given to statistical information on the number and magnitude of the plastic deformation ranges which define the damage index D_2 for low-cycle fatigue (see Eq. (6.3)). For a given system, their probability distribution is investigated based on the plastic deformation ranges produced by the family of 100 artificial earthquakes, providing a large data base enabling reliable statistical estimation. In addition to the statistical analysis results, the structural response simulation tools developed allow the generation of individual response time histories such as deformation, force, energy and rate of energy. In the presentation of the results, graphical representation is

emphasized for visual inspection of patterns and trends in response behavior.

As an illustration of the earthquake response simulation capabilities mentioned above,

- Figs. 6.7(a), (b), (c) and (d) show the hysteresis behavior of the four systems included in this study, all corresponding to the same bilinear skeleton curve and subjected to the same artificial record derived from El Centro 1940 (see Fig. 5.25).
- Figs. 6.8(a), (b), (c) and (d) show the normalized energy histories of the same four systems subjected to the same artificial earthquake.
- Figs. 6.9(a), (b), (c) and (d) show the normalized rate of hysteretic energy time histories of the same four systems subjected to the same artificial earthquake. The case of the bilinear elastic system is trivial since it does not dissipate hysteretic energy.
- Figs. 6.10(a) and (b) present the convergence of the second order statistics of the displacement ductility and normalized hysteretic energy ductility of a given system to the number of artificial earthquakes for the ARMA(2,1) El Centro earthquake process.
- Fig. 6.11 shows the histogram and a lognormal probabilistic model fit of the plastic deformation ranges produced by 100 artificial earthquakes from the ARMA(2,1) El Centro process on a given bilinear inelastic structure.

6.5 Comprehensive Parametric Study

With the nonstationary stochastic earthquake modeling and inelastic structural response simulation tools in hand, a comprehensive parametric study has been undertaken to better understand the complex relationships between ground motion features, structural properties and response (damage) parameters in a probabilistic framework. Such a parametric study provides insight into the probabilistic nature of seismic response of structures. Another objective of the study is to find the hierarchy of sensitivities of structural response statistics with respect to ground motion and structural parameters. For the purpose of the sensitivity study, three different approaches are taken. In the first approach,

the target earthquake record and the fitted stochastic process are kept fixed. First structural parameters and then structural models are varied to study their influence on the probabilistic seismic response (motion-to-motion variability within an earthquake process). In the second approach, the target earthquake record as well as the structural model and parameters are kept fixed. The fitted stochastic earthquake model is varied to study its influence on the stochastic response process. In the third approach, the structural model and parameters are kept fixed and the target earthquake record is varied to study its influence on the response parameter statistics. The flow chart of Fig. 6.12 summarizes the various options of the sensitivity analysis. The results of this parametric and sensitivity study are presented in Chapter 8.

CHAPTER 7

STATISTICAL RESPONSE OF LINEAR ELASTIC STRUCTURES

7.1 Introduction

Before focusing on inelastic SDOF systems, this Chapter is concerned with the probabilistic nature of the peak responses of linear elastic SDOF systems to seismic loading. In earthquake engineering, the concept of response spectrum is used to characterize the peak response of a SDOF linear oscillator with undamped natural period T and damping ratio ξ to a ground motion input. For a deterministic earthquake ground motion input, the response spectrum is defined as a function of T and ξ as:

$$RS(T,\xi) = \max_{0 \le t \le \infty} |r(t)| \tag{7.1}$$

where the response quantity under consideration $r(t)$ is either the displacement or velocity or acceleration of the oscillator. The response spectra corresponding to individual measured acceleration records are quite irregular in shape with numerous sharp peaks and valleys. Therefore, such individual response spectra cannot be used for design purposes, since these irregularities are considered to be random variations which do not represent a reliable property of the earthquake process for design [91]. For this reason, Housner [40] developed a smoothed design spectrum by computing the response spectra of different earthquake records and then normalizing, averaging and smoothing the resulting curves. However, smoothed design spectra derived in this fashion have no guarantee of risk-consistency or uniform hazard level. In other words, their values at different natural frequencies do not necessarily correspond to the same level of probability.

If an earthquake ground excitation is defined as a stochastic process, then the oscillator response $r(t)$ will be a stochastic process as well. In this case, an extension to the deterministic response spectrum (Eq. (7.1)) is necessary. This leads to the concept of probabilistic response spectra, which is very useful for probabilistic seismic design and seismic

safety assessment. Such spectra correspond to a uniform hazard level for different structural natural frequencies. They provide a tool to answer in a probabilistic sense the question of whether a structure will safely sustain a given class of stochastic ground excitation. In this study, a methodology is proposed to derive such probabilistic response spectra using the ARMA stochastic earthquake modeling. The derived probabilistic spectra are also used to check the adequacy of the stochastic earthquake models fitted to real target earthquake records (i.e., third level of model checking).

7.2 Probabilistic Response Spectra

For a given stochastic ground motion, the probabilistic response spectrum (PERS) for a confidence level p is defined as a function of T, ξ and p:

$$\mathrm{PERS}(T, \xi, p) \tag{7.2}$$

such that the following probability relation holds:

$$P\,[\,\mathrm{RS}(T, \xi) \leq \mathrm{PERS}(T, \xi, p)\,] = p \tag{7.3}$$

Therefore $(1 - p)$ corresponds to the probability of exceedence of the response level, $\mathrm{PERS}(T, \xi, p)$.

Even in the idealized case of stationary Gaussian input excitation, there is no exact closed-form solution for the probability distribution of the peak response of a linear SDOF oscillator over a specified duration. Indeed, such a solution depends on the well known first-passage problem which has not yet been solved in an exact form. Several researchers have provided approximate closed-form solutions to this problem by using various assumptions [26,92,93]. For example, Vanmarcke [92] has shown that in the special case of Gaussian response, the mean, variance and distribution of the peak response over a specified duration can be approximated in terms of the spectral moments of the response power spectral density. In Ref. [28], Der Kiureghian derived closed-form solutions for the spectral moments of the response of single and multi-degree-of-freedom structures to the classes of white-noise and filtered white-noise input excitations. These spectral moments are func-

tions of the parameters of the input power spectral density and of the dynamic structural characteristics (natural frequencies and damping ratios). To solve the realistic case of a nonstationary excitation in both amplitude and frequency content, analytical methods become extremely complicated and can give unreliable results due to the crudeness of the assumptions made. In this case, a solution using Monte Carlo simulation is justified and has been used in the present study.

Beck and Dowling's quick numerical algorithm to compute elastic response spectra [10] has been used to generate the population of response spectra. PERS corresponding to the ARMA stochastic models fitted to real earthquake records (see Chapter 5) have been generated using two methods: (i) the "statistical fractile method" described in Section 6.4 and (ii) an "analytical fractile method" which uses a fitted probability distribution of the peak responses. In both cases, the larger the number of artificial earthquakes, the smoother the PERS curves. However, for a given number of artificial earthquakes, the second method provides smoother PERS curves.

Figs. 7.1(a) and (b) show the convergence of the second order statistics of the peak pseudo-acceleration response Pa [g] of a given linear oscillator to the ARMA(2,1) earthquake models derived from the E02NS and El Centro records. It is observed that a sample of 20 artificial accelerograms, typically used in the literature, may be too optimistic if a statistical convergence within a few percent is required. In the present study, a sample size of 100 has been used to generate the PERS.

Probabilistic Response Spectra Using the "Statistical Fractile Method"

Fig. 7.2 displays the probabilistic relative displacement, relative velocity and absolute acceleration response spectra (dashed lines and dash-dot line for the median ERS) together with the corresponding deterministic response spectra (solid lines) related to the E02NS target record. The PERS of Fig. 7.2(a) have been generated from the ARMA(2,1) stochastic model fitted to E02NS, whereas Fig. 7.2(b) corresponds to the ARMA(4,2) model fitted to the same target record (see Chapter 5). Fig. 7.3(a) shows similar results for the

ARMA(2,1) model fitted to El Centro 1940. In all cases, the PERS correspond to confidence levels (or probability of non-exceedence) p = 5, 10, 30, 50, 70, 90 and 95 %. From these figures, the following remarks are made:

- For the E02NS target record, the ARMA(4,2) model provides a better match between probabilistic and target elastic spectra than the ARMA(2,1) model. This is in agreement with the relative rating of these two ARMA models given by the first level of model checking (residuals checks, see Section 3.7). However, for both models the target spectra are not contained within the (5-95%) statistical range for periods larger than T_0 = 1.40 second. At these periods, the two ARMA earthquake models overestimate the peak elastic response, since, as seen previously, these ARMA models are too rich in low frequency content. In the lower period range (T_0 < 1.40 second), the target spectra tend to lie above the corresponding median spectra (p=50%), suggesting an underestimation of the peak elastic response by the earthquake models in this period range. However, this is not necessarily a sign of model inadequacy, since the deterministic spectra derived from specific realizations of a stochastic process may not oscillate symmetrically around the corresponding median spectra as illustrated in Fig. 7.6.
- The match between probabilistic and target response spectra is better for the El Centro target record than for the E02NS target record. In the case of El Centro, the target spectra are contained in the (5-95%) statistical range up to a period of T_0 = 3.50 seconds. The wider period range of "good match" for El Centro than for E02NS is explained by the noticeably broader and higher frequency content of the E02NS record (compare Figs. 5.2 and 5.4). In the latter case, the model fitting algorithm accomodates the capture of the predominant high frequency components of the target record at the cost of a lesser quality representation of the longer period components.

Probability Distribution of Peak Responses of Linear SDOF Systems

The probability distribution of the peak responses (displacement, velocity and acceleration) of linear SDOF oscillators subjected to the stochastic ground motion inputs has been studied. Histograms of the peak responses of specific SDOF systems have been plotted to suggest the underlying distribution. Some of these have been reported on Fig. 7.4 where the distributions are observed to be unsymmetric with a positive skewness coefficient (longer tail to the right).

The simulated peak response values have been plotted on different probability papers such as, Gaussian, lognormal, Rayleigh and Gumbel type I(1) extreme value distribution. Fig. 7.5 presents two of these attempts of probabilistic model fitting, namely, Gumbel type I and lognormal, for a specific stochastic model and a given oscillator. It was found that a lognormal distribution represented the data reasonably well for all the individual cases examined.

Probabilistic Response Spectra Using the "Analytical Fractile Method"

For a given number of artificial accelerograms, smoother PERS than the ones generated using the "statistical fractile method" can be obtained by assuming an underlying probability distribution for the peak responses. In this study, the lognormal distribution has been assumed. The parameters of the lognormal distribution, λ and ζ, are estimated using the simulated data:

$$\lambda = E[\ln(r_{max}(T,\xi))] \approx (\sum_{i=1}^{N} r_{max,i})/N = \bar{\lambda}(T,\xi) \tag{7.4}$$

$$\zeta^2 = Var[\ln(r_{max}(T,\xi))] \approx (\sum_{i=1}^{N} (r_{max,i} - \bar{\lambda})^2)/N = \bar{\zeta}^2(T,\xi) \tag{7.5}$$

(1) It is known from the theory of random vibration [56,65] that for a narrow-band stationary random process, the distribution of the peaks (all peaks independently of magnitude) is the Rayleigh distribution. The stationary response of a lightly damped SDOF linear system to a stationary Gaussian excitation is often a narrow-band process. It is also known [5] that in the case of an initial variate with the Rayleigh probability distribution, the distribution of the largest value (out of a sample of n outcomes) from this initial variate will converge, for large n, to the Gumbel type I asymptotic form. These results, valid in the stationary case, justify the attempt to fit a Gumbel type I distribution to the simulated results. Apparently, they don't extend to the nonstationary case considered in this study.

Where $N = 100$ and the $(r_{max,i}, i = 1, \cdots, N)$ are the individual peak responses corresponding to the artificial earthquakes. These estimated parameters are then used to compute the 5, 10, 30, 50, 70, 90 and 95 percentile values of the random peak response variable as

$$\ln[\mathrm{PERS}(T,\xi,p)] = \bar{\zeta}(T,\xi)\Phi^{-1}(p) + \bar{\lambda}(T,\xi) \tag{7.6}$$

$$\mathrm{PERS}(T,\xi,p) = \exp[\bar{\zeta}(T,\xi)\Phi^{-1}(p) + \bar{\lambda}(T,\xi)] \tag{7.7}$$

in which $\Phi^{-1}(\ )$ represents the inverse standard normal probability function. Fig. 7.3(b) shows the PERS corresponding to the ARMA(2,1) model of El Centro 1940 and derived using Monte Carlo simulation and the assumption of a lognormal underlying distribution. They are smoother than those illustrated in Fig. 7.3(a) derived using the "statistical fractile method".

Finally, to conclude the topic of probabilistic response spectra, Fig. 7.6 shows, on the same graph, the acceleration PERS corresponding to the ARMA(2,1) model of El Centro 1940 and two deterministic response spectra derived from two single realizations of this stochastic process. This illustrates the risk-inconsistency of response spectra derived from single earthquake records and demonstrates that the irregularities (peaks and valleys) of such spectra are random variations which do not represent a reliable property of the earthquake process.

7.3 Probabilistic Seismic Design and Seismic Safety Analysis of Elastic Structures

In earthquake engineering, probabilistic design spectra are very useful in two different situations, namely, for the seismic design of a new structure and for the seismic safety assessment of an existing structure. These two situations will be examined in more detail after the use of probabilistic response spectra for MDOF linear elastic structures is discussed.

Probabilistic Response of MDOF Linear Elastic Structures

In the case of a classically damped (proportional damping) MDOF linear elastic structure, the coupled equations of motion expressed in terms of the geometric coordinates (nodal displacements) can be completely uncoupled by making use of the modal or normal coordinates (amplitudes of normalized undamped mode shapes) [22]. Each uncoupled modal equation of motion is identical, except for a modal participation factor scaling the input excitation, to the equation of motion of a linear viscously damped SDOF oscillator having, for dynamic characteristics, the natural frequency and damping coefficient of the mode under consideration. After the time-history solutions for the normal coordinates are computed, any total structural response can be obtained as a linear combination of these modal response time histories.

However, in practical applications, the lengthy modal response time histories are not computed. Instead, the maximum total response of interest is approximated using a technique for combining modal maxima. Examples of these modal combination methods are: square-root-of-sum-of-squares (SRSS), sum of absolute values, complete quadratic combination (CQC). The maximum modal responses are directly obtained from the corresponding response spectra. This analysis procedure is called the "response spectrum method".

The simple response spectrum analysis technique can still be applied in the case of the stochastic response of a MDOF structure to a stochastic ground motion provided:

(i) risk-consistent response spectra are used. In other words, the peak modal responses (corresponding to different natural frequencies) read from the response spectra should all correspond to the same level of probability (risk or hazard).

(ii) The statistical correlation between the modal responses are accounted for. The cross-modal contributions can be highly significant for structures with closely spaced natural frequencies [98].

The requirement (i) above, which is the same as for SDOF structures, is satisfied if use is made of the probabilistic response spectra (PERS) defined and computed in Section 7.2.

By definition, these PERS are risk-consistent for a specific stochastic ground motion. The requirement (ii) is specific to MDOF structures only. In general, the cross-modal contributions depend on the properties of the stochastic ground motion (duration and frequency content) and on the modal dynamic characteristics $(\omega_i, \omega_j, \xi_i, \xi_j)$. Modal correlation coefficients have been defined analytically for the classes of white-noise and filtered white-noise input excitations [28]. They are at the origin of the development of the CQC method [29]. In the case of the non-parametric nonstationary ARMA stochastic earthquake ground motion models used in this study, the cross-modal contributions could be approximated in three different ways:

(i) by using ARMA Monte Carlo simulation for several characteristic pairs of SDOF oscillators $[(\omega_i, \xi_i), (\omega_j, \xi_j)]$. Of course, this would require a large computational effort, but for a given earthquake process, it would have to be done only once.

(ii) by using the expressions for the modal correlation coefficients based on a white-noise input (found in Ref. [28]) as an approximation for the nonstationary stochastic excitation considered here.

(iii) by deriving approximate analytical results using random vibration theory and analytical parametrizations of the ARMA stochastic ground motion models.

Probabilistic Seismic Design of Linear Elastic Structures

Imagine the general situation in which a structure has to be designed to resist elastically, with a specified reliability level, an ensemble of n stochastic earthquake ground motions. The stochastic ground motion models characterize different seismotectonic zones (e.g., faults) or seismogenic zones. The seismic activities of these different seismic sources are assumed to be independent. Suppose that, at the time of the design, the annual probability of occurrence of an earthquake is known for each seismic source:

$$P[E_i] = \nu_i \tag{7.8}$$

where E_i = the event that an earthquake occurs in source i. The annual probability of

occurrence υ_i is given by an earthquake occurrence model in time such as the Poisson model [27], the Markov and Semi-Markov models [48], calibrated for a given source-site condition. For example, if the homogeneous Poisson model is used, the annual probability of occurrence of an earthquake corresponds approximately with the average rate of earthquake occurrences (No. of earthquakes/year) provided this number is small (< 0.1).

The uniform hazard elastic response spectrum $\mathrm{UHERS}(T, \xi, p)$ for a confidence level p, corresponding to a given site and multi-source uncertain seismic environment, is defined such that:

$$P[\mathrm{RS}(T, \xi) \leq \mathrm{UHERS}(T, \xi, p)] = p \tag{7.9}$$

In fact, the $\mathrm{UHERS}(T, \xi, p)$ plays the role of the inverse cumulative distribution function of the random response spectrum variable. Its inverse, the function $\mathrm{UHERS}^{-1}(T, \xi, rs)$ satisfies the following probability statement:

$$P[\mathrm{RS}(T, \xi) \leq rs] = \mathrm{UHERS}^{-1}(T, \xi, rs) \tag{7.10}$$

and plays the role of the cumulative distribution function of the random response spectrum variable. By use of the total probability theorem, $\mathrm{UHERS}^{-1}(T, \xi, rs)$ is obtained from the probabilistic response spectra conditional on a given earthquake process (seismic source) derived in Section 7.2:

$$\begin{aligned} \mathrm{UHERS}^{-1}(T, \xi, rs) &= P[E \cap (\mathrm{RS}(T, \xi) \leq rs)] \\ &= \sum_{i=1}^{n} P[(\mathrm{RS}(T, \xi) \leq rs) \mid E_i]\, P[E_i] \\ &= \sum_{i=1}^{n} \mathrm{PERS}_i^{-1}(T, \xi, rs)\, \upsilon_i \end{aligned} \tag{7.11}$$

In the above, E = the event that an earthquake occurs in one of the seismic sources, i.e., $E \equiv E_1 \cup E_2 \cup \cdots \cup E_n$ and the total probability theorem is applicable since the E_i are mutually exclusive and collectively exhaustive events. The inverse conditional probabilistic response spectra $\mathrm{PERS}_i^{-1}(T, \xi, rs)$ are defined such that:

$$P[RS(T,\xi) \leq rs \mid E_i] = PERS_i^{-1}(T,\xi,rs) \tag{7.12}$$

and can be derived from the $PERS_i(T,\xi,p)$ discussed in Section 7.2, by linear interpolation, for example.

In the context of probabilistic design, the design criteria are reliability-based. For example, in order to maintain the structure in the elastic range of behavior, one or several elastic limit states such as maximum admissible displacement, deformation or force, have to be satisfied within a specified target reliability level. In the iterative design process, the engineer selects the design parameters (structural system, geometrical configuration, stiffness, strength) and evaluates the inverse cumulative distribution function(1) $F_{R_i}^{-1}(p)$ of the response quantities R_i defining the various limit states. The functions $F_{R_i}^{-1}(p)$ are evaluated using the previously defined $UHERS(T,\xi,p)$ in the context of the probabilistic response spectrum method. Finally, by comparing the computed reliability levels p_i with the target reliability levels $p_{targ,i}$ corresponding to the specified maximum admissible response values, the trial design is accepted or the iterative design process is continued.

Seismic Safety Analysis of Linear Elastic Structures

Sometimes, the safety of an existing structure with known structural properties (geometry, stiffness, strength) has to be evaluated for a given uncertain multi-source seismic environment. In this case, the uniform hazard response spectra $UHERS(T,\xi,p)$ corresponding to the stochastic seismic environment, are developed as described above. At this point, they are used with the probabilistic response spectrum method to derive the cumulative distribution function(2) $F_{R_i}(r_i)$ of the various controlled response quantities. The reliability levels corresponding to the various elastic limit states are given by:

---

(1) The inverse cumulative distribution function $F_{R_i}^{-1}(p)$ is defined such that:

$$P[R_i \leq F_{R_i}^{-1}(p)] = p$$

(2) The cumulative distribution function $F_{R_i}(r_i)$ is defined such that:

$$P[R_i \leq r_i] = F_{R_i}(r_i)$$

$$p_i = P[R_i \leq r_{i,max}] = F_{R_i}(r_{i,max}) \tag{7.13}$$

These reliability levels are safety indicators for the structure.

CHAPTER 8

STATISTICAL RESPONSE OF INELASTIC SDOF STRUCTURES

8.1 Introduction

In this Chapter, the results of the inelastic structural response simulations and parametric study are presented, analyzed and discussed in the context of the two main objectives of this research. The first objective is to examine the "match" between the inelastic structural response to the target earthquake motion and the probabilistic inelastic response to the fitted stochastic earthquake model. This serves as a basis for the third level of earthquake model checking (see Section 3.7). The second objective is to investigate the sensitivity of the stochastic inelastic response with respect to the earthquake ground motion model, the structural hysteretic model and the structural parameters. These results provide insight into the probabilistic nature of the seismic response of structures, e.g., the structural response variability to be expected in case of an earthquake. The results are presented graphically to better capture the general patterns and trends in response behavior.

8.2 Presentation of Simulation Results

The entire parametric earthquake response simulation study is represented in the form of a flow chart in Fig. 8.1. Two target earthquake records have been used: the E02NS record from Event 39 of the SMART I Array and the El Centro record from the 1940 Imperial Valley earthquake. The ARMA(2,1) and ARMA(4,2) models fitted to the E02NS record as well as the ARMA(2,1) model fitted to the El Centro record (see Chapter 5) have been employed as earthquake "simulators". The structural hysteretic behavior has been represented by four different restoring force models, namely: (1) the bilinear nondegrading inelastic model (BILIN), (2) Clough's stiffness degrading model (CLD), (3) the slip model (SLIP) and (4) the bilinear elastic model (BILEL). A damping ratio of 5 percent has been used throughout the study. The structural parameters defining the bilinear

skeleton curve of the restoring force models, namely: (1) the initial stiffness or undamped natural period T_0, (2) the strength coefficient η and (3) the strain-hardening/softening ratio α are also indicated in Fig. 8.1 for each simulation case. The following ensemble of undamped natural periods has been used: T_0 = 0.10, 0.20, 0.30, 0.40, 0.50, 0.60, 0.70, 0.80, 0.90, 1.00, 1.20, 1.40, 1.60, 1.80, 2.00, 2.50, 3.00 [seconds].

In earthquake engineering, the concept of the elastic response spectrum has been extended to the case of inelastic SDOF systems [59]. An inelastic response spectrum (IRS) characterizes a response parameter (or damage parameter) of an inelastic SDOF system subjected to a ground motion input. In general, for a deterministic earthquake ground motion input, the inelastic response spectrum is defined as a function of the restoring force model, the response parameter rp under consideration, the initial undamped natural period T_0 and the damping ratio ξ_0, i.e., the function can be expressed as:

$$IRS_{MODEL}(rp, T_0, \xi_0) \tag{8.1}$$

As world-wide design procedures change from elastic to ultimate state design, inelastic response spectra are gaining greater importance than elastic spectra for certain classes of structures.

For a given stochastic ground motion, the probabilistic inelastic response spectrum (PIRS) for a confidence level p, $PIRS_{MODEL}(rp, T_0, \xi_0, p)$, is defined such that the following probability relation holds:

$$P[IRS_{MODEL}(rp, T_0, \xi_0) \leq PIRS_{MODEL}(rp, T_0, \xi_0, p)] = p \tag{8.2}$$

In other words, p corresponds to the probability of non-exceedence of the response level $PIRS_{MODEL}(rp, T_0, \xi_0, p)$. In this study, the PIRS's corresponding to the response or damage parameters defined in Section 6.3 have been estimated using the statistical fractile method described in Section 6.4. The various confidence levels considered were p = 5, 10, 30, 50, 70, 90 and 95 %.

Figs. 8.2 through 8.11 show the probabilistic inelastic response spectra corresponding

to the ARMA(2,1) and ARMA(4,2) models fitted to the E02NS record and to the different hysteretic models with several sets of structural parameters. In these figures, the solid curve represents the deterministic inelastic response spectrum corresponding to the target record. The estimates of the probabilistic inelastic response spectra are shown as dashed lines, except for the median IRS (p= 50%) which is shown as a dash-dot line. All these figures contain the whole set of response parameters defined in Section 6.3. Figs. 8.12 through 8.20 display exactly the same information as Figs. 8.3 through 8.11, but for the ARMA(2,1) model fitted to the El Centro 1940 record.

Figs. 8.30 through 8.36 and Figs. 8.37 through 8.43 show the histograms and lognormal distribution fits for the plastic deformation ranges generated by the various simulation cases corresponding to the E02NS and El Centro 1940 target records, respectively. Each sample of plastic deformation ranges is produced by an ensemble of 100 artificial earthquakes. Comparisons between lognormal and shifted exponential distribution fits are presented in Figs. 8.31 and 8.38.

8.3 Earthquake Model Checking Based on Inelastic Response Parameters

A comparison between probabilistic inelastic response spectra (PIRS) derived from a stochastic ground motion process and the corresponding deterministic IRS derived from two single realizations of this stochastic process is shown in Fig. 8.21. As already observed by Housner [38], the spectrum of a specific earthquake realization may show a tendency to be high or low in certain regions instead of having rather symmetrical fluctuations about the mean (or median). Since, in a probabilistic approach, the target earthquake record is viewed as a single realization of the earthquake process, Fig. 8.21 illustrates the type of "match" to be expected between a PIRS and the corresponding deterministic IRS derived from the target record.

As mentioned in Section 3.7, a way to check the earthquake model capability in characterizing earthquake accelerograms for inelastic structural response studies is to compare the derived probabilistic response spectra with the corresponding deterministic

response spectra of the analyzed "target" accelerogram. This comparison is shown in Figs. 8.2 through 8.11 for the E02NS target record and in Figs. 8.12 through 8.20 for the El Centro 1940 target record. The following remarks can be made regarding these figures:

- For the two target records analyzed (with a few exceptions), the target IRS lie between the corresponding PIRS's of confidence levels p = 5 and 95%. In general, they do not oscillate around the median spectra (p=50%), but this is not a condition of model adequacy, as seen at the beginning of this Section (see Fig. 8.21).
- In the case of the E02NS target accelerogram with a bilinear hysteretic model, the ARMA(4,2) model allows a better "match" between PIRS's, median spectra and target IRS's than the ARMA(2,1) model (see Figs. 8.2 and 8.3). Hence, in this case, the third level of model checking confirms the results from the first and second levels of model checking (see Section 5.4).
- Based on the two examples considered in this study, the quality of the "match" between PIRS's and corresponding target spectra does not seem to be dependent on the hysteretic models or on the structural parameters.
- A major deficiency of both the ARMA(2,1) and ARMA(4,2) models for the E02NS record is the overestimation of the target maximum displacement ductility μ_d at long periods ($T_0 \geq 1.20$ sec) as shown in Figs. 8.2, 8.3, 8.4, etc. This deficiency exists for all hysteretic models and is due to the low frequency error (already pointed out) for these two earthquake models. This low frequency error is also visible in the probabilistic elastic displacement response spectra (see Figs. 7.2 and 7.3). In spite of the high-pass filtering, these two stochastic ground motions are still too rich in low frequency content. This model deficiency is also responsible for the overestimation of the target input energy spectra ($E^*_{I,max}$ or $E^*_{I,end}$) at long periods ($T_0 \geq 2.0$ secs) visible in Figs. 8.2, 8.3, etc.

8.4 Influence of Earthquake Model and Structural Parameters on Stochastic Response Parameters

8.4.1 Type of Probability Distributions

The statistical distribution of the various response (damage) parameters defined in Section 6.3 is obtained through the structural response simulations performed using the derived stochastic earthquake ground motion models. These statistical distributions displayed in the form of histograms or PIRS curves estimated using the fractile method are used to suggest underlying theoretical probability distributions. These analytical distributions characterizing the structural demand from the earthquake can then be used for seismic reliability calculations in which the failure probability is obtained as the convolution of the probability distributions of the demand and the corresponding structural capacity.

From the PIRS shown in Figs. 8.2 through 8.11 and 8.12 through 8.20 for the E02NS and El Centro cases, respectively, and from numerous probability model fits not shown here, the following observations can be made:

- The PIRS curves corresponding to the response parameters μ_d, μ_E, $E^*_{I,max}$, $E^*_{I,end}$, $P^*_{I,max}$ and $P^*_{D,max}$ tend to be symmetrically distributed with respect to the median curve (p=50%) when plotted on a logarithmic scale. From model fits on probability paper, it was found that the statistical distribution of these six positive-definite (always > 0) response parameters is very well described by a lognormal distribution. In the case of the normalized hysteretic energy ductility factor μ_E which takes the value of 1.0 when the system remains elastic, only the distribution of μ_E conditional on yielding of the system is well described by a lognormal distribution.
- The PIRS curves corresponding to the response parameters μ_{acc}, μ_{res}, $(\Delta u_p/U_y)_{max}$, $(\overline{\Delta u_p}/U_y)$, E^*_H and P^*_H exhibit a pronounced degree of asymmetry when plotted on a decimal scale. This asymmetry is characterized by a positive skewness coefficient (i.e., large values are more widely dispersed than small values). From model fits on

probability paper, it was found that the statistical distribution of μ_{acc} ($\geq$ 1) and of the other five positive-semi-definite ($\geq$ 0) response parameters is well represented by a lognormal distribution, conditional on the yielding of the system. The conditional statistical distribution of $(\Delta u_p / U_y)_{max}$ is very well described by a lognormal distribution.

- The PIRS curves corresponding to the discrete response parameters $n^{(+)}$, $n^{(-)}$ and n_{rev} characterizing the number of yield excursions and reversals tend to be symmetrically distributed with respect to the median curve, when plotted on a decimal scale. Plots on probability paper have shown that these three discrete parameters treated as continuous random variables are very well described by a normal distribution provided the probability of no yielding is small. If the latter condition is not satisfied, a truncated (to the left) normal distribution seems very appropriate.
- The PIRS curves corresponding to the response parameter E_H/TDE ($\geq$0) are asymmetric on a decimal scale. The skewness coefficient is negative (i.e., small values are more widely dispersed than large values). Therefore, a probability distribution allowing for a negative skewness coefficient such as the Gumbel type I smallest value distribution should be used to describe this random response parameter.
- For all the response parameters whose probability distributions are conditional on the yielding of the system, the unconditional probability distributions are of the mixed type (probability mass function at the lower bound value and probability density function for the positive range of values).
- From the results of the parametric simulation study, it seems that the type of probability distribution of the various response parameters is insensitive to (i) the target accelerogram, (ii) the ARMA model order, (iii) the type of hysteretic model and (iv) the structural parameters.

8.4.2 Influence of Target Earthquake

In an attempt to determine if the dependence of PIRS's on structural period varies across earthquakes, a double comparison has been made: (i) comparison case A - case B

and (ii) comparison case A - case C, where cases A, B and C are defined below (see also Fig. 8.1).

Case A : E02NS target record

ARMA(2,1) model

Elastoplastic hysteretic model

$\xi_0 = 0.05$, $\eta = 0.05$, $\alpha = 0.00$.

Case B : El Centro 1940 target record

ARMA(2,1) model

Elastoplastic hysteretic model

$\xi_0 = 0.05$, $\eta = 0.10$, $\alpha = 0.00$.

Case C : El Centro 1940 target record

ARMA(2,1) model

Elastoplastic hysteretic model

$\xi_0 = 0.05$, $\eta = 0.20$, $\alpha = 0.00$.

The PIRS's corresponding to these 3 cases are shown in Figs. 8.2, 8.12 and 8.18, respectively. The comparison between cases A and B indicates that the El Centro stochastic ground motion produces a larger response in the elastoplastic (EP) structure whose strength coefficient $\eta = 0.10$, in comparison to the E02NS stochastic ground motion in the EP structure whose strength coefficient $\eta = 0.05$. The relative effectiveness of the El Centro earthquake process is manifested in all the inelastic response parameters considered and over the whole structural period range ($0.10 \leq T_0 \leq 3.0$ sec.). From the comparison between cases A and C, it is seen that the E02NS earthquake process produces a larger response in the EP structure whose strength coefficient $\eta = 0.05$, in comparison to the El Centro earthquake process in the EP structure whose strength coefficient $\eta = 0.20$, only in the short period range ($T_0 \leq 0.30$ sec.). For larger structural periods, the situation is reversed. In addition, it is seen that the relative destructiveness of an earthquake depends on the relative spectral properties of the structure and of the earthquake. This example is

also able to show that the relative destructiveness of two target earthquakes with respect to a given structure, given by the comparison of (i) the deterministic inelastic spectra and (ii) the probabilistic inelastic spectra, can be different. More confidence can be placed in the answer given by comparison of the PIRS's, since the latter eliminate the random effects attached to a particular earthquake realization.

From the same comparisons, it is also observed that the shape of the PIRS curves for a given inelastic response parameter can change for two different target earthquakes (as illustrated by a comparison of Fig. 8.2 with Fig. 8.12 for the response parameters $n^{(+)}$, $n^{(-)}$, n_{rev}, $E^*_{I,max}$ and $E^*_{I,end}$. Another noticeable difference between the two earthquake processes is the larger ratio "$n_{rev}/(n^{(+)} + n^{(-)})$" for the E02NS earthquake process, indicating that in the case of the El Centro process, elastoplastic structures have more tendency to yield consecutively in the same direction (less yield reversals for a given number of yield excursions).

The coefficients of variation (c.o.v. = standard deviation / mean) of the various inelastic response parameters as a function of structural period have been compared between cases A, B and C. It has been observed that, (i) the trends of the c.o.v.'s as a function of period are very similar between cases B and C and, (ii) except for a few local exceptions, the same trends also prevail between case A and case B or case C.

8.4.3 Influence of ARMA Model Order

Two different ARMA models, the ARMA(2,1) and the ARMA(4,2), have been fitted to the same target accelerogram E02NS. By subjecting a class of inelastic structures to these two stochastic ground motion models, the influence of the model order on the structural response statistics can be evaluated. With this in mind, two simulation cases are compared (see Fig. 8.1).

Case I : E02NS target record

ARMA(2,1) model

Elastoplastic hysteretic model

$\xi_0 = 0.05$, $\eta = 0.05$, $\alpha = 0.00$.

Case II : E02NS target record

ARMA(4,2) model

Elastoplastic hysteretic model

$\xi_0 = 0.05$, $\eta = 0.05$, $\alpha = 0.00$.

The PIRS's corresponding to these two cases are shown in Figs. 8.2 and 8.3, respectively. Comparison of these PIRS's leads to the conclusion that for all the inelastic response parameters considered, except for the number of yield excursions and reversals ($n^{(+)}$, $n^{(-)}$ and n_{rev}), the ARMA(4,2) earthquake model appears a little more intense than the ARMA(2,1) model over the whole period range. In terms of their effects on the number of yield excursions and reversals, these two earthquake models are very similar.

In this comparison, the earthquake model dependence of the c.o.v. of the various inelastic response parameters as a function of structural period has been carefully studied. For elastoplastic structures, it was found that the ARMA(4,2) earthquake model produces a larger structural response variability (dispersion) than the ARMA(2,1) model, except in the following cases: (i) μ_R, $(\Delta u_p/U_y)_{max}$ and $\overline{\Delta u_p}/U_y$ for $T_0 \geq 0.7$ sec, (ii) $n^{(+)}$, $n^{(-)}$ and n_{rev}, (iii) E_H/TDE and (iv) $P^*_{H,max}$ for $T_0 \geq 0.7$sec. Therefore, the ARMA(4,2) model does not systematically produce less structural response variability than the ARMA(2,1) model, even though it has been diagnosed better than the ARMA(2,1) model for the three levels of model diagnostic checking in the case of the E02NS record. The response statistics showed that the trends of the c.o.v. of the various inelastic response parameters as a function of structural period were similar for the two earthquake models fitted to the same target record.

8.4.4 Influence of Hysteretic Model

The restoring force models considered in this study are (see Section 6.1): (i) the bilinear inelastic model (BILIN), (ii) modified Clough's stiffness degrading model (CLD), (iii) the slip model (SLIP) and (iv) the bilinear elastic model (BILEL). The influence of

the restoring force model on the statistics of the inelastic response parameters is examined for two simulation cases (see Fig. 8.1): (i) the ARMA(4,2) simulation of the E02NS target record with: $\xi_0 = 0.05$, $\eta = 0.05$ and $\alpha = 0.00$, for all structural models and (ii) the ARMA(2,1) simulation of El Centro with: $\xi_0 = 0.05$, $\eta = 0.10$ and $\alpha = 0.00$, also for all structural models. It was established in Section 8.4.2 that the ARMA(2,1) El Centro stochastic ground motion is more destructive than the ARMA(4,2) E02NS stochastic ground motion in terms of all inelastic response parameters, over the whole structural period range for all restoring force models. Some of the differences found when comparing response statistics for various hysteretic models for these stochastic ground motions may be caused by the different levels of inelastic behavior. It is also noted from Section 8.4.1 that the type of probability distribution of the various inelastic response parameters seems to be insensitive to the type of restoring force model. The comparisons between different hysteretic models have been made based on the PIRS's shown in Figs. 8.3 through 8.6 for the ARMA(4,2) E02NS simulation and in Figs. 8.12 through 8.15 for the ARMA(2,1) El Centro simulation. Also, use has been made of Figs. 8.22 and 8.23 which represent the coefficient of variation (c.o.v.) of the various response parameters as a function of structural period for the different restoring force models. Listed below are the main differences with respect to the hysteretic models which have been observed for the two stochastic ground motions considered. Other differences across hysteretic models differed from one target earthquake to the other.

μ_d : For a given confidence level p, the maximum displacement ductility factor is:

- largest for the SLIP model in the period range[(1)] $T_0 \leq 0.80$ sec;
- larger for the CLD model than for the BILIN model in the short period range $T_0 \leq 0.20$ sec;
- larger for the BILEL model than for the BILIN and the CLD models.

(1) When the period range is not specified, the entire period range is implied: $[0.10 \leq T_0 \leq 3.0\,\text{sec}]$.

The μ_d response parameter produced by the SLIP model has a lower variability than for the other models in the period range $T_0 \leq 0.60$ sec (see Figs. 8.22 and 8.23 for μ_d).

μ_E (E_H^*) : For a given confidence level p, the hysteretic energy ductility factor μ_E or normalized hysteretic energy dissipated (E_H^*) is:

- lowest for the SLIP model. This result is obvious from the pinched hysteresis loops of the slip model.
- larger for the CLD model than for the BILIN model in the period range $T_0 \geq 0.20$ sec.

The SLIP model produces a μ_E response with a lower variability than the other models in the period range $T_0 \leq 0.70$ sec (see Figs. 8.22 and 8.23 for μ_E or E_H^*).

μ_R : For a given confidence level p, the residual displacement ductility factor μ_R is:

- largest for the BILIN model. This result is in agreement with previous deterministic studies regarding the large permanent offset developed by elastoplastic structures [21,94].

For the SLIP model, the PIRS curves don't decay as fast with period as for the other models.

$(\Delta u_p / U_y)_{max}$: For a given confidence level p, the maximum normalized plastic deformation range is:

- largest for the CLD and BILEL models;
- lowest for the SLIP and BILIN models. However, it tends to be larger for the SLIP model than for the BILIN model as the ground motion intensity increases;

$(\overline{\Delta u_p} / U_y)$: For a given confidence level p, the normalized mean deformation with respect to the undeformed configuration is:

- lowest for the BILEL model. This result means that the centroid of all plastic deformation ranges is much more centered for the BILEL model than for the other models, which could be expected.

The $(\overline{\Delta u_p}/U_y)$ response produced by the BILEL model has a larger variability than the other models in the period range $T_0 \leq 0.50$ sec (see Figs. 8.22 and 8.23 for $(\overline{\Delta u_p}/U_y)$).

$\mathbf{n^{(+)}, n^{(-)}}$: For a given confidence level p, the number of yield excursions, $N = n^{(+)} + n^{(-)}$, is:

- largest for the CLD model. This result is obvious from the definition of the CLD model (see Fig. 6.5(b)) which, after the first yielding, yields twice per cycle;
- lowest, by far, for the SLIP model;
- larger or equal for the BILEL model relative to the BILIN model, which indicates that inelasticity tends to reduce the number of yield excursions. In the case of a larger number of yield excursions by the BILEL model, the corresponding variability is also larger (see Fig. 8.23 for $n^{(+)}$ and $n^{(-)}$).

$\mathbf{\frac{n_{rev}}{n^{(+)} + n^{(-)}}}$: For a given confidence level p, the ratio of the number of yield reversals to the total number of yield excursions is:

- larger for the BILEL model than for the BILIN model, which means that the BILIN model tends more to yield consecutively in the same direction than the BILEL model.

$\mathbf{E^*_{I,max}}$: For a given confidence level p, the normalized seismic input energy is:

- lowest for the BILIN model, which means that the "fatter" the hysteresis loop, the more reduction in seismic energy input;
- not necessarily the largest for the BILEL model (nonlinear elastic);
- comparable for the CLD model and the SLIP model.

The normalized seismic input energy has the largest variability in the case of the BILEL model and the lowest in the case of the BILIN model (see Figs. 8.22 and 8.23 for $E^*_{I,max}$).

$\mathbf{E_H/TDE}$: For a given confidence level p, the ratio of the hysteretic energy dissipated to the total energy dissipated ($TDE = E_H + E_D$) is:

- much smaller for the SLIP model than for the other models, especially in the period range $T_0 \leq 0.60$ sec. This means that, in the case of the SLIP model, most of the seismic input energy has to be dissipated through viscous damping.

The "E_H/TDE" response has the lowest variability for the CLD model in the period range $T_0 \geq 0.5$ sec.

$\mathbf{P^*_{I,max}}$: For a given confidence level p, the normalized peak rate of seismic input energy is:

- lowest for the BILIN model, which already had the lowest normalized seismic input energy. However, the ratio "$P_{I,max}/E_{I,max}$" is not the smallest for the BILIN model. It is smaller for the BILEL model, indicating a smoother flow of seismic input energy into the BILEL model than into the BILIN model.

$\mathbf{P^*_{H,max}}$: For a given confidence level p, the normalized peak rate of hysteretic energy dissipation is:

- largest for the SLIP model;
- lowest for the BILIN model, which is another advantage of the BILIN model if structural damage is produced by a threshold value of the rate of hysteretic energy dissipation. However, the ratio "$P_{H,max}/E_H$" is not necessarily the smallest for the BILIN model. For example, in the case of El Centro, it is smaller for the CLD model than for the BILIN model, which means a smoother dissipation of hysteretic energy for the CLD model. The latter can be explained from the yielding at every half cycle of the CLD model after it has first yielded, which represents a more "continuous" yielding process than in the case of the BILIN model.

The $P^*_{H,max}$ response from the BILEL model has the lowest variability in the short period range $T_0 \leq 0.4$sec.

- $\mathbf{P^*_{D,max}}$: For a given confidence level p, the normalized peak rate of viscous damping energy dissipated is:

- lowest for the BILIN model, since most of the seismic input energy is dissipated through hysteretic behavior;
- largest for the SLIP model which must dissipate most of the seismic input energy through viscous damping.

In the short period range ($T_0 \leq 0.4$sec) this response parameter has the smallest variance for the BILEL model and the largest for the BILIN model.

8.4.5 Influence of Structural Parameters

The structural parameters characterizing the four restoring force models considered in this study are: (i) the initial undamped natural period of the structure T_0, (ii) the strain-hardening (or softening) ratio α, and (iii) the strength coefficient η. The sensitivity of the response parameter statistics with respect to these structural parameters is examined based on several structural response simulation cases summarized in Fig. 8.1. The statistical results used to describe the desired sensitivities are the PIRS curves (shape and amplitude) and the c.o.v. vs. period curves corresponding to the various inelastic response parameters.

Influence of Structural Period T_0:

Since the statistical results used in this study (PIRS's and c.o.v.'s) are plotted as a function of structural period T_0, the influence of T_0 on the statistics of the various response parameters is readily available on all the plots (Figs. 8.2 through 8.23). Only the main results from this sensitivity study are listed below.

- For given strength and confidence levels η and p, the μ_d, $P^*_{I,max}$ and $P^*_{D,max}$ response parameters plotted on a logarithmic scale decrease nearly linearly with respect to the logarithm of initial structural period. This result is observed for all four restoring force models. In the E02NS case, this close-to-linear relationship also applies to the response parameters μ_E, $E^*_{I,max}$ and $E^*_{I,end}$. Turkstra and Tallin have also reported this property [91] for average nonlinear spectra. The above result signifies that the sensitivities of the maximum displacement and hysteretic energy ductility factors (μ_d and μ_E) decrease

dramatically with structural period in the short period range. This is a well known result from deterministic studies [21,94].

- For a given probability level p and with other structural parameters fixed, all the inelastic response parameters considered in this study, except the ratio E_H/TDE are very sensitive to structural period in the short period range ($T_0 \leq 0.4$ sec). This is a general result observed for all hysteretic models.
- In the case of the El Centro ARMA(2,1) earthquake model, the PIRS's corresponding to the number of yield excursions and reversals exhibit a stationary level (maximum) at $T_0 = 0.20$ sec (see Figs. 8.12 and 8.14 for $n^{(+)}$, $n^{(-)}$ and n_{rev}) for the bilinear (elastic and inelastic) models.
- The PIRS curves corresponding to the ratio E_H/TDE exhibit a maximum (see Figs. 8.3, 8.4, 8.5 and 8.12, 8.13, 8.14 for E_H/TDE) for the three hysteretic models (BILIN, CLD and SLIP). However, the structural period at which this maximum occurs is different for the three models; it is lowest for the BILIN model and highest for the SLIP model.
- From the c.o.v. vs. period curves represented in Figs. 8.22 and 8.23, it is obvious that the c.o.v. of the response parameters characterized by a zero value at the transition point between elastic and inelastic behaviors (i.e., μ_R, $(\Delta u_p/U_y)_{max}$, $\overline{\Delta u_p}/U_y$, $n^{(+)}$, $n^{(-)}$, n_{rev}, $E^*_{H,max}$, E_H/TDE, $P^*_{H,max}$) are very large (> 2) at long periods ($T_0 \geq 2.0$ sec). This result is explained by the mixed behavior of structures at long period, i.e., within a sample of structural responses, only a few structures undergo inelastic behavior, resulting in large standard deviations of the response parameters compared to their very small mean values.
- Aside from the behavior of the c.o.v. of certain response parameters at long periods as described above, the following trends with respect to the c.o.v. vs. period are noticed:

(i) The c.o.v. of the maximum and residual displacement ductility factors (μ_d and μ_R) do not vary significantly with structural period (see Figs. 8.22 and 8.23 for μ_d and

μ_{res}). The amplitude of the c.o.v. of μ_d decreases with the intensity of the inelastic behavior;

(ii) In the period range $T_0 \leq 1.0$ sec, the c.o.v. of $(\Delta u / U_y)_{max}$ is almost constant with respect to structural period;

(iii) The c.o.v. of the number of yield excursions and reversals is constant with respect to period in the period range $T_0 \leq 0.60$ sec;

(iv) The c.o.v. of $E^*_{I,max}$ increases slightly with period;

(v) The c.o.v. of $P^*_{I,max}$, $P^*_{H,max}$ and $P^*_{D,max}$ is nearly constant over structural periods.

Influence of Positive Strain-Hardening

The influence of a positive strain-hardening ratio α on the response parameter statistics is examined through the parametric simulation cases I and II described below (see also Fig. 8.1).

Case I : E02NS target record

ARMA(4,2) earthquake model

Bilinear inelastic hysteretic model with $\xi_0 = 0.05$ and $\eta = 0.05$

Values of strain-hardening ratio: $\alpha = 0.00, 0.01, 0.05$

The corresponding PIRS's and c.o.v. vs. period curves are found in Figs. 8.3, 8.7, 8.8 and 8.24, respectively.

Case II : El Centro target record

ARMA(2,1) earthquake model

Bilinear inelastic hysteretic model with $\xi_0 = 0.05$ and $\eta = 0.10$

Values of strain-hardening ratio: $\alpha = 0.00, 0.01, 0.05$

The corresponding PIRS's and c.o.v. vs. period curves are found in Figs. 8.12, 8.16, 8.17 and 8.25, respectively.

The chosen values of 1 and 5 percent for the strain-hardening ratio are characteristic of real material (e.g., steel). The following observations can be made from the simulated sta-

tistical data. For a given probability level p, a few percent of positive strain-hardening:

- substantially decreases (e.g., more than a 40% decrease for 5% of strain-hardening) the maximum displacement ductility factor (μ_d) of short period structures only ($T_0 \leq 0.4$ sec); For longer period structures, the effect is much smaller (negligible);
- can have a slight increasing or decreasing effect on the hysteretic ductility factor (μ_E) of short period structures ($T_0 \leq 0.3$ sec);
- tremendously decreases the residual displacement ductility factor (μ_R) for structures in the period range ($T_0 \leq 0.60$ sec). This confirms a well known result from deterministic studies [59,94] where a very small amount of positive strain-hardening suffices to center the nonlinear oscillation of a bilinear inelastic hysteretic structure around the undeformed configuration;
- substantially decreases the $(\Delta u_p / U_y)_{max}$ and $(\overline{\Delta u_p} / U_y)$ response parameters for short period structures ($T_0 \leq 0.4$ sec);
- can slightly increase the number of yield excursions without increasing the number of yield reversals, indicating slightly more consecutive yielding in the same direction;
- slightly decreases the normalized seismic input energy and normalized hysteretic energy dissipation for short period structures ($T_0 \leq 0.3$ sec);
- has no effect at all on the ratio E_H / TDE;
- decreases the normalized peak rates of seismic input energy and viscous damping energy dissipation for short period structures ($T_0 \leq 0.3$ sec);
- significantly increases (by 50 %) the normalized peak rate of hysteretic energy dissipation.

From Figs. 8.24 and 8.25 representing the c.o.v. vs. period curves for the various response parameters and for different strain-hardening ratios, it is seen that a few percent of positive strain-hardening has no influence on the c.o.v. of the response parameters, except in the following cases:

- it slightly reduces the c.o.v. of μ_d and $(\Delta u_p / U_y)_{max}$ in the period range $T_0 \leq 0.4$ sec;
- it slightly increases the c.o.v. of the number of yield excursions in the period range $T_0 \leq 0.4$ sec;
- it increases the c.o.v. of $P^*_{H,max}$ in the period range $T_0 \leq 0.6$ sec.

Influence of Negative Strain-Hardening (P-Δ Effect)

In structural engineering, when geometric effects are taken into account, they soften the structure. A first order treatment of geometric effects consists in adding a negative stiffness (of value $-W/h$ where W is the weight of the structure and h its height) to the restoring force model [22]. This first order geometric effect is commonly called the "P-Δ effect". When the negative geometric stiffness is added to the post-yield stiffness (αk_0) of the restoring force model of the structure, the resulting effective post-yield stiffness can become negative (strain-softening). The effect of strain-softening (or negative strain-hardening) on the response parameter statistics is examined using the parametric simulation cases III and IV described below (see also Fig. 8.1).

Case III : E02NS target record

ARMA(4,2) earthquake model

Bilinear inelastic hysteretic model with $\xi_0 = 0.05$ and $\eta = 0.10$

Values of strain-softening ratio: $\alpha = 0.00, -0.01$

The corresponding PIRS's are found in Figs. 8.9 and 8.11.

Case IV : El Centro target record

ARMA(2,1) earthquake model

Bilinear inelastic hysteretic model with $\xi_0 = 0.05$ and $\eta = 0.20$

Values of strain-softening ratio: $\alpha = 0.00, -0.005$

The corresponding PIRS's are found in Figs. 8.18 and 8.20.

A very small strain-softening ratio has been selected ($\leq 1\%$) in order to keep all the structures out of the collapse range (i.e., zero or negative residual strength) for each artificial

ground motion. Violation of this restriction significantly complicates the statistical treatment of the response parameters. Examination of the statistical simulated data indicates that for a given probability level p, a very small ($\leq 1\%$) strain-softening ratio:

- significantly increases the maximum displacement ductility factor (μ_d) for short period structures only ($T_0 \leq 0.4$ sec);
- can slightly increase or decrease the hysteretic ductility factor (μ_E) for short period structures only ($T_0 \leq 0.3$);
- increases the μ_R and $(\overline{\Delta u_p}/U_y)$ response parameters for short period structures only;
- slightly increases the number of yield excursions with a simultaneous slight decrease in the number of yield reversals. This indicates a greater tendency for the structure to drift in a given direction;
- slightly decreases the normalized peak rates of seismic input energy, hysteretic and viscous damping energy dissipation for short period structures only ($T_0 \leq 0.3$ sec).

The c.o.v. vs. period curves, not represented here, show no effect of a small strain-softening on the c.o.v. of the various inelastic response parameters.

Influence of Strength Level:

The influence of the strength level on the response parameter statistics is studied through the parametric simulation cases V and VI described below (see Fig. 8.1):

Case V : E02NS target record

ARMA(4,2) earthquake model

Bilinear inelastic and Modified Clough's hysteretic models

with $\xi_0 = 0.05$ and $\alpha = 0.00$

Values of strength coefficient: $\eta = 0.05, 0.10$

The corresponding PIRS's and c.o.v. vs. period curves are shown in Figs. 8.3, 8.4, 8.9, 8.10 and Figs. 8.26, 8.27, respectively.

Case VI : El Centro target record

ARMA(2,1) earthquake model

Bilinear inelastic and Modified Clough's hysteretic models

with $\xi_0 = 0.05$ and $\alpha = 0.00$

Values of strength coefficient: $\eta = 0.10, 0.20$

The corresponding PIRS's and c.o.v. vs. period curves are shown in Figs. 8.12, 8.13, 8.18, 8.19 and Figs. 8.28, 8.29, respectively.

Hence, in each of these two cases, the effect of doubling the strength level (yield force) keeping all the other parameters fixed has been studied. The following observations are made from the simulated data statistics. For a given confidence level p:

- the relationship between the amplitude of the inelastic response parameters and the strength level is clearly nonlinear. In these two cases, most response parameters were reduced by a factor 3 to 10 in the short period range when the strength level was doubled. The exception is the number of yield excursions and reversals which responded almost linearly to the strength level change;
- the influence of the strength level is more significant in the short period range than in the long period range;
- overall, the influence of the strength level tends to be more significant for the bilinear inelastic hysteretic model than for the modified Clough's model;
- the more intense the inelastic behavior of a structure, the more influence its strength level has on the reduction of the inelastic behavior.

From the c.o.v. vs. period curves for the various inelastic response parameters (Figs. 8.26 through 8.29), the following trends are observed for the E02NS and El Centro cases for both the BILIN and CLD models. An increase of the strength level (yield force):

- increases the c.o.v. of the maximum displacement and hysteretic energy ductility factors (μ_d and μ_E) in the short period range and decreases it elsewhere;

- increases the c.o.v. of the number of yield excursions and reversals for the bilinear inelastic hysteretic model;
- increases substantially the c.o.v. of the response parameters E_H^*, E_H/TDE and P_H^* for long period structures, because of the mixed elastic-inelastic behavior mentioned previously;
- decreases the c.o.v. of $P_{I,max}^*$ and $P_{D,max}^*$ in the intermediate period range.

8.5 Probability Distribution of Plastic Deformation Ranges

This Section is concerned with the normalized plastic deformation ranges (PDR's) $\Delta u_{p,i}/U_y$, their probability distribution and their sensitivity with respect to hysteretic models and structural parameters. Plastic deformation ranges are very important inelastic response parameters, since they define the low-cycle fatigue damage index presented in Eq. (6.3). Their probability distribution is investigated based on very large samples of PDR's produced by a family of 100 artificial earthquakes. For a given hysteretic model and a given set of structural parameters, the histogram of the corresponding sample of PDR's is determined by subdividing the interval between the minimum and maximum PDR into 100 equal subintervals. For comparison purposes, the maximum abscissa value of each histogram corresponds to the maximum PDR, $(\Delta u_p/U_y)_{max}$, of the case under consideration. Such histograms are represented in Figs. 8.30 and 8.32 through 8.36 for the ARMA(4,2) E02NS simulation and in Figs. 8.37 and 8.39 through 8.43 for the ARMA(2,1) El Centro simulation. Each figure corresponds to a given restoring force model with a given set of structural parameters (ξ_0, η and α). Five natural periods are represented in each figure: T_0 = 0.10, 0.50, 1.00, 1.40 and 2.50 seconds.

The most representative theoretical probability distribution among several candidate distributions (normal, Rayleigh, shifted exponential and Gumbel type I) has been determined to be the lognormal distribution using the visual method of inspection of plots on probability paper. This result agrees with another statistical study on the distribution of PDR's based on a sample of real earthquake accelerograms [52]. To the right of each

histogram is the corresponding lognormal distribution fit on probability paper. Superimposed on each histogram is the lognormal distribution function corresponding to the least squares linear fit on probability paper. The total number of PDR's is also indicated for each histogram. The quality of the lognormal distribution fit to the simulated PDR's decreases with increasing natural period, possibly due the decreasing sample size of PDR's with increasing period. The general appearance of the histograms suggests a shifted exponential distribution; however, as shown in Figs. 8.31 and 8.38, which compare lognormal and exponential probability fits for two simulation cases, this is not true. The fitted lognormal distributions appear to be very asymmetric with a very narrow peak close to the origin.

Influence of Positive Strain-Hardening:

The influence of a positive strain-hardening of 5% on the PDR's is seen by comparing Figs. 8.30 and 8.32 for the E02NS case and Figs. 8.37 and 8.39 for the El Centro case. These figures correspond to bilinear inelastic structural models and show that a few percent of positive strain-hardening:

- substantially reduces the maximum PDR, $(\Delta u_p / U_y)_{max}$, for short period structures (this confirms a previous result);
- increases the number of PDR's (or number of yield excursions) over the whole period range $[0.10 \leq T_0 \leq 3.0 \text{ seconds}]$;
- does not produce a noticeable change in shape of the PDR histograms. However, it does slightly degrade the quality of the fit of the simulated PDR's by a lognormal distribution (see fits on probability paper).

Influence of Strength Level:

The influence of the strength level on the simulated PDR's is seen by comparing Figs. 8.30 and 8.33 for E02NS and Figs. 8.37 and 8.40 for El Centro. These figures correspond to bilinear inelastic structures. They demonstrate that doubling the strength level in these

two cases:

- reduces the largest PDR, $(\Delta u_p / U_y)_{max}$, by 70 to 80%;
- reduces, by 40 to 70% in the E02NS case and by 60 to 70% in the El Centro case, the number of PDR's for the periods illustrated. This relative reduction in the number of PDR's is increasing, with natural period T_0;
- only slightly reduces the quality of a lognormal distribution fit (see fits on probability paper). Hence, the shape of the underlying probability distribution of the PDR's does not appear very sensitive to the strength coefficient η.

The effects of doubling the strength level on the PDR's produced by the modified Clough's model are the following:

- it has the same effect on $(\Delta u_p / U_y)_{max}$ as in the case of the bilinear inelastic model;
- it noticeably increases (up to 40%) the number of PDR's in a short period range, the size of which depends on the intensity of the ground motion.

Influence of the Restoring Force Model:

To investigate the influence of the restoring force model on the PDR's, the modified Clough's model (CLD), the slip model (SLIP) and the bilinear elastic model (BILEL) are compared to the bilinear inelastic model (BILIN) which serves as a reference model.

Modified Clough's Model:

(compare Figs. 8.30 and 8.34 for E02NS and Figs. 8.37 and 8.41 for El Centro).

- the maximum PDR, $(\Delta_p / U_y)_{max}$, is much larger in the low period range for the CLD model;
- the total number of PDR's is much larger for the CLD model. This result is obvious from the definition of the CLD model (see Fig. 6.5(b)). The ratio of the number of PDR's produced by the CLD model to the ones produced by the BILIN model is increasing with structural period;

- the histogram of the PDR's decays much faster, especially in the period range $T_0 \leq 0.50$ second. This indicates that the CLD model has relatively smaller PDR's with respect to the BILIN model;
- for the El Centro case, the quality of a lognormal distribution fit for the PDR's of the CLD model is not as good as in the case of the BILIN model: the smallest PDR sizes as well as the largest are too small.

Slip Model:

(compare Figs. 8.30 and 8.35 for E02NS and Figs. 8.37 and 8.42 for El Centro).

- the largest PDR, $(\Delta_p/U_y)_{max}$, tends to be larger for the SLIP model when the ground motion intensity increases;
- for the same stochastic ground motion and structural parameters, the SLIP model has the lowest number of PDR's (or yield excursions) among the hysteretic models investigated. In the low period range, the number of PDR's produced by the SLIP model is considerably lower than for the other models;
- the PDR histograms decay slower than in the case of the BILIN model as the ground motion intensity increases (compare Figs. 8.37 and 8.42). This signifies that for the SLIP model, the medium size PDR's are relatively more frequent;
- the quality of a lognormal distribution fit is the same for the SLIP and BILIN models in the E02NS case. It is not as good for the SLIP model as for the BILIN model in the short period range for El Centro.

Bilinear Elastic Model:

(compare Figs. 8.30 and 8.36 for E02NS and Figs. 8.37 and 8.43 for El Centro).

- the largest PDR, $(\Delta u_p/U_y)_{max}$, is larger for the BILEL model than for the BILIN model in general;
- the number of PDR's is larger for the BILEL model than for the BILIN model in general;

- the PDR histograms tend to decay slower, indicating relatively more medium size PDR's for the BILEL model;
- the lognormal distribution fit is not as good for the BILEL model as for the BILIN model.

8.6 Variability of Structural Response Parameters vs. Variability of Ground Motion Parameters.

The variability, expressed in terms of the coefficient of variation (c.o.v.), of the traditional ground motion parameters defined in Section 5.4, are found in Table 5.6 for the ARMA(2,1) and ARMA(4,2) simulations of E02NS and in Table 5.7 for the ARMA(2,1) simulation of El Centro. The c.o.v. of the peak elastic response parameters (displacement, velocity and acceleration) as a function of period have been plotted in Figs. 8.44 and 8.45 for E02NS and El Centro, respectively(1). The lower and upper bounds of the c.o.v. corresponding to the various elastic and inelastic response parameters have been reported in Table 8.1 from Figs. 8.22, 8.23, 8.44 and 8.45. These lower and upper bounds include all hysteretic models considered (with structural parameters: $\xi_0 = 0.05$, $\alpha = 0.00$, $\eta = 0.05$ for E02NS and $\eta = 0.10$ for El Centro) and correspond to the period range $[0.10 \leq T_0 \leq 3.0 \text{ seconds}]$. Observation of Tables 5.6, 5.7 and 8.1 leads to the following remarks:

- In general, the lower and upper bounds correspond to short and long period structures, respectively;
- The variability of the ground motion parameters (see Table 5.6) and of the peak elastic response parameters (see Fig. 8.44) depend on the order of the ARMA model. For example, the c.o.v.'s generated by the ARMA(4,2) E02NS earthquake model are

(1) It is noticed that the c.o.v. of the relative displacement (S_d) and absolute acceleration (S_a) are almost identical, independently of the structural period. This is explained by the fact that for small damping values (here $\xi_0 = 0.05$), the absolute acceleration (S_a) and pseudo-acceleration (P_a) response spectra are almost identical. Moreover, the relative displacement and pseudo-acceleration response spectra are simply related as: $P_a = (2\pi / T_0)^2 S_d$. Hence, S_d and P_a have exactly the same c.o.v.

consistently larger than the c.o.v.'s generated by the ARMA(2,1) E02NS earthquake model;

- The upper bounds of the c.o.v.'s of the inelastic response parameters characterized by a zero value in the elastic range are considerably larger for E02NS than for El Centro. As already explained in Section 8.4.5, this results from the larger intensity of the El Centro stochastic ground motion with respect to the E02NS stochastic ground motion. In the El Centro case, more artificial ground motions drive long period structures into the plastic range than in the case of E02NS;
- The c.o.v.'s of the peak elastic response parameters (S_d, S_v and S_a) are inside the range defined by the minimum ground motion parameter c.o.v. (RMSA) and the maximum ground motion parameter c.o.v. (PGD, RMSD);
- In the E02NS case, several inelastic response parameters (μ_{acc}, μ_E, n^+, n^-, n_{rev}, E_H/TDE) have a lower variability in the low period range, than the least dispersed ground motion parameter (RMSA). This is not the case for El Centro. However, in the El Centro case, the majority of inelastic response parameters have a lower bound c.o.v. substantially smaller than the maximum ground motion parameter c.o.v;
- In the long period range, inelastic response parameters have a c.o.v. considerably larger than the largest ground motion parameter c.o.v;
- The majority of the inelastic response parameters have a larger variability over the whole period range than the elastic peak response parameters. However, some inelastic response parameters, such as μ_{acc}, μ_E, n^+, n^-, n_{rev}, E_H^* and E_H/TDE, have a lower variability in the low period range than the peak elastic response parameters;
- The relative difference between c.o.v. lower and upper bounds is considerably larger for inelastic than for elastic response parameters. This is due to the mixed elastic-plastic behavior already mentioned.

CHAPTER 9

CONCLUDING REMARKS

9.1 Summary of Work

The first part of the present work was undertaken as an initial step toward solving the complicated and important problem of realistically modeling the inherent variability associated with the ground motion time histories corresponding to a specific source-site pair. The solution to this problem is crucial for a realistic solution to the more general problem of seismic risk analysis of structures. The quantitative description of the uncertainty of the earthquake input into structures is critical in earthquake engineering, because the variability of the seismic response of structures is mainly driven by the input uncertainty.

To account for their uncertainty or variability, real earthquake ground motions are viewed as particular realizations of underlying earthquake stochastic processes. The versatile family of discrete stochastic linear ARMA models is used for the stochastic process representation. The discrete-time ARMA models are of generality equal to linear continuous-time analytical models, but have a number of significant advantages for digital analysis and simulation purposes. For example, they fulfill the desirable condition of model parsimony. Because their parameters are estimated directly form data in the time domain, the number of steps from analysis to simulation is also reduced since it is not necessary to convert back and forth between discrete and continuous models, or between time domain and frequency domain characterizations.

Chapter 2 contains a review of the state-of-the-art continuous-time stochastic earthquake models. It emphasizes the similarity between continuous and discrete stochastic models. The concepts used in continuous stochastic processes and in time series analysis are shown to be the same. The complete equivalence between the low order ARMA(2,1) model described by a stochastic second order difference equation and the continuous

second order stochastic differential equation is described in detail in Chapter 4. The derived parameter relationships between ARMA parameters and physical parameters provide a very useful physical insight for ARMA models.

An existing Kalman filter algorithm for the estimation of a time-varying stochastic ARMA model from a real earthquake accelerogram has been improved and applied to two earthquake records very different in nature: (i) Seismic event no. 39 (M_L = 6.5, January 1986) recorded at the rock station E-02 of the SMART 1 Array in Taiwan (E02NS) and (ii) the North-South component of the 1940 Imperial Valley earthquake recorded at El Centro, California. The time-varying property of the ARMA models used is necessary to account for both temporal and spectral nonstationarities characterizing real earthquake motions. The spectral nonstationarity, often neglected in the past, is very important to predict the response of inelastic degrading structures.

An ARMA(2,1) and an ARMA(4,2) model have been fitted to the E02NS record and an ARMA(2,1) model has been fitted to the El Centro record. The Kalman filter results were compared to a more traditional nonstationary estimation technique using the concept of a stationary moving time window.

Goodness of fit of the ARMA models was performed at three different levels: (i) check of the residuals for both uncorrelation and normality, (ii) comparison between the properties (both individual and statistical) of the simulated earthquake motions and the corresponding properties of the target earthquake and (iii) comparison between the probalistic elastic and inelastic response characteristics of single-degree-of-freedom (SDOF) systems produced by the fitted ARMA earthquake models and the corresponding deterministic response parameters associated with the target record.

Using the fitted nonstationary ARMA models, populations of 100 artificial earthquake ground accelerations were generated. The corresponding populations of traditional ground motion parameters used to characterize earthquake records were computed and analyzed stochastically to investigate their underlying probability distributions and their

relative variabilities (measured by their c.o.v.).

In the second part of the present work (from Chapter 6), the populations of artificial earthquakes were used to perform a comprehensive parametric study of the stochastic elastic and inelastic response of SDOF representations of structures by Monte Carlo simulation. To represent the nonlinear force-deformation characteristics of a structure, four different models were used, namely (1) the bilinear nondegrading inelastic model, (2) modified Clough's stiffness degrading model, (3) the slip model and (4) the bilinear elastic model. All these restoring force models are characterized by the same bilinear skeleton curve. Each of the nonlinear elastic or inelastic dynamic SDOF systems is uniquely defined by four structural parameters: (1) the initial natural period T_0, (2) the initial damping ratio ξ_0, (3) the strength coefficient η expressing the yield strength of a system as a fraction of its weight and (4) the strain-hardening (or -softening) ratio defined as the ratio of the post-yield stiffness to the initial stiffness.

The dynamic response of the nonlinear SDOF systems to the earthquake loading is characterized by several response parameters. Some of these response parameters have been correlated experimentally by several investigators to the most common damage mechanisms experienced by steel and reinforced concrete structures during major earthquakes or during earthquake like cyclic dynamic loading under laboratory conditions. These damage mechanisms are (i) the largest excursion failure, for which a pertinent damage index is the well known maximum displacement ductility factor and (ii) the low cycle fatigue damage, a cumulative type of damage which can be characterized by the cumulative hysteretic energy dissipation response parameter or by some linear or nonlinear aggregation of the plastic deformation ranges response quantities. Additional single or cumulative response quantities based on the deformation, the energy and the power responses have also been included in this study.

The stochastic response parameters were represented in terms of (i) probabilistic elastic response spectra (PERS), (ii) probabilistic inelastic response spectra (PIRS) and (iii)

coefficient-of-variation (c.o.v.) vs. structural period curves for the various response parameters examined. All these statistical results were obtained by the ARMA Monte Carlo simulation procedure.

The parametric study mentioned above has been adopted as a first step to investigate the complex relationships existing among earthquake ground motion processes, structural properties and structural response characteristics in a probabilistic framework. Compared to the traditional deterministic methods used to solve this complex problem, the stochastic approach selected has the following advantages:

- it eliminates the statistical bias introduced by the random details of a single ground motion time history;
- it provides insight into the inherent variability of the structural seismic response caused by the uncertainty of the ground motion time history.

Statistical analyses of the simulated populations of response parameters were performed to identify or approximate their underlying probability distributions, essential for seismic risk studies. The parametric study undertaken permitted extraction of the sensitivities of the various response or damage parameters with respect to: (i) the target earthquake, (ii) the ARMA model order, (iii) the structural model and (iv) the structural parameters. These sensitivities permit examination of the problem under consideration from two complementary view points: (1) for a fixed earthquake process, study the effects of changing the structural model and/or the structural parameters and (2) for a fixed structure, study the effects of changing the earthquake process.

In Chapter 7, a methodology is described combining probabilistic elastic spectra corresponding to a given site and several statistically independent seismic sources to derive uniform hazard elastic response spectra. Such uniform hazard spectra account rationally for a multi-source seismic environment and provide a very useful tool for probabilistic seismic design or seismic safety analysis of structures. This methodology can be directly extended to the inelastic response spectra without further complications. In the latter case,

uniform hazard inelastic or damage spectra are obtained, very useful for damage-control seismic design.

9.2 Summary of Findings

The most significant findings of the present research are separated into two different classes and summarized:

Nonstationary ARMA Modeling of Earthquake Ground Motions and Simulated Ground Motion Parameters:

- The general trends of the estimation results for time-varying ARMA models using (1) the iterative Kalman filter algorithm and (2) the stationary moving time window technique, were found in good agreement for low order ARMA models such as the ARMA(2,1) model, for example. However, this agreement deteriorates with growing ARMA model order.
- The Kalman filter algorithm provides a much more efficient, computationally faster, model estimation technique than the more traditional moving time window technique, which uses a maximum likelihood estimation procedure at each window position.
- The selection of the tuning parameter of the Kalman filter (variance of the step size of the random walk) requires a trade-off between the learning rate of the Kalman filter compared to the rate of change of the earthquake spectral properties and realistically smooth time histories of the estimated ARMA parameters. The starting conditions for the Kalman filter (initial values of the estimated ARMA model parameters) are very important for the success of Kalman filtering.
- Earthquake records which are predominantly uni-modal (energy mostly contained in a single fixed or time-varying frequency band) can be well modeled by the low order ARMA(2,1) model. For multi-modal type of earthquakes (energy distributed more or less equally in several fixed or time-varying non-contiguous frequency bands), higher order ARMA models are needed. In the latter case, it is useful for the engineer if these

higher order ARMA models can be expressed as multiple-cascading (uncoupled series system) of physically interpretable low order ARMA models, such as the ARMA(2,1) model.

- The low order ARMA models used in this study exhibit a low frequency error whose consequences on the structural response simulation results depend on the relative spectral properties of the fitted ARMA model and of the earthquake record to be fitted. Usually this low frequency error is responsible for "mismatches" between probabilistic and target elastic and inelastic response spectra in the long period range. This defect can be at least partially corrected by shaping the low frequency components of the simulated earthquakes using a high-pass filter such as the two-way Butterworth filter used in this study.
- The well known Kanai-Tajimi stochastic earthquake model is the continuous version of a subset of the discrete ARMA(2,1) model. The physical parameters T_g and ξ_g (indicating the instantaneous predominant frequency and frequency bandwidth of the earthquake accelerogram) obtained from the estimated ARMA(2,1) parameters agree well with a visual inspection of the corresponding target accelerogram.
- Provided a comprehensive implementation of the Kalman filtering algorithm is made, the estimated time-varying ARMA models are able to capture reasonably well for engineering purposes the amplitude and spectral nonstationarities of a target earthquake accelerogram.
- For the examples considered in this study, a good match was achieved between simulated statistics and corresponding target values of the following traditional ground motion parameters: peak ground acceleration (PGA), root-mean-square acceleration (RMSA), Arias intensity and spectral intensity.
- Due to the low frequency error remaining after high-pass filtering of the simulated motions, a bad match was obtained between simulated statistics and target values of ground displacement related ground motion parameters such as: peak ground displacement (PGD), PGD/PGA, root-mean-square displacement.

- Based on the examples of this study, the statistical distributions of the simulated traditional ground motion parameters were found to be well approximated by lognormal distributions. For a given earthquake process, the root-mean-square acceleration parameter was found to be the least scattered parameter among the set of ground motion parameters investigated. In particular, the RMSA parameter was found much less scattered than the peak ground acceleration parameter (PGA) extensively used in the past and still used today to characterize the damage potential of earthquake ground motions. The choice of a ground motion parameter characterized by a large variability and obtained from a single earthquake realization is not reliable. The variability (measured by the c.o.v.) of the various ground motion parameters was found to be noticeably dependent on the ARMA model order.

Structural Response Simulation of Elastic and Inelastic SDOF Systems:

- A good match was observed between simulated probabilistic and target elastic and inelastic (or damage) response spectra, except in the long period range, the lower bound of which depends on the relative spectral properties of the fitted ARMA model and of the target earthquake record analyzed. The overestimation of the target elastic and inelastic response spectra in the long period range is a consequence of the low frequency error characteristic of low order ARMA models fitted to earthquake accelerograms. From the examples studied, the relative rating of ARMA models of different orders appears to remain the same for the three levels of model checking. In the case of the nonlinear SDOF systems, it appears that the quality of the match between probalistic and target spectra is independent of the structural model and of the structural parameters.
- The visual method using probability paper has shown that the statistical distributions of the peak elastic responses and the various inelastic response parameters considered are well approximated by lognormal distributions with the following exceptions: (i) the statistical distributions of the number of yield excursions and of the number of yield reversals are better approximated by normal distributions and (ii) the distribution of the ratio

of the hysteretic energy dissipation to the total dissipated energy response parameter (E_H/TDE) is characterized by a negative skewness coefficient. The response parameters characterized by a lower limit value in the case of elastic behavior have a distribution of the mixed type (combination of a probability mass function and a probability density function) and in their case, the aforementioned lognormal distributions are in fact conditional on the yieding of the system. The lognormal nature of the plastic deformation ranges (PDR's) identified using the stochastic approach of this study confirms the result of another statistical study on the distribution of the PDR's based on a sample of real earthquake accelerograms. It was found that the relative levels of variabiliy of the various elastic and inelastic response parameters were conserved between ARMA models of different order. However, the overall level of these variabilities depends on the ARMA model order.

The comprehensive probabilistic parametric study undertaken offered a very large data base concerning the seismic response behavior of simple structural models. Numerous results were found, some of which confirmed, in a probabilistic framework, previous results obtained from traditional deterministic methods. The most important results are:

- The type of probability distribution of the various elastic and inelastic response parameters considered appear to be insensitive to (i) the target accelerogram, (ii) the ARMA model order, (iii) the type of hysteretic model and (iv) the structural parameters.
- The relative destructiveness of two target earthquake motions with respect to a given structure given by (i) the comparison of the corresponding deterministic inelastic spectra and (ii) the comparison of the corresponding probabilistic inelastic spectra, may not agree. More confidence can be placed in the answer given by (ii).
- The shape of the PIRS curves can change from one target earthquake to another, indicating that the dependence of inelastic response parameters on structural period varies across earthquakes. However, this question should be re-examined in the light of more than two target earthquakes. On the other hand, the general trends of the c.o.v. vs.

period curves of the various response parameters were maintained across the two target earthquakes, but this also should be verified using a larger sample of target earthquakes.

- A better fitted ARMA earthquake model does not necessarily generate less structural response variability.
- For a given confidence level,
  - The number of yield excursions is larger or equal for the bilinear elastic model than for the bilinear inelastic model, indicating that the inelastic behavior tends to reduce the number of yield excursions.
  - Among the different restoring force models investigated, the maximum normalized earthquake input energy and rate of earthquake input energy are lowest for the bilinear inelastic model indicating that the "fatter" the hysteresis loop, the more reduction in seismic input energy can be expected. The c.o.v. of the seismic input energy is also lowest for the bilinear inelastic model.
  - the maximum normalized rate of hysteretic energy is also lowest for the bilinear inelastic model which is another advantage of this type of behavior if structural damage is produced by the crossing of a threshold level by the rate of hysteretic energy dissipation response parameter.
  - the maximum displacement ductility factor, maximum normalized rates of hysteretic energy and damping energy dissipation response parameters plotted on a logarithmic scale decrease nearly linearly with respect to the logarithm of initial structural period. This result was observed for all restoring force models considered. In the case of the E02NS record, this result also extended to the normalized hysteretic ductility factor and to the normalized seismic input energy response parameters. Some of these results had also been reported in the literature in the case of average nonlinear spectra.
- For a fixed confidence level and with other structural parameters fixed, all inelastic response parameters considered in this study, except the ratio E_H/TDE are sensitive or very sensitive to structural period, to a small amount (few percent) of strain-hardening or

strain-softening (P-Δ effect) or to the strength level, in the short period range. These are general results valid for all force-deformation models examined. They agree with the results of similar studies but undertaken in a deterministic framework.

- The more intense the inelastic behavior of a structure, the more influence its strength level has on the reduction of the inelastic behavior.
- The parameters of the probability distributions characterizing the various response parameters are very much influenced by the spectral nonstationarity of the earthquake model.
- The c.o.v.'s of the peak elastic response parameters lie between the minimum and maximum c.o.v.'s corresponding to the traditional ground motion parameters considered. In the case of the E02NS record, several inelastic response parameters have a lower variabilityi, in the low period range, than the least scattered ground motion parameter. In the long period range, the inelastic response parameters have a c.o.v. considerably larger than the largest ground motion parameter c.o.v. This is due to the mixed elastic-plastic behavior in this period range.

Since no adequate sample of earthquake strong motion records corresponding to the same source-site pair is available in the world, it is impossible to directly compare the seismic response variability generated by the ARMA earthquake models with the "true" seismic response variability produced by a given physical earthquake mechanism at a given site. This remark raises a shortcoming of the ARMA modeling of earthquake ground motions, namely that ARMA models disguise the direct influence of the physical parameters involved in the earthquake generation process, such as the rupture mechanism at the source, the amount of energy release, the propagation of seismic waves through the ground medium and the local site conditions. They depend only on recorded earthquake time series, which aggregate the above physical parameters and explicitly assume that given these historical recorded values, the future is independent of all other factors.

9.3 Recommendations for Future Research

In consideration of the work done in the present study, recommendations for future research can be made:

- Some of the results obtained from the parametric probabilistic study should be revisited using a larger set of target earthquake accelerograms and of ARMA model orders. This would confirm or extend the generality of the results obtained from the present study.
- The effects of the spectral nonstationarity of the earthquake input on the seismic response of structures, identified qualitatively in this study, should be quantified. Such a quantification could be obtained by systematically comparing the seismic responses to earthquake models with and without spectral nonstationarities included.
- The discrete-time stochastic earthquake models estimated from real earthquake records can be used as a basis to derive equivalent continuous-time analytical models. The latter is the required form of ground motion input for analytical random vibration analysis. Nonlinear random vibration techniques could then be tested by comparing their results with the simulated results obtained using the discrete models. This conversion from discrete to continuous model is appealing since continuous stochastic models are more difficult to estimate from real earthquake data than discrete ARMA models.
- A seismic reliability assessment of structures could be obtained by convolving probability distributions of demands, identified in this study, and corresponding capacities assumed to be uncertain and described by random variables as well. Such a method provides a stochastic assessment of structures in which the randomness of the seismic input and the structural capacity are systematically and realistically accounted for. The proposed reliability assessment algorithm could be used to conduct a sensitivity study of the seismic reliability of a structure with respect to earthquake processes, structural systems and structural properties.
- For practical applications in earthquake-resistant design, the time-varying ARMA parameters need to be related to physical parameters characterizing the earthquake

generation mechanism such as magnitude and epicentral distance. This can be done by regressing the ARMA parameters time histories against the earthquake source variables for a large number of recorded seismic events.

- The ARMA model identification, estimation and identification procedures could be completely automated and integrated in a software package useful for the practicing earthquake engineer.
- The Kalman estimation procedure for time-varying ARMA models from real earthquake records could be improved by including some physical knowledge about the earthquake process in the state equation of the Kalman filter. Also, some state-of-the-art deterministic models from ground motion seismology could be combined with the probabilistic ARMA models to correctly shape the low frequency content of the artificial earthquake motions.
- The problem of local instability of time-varying ARMA models estimated without imposing stability constraints (as in this study) deserves special attention. This problem appeared once in the course of this study for an unpresented case.
- The damage characterization of structures subjected to cyclic dynamic loading such as earthquakes should be improved by developing comprehensive damage-coupled constitutive models by using concepts from continuum mechanics and results from experimental work on scaled-models of entire structures or real size substructures.

REFERENCES

[1] Abrahamson, N. A. et al., "The SMART I Accelegraph Array (1980-1987): A Review," Earthquake Spectra, Vol. 3, No. 2, pp. 263-287, May 1987.

[2] Anderson, B. D. O. and Moore, J. B., "**Optimal Filtering**," Prentice-Hall, New Jersey.

[3] Anderson, J. C., and Bertero, V. V., "Uncertainties in Establishing Design Earthquakes," Journal of the Engineering Structural Division, ASCE, Vol. 113, No. ST8, pp. 1709-1725, 1987.

[4] Ang, A. H.-S. and Tang, W. H., "**Probability Concepts in Engineering Planning and Design**," Volume I: Basic Principles, John Wiley & Sons, New York, N. Y., 1975.

[5] Ang, A. H.-S. and Tang, W. H., "**Probability Concepts in Engineering Planning and Design**," Volume II: Decision, Risk and Reliability, John Wiley & Sons, New York, N. Y., 1984.

[6] Araya, R., "Seismic Hazard Analysis: Improved Models, Uncertainty and Sensitivities," Ph.D. Thesis, University of California, Berkeley, 1988.

[7] Austin, M. A., Pister, K. S. and Mahin, S. A., "A Methodology for Computer-Aided Design of Earthquake-Resistant Steel Structures," Report No. UCB/EERC-85/13, Earthquake Engineering Research Center, University of California, Berkeley, CA, 1985.

[8] Baber, T. T. and Wen, Y. K., "Stochastic Equivalent Linearization for Hysteretic, Degrading, Multistory Structures," Civil Engineering Studies, Structural Research Series No. , University of Illinois at Urbana-Champaign, Urbana, Ill. April 1980.

[9] Bartlett, M. S., "The Theoretical Specification and Sampling Properties of Autocorrelated Time Series," Journal of the Royal Statistical Society, Supplement 8, pp. 27-40, 1940.

[10] Beck, J. L. and Dowling, M. J., "Quick Algorithms for Computing either Displacement, Velocity or Acceleration of an Oscillator," Journal of Earthquake Engineering and Structural Dynamics, Vol. 16, pp. 245-253, 1988.

[11] Biggs, J. M., "**Introduction to Structural Dynamics**," McGraw-Hill Book Company, New York, N.Y., 1964.

[12] Bogdanoff, J. L. and Krieger, W., "A New Cumulative Damage Model - Parts 1 and 2," Journal of Appl. Mech., Transactions of the ASME, Vol. 45, pp. 246-257, June 1978.

[13] Bogdanoff, J. L., "A New Cumulative Damage Model - Part 3," Journal of Appl. Mech., Transactions of the ASME, Vol. 45, pp. 733-739, Dec 1978.

[14] Bogdanoff, J. L. and Kozin, F., "A New Cumulative Damage Model - Part 4," Journal of Appl. Mech., Transactions of the ASME, Vol. 47, pp. 40-44, March 1980.

[15] Bolt, B. A., "**Seismic Strong Motion Synthetics**," Academic Press, 1987.

[16] Box, G. E. P., and Jenkins, G. M., "**Time Series Analysis: Forecasting and Control**," Revised Edition, Holden-Day, San Francisco, 1976.

[17] Brillinger, D. R., "**Time Series: Data Analysis and Theory**," Expanded Edition, Holden-Day, 1981.

[18] Brune, J. N., "Tectonic Stress and the Spectra of Seismic Shear Waves from Earthquakes," J. Geophys. Res., Vol. 75, No. 26, pp. 4997-5009, 1970.

[19] Chang, M. K., Kwiatkowski, J. W. and Nau, R. F., "ARMA Models for Earthquake Ground Motions," Journal of Earthquake Engineering and Structural Dynamics, Vol. 10, pp. 651-662, 1982.

[20] Chopra, A. K. and Kan, C., "Effects of Stiffness Degradation of Earthquake Ductility Requirements for Multistory Buildings," Journal of Earthquake Engineering and Structural Dynamics, Vol. 2, pp. 35-45, 1973.

[21] Clough, R. W. and Johnston, S. B., "Effect of Stiffness Degradation on Earthquake Ductility Requirements," Proc. Second Japan Earthquake Eng. Symp., Tokyo, pp. 227-232, 1966.

[22] Clough, R. W. and Penzien, J., "**Dynamics of Structures**," McGraw-Hill Book Co., New York, N. Y., 1975.

[23] Coffin, L. F., "A Study of the Effect of Cyclic Thermal Stresses in Ductile Metals," Transactions of ASME, Vol. 76, pp. 931-950, 1954.

[24] Conte J. P., "ARMA Models for Earthquake Excitation and Structural Response Simulation," CE299 Report, Department of Civil Engineering, University of California, Berkeley, 1988.

[25] Crandall, S. H. and Mark, W. D., "**Random Vibration in Mechanical Systems**," New York, Academic Press, 1963.

[26] Davenport, A. G., "Note on the Distribution of the Largest Value of a Random Function with Application to Gust Loading," Proc., Institution of Civil Engineers, Vol. 28, pp. 187-196, 1964.

[27] Der Kiureghian, A. and Ang, A., H.-S., "A Fault-Rupture Model for Seismic Risk Analysis," Bull. Seism. Soc. Am., Vol. 67, No. 4, pp. 1173-1194, 1977.

[28] Der Kiureghian, A., "Structural Response to Stationary Excitation," Journal of the Engineering Mechanics Division, ASCE, Vol. 106, No. EM6, pp. 1195-1213, 1980.

[29] Der Kiureghian, A., "A Response Spectrum Method for Random Vibration Analysis of MDF Systems," Journal of Earthquake Engineering and Structural Dynamics, Vol. 9, pp. 419-435, 1981.

[30] DiPasquale, E. and Cakmak, A. S., "Detection and Assessment of Seismic Structural Damage," Report NCCER-87-0015, Nat. Ctr. for Earthquake Engrg. Res., State Univ. of New York at Buffalo, Buffalo, N. Y., 1987.

[31] DiPasquale, E. and Cakmak, A. S., "Identification of the Serviceability Limit State and Detection of Seismic Structural Damage," Report NCCER-88-0022, Nat. Ctr. for Earthquake Engrg. Res., State Univ. of New York at Buffalo, Buffalo, N. Y., 1988.

[32] DiPasquale, E., Ju, J.-W., Askar, A. and Cakmak, A. S., "Relation Between Global Damage Indices and Local Stiffness Degradation," Journal of the Engineering Structural Division, ASCE, Vol. 116, No. ST5, pp. 1440-1456, 1990.

[33] Gawronski, W. and Natke, H. G., "On ARMA Models for Vibrating Systems," Journal of Computational Mechanics, June 1986.

[34] Gersch, W. and Liu, R. S-Z, "Time Series Methods for the Synthesis of Random Vibration Systems," Journal of Applied Mechanics, Vol. 43, pp. 159-165, 1976.

[35] Hadidi-Tamjed, H., "Statistical Response of Inelastic SDOF Systems Subjected to Earthquakes," Ph.D. Thesis, Stanford University, Stanford, CA, December 1987.

[36] Hamming, R. W., "**Digital Filters**," 2nd Ed., Prentice-Hall, 1983.

[37] Hart, J. D., "Simplified Earthquake Analysis of Buildings Including Site Effects," Ph.D. Thesis, University of California, Berkeley, 1989.

[38] Housner, G. W., "Characteristics of Strong-Motion Earthquakes," Bull. Seism. Soc. Am., Vol. 37, pp. 19-31, 1947.

[39] Housner, G. W., "Properties of Strong Ground Motion Earthquakes," Bull. Seism. Soc. Am., Vol. 45, pp. 187-218, 1955.

[40] Housner, G. W., "Behavior of Structures during Earthquakes," Proc. ASCE, Vol. 85, No. EM-4, October 1959.

[41] Housner, G.W. and Jennings, P.C., "Generation of Artificial Earthquakes," Journal of the Engineering Mechanics Division, ASCE, Vol. 90, No. EM1, pp. 113-150, 1964.

[42] Housner, G. W. and Jennings, P. C., "The Capacity of Extreme Earthquake Motions to Damage Structures," in **Structural an Geotechnical Mechanics**, Edited by W. J. Hall, Prentice-Hall, 1977.

[43] Housner, G. W., "Statistics of Pulses on Strong-motion Accelerograms," N.S.F. Seminar-Workshop on Strong Ground Motion, San Diego, California, 1978.

[44] Hudson, D. E., "Reading and Interpreting Strong Motion Accelerograms," EERI Monograph, 1979.

[45] IMSL, The International Mathematical and Statistical Library, User's Manual, Version 2.0, April 1987.

[46] Ju, J. W., "On Novel Energy-Based Coupled Elastoplastic Damage Models," 25th Annual Technical Meeting Society of Engineering Science, Berkeley, California, 1988.

[47] Kanai, K., "Semi-Empirical Formula for Seismic Characterization of the Ground," Bulletin of Earthquake Research Institute, University of Tokyo, Tokyo, Japan, Vol. 35, June, 1967.

[48] Kiremidjian, A. S. and Anagnos, T., "Stochastic Models for Earthquake Occurence," Report, The John A. Blume Earthquake Engineering Center, Stanford University, May 1983.

[49] Kitagawa, G., "Changing Spectrum Estimation," Journal of Sound and Vibration, Vol. 89, NO. 3, pp. 433-445, 1983.

[50] Kitagawa, G. and Gersch, W., "A Smoothness Priors Time-Varying AR Coefficient Modeling of Nonstationary Covariance Time Series," IEEE Transactions on Automatic Control, Vol. AC-30, NO. 1, pp. 48-56, January 1985.

[51] Krawinkler, H. et al., "Recommendations for Experimental Studies on the Seismic Behavior of Steel Components and Materials," The John A. Blume Earthquake Engineering Center, Report No. 61, Department of Civil Engineering, Stanford University, Stanford, CA, August 1983.

[52] Lashkari-Irvani, B., "Cumulative Damage Parameters for Bilinear Systems Subjected to Seismic Excitations," Ph.D. Thesis, Stanford University, Stanford, CA, August 1983.

[53] Lemaitre, J., "How to Use Damage Mechanics," Nuclear Engineering Design, 80(2), pp. 233-245, 1984.

[54] Lemaitre, J., "Plasticity and Damage Under Random Loading," 10th US Natl. Cong. of Appl. Mech., Austin, Texas, 1986.

[55] Lin, Y. K., "Application of Nonstationary Shot Noise in the Study of System Response to a Class of Nonstationary Excitations," Journal of Applied Mechanics, Vol. 30, pp. 555-558, 1963.

[56] Lin, Y. K., "**Probabilistic Theory of Structural Dynamics**," McGraw-Hill, New York, 1967.

[57] Lin, Y. K., "On Random Pulse Train and its Evolutionary Spectral Representation," Probabilistic Engineering Mechanics 1, pp. 219-223, 1986.

[58] Lin, Y. K. and Yong, Y., "Evolutionary Kanai-Tajimi Earthquake Models," Journal of the Engineering Mechanics Division, ASCE, Vol. 113, No. EM8, pp. 1119-1137, 1987.

[59] Mahin, S. A. and Lin, J., "Construction of Inelastic Response Spectra for Single-Degree-of-Freedom Systems," Report No. UCB/EERC-83/17, Earthquake Engineering Research Center, University of California, Berkeley, CA, 1983.

[60] Manson, S. S., "Behavior of Materials under Conditions of Thermal Stress," NACA, TN 2933, 1954.

[61] Marco, S. M. and Starkey, W. L., "A Concept of Fatigue Damage," Transactions of ASME, Vol. 76, pp. 627-632, 1954.

[62] Miner, M. A., "Cumulative Damage in Fatigue," Journal of Applied Mechanics, September 1945.

[63] Nau, R. F. and Oliver, R. M., "Adaptive Filtering Revisited," Journal of the Operational Research Society, Vol. 30, No. 9, pp. 825-831, 1979.

[64] Nau, R. F., Oliver, R. M. and Pister, K. S., "Simulating and Analyzing Artificial Non-Stationary Earthquake Ground Motions," Bull. Seism. Soc. Am., Vol. 72, No. 4, pp. 615-636, 1982.

[65] Nigam, N. C., "**Introduction to Random Vibrations**," MIT Press, Cambridge, Massachusetts, 1983.

[66] Ohi, K., Takanashi, K. and Homma, Y., "Energy Input Rate Spectra of Earthquake Ground Motions," Bull. ERS, No. 23, 1990.

[67] Page, C. H., "Instantaneous Power Spectra," Journal of Applied Physics, Vol. 23, pp. 103-106, 1952.

[68] Palmgren, A., "Die Lebensdauer von Kugellagern," Z. Vereines Deutscher Ingenieure, 68, 1924 (in German).

[69] Papadimitriou, K. and Beck, J. L., "Nonstationary Stochastic Characterization of Strong-Motion Accelerograms," submitted for publication in Earthquake Engineering and Structural Dynamics, November 1989.

[70] Papageorgiou, A. and Aki, K., "A Specific Barrier Model for the Quantitative Description of Inhomogeneous Faulting and the Prediction of Strong Ground Motion," Bull. Seism. Soc. Am., Vol. 73, pp. 693-722 and 953-978, 1983.

[71] Park, Y. J. and Ang, A. H.-S., "Mechanistic Seismic Damage Model for Reinforced Concrete", Journal of the Engineering Structural Division, ASCE, Vol. 111, No. ST4, pp. 722-739, 1985.

[72] Park, Y. J., Ang, A. H.-S. and Wen, Y. K., "Seismic Damage Analysis of Reinforced Concrete Buildings", Journal of the Engineering Structural Division, ASCE, Vol. 111, No. ST4, pp. 740-757, 1985.

[73] Powell, G. H. and Row, D. G., "Influence of Analysis and Design Assumptions on Computed Inelastic Response of Moderately Tall Frames," Report No. UCB/EERC-76/11, Earthquake Engineering Research Center, University of California, Berkeley, CA, 1976.

[74] Powell, G. H. and Allahabadi, R., "Seismic Damage Prediction by Deterministic Methods: Concepts and Procedures," Journal of Earthquake Engineering and Structural Dynamics, Vol. 16, pp. 719-734, 1988.

[75] Press, W. H. et al., "**Numerical Recipes: The Art of Scientific Computing**," Cambridge University Press, 1986.

[76] Priestley, M. B., "**Spectral Analysis and Time Series**," 2 vols. Academic Press, London and New York, 1981.

[77] "Proceedings of the Second Workshop on Processing of Seismic Strong Motion Records," (Part 2), Tokyo, Japan, August 1988.

[78] Richter, C. F., "**Elementary Seismology**," W. H. Freeman, San Francisco, 1958.

[79] Saiidi, M. and Sozen, M. A., "Simple and Complex Models for Nonlinear Seismic Response of Reinforced Concrete Structures," Civil Engineering Studies, Structural Research Series No. 465, University of Illinois at Urbana-Champaign, Urbana, Ill. August 1979.

[80] Saiidi, M. and Sozen, M. A., "Simple Nonlinear Seismic Analysis of R/C Structures," J. of the Eng. Structural Division, ASCE, Vol. 107, No. ST5, pp. 937-952, 1981.

[81] Sewell, R. T., "Damage Effectiveness of Earthquake Ground Motion: Characterization Based on the Performance of Structures and Equipment," Ph.D. Thesis, Stanford University, Stanford, CA, December 1988.

[82] Sharma, M. P. and Shah, H. C., "Time Varying Parametric Time Domain Modeling of Strong Ground Motion," Proc., 8th ECEE, Lisbon, 1986.

[83] Shinozuka, M. and Sato, Y., "Simulation of Nonstationary Random Processes," J. of the Eng. Mechanics Division, ASCE, Vol. 93, No. EM1, pp. 11-40, 1967.

[84] Shinozuka, M. and Jan, C. M., "Digital Simulation of Random Processes and its Applications," Journal of Sound and Vibration, Vol. 25, NO. 1, pp. 111-128, 1972.

[85] Shinozuka, M., "Stochastic Fields and their Digital Simulation," Stochastic Methods in Structural Dynamics, (Eds G. I. Schueller and M. Shinozuka), Martinus Nijhoff Publishers, Dordrecht, pp. 93-133, 1987.

[86] Simo, J. C. and Ju, J. W., "Strain- and Stress-Based Continuum Damage Models - I. Formulation," Int. J. Solids Struct., 23(7), pp. 821-840, 1987.

[87] Simo, J. C. and Ju, J. W., "Strain- and Stress-Based Continuum Damage Models - II. Applications," Int. J. Solids Struct., 23(7), pp. 841-869, 1987.

[88] Tajimi, H., "A Standard Method of Determining the Maximum Response of a Building Structure During an Earthquake," Proc., Second World Conference on Earthquake Engineering, Tokyo, Japan, Vol. II, pp. 781-798, July 1960.

[89] Trifunac, M. D. and Brune, J. N., "Complexity of Energy Release During the Imperial Valley, California, Earthquake of 1940," Bull. Seism. Soc. Am., Vol. 60, No. 1, pp. 137-160, 1970.

[90] Trifunac, M. D., "Tectonic Stress and the Source Mechanism of the Imperial Valley, California, Earthquake of 1940," Bull. Seism. Soc. Am., Vol. 62, No. 5, pp. 1283-1302, 1972.

[91] Turkstra, C. J. and Tallin, A. G., "A Re-evaluation of Design Spectra for Seismic Damage Control," Report NCCER-88-0032, Nat. Ctr. for Earthquake Engrg. Res., State Univ. of New York at Buffalo, Buffalo, N. Y., 1988.

[92] Vanmarcke, E. H., "Properties of Spectral Moments with Applications to Random Vibration," Journal of the Engineering Mechanics Division, ASCE, Vol. 98, No. EM2, pp. 425-446, 1972.

[93] Vanmarcke, E. H., "On the Distribution of the First-Passage Time for Normal Stationary Random Processes," J. of Applied Mechanics, Vol. 42, pp. 215-220, 1975.

[94] Veletsos, A. S., "Maximum deformations of Certain Nonlinear Systems," Proc. Fourth World Conf. in Earthquake Eng., Santiago, Chile, 1969.

[95] Wakabayashi, M., "**Design of Earthquake-Resistant Buildings**," McGraw-Hill Book Company, New York, N.Y., 1986.

[96] Walker, A. M., "Note on a Generalization of the Large Sample Goodness of Fit Test for Linear Autoregressive Schemes," Journal of the Royal Statistical Society, Series B, Vol. 12, pp. 102-107, 1950.

[97] Wen, Y. K., "Methods of Random Vibration for Inelastic Structures," Appl. Mech. Rev. Vol. 42, no. 2, Feb 1989.

[98] Wilson, E. L., Der Kiureghian, A., and Bayo, E. P., "A Replacement for the SRSS Method in Seismic Analysis", Journal of Earthquake Engineering and Structural Dynamics, Vol. 9, pp. 187-192, 1981.

[99] Zohrei, M., "Cumulative Damage in Components of Steel Structures Under Cyclic Inelastic Loading," Ph.D. Thesis, Stanford University, Stanford, CA, December 1982.

TABLE 4.1

Roots of Characteristic Equation $r^2 - \phi_1 r - \phi_2 = 0$

Zone #	Roots $r_{1,2}$	Properties of $r_{1,2}$
1	$r_{2,1} = \sqrt{-\phi_2}\, e^{\pm i \frac{\sqrt{-(\phi_1^2 + 4\phi_2)}}{\phi_1}}$	complex conjugate
2	$r_{2,1} = \frac{\phi_1 \pm \sqrt{\phi_1^2 + 4\phi_2}}{2}$	$r_1 > 0$ $0 < r_2 < \phi_1$ $\lvert r_2 \rvert > \lvert r_1 \rvert$
3		$\phi_1 < r_1 < 0$ $r_2 < 0$ $\lvert r_1 \rvert > \lvert r_2 \rvert$
4		$r_1 < 0$ $r_2 > \phi_1 > 0$ $\lvert r_1 \rvert > \lvert r_2 \rvert$
5		$r_1 < \phi_1 < 0$ $r_2 > 0$ $\lvert r_1 \rvert > \lvert r_2 \rvert$

TABLE 4.2

Discrete Autocorrelation Coefficient Function ρ_n

Zone #	$\rho_n = \rho(n\Delta t), n = 0, 1, 2 \cdots$
1	$\rho_n = \rho(n\Delta t) = e^{\frac{n}{2}\ln(-\phi_2)} \dfrac{\cos(n\theta - \mu_d)}{\cos(-\mu_d)}$ where $\mu_d = \tan^{-1}\left(\dfrac{2\rho_1 - \phi_1}{\sqrt{-(\phi_1^2 + 4\phi_2)}}\right)$, $\theta = \cos^{-1}\left(\dfrac{\phi_1}{2\sqrt{-\phi_2}}\right)$ and ρ_1 as defined in Eq. (4.6b)
2	$\rho_n = \rho(n\Delta t) = e^{cn}\left[\cosh(dn) + \dfrac{e^{-c}\rho_1 - \cosh(d)}{\sinh(d)}\sinh(dn)\right]$ where $c = \dfrac{1}{2}\ln(-\phi_2)$, $d = \dfrac{1}{2}\ln\dfrac{\phi_1 + \sqrt{\phi_1^2 + 4\phi_2}}{\phi_1 - \sqrt{\phi_1^2 + 4\phi_2}}$ and ρ_1 as defined in Eq. (4.6b)
3	$\rho_n = \rho(n\Delta t) = e^{cn}\left[(-1)^n\cosh(dn) + (-1)^{n+1}\dfrac{e^{-c}\rho_1 + \cosh(d)}{\sinh(d)}\sinh(dn)\right]$ where c, d and ρ_1 as defined for zone 2
4 , 5	$\rho_n = \rho(n\Delta t) = e^{cn}\left[\cosh(dn) + (-1)^{n+1}\dfrac{e^{-c}\rho_1 - \cosh(d)}{\sinh(d)}\sinh(dn)\right]$ where $c = \dfrac{1}{2}\ln(\phi_2)$ and $d = \dfrac{1}{2}\ln\left(\dfrac{\phi_1 + \sqrt{\phi_1^2 + 4\phi_2}}{\phi_1 - \sqrt{\phi_1^2 + 4\phi_2}}\right)$

TABLE 4.3

Discrete/Continuous Parameter Relationships for Zone 1
(Underdamped Case: $\xi_g < 1$)

Continuous-to-discrete conversion : $(\omega_g , \xi_g , \frac{C_s}{C_d}) \rightarrow (\phi_1 , \phi_2 , \theta_1)$

$$\phi_1 = 2\, e^{-\xi_g \omega_g \Delta t} \cos(\omega_g \sqrt{1 - \xi_g^2}\ \Delta t)$$

$$\phi_2 = -\, e^{-2 \xi_g \omega_g \Delta t}$$

$$\theta_1 = \text{solution of :}\quad \theta_1^2 + \frac{2\rho_1\phi_1 - \phi_1^2 + \phi_2^2 - 1}{\phi_1 - \rho_1 (1 - \phi_2)}\, \theta_1 + 1 = 0 \quad , \quad |\theta_1| < 1$$

$$\text{where}\quad \rho_1 = \rho(\Delta t) = \frac{1}{2}\, \frac{(\frac{C_s}{C_d})^2 - 4\,\xi_g^2}{(\frac{C_s}{C_d})^2 + 4\,\xi_g^2}\, \frac{\xi_g}{\sqrt{1 - \xi_g^2}}\, \sqrt{-(\phi_1^2 + 4\,\phi_2)} + \frac{1}{2}\,\phi_1$$

$$0 < \omega_g \sqrt{1 - \xi_g^2} \le \frac{\pi}{\Delta t}$$

Discrete-to-continuous conversion : $(\phi_1 , \phi_2 , \theta_1) \rightarrow (\omega_g , \xi_g , \frac{C_s}{C_d})$

$$\omega_g = \frac{\sqrt{4\,\lambda_d^2 + \ln^2(-\phi_2)}}{2\,\Delta t}$$

$$\xi_g = \frac{-\ln(-\phi_2)}{\sqrt{4\,\lambda_d^2 + \ln^2(-\phi_2)}}$$

$$\left(\frac{C_s}{C_d}\right)^2 = 4\,\xi_g^2 \left(\frac{\xi_g + \sqrt{1 - \xi_g^2}\ \tan\mu_d}{\xi_g - \sqrt{1 - \xi_g^2}\ \tan\mu_d}\right)$$

$$\text{where}\quad \lambda_d = \cos^{-1}\left(\frac{\phi_1}{2\sqrt{-\phi_2}}\right), \qquad 0 \le \lambda_d \le \pi$$

$$\text{and}\quad \mu_d = \tan^{-1}\left(\frac{2\,\rho_1 - \phi_1}{\sqrt{-(\phi_1^2 + 4\,\phi_2)}}\right), \qquad -\frac{\pi}{2} \le \mu_d \le \frac{\pi}{2}$$

$$\text{where}\quad \rho_1 = \frac{\phi_1\,(1 + \theta_1^2 - \theta_1\,\phi_1) - \theta_1\,(1 - \phi_2^2)}{(1 - \phi_2)\,(1 + \theta_1^2 - \theta_1\,\phi_1) - \theta_1\,\phi_1\,(1 + \phi_2)}$$

TABLE 4.4

Discrete/Continuous Parameter Relationships for Zone 2
(Overdamped Case: $\xi_g > 1$)

Continuous-to-discrete conversion : $(\omega_g , \xi_g , \frac{C_s}{C_d}) \rightarrow (\phi_1 , \phi_2 , \theta_1)$

$$\phi_2 = -e^{-2\xi_g \omega_g \Delta t}$$

$$\phi_1 = -\frac{2}{\kappa}\phi_2 + \frac{\kappa}{2} \quad \text{where} \quad \kappa = 2\,e^{-\omega_g\left[\xi_g - \sqrt{\xi_g^2 - 1}\right]\Delta t}$$

$$\theta_1 = \text{solution of :} \quad \theta_1^2 + \frac{2\rho_1\phi_1 - \phi_1^2 + \phi_2^2 - 1}{\phi_1 - \rho_1(1-\phi_2)}\theta_1 + 1 = 0 \quad , \quad |\theta_1| < 1$$

$$\text{where} \quad \rho_1 = \sqrt{-\phi_2}\left[\cosh(d) + \frac{\left(\frac{C_s}{C_d}\right)^2 - 4\xi_g^2}{\left(\frac{C_s}{C_d}\right)^2 + 4\xi_g^2}\,\frac{\xi_g}{\sqrt{\xi_g^2 - 1}}\sinh(d)\right]$$

$$\text{and} \quad d = \frac{1}{2}\ln\left[\frac{\phi_1 + \sqrt{\phi_1^2 + 4\phi_2}}{\phi_1 - \sqrt{\phi_1^2 + 4\phi_2}}\right]$$

Discrete-to-continuous conversion : $(\phi_1 , \phi_2 , \theta_1) \rightarrow (\omega_g , \xi_g , \frac{C_s}{C_d})$

$$\xi_g = \frac{1}{\sqrt{2K - K^2}} \quad \text{where} \quad K = \frac{2}{\ln(-\phi_2)}\ln\left[\frac{\phi_1 + \sqrt{\phi_1^2 + 4\phi_2}}{2}\right]$$

$$\omega_g = -\frac{1}{2\xi_g\Delta t}\ln(-\phi_2)$$

$$\left(\frac{C_s}{C_d}\right)^2 = \frac{-4\xi_g^2\left[\left(\frac{\rho_1}{\sqrt{-\phi_2}} - \cosh(d)\right)\sqrt{\xi_g^2 - 1} + \sinh(d)\,\xi_g\right]}{\left(\frac{\rho_1}{\sqrt{-\phi_2}} - \cosh(d)\right)\sqrt{\xi_g^2 - 1} - \sinh(d)\,\xi_g}$$

$$\text{where} \quad \rho_1 = \frac{\phi_1(1 + \theta_1^2 - \theta_1\phi_1) - \theta_1(1 - \phi_2^2)}{(1 - \phi_2)(1 + \theta_1^2 - \theta_1\phi_1) - \theta_1\phi_1(1 + \phi_2)}$$

and d as defined above

TABLE 5.1

Summary of Earthquake Data

Location	Earthquake Date & Time	Magnitude	Mechanism	Station & Comp. used in this study	Record Identification
SMART 1 Accelerograph Array (Taiwan) Event 39	1/16/86 13:04:32 UTC	6.5 (M_L) 5.8 (M_S)	?	E02, N-S	E-02NS*
Imperial Valley, California	5/18/40 20:37 PST	6.3	Strike Lateral Slip on Imperial Fault	El Centro, N-S	A001.S00** (EERL)

* Uncorrected digital record ($\Delta t = 0.01$ sec)

** Baseline corrected digitized analog record ($\Delta t = 0.02$ sec)

TABLE 5.2

Characteristics of Target Earthquake Records

Record Station and Component	SMART 1 Array Event 39, 1/16/86, N-S	El Centro 5/18/40, N-S
Magnitude	6.5 (M_L)	6.3
Depth [km]	10	?
Epicentral Dist. [km]	22	8.1
Site Geology	rock	firm deep alluvium deposit
Record Duration [sec]	18.5	35.0
PGA [in/sec^2]	78.26	134.52
PGV [in/sec]	4.495	13.17
PGD [in]	0.419	4.28
PGV/PGA [sec]	0.057	0.098
PGD/PGA [sec^2]	0.0054	0.032
RMSA [in/sec^2]	11.902	21.80
RMSV [in/sec]	0.49	3.01
RMSD [in]	0.10	2.09
AI [in/sec]	10.66	67.67
SI [in]	8.266	53.43

TABLE 5.3

High-Pass Filters

Filter	Type	Parameters
Filter I	Two-Way Butterworth*	$\epsilon = 0.17$, $A = 2.0$, $f_p = 0.065$ Hz , $f_s = 0.095$ Hz → 7 POLES
Filter II	Two-Way Butterworth	$\epsilon = 0.17$, $A = 2.0$, $f_p = 0.080$ Hz , $f_s = 0.120$ Hz → 6 POLES
Filter III	Two-Way Butterworth	$\epsilon = 0.17$, $A = 2.0$, $f_p = 0.100$ Hz , $f_s = 0.140$ Hz → 7 POLES
Filter IV	Brune's Model**	$f_c = 0.10$ Hz

* see Appendix A

** see Section 3.6

TABLE 5.4

Statistical Tests for the ARMA Models Fitted to the E02NS Record

Model	Q	# d.o.f.	Percentage of $\hat{\rho}(k\Delta t)$ outside 95% conf. interval
ARMA(2,1)	883	375	16.1 %
ARMA(4,2)	567	372	9.3 %
Discrete White-Noise # 1	293	378	3.2 %
Discrete White-Noise # 2	334	378	1.9 %
Discrete White-Noise # 3	358	378	4.5 %
Ampl.-Demod. E02NS rec.	4774	370	

TABLE 5.5

Statistical Tests for the ARMA(2,1) Model Fitted to El Centro 1940

Model	Q	# d.o.f.	Percentage of $\hat{\rho}(k\Delta t)$ outside 95% conf. interval
ARMA(2,1)	447	347	6.8 %
Discrete White-Noise # 1	273	350	2.6 %
Discrete White-Noise # 2	311	350	2.9 %
Discrete White-Noise # 3	322	350	4.6 %
Ampl.-Demod. EL Centro rec.	4961	350	

TABLE 5.6

Ground Motion Parameters of E02NS and Statistics from ARMA(2,1) and ARMA(4,2) Earthquake Models

Parameter	Target	Mean	Std	C.O.V.
PGA [in/sec^2]	78.26	70.76* 73.82**	13.43 23.53	0.19 0.32
PGV [in/sec]	4.50	4.35 4.92	1.10 1.67	0.25 0.34
PGD [in]	0.42	2.34 3.02	1.12 1.94	0.48 0.64
PGV/PGA [sec]	0.057	0.063 0.068	0.020 0.019	0.31 0.28
PGD/PGA [sec^2]	0.0054	0.0342 0.0400	0.0176 0.0200	0.51 0.50
RMSA [in/sec^2]	11.90	9.61 9.16	1.13 1.51	0.12 0.17
RMSV [in/sec]	0.49	0.95 1.16	0.30 0.51	0.32 0.44
RMSD [in]	0.10	0.85 1.06	0.39 0.59	0.46 0.56
AI [in/sec]	10.66	7.05 6.49	1.69 2.36	0.24 0.36
SI [in]	8.27	10.95 13.86	2.60 5.67	0.24 0.41

* ARMA(2,1) Model

** ARMA(4,2) Model

TABLE 5.7

Ground Motion Parameters of El Centro 1940 and Statistics from ARMA(2,1) Earthquake Model

Parameter	Target	Mean	Std	C.O.V.
PGA [in/sec^2]	134.52	136.32	21.25	0.16
PGV [in/sec]	13.17	21.45	5.36	0.25
PGD [in]	4.28	14.02	4.99	0.36
PGV/PGA [sec]	0.098	0.159	0.04	0.25
PGD/PGA [sec^2]	0.032	0.105	0.04	0.38
RMSA [in/sec^2]	21.80	20.76	1.36	0.07
RMSV [in/sec]	3.01	5.03	1.12	0.22
RMSD [in]	2.09	4.63	1.56	0.34
AI [in/sec]	67.67	61.62	8.14	0.13
SI [in]	53.43	58.68	12.00	0.20

TABLE 8.1

Lower and Upper Bounds of the C.O.V. of Elastic and Inelastic Response Parameters in Period Range [$0.10 \leq T_0 \leq 3.0$ sec]

Parameter	ARMA(2,1) E02NS	ARMA(4,2) E02NS	ARMA(2,1) El CENTRO
S_d or S_a	0.22* / 0.40**	0.27 / 0.59	0.18 / 0.34
S_v	0.20 / 0.34	0.24 / 0.49	0.19 / 0.32
μ_d		0.53 / 0.83	0.30 / 0.60
μ_{acc}		0.15 / 0.93	0.13 / 0.93
μ_E		0.13 / 0.68	0.13 / 0.51
μ_R		0.75 / 2.80	0.63 / 1.00
$(\Delta u_p / U_y)_{max}$		0.71 / 2.70	0.40 / 0.90
$(\overline{\Delta u_p} / U_y)$		0.90 / 2.30	0.60 / 1.50
n^+		0.13 / 2.50	0.08 / 0.70
n^-		0.14 / 3.30	0.13 / 0.70
n_{rev}		0.15 / 4.40	0.09 /0.90
$E^*_{I,max}$		0.38 / 0.83	0.21 / 0.60
$E^*_{I,end}$		0.40 / 0.95	0.21 / 0.63
E^*_H		0.27 / 2.70	0.16 / 0.90
E_H/TDE		0.05 / 2.50	0.025 / 0.50
$P^*_{I,max}$		0.70 / 0.87	0.39 / 0.57
$P^*_{H,max}$		0.32 / 2.40	0.20 / 0.50
$P^*_{D,max}$		0.70 / 1.10	0.40 / 0.67

* Minimum (C.O.V.)

** Maximum (C.O.V.)

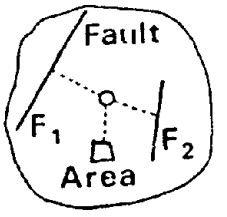

STEP 1: Earthquake Sources

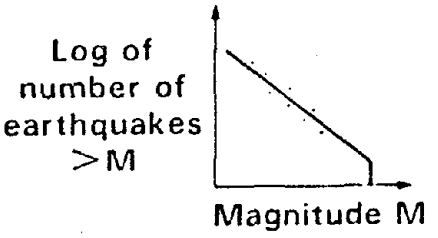

STEP 2: Magnitude Recurrence

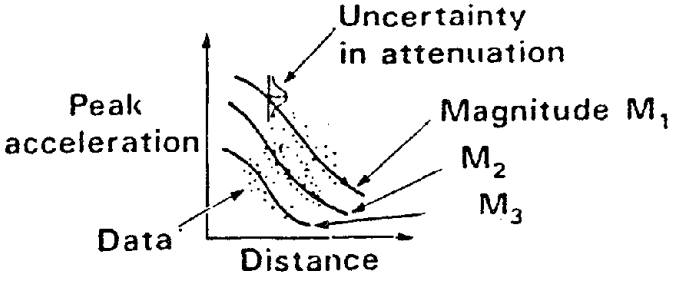

STEP 3: Intensity Attenuation Relationship

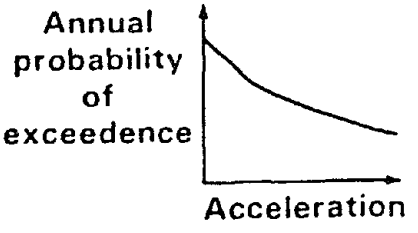

STEP 4: Evaluation of the Hazard Curve

Fig. 1.1 Probabilistic Seismic Hazard Analysis Procedure (from Ref. [6])

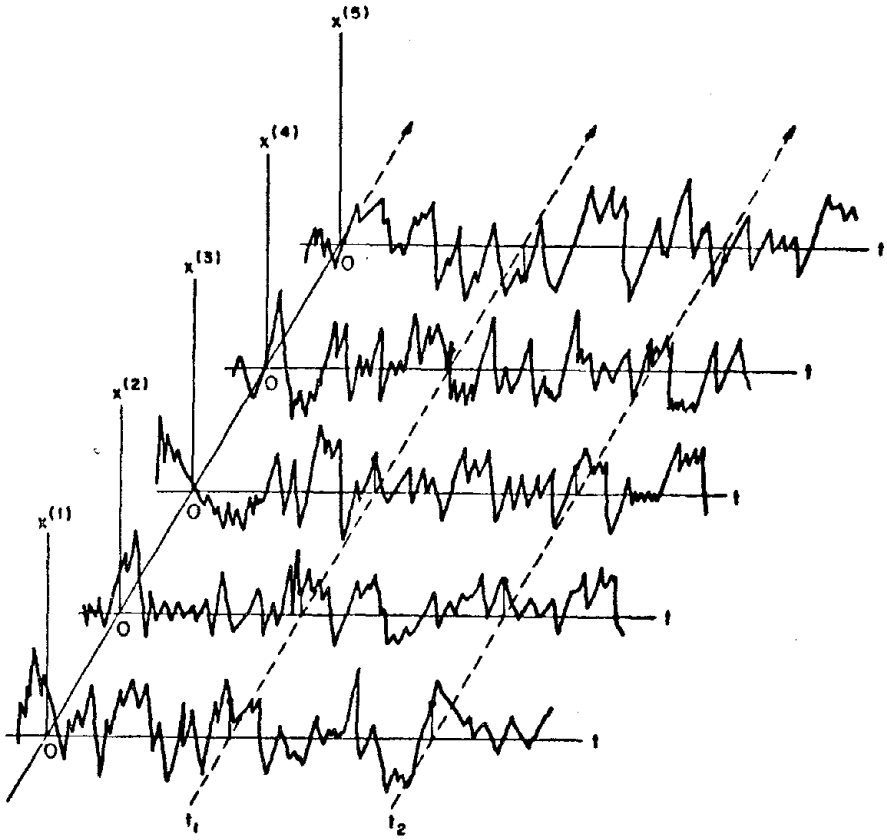

Fig. 2.1 Schematic Representation of a Random Process X(t) (from Ref. [25])

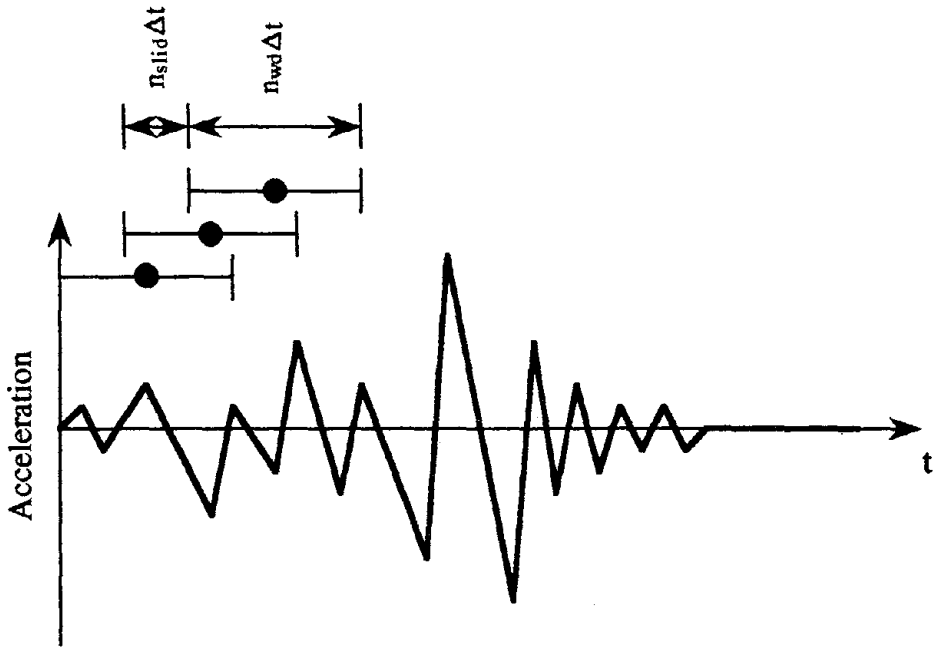

Fig. 3.1 Time Windowing of an Accelerogram

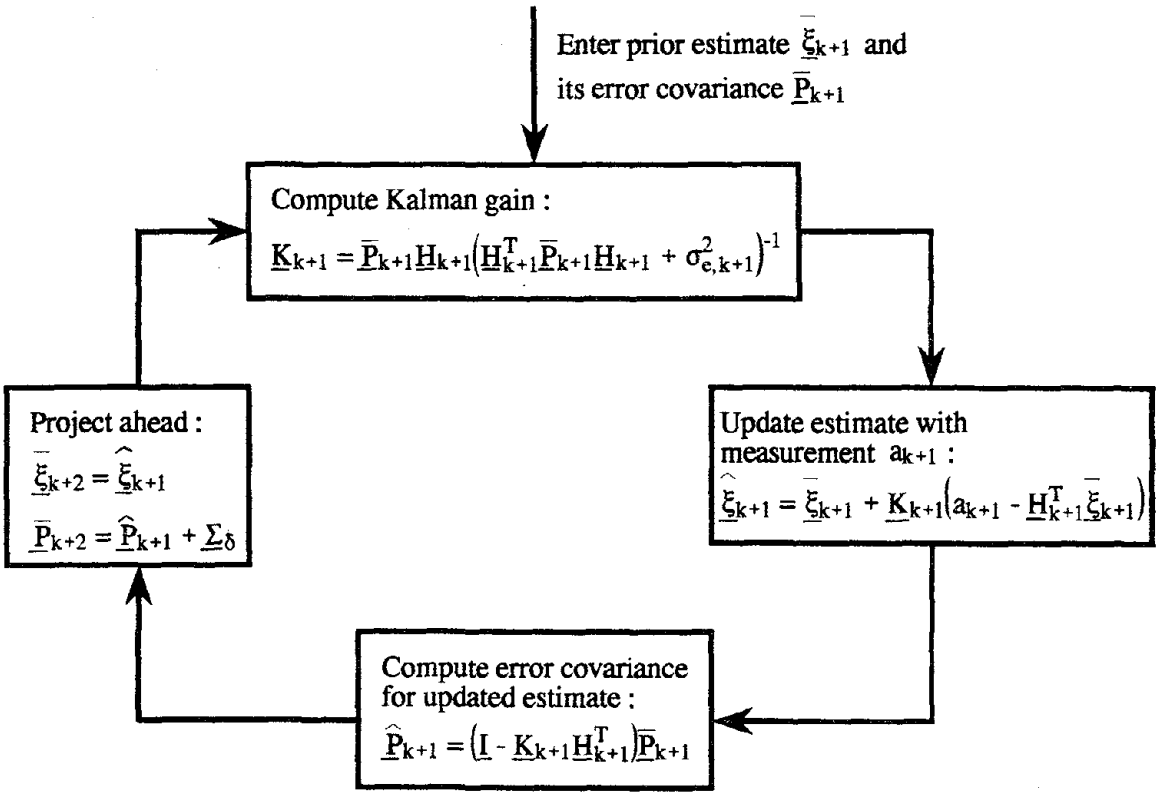

Fig. 3.2 Kalman Filter Loop

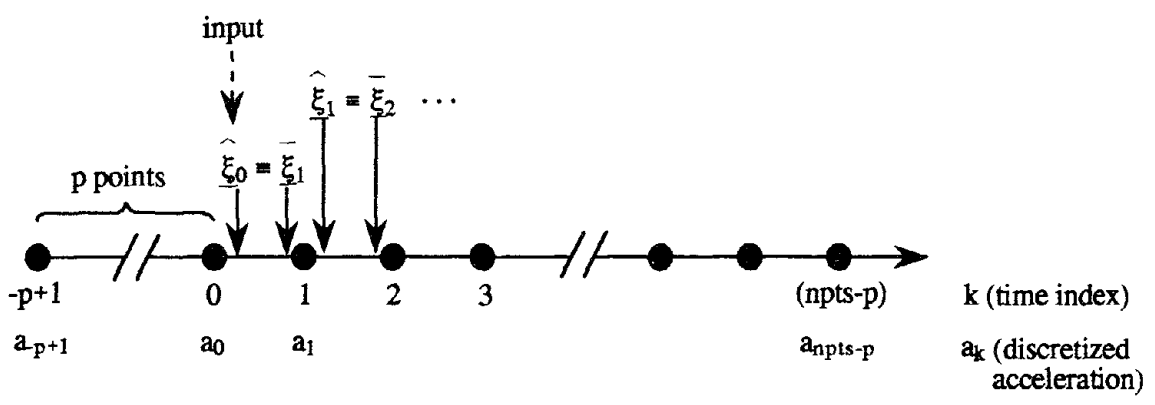

Fig. 3.3 Starting Conditions for Kalman Filtering

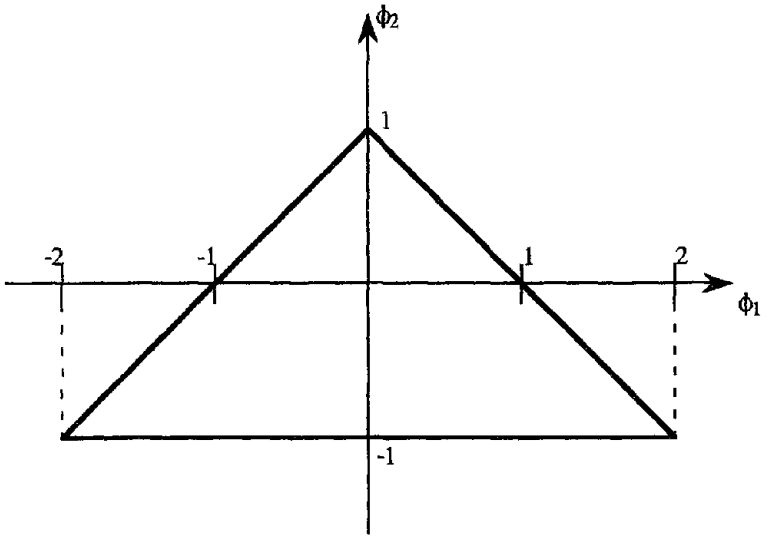

Fig. 4.1 Stability Region for the ARMA(2,1) Model

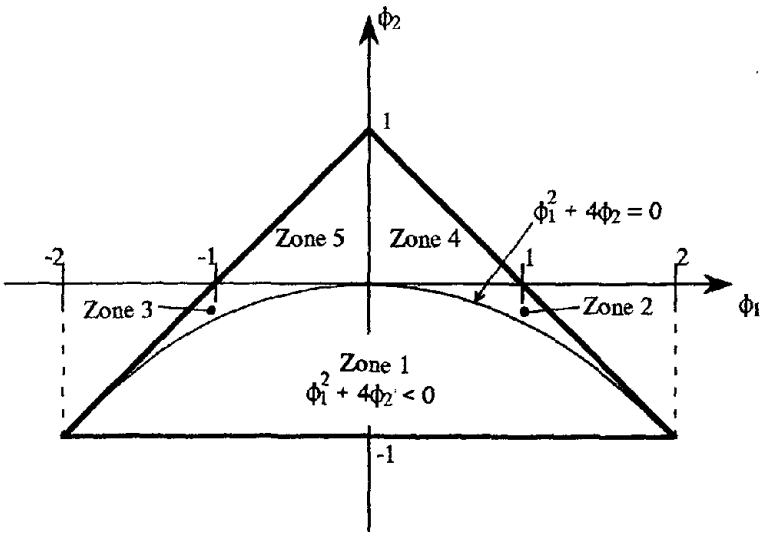

Fig. 4.2 Definitions of Zones 1 to 5

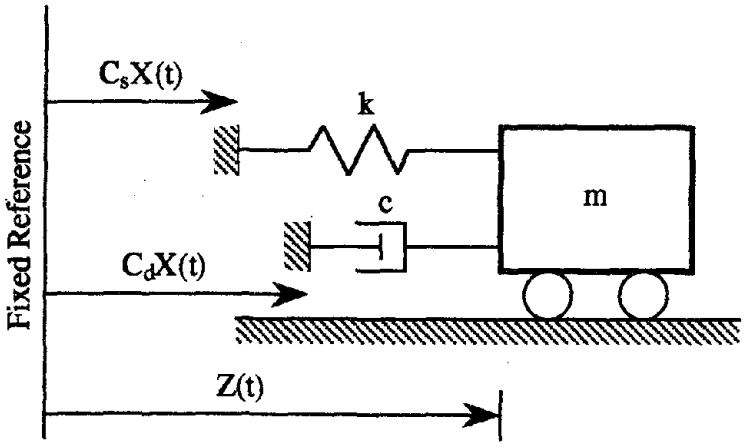

Fig. 4.3 Underlying Physical System

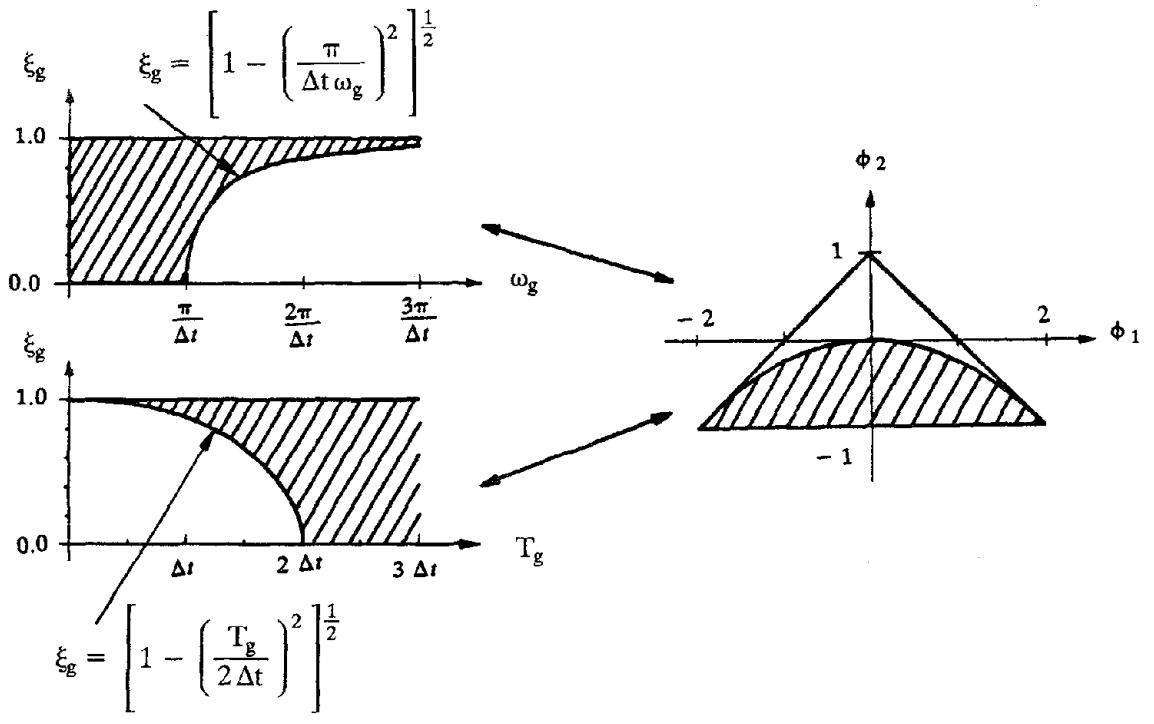

Fig. 4.4 Reduced Mapping $(\phi_1, \phi_2) \longleftrightarrow (\omega_g, \xi_g)$ for Underdamped Case

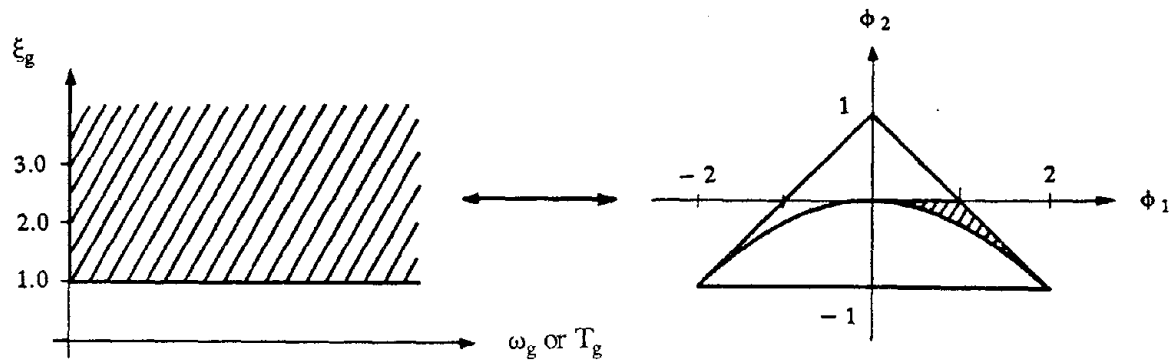

Fig. 4.5 Reduced Mapping $(\phi_1, \phi_2) \longleftrightarrow (\omega_g, \xi_g)$ for Overdamped Case

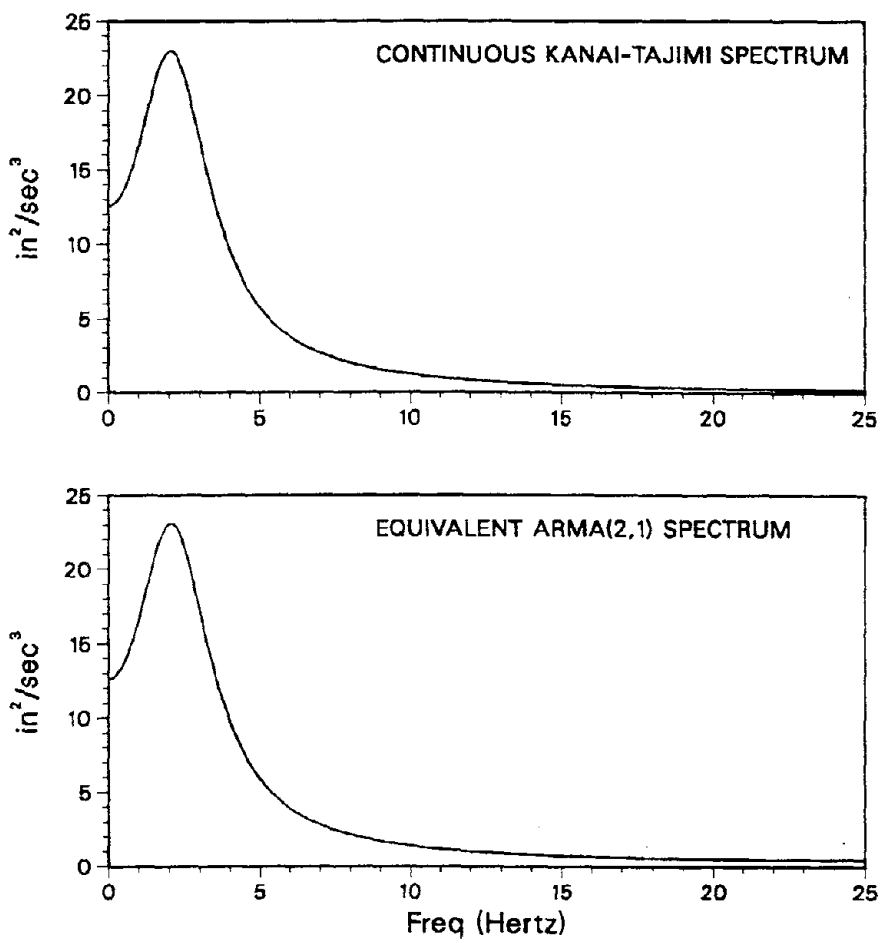

Fig. 4.6 Kanai-Tajimi and Corresponding ARMA(2,1) PSD

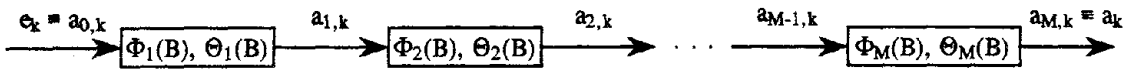

Fig. 4.7 Multiple Cascading of Low Order ARMA Models

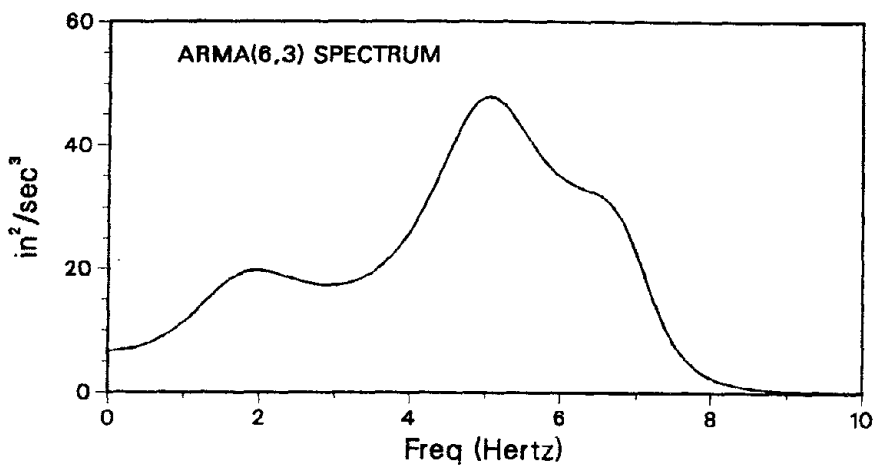

Fig. 4.8 Tri-Modal PSD Corresponding to an ARMA(6,3) Model

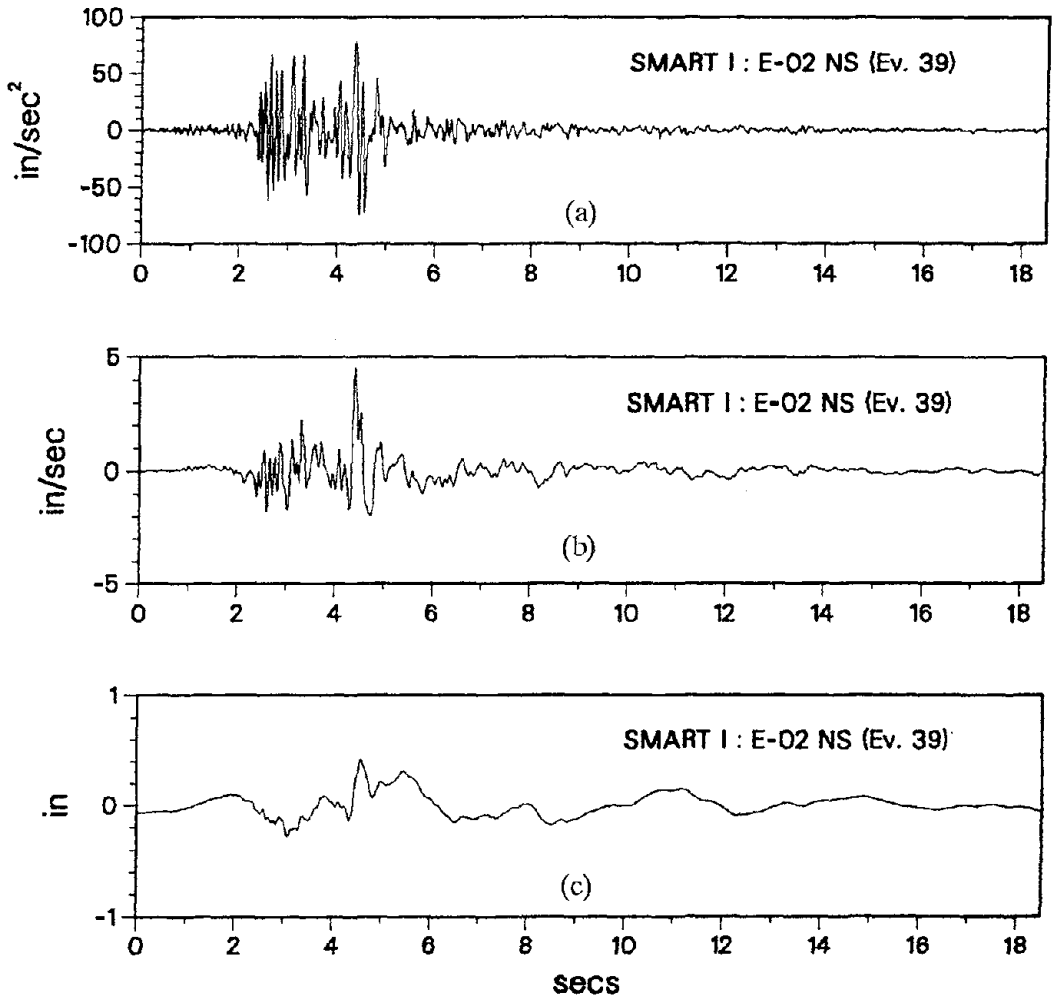

Fig. 5.1 Ground Acceleration (a), Velocity (b) and Displacement (c) Time Histories of the E02NS Record

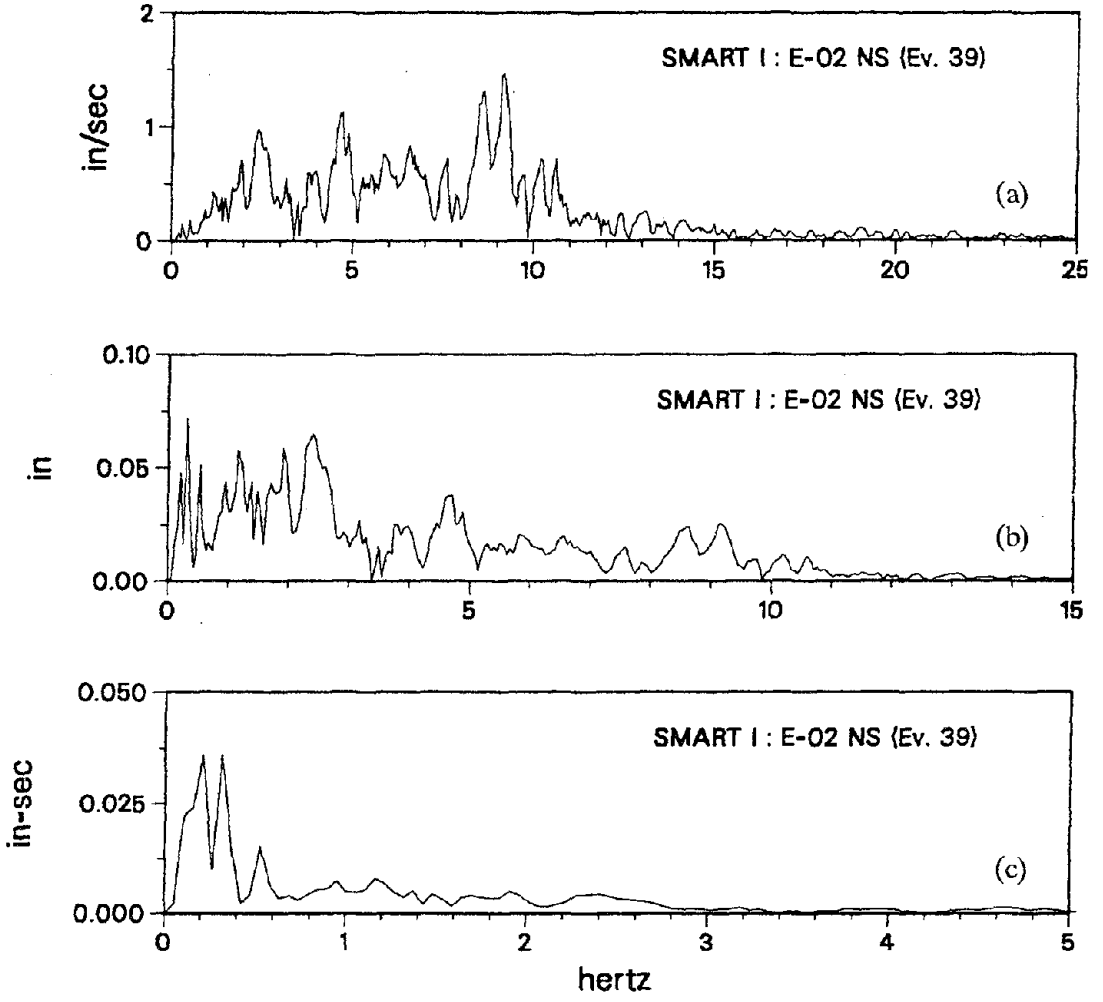

Fig. 5.2 Ground Acceleration (a), Velocity (b) and Displacement (c) Fourier Amplitude Spectra of the E02NS Record

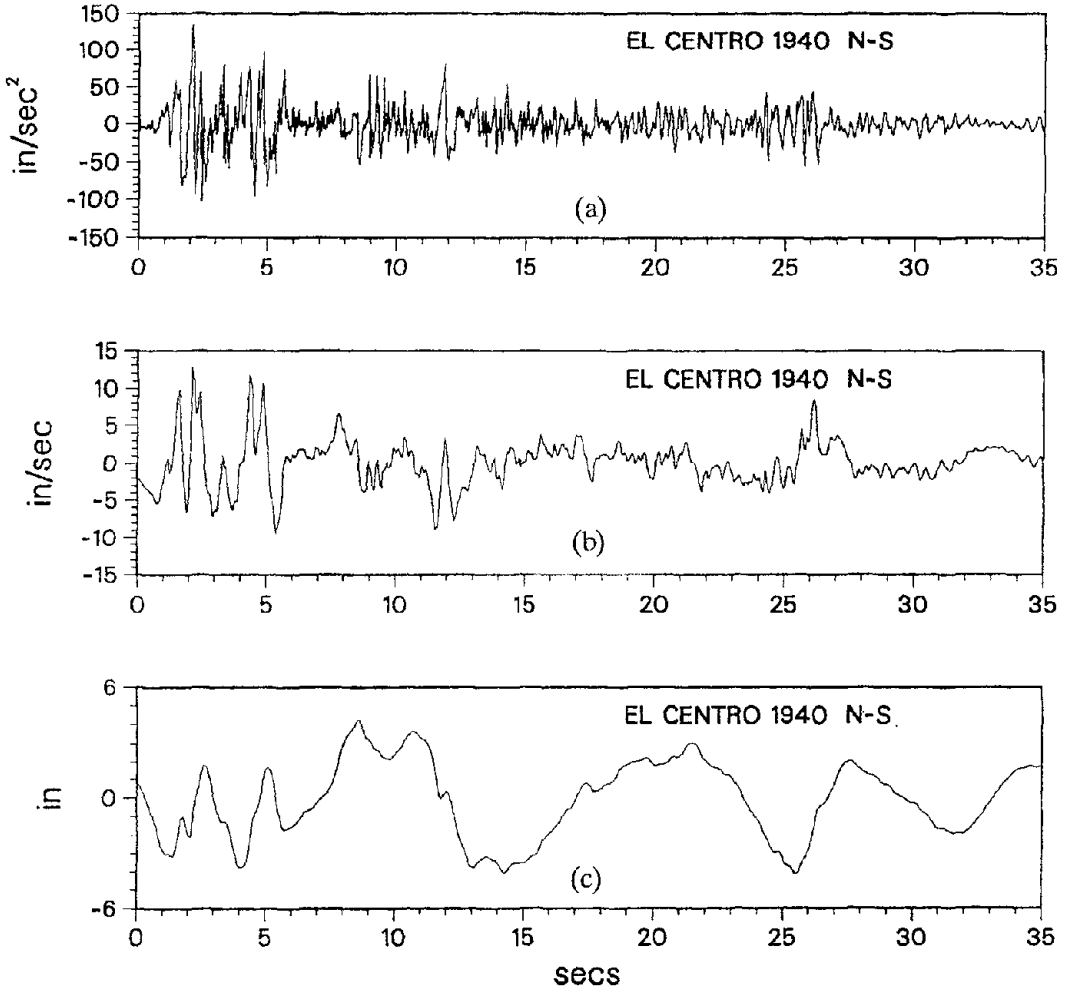

Fig. 5.3 Ground Acceleration (a), Velocity (b) and Displacement (c) Time Histories of the El Centro 1940 Record

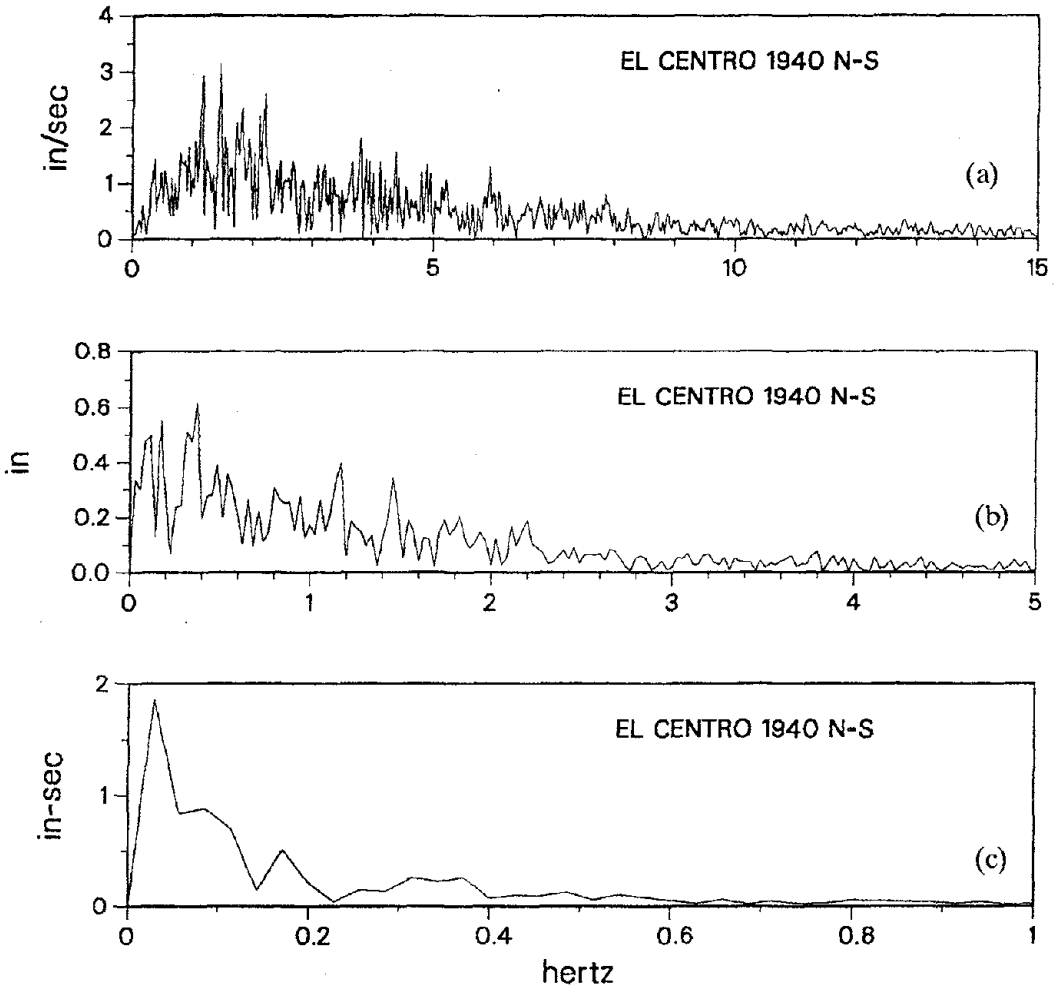

Fig. 5.4 Ground Acceleration (a), Velocity (b) and Displacement (c) Fourier Amplitude Spectra of the El Centro 1940 Record

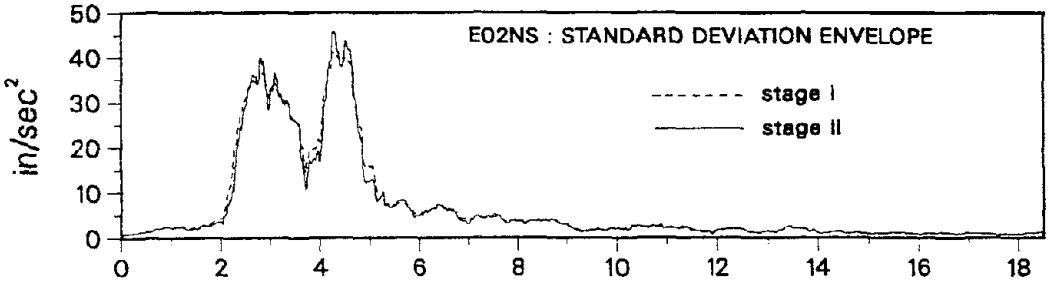

Fig. 5.5 Standard Deviation Envelope of the E02NS Record

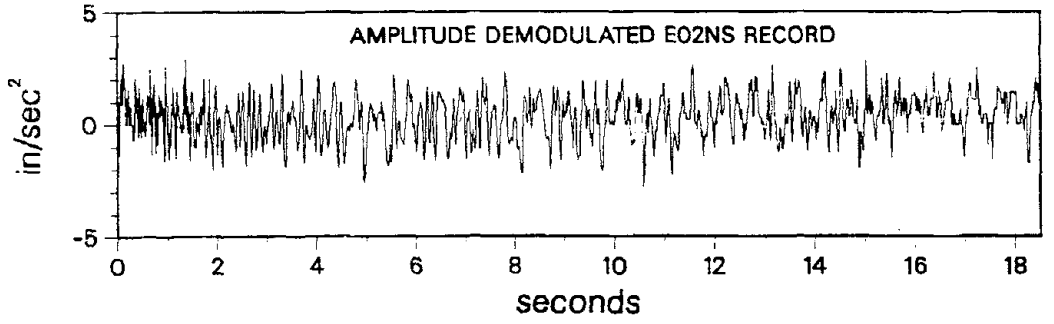

Fig. 5.6 Amplitude Demodulated E02NS Record

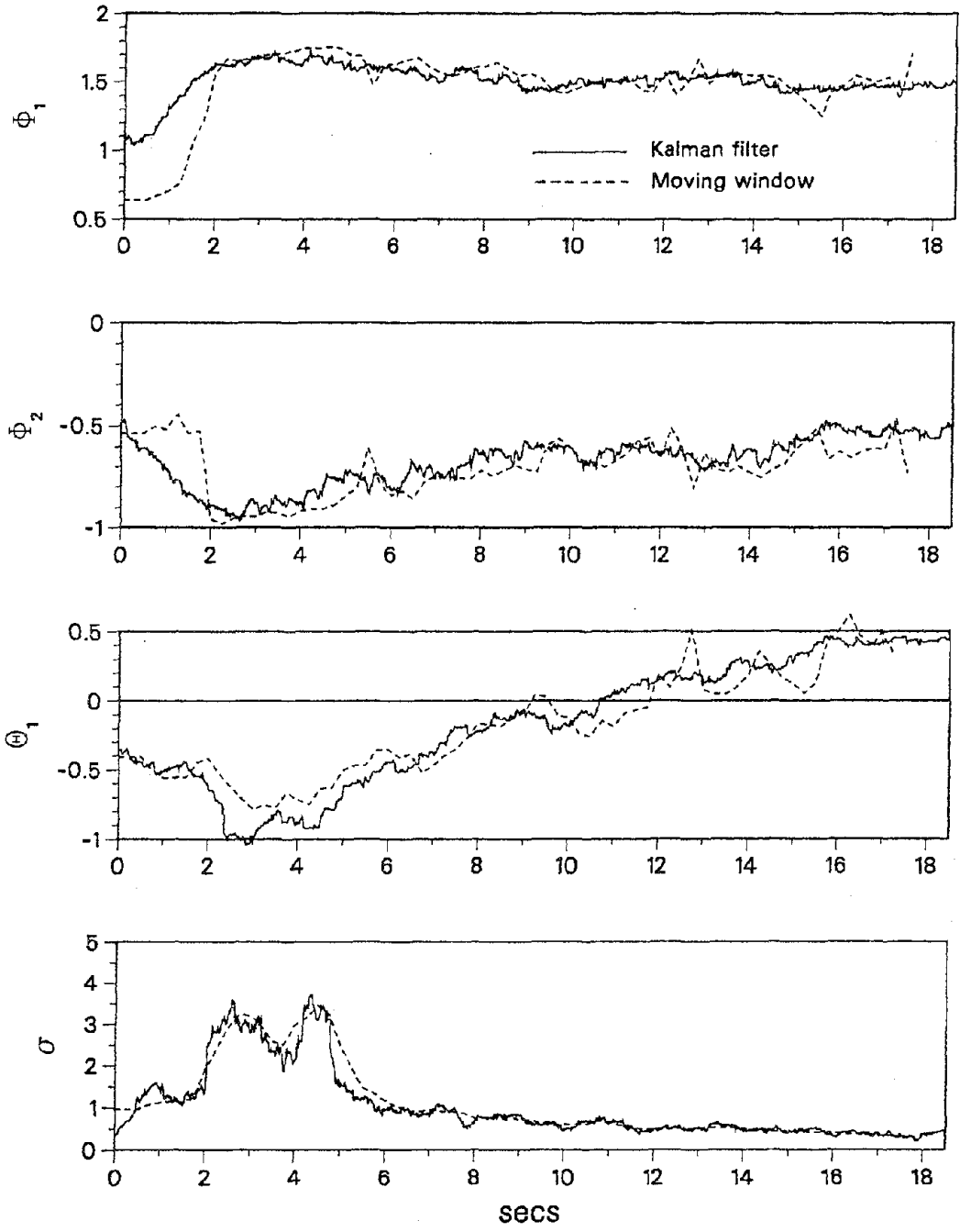

Fig. 5.7 ARMA(2,1) Model Parameter Estimates for the E02NS Record

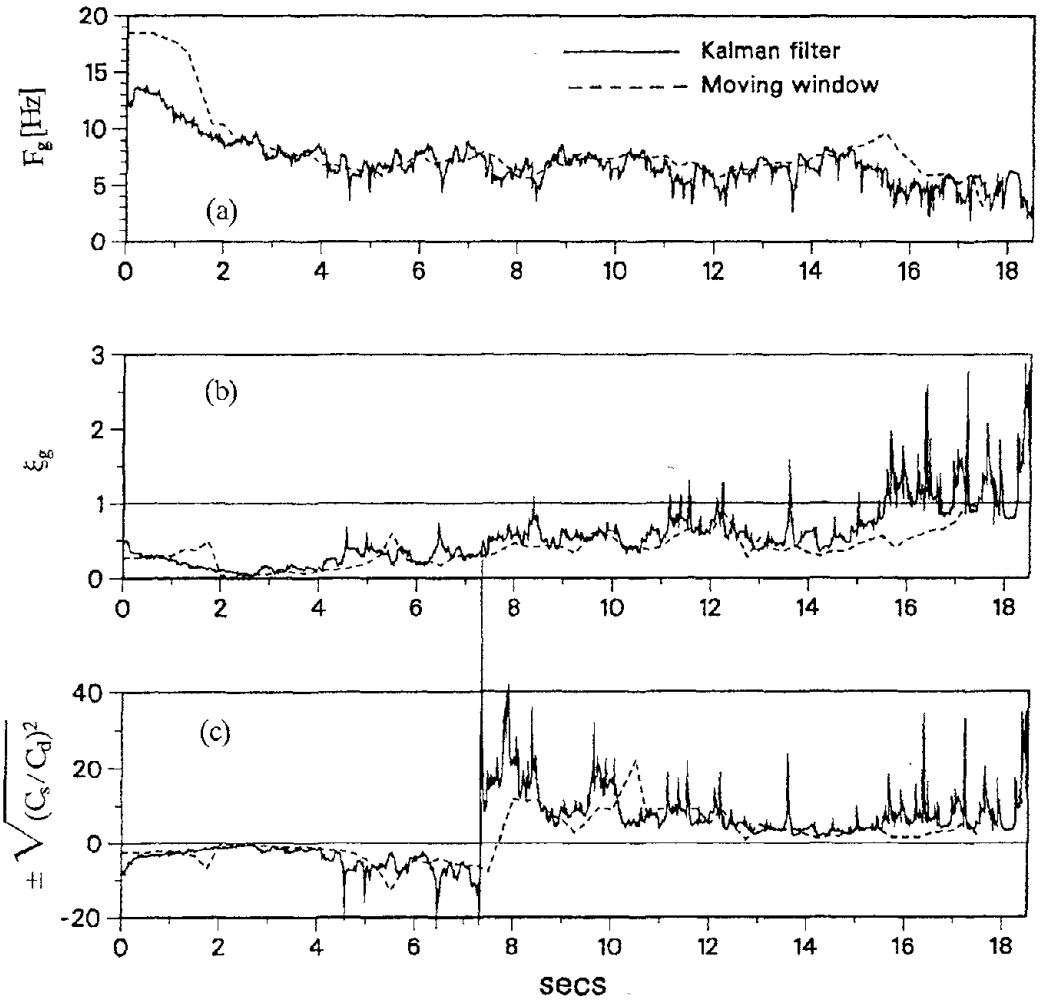

Fig. 5.8 Time Histories of Physical Parameters for the E02NS Record

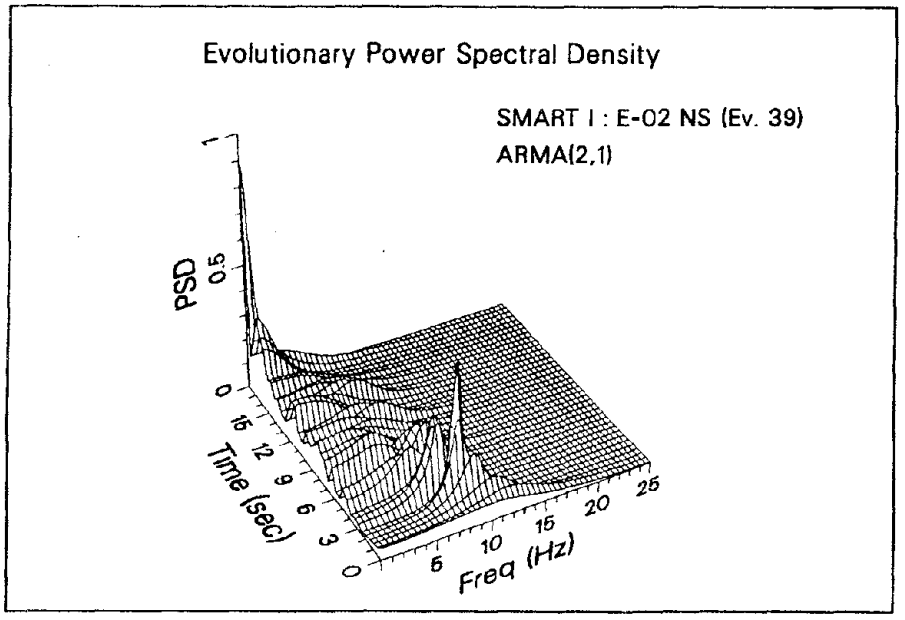

Fig. 5.9 Normalized ARMA(2,1) Evolutionary Power Spectral Density Estimate of the E02NS Record

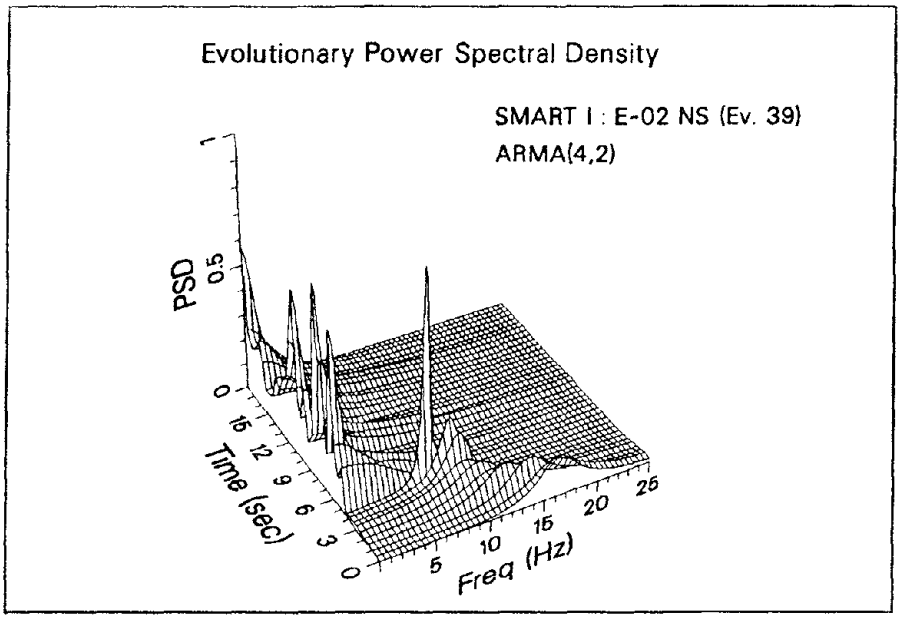

Fig. 5.10 Normalized ARMA(4,2) Evolutionary Power Spectral Density Estimate of the E02NS Record

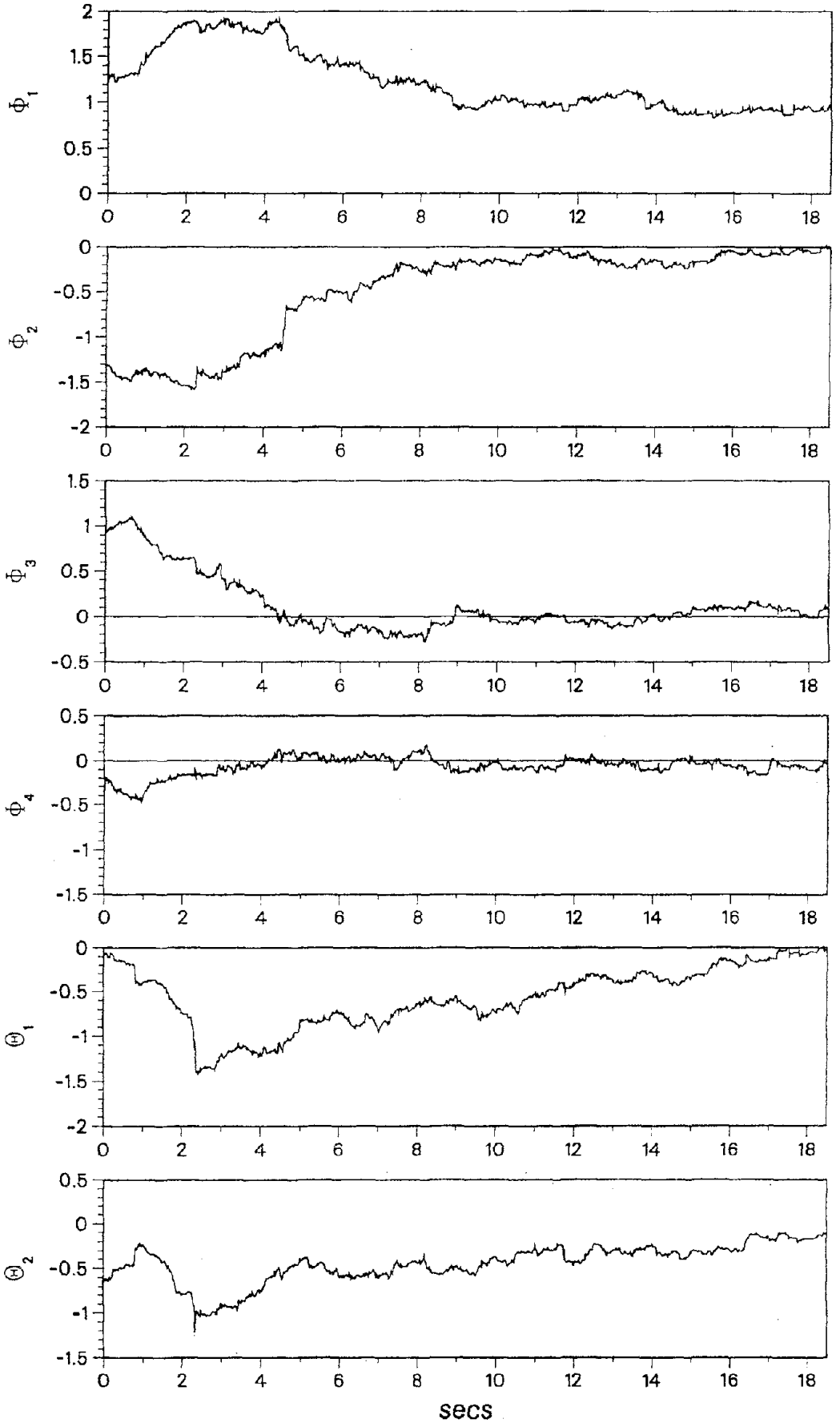

Fig. 5.11 ARMA(4,2) Model Parameter Estimates for the E02NS Record

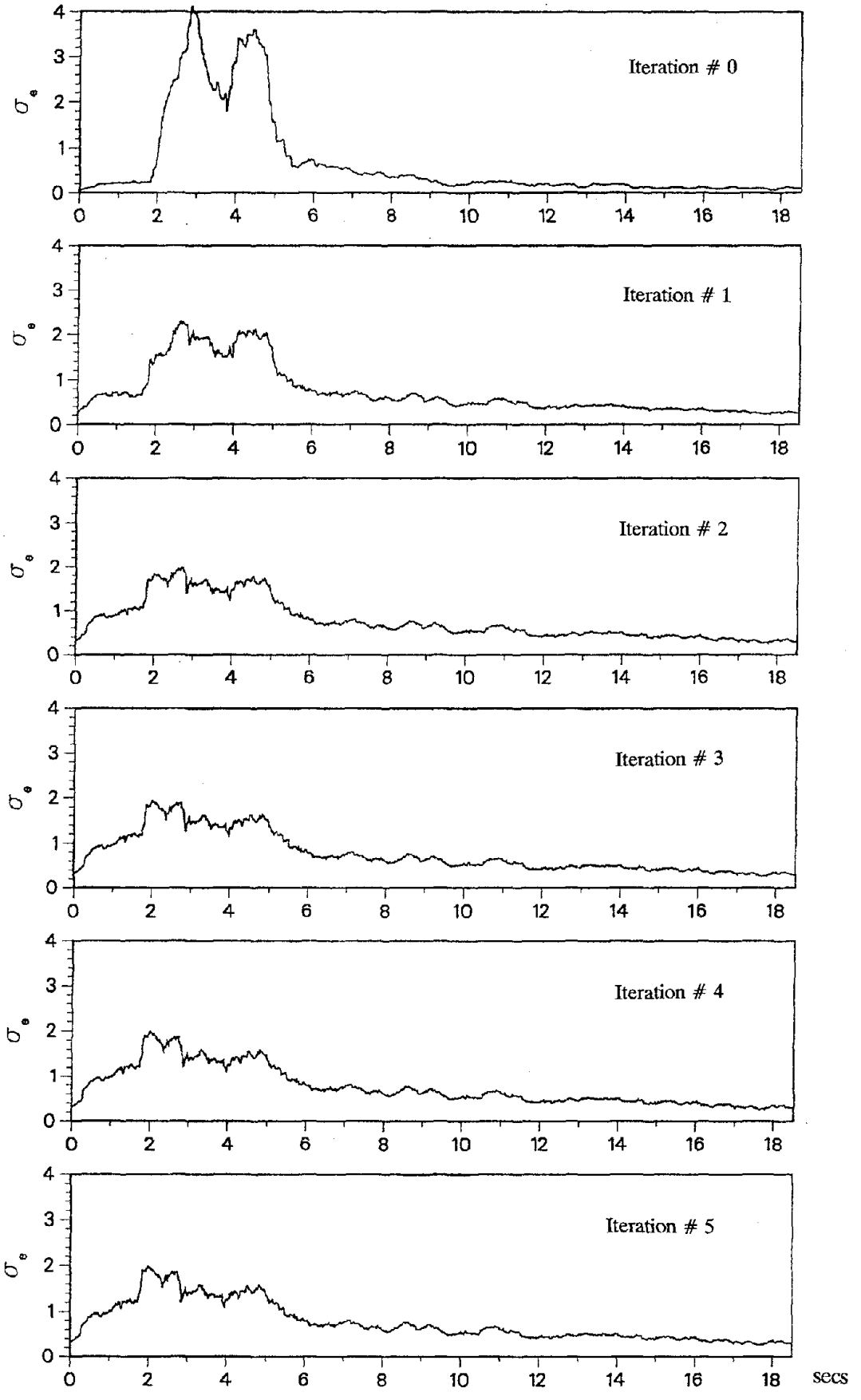

Fig. 5.12 Convergence of the Iterative Kalman Filtering Scheme

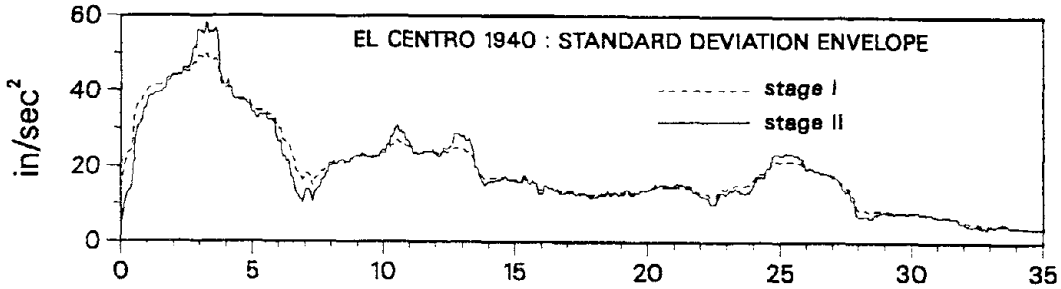

Fig. 5.13 Standard Deviation Envelope of the El Centro 1940 Record

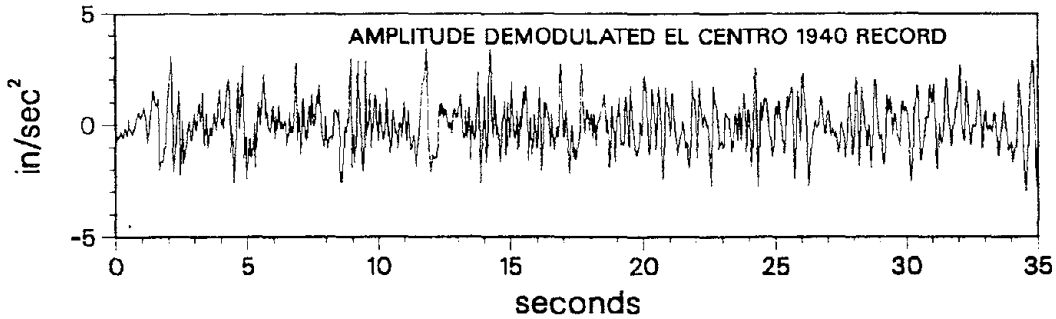

Fig. 5.14 Amplitude-Demodulated El Centro Record

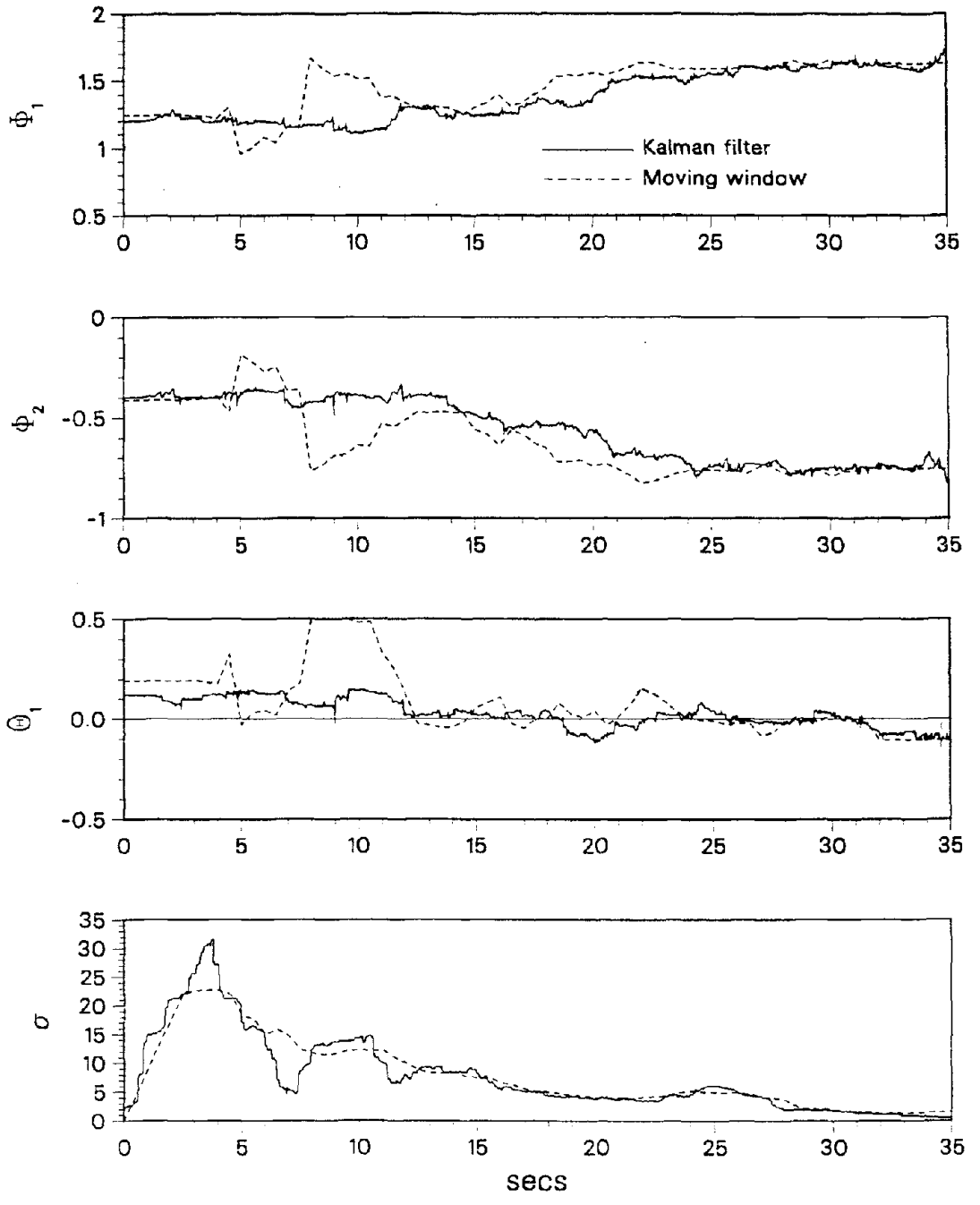

Fig. 5.15 ARMA(2,1) Model Parameter Estimates for El Centro 1940

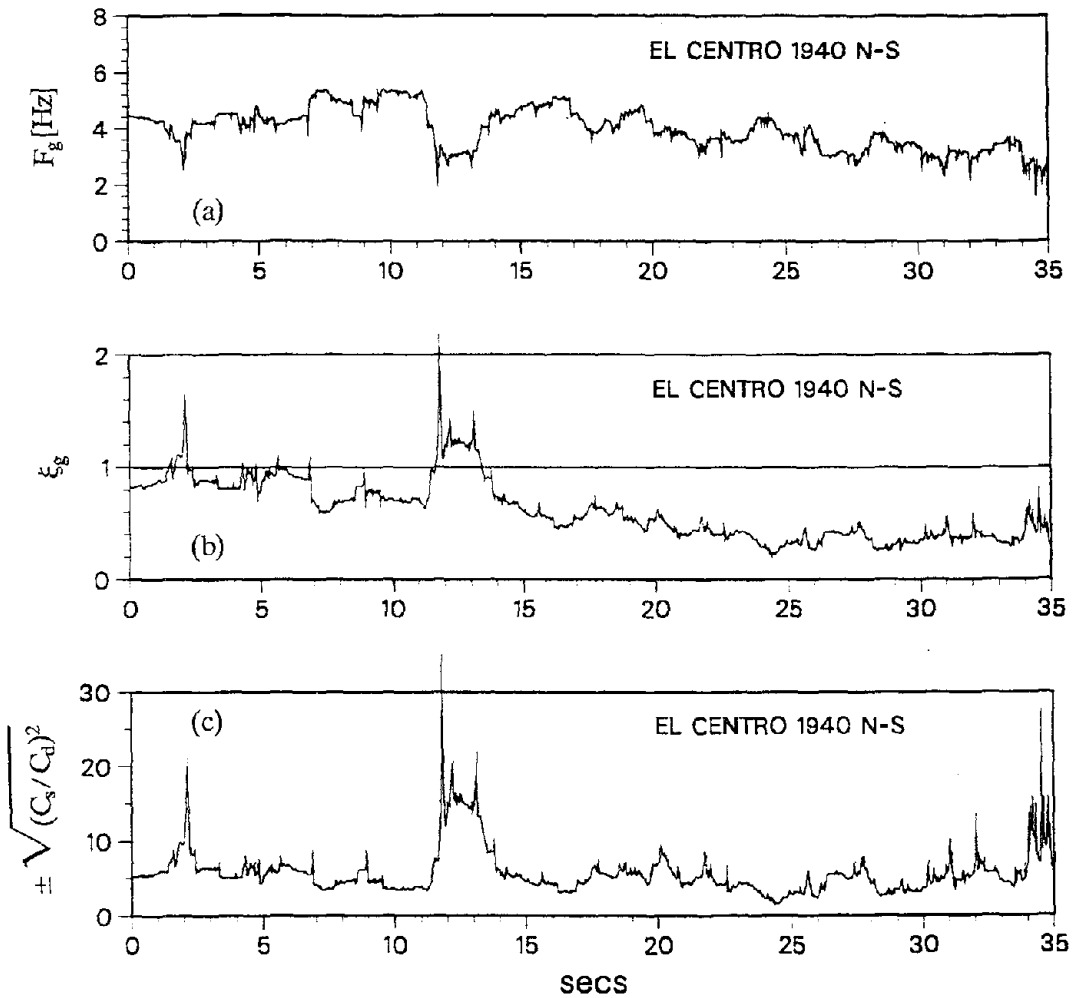

Fig. 5.16 Time Histories of Physical Parameters for El Centro 1940

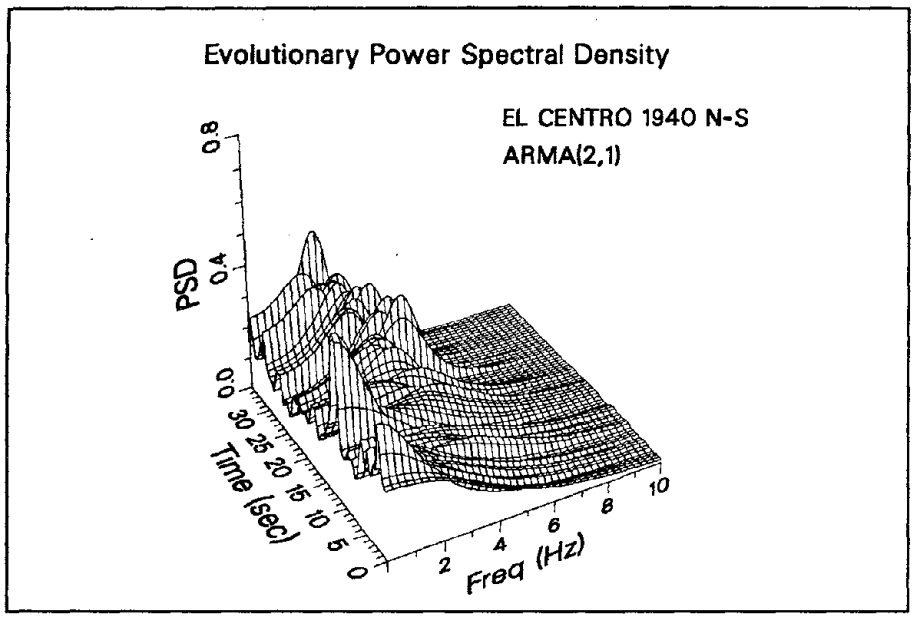

Fig. 5.17 Normalized ARMA(2,1) Evolutionary Power Spectral Density Estimate of the El Centro record

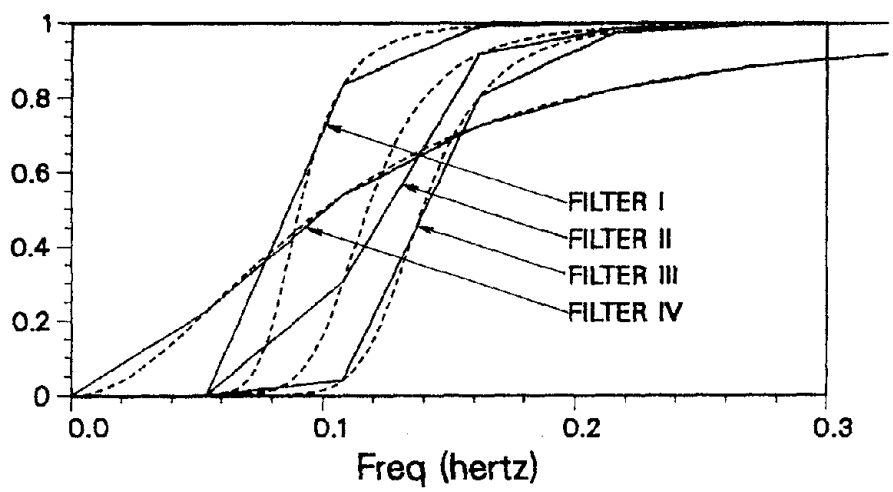

Fig. 5.18 Four Different High-Pass Filters

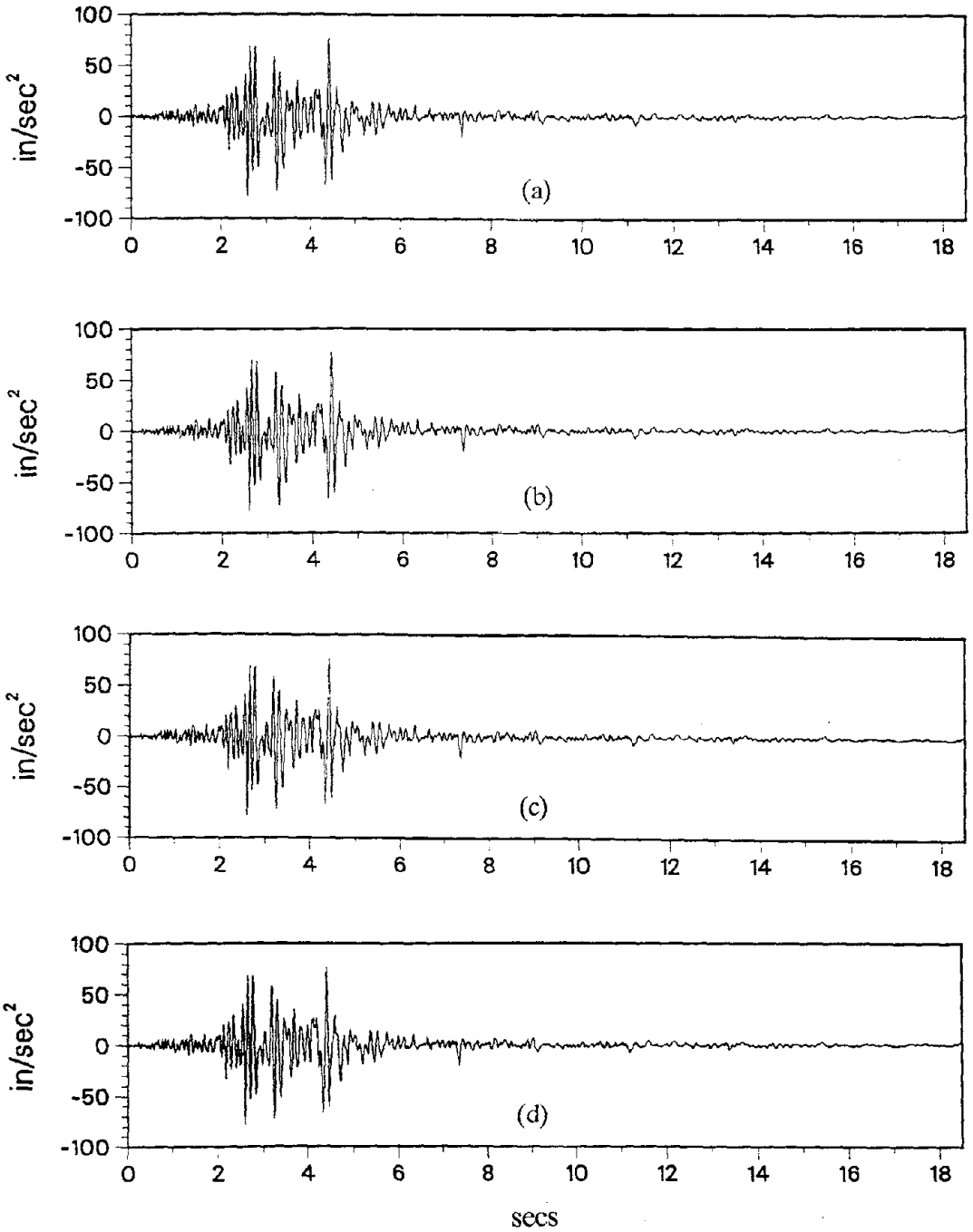

Fig. 5.19 Single ARMA(2,1) Artificial Earthquake Ground Acceleration for the E02NS Target Record Using Four Different High-Pass Filters: (a) Filter I, (b) Filter II, (c) Filter III, and (d) Filter IV

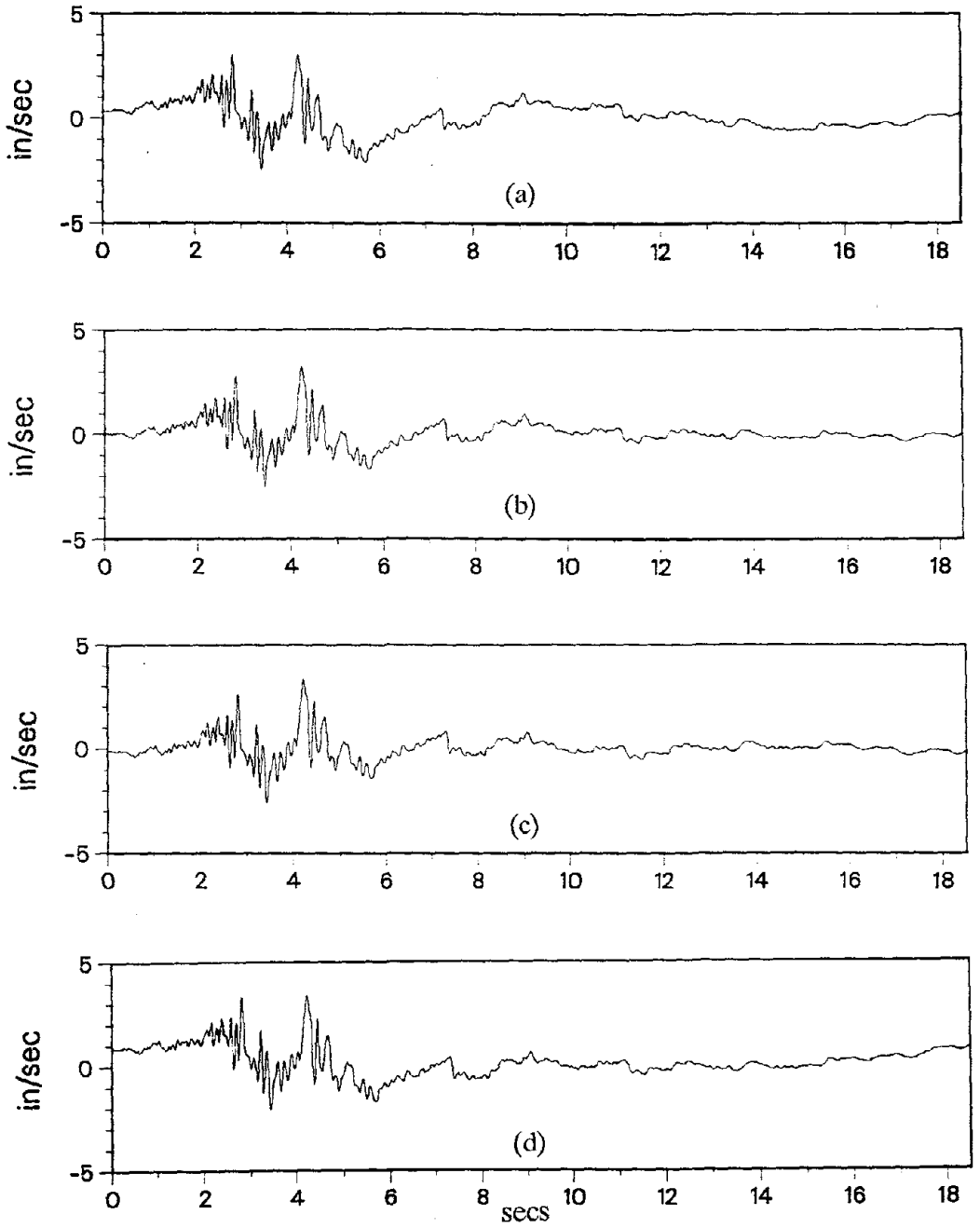

Fig. 5.20 Single ARMA(2,1) Artificial Earthquake Ground Velocity for the E02NS Target Record Using Four Different High-Pass Filters: (a) Filter I, (b) Filter II, (c) Filter III, and (d) Filter IV

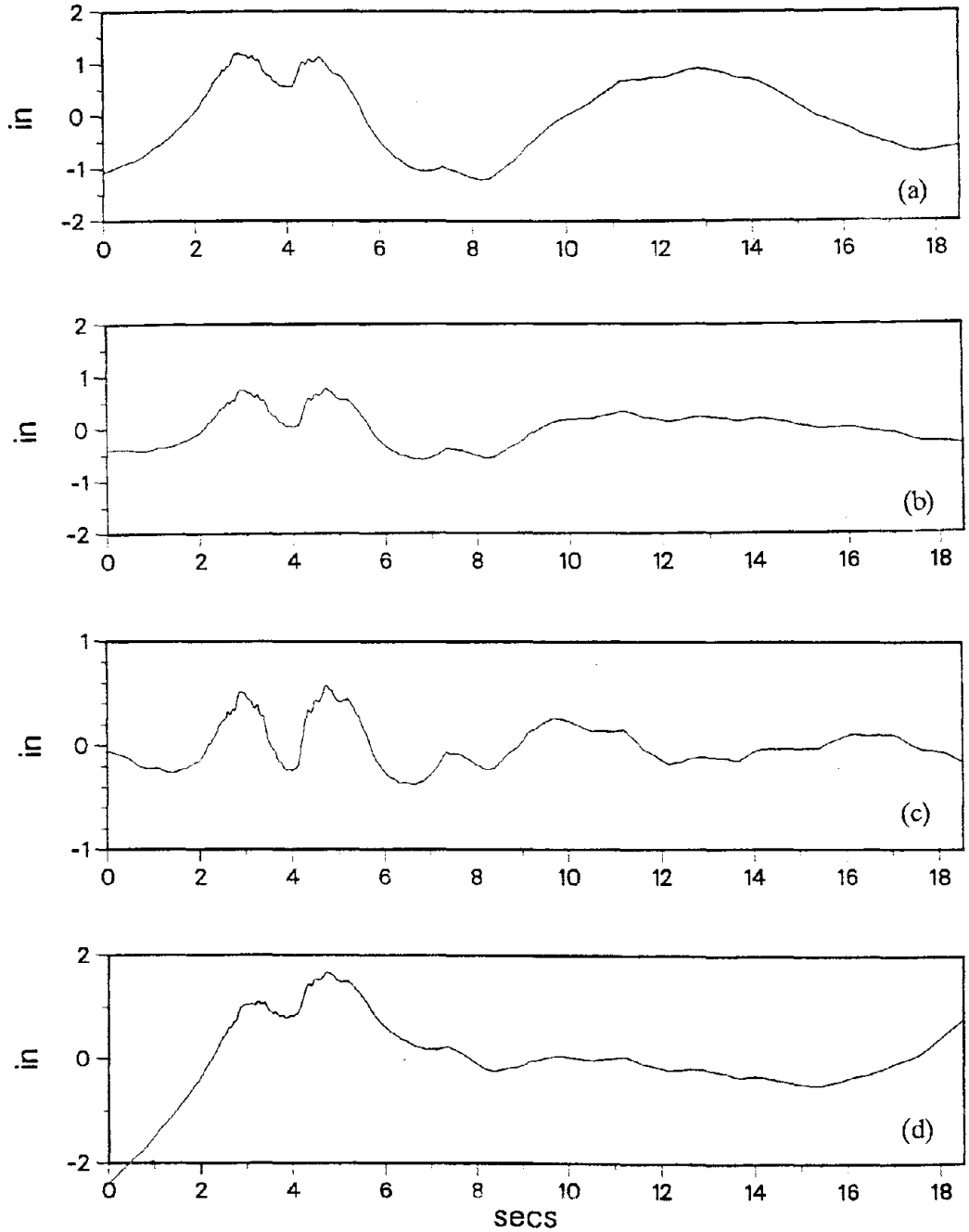

Fig. 5.21 Single ARMA(2,1) Artificial Earthquake Ground Displacement for the E02NS Target Record Using Four Different High-Pass Filters: (a) Filter I, (b) Filter II, (c) Filter III, and (d) Filter IV

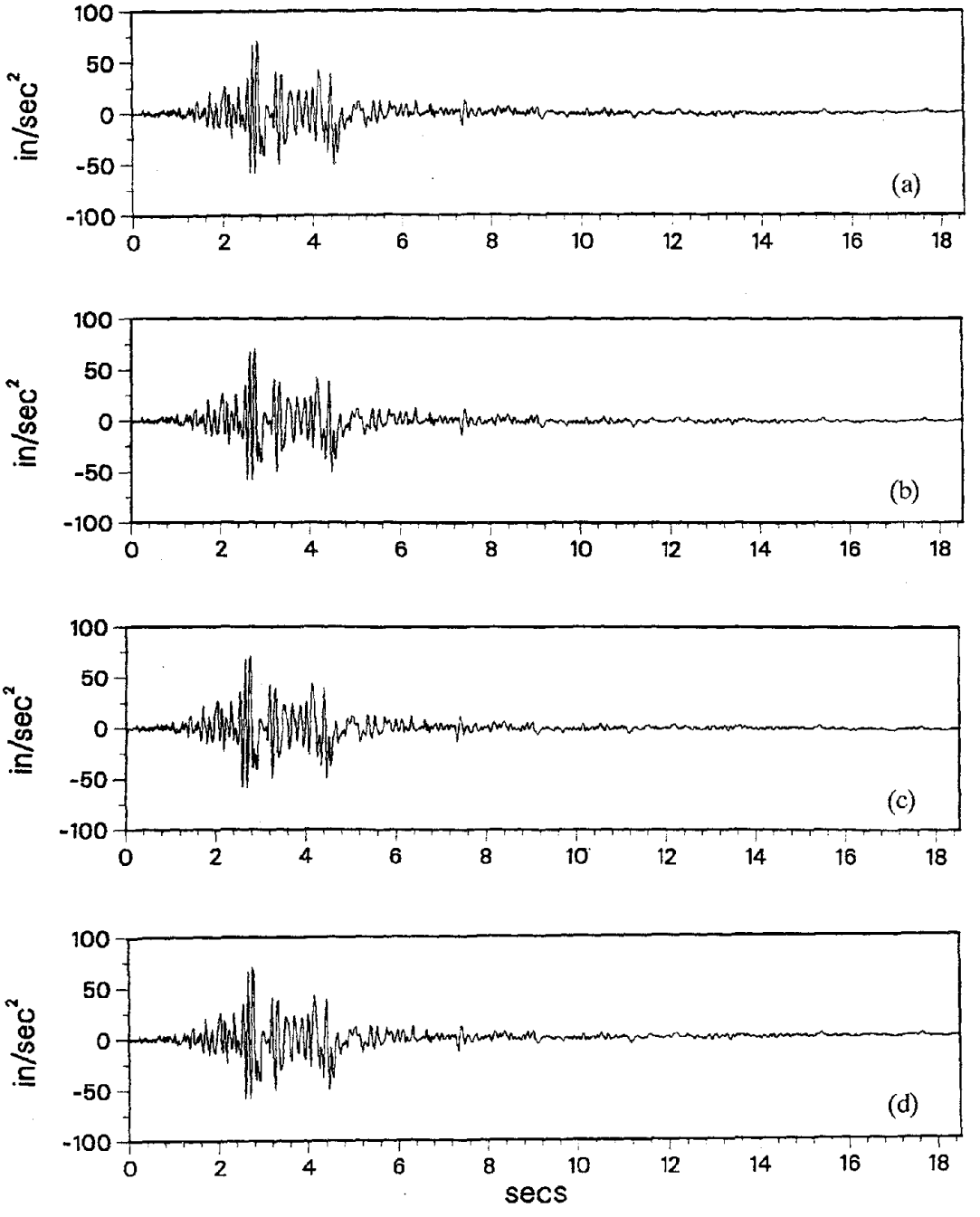

Fig. 5.22 Single ARMA(4,2) Artificial Earthquake Ground Acceleration for the E02NS Target Record Using Four Different High-Pass Filters: (a) Filter I, (b) Filter II, (c) Filter III, and (d) Filter IV

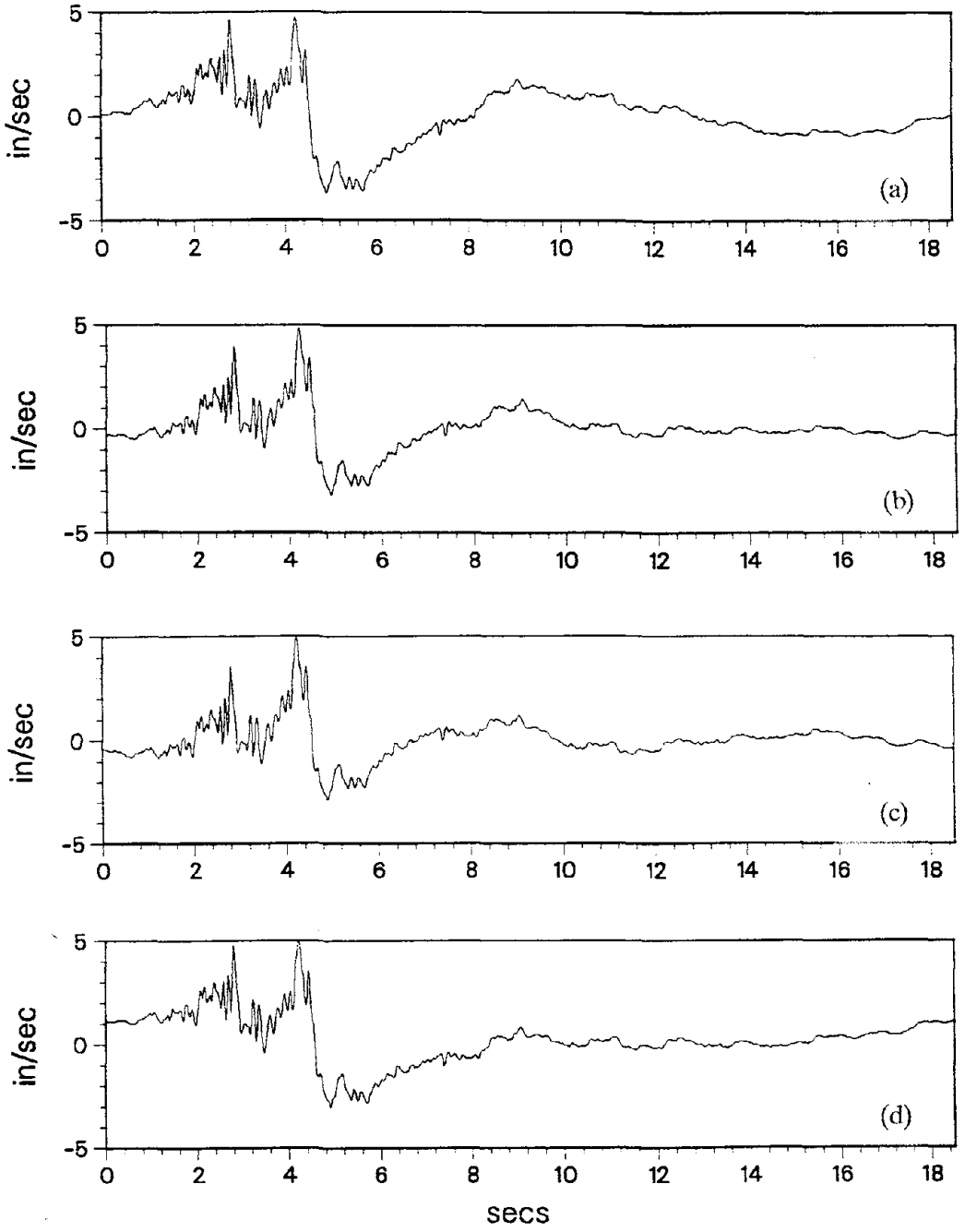

Fig. 5.23 Single ARMA(4,2) Artificial Earthquake Ground Velocity for the E02NS Target Record Using Four Different High-Pass Filters: (a) Filter I, (b) Filter II, (c) Filter III, and (d) Filter IV

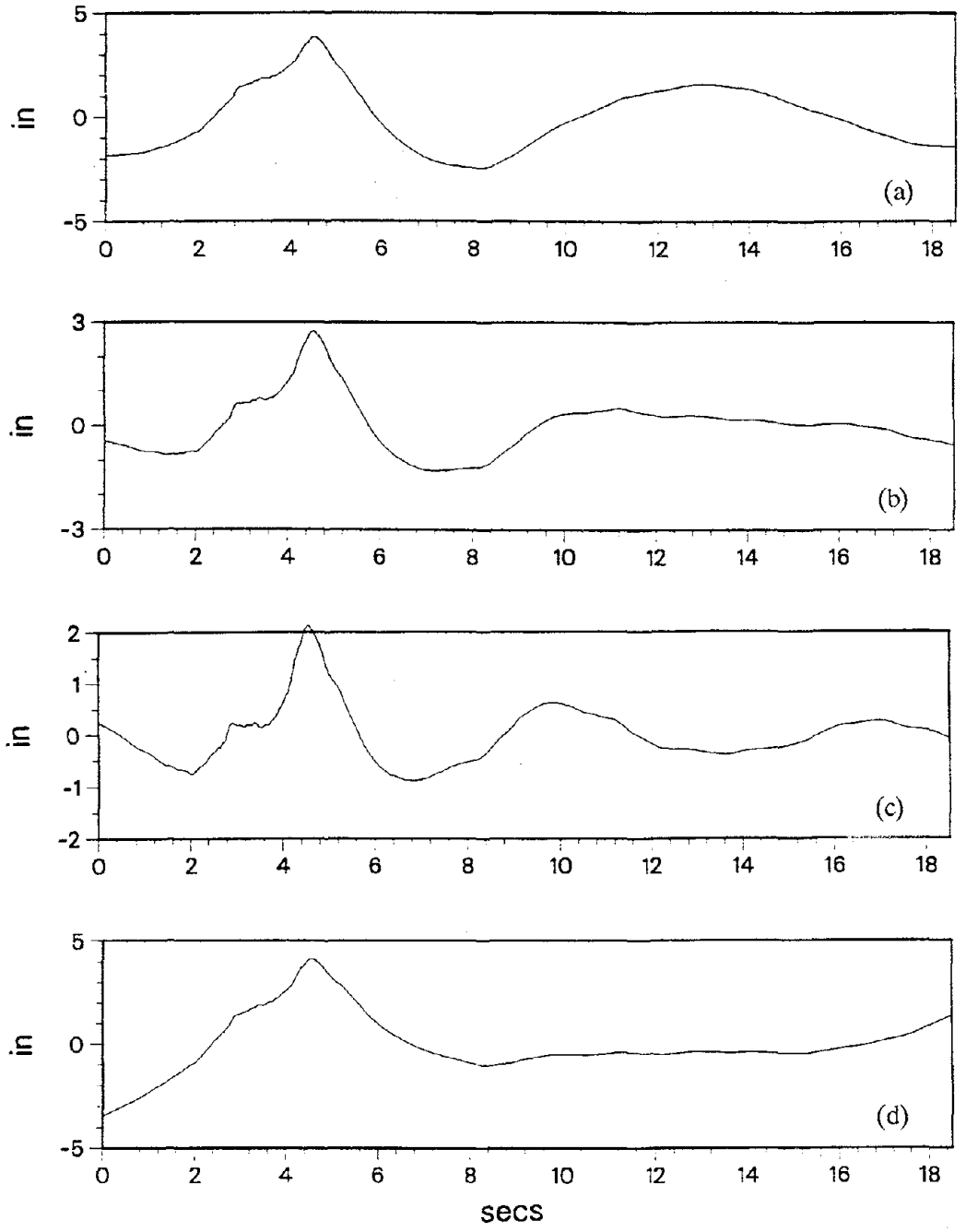

Fig. 5.24 Single ARMA(4,2) Artificial Earthquake Ground Displacement for the E02NS Target Record Using Four Different High-Pass Filters: (a) Filter I, (b) Filter II, (c) Filter III, and (d) Filter IV

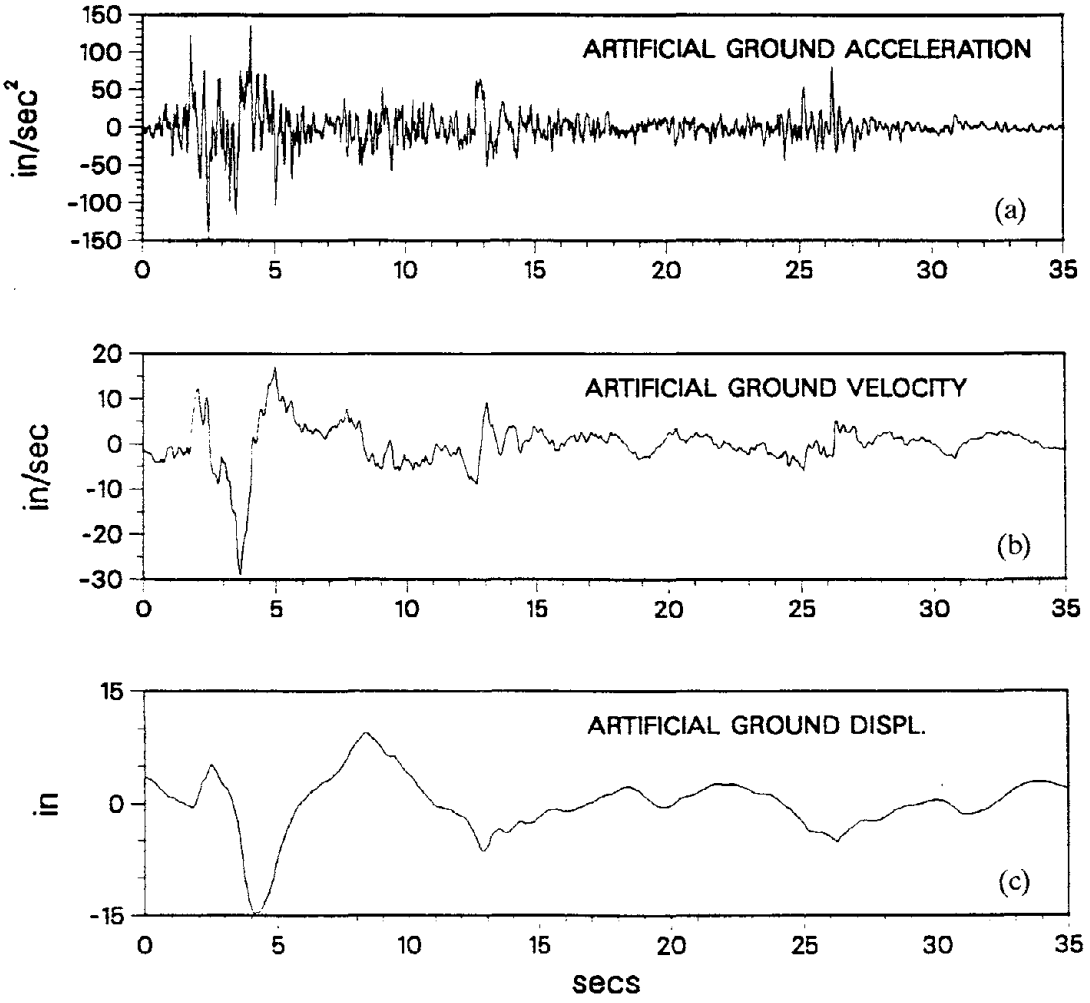

Fig. 5.25 Single ARMA(2,1) Artificial Earthquake for El Centro 1940 Ground (a) Acceleration, (b) Velocity, and (c) Displacement

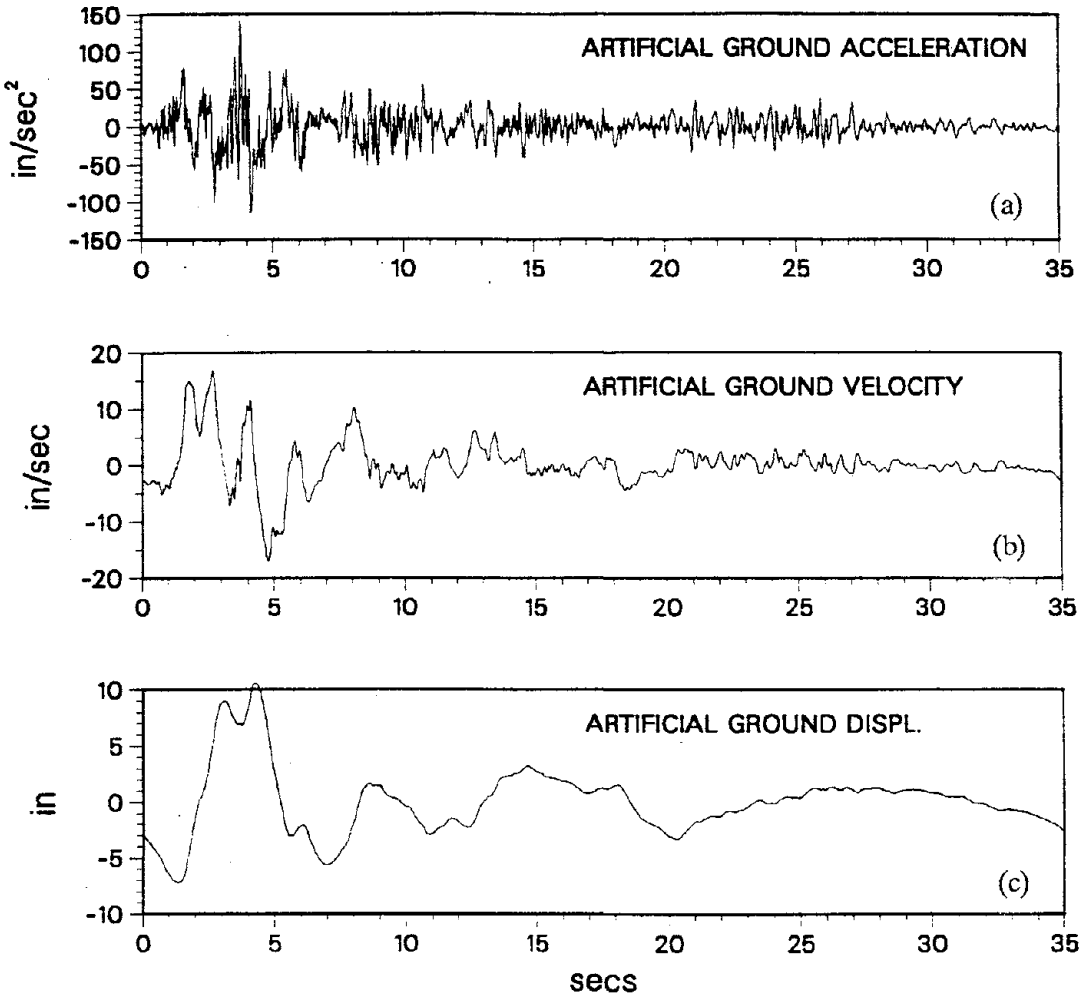

Fig. 5.26 Single ARMA(2,1) Artificial Earthquake for El Centro 1940 Ground (a) Acceleration, (b) Velocity, and (c) Displacement

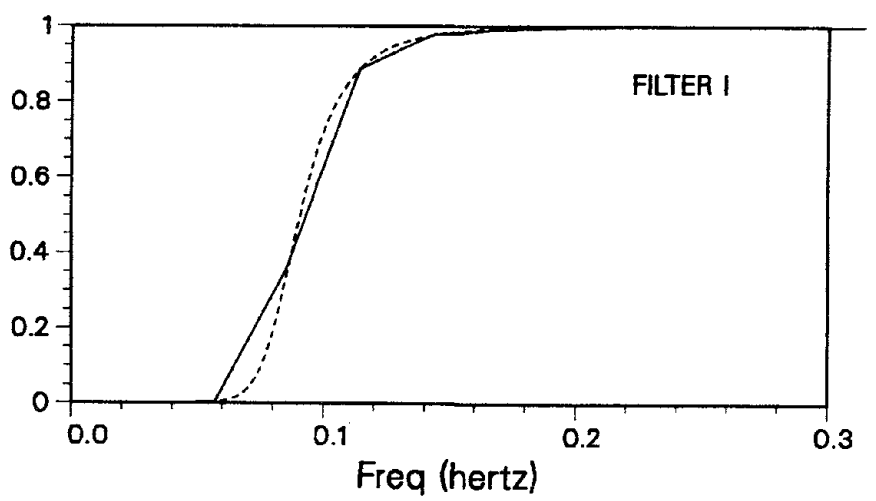

Fig. 5.27 Butterworth High-Pass Filter for the ARMA(2,1) El Centro 1940 Earthquake Process

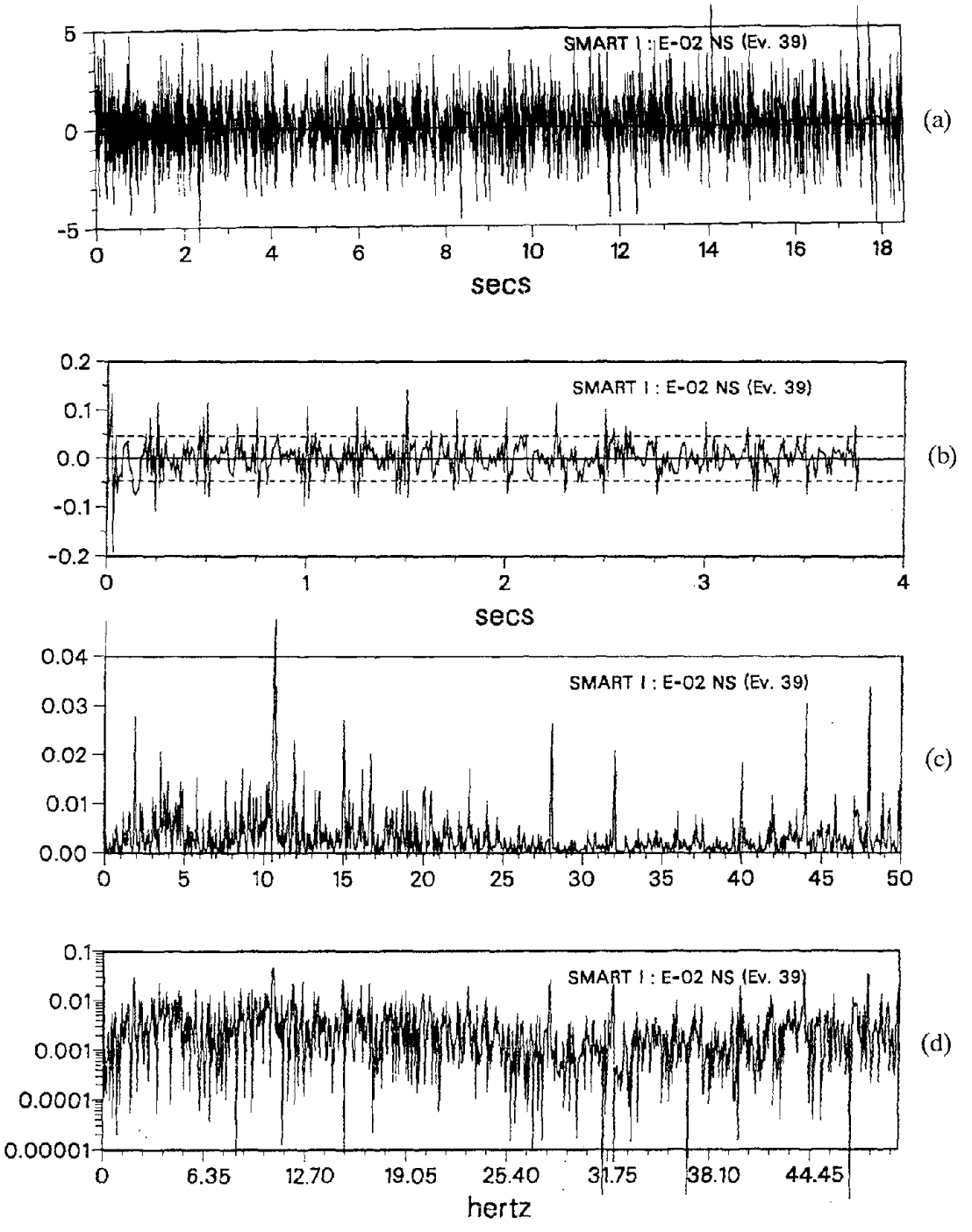

Fig. 5.28 Residuals from the ARMA(2,1) Model Fitted to the E02NS Record: (a) Time History, (b) Sample Autocorrelation Function, Periodogram in (c) Decimal Scale, and (d) Logarithmic Scale

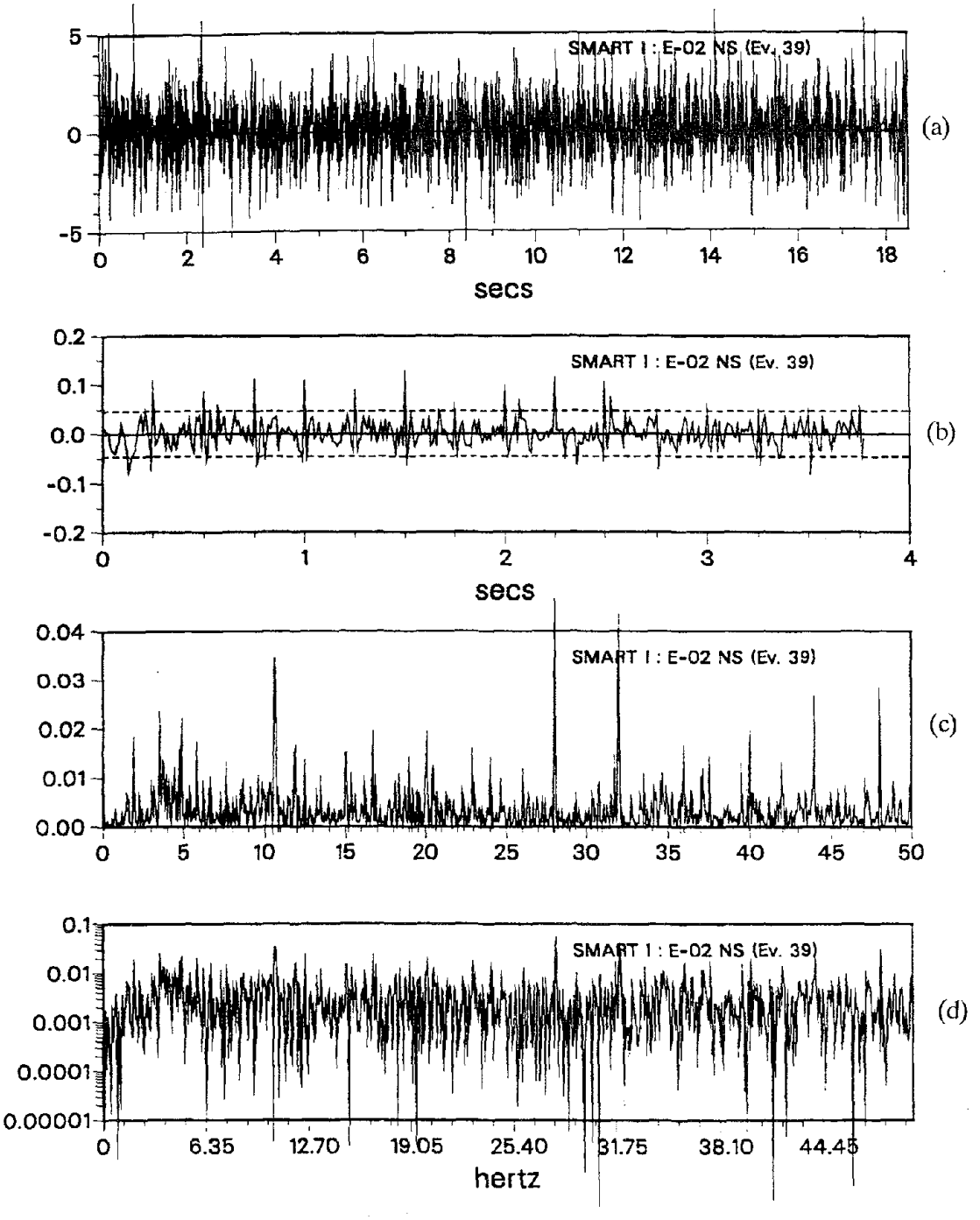

Fig. 5.29 Residuals from the ARMA(4,2) Model Fitted to the E02NS Record: (a) Time History, (b) Sample Autocorrelation Function, Periodogram in (c) Decimal Scale, and (d) Logarithmic Scale

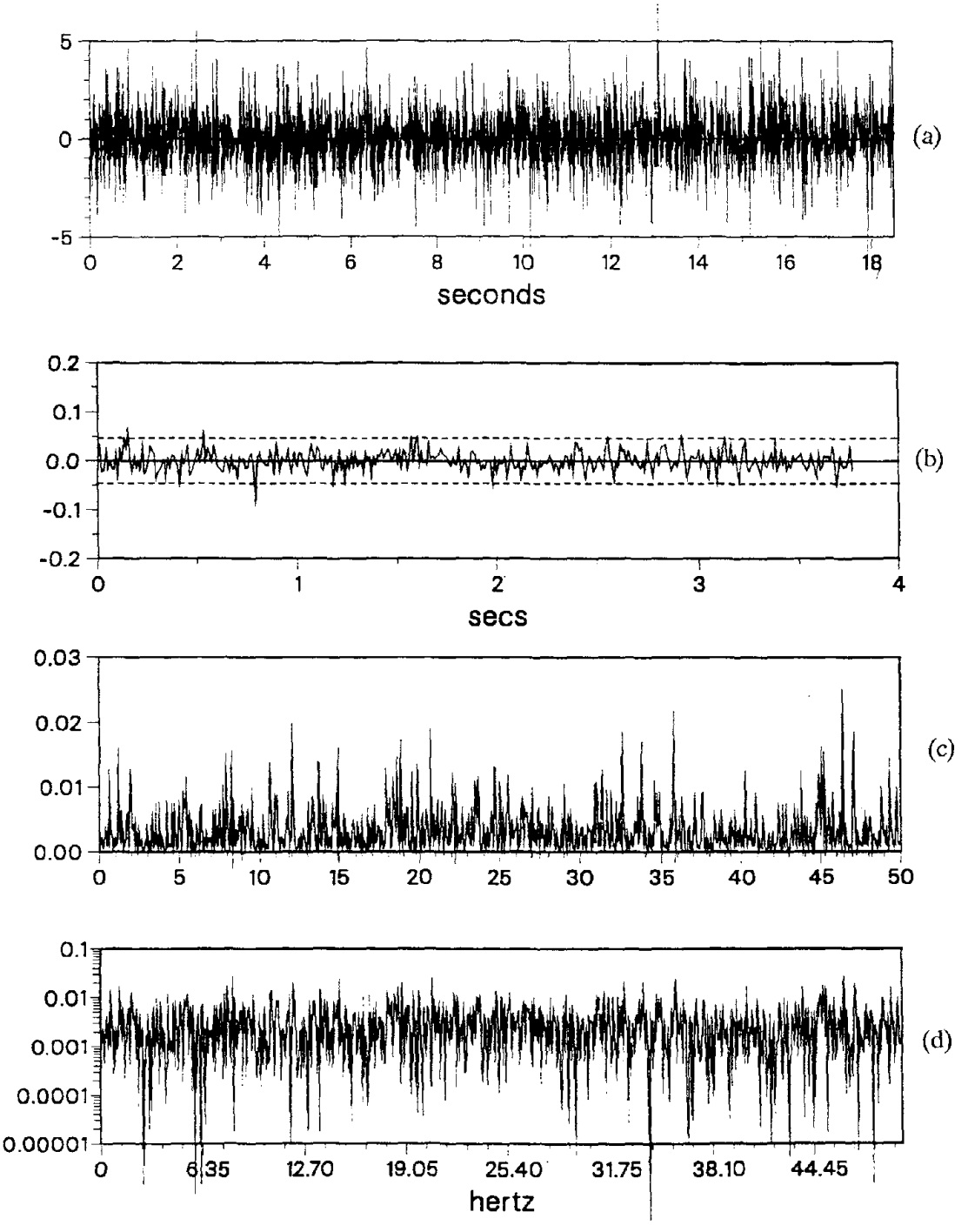

Fig. 5.30 Computer Generated Discrete White-Noise:
(a) Time History, (b) Sample Autocorrelation Function,
Periodogram in (c) Decimal Scale, and (d) Logarithmic Scale

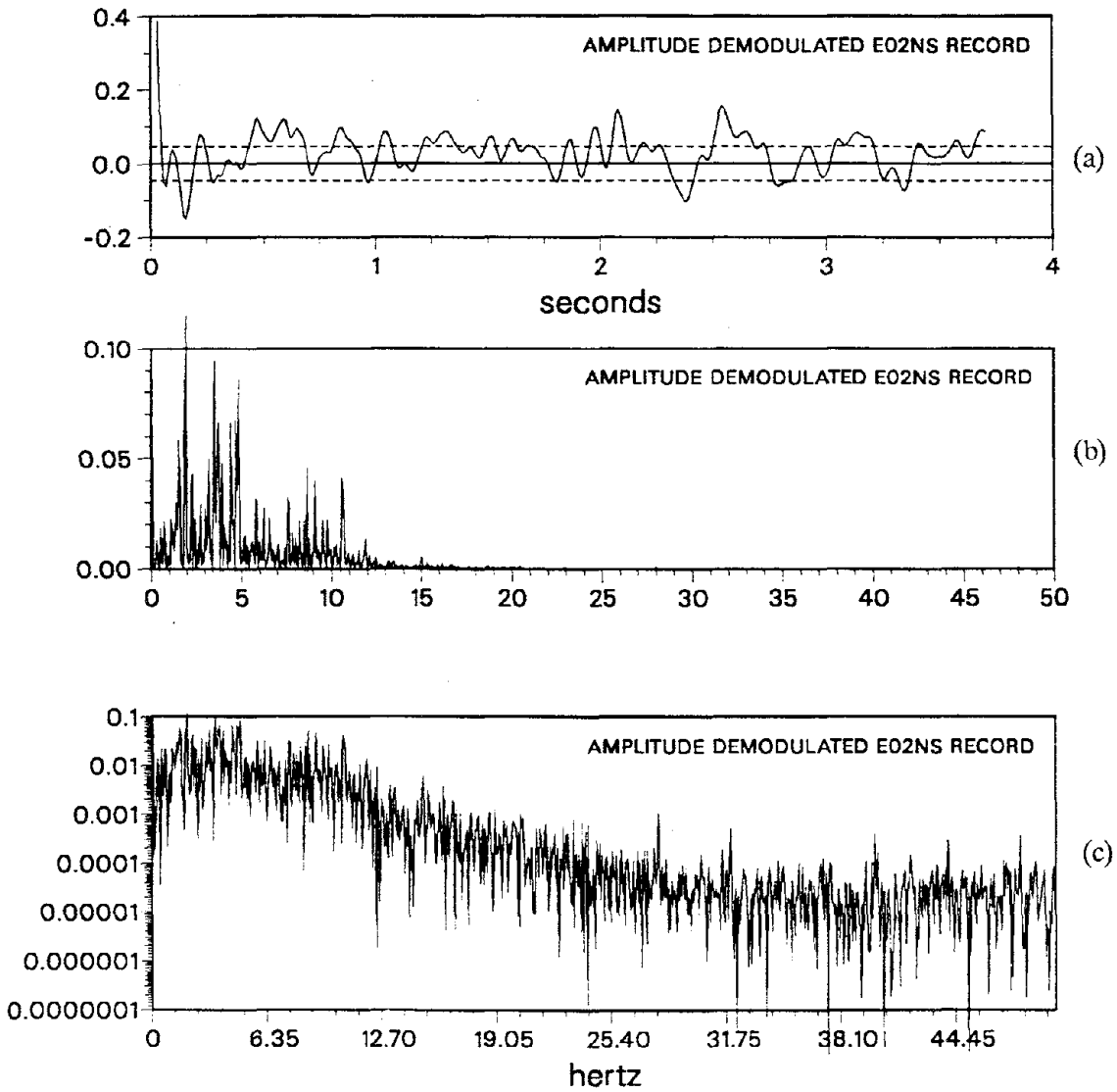

Fig. 5.31 Sample Autocorrelation Function and Periodogram of the Amplitude-Demodulated E02NS Record

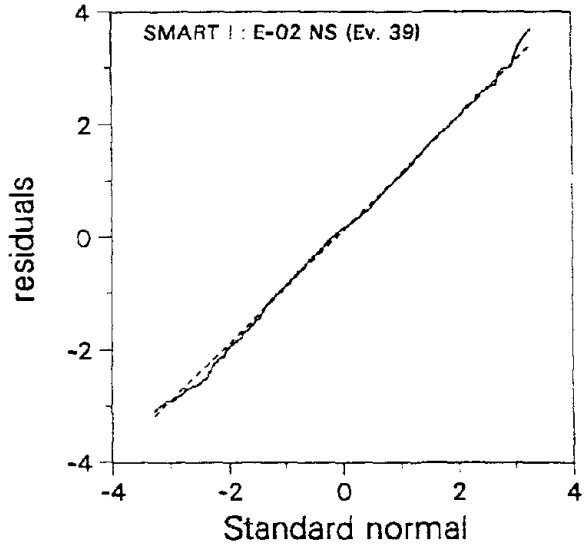

Fig. 5.32 Normality Test of the Residuals from the ARMA(2,1) Model Fitted to the E02NS Record

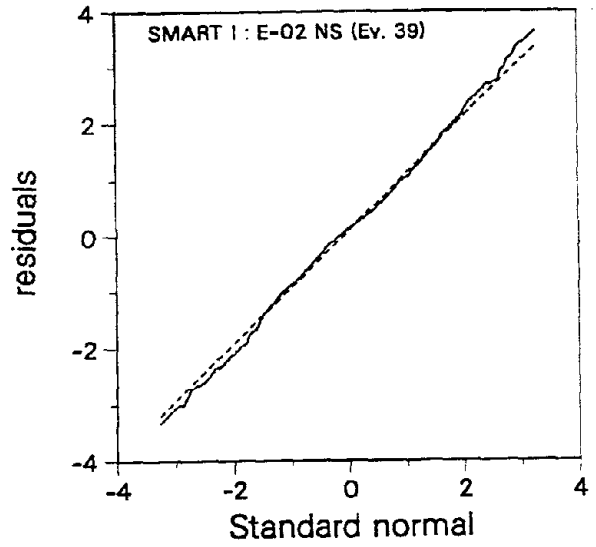

Fig. 5.33 Normality Test of the Residuals from the ARMA(4,2) Model Fitted to the E02NS Record

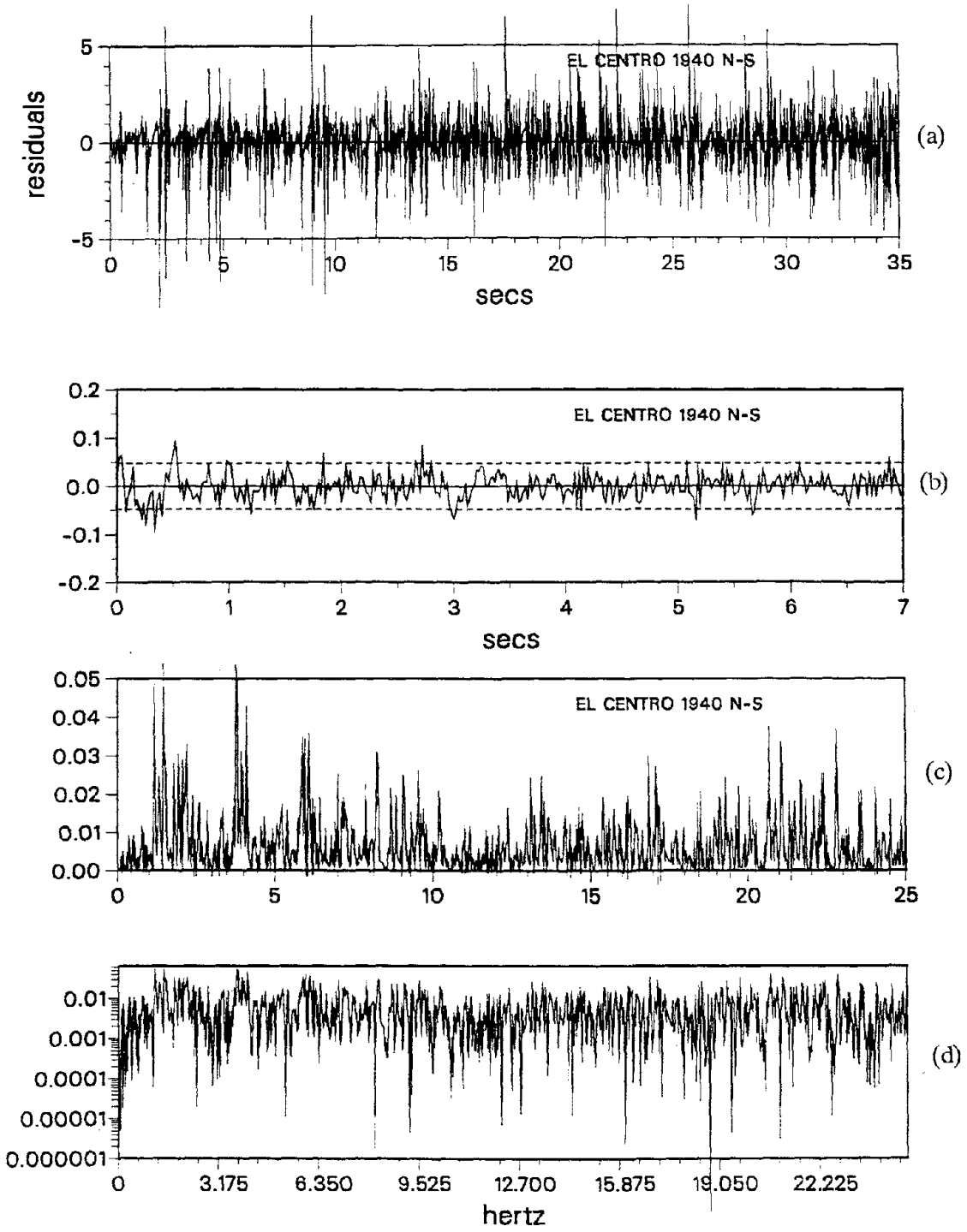

Fig. 5.34 Residuals from the ARMA(2,1) Model Fitted to the El Centro 1940 Record: (a) Time History, (b) Sample Autocorrelation Function, Periodogram in (c) Decimal Scale, and (d) Logarithmic Scale

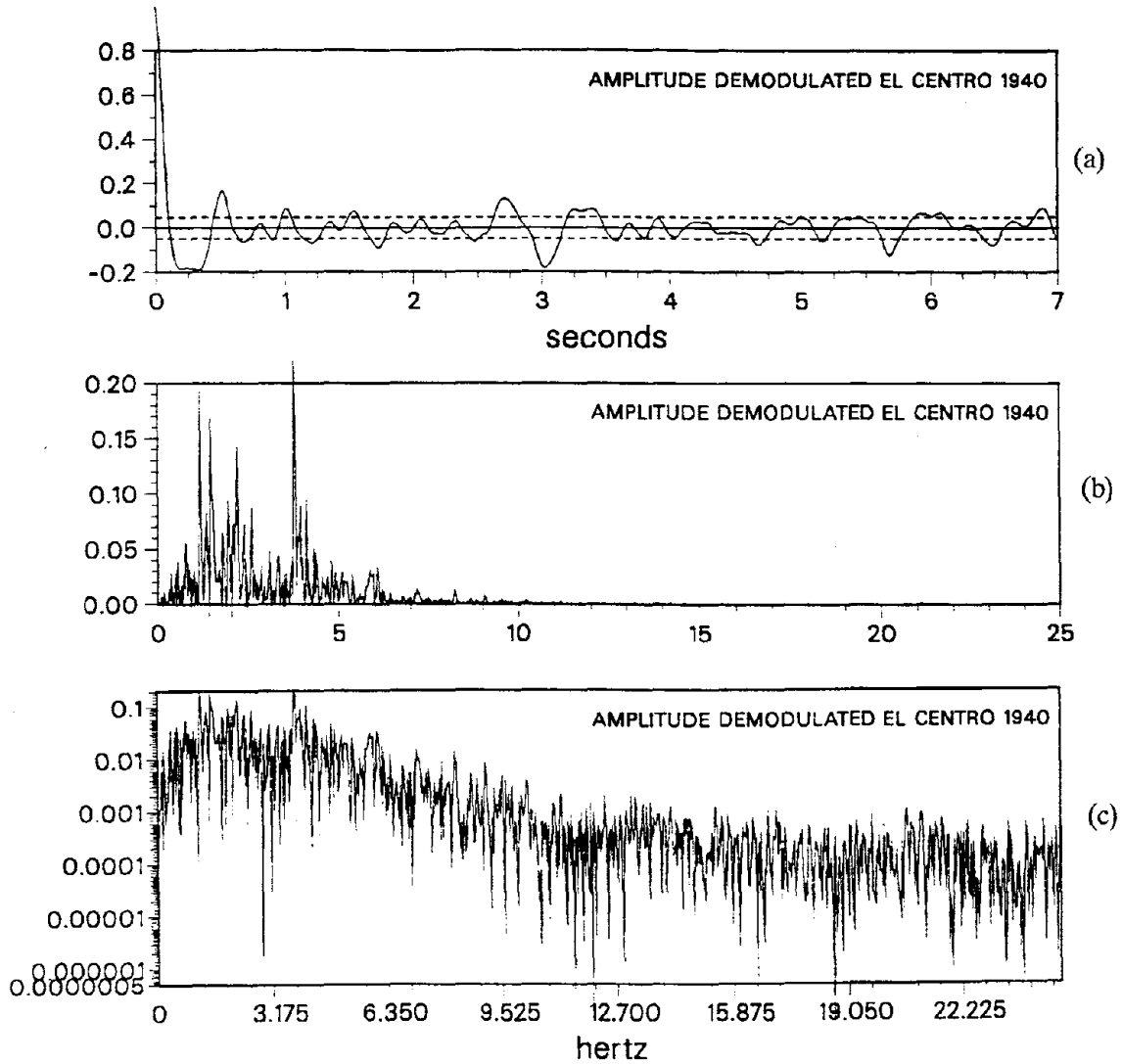

Fig. 5.35 Sample Autocorrelation Function and Periodogram of the Amplitude-Demodulated El Centro 1940 Record

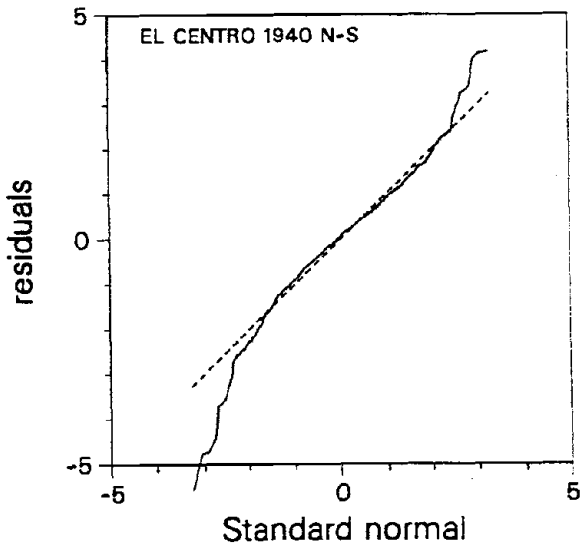

Fig. 5.36 Normality Test of the Residuals from the ARMA(2,1) Model Fitted to the El Centro 1940 Record

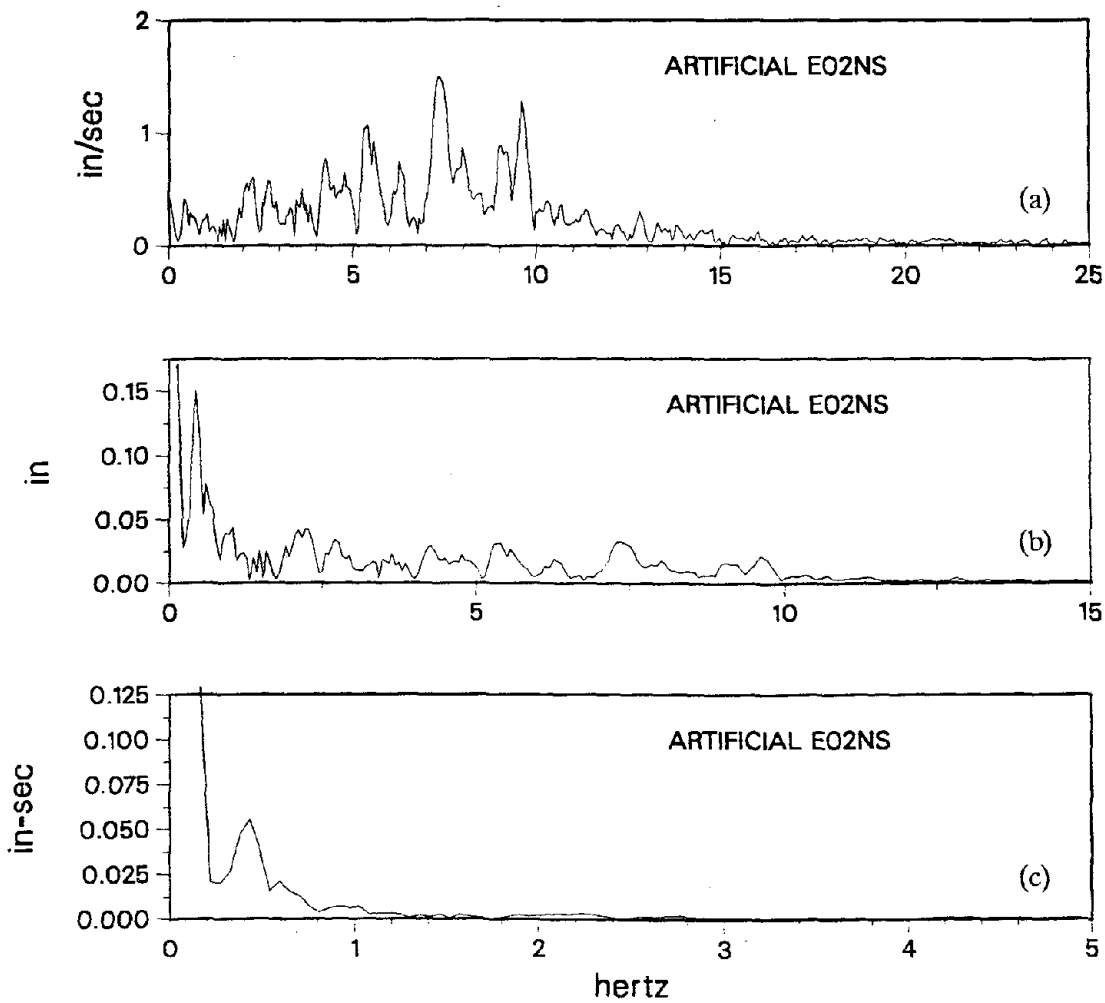

Fig. 5.37 Fourier Amplitude Spectra of an Artificial Ground Motion (acceleration, velocity, and displacement) Generated from the ARMA(2,1) Model Fitted to the E02NS Record

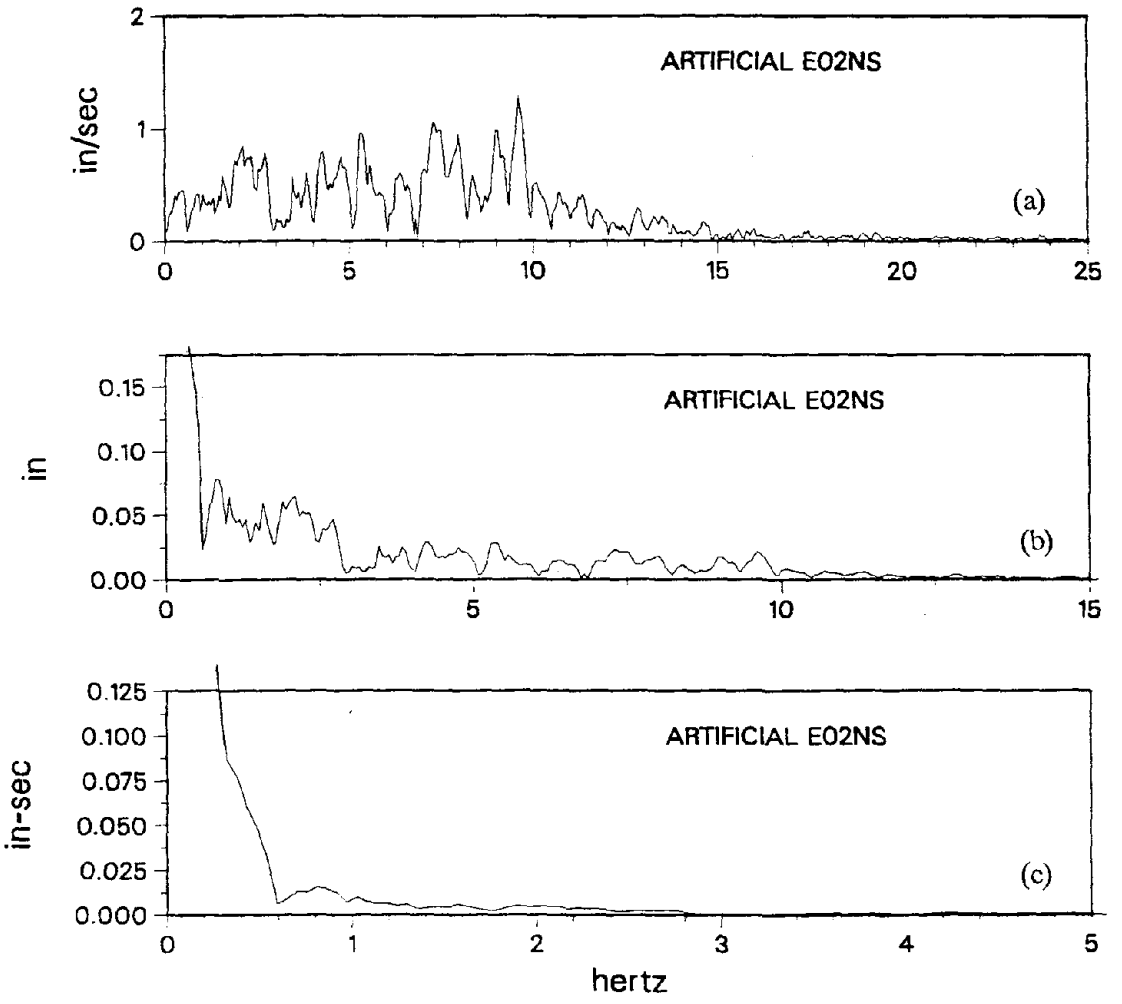

Fig. 5.38 Fourier Amplitude Spectra of an Artificial Ground Motion (acceleration, velocity, and displacement) Generated from the ARMA(4,2) Model Fitted to the E02NS Record

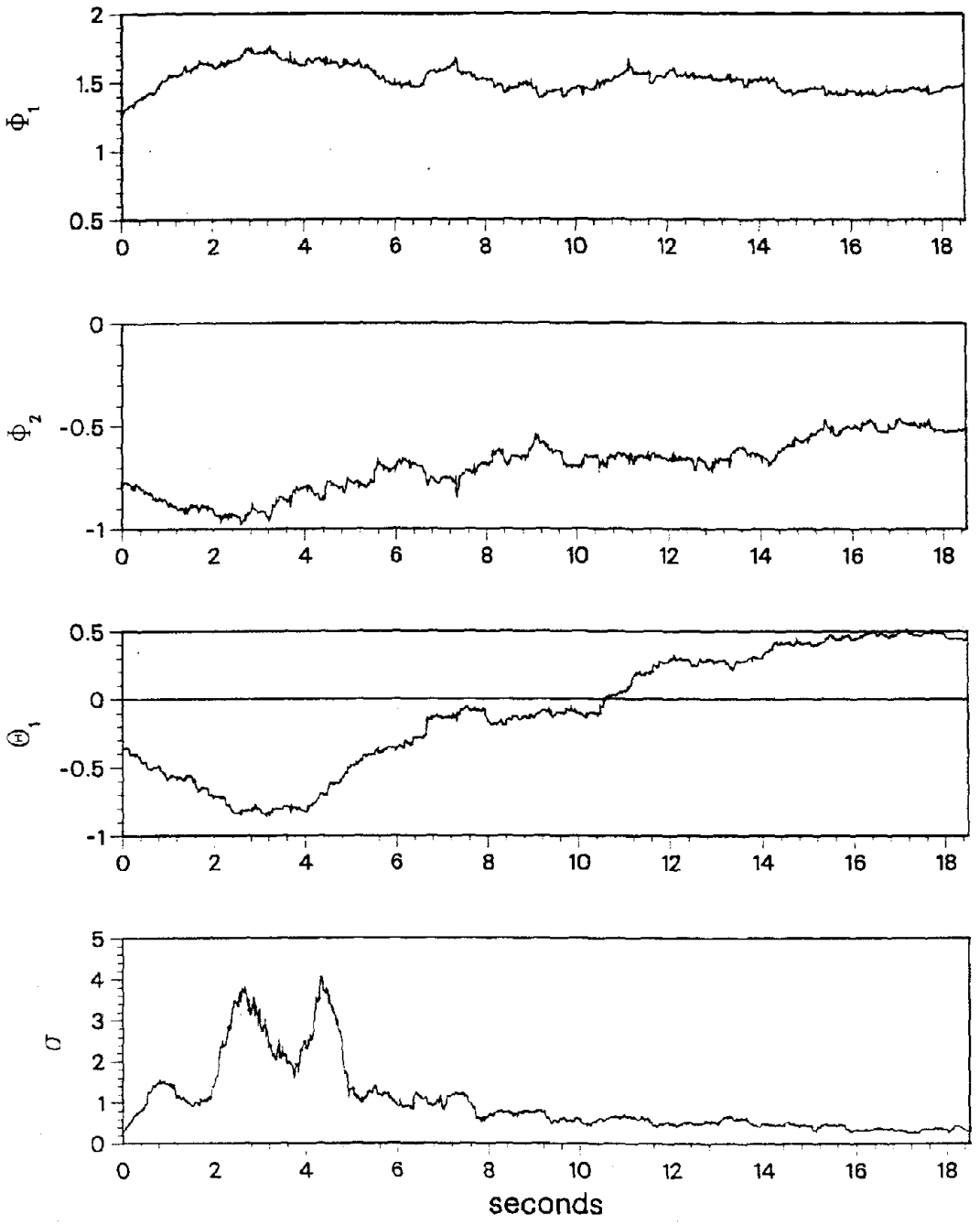

Fig. 5.39 ARMA(2,1) Model Parameter Estimates for an ARMA(2,1) Artificial Realization of the E02NS Earthquake Process

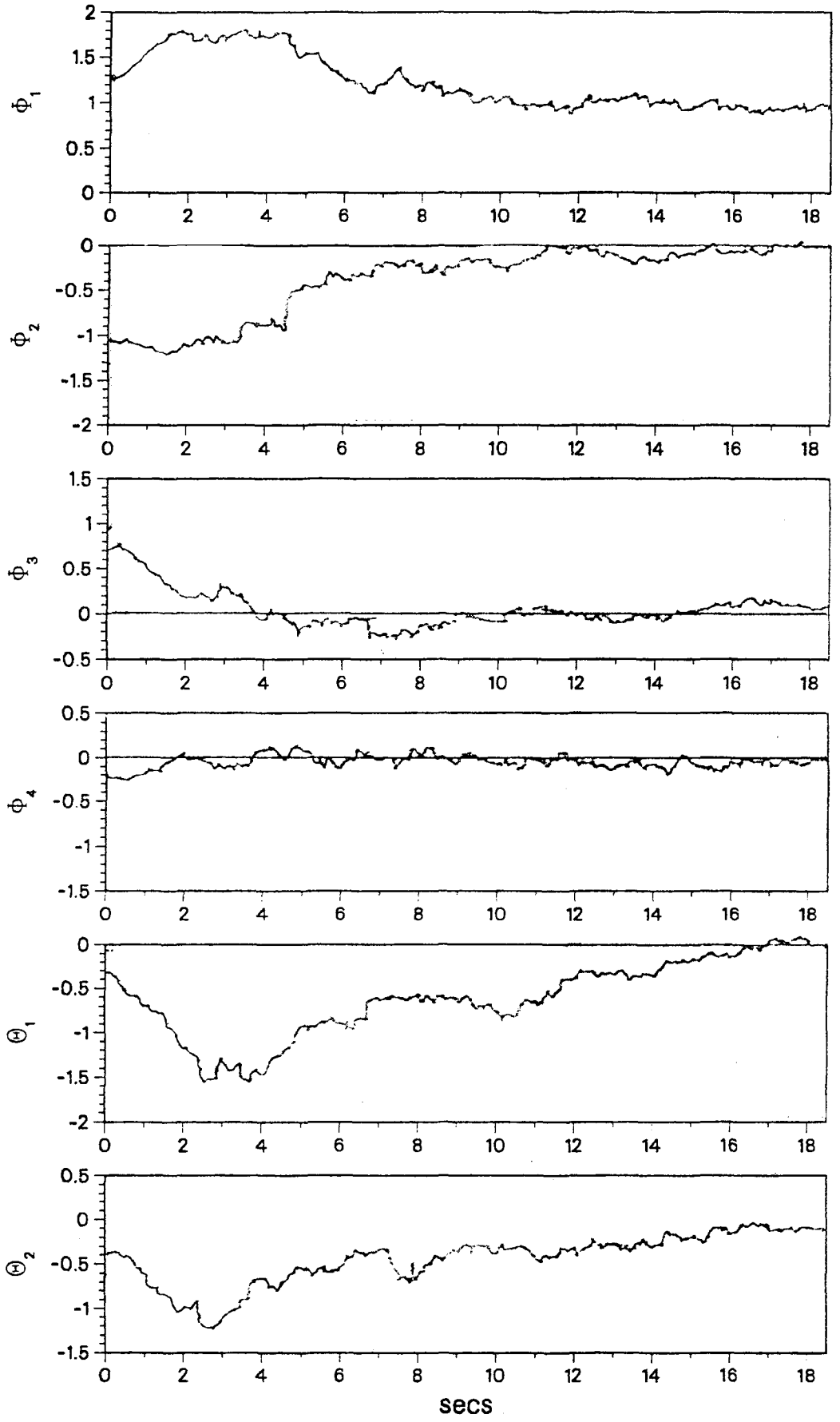

Fig. 5.40 ARMA(4,2) Model Parameter Estimates for an ARMA(4,2) Artificial Realization of the E02NS Earthquake Process

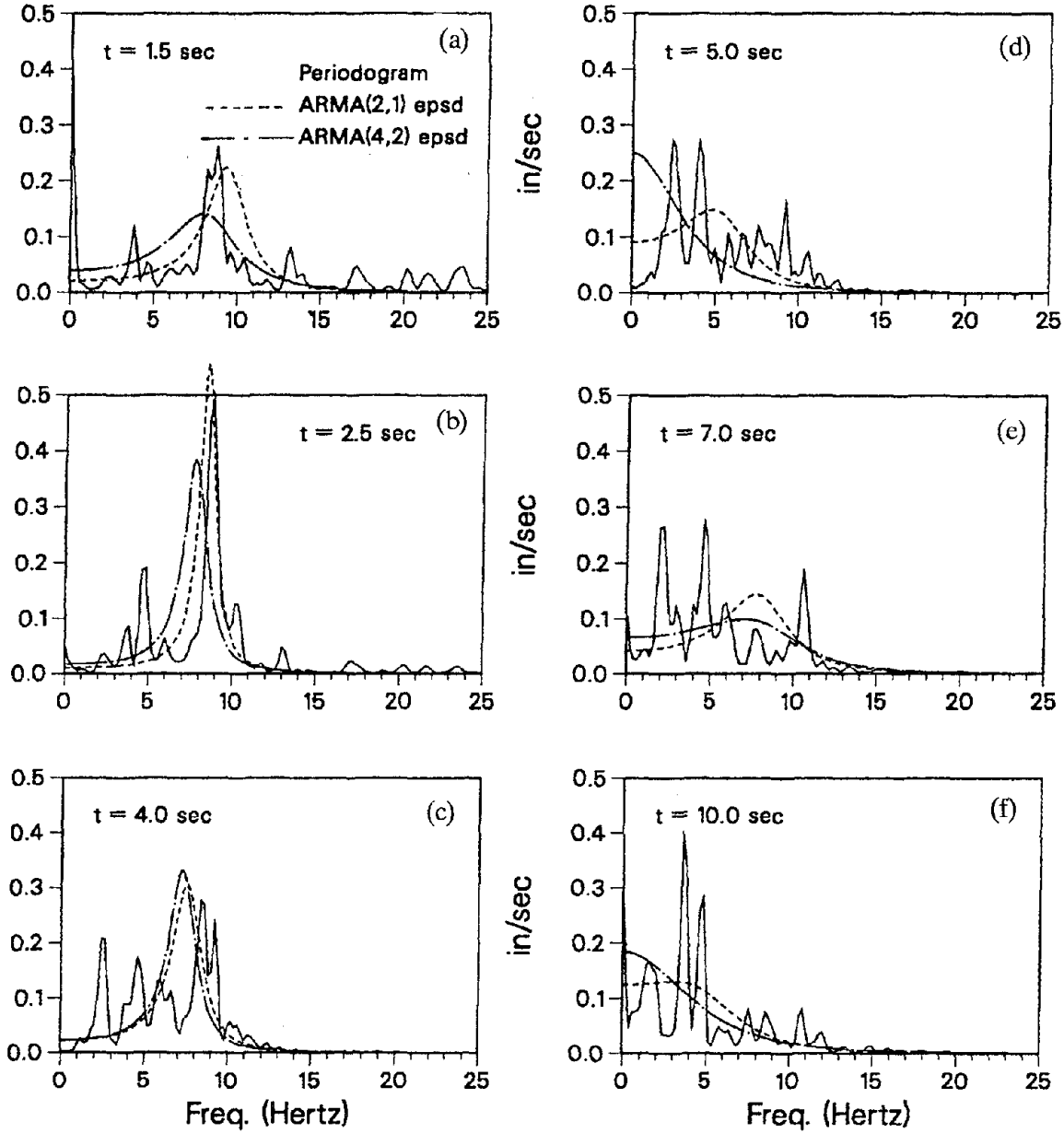

Fig. 5.41 Comparison Between the Normalized ARMA EPSD Estimate and the Normalized Moving Periodogram Estimate of the EPSD of the E02NS Earthquake Process

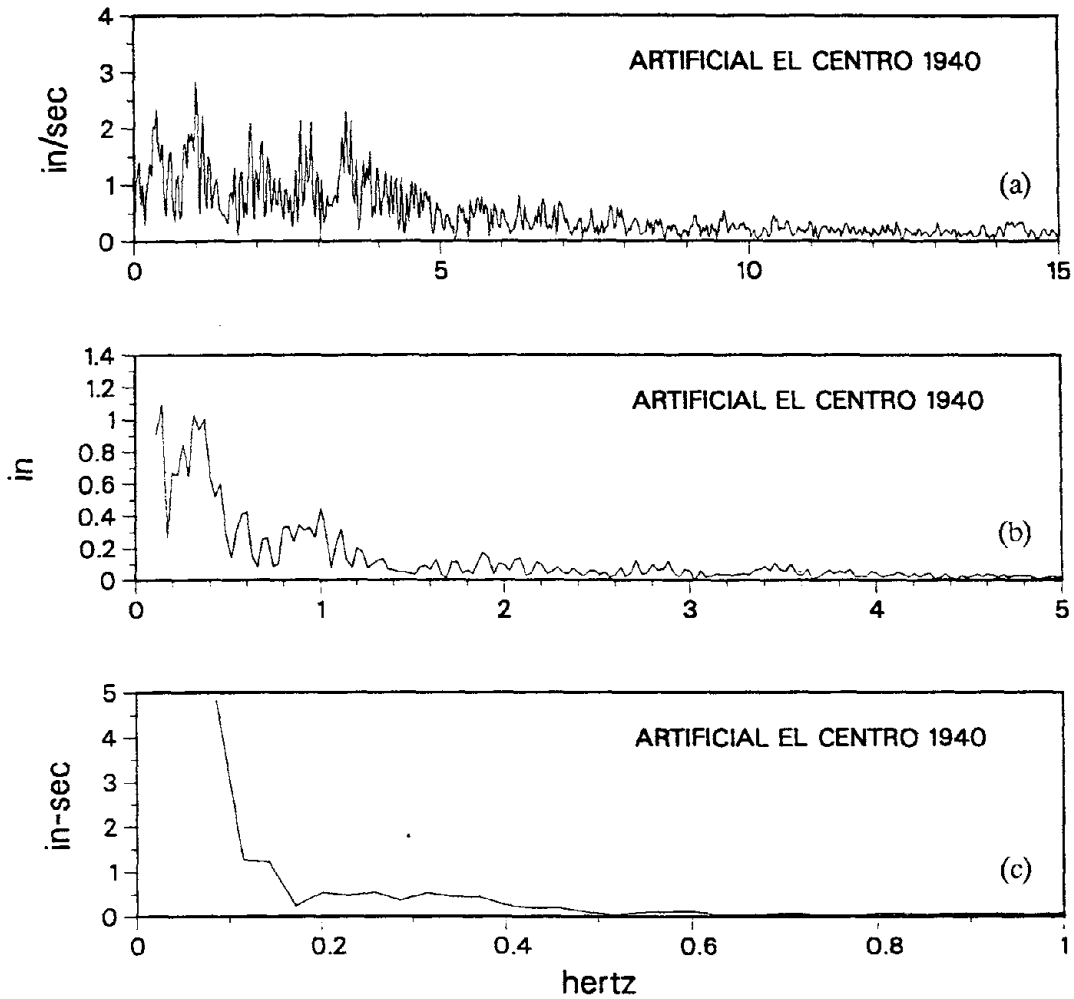

Fig. 5.42 Fourier Amplitude Spectra of an Artificial Ground Motion (acceleration, velocity, and displacement) Generated from the ARMA(2,1) Model Fitted to the El Centro 1940 Record

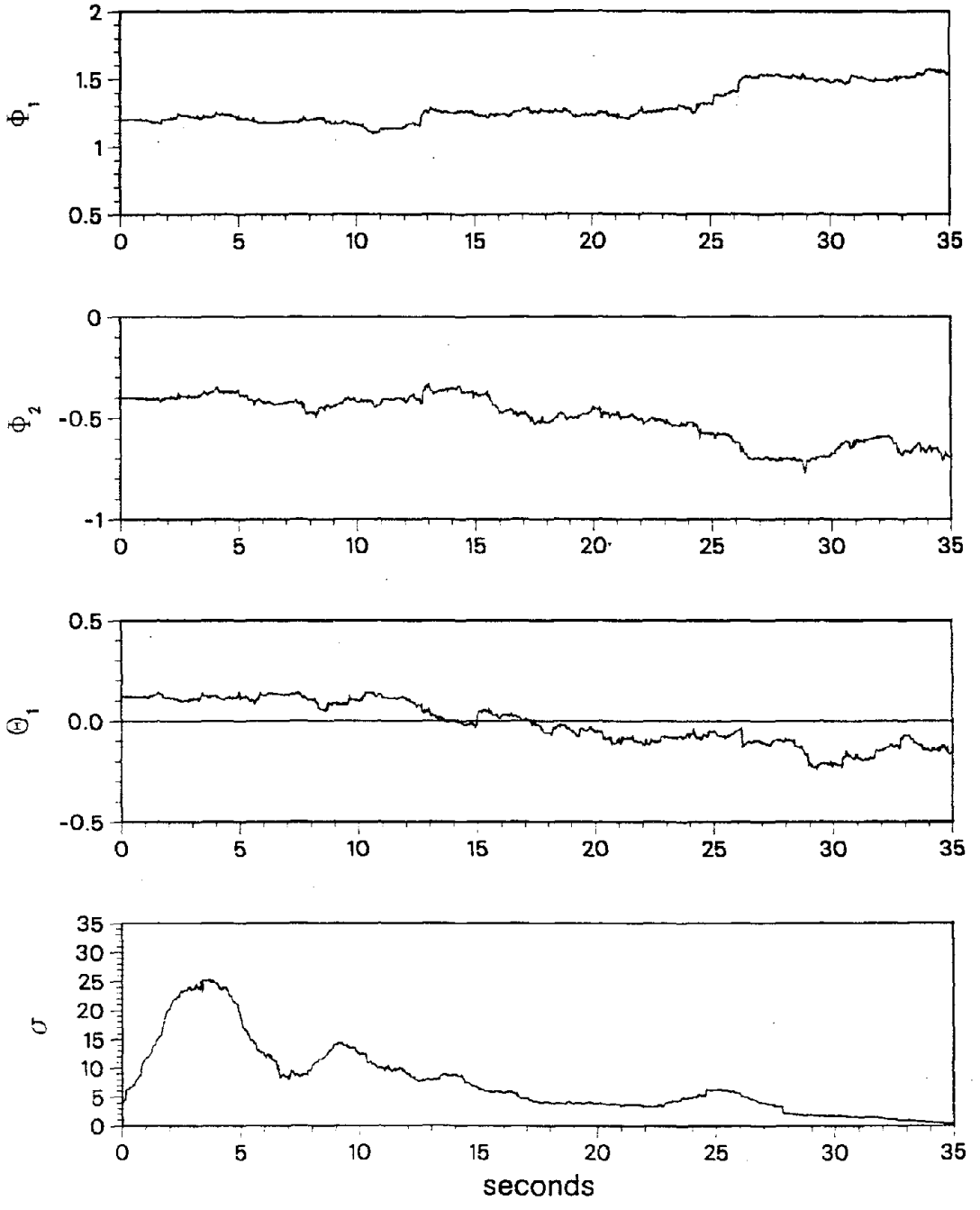

Fig. 5.43 ARMA(2,1) Model Parameter Estimates for an ARMA(2,1) Artificial Realization of the El Centro Earthquake Process

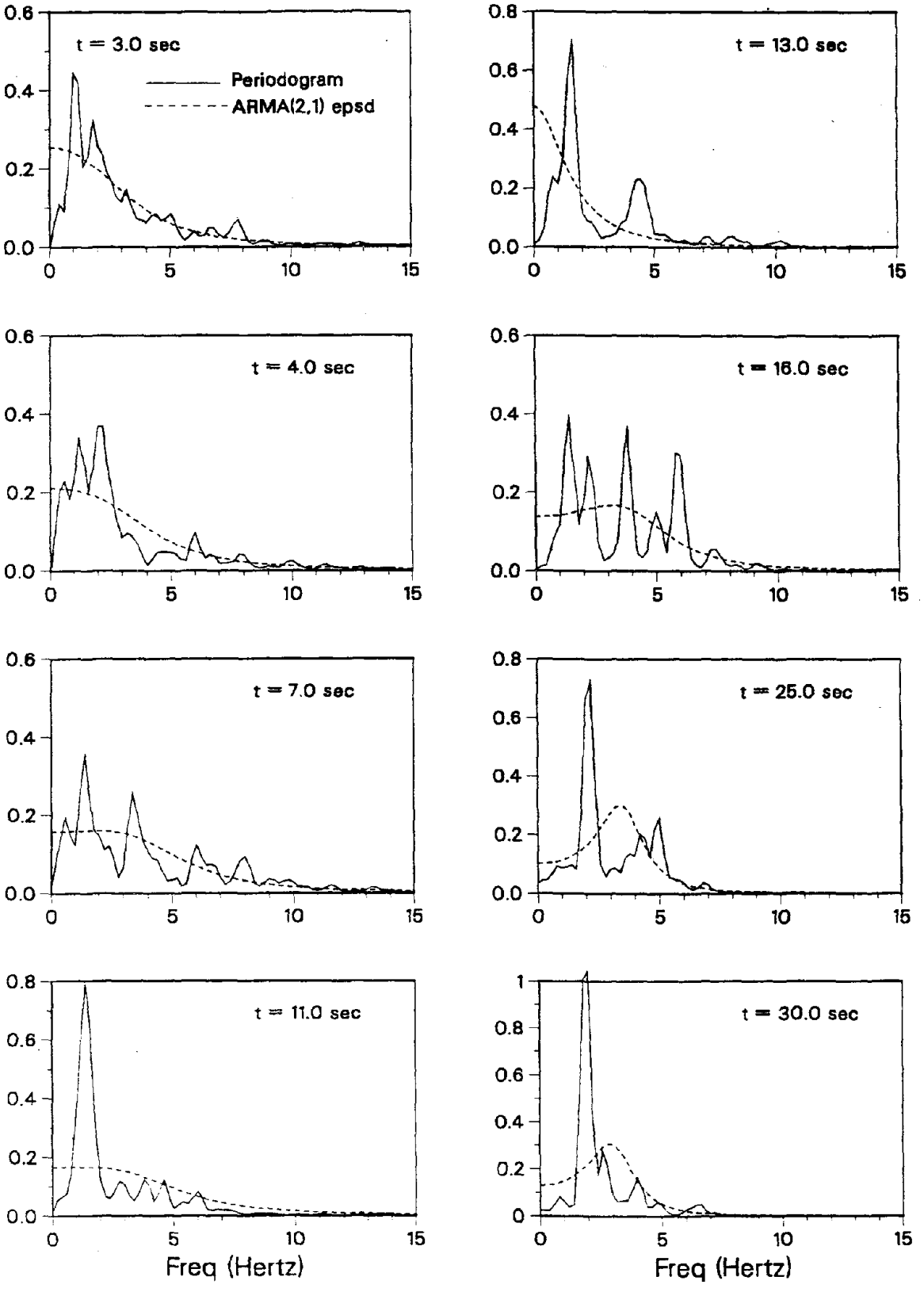

Fig. 5.44 Comparison Between the Normalized ARMA EPSD Estimate and the Normalized Moving Periodogram Estimate of the EPSD of the El Centro Earthquake process

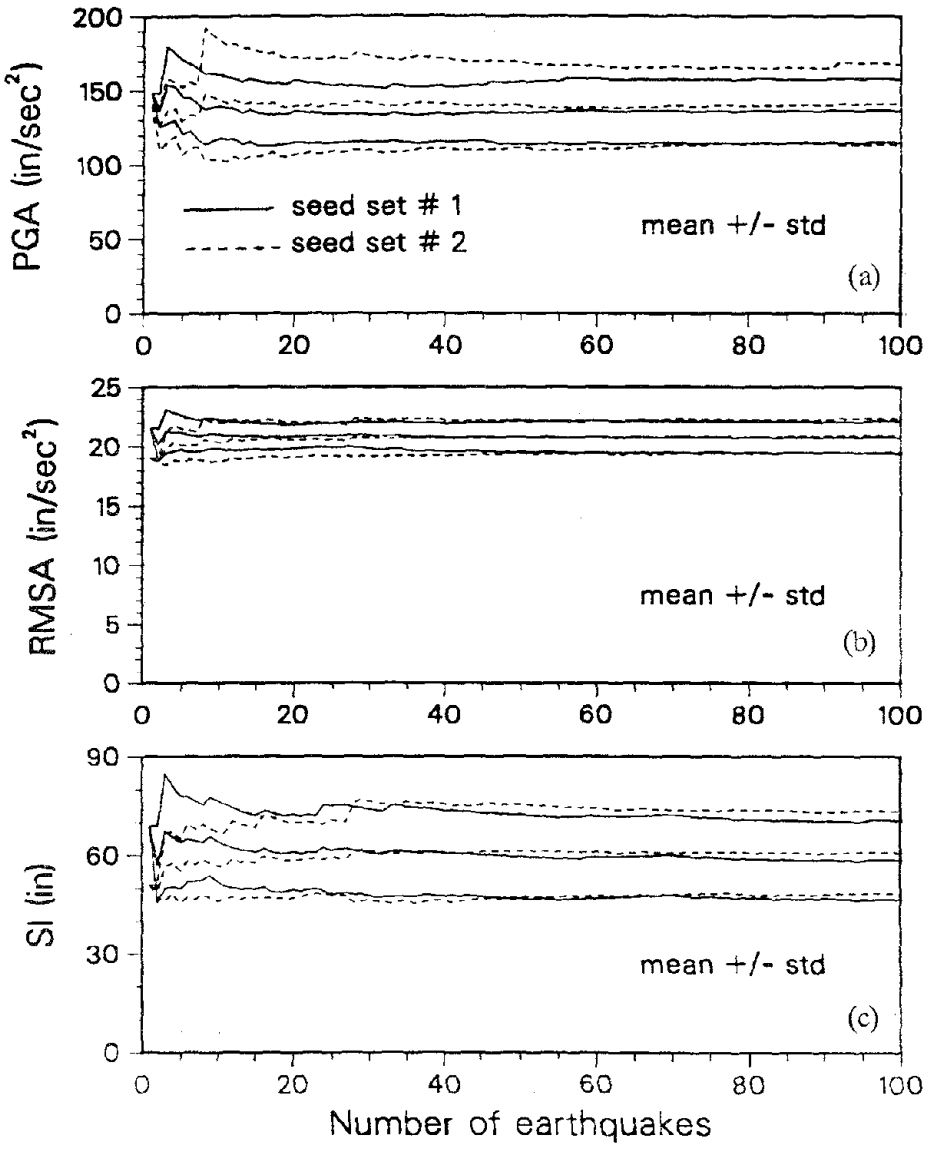

Fig. 5.45 Statistical Convergence of the Ground Motion Parameters Simulated from the ARMA(2,1) Model of El Centro 1940

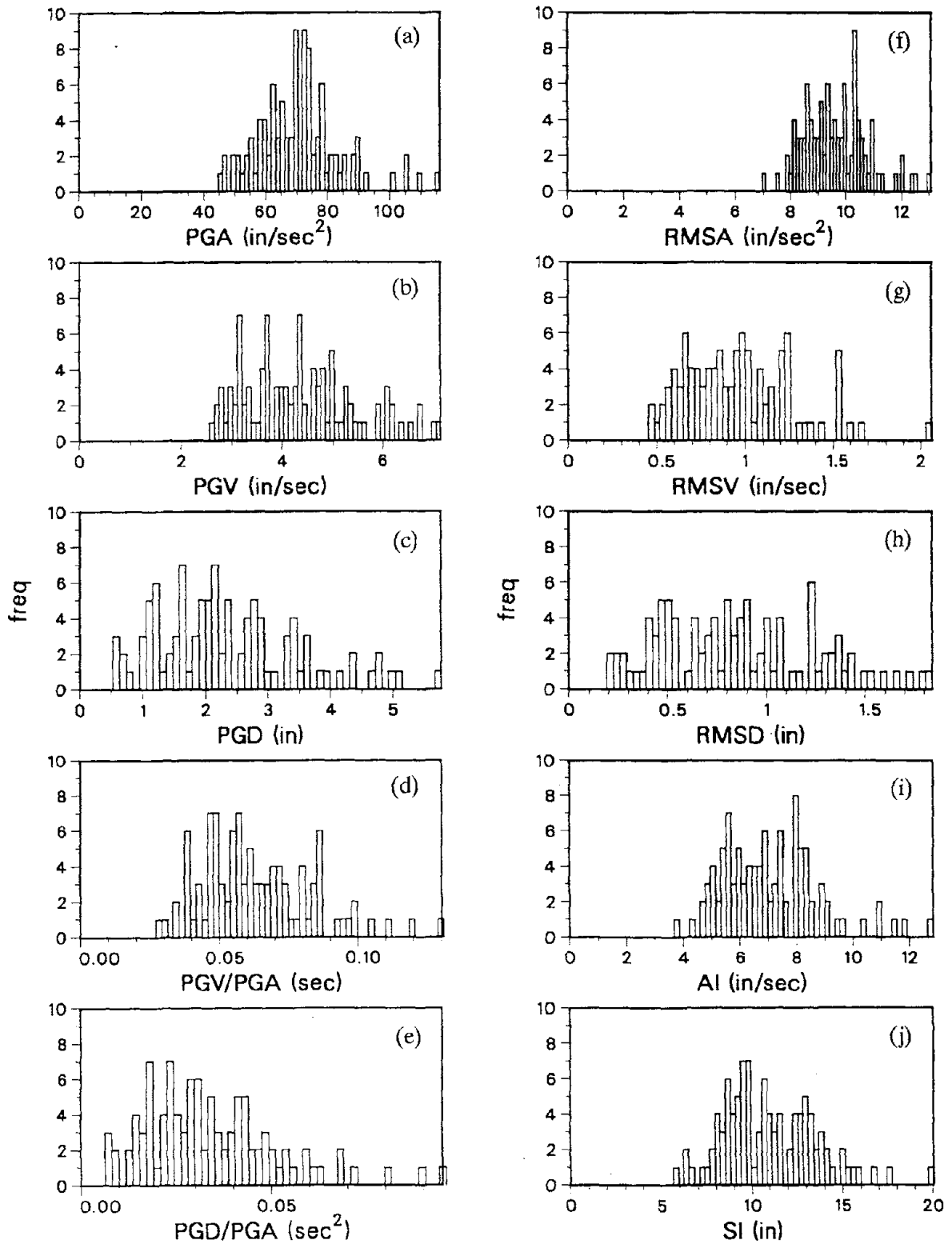

Fig. 5.46 Histograms of the Ground Motion Parameters Simulated from the ARMA(2,1) Model of E02NS

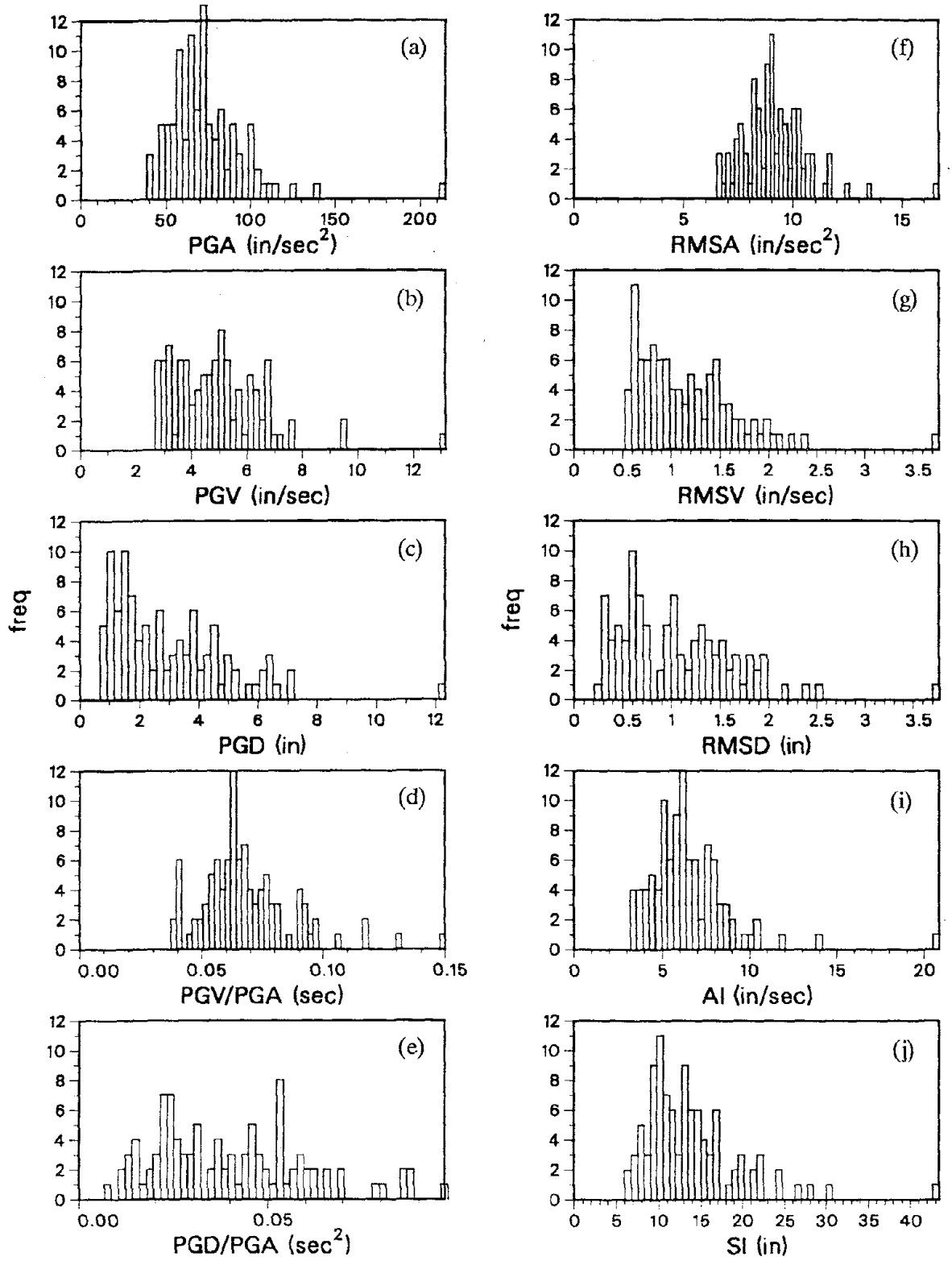

Fig. 5.47 Histograms of the Ground Motion Parameters Simulated from the ARMA(4,2) Model of E02NS

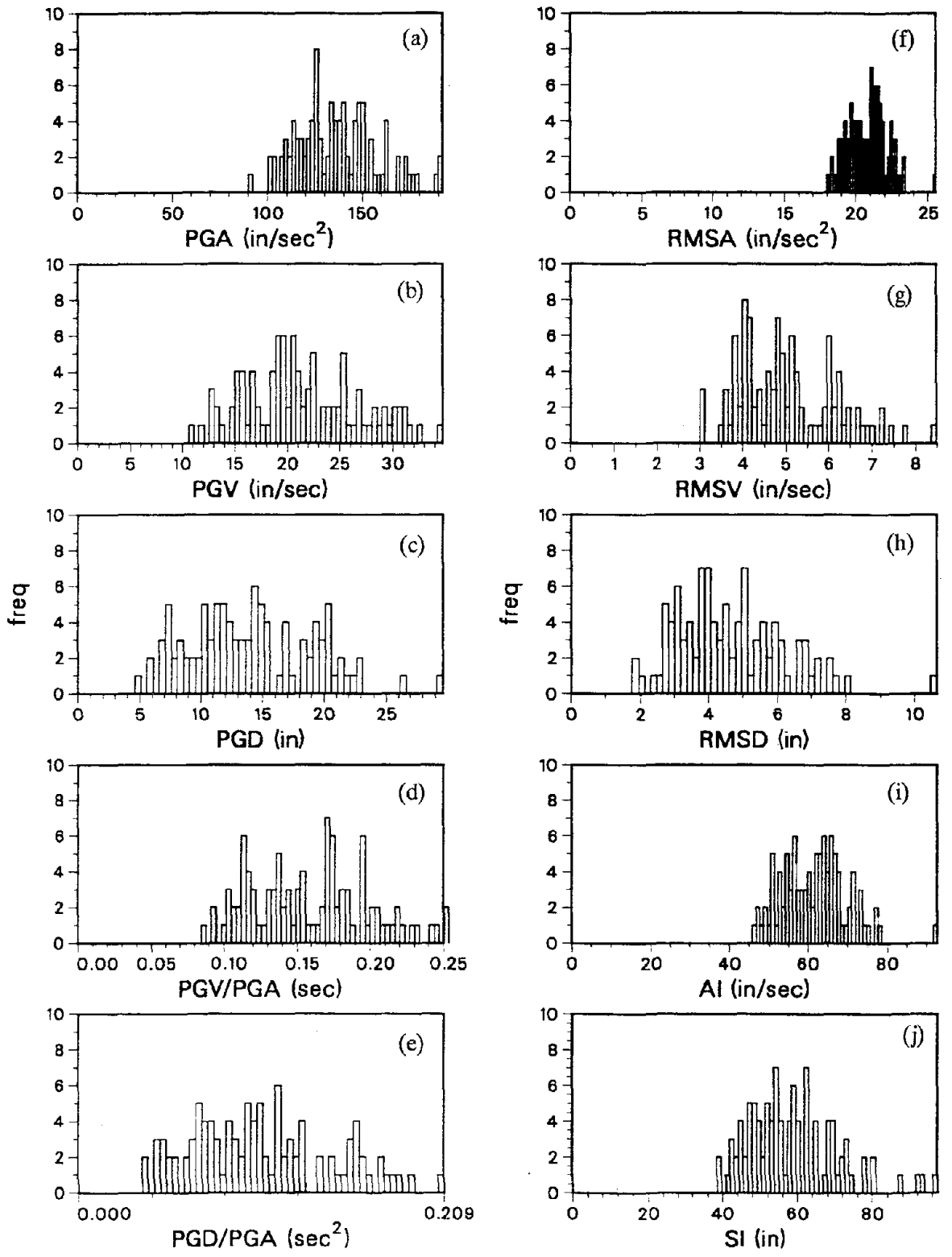

Fig. 5.48 Histograms of the Ground Motion Parameters Simulated from the ARMA(2,1) Model of El Centro 1940

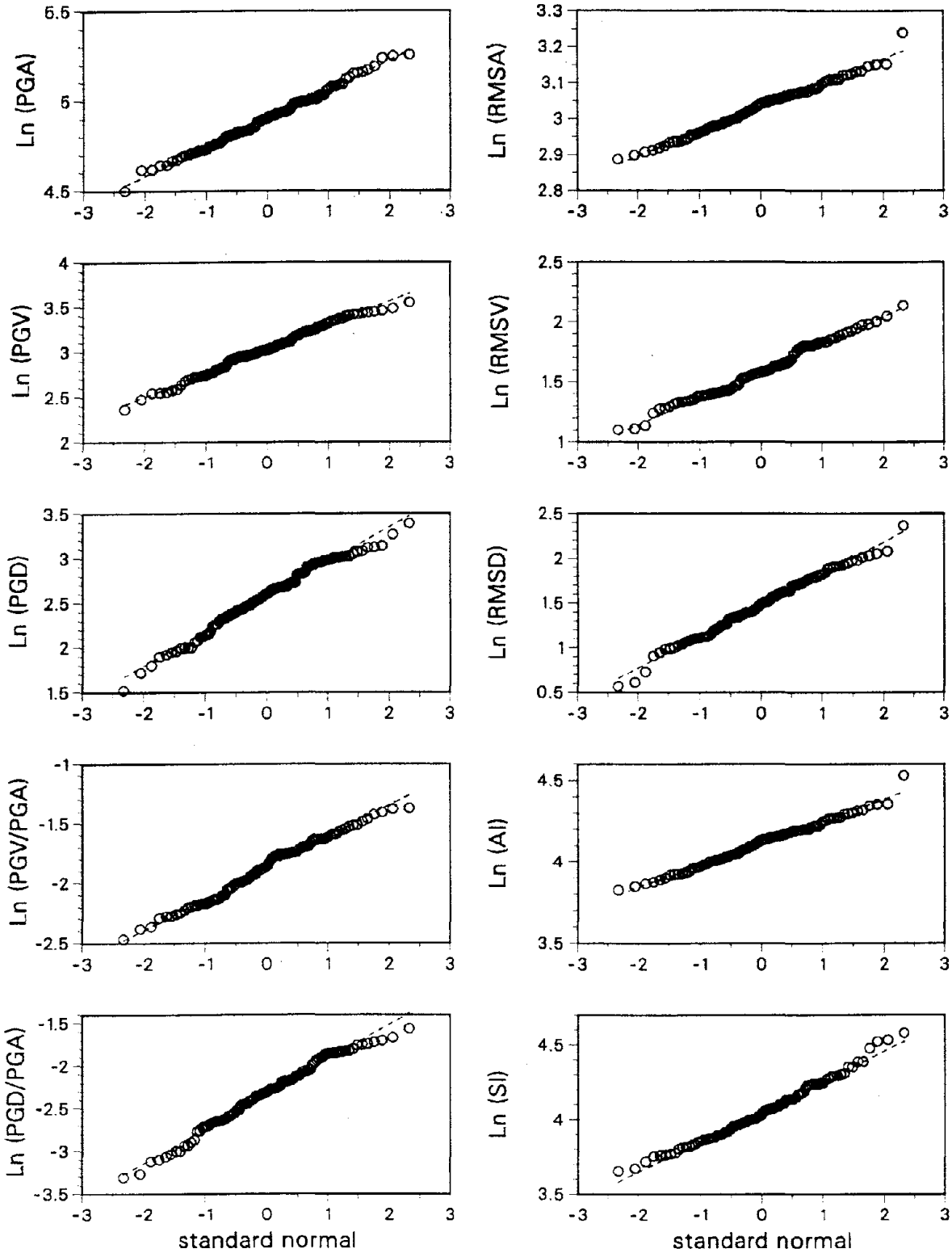

Fig. 5.49 Lognormal Distribution Fit of Ground Motion Parameters on Probability Paper (El Centro 1940, ARMA(2,1))

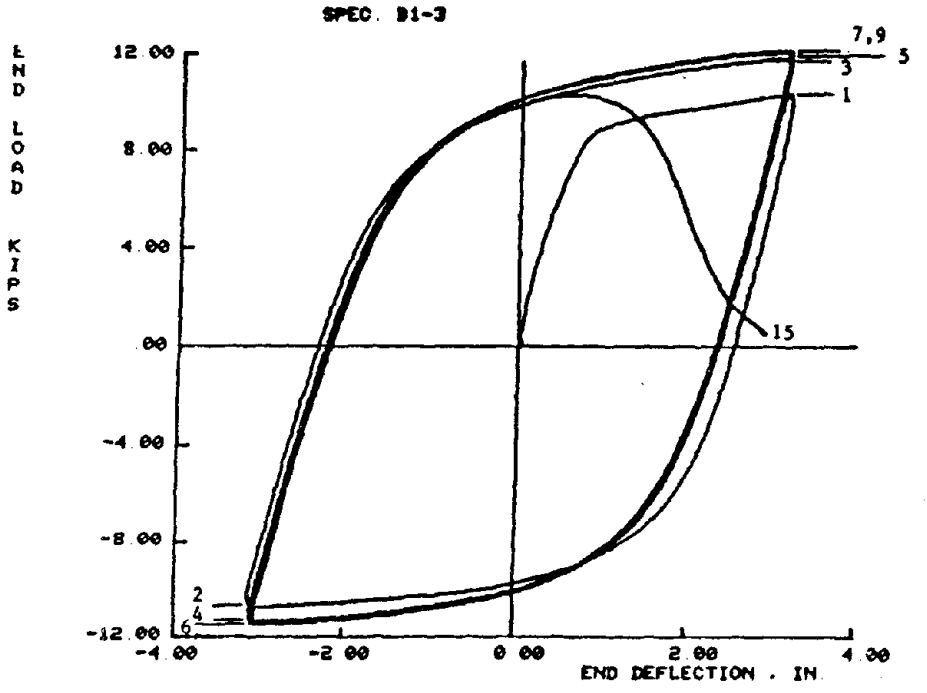

Fig. 6.1 Cyclic Load-Deflection Diagram for constant amplitude cycling of a Wide-Flange Component of Steel Structure ("crack propagation at weldment" damage mode from Ref. [51])

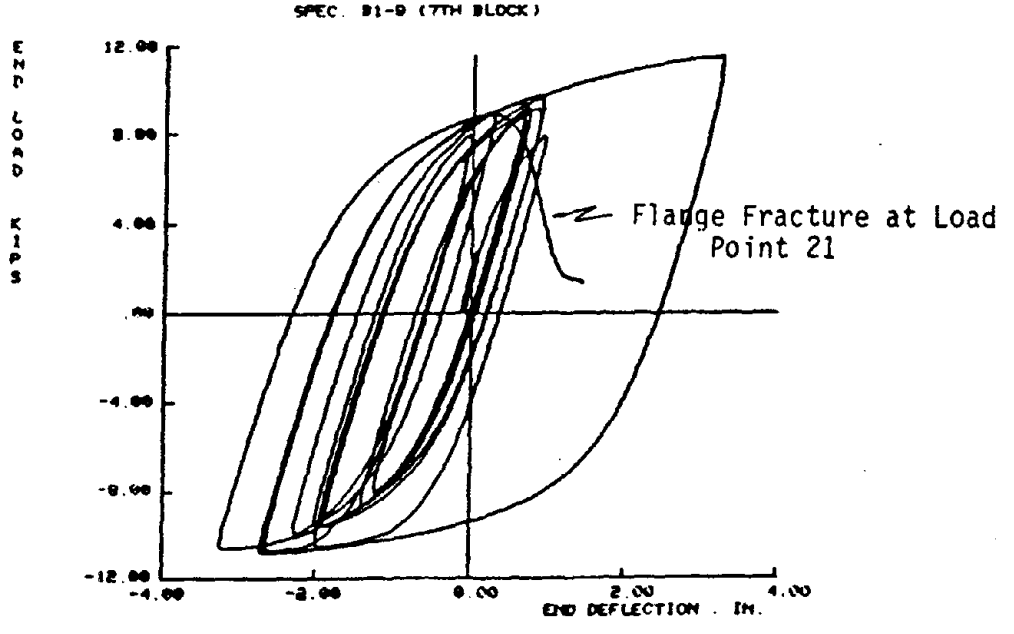

Fig. 6.2 Cyclic Load-Deflection Diagram for variable amplitude cycling of a Wide-Flange Component of Steel Structure ("crack propagation at weldment" damage mode from Ref. [51])

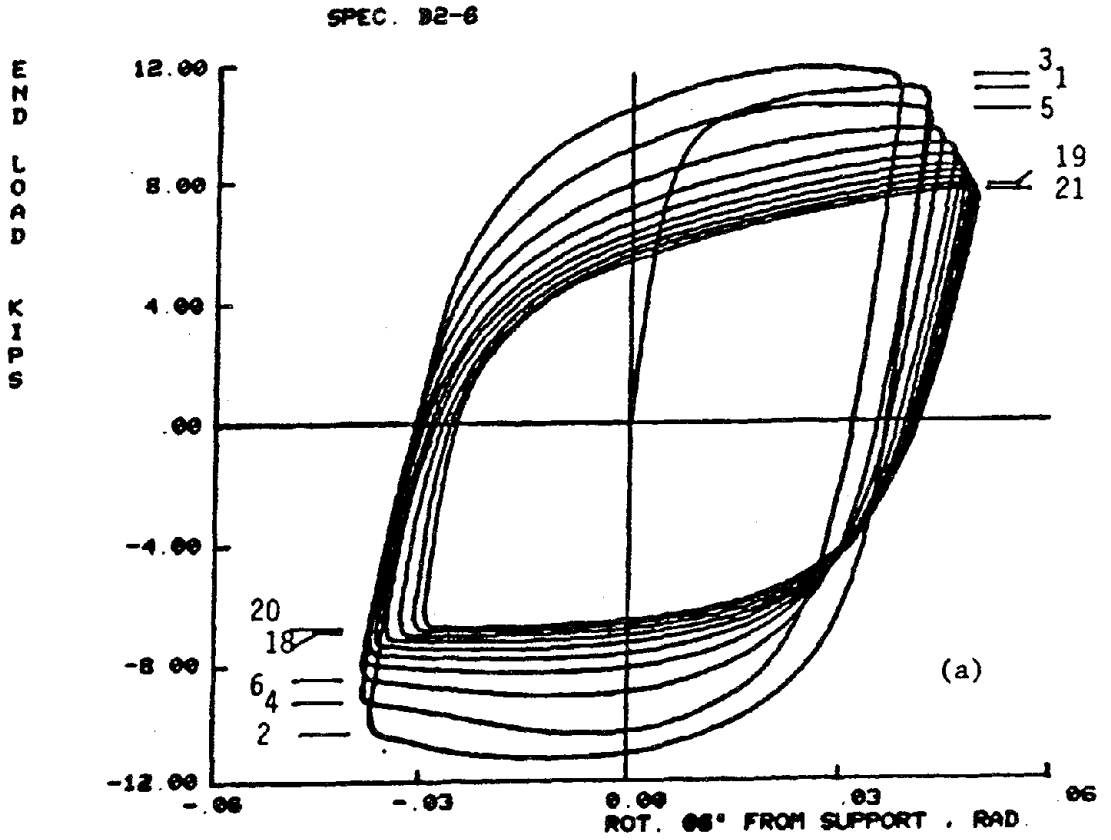

Fig. 6.3 Cyclic Load-Deflection Diagram for constant amplitude cycling of a Wide-Flange Component of Steel Structure ("flange local buckling" damage mode from Ref. [51])

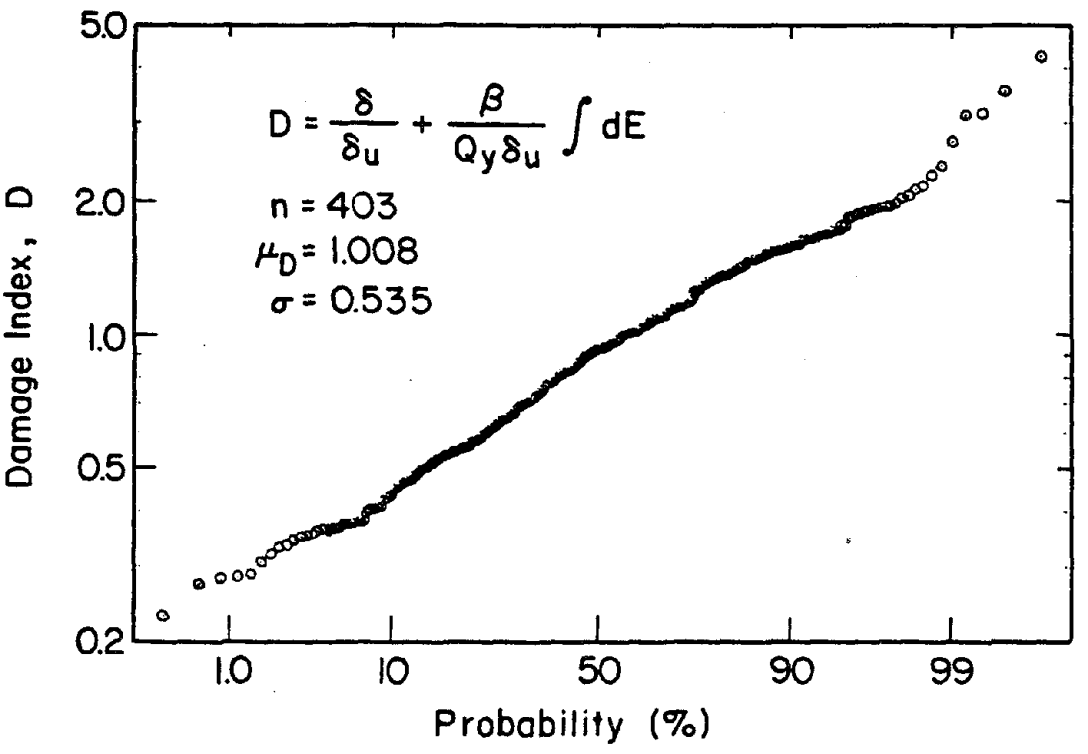

Fig. 6.4 Damage Index D_1 plotted on Lognormal Probability Paper, from Ref. [71])

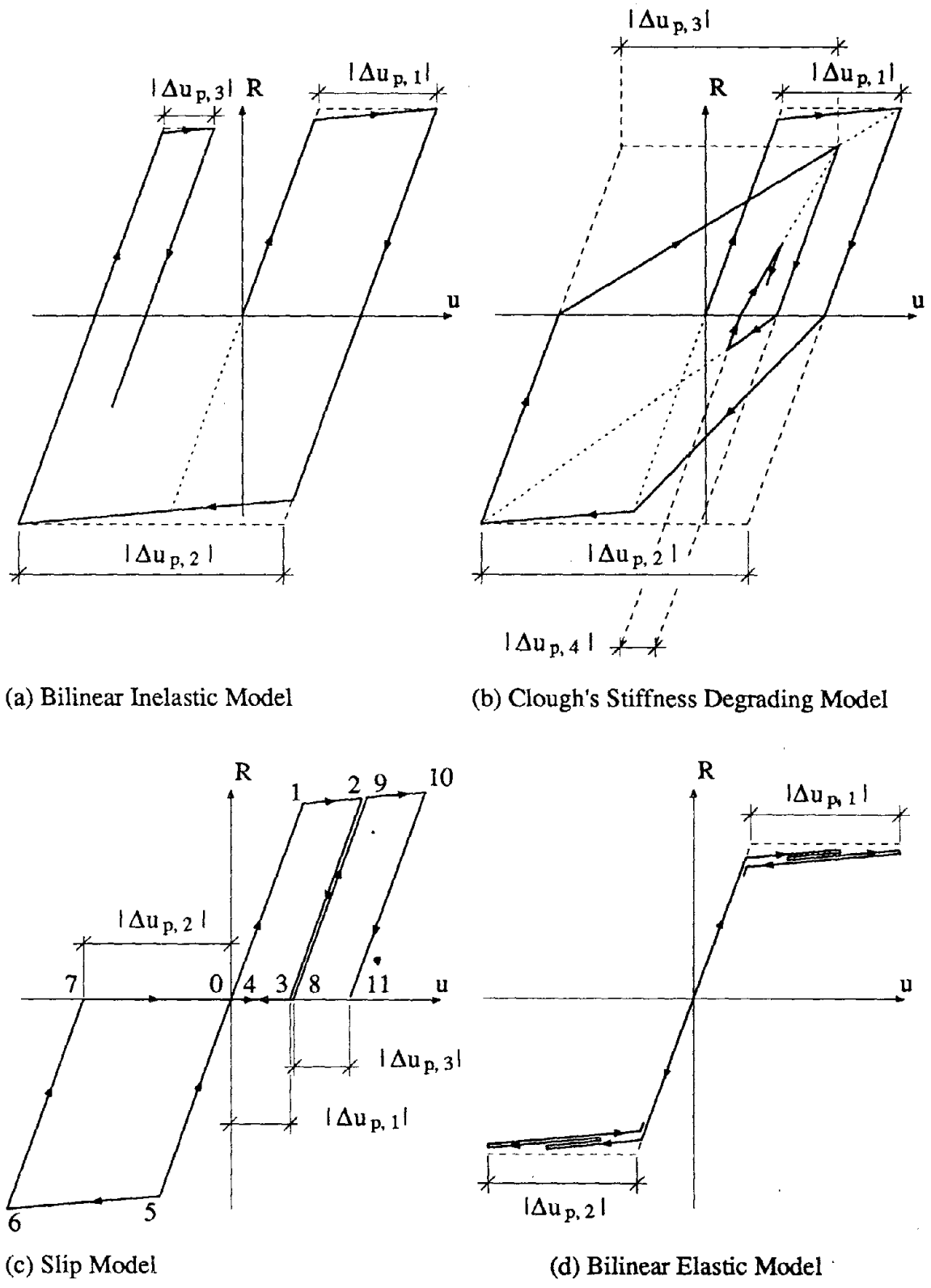

Fig. 6.5 Definition of Plastic Deformation Ranges for Different Hysteretic Models

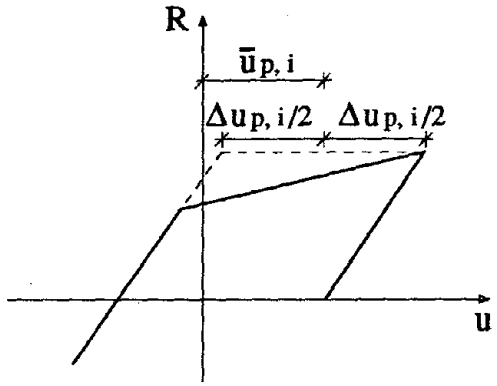

Fig. 6.6 Centroid of Plastic Deformation Range, $\bar{u}_{p,i}$

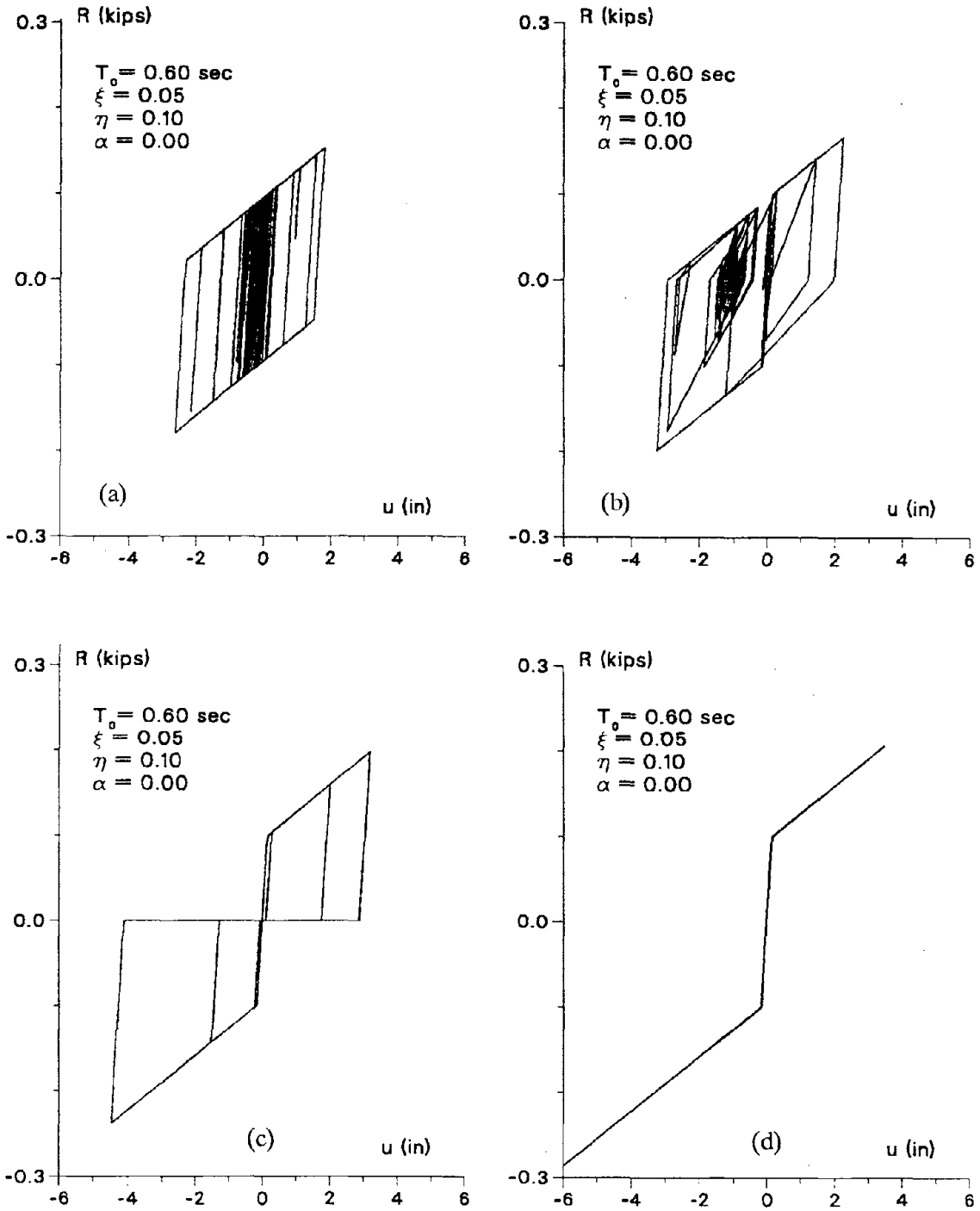

Fig. 6.7 Hysteretic Behavior of Four Different Systems in Response to the Same Artificial Earthquake Derived From El Centro 1940

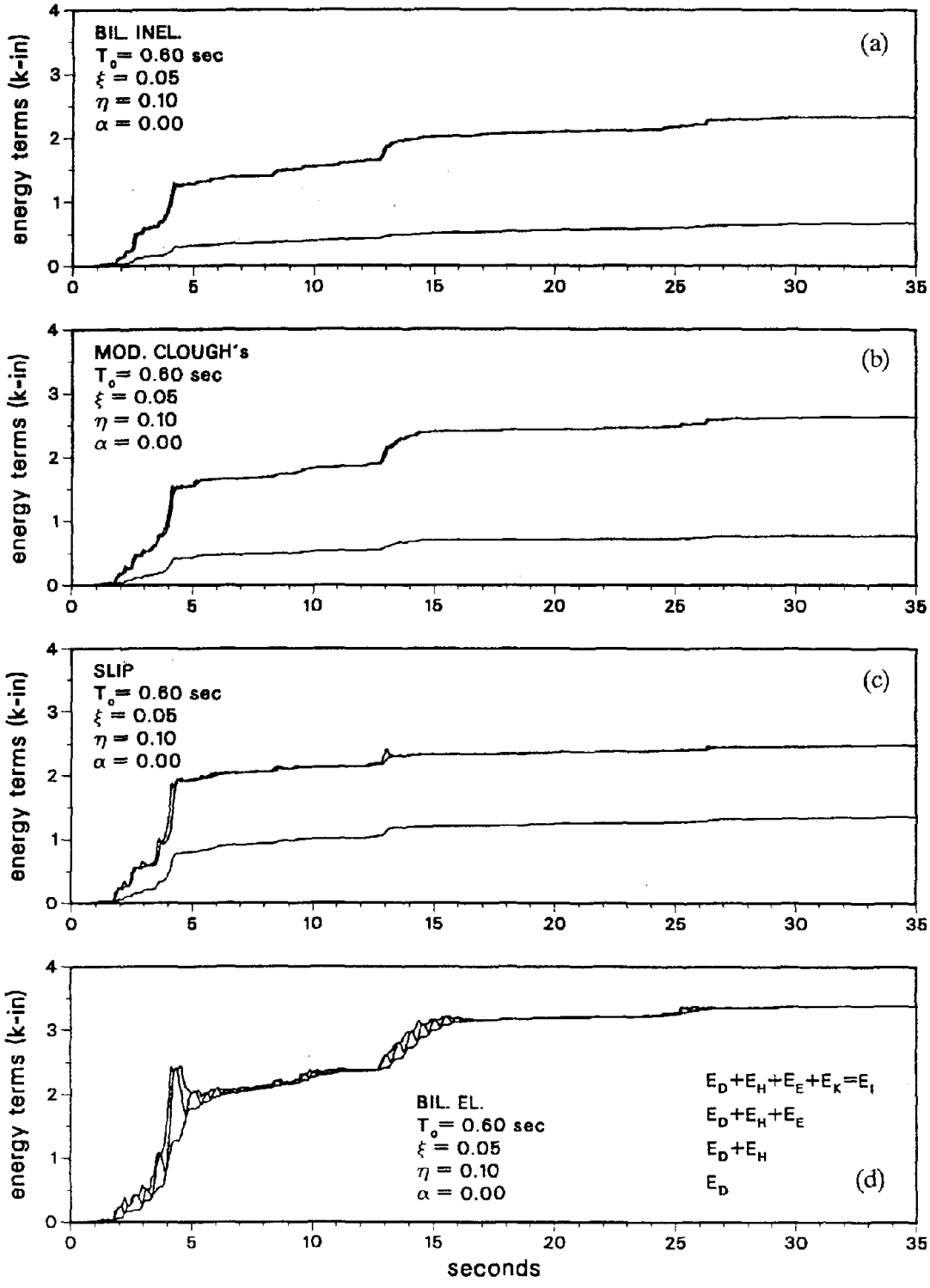

Fig. 6.8 Energy Response Time Histories of Four Different Systems to the Same Artificial Earthquake Derived From El Centro 1940

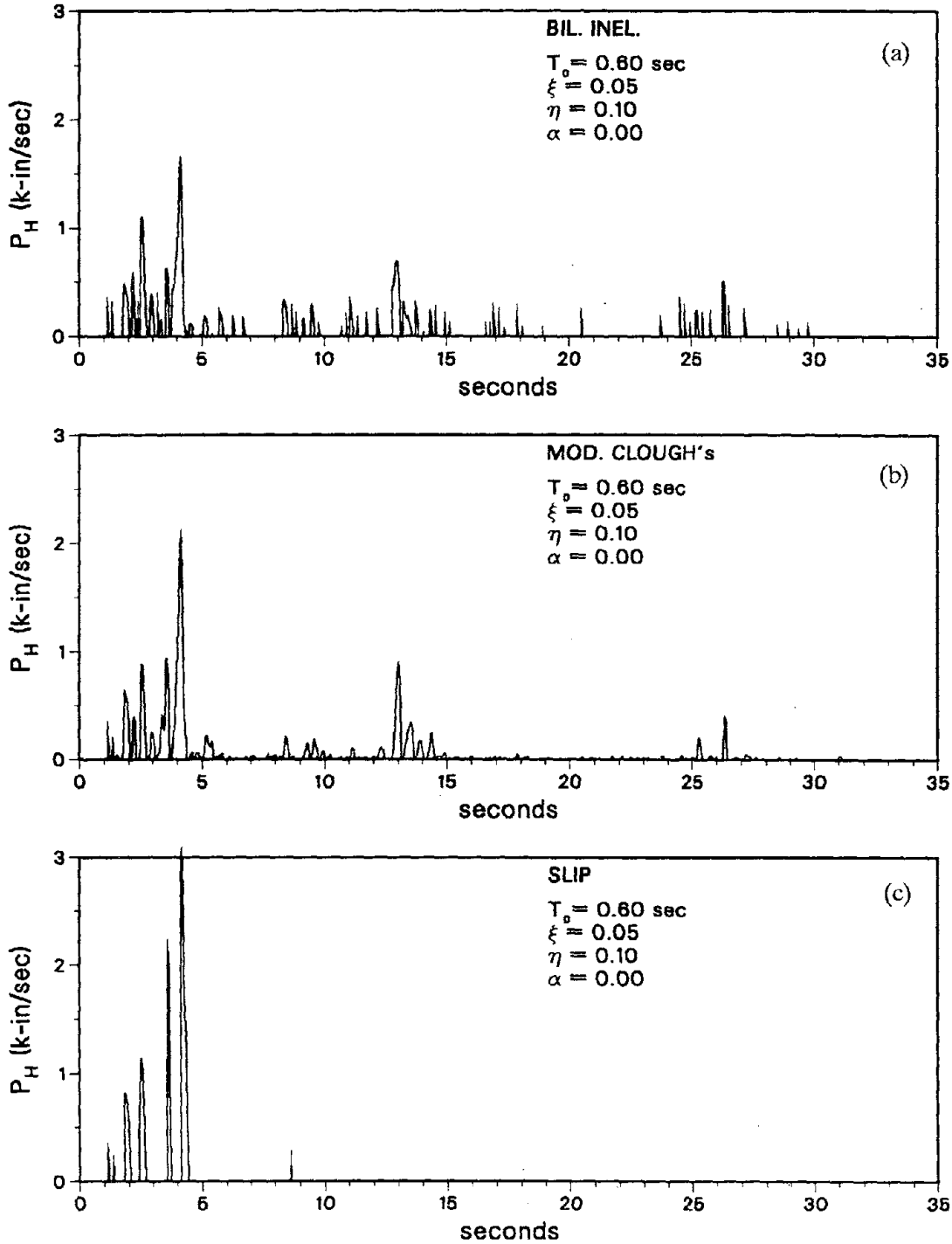

Fig. 6.9 Rate of Hysteretic Energy Response Time Histories of Four Different Systems to the Same Artificial Earthquake Derived from El Centro 1940

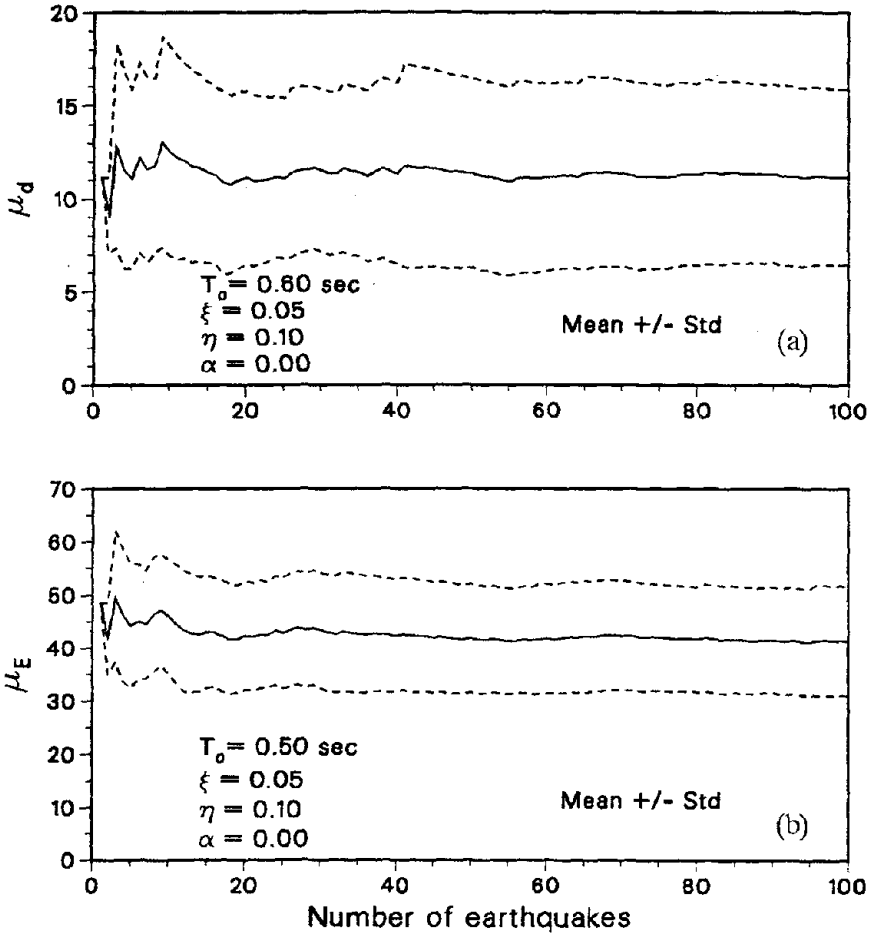

Fig. 6.10 Convergence of the Second Order Statistics of Two Response Parameters to the Number of Artificial Earthquakes from the ARMA(2,1) El Centro Process

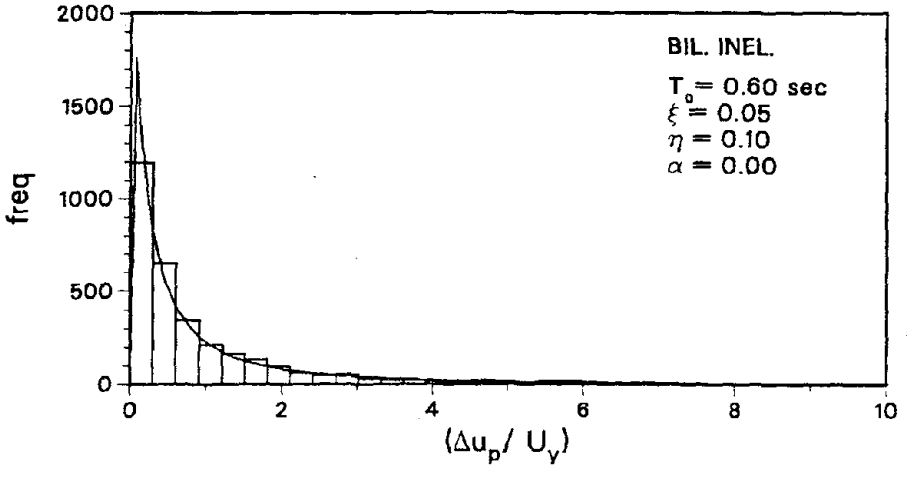

Fig. 6.11 Histogram and Lognormal Probability Model Fit of the Plastic Deformation Ranges Generated by the ARMA(2,1) El Centro Process

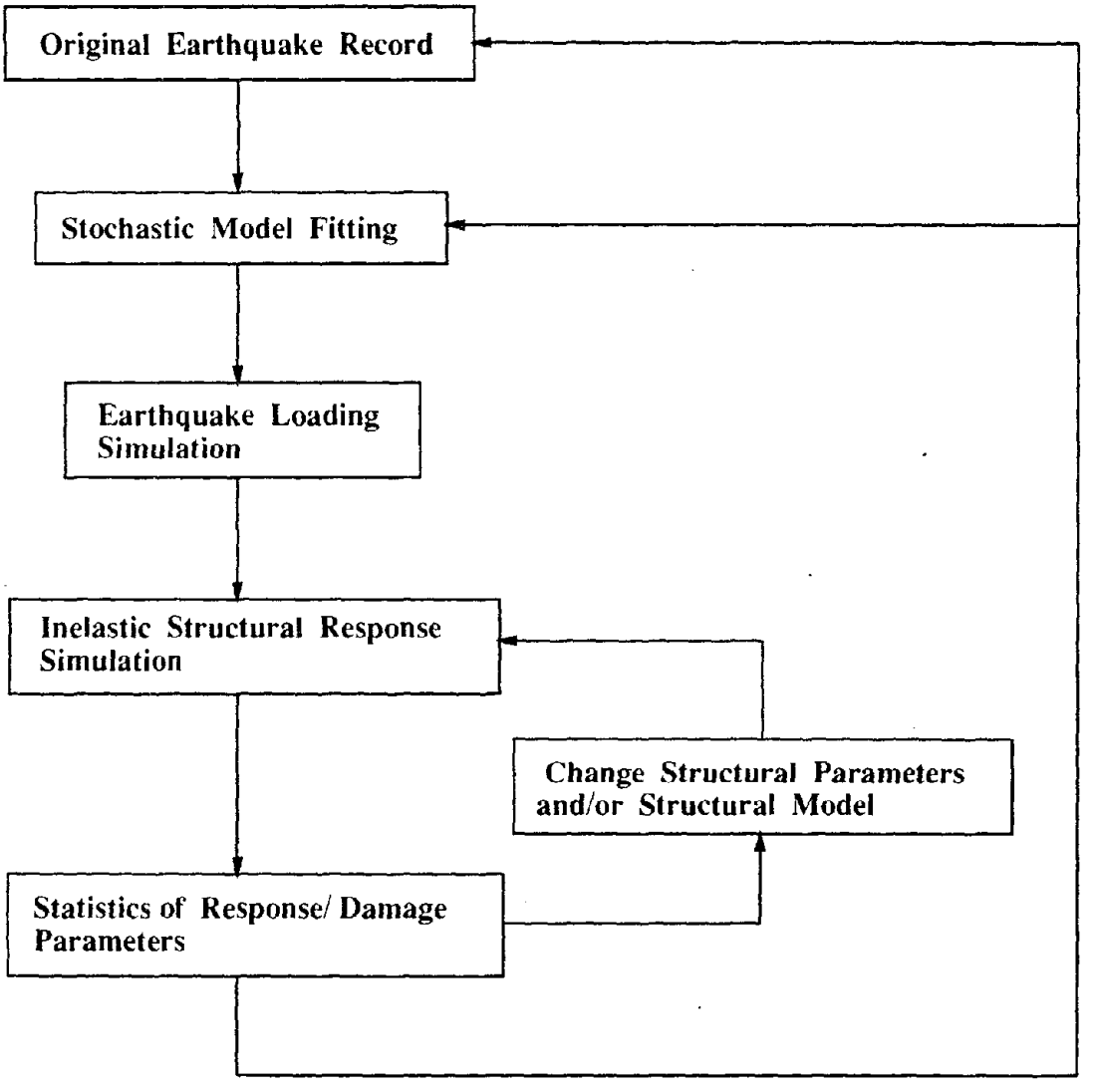

Fig. 6.12 Flow Chart of Statistical Parametric (Sensitivity) Study

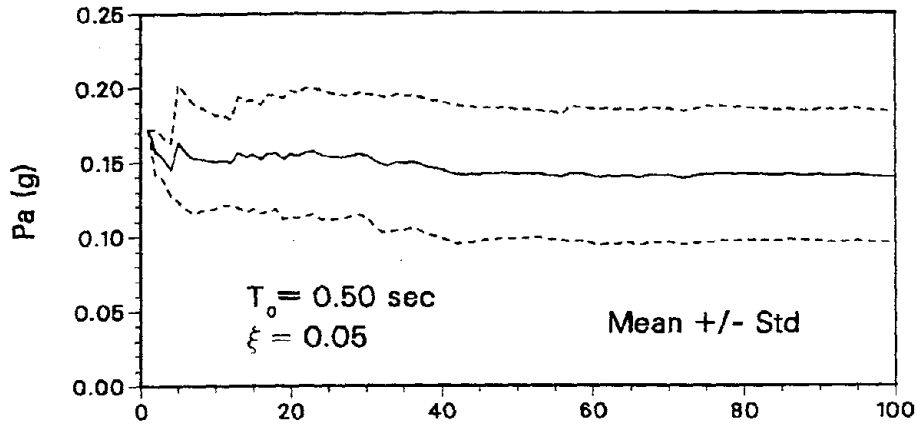

(a) From ARMA(2,1) Model of E02NS

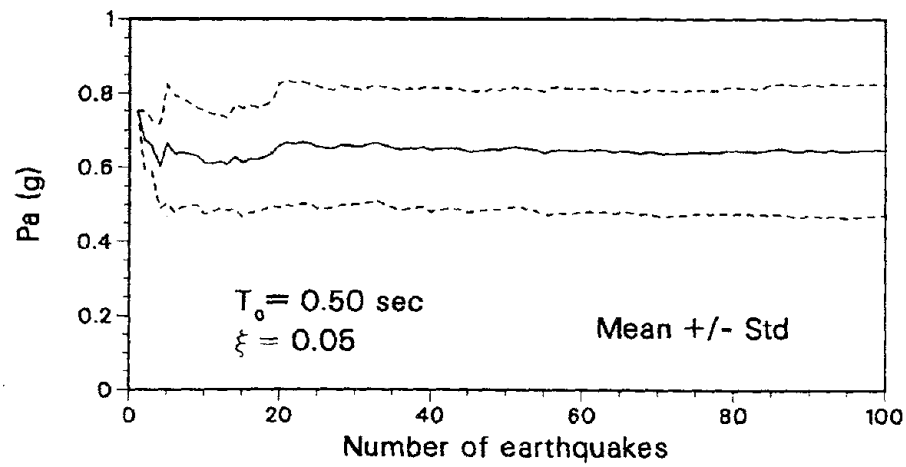

(b) From ARMA(2,1) Model 0f El Centro 1940

Fig. 7.1 Statistical Convergence of the Pseudo-Acceleration Rcsponse

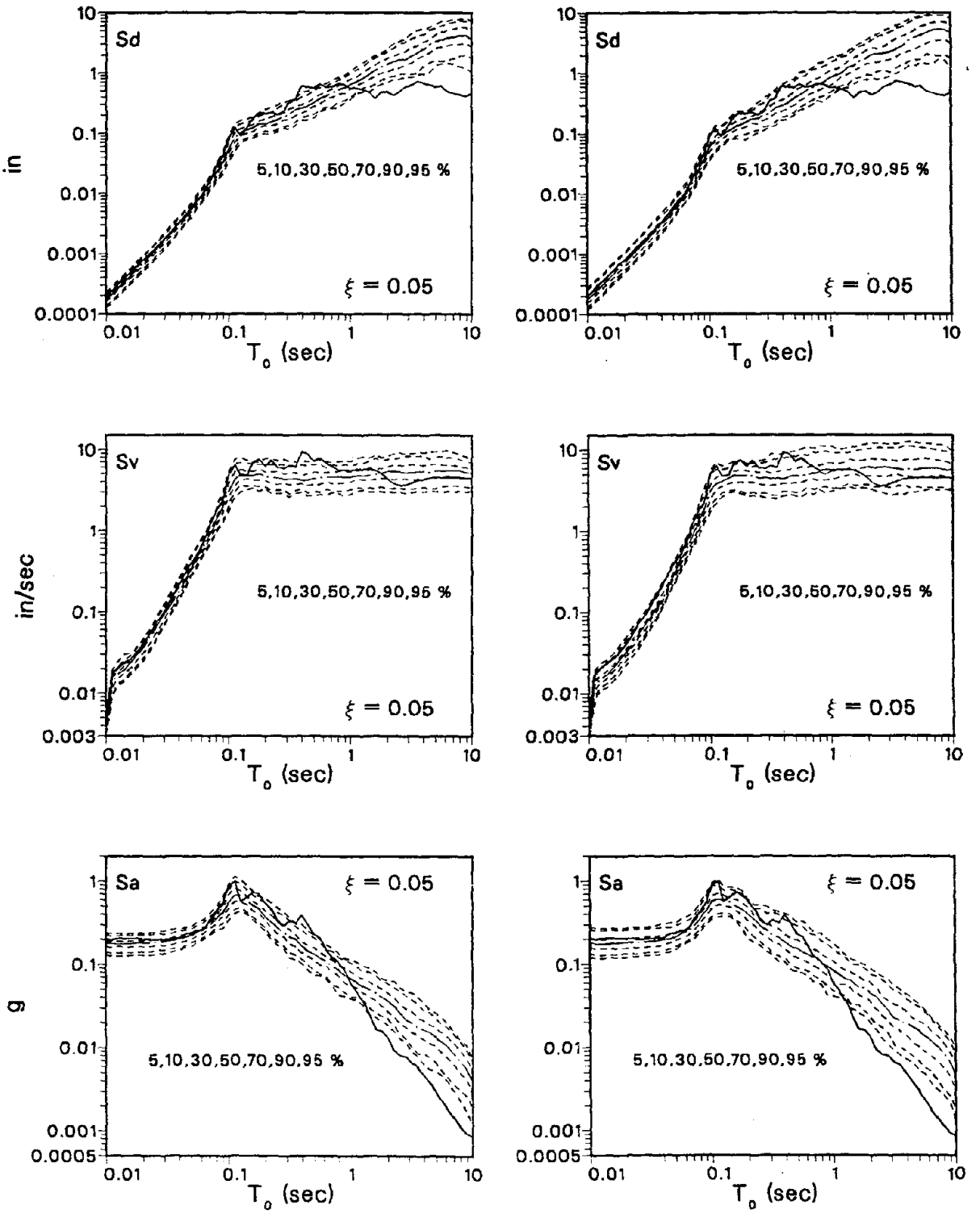

(a) ARMA(2,1) Model of E02NS

(b) ARMA(4,2) Model of E02NS

Fig. 7.2 Probabilistic and Target Elastic Response Spectra for E02NS (Statistical "Fractile Method")

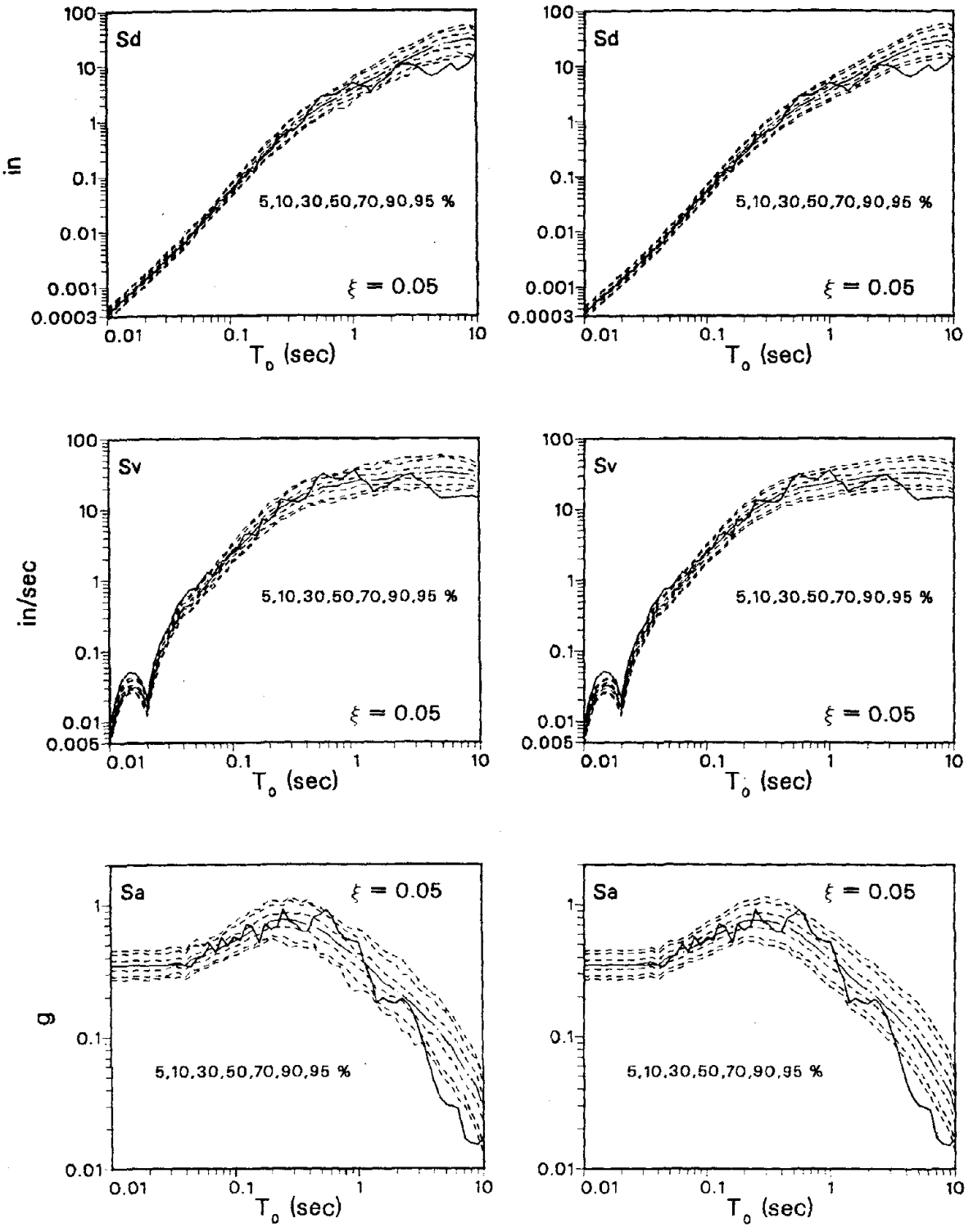

(a) "Statistical Fractile Method"

(b) "Analytical Fractile Method"

Fig. 7.3 Probabilistic and Target Elastic Response Spectra for El Centro 1940

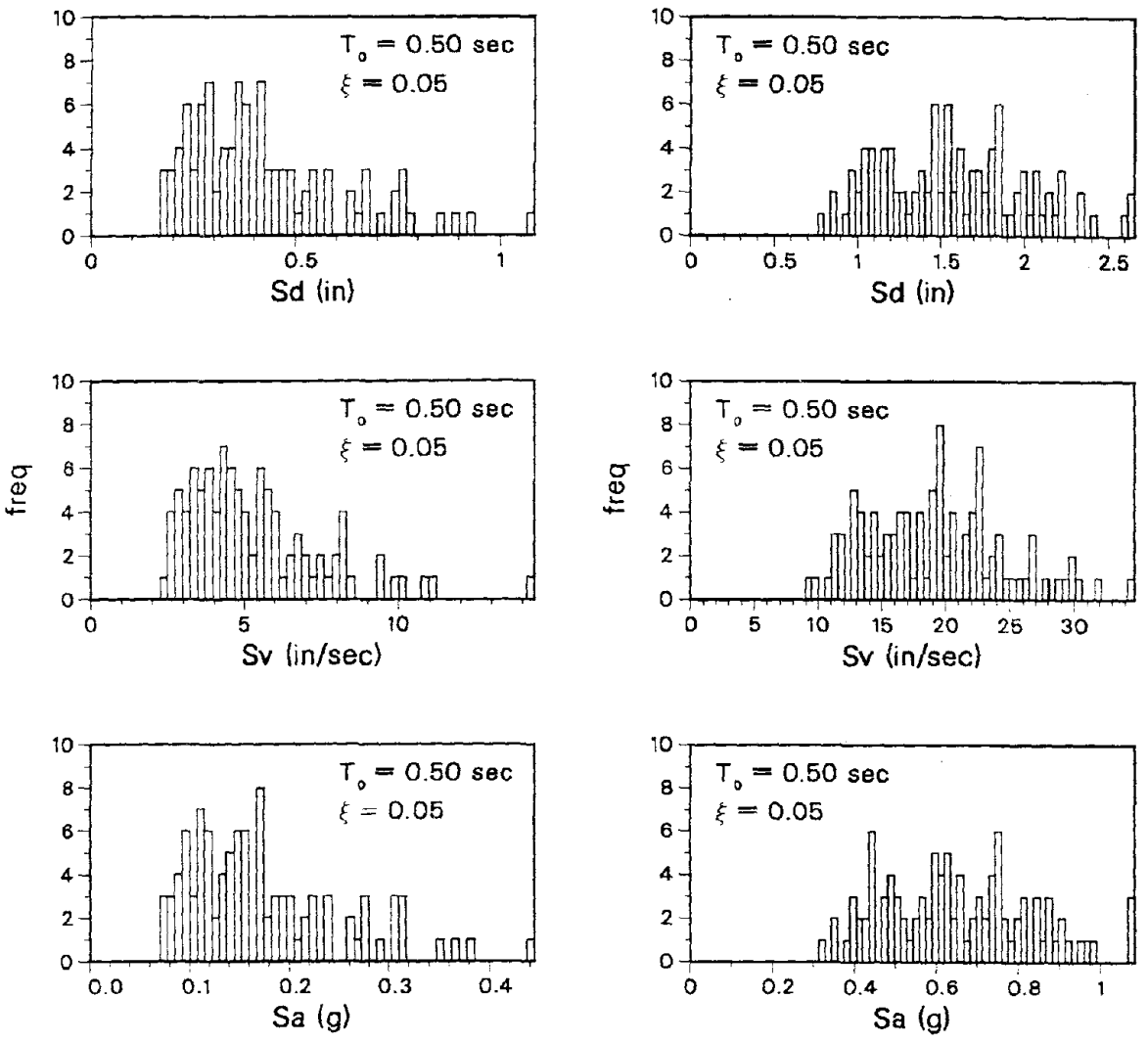

(a) ARMA(4,2) Model of E02NS

(b) ARMA(2,1) Model of El Centro 1940

Fig. 7.4 Histograms of the Peak Responses of Linear SDOF Oscillators

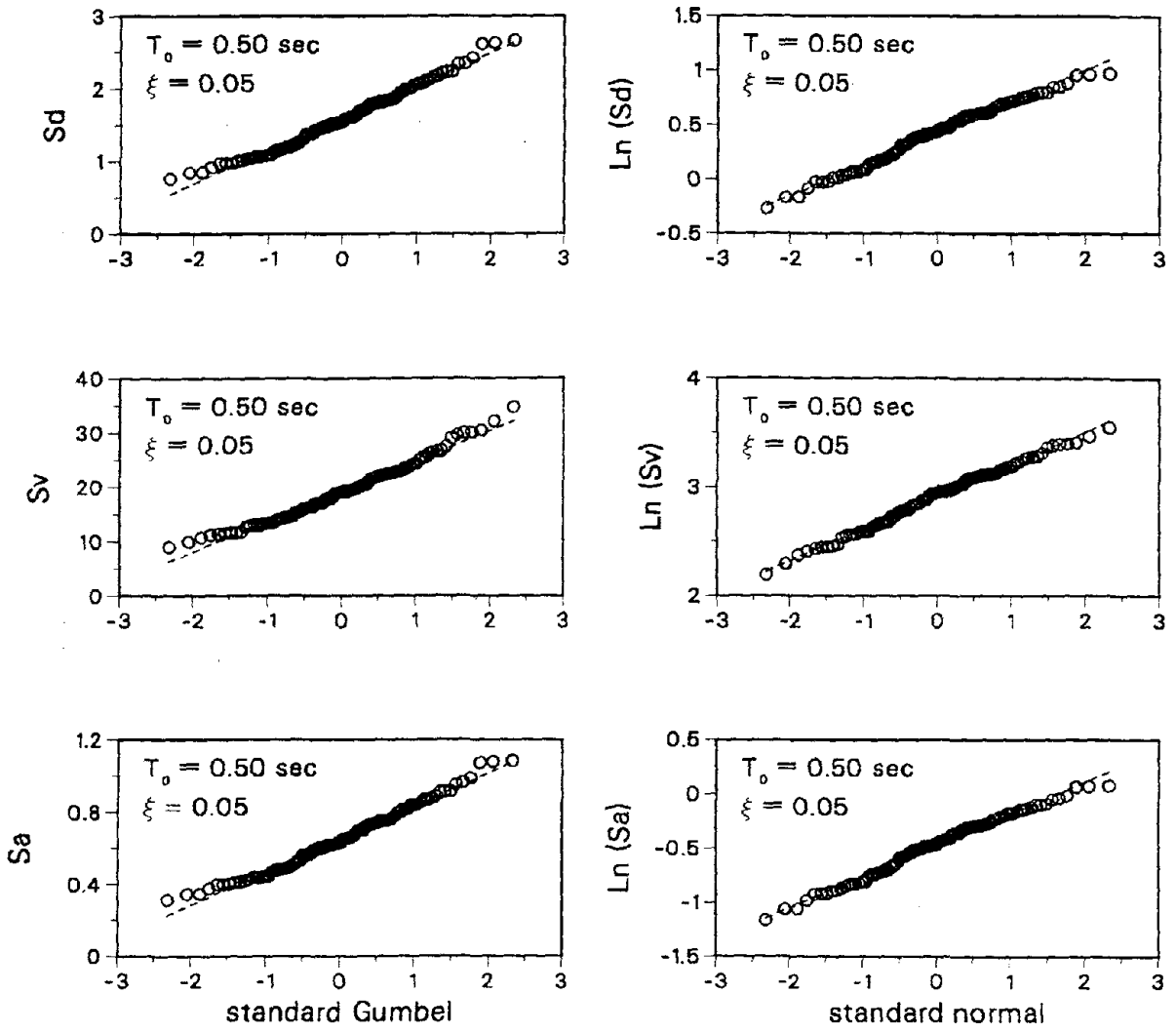

(a) Gumbel Type I

(b) Lognormal

Fig. 7.5 Probability Model Fit of the Peak Elastic Responses Simulated from the ARMA(2,1) Model of El Centro 1940

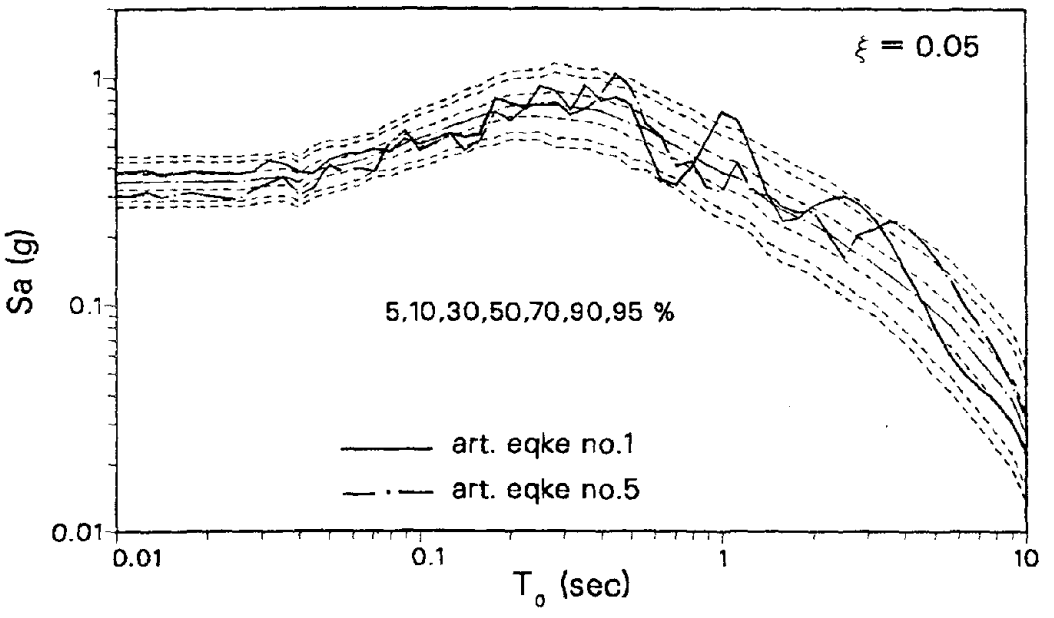

Fig. 7.6 Risk-Inconsistence of Elastic Response Spectra Derived From Single Earthquake Realizations

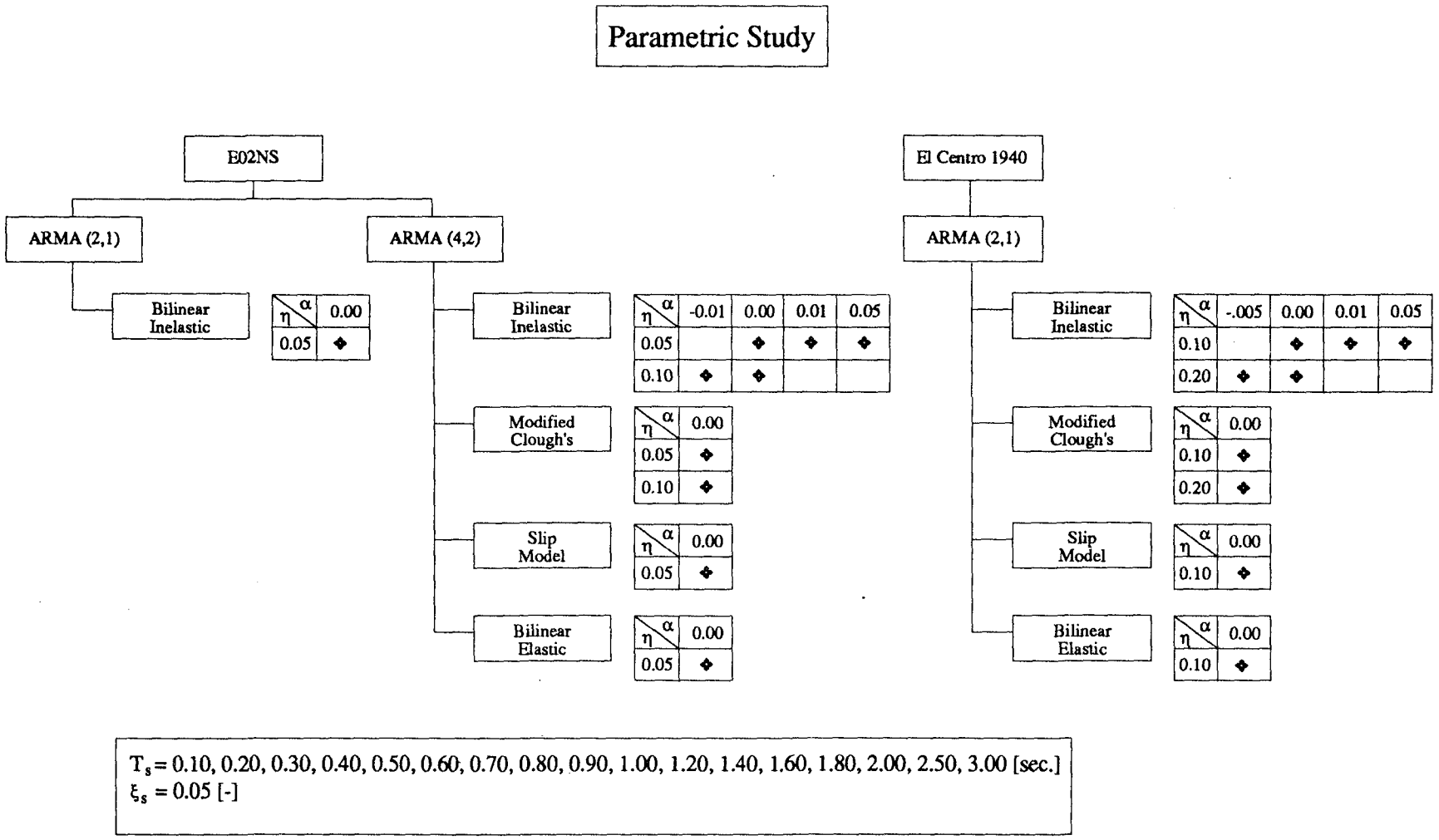

Fig. 8.1 Flow Chart of Parametric Study

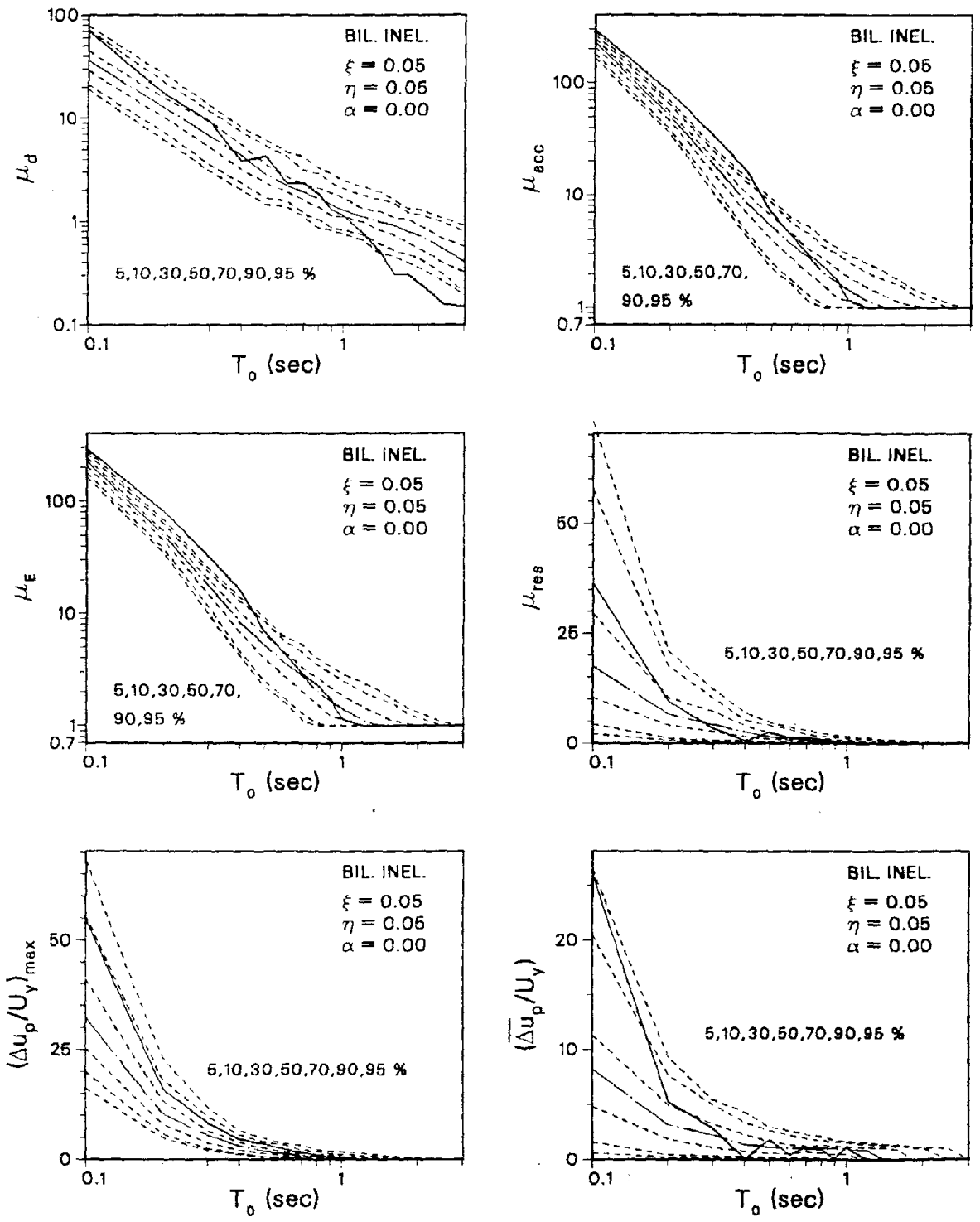

Fig. 8.2 Probabilistic Inelastic Response Spectra for the E02NS Target Record (ARMA(2,1) Earthquake Model and Bilinear Inelastic Structural Model)

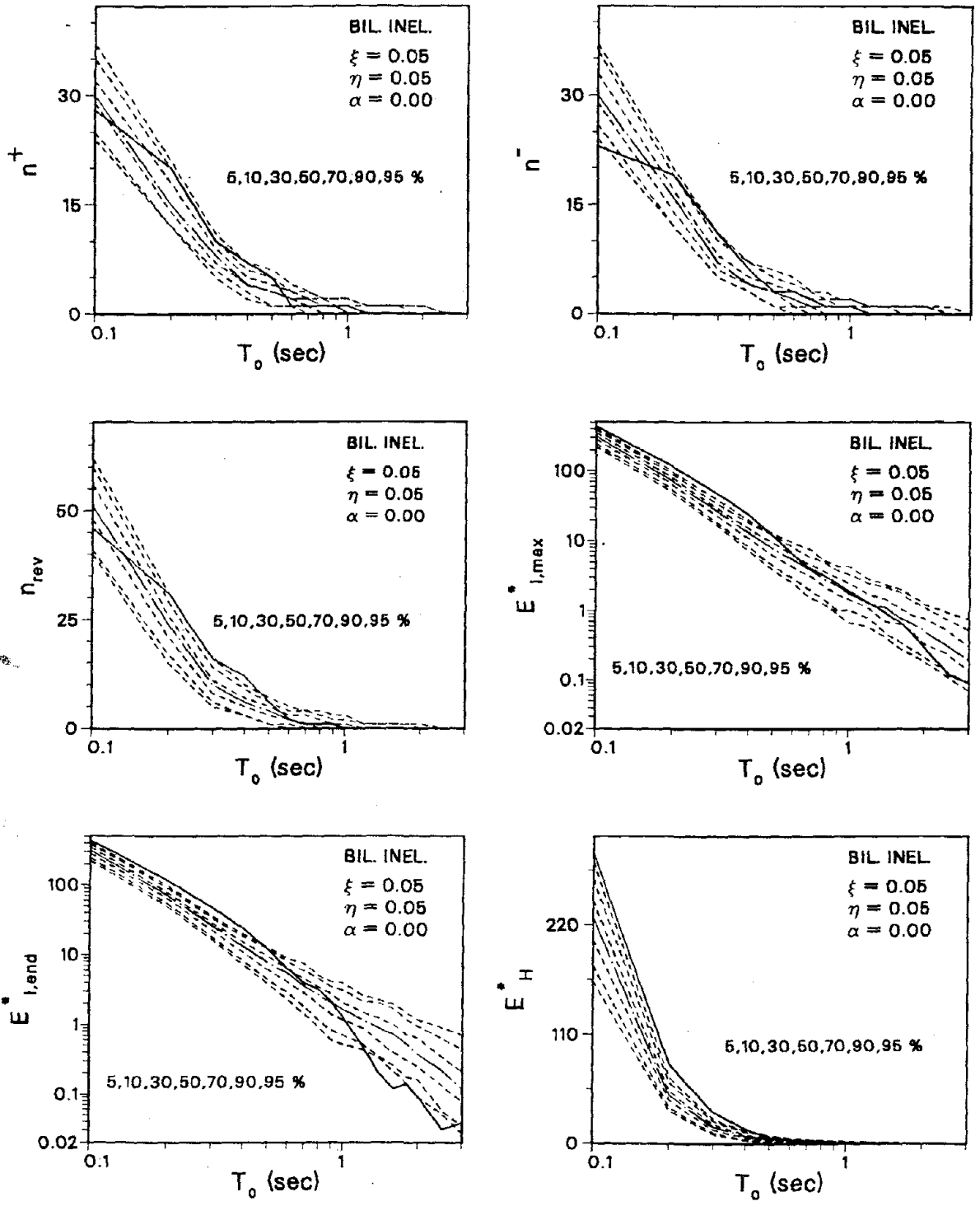

Fig. 8.2 (continued)

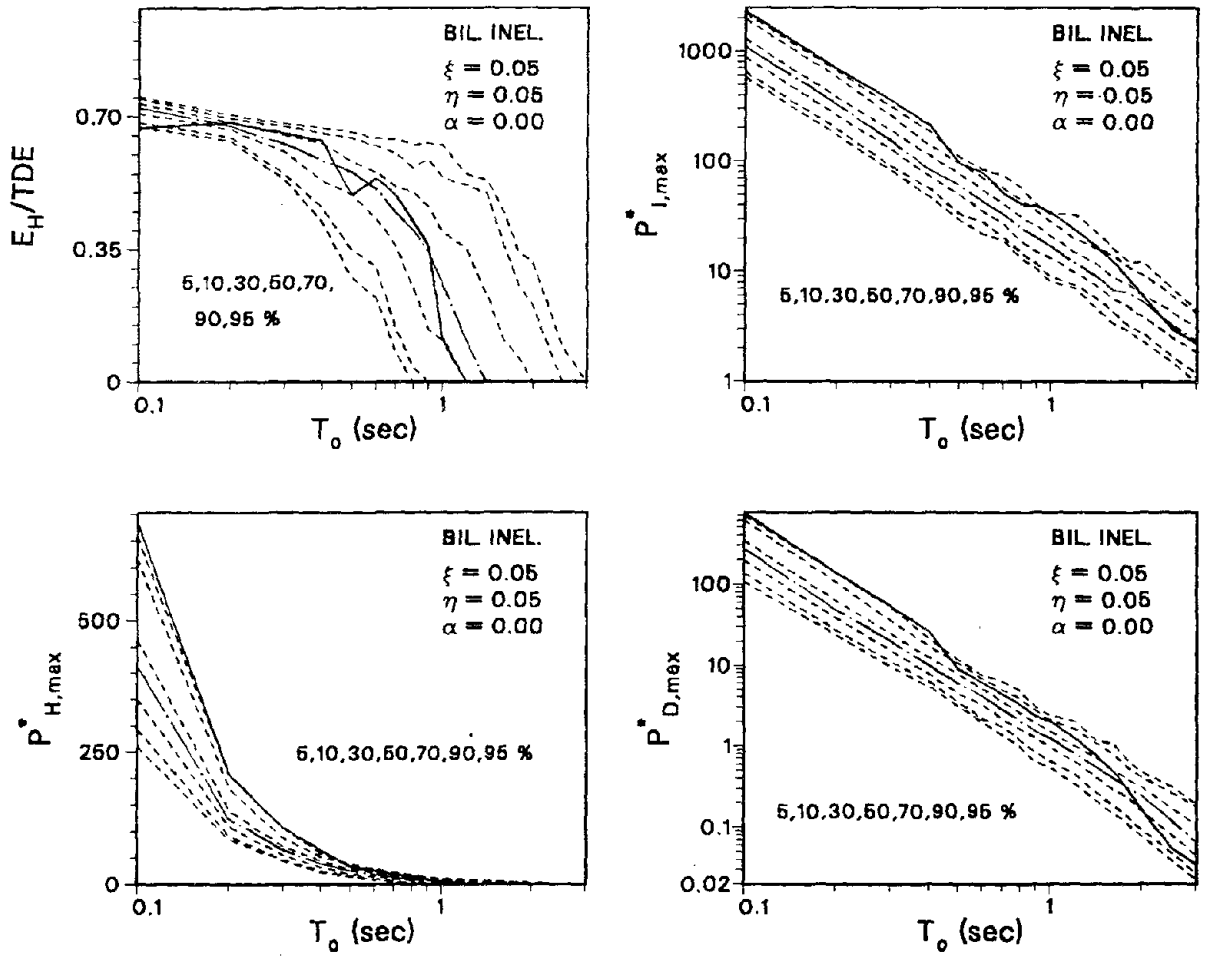

Fig. 8.2 (continued)

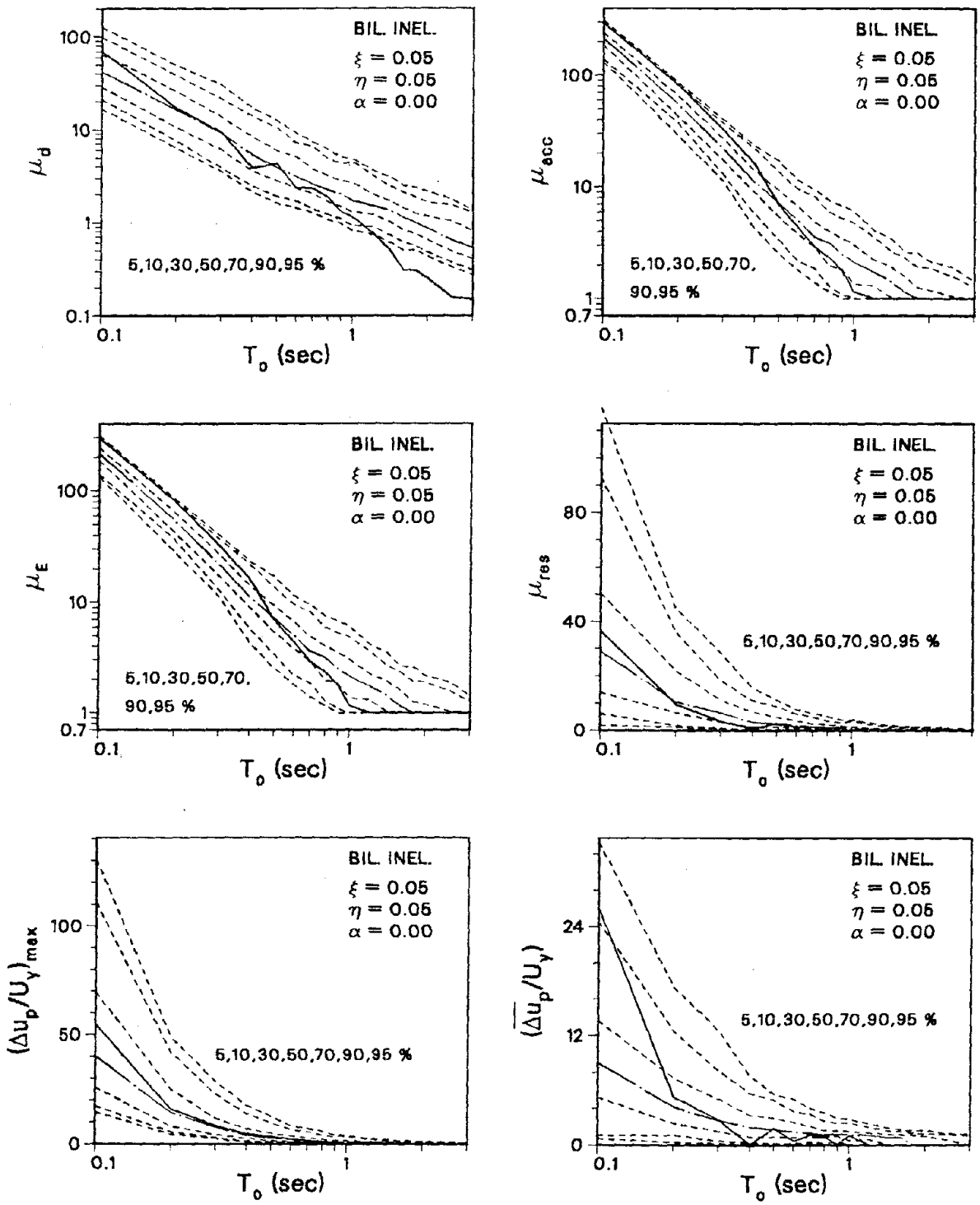

Fig. 8.3 Probabilistic Inelastic Response Spectra for the E02NS Target Record (ARMA(4,2) Earthquake Model and Bilinear Inelastic Structural Model)

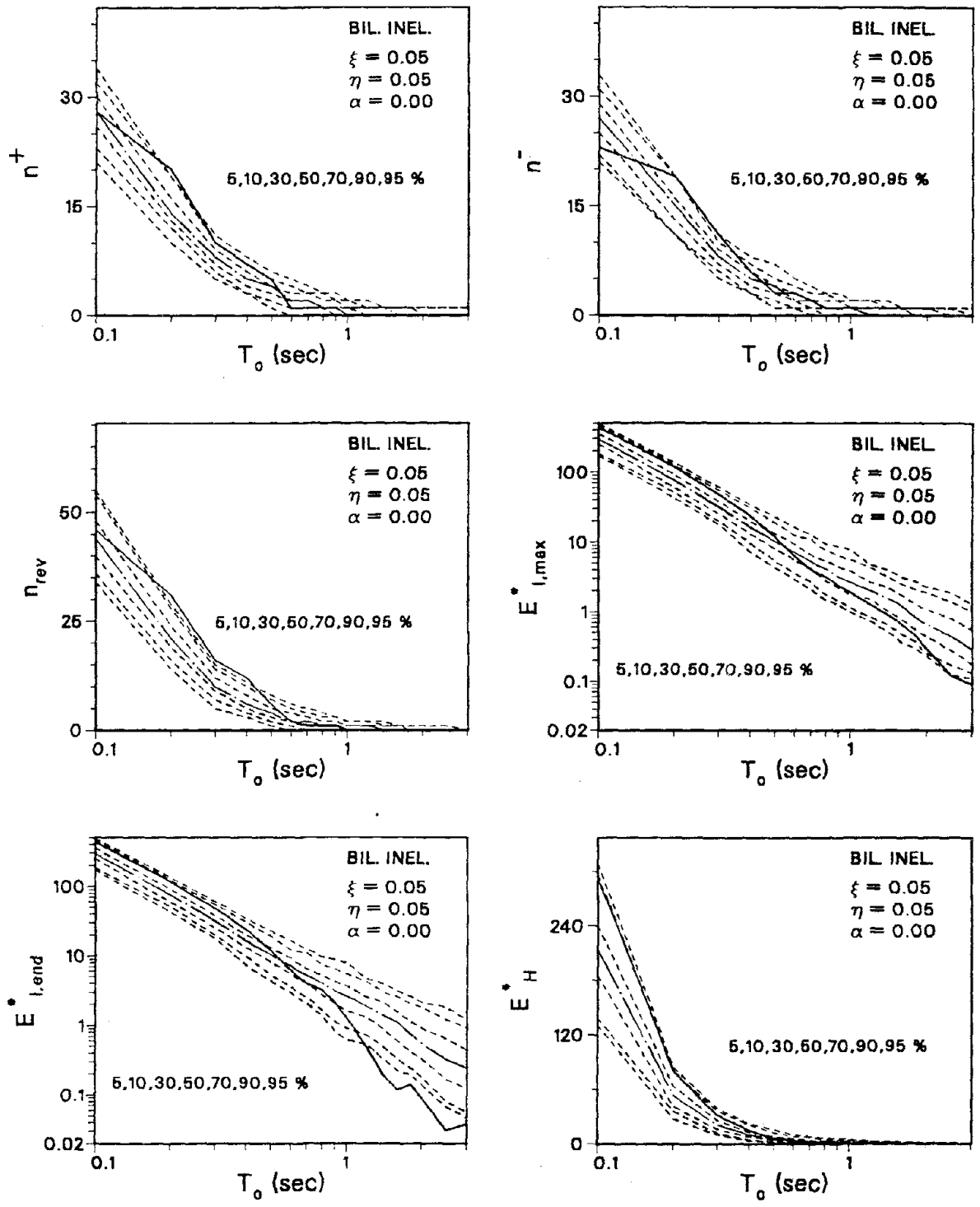

Fig. 8.3 (continued)

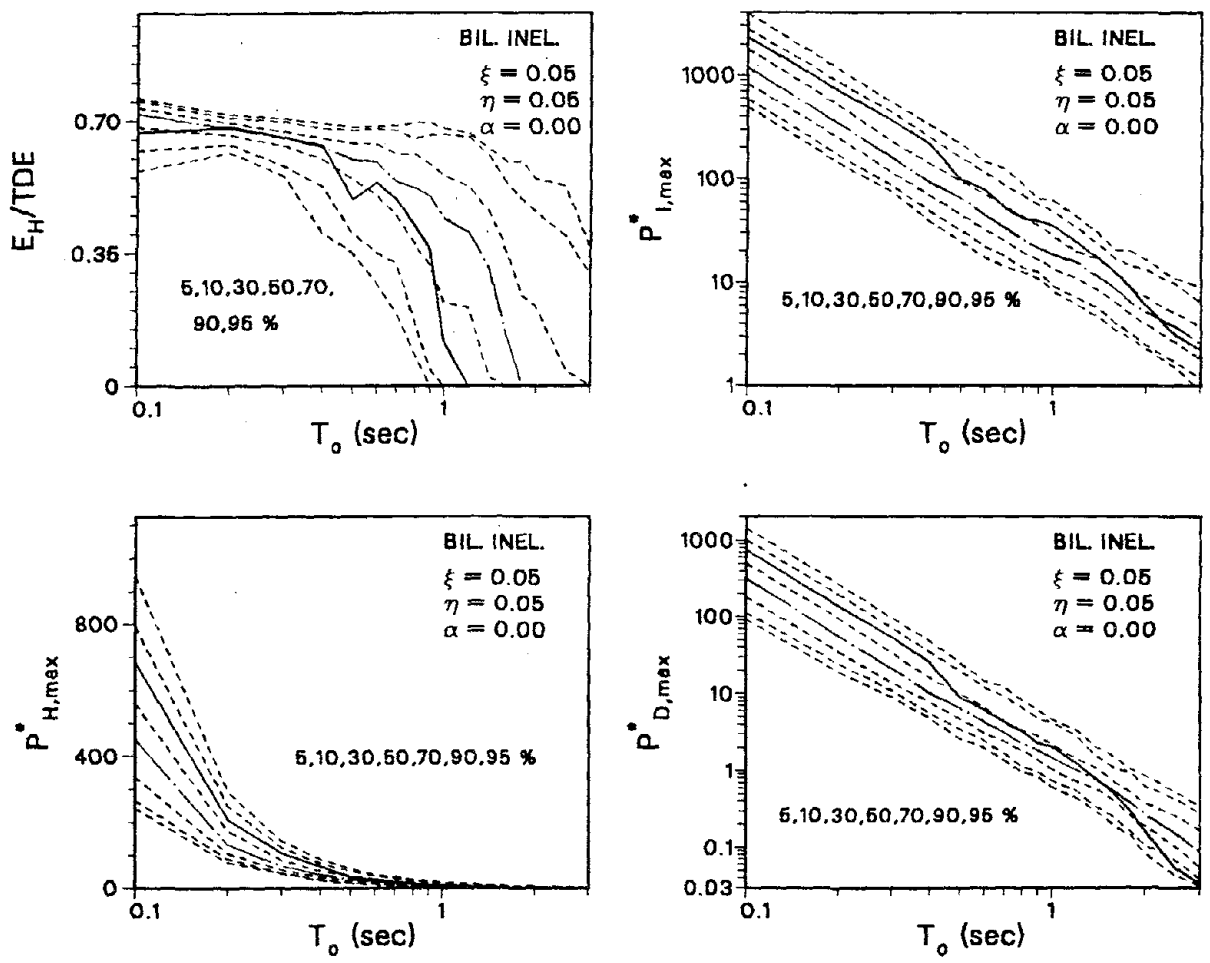

Fig. 8.3 (continued)

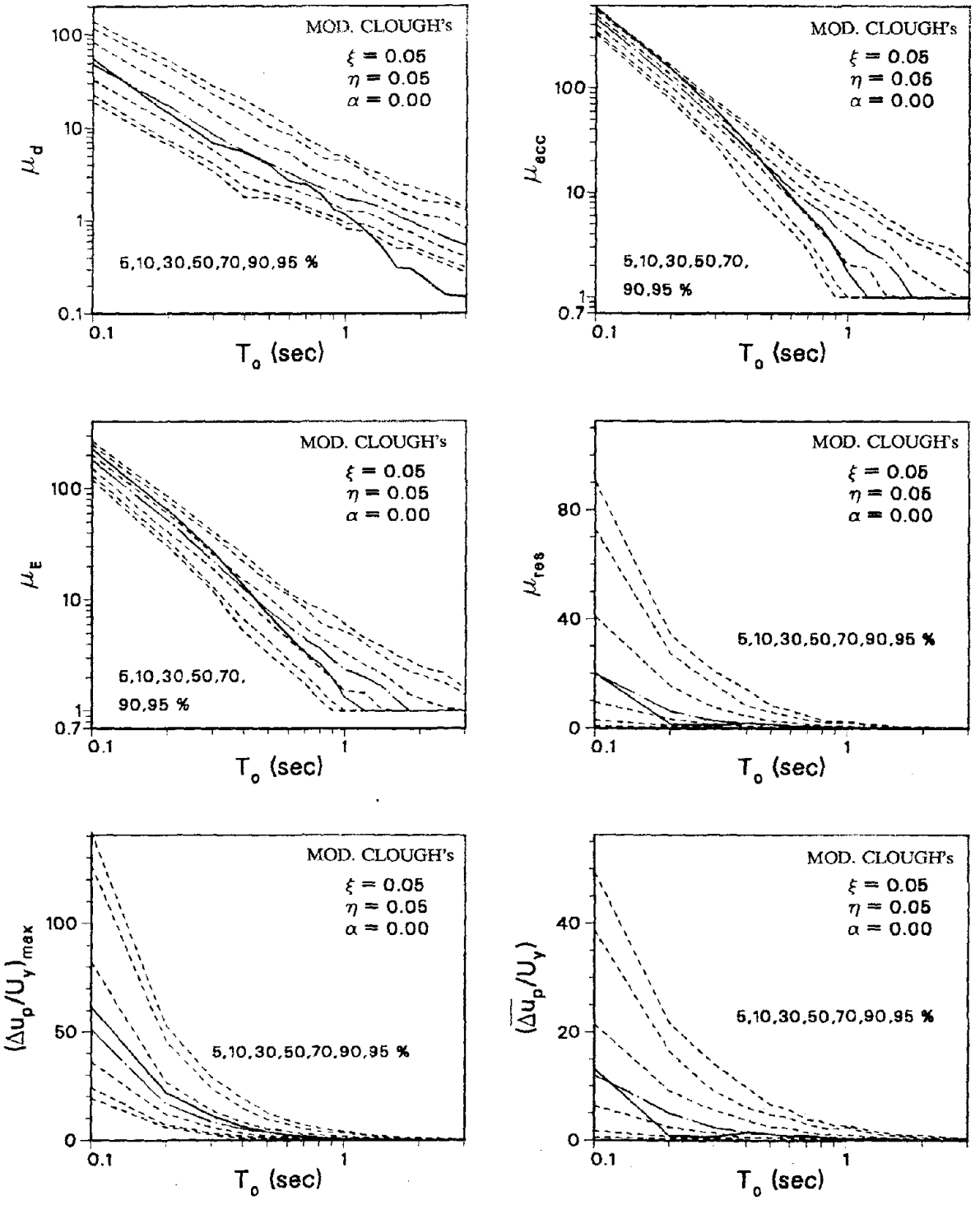

Fig. 8.4 Probabilistic Inelastic Response Spectra for the E02NS Target Record (ARMA(4,2) Earthquake Model and Modified Clough's Structural Model)

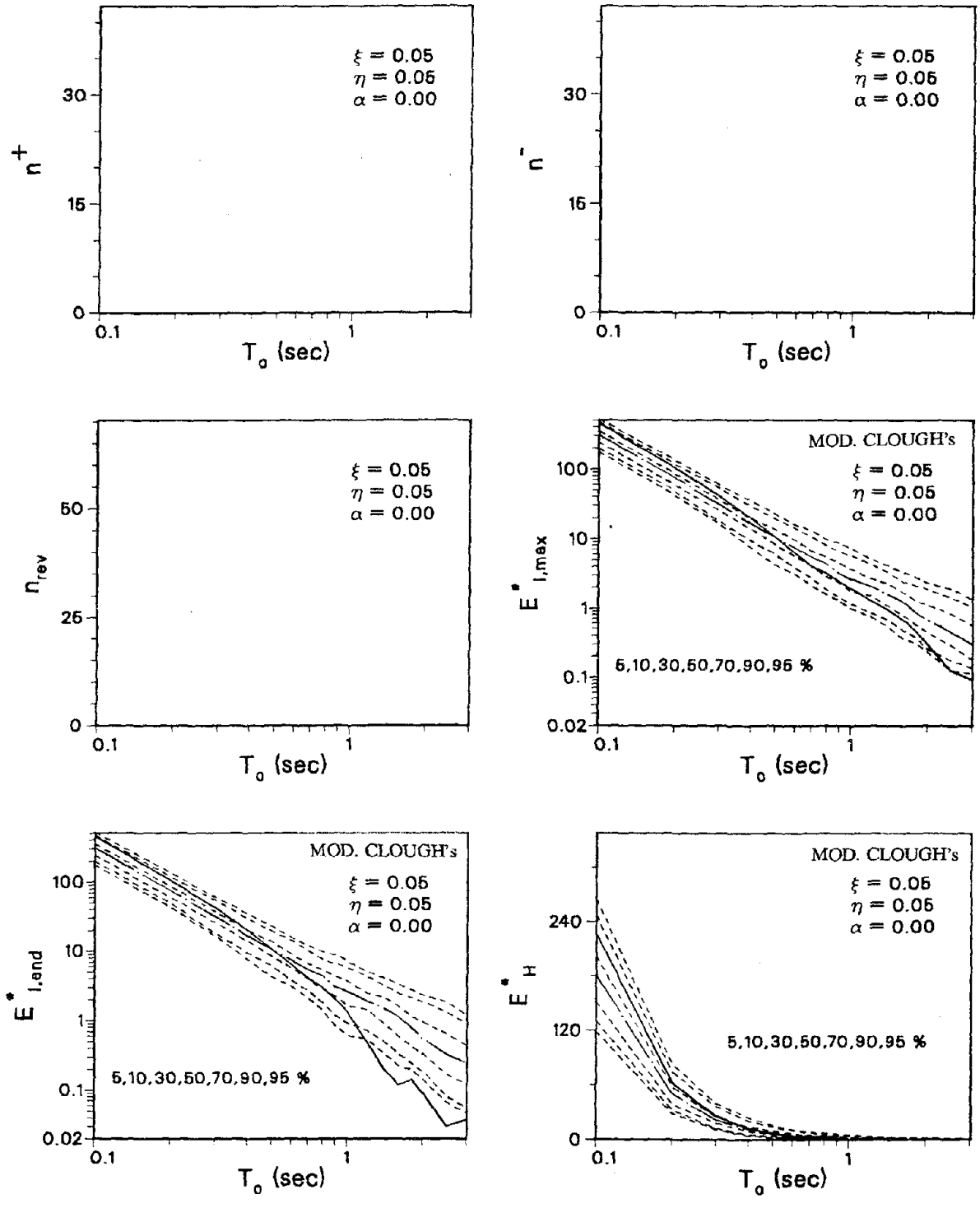

Fig. 8.4 (continued)

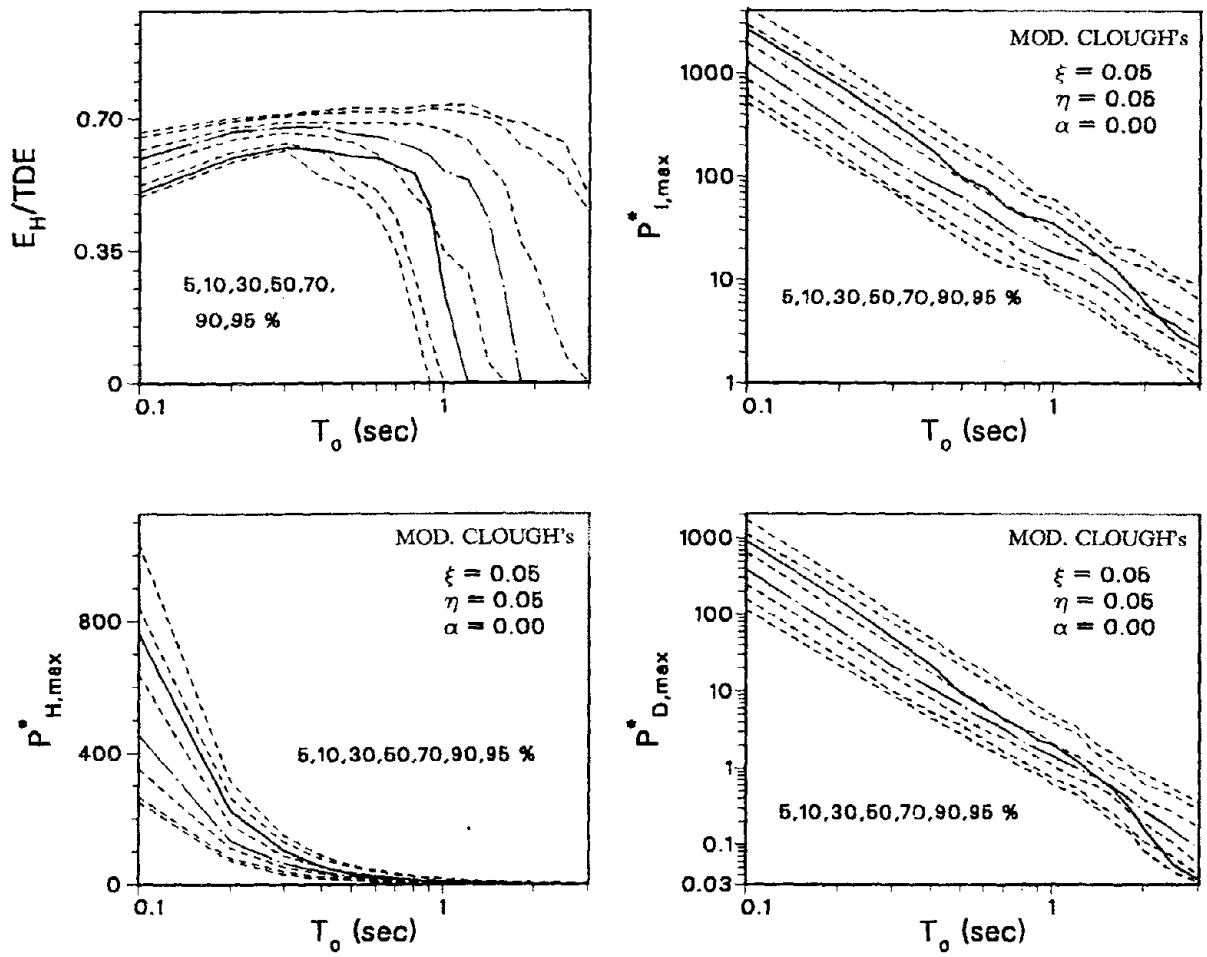

Fig. 8.4 (continued)

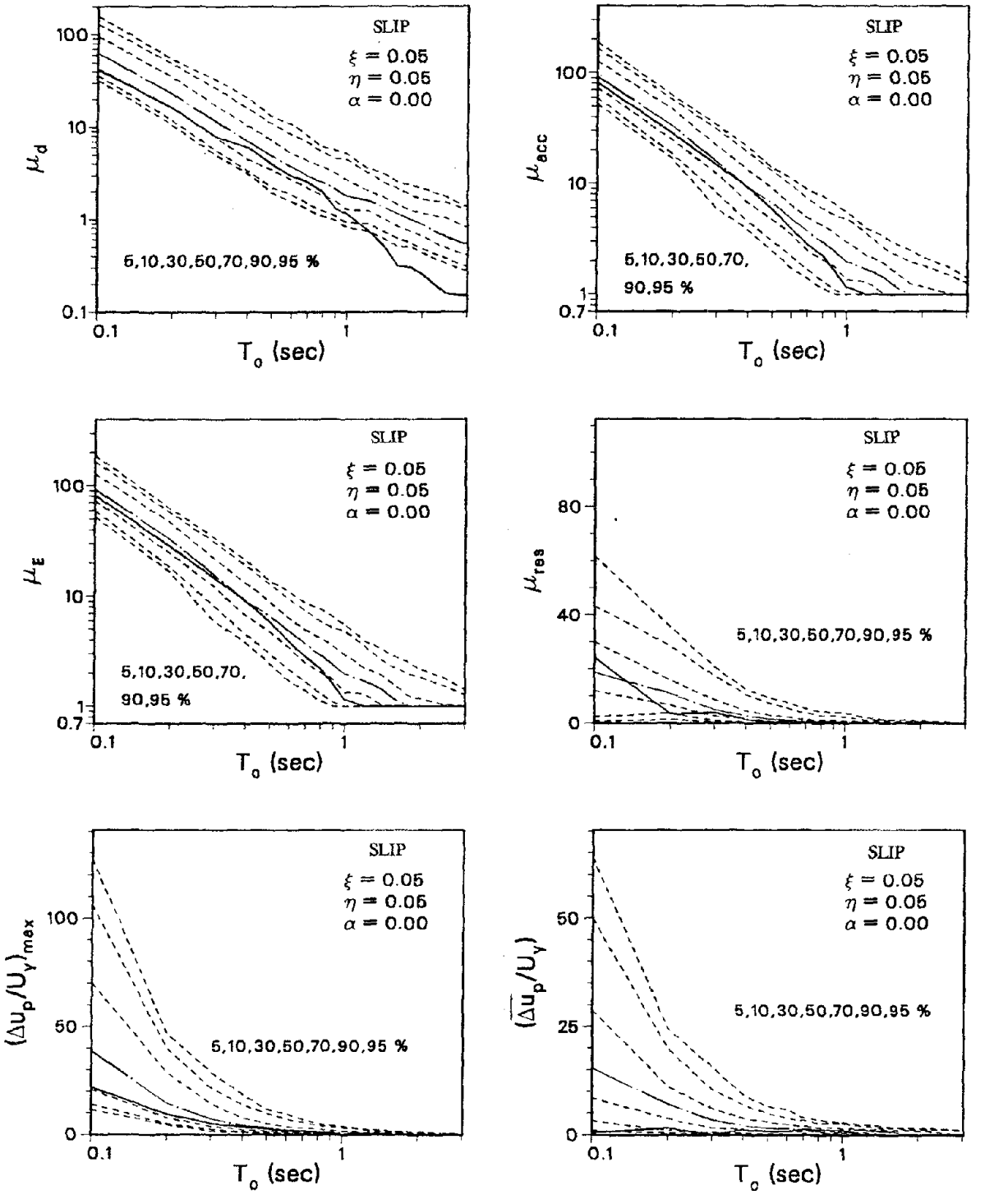

Fig. 8.5 Probabilistic Inelastic Response Spectra for the E02NS Target Record (ARMA(4,2) Earthquake Model and Slip Structural Model)

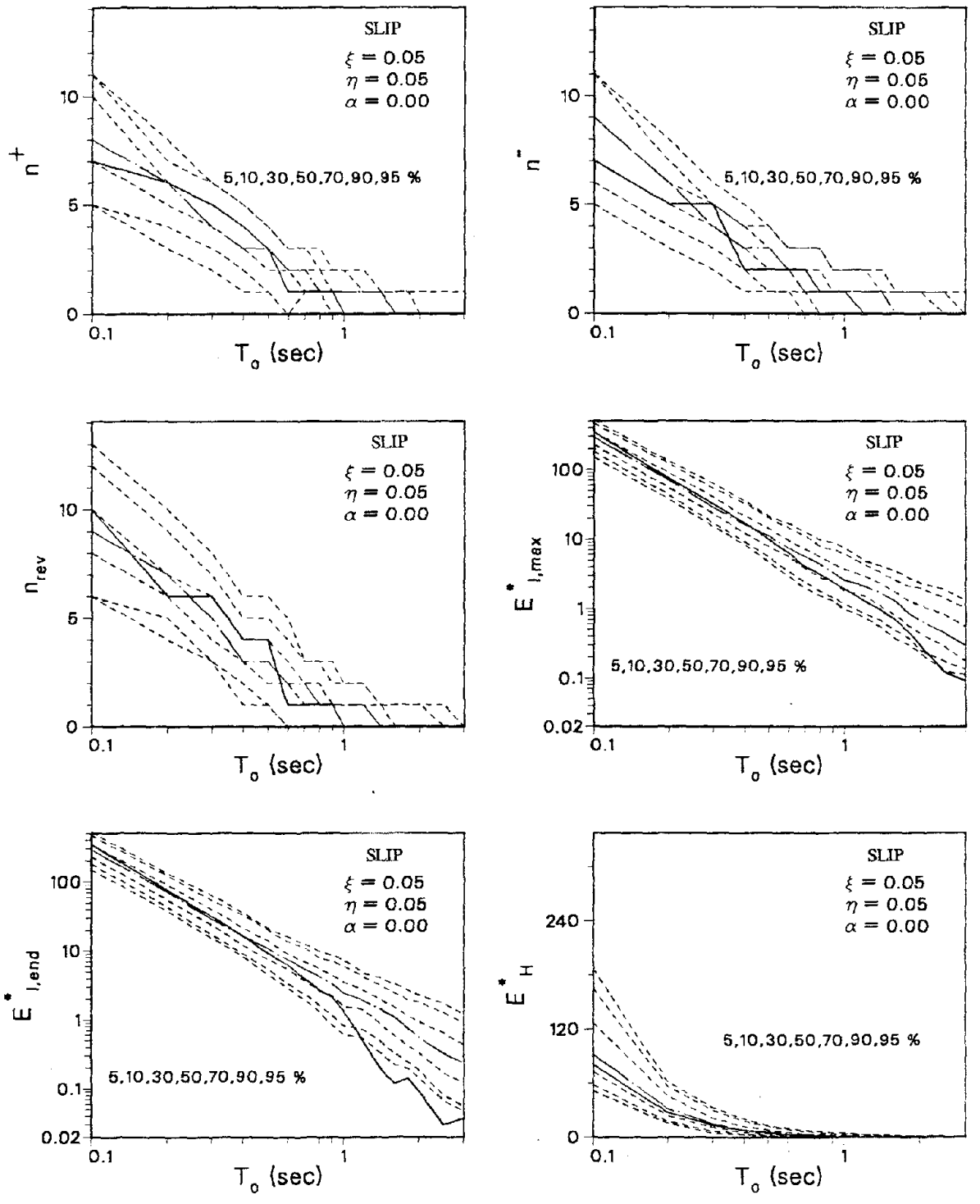

Fig. 8.5 (continued)

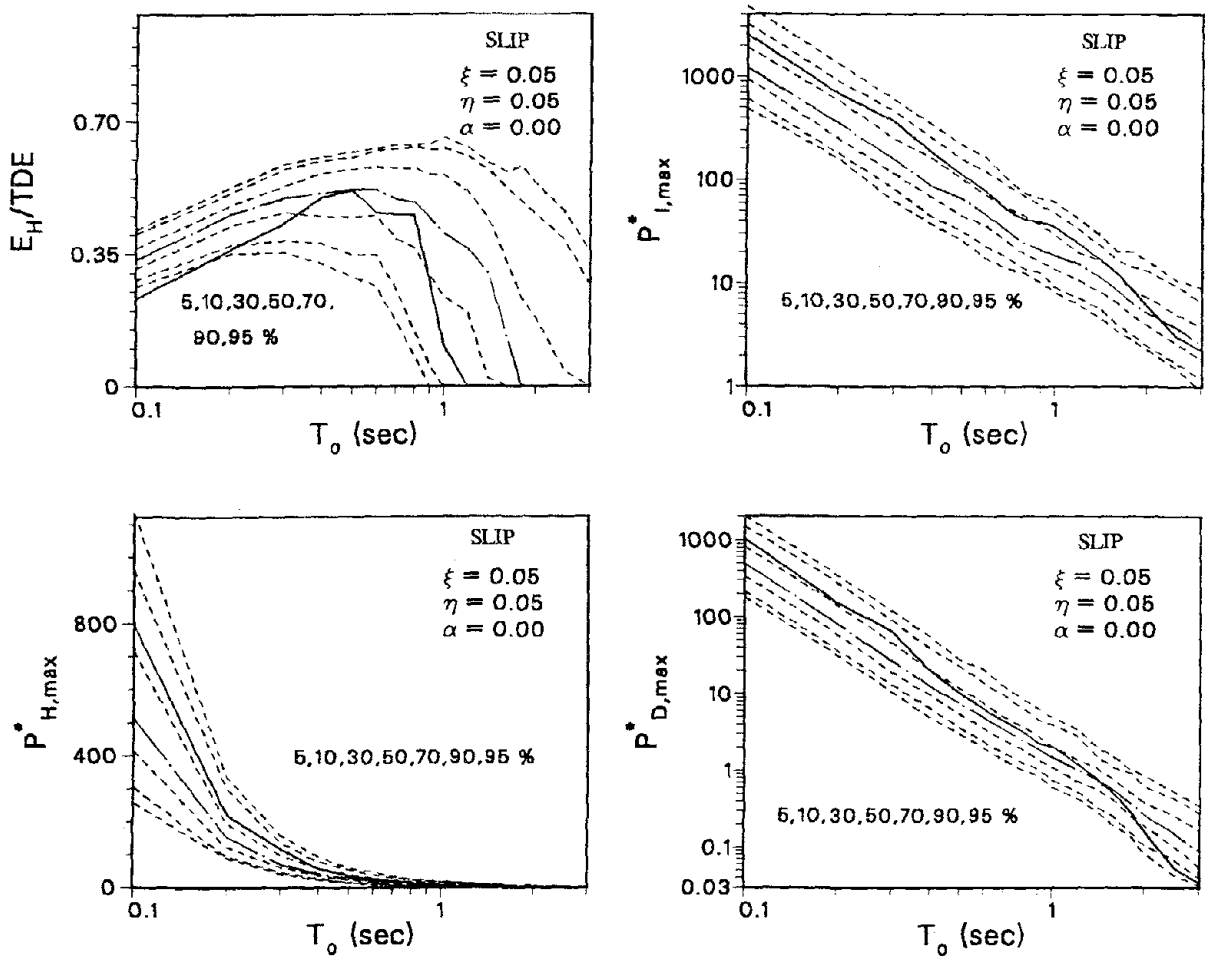

Fig. 8.5 (continued)

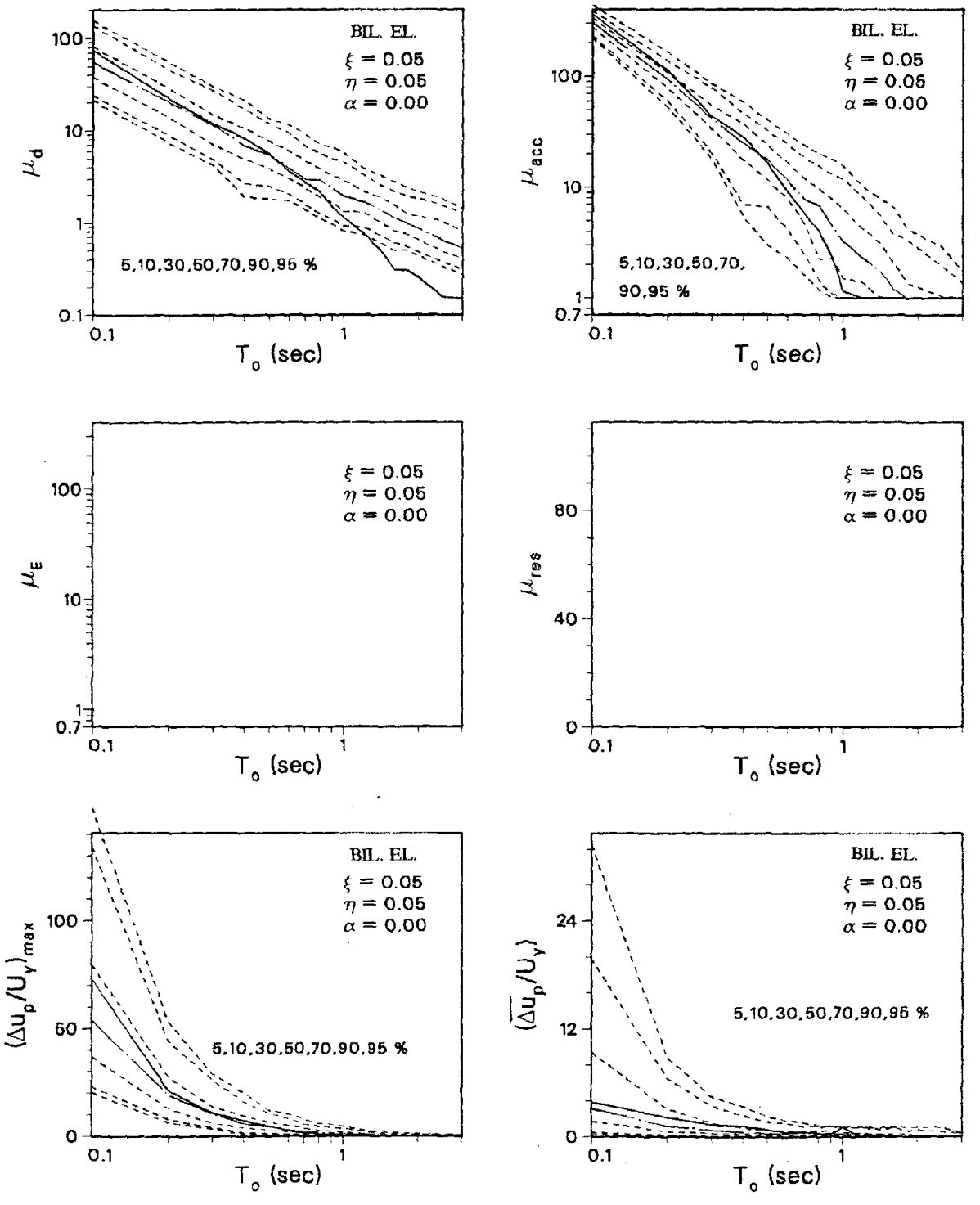

Fig. 8.6 Probabilistic Inelastic Response Spectra for the E02NS Target Record (ARMA(4,2) Earthquake Model and Bilinear Elastic Structural Model)

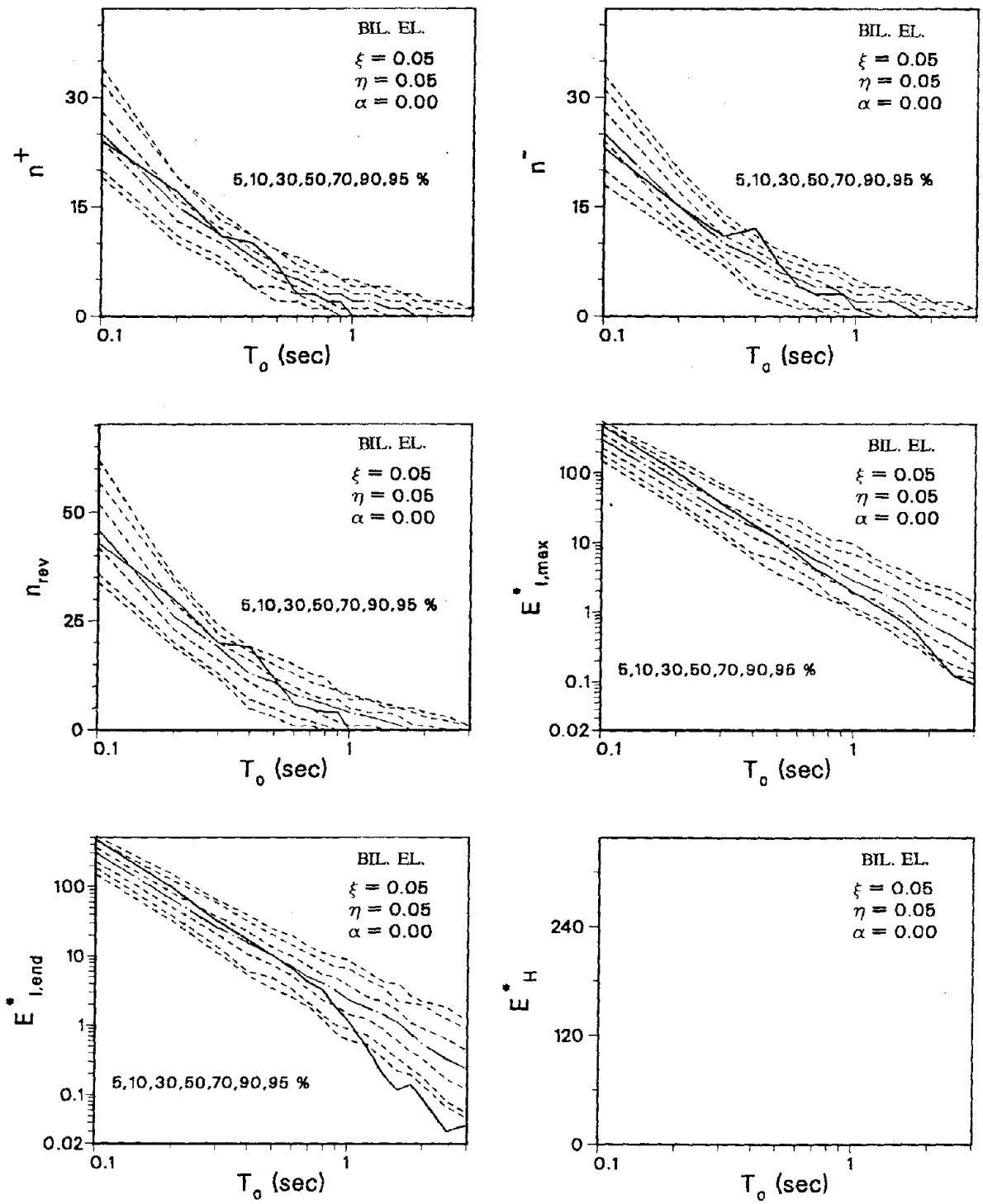

Fig. 8.6 (continued)

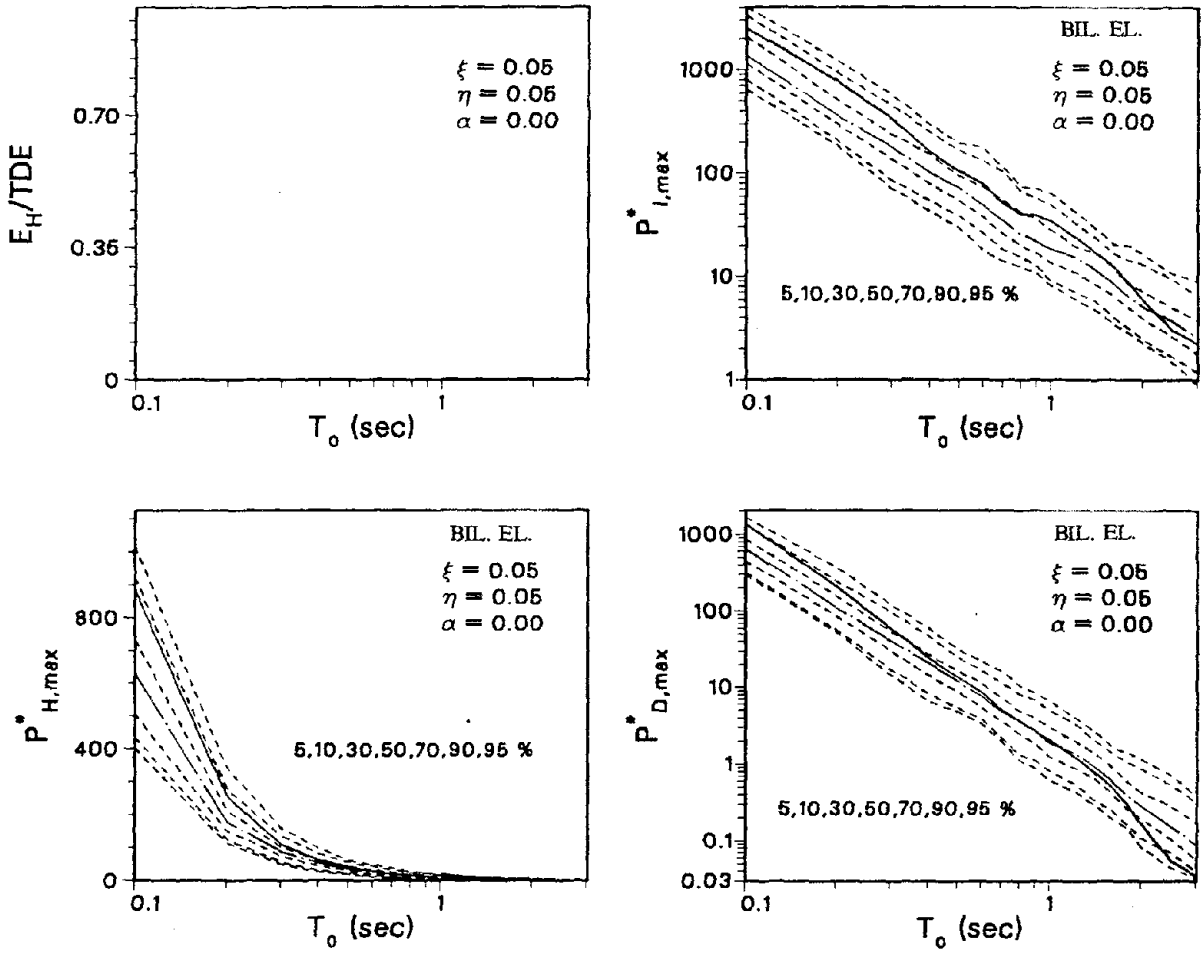

Fig. 8.6 (continued)

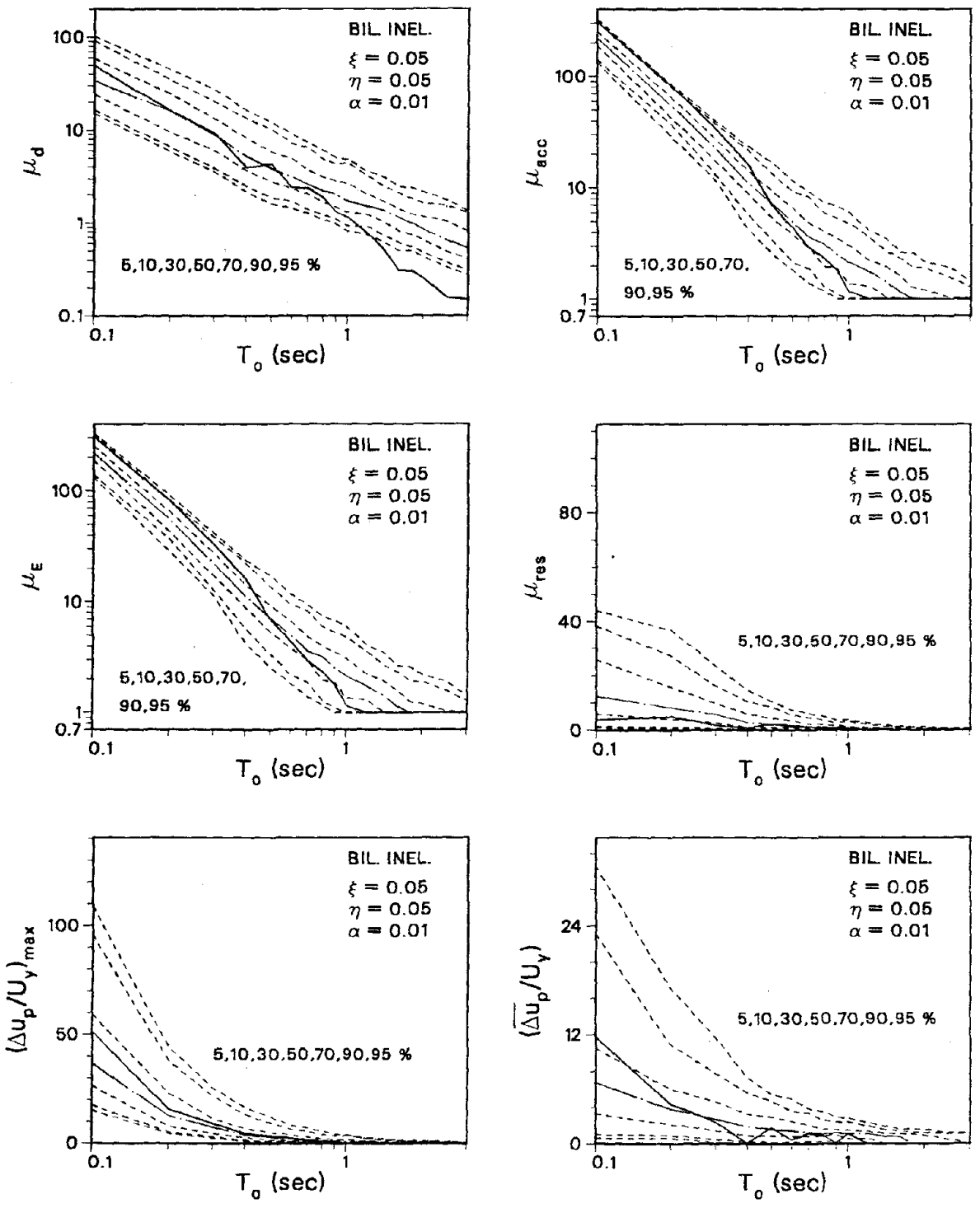

Fig. 8.7 Probabilistic Inelastic Response Spectra for the E02NS Target Record (ARMA(4,2) Earthquake Model and Bilinear Inelastic Structural Model)

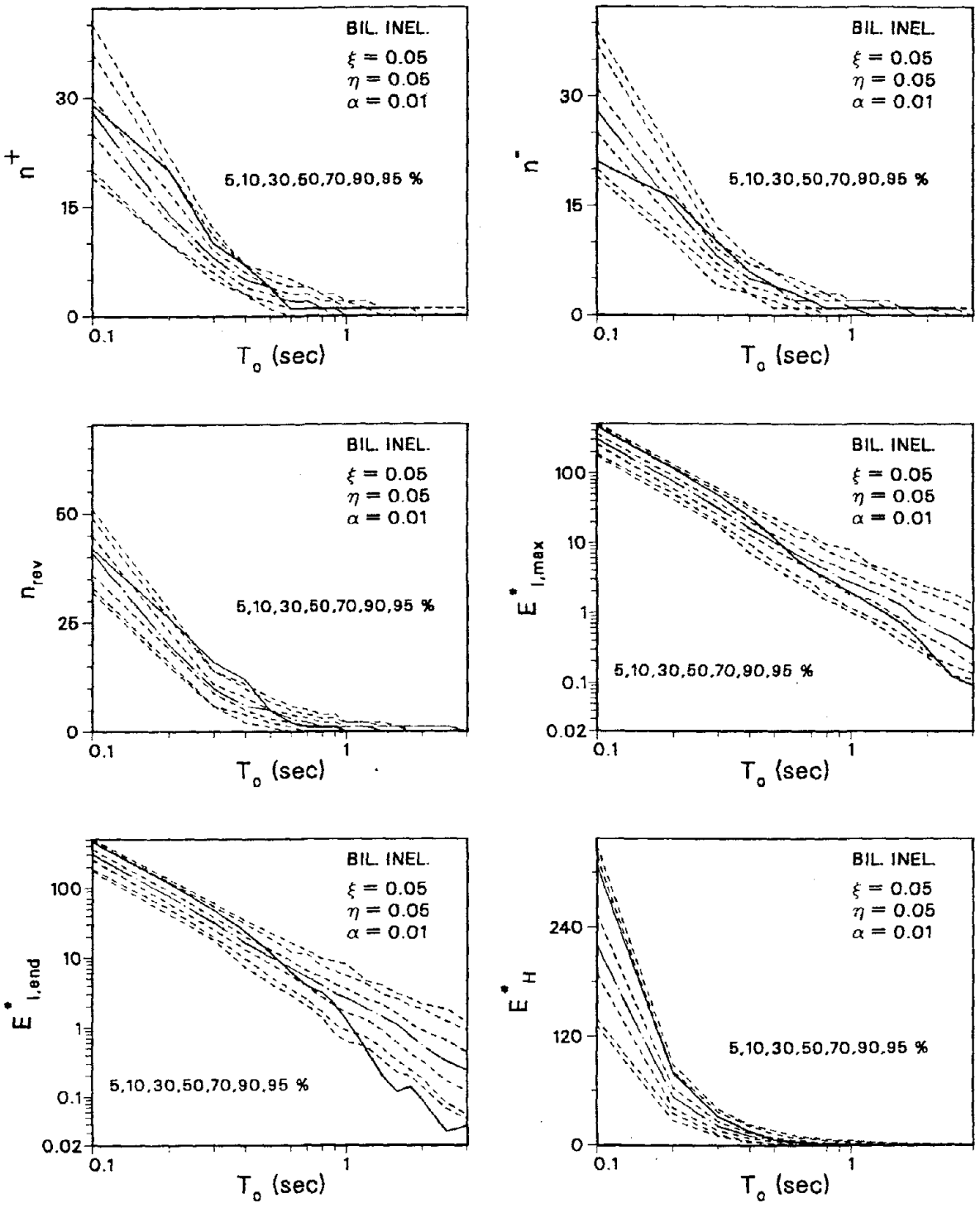

Fig. 8.7 (continued)

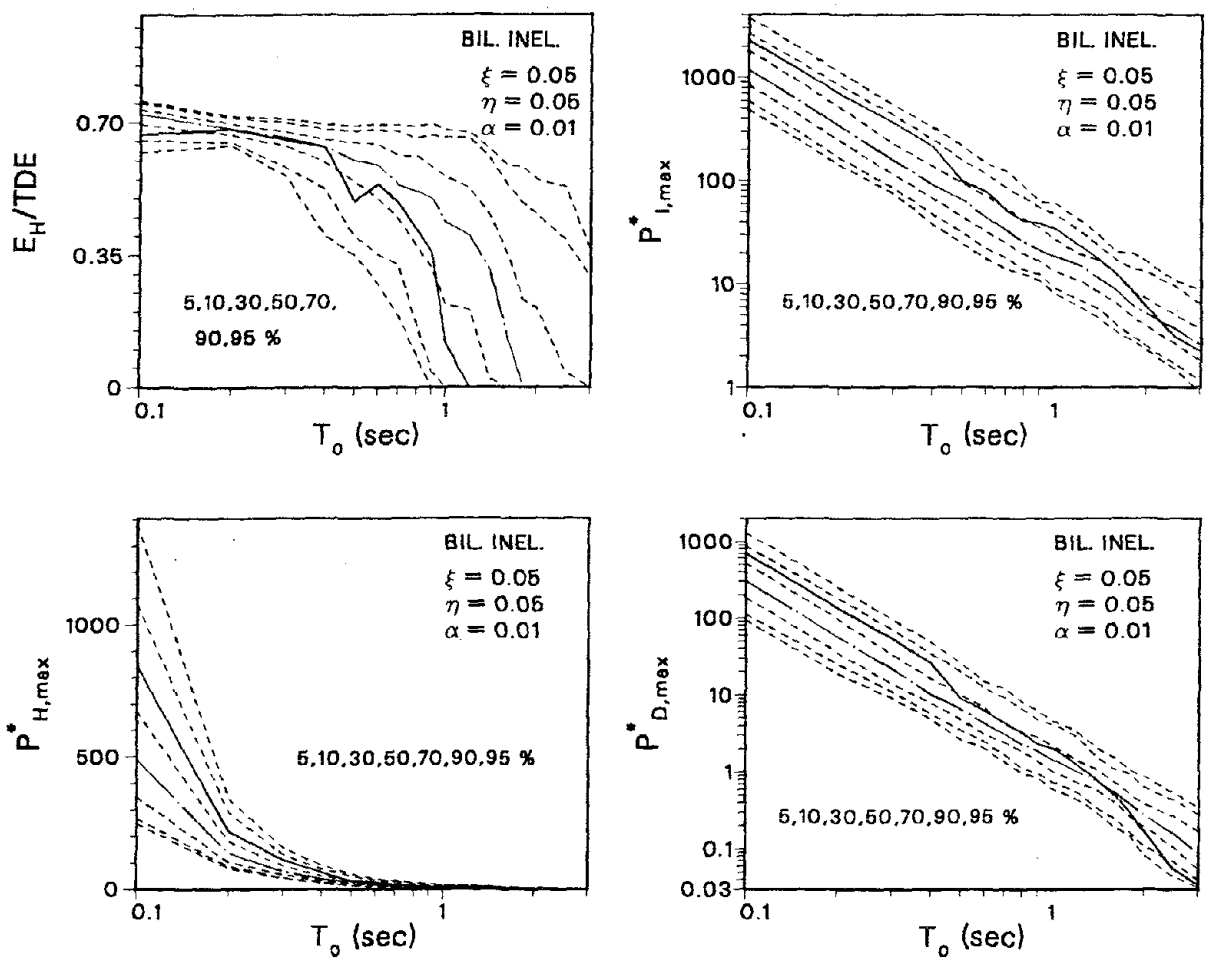

Fig. 8.7 (continued)

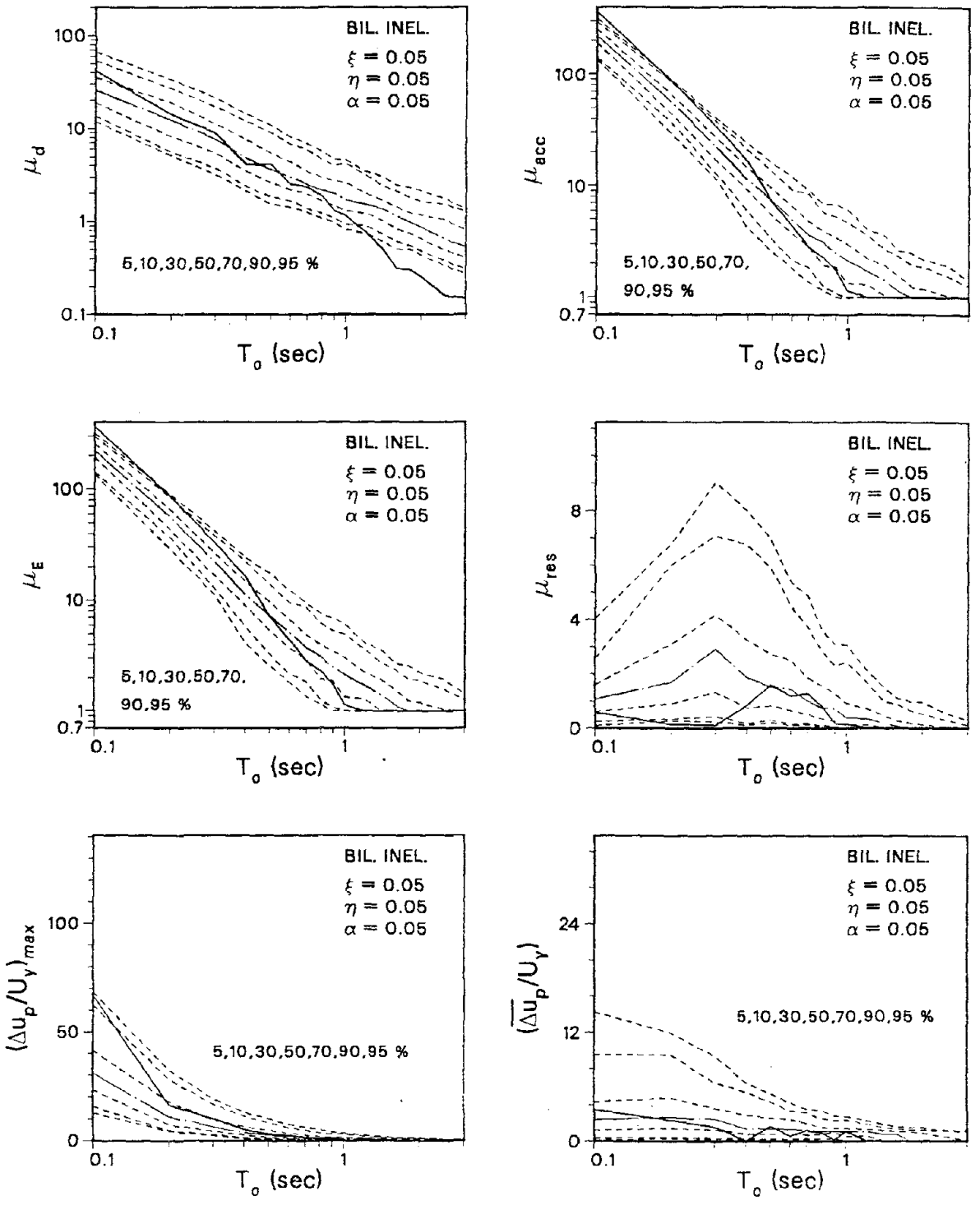

Fig. 8.8 Probabilistic Inelastic Response Spectra for the E02NS Target Record (ARMA(4,2) Earthquake Model and Bilinear Inelastic Structural Model)

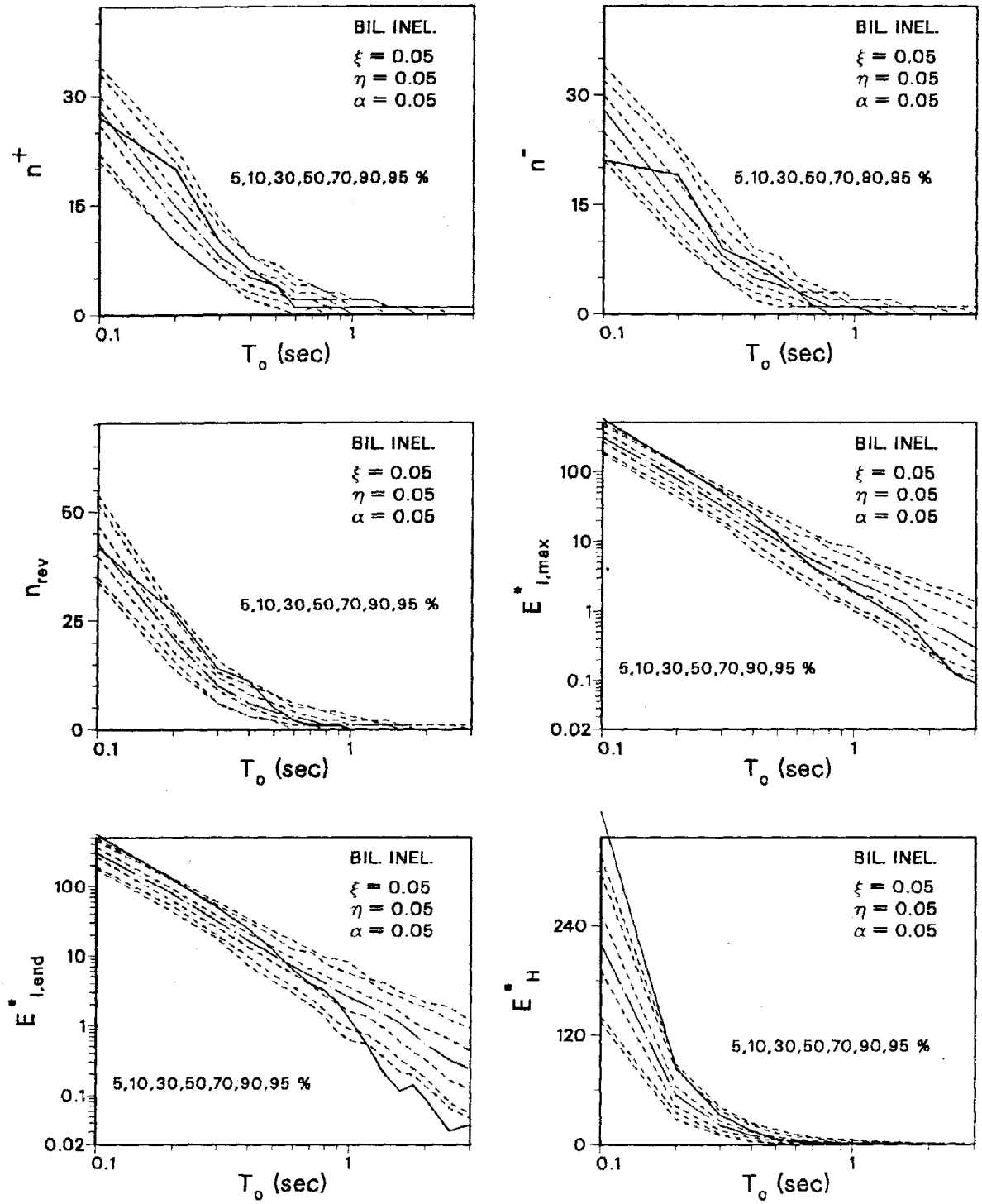

Fig. 8.8 (continued)

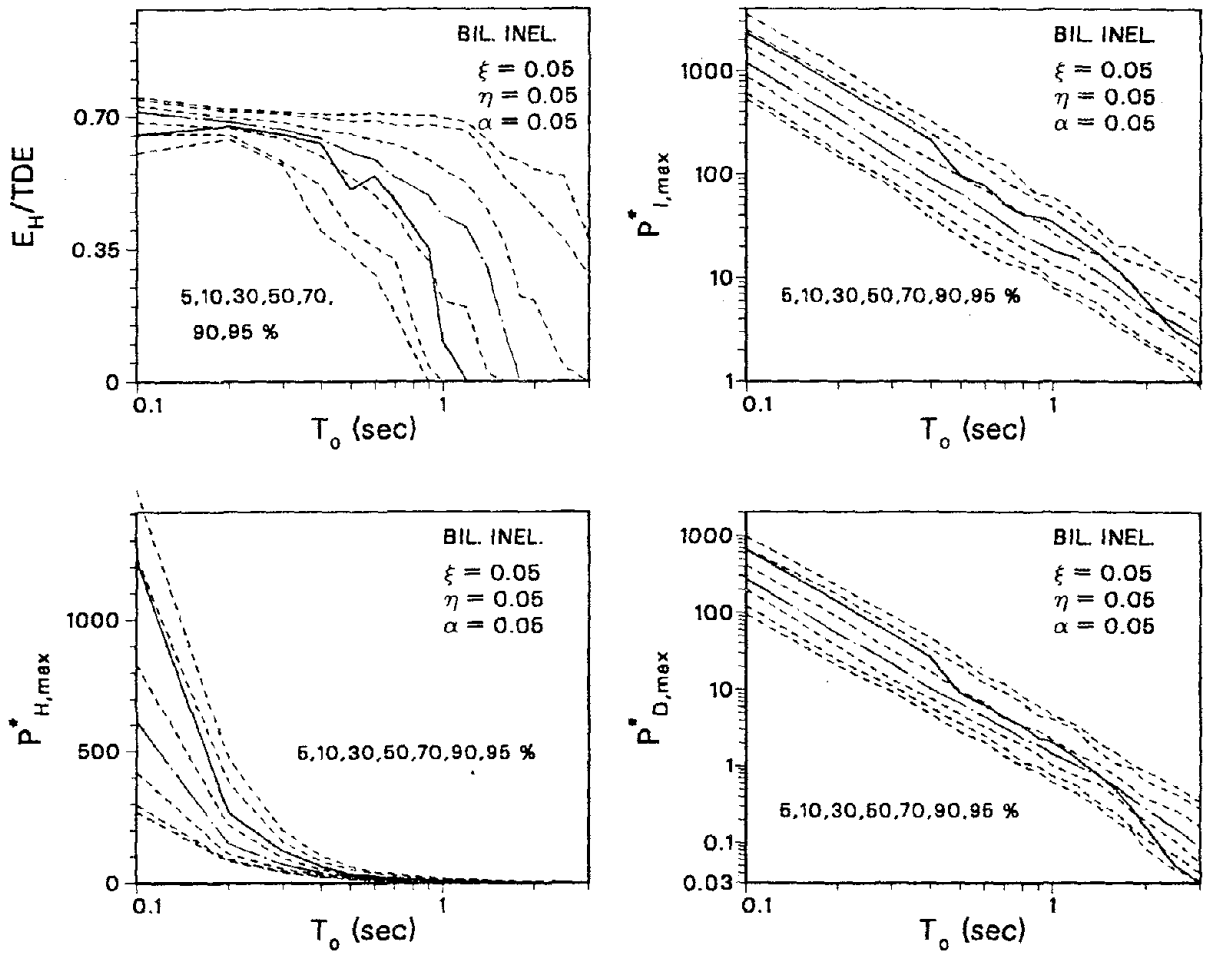

Fig. 8.8 (continued)

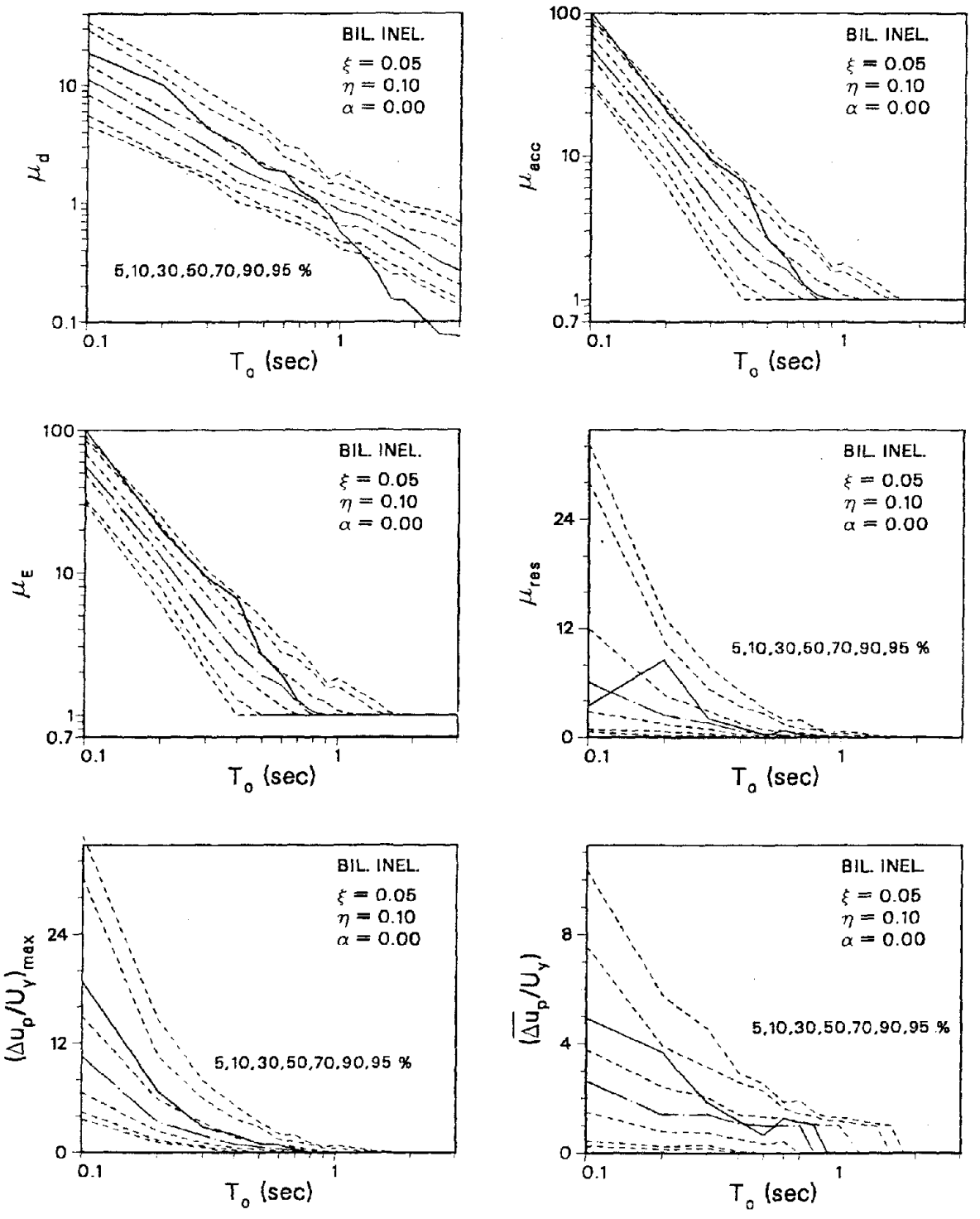

Fig. 8.9 Probabilistic Inelastic Response Spectra for the E02NS Target Record (ARMA(4,2) Earthquake Model and Bilinear Inelastic Structural Model)

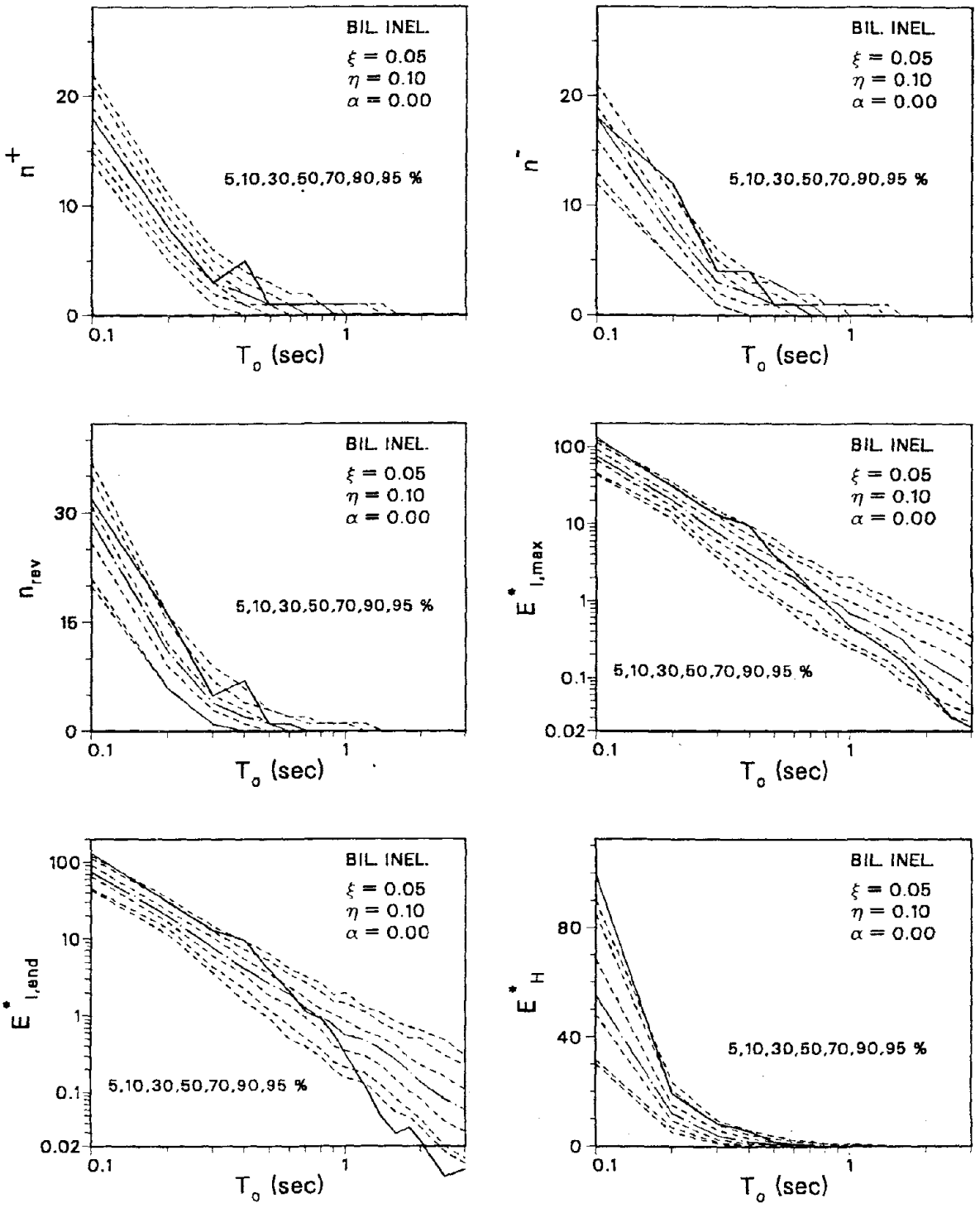

Fig. 8.9 (continued)

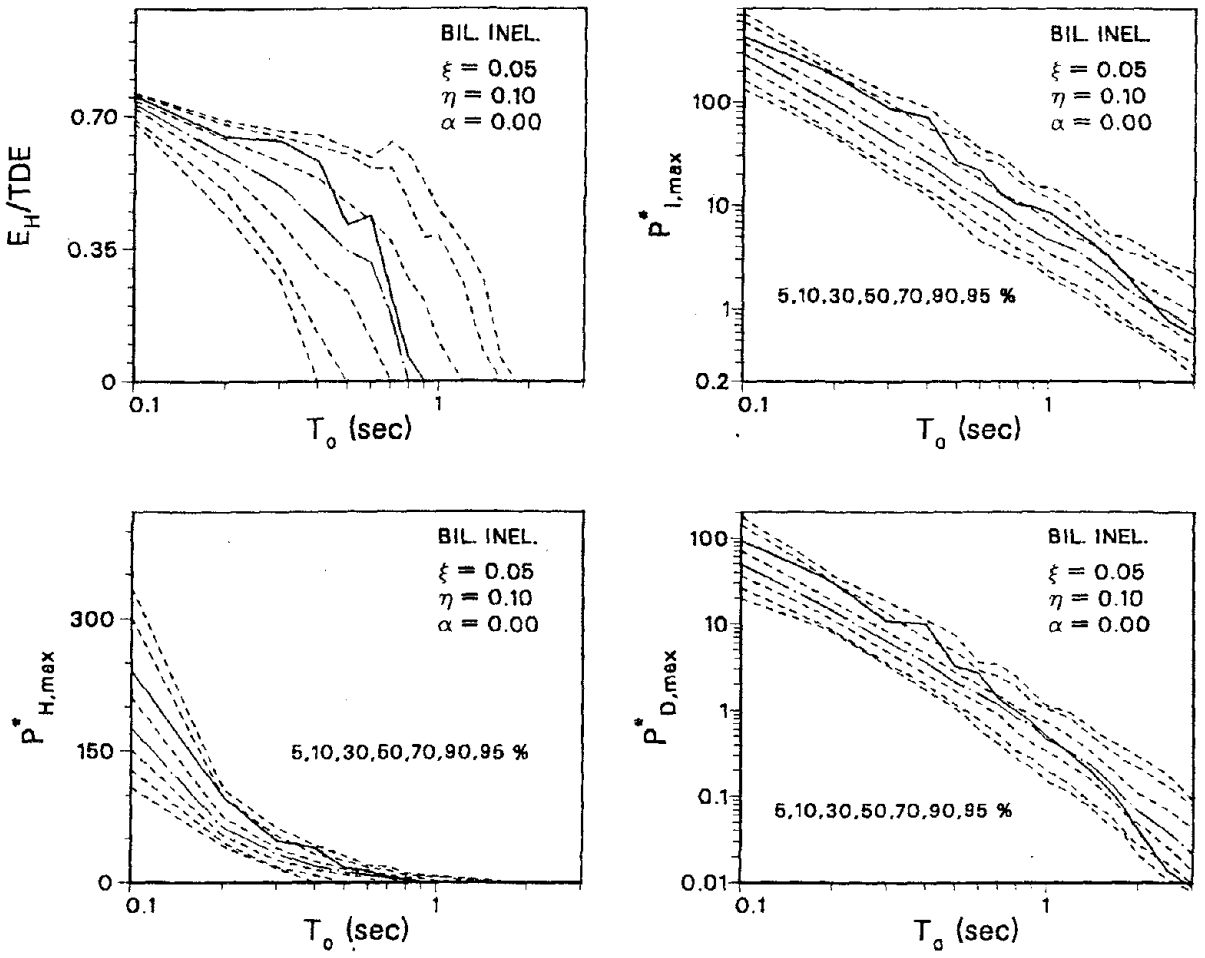

Fig. 8.9 (continued)

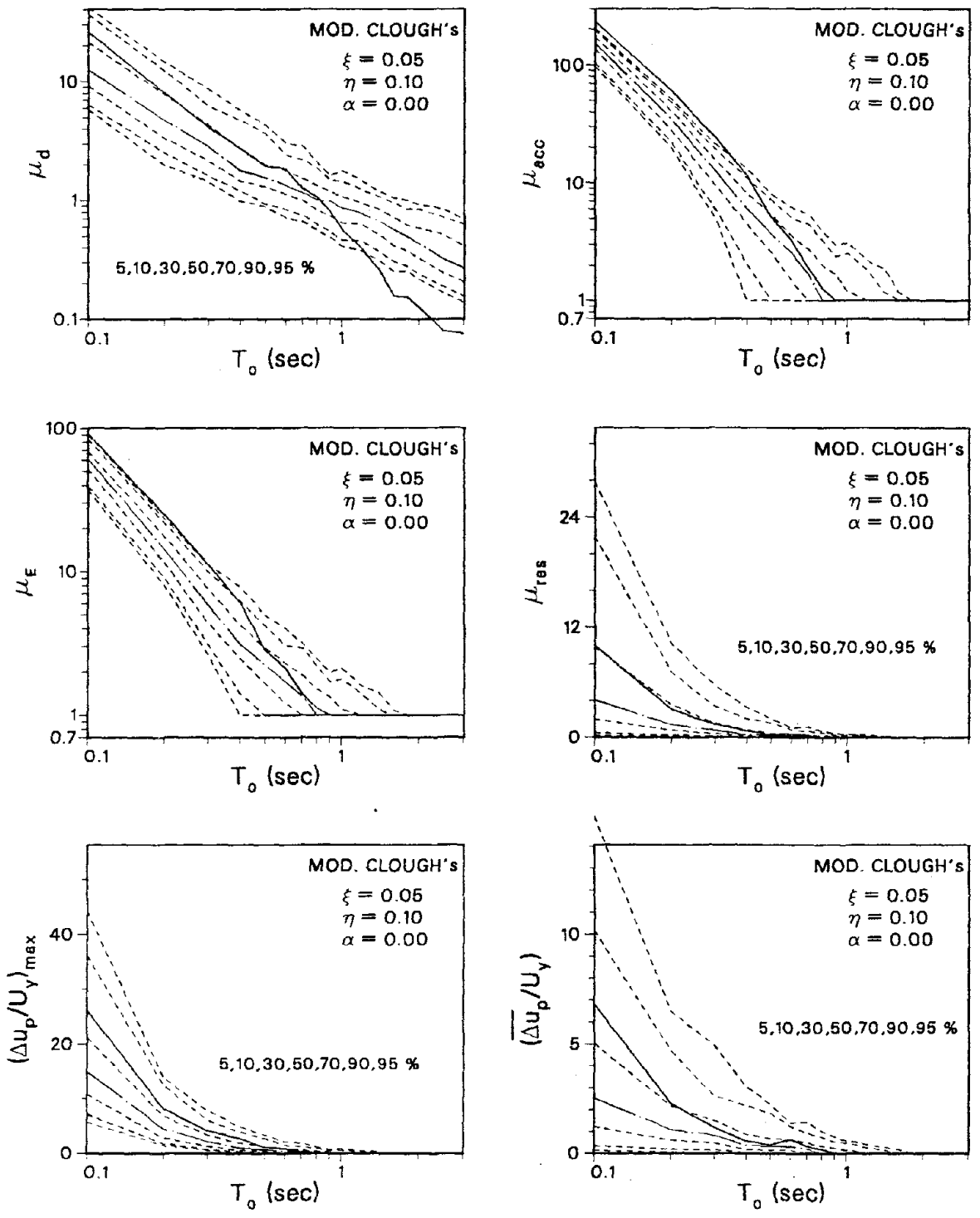

Fig. 8.10 Probabilistic Inelastic Response Spectra for the E02NS Target Record (ARMA(4,2) Earthquake Model and Modified Clough's Structural Model)

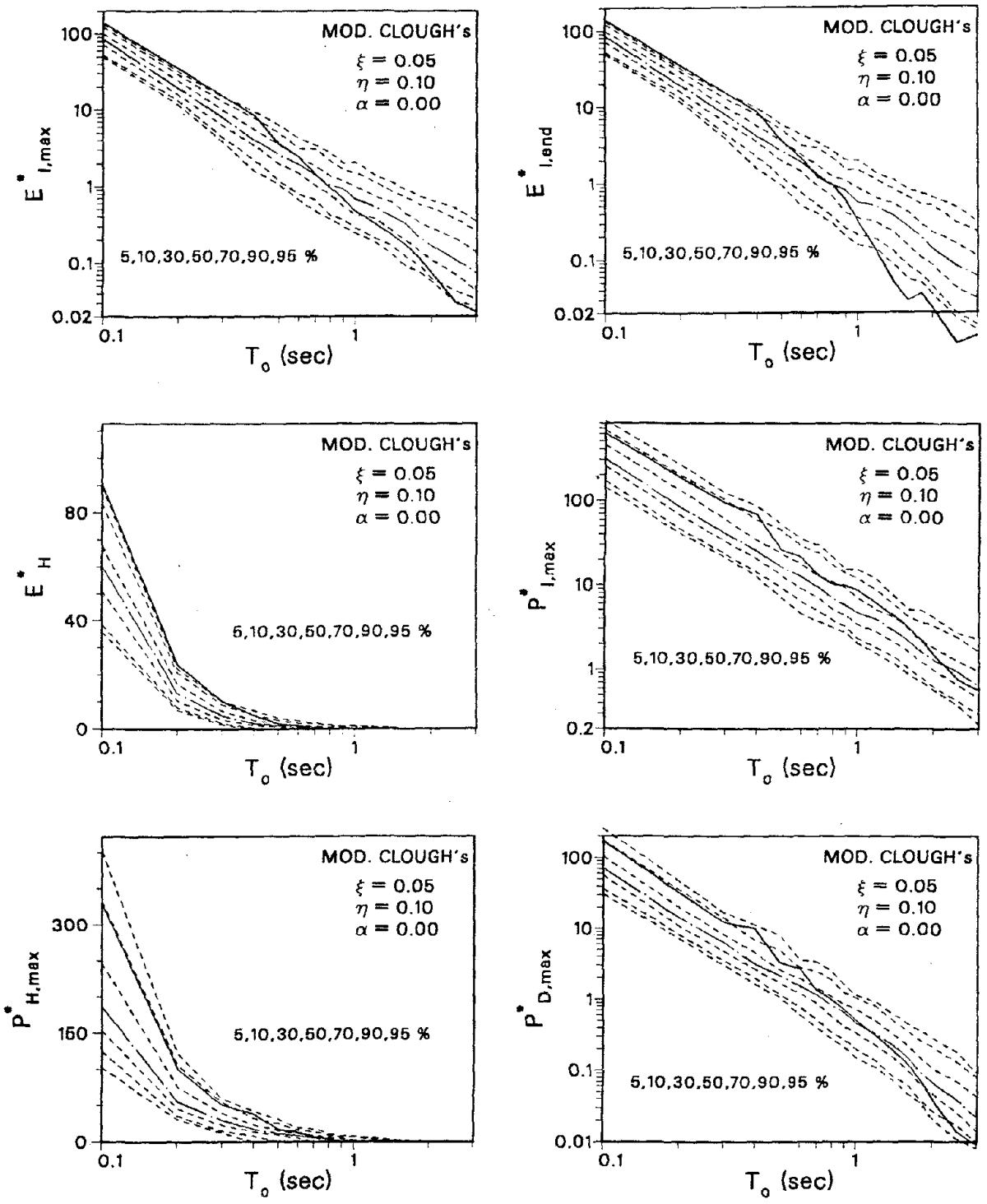

Fig. 8.10 (continued)

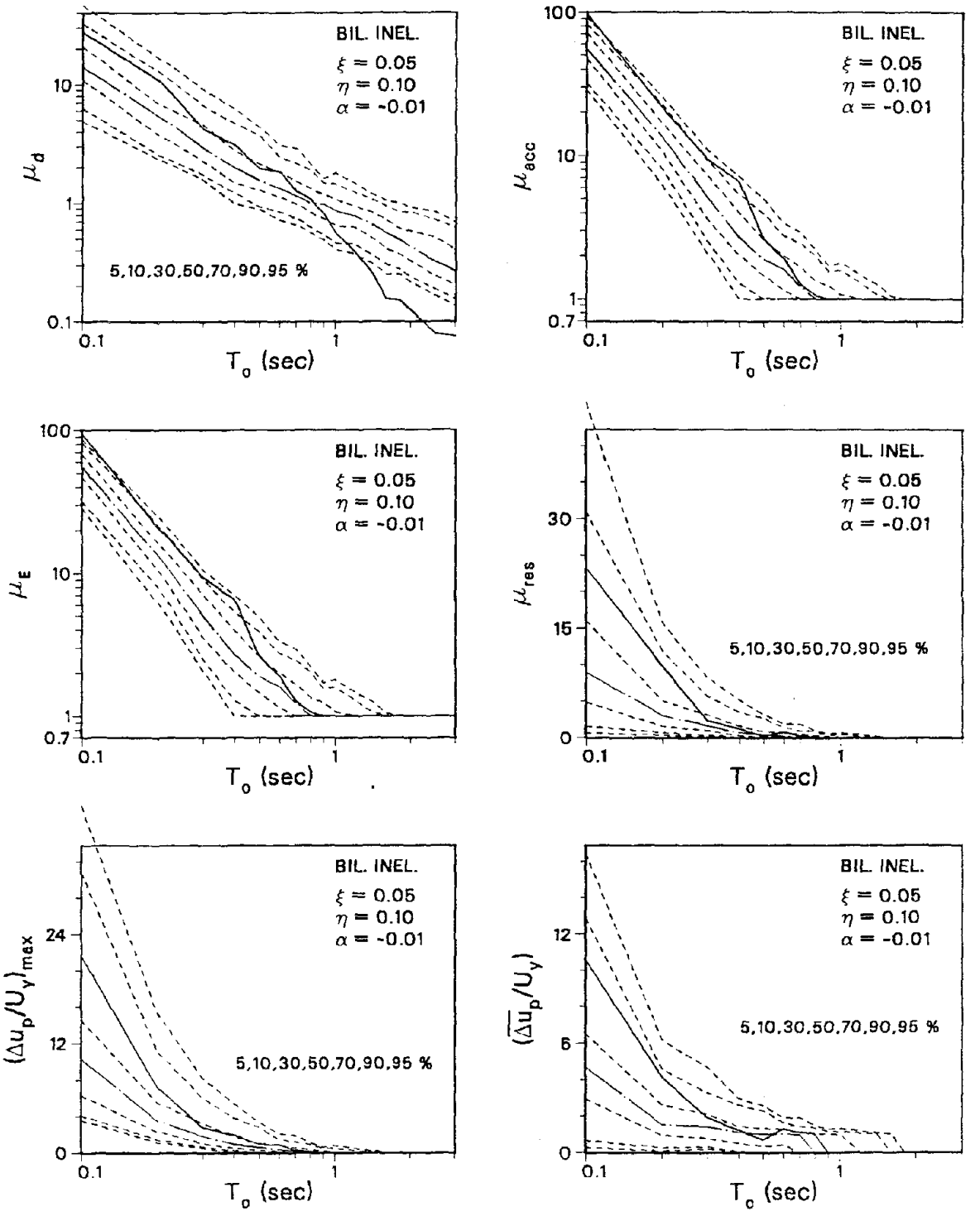

Fig. 8.11 Probabilistic Inelastic Response Spectra for the E02NS Target Record (ARMA(4,2) Earthquake Model and Bilinear Inelastic Structural Model)

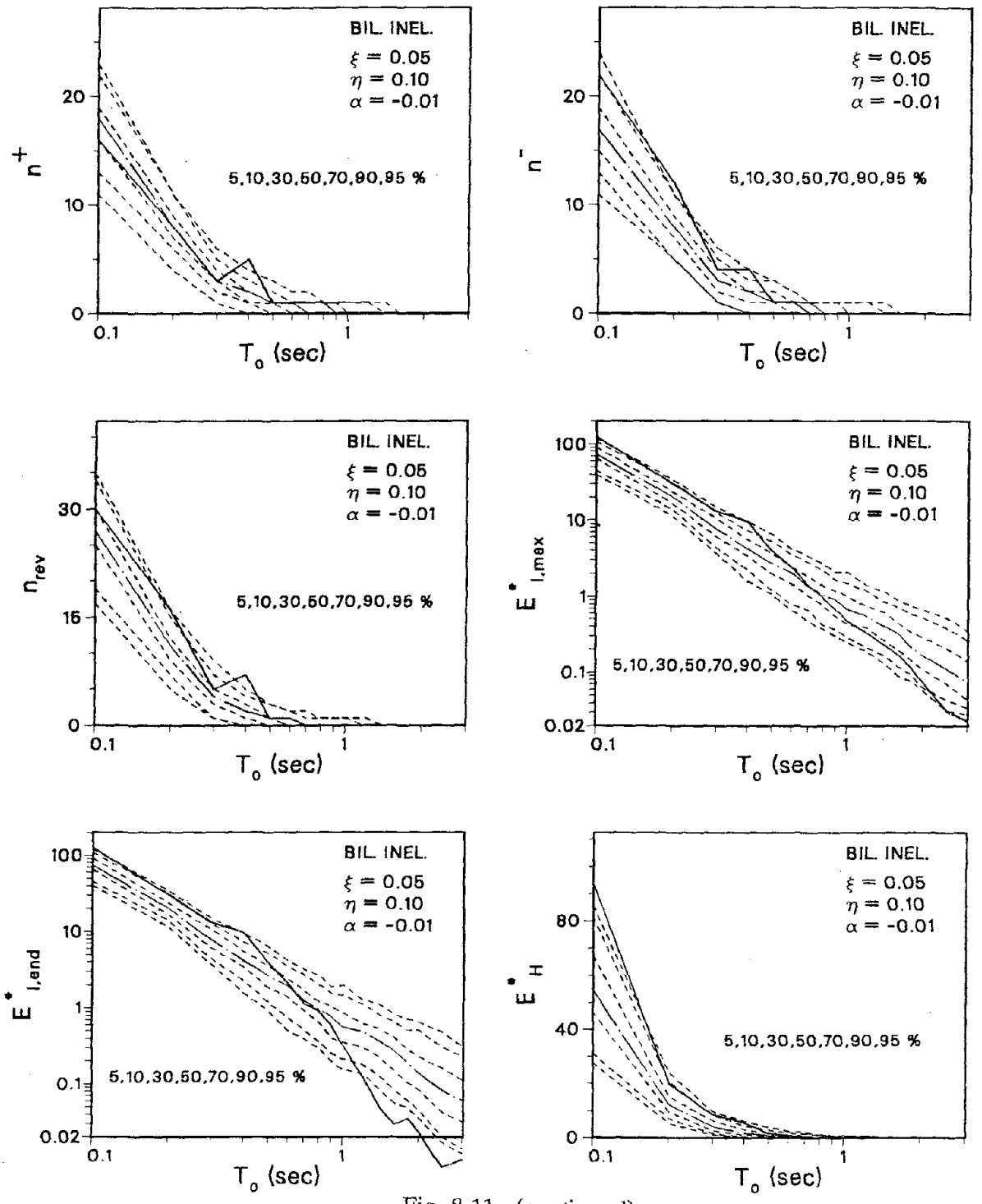

Fig. 8.11 (continued)

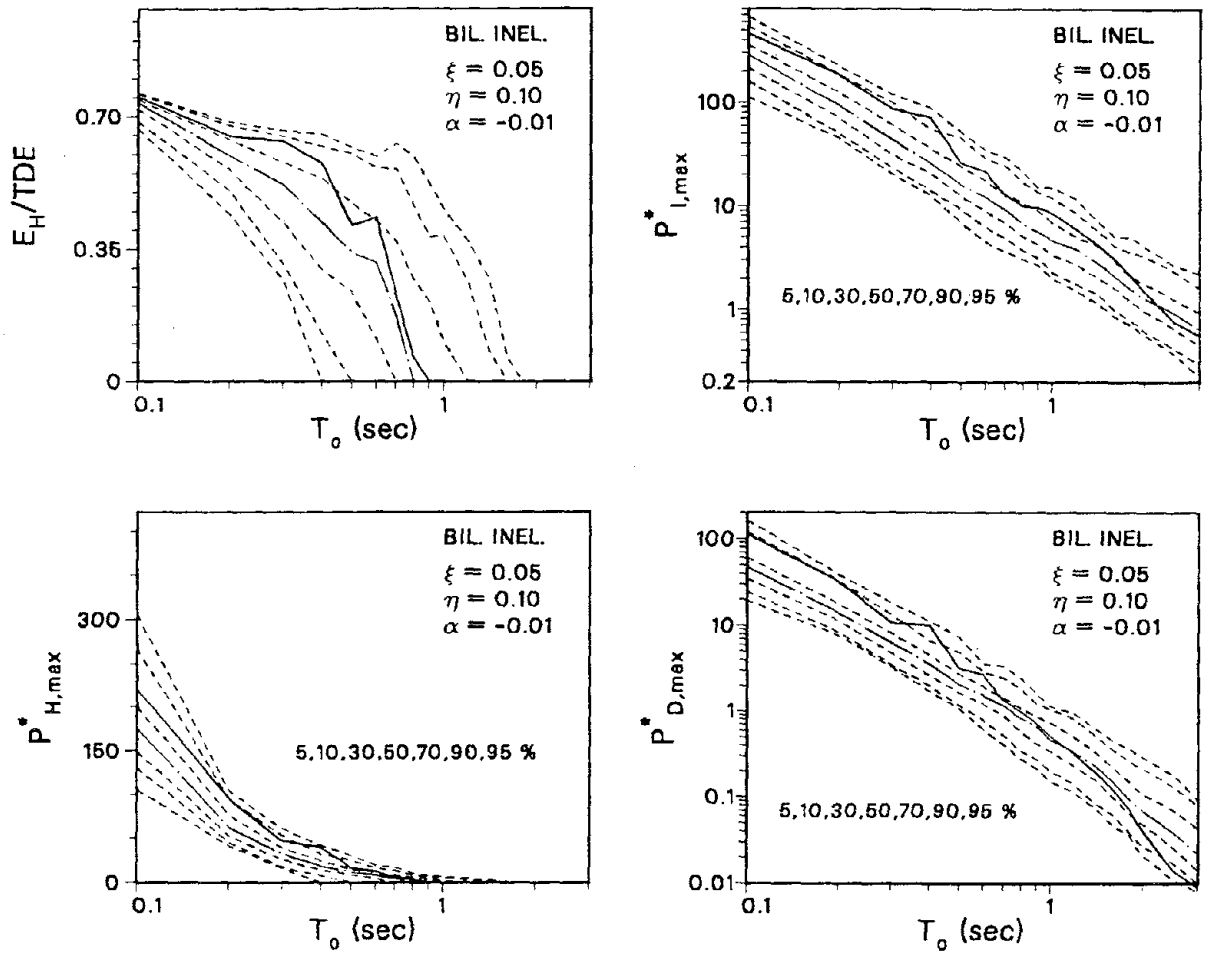

Fig. 8.11 (continued)

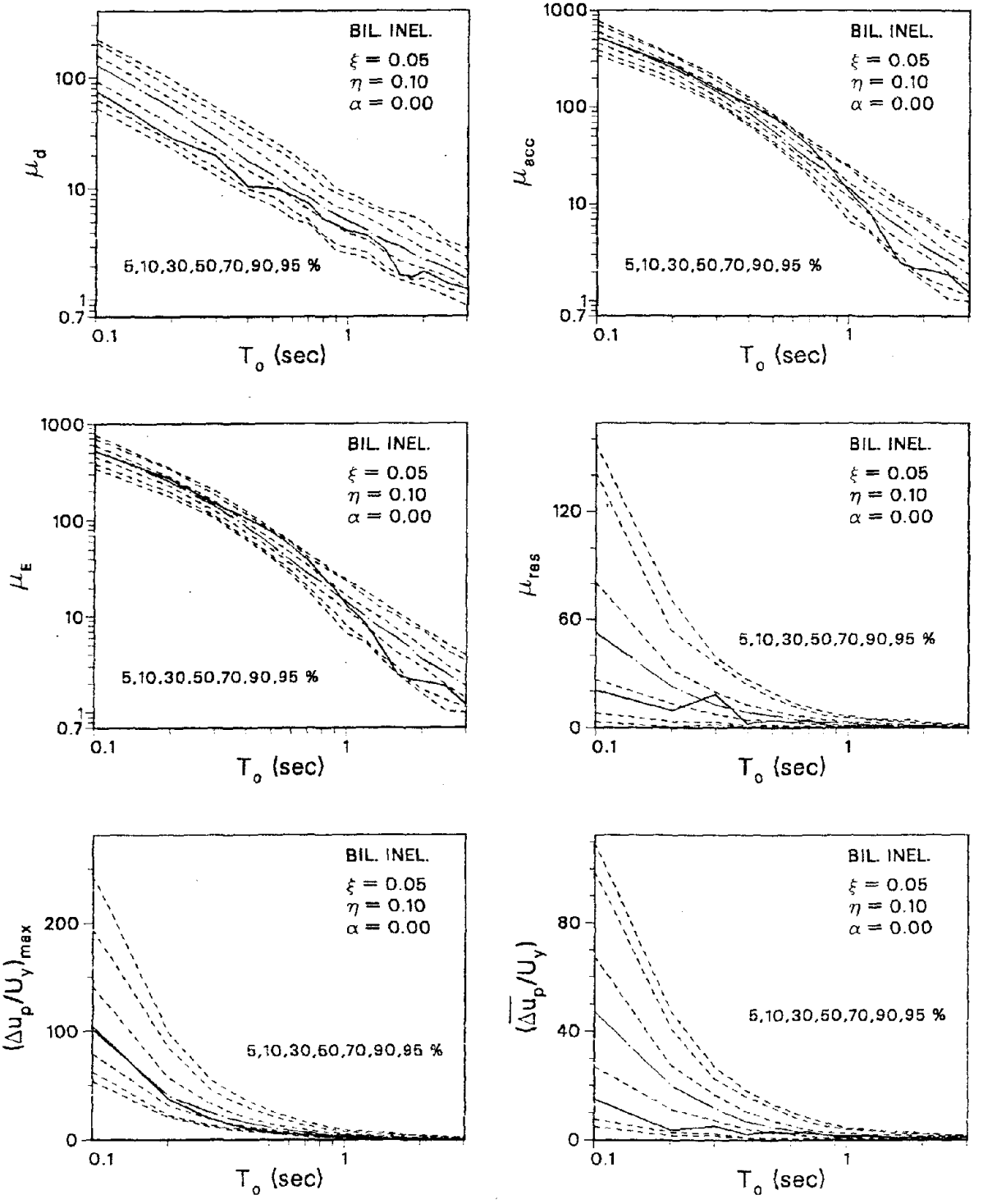

Fig. 8.12 Probabilistic Inelastic Response Spectra for the El Centro Target Record (ARMA(2,1) Earthquake Model and Bilinear Inelastic Structural Model)

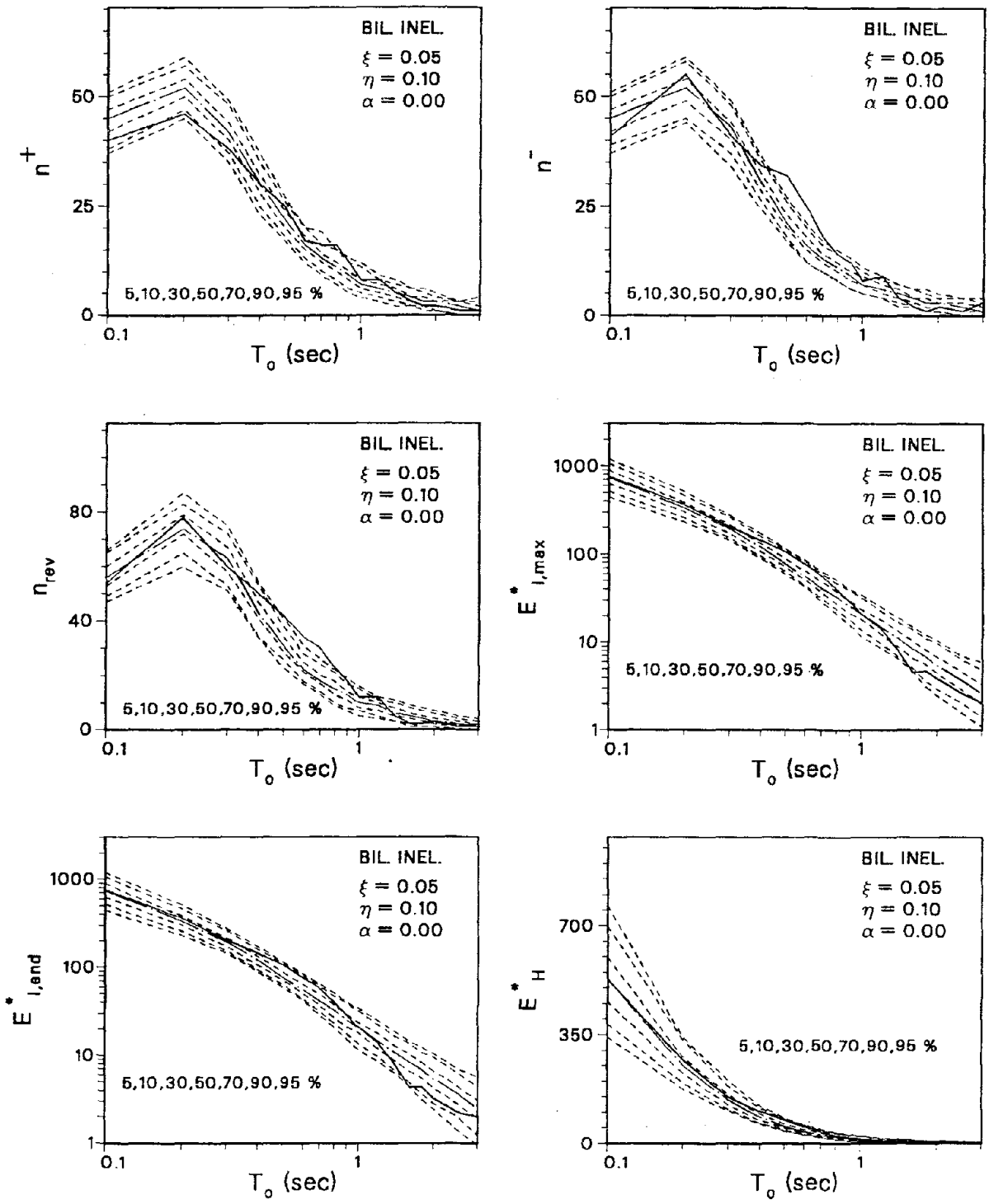

Fig. 8.12 (continued)

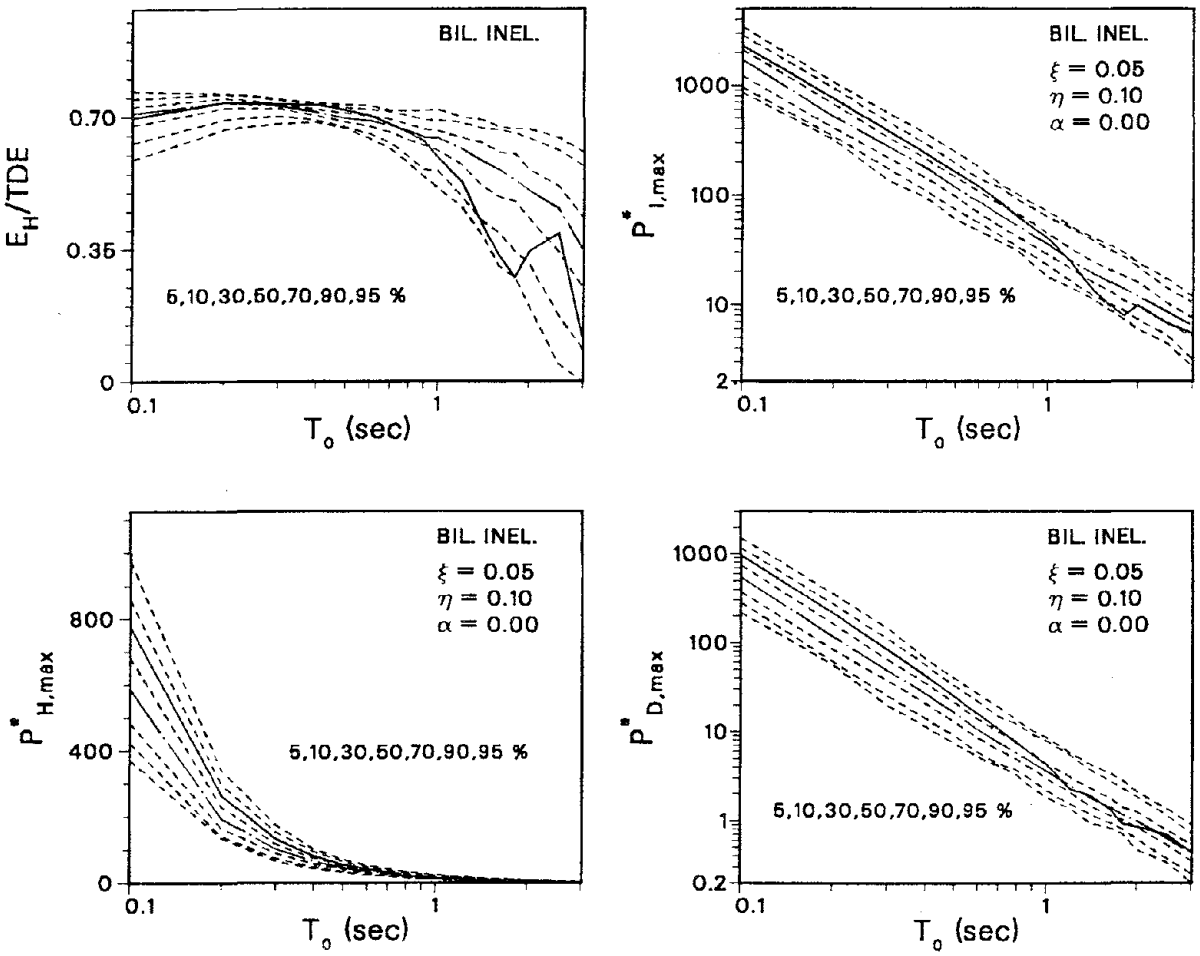

Fig. 8.12 (continued)

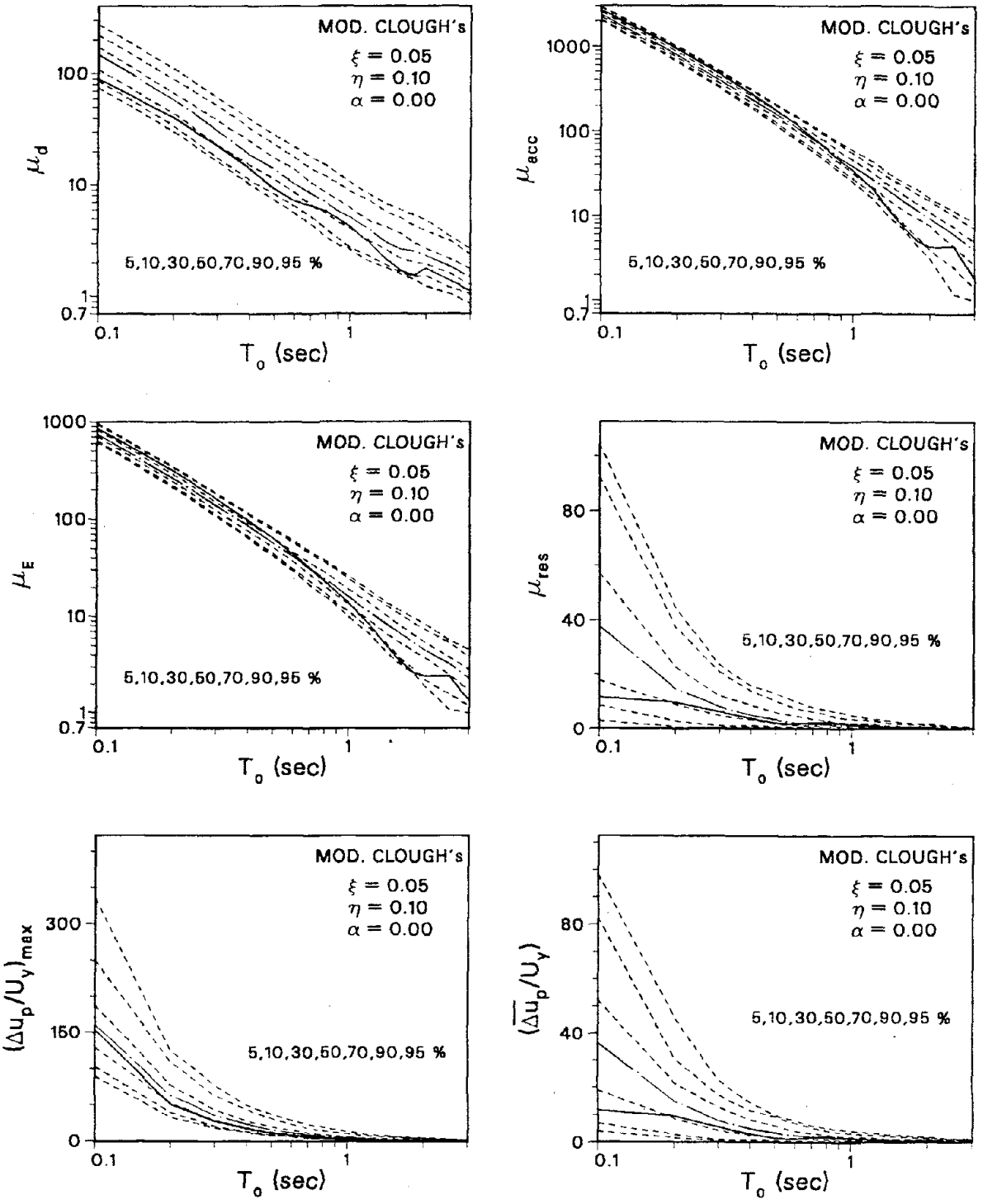

Fig. 8.13 Probabilistic Inelastic Response Spectra For the El Centro Target Record (ARMA(2,1) Earthquake Model and Modified Clough's Structural Model)

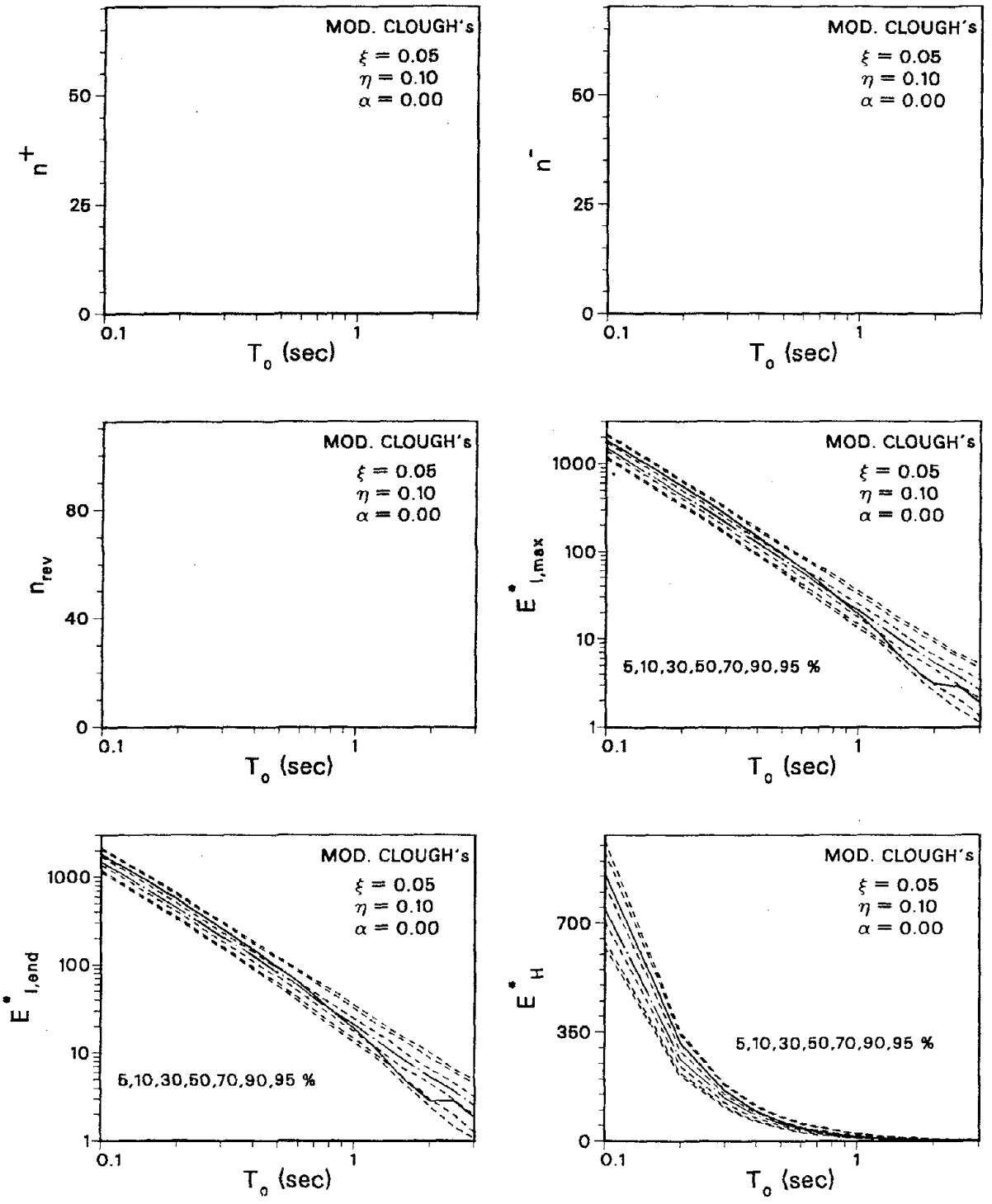

Fig. 8.13 (continued)

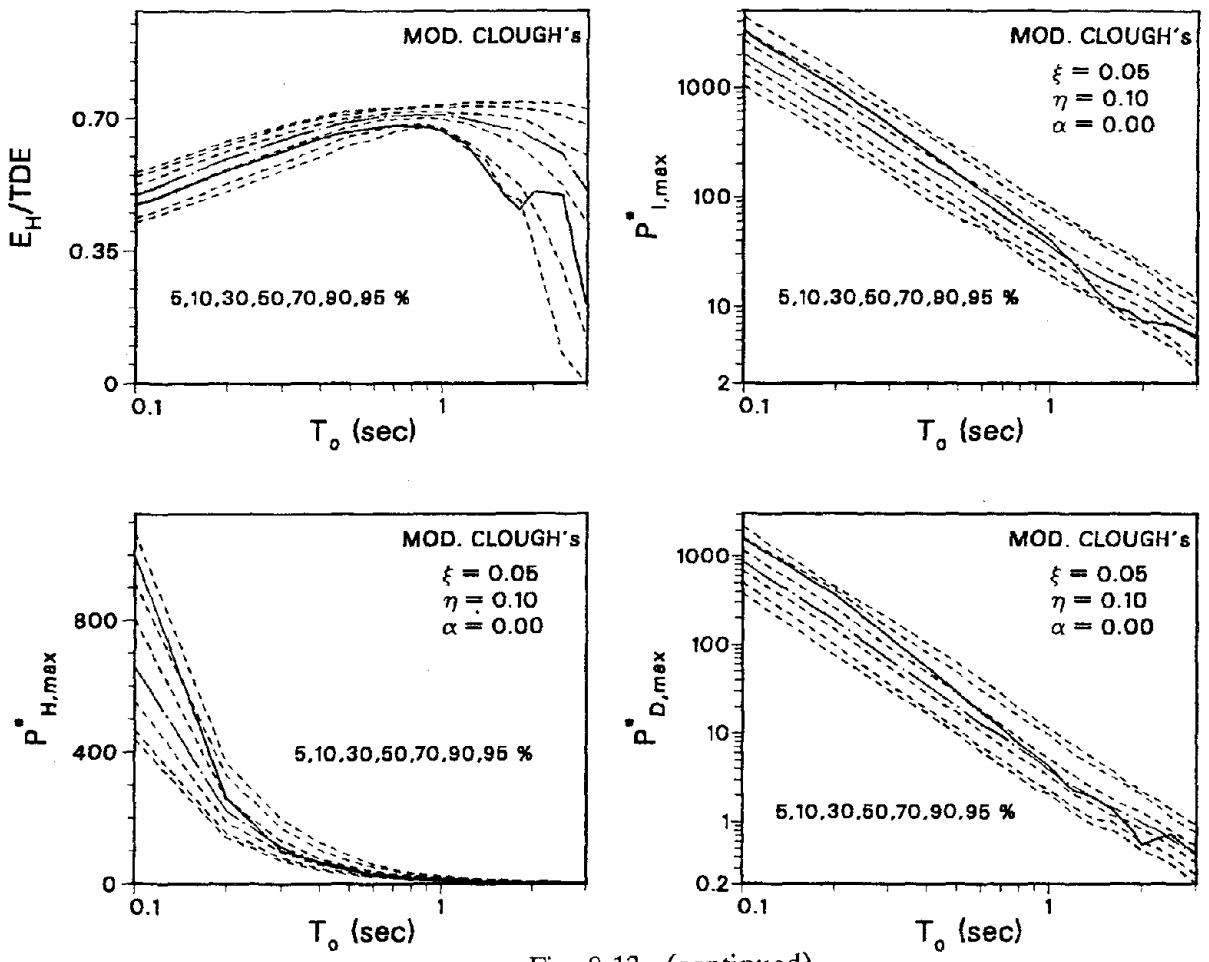

Fig. 8.13 (continued)

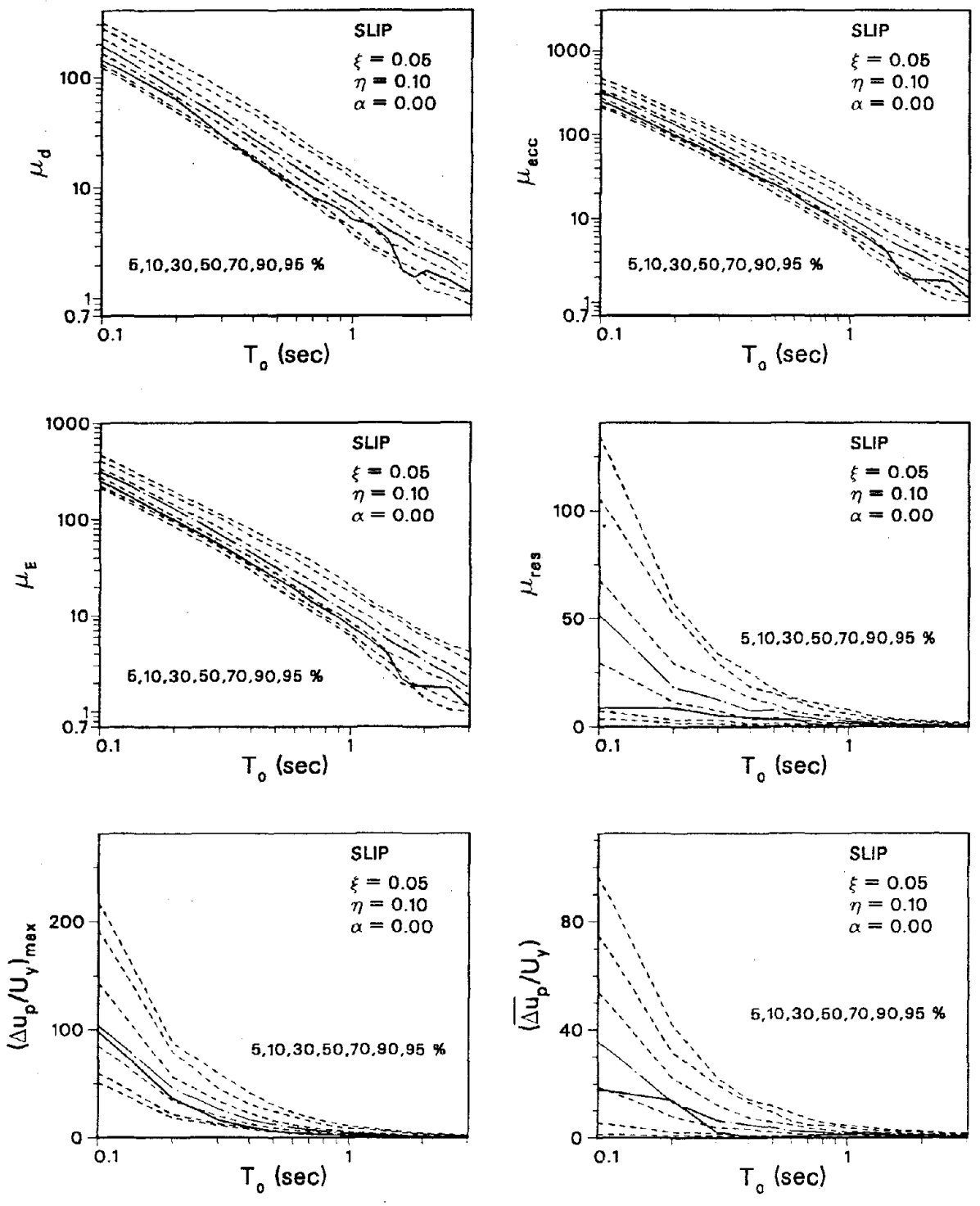

Fig. 8.14 Probabilistic Inelastic Response Spectra For the El Centro Target Record (ARMA(2,1) Earthquake Model and Slip Structural Model)

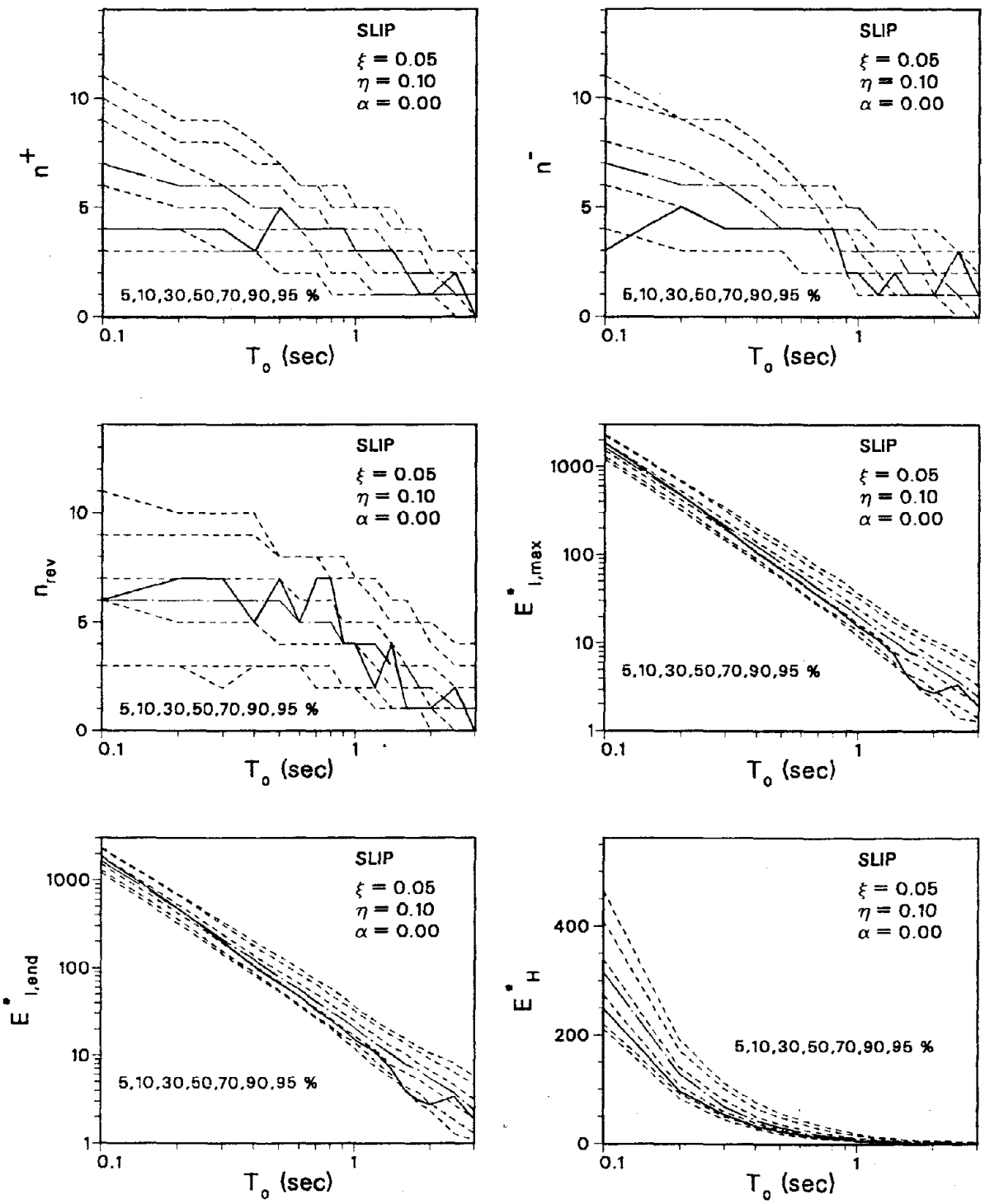

Fig. 8.14 (continued)

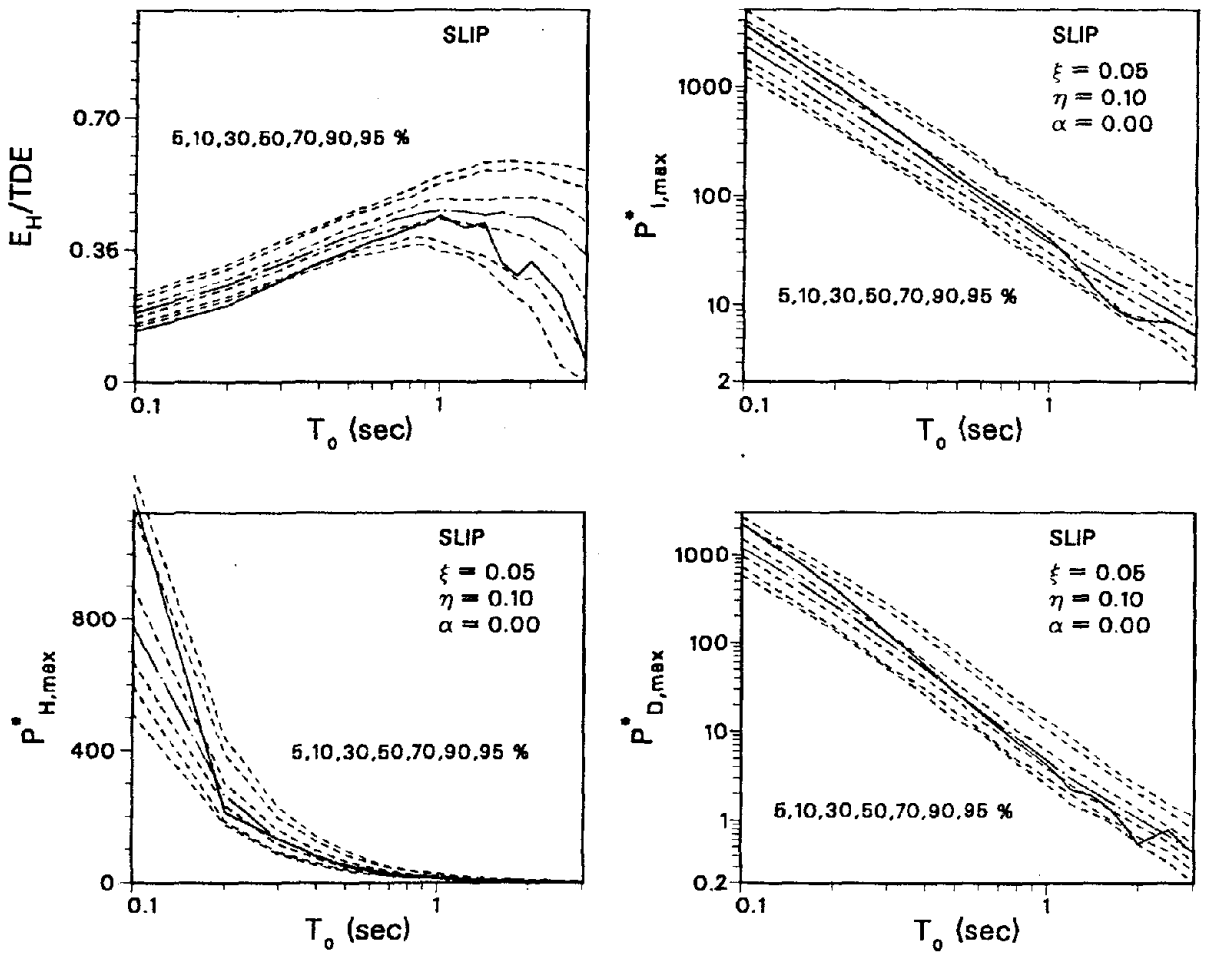

Fig. 8.14 (continued)

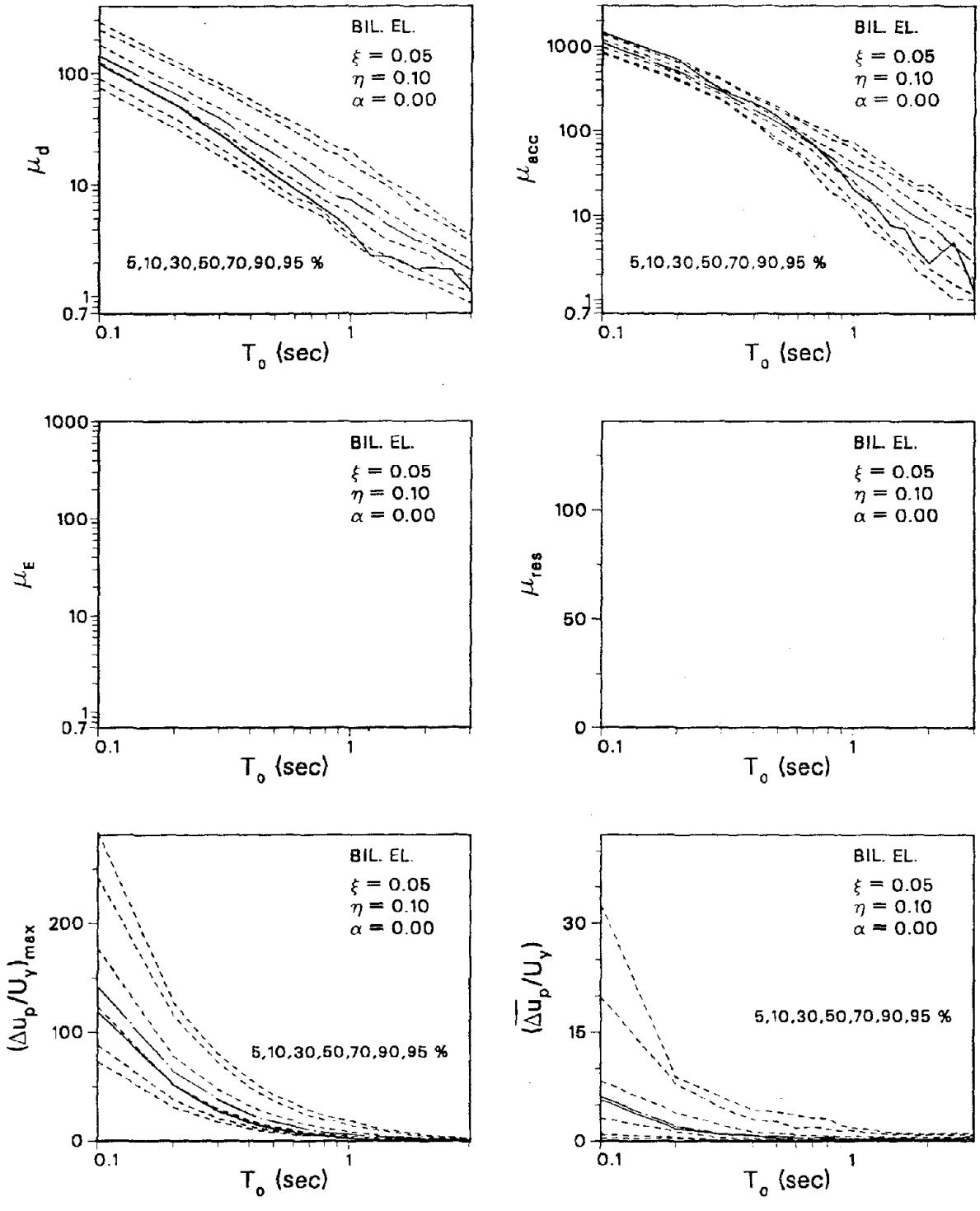

Fig. 8.15 Probabilistic Inelastic Response Spectra For the El Centro Target Record (ARMA(2,1) Earthquake Model and Bilinear Elastic Structural Model)

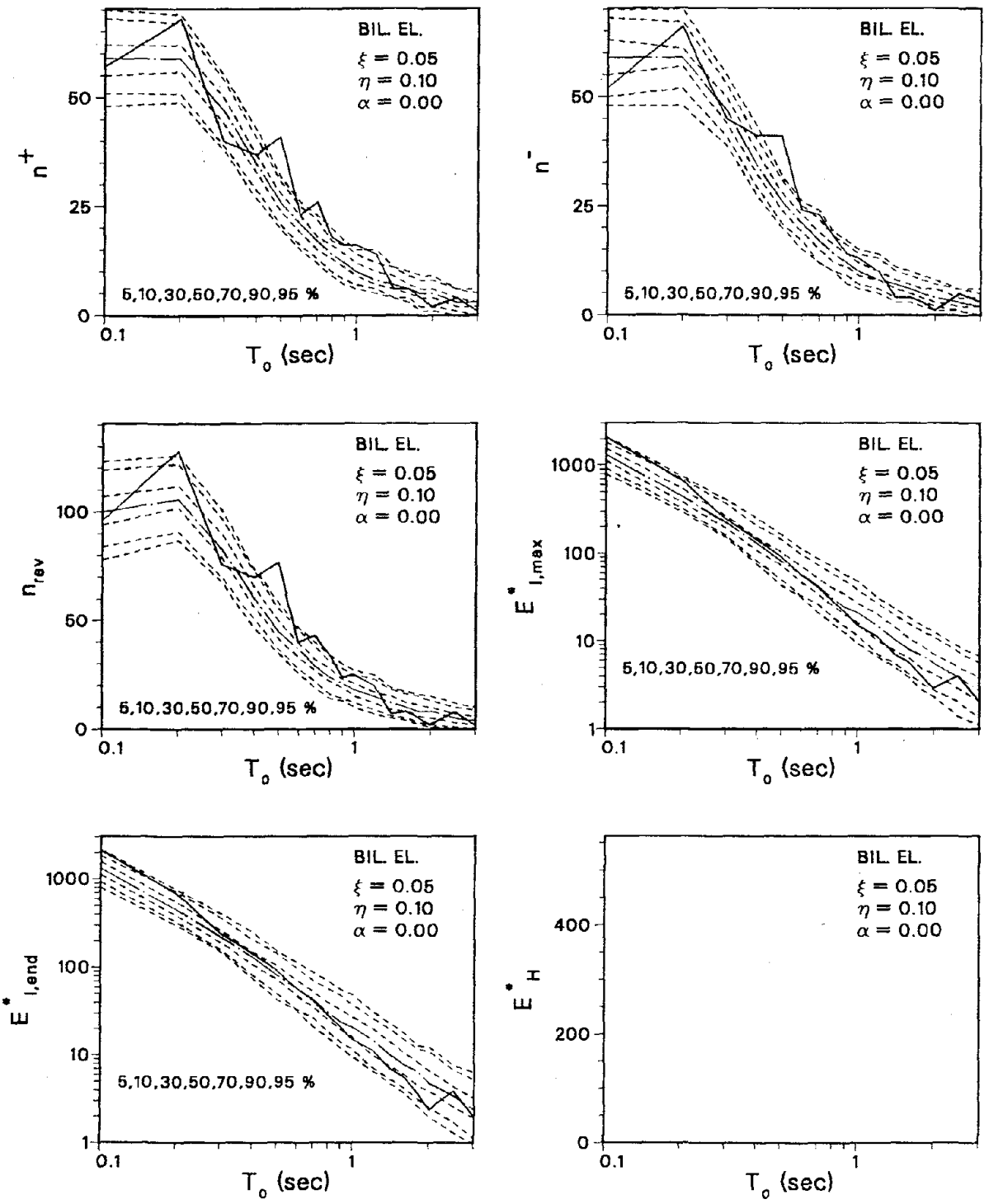

Fig. 8.15 (continued)

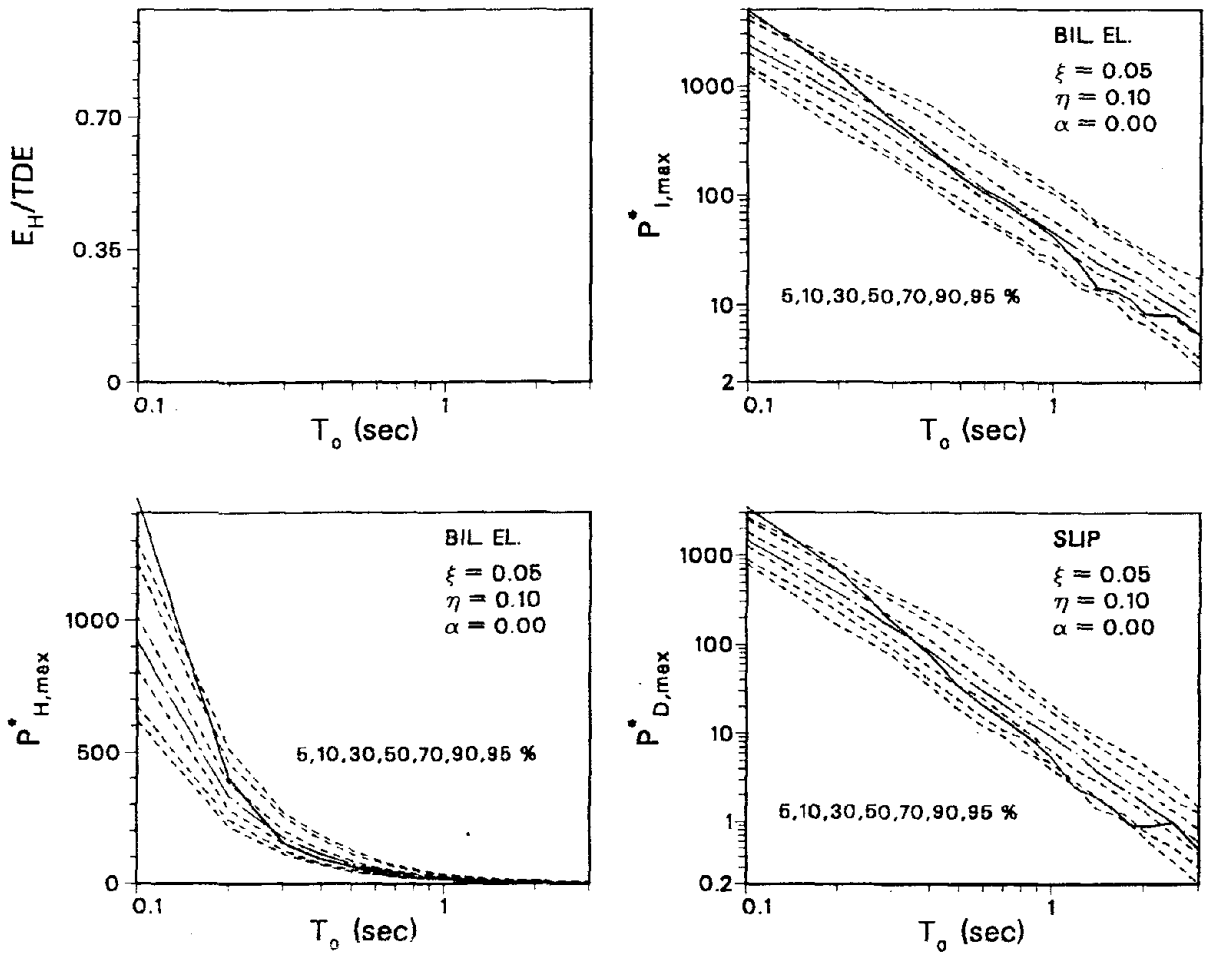

Fig. 8.15 (continued)

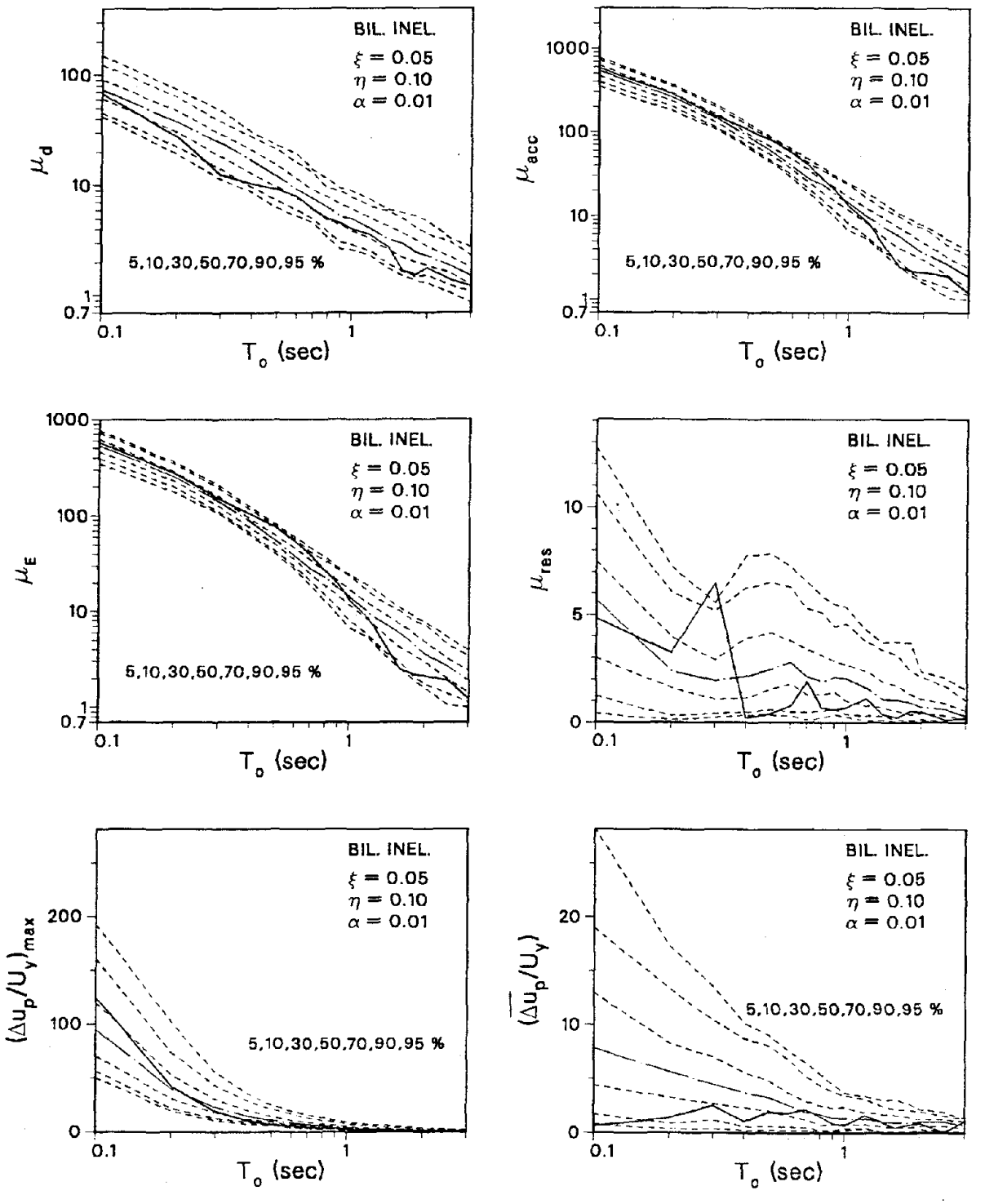

Fig. 8.16 Probabilistic Inelastic Response Spectra For the El Centro Target Record (ARMA(2,1) Earthquake Model and Bilinear Inelastic Structural Model)

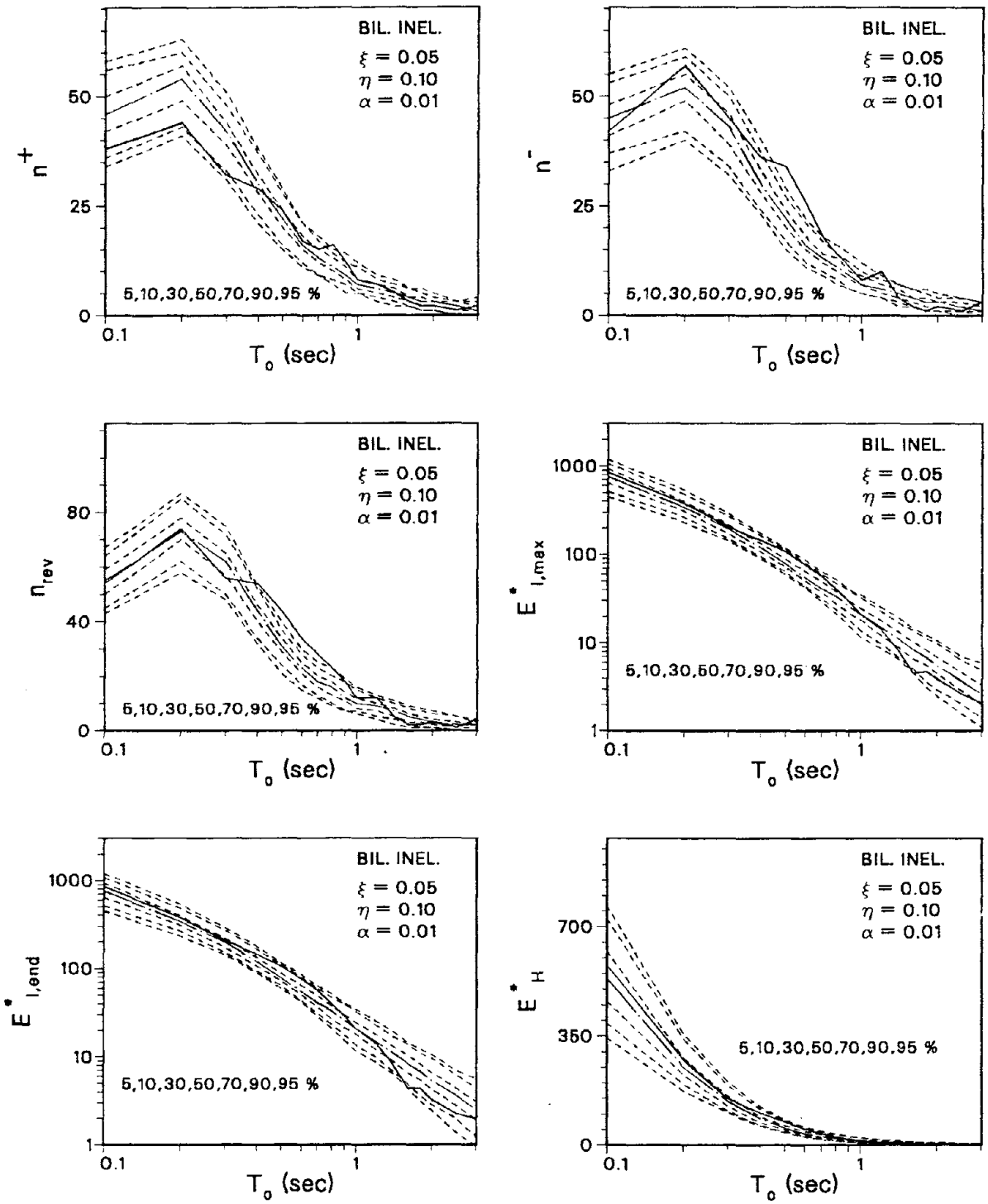

Fig. 8.16 (continued)

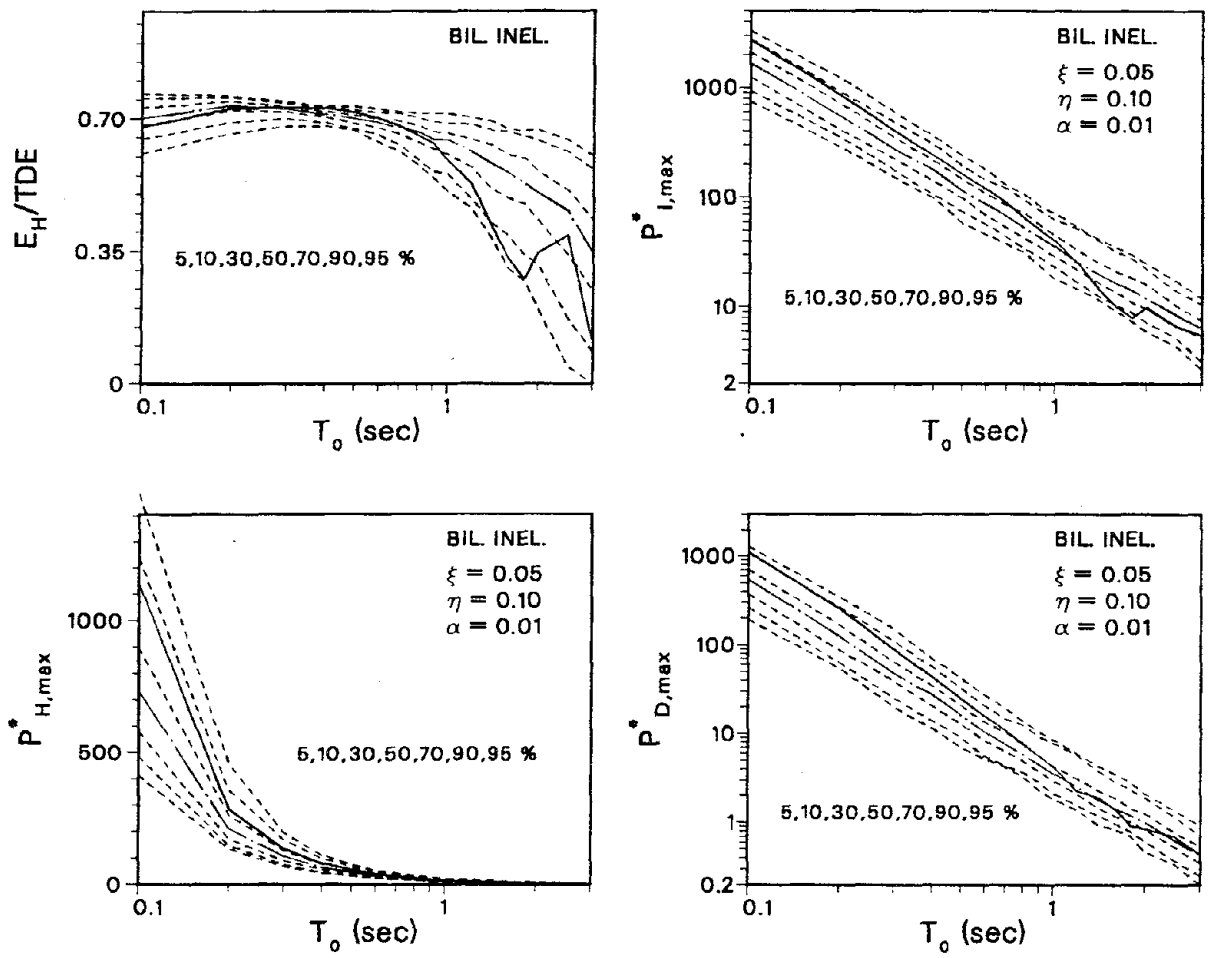

Fig. 8.16 (continued)

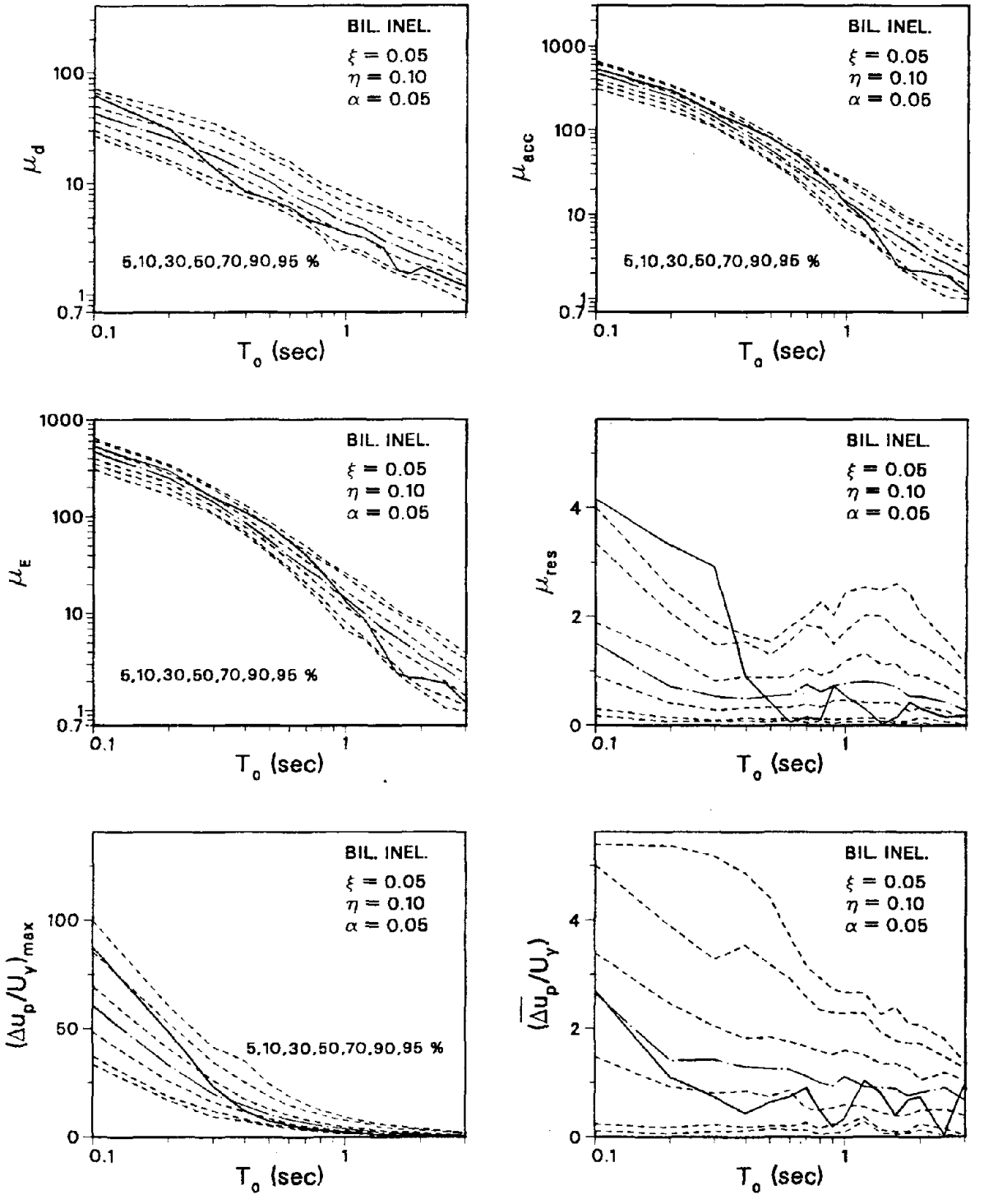

Fig. 8.17 Probabilistic Inelastic Response Spectra For the El Centro Target Record (ARMA(2,1) Earthquake Model and Bilinear Inelastic Structural Model)

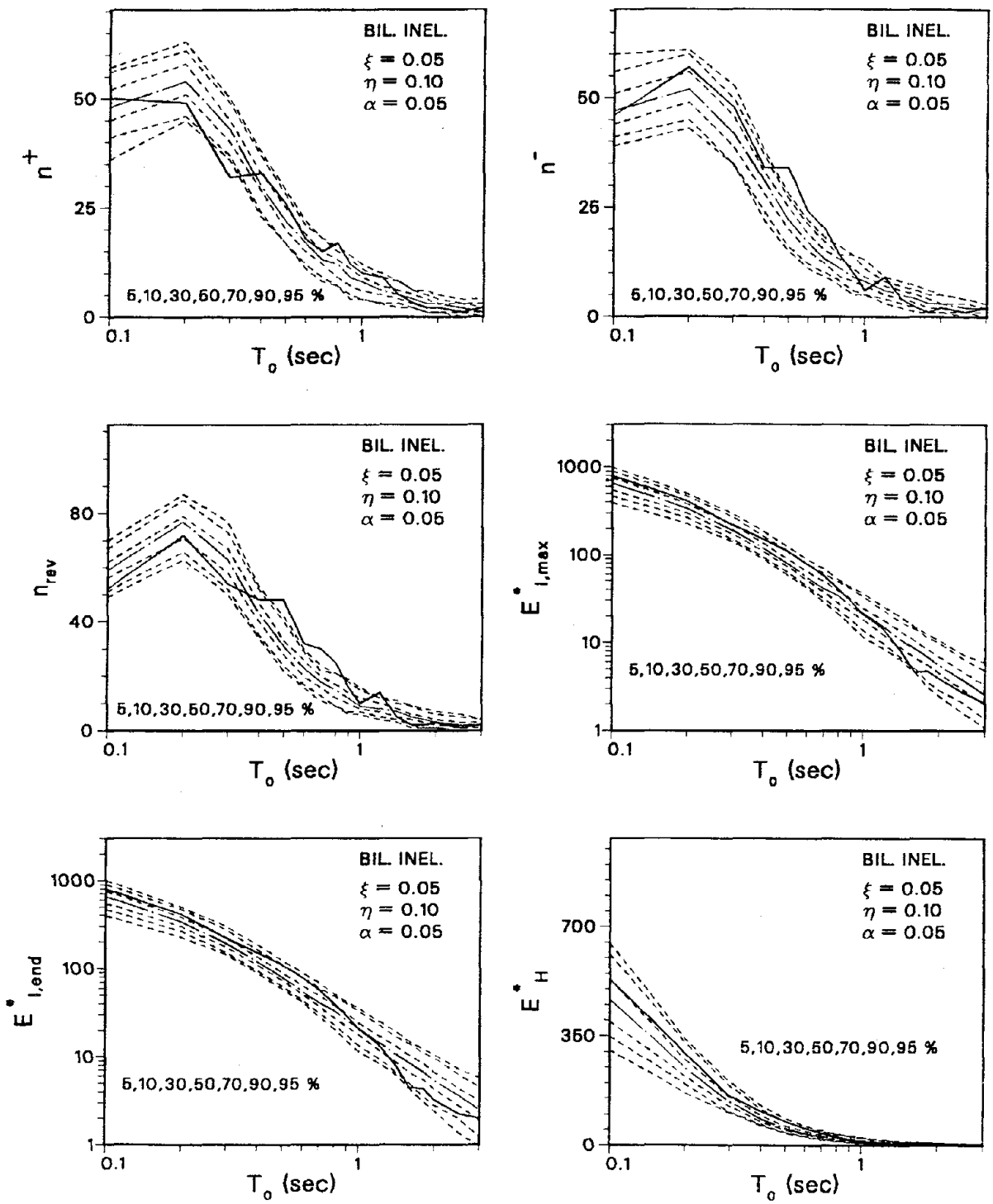

Fig. 8.17 (continued)

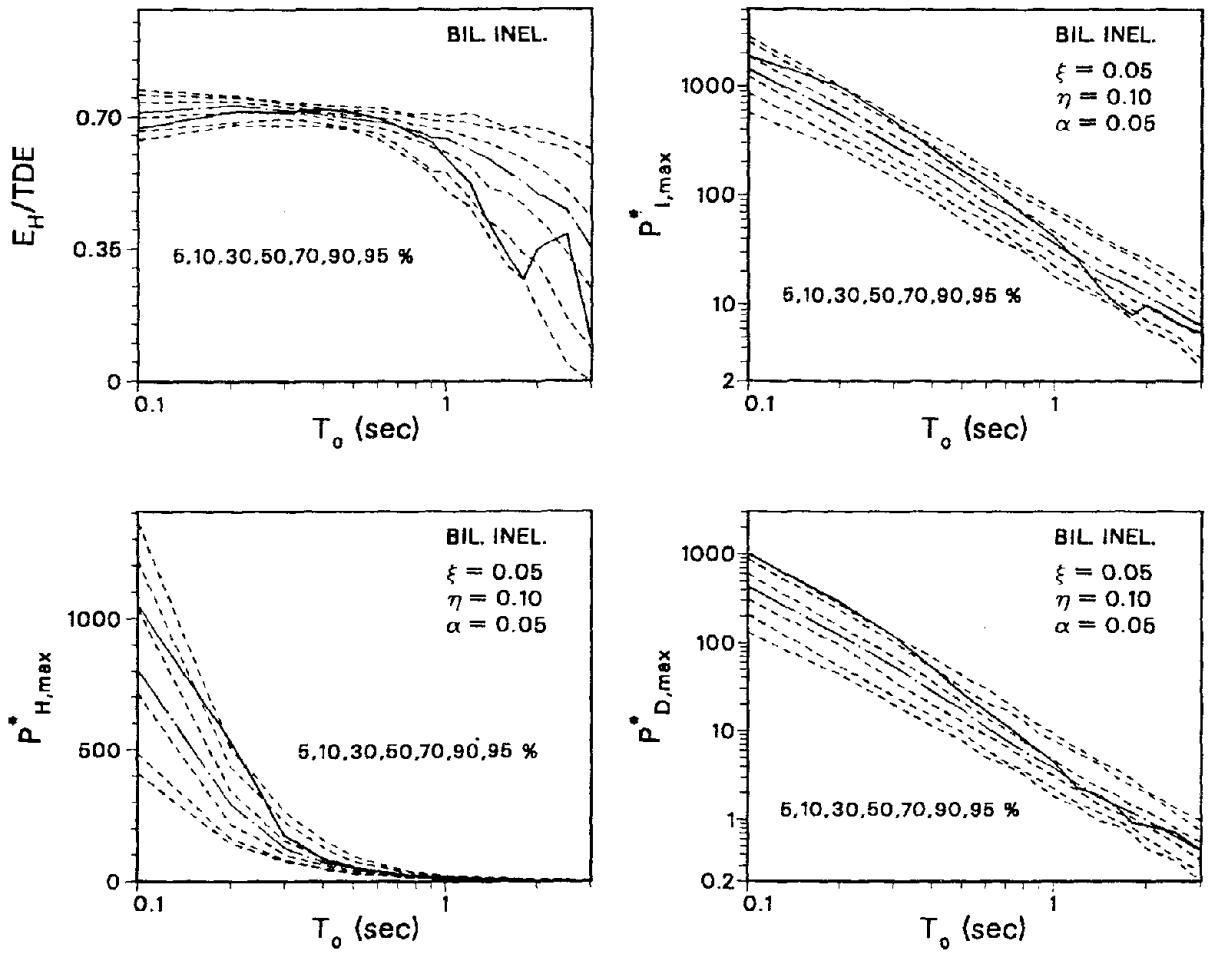

Fig. 8.17 (continued)

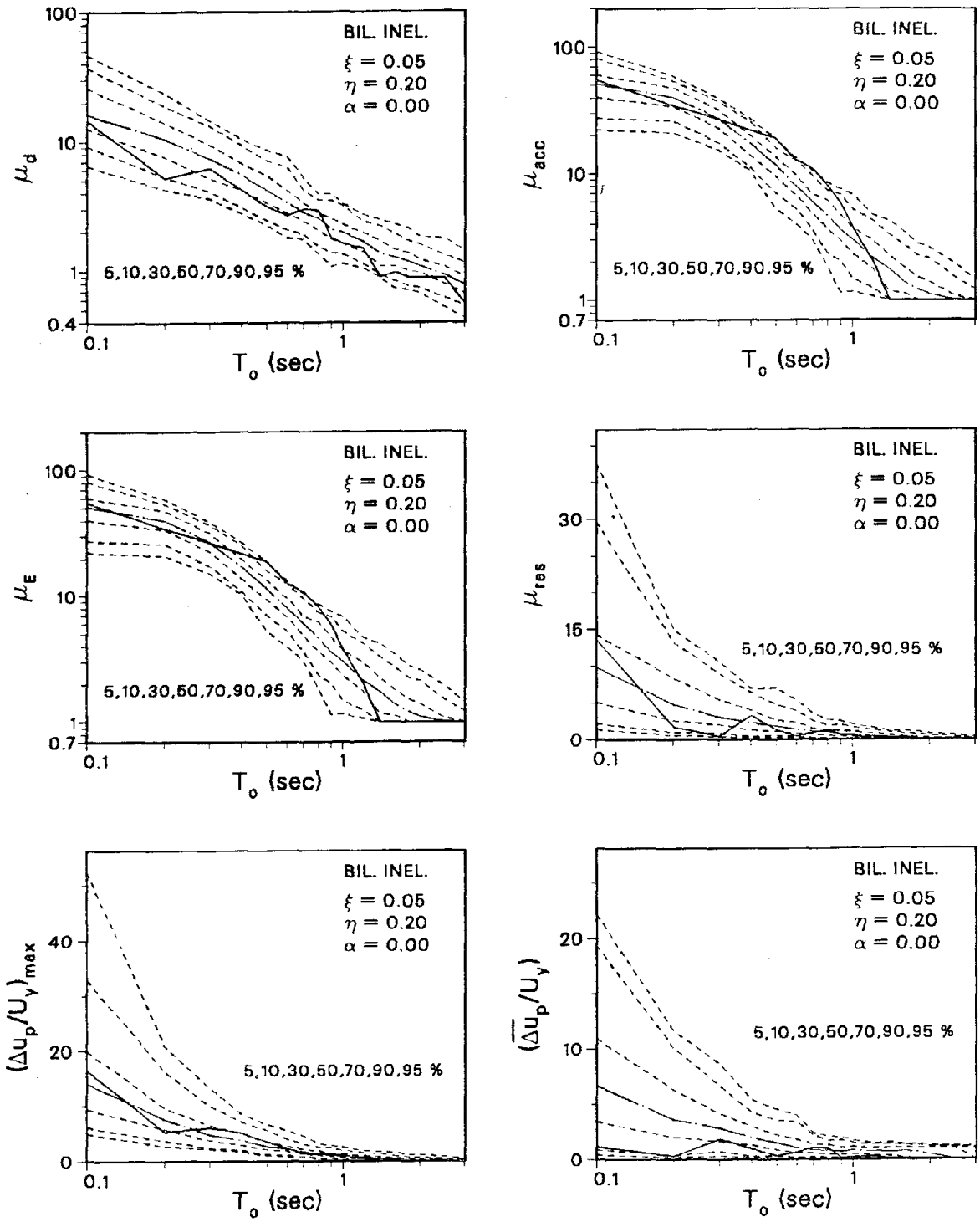

Fig. 8.18 Probabilistic Inelastic Response Spectra For the El Centro Target Record (ARMA(2,1) Earthquake Model and Bilinear Inelastic Structural Model)

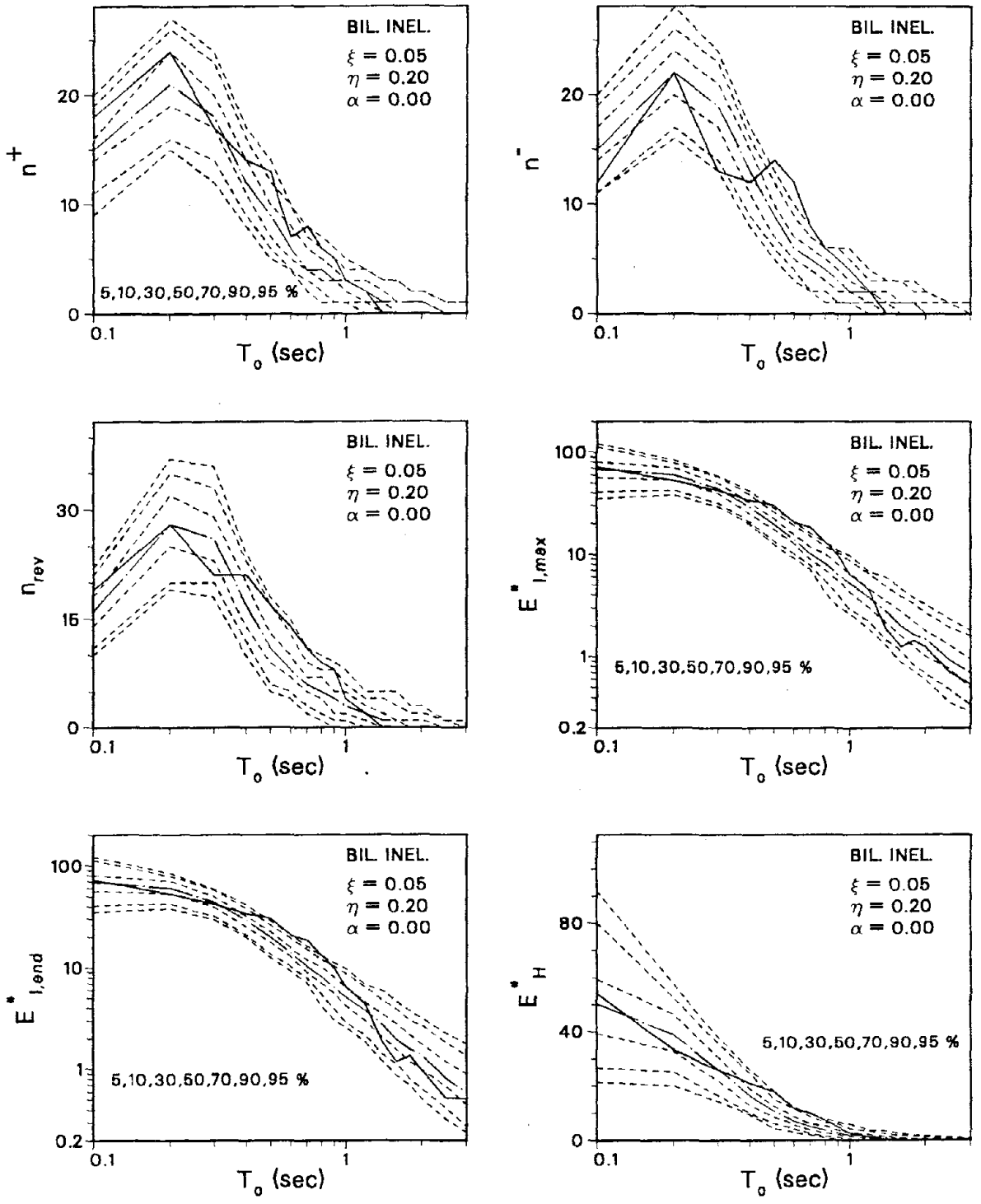

Fig. 8.18 (continued)

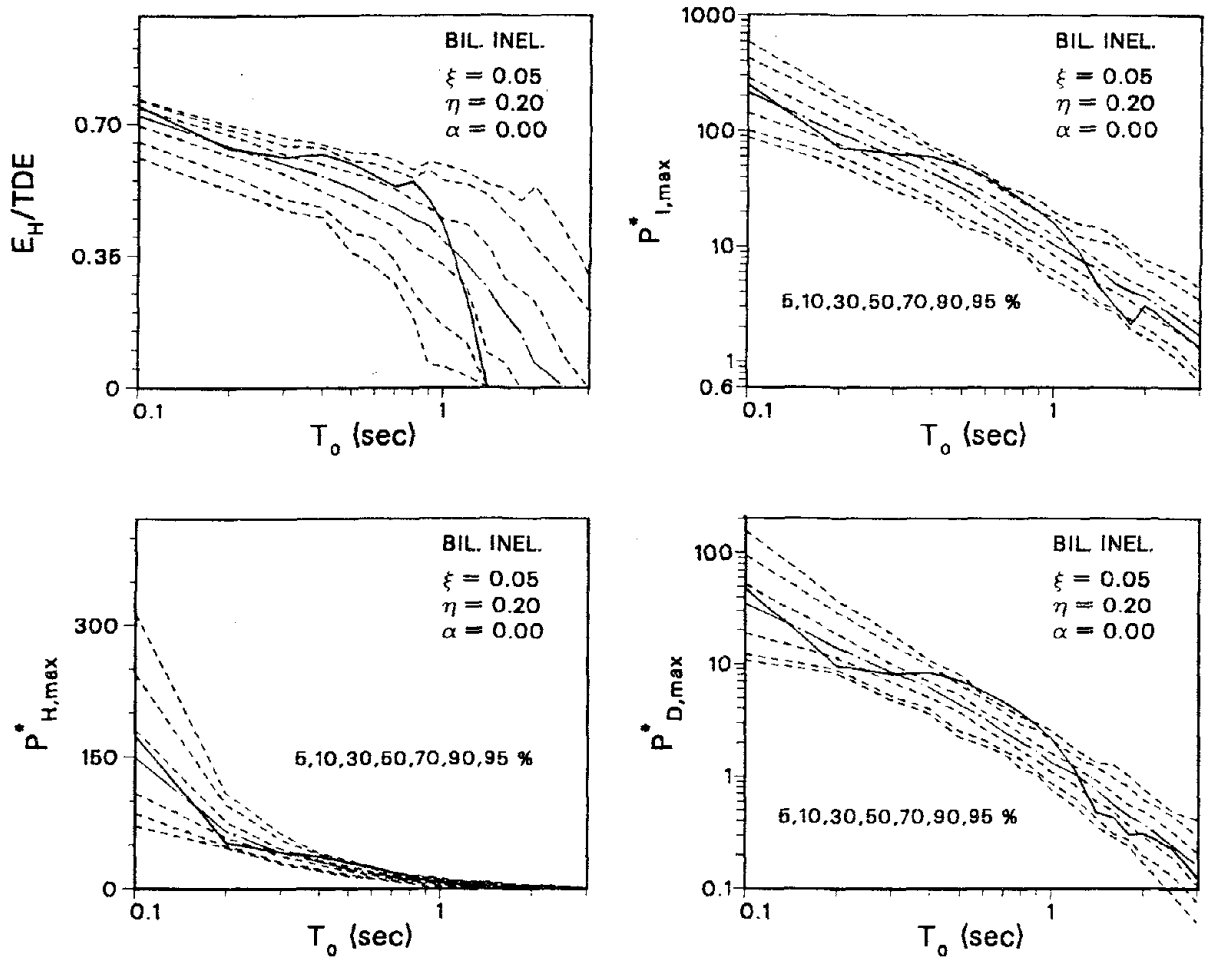

Fig. 8.18 (continued)

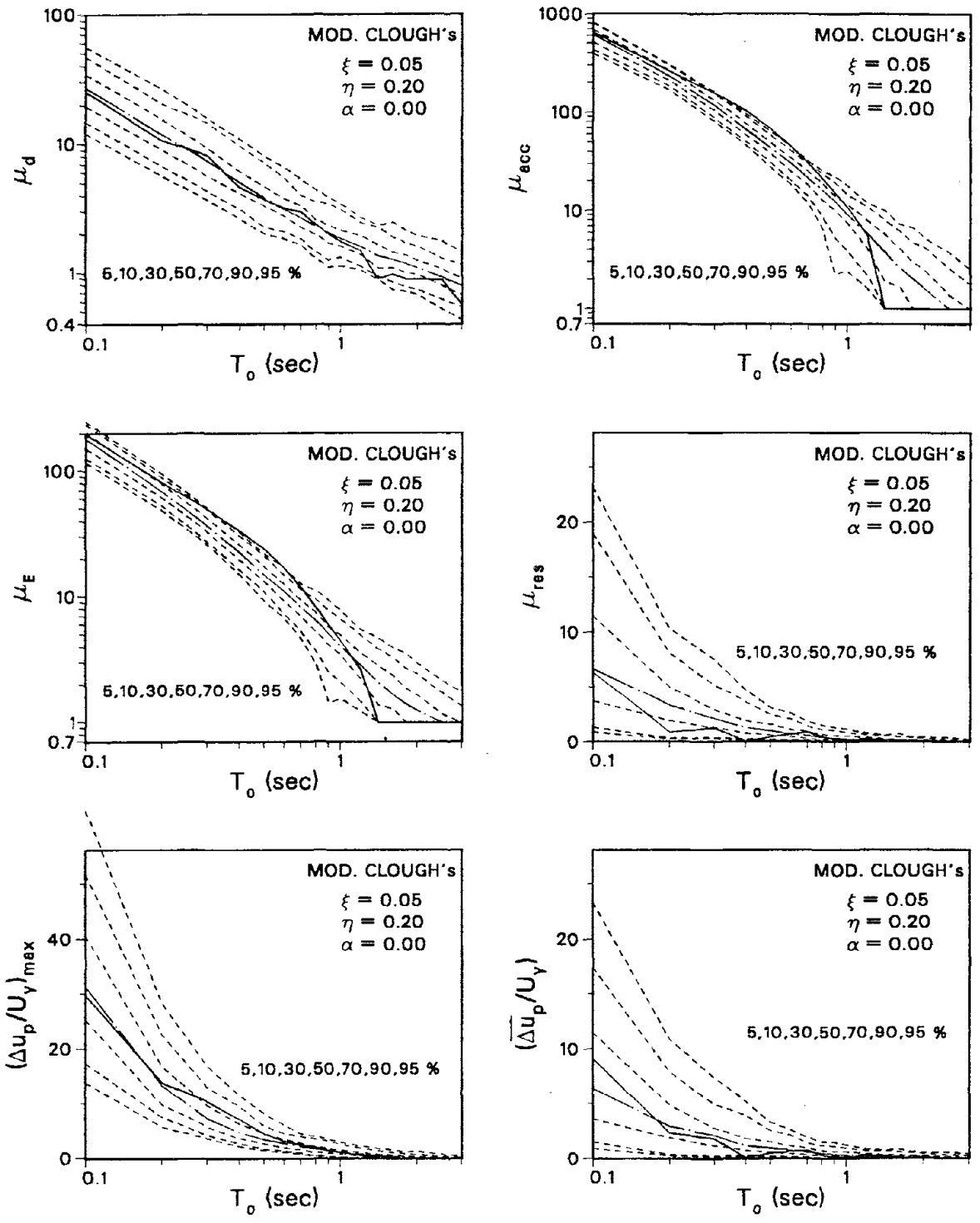

Fig. 8.19 Probabilistic Inelastic Response Spectra For the El Centro Target Record (ARMA(2,1) Earthquake Model and Modified Clough's Structural Model)

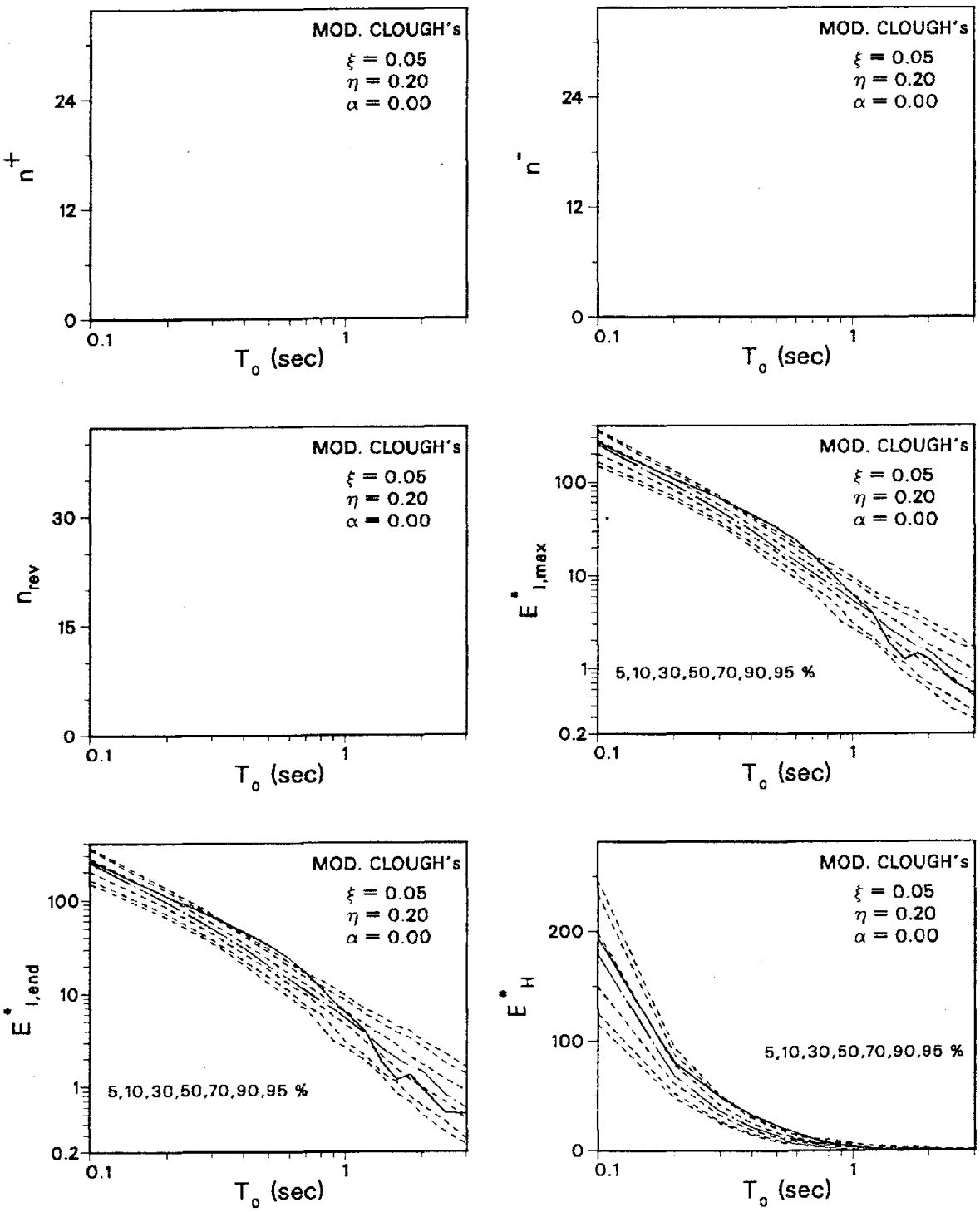

Fig. 8.19 (continued)

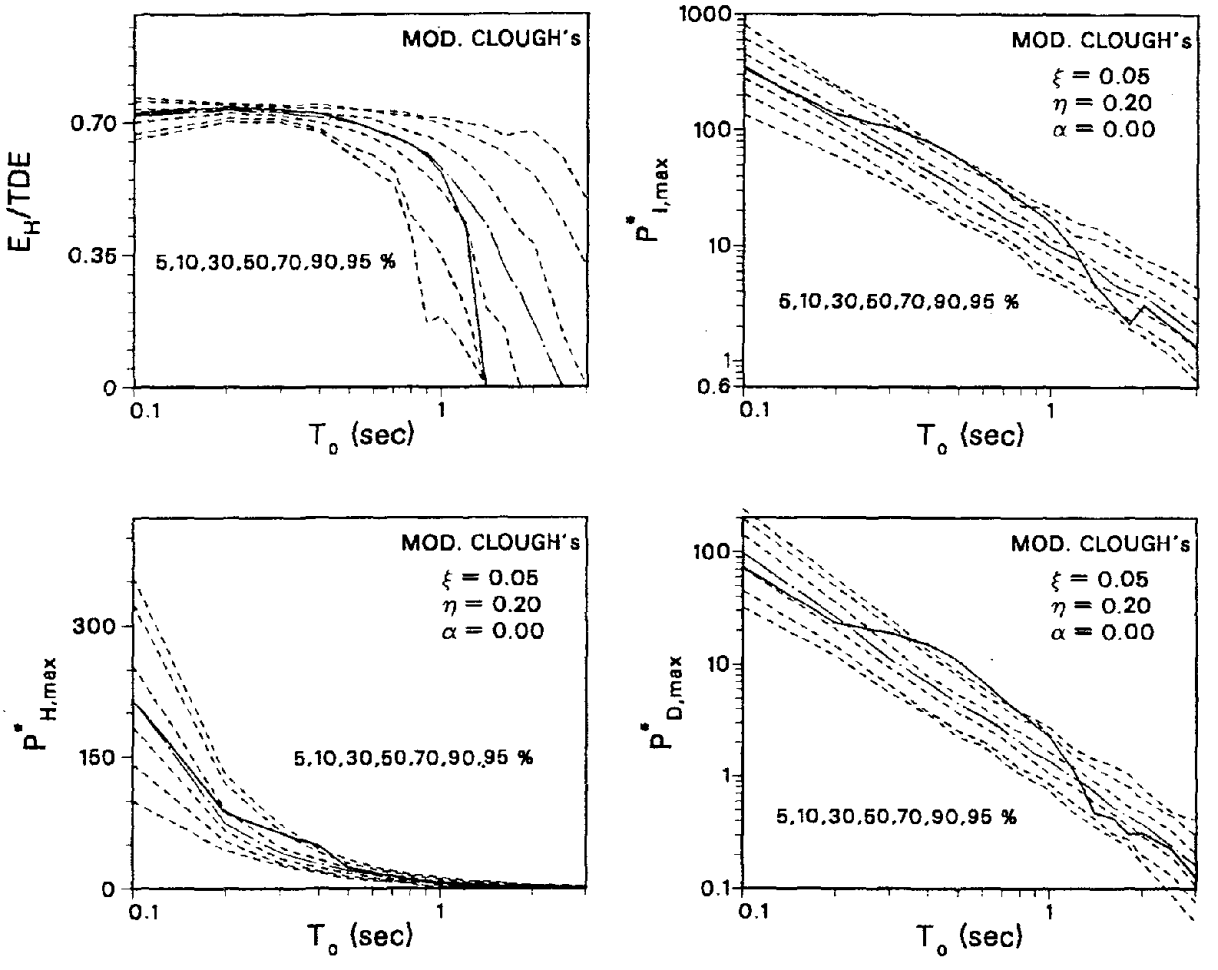

Fig. 8.19 (continued)

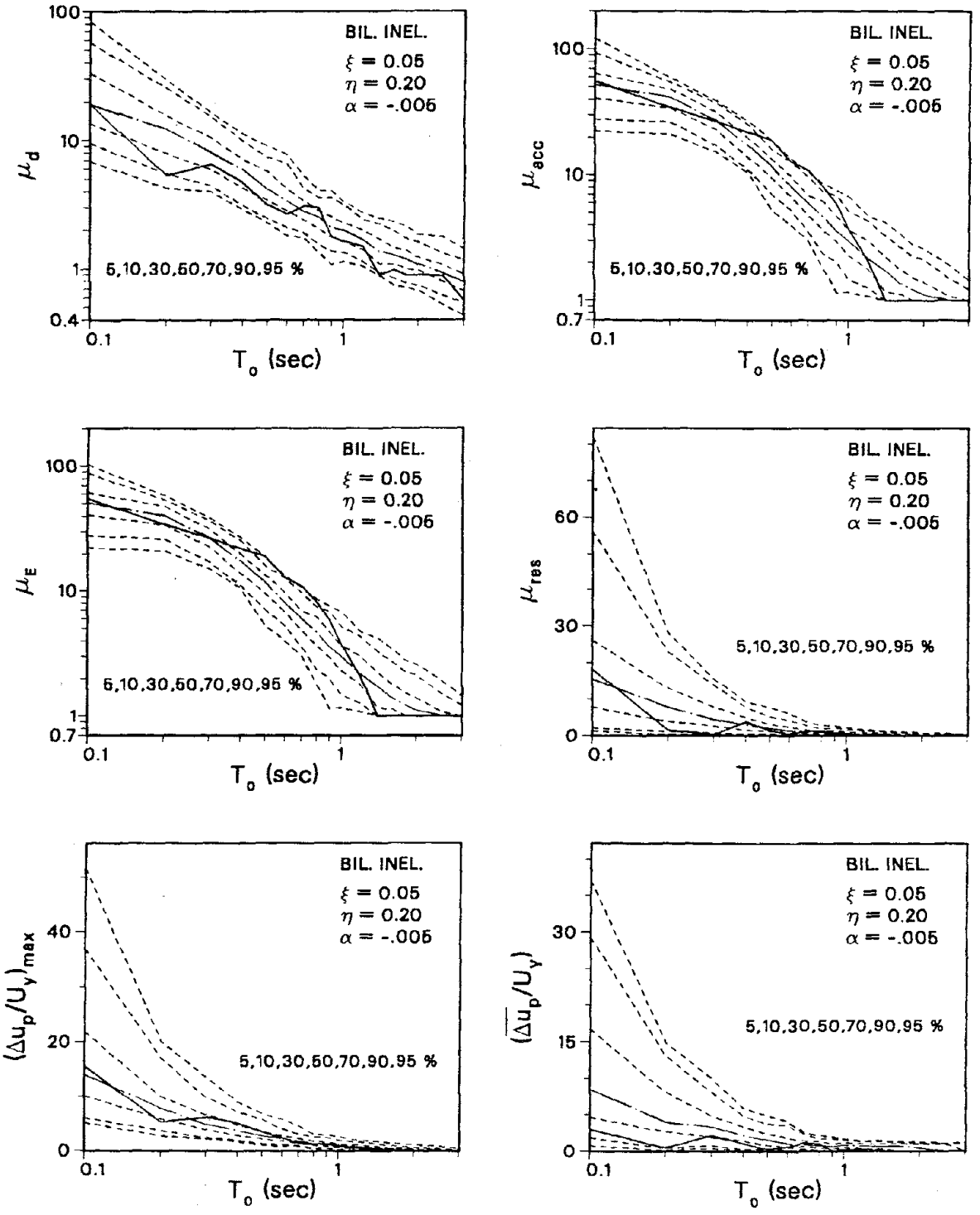

Fig. 8.20 Probabilistic Inelastic Response Spectra For the El Centro Target Record (ARMA(2,1) Earthquake Model and Bilinear Inelastic Structural Model)

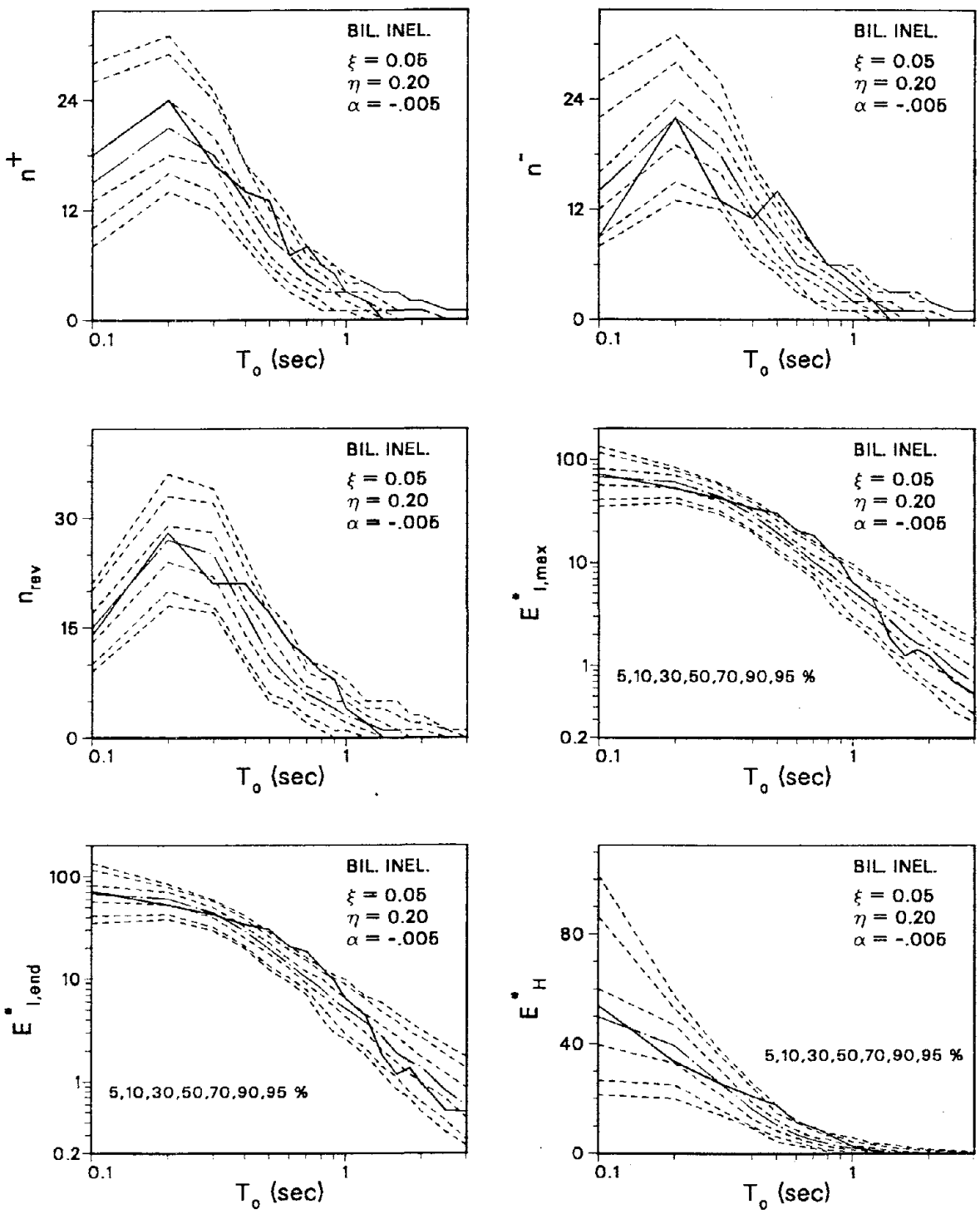

Fig. 8.20 (continued)

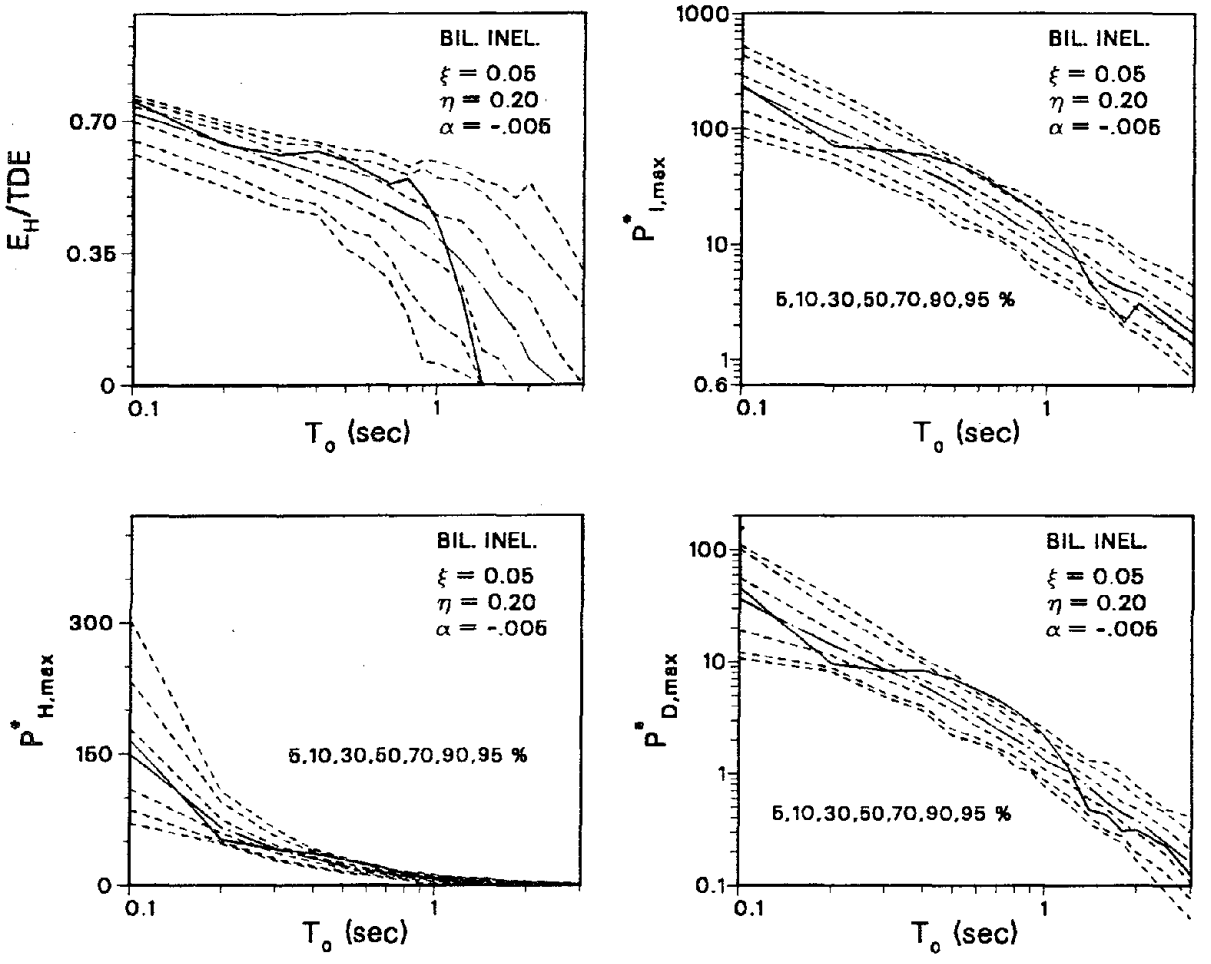

Fig. 8.20 (continued)

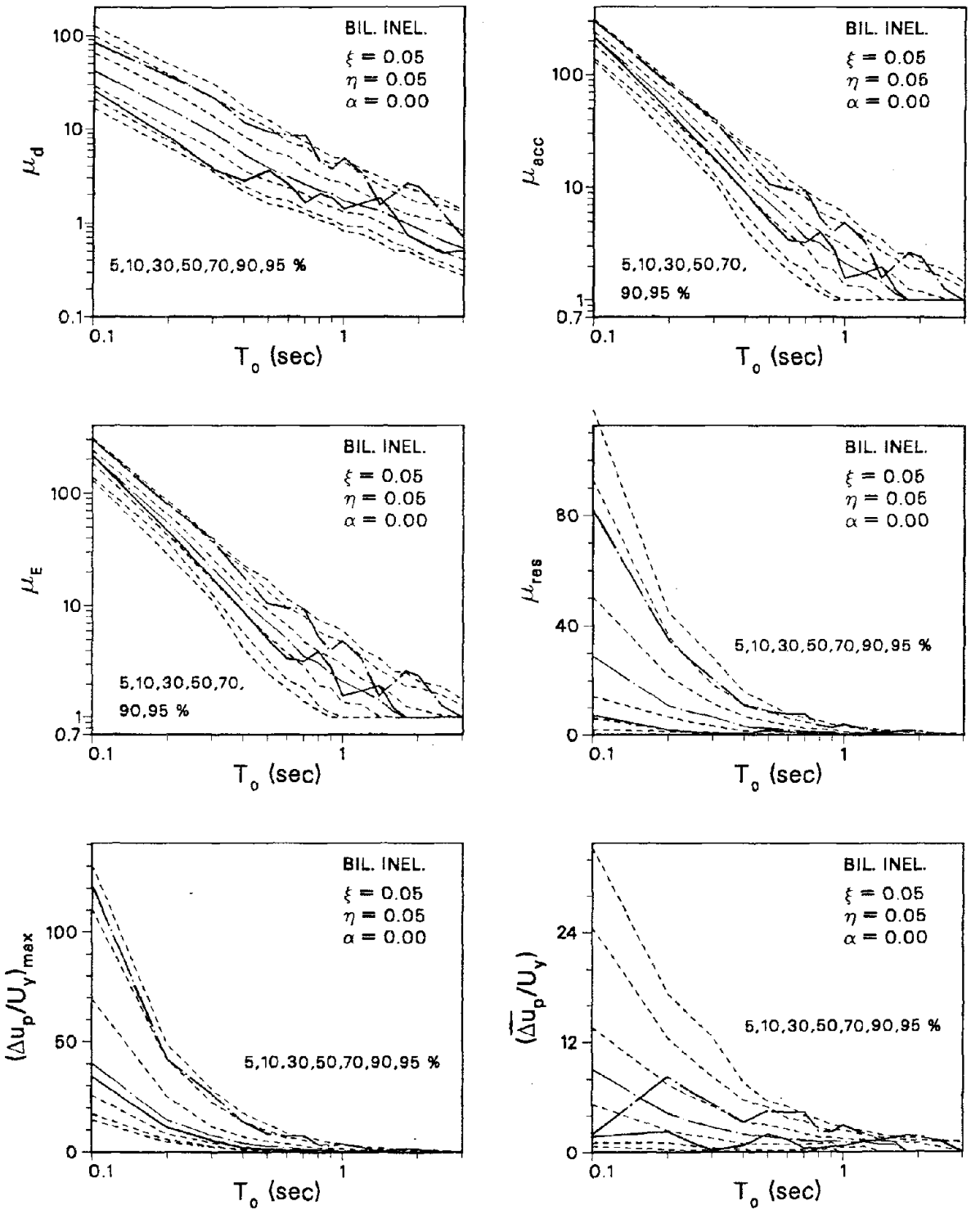

Fig. 8.21 Comparison Between Probabilistic Inelastic Response Spectra and Deterministic Inelastic Response Spectra Derived From Single Earthquake Realizations (ARMA(4,2) Model of E02NS)

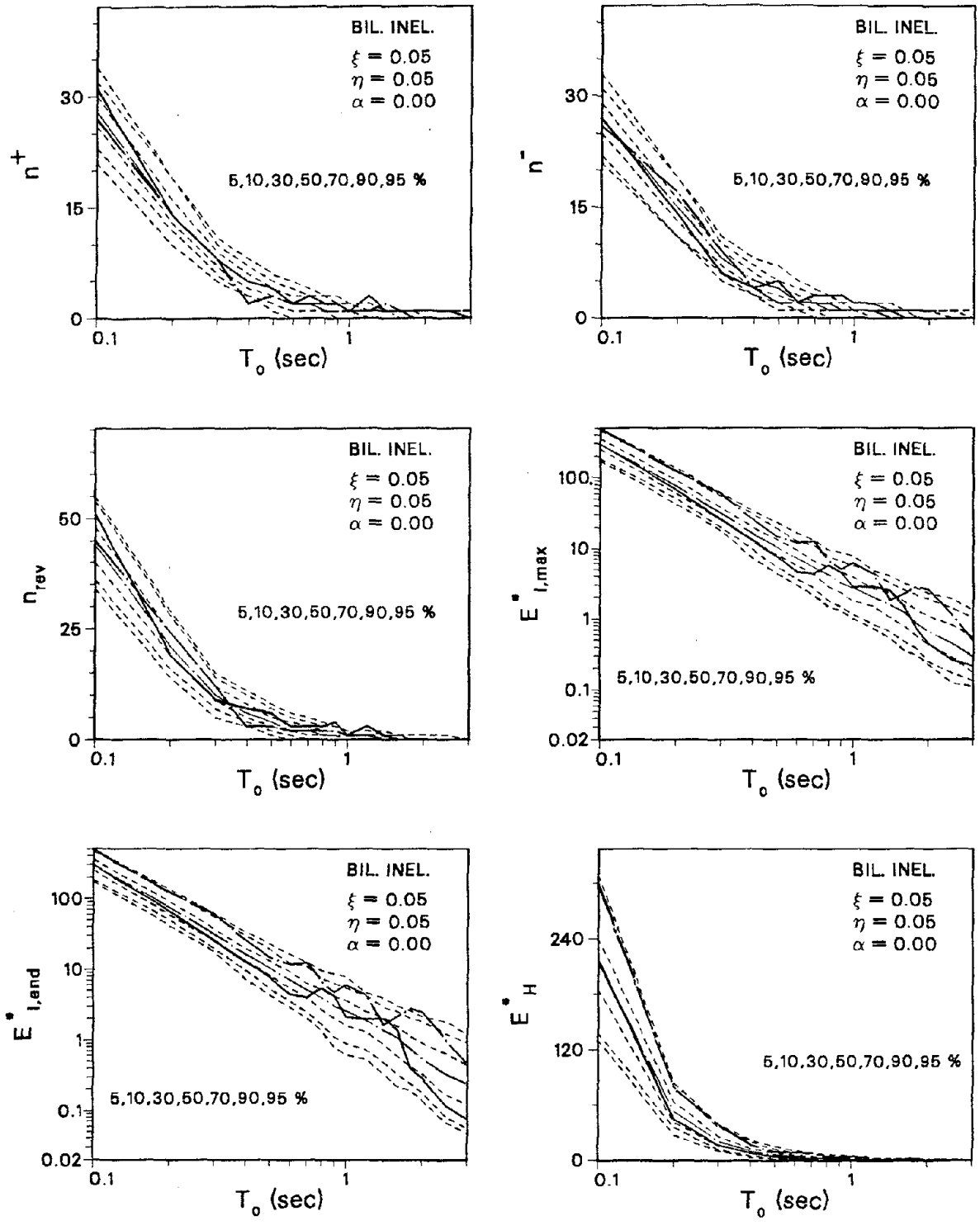

Fig. 8.21 (continued)

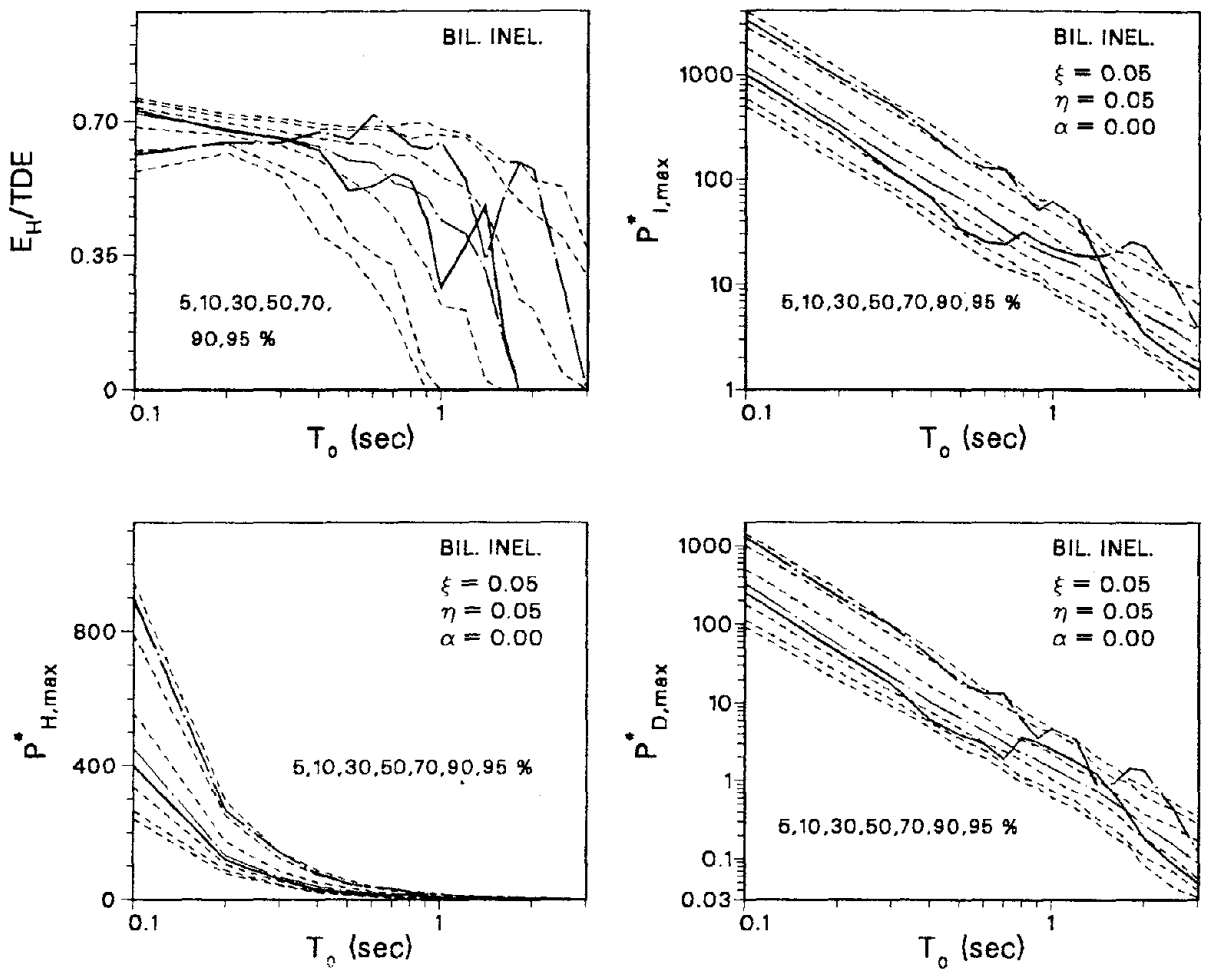

Fig. 8.21 (continued)

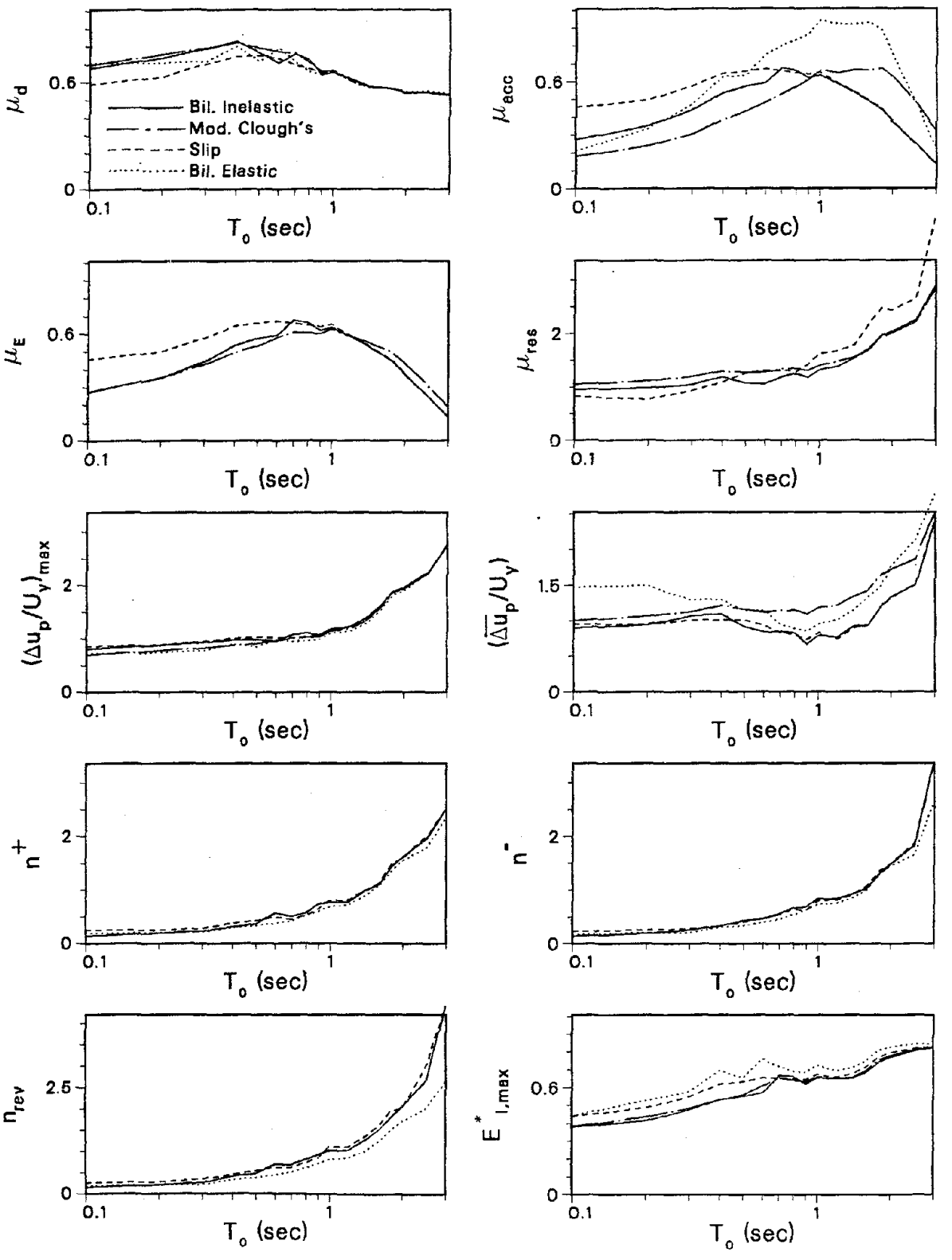

Fig. 8.22 C.O.V. of Inelastic Response Parameters for Different Hysteretic Models (ARMA(4,2) Simulation of E02NS)

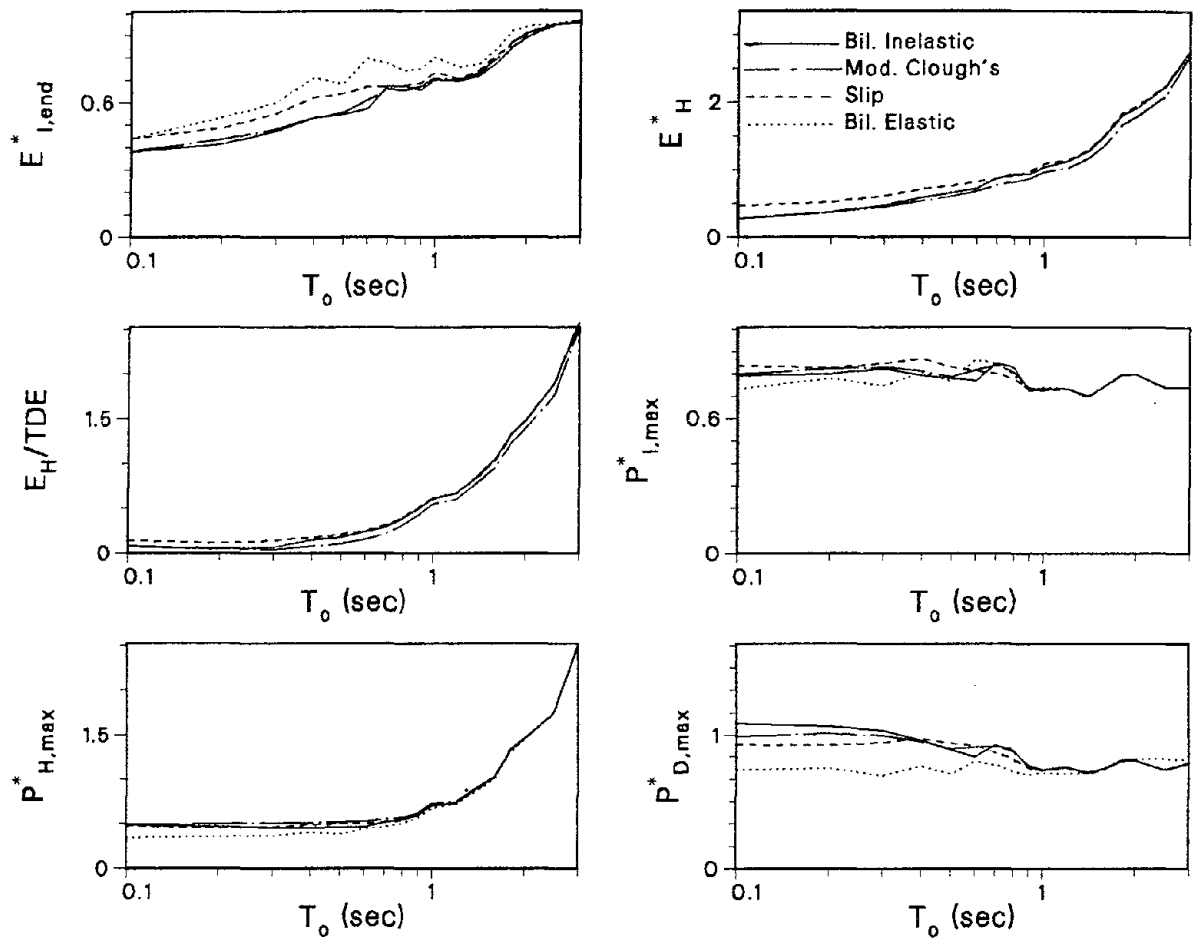

Fig. 8.22 (continued)

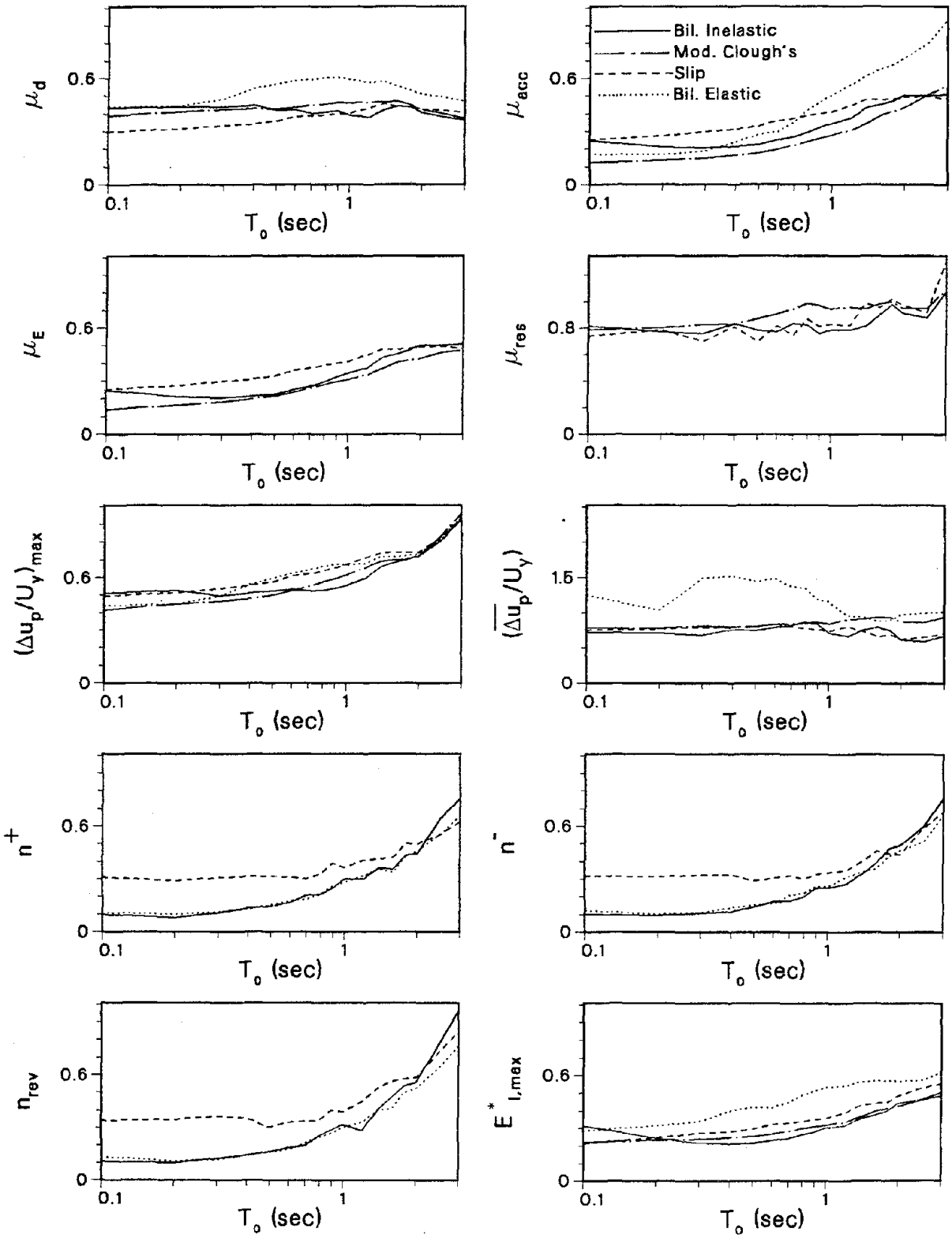

Fig. 8.23 C.O.V. of Inelastic Response Parameters for Different Hysteretic Models (ARMA(2,1) Simulation of El Centro 1940)

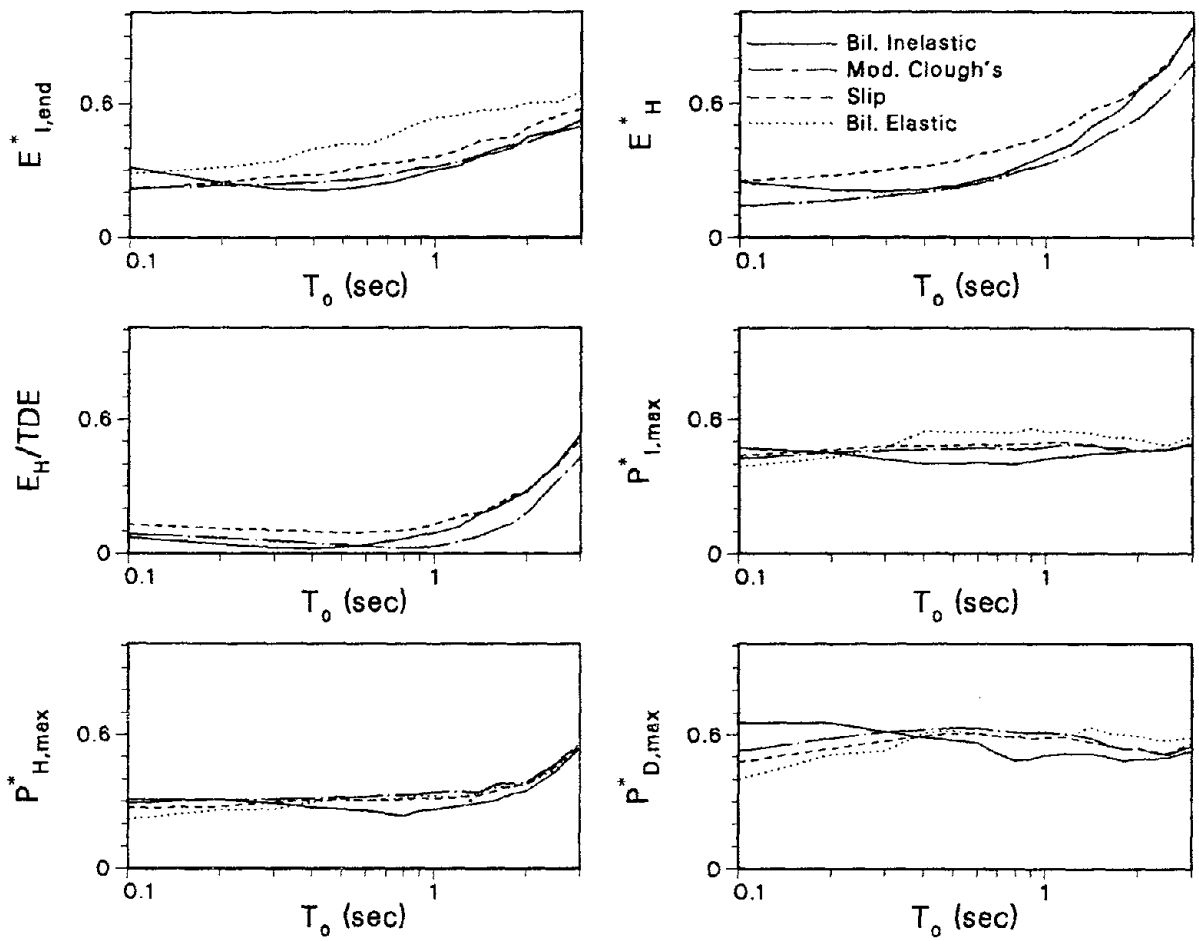

Fig. 8.23 (continued)

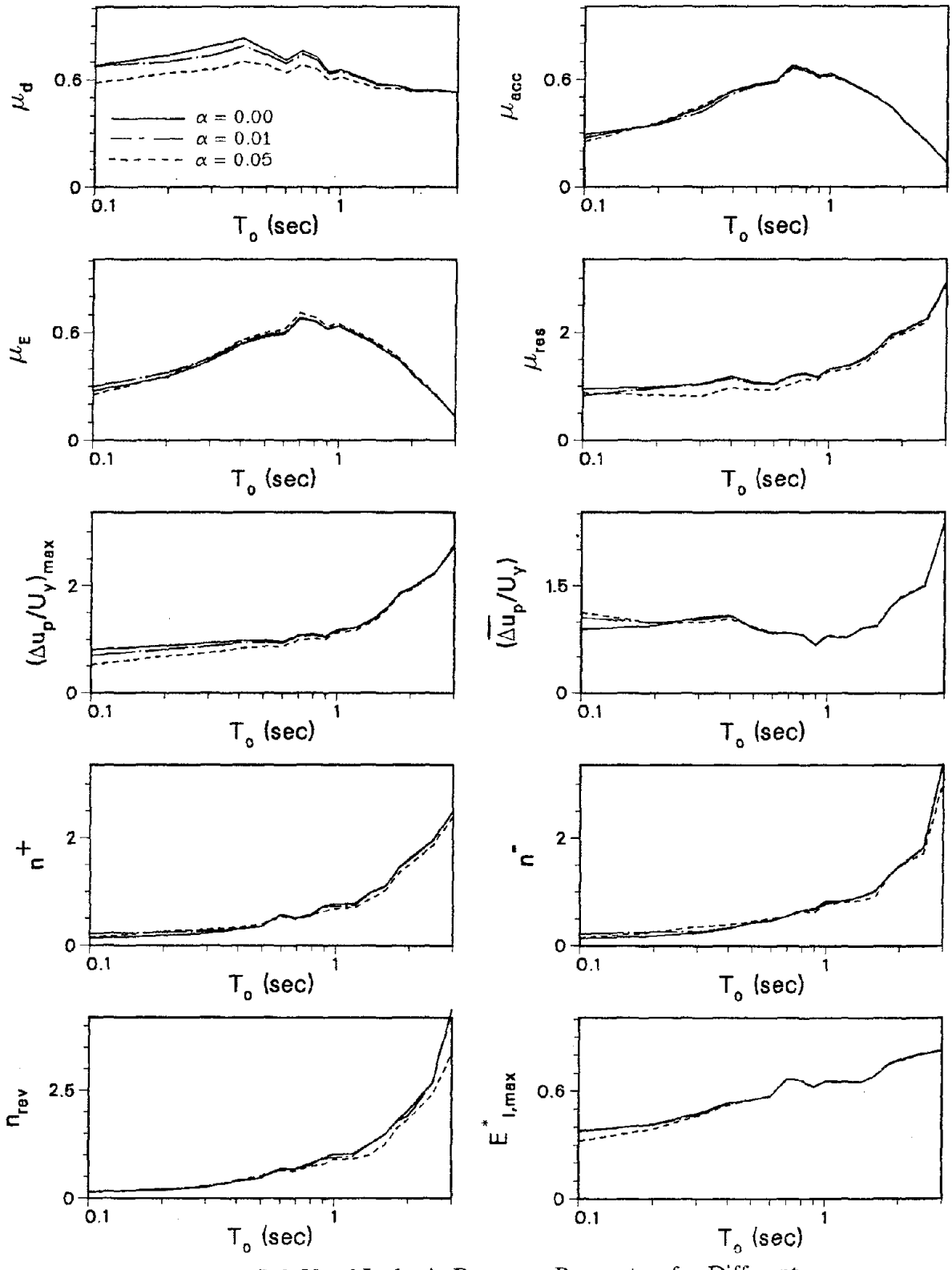

Fig. 8.24 C.O.V. of Inelastic Response Parameters for Different Values of Strain-Hardening Ratio (ARMA(4,2) Simulation of E02NS and Bilinear Inelastic Structural Model)

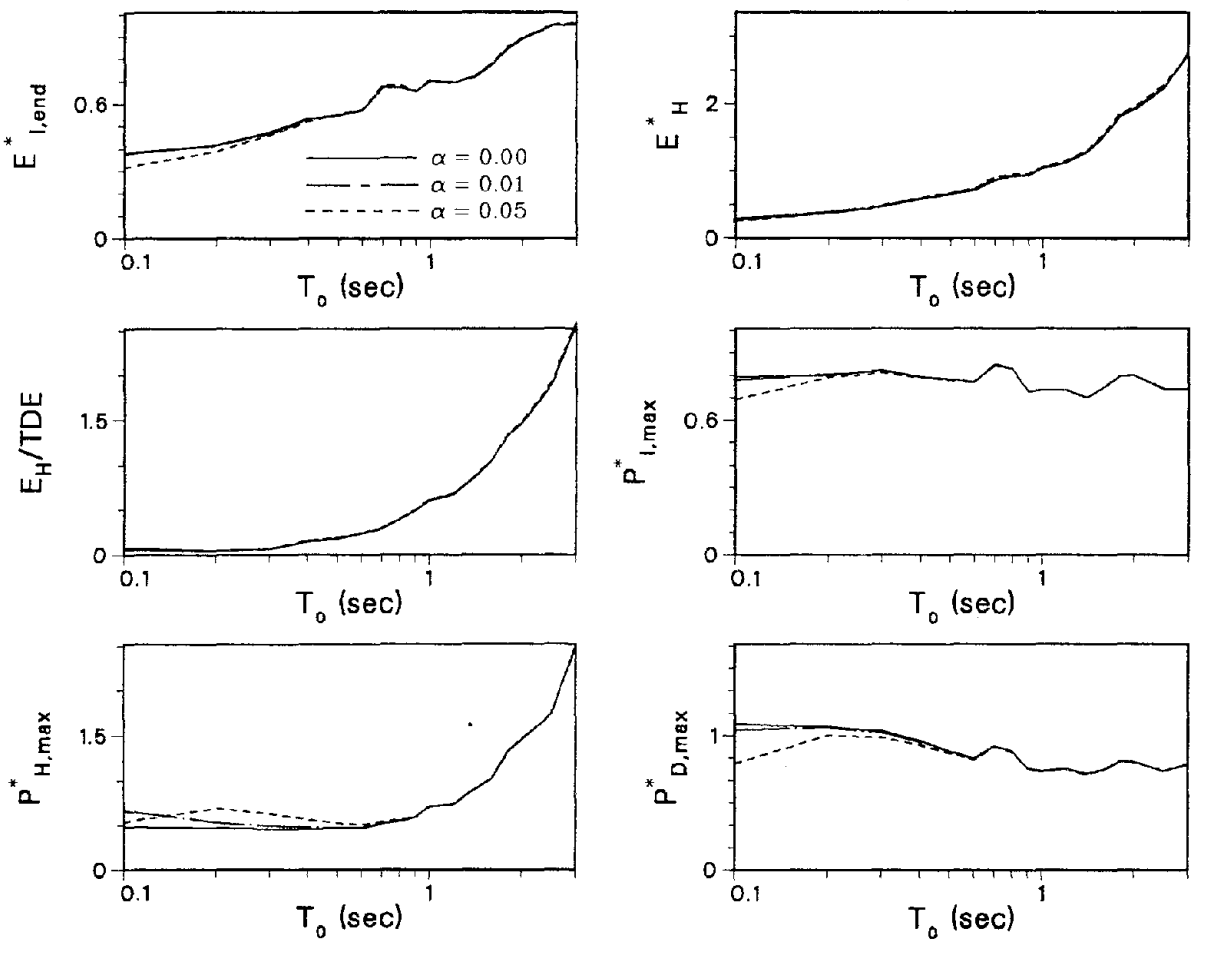

Fig. 8.24 (continued)

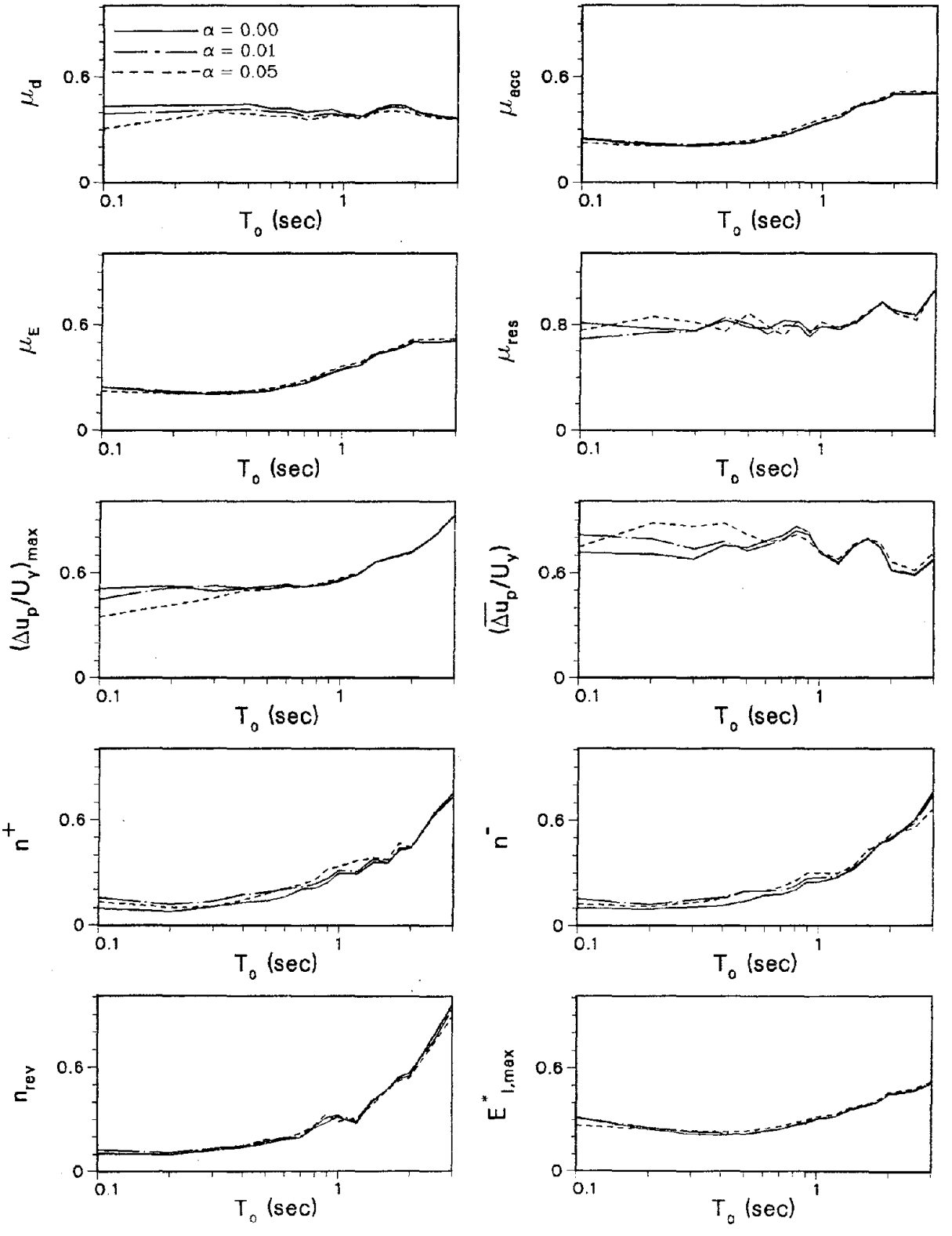

Fig. 8.25 C.O.V. of Inelastic Response Parameters for Different Values of Strain-Hardening Ratio (ARMA(2,1) Simulation of El Centro and Bilinear Inelastic Structural Model)

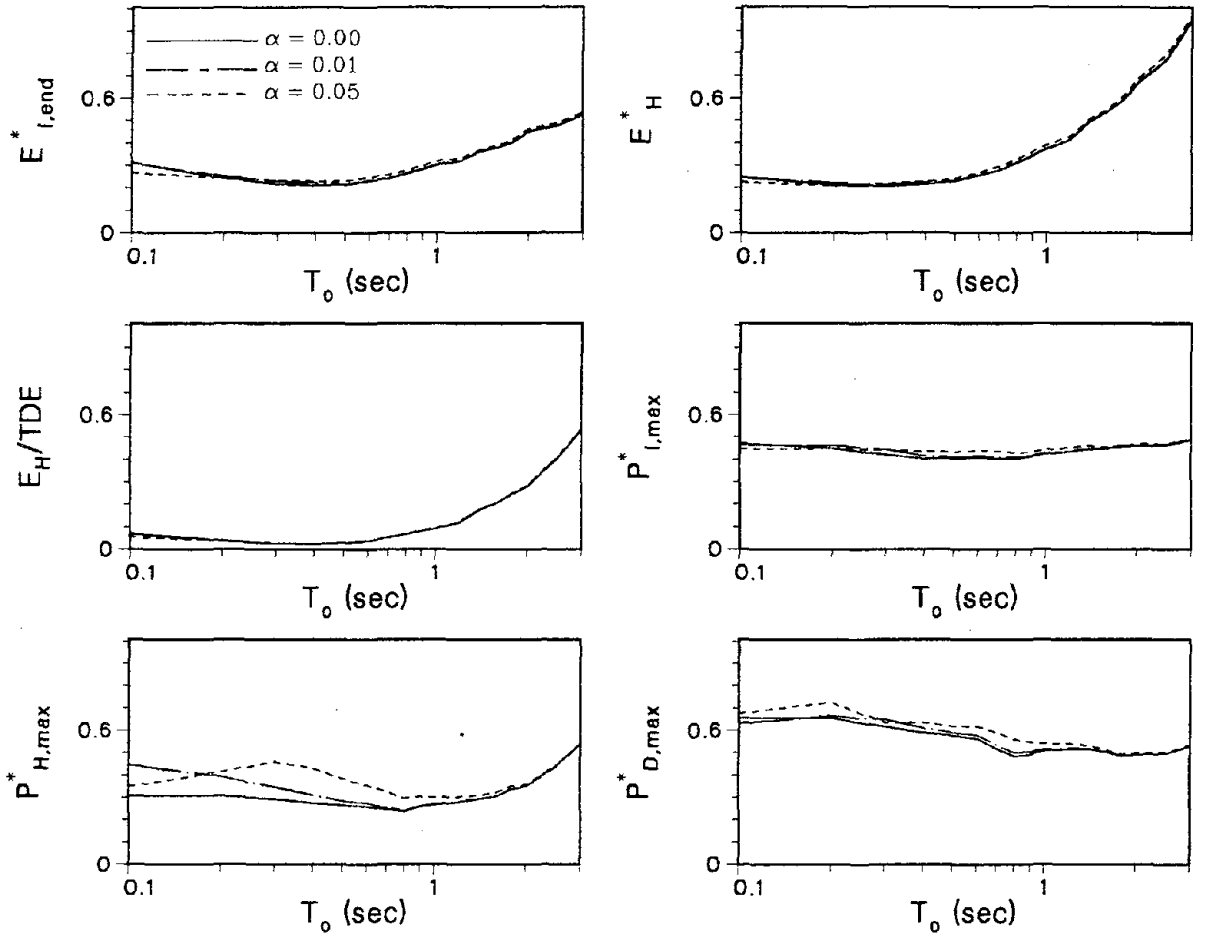

Fig. 8.25 (continued)

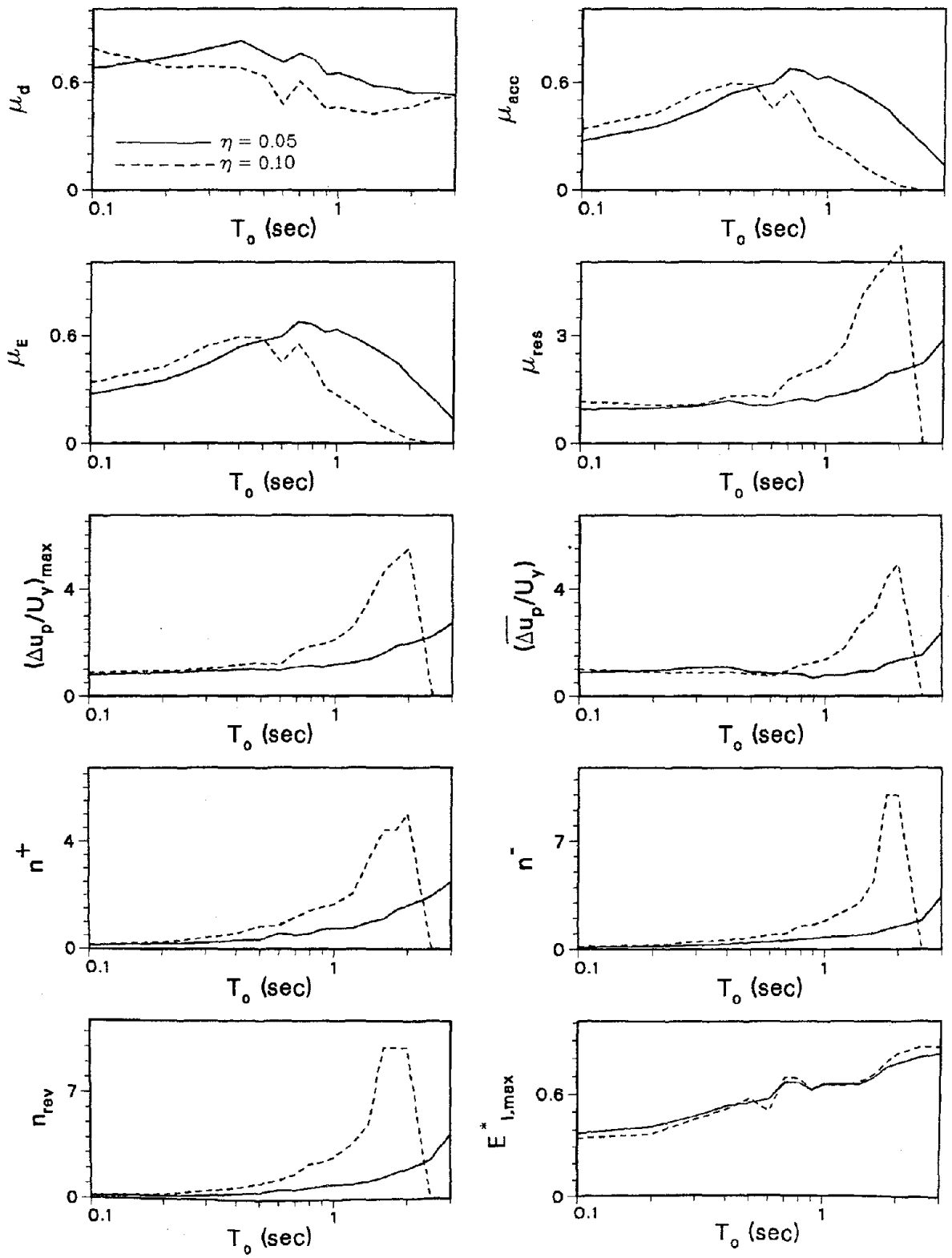

Fig. 8.26 C.O.V. of Inelastic Response Parameters for Different Strength Levels (ARMA(4,2) Simulation of E02NS and Bilinear Inelastic Structural Model)

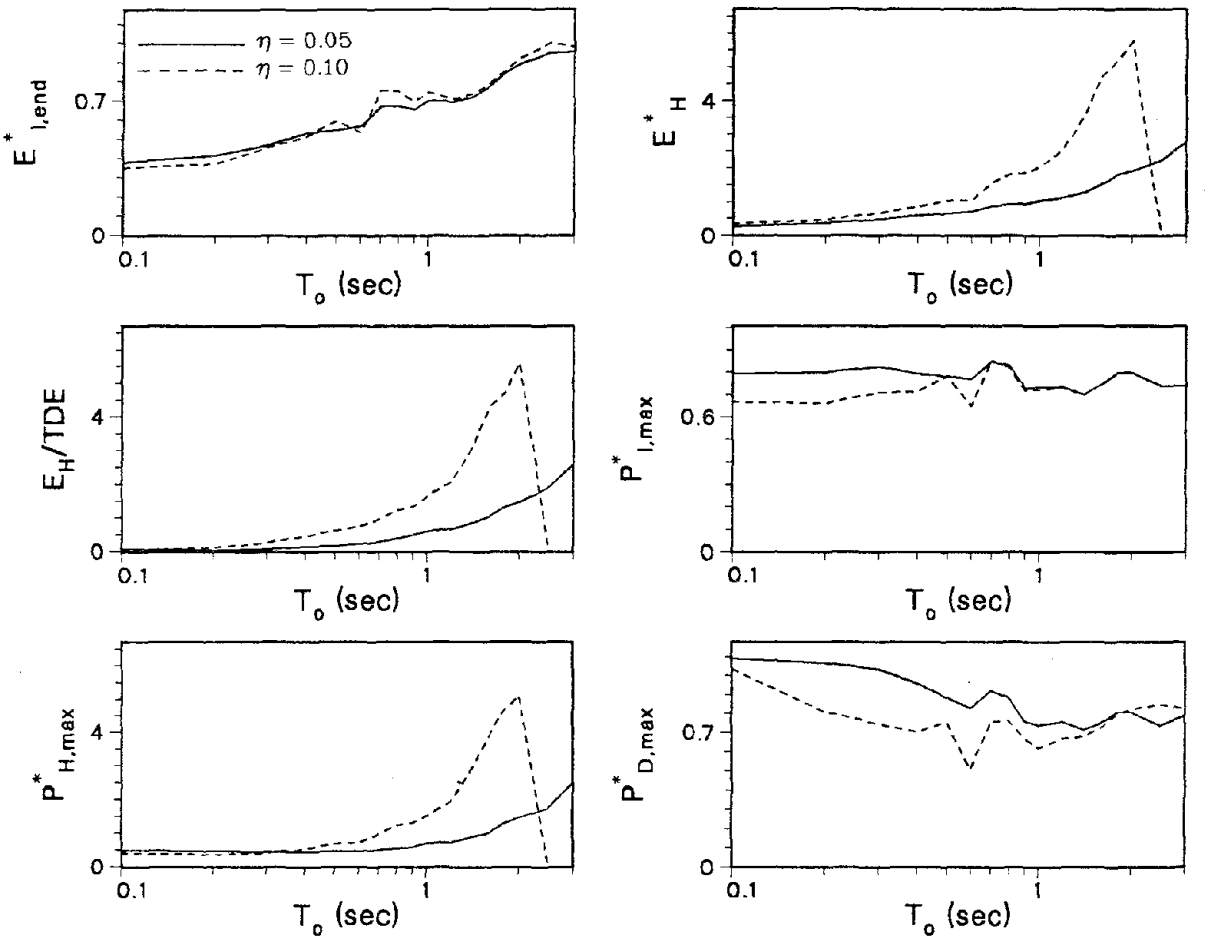

Fig. 8.26 (continued)

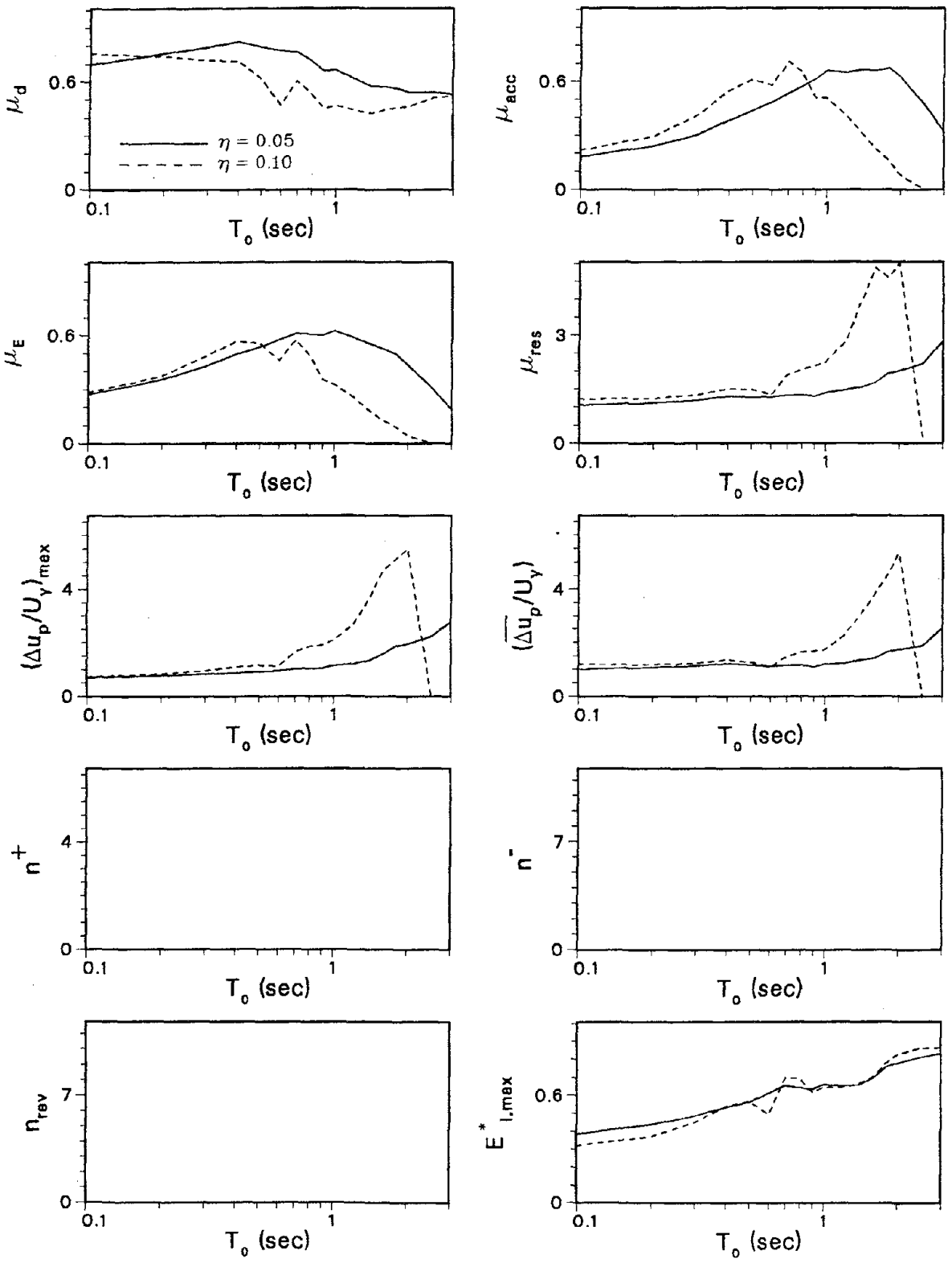

Fig. 8.27 C.O.V. of Inelastic Response Parameters for Different Strength Levels (ARMA(4,2) Simulation of E02NS and Modified Clough's Structural Model)

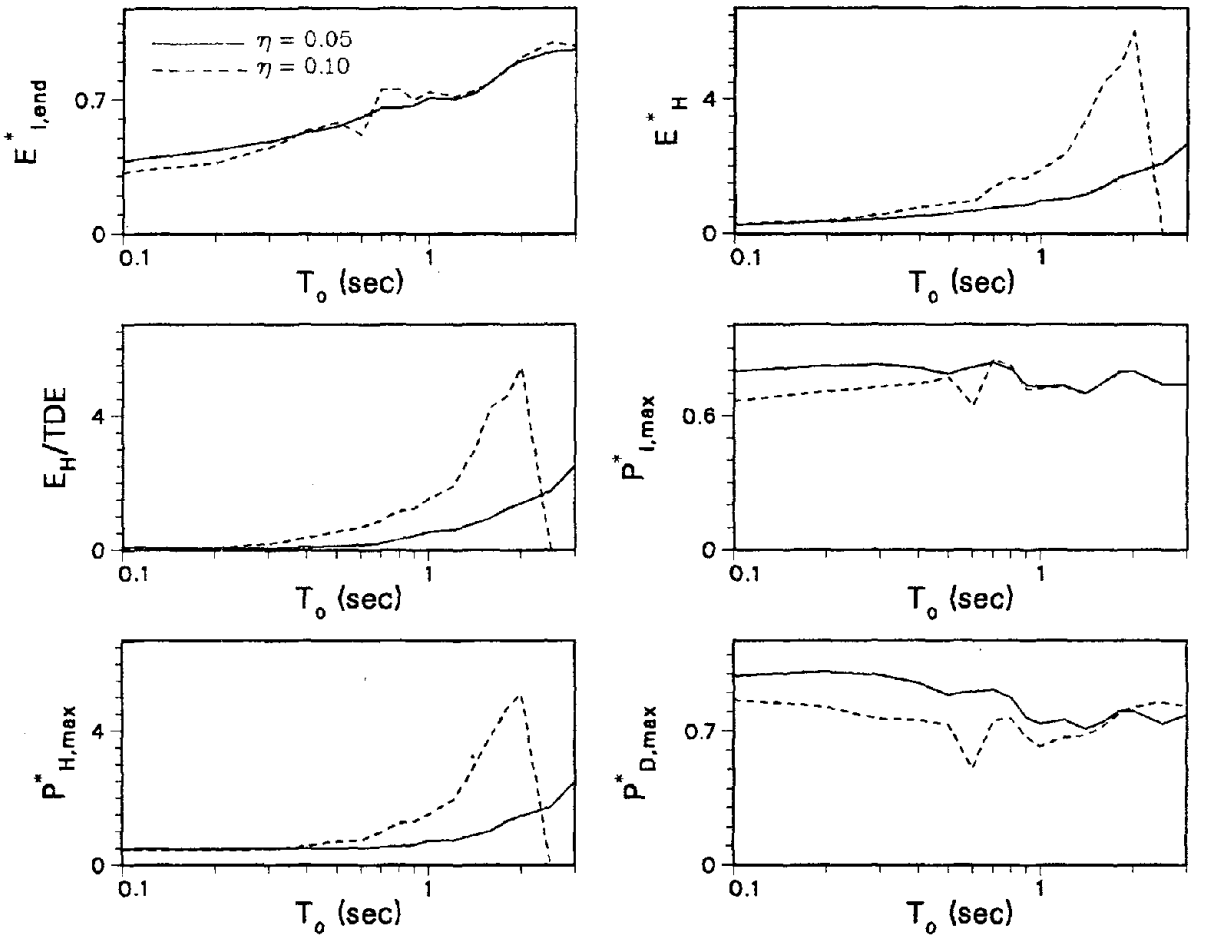

Fig. 8.27 (continued)

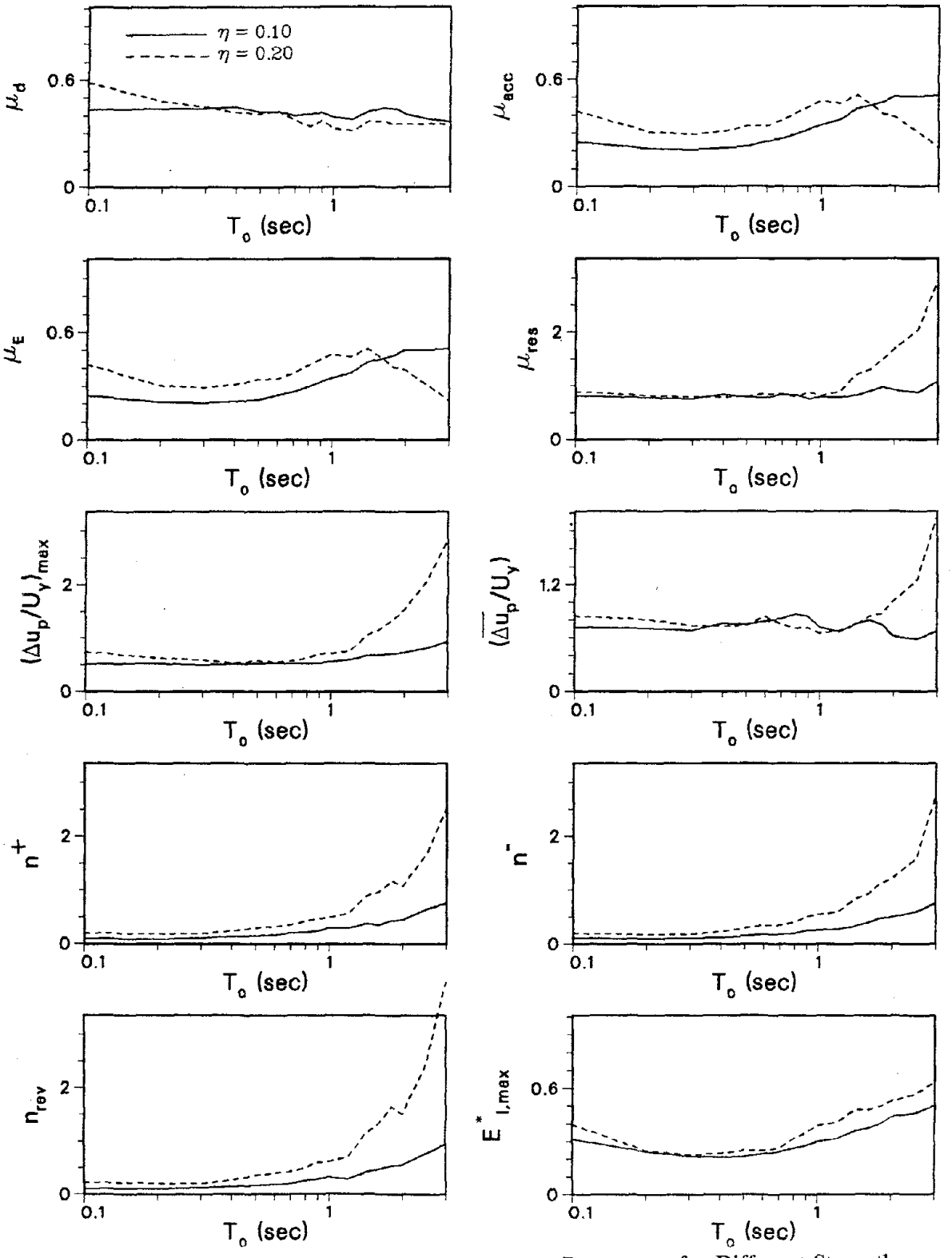

Fig. 8.28 C.O.V. of Inelastic Response Parameters for Different Strength Levels (ARMA(2,1) Simulation of El centro and Bilinear Inelastic Structural Model)

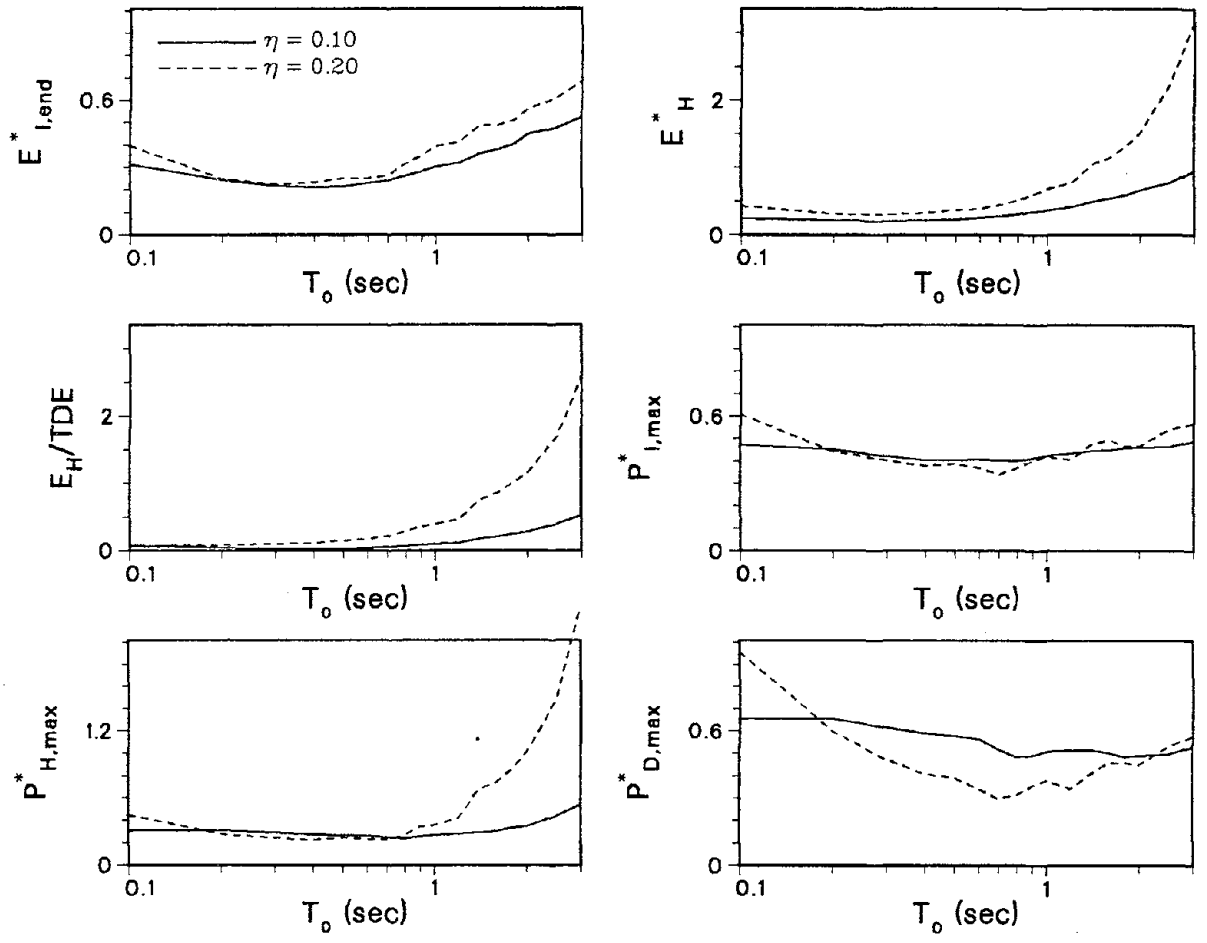

Fig. 8.28 (continued)

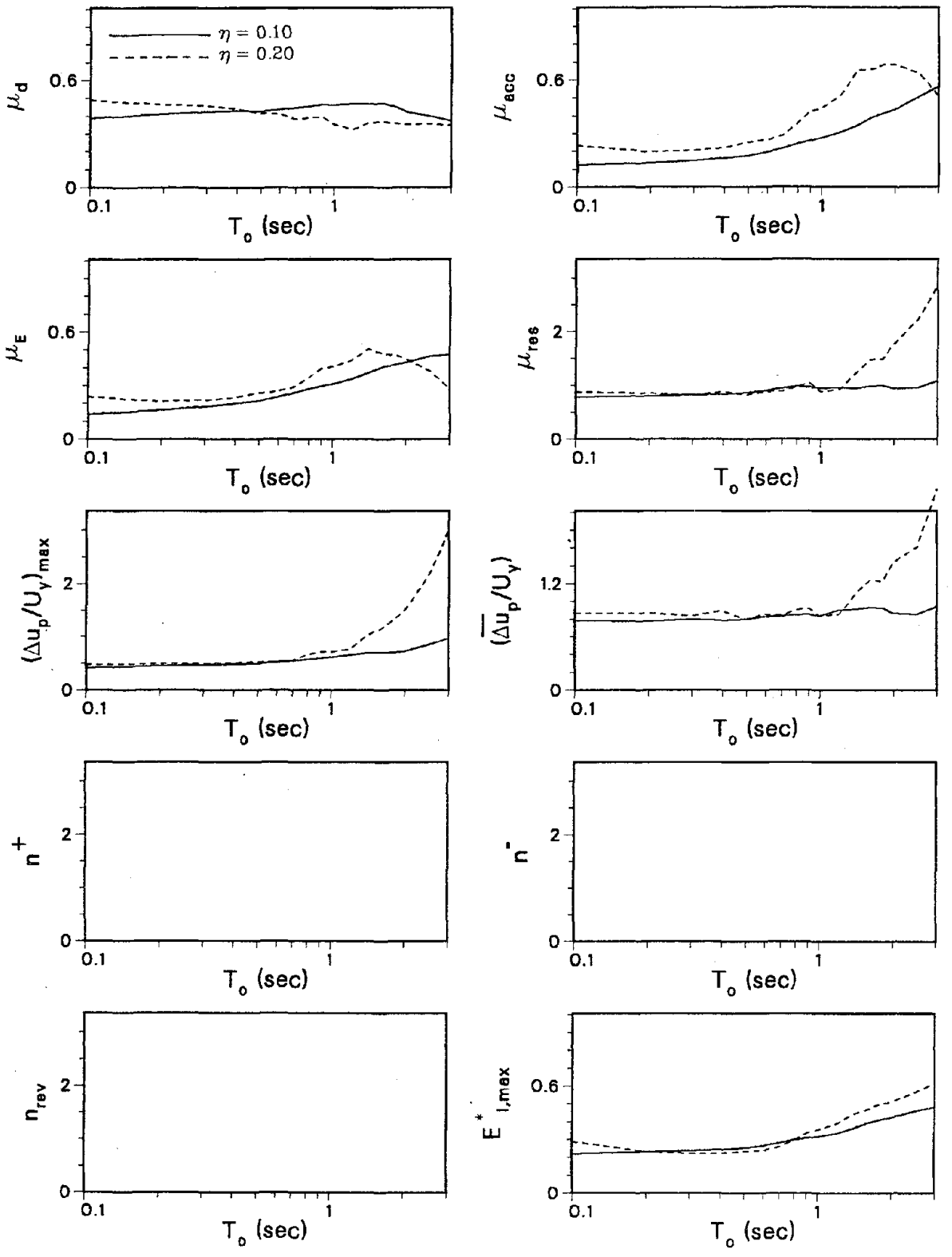

Fig. 8.29 C.O.V. of Inelastic Response Parameters for Different Strength Levels (ARMA(2,1) Simulation of El Centro and Modified Clough's Structural Model)

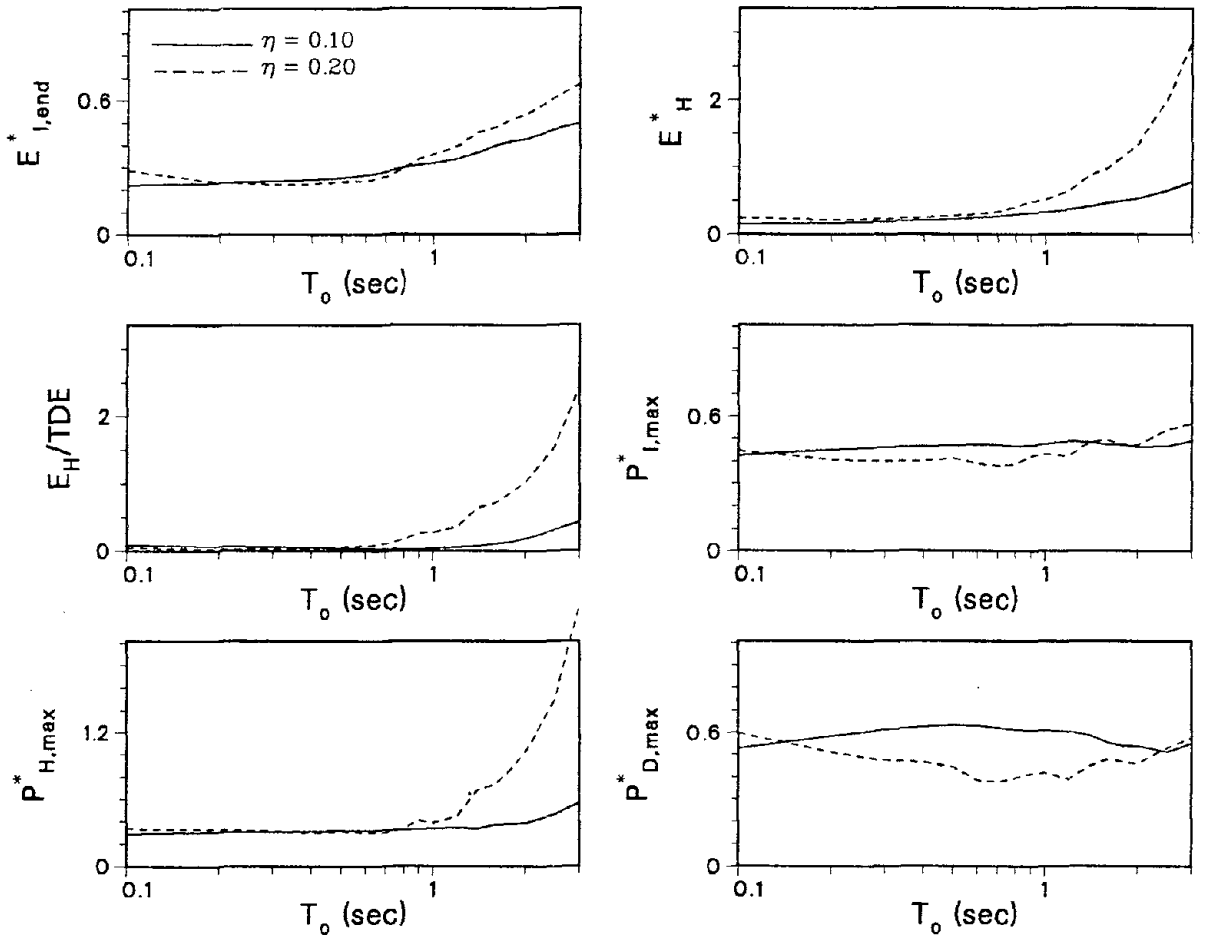

Fig. 8.29 (continued)

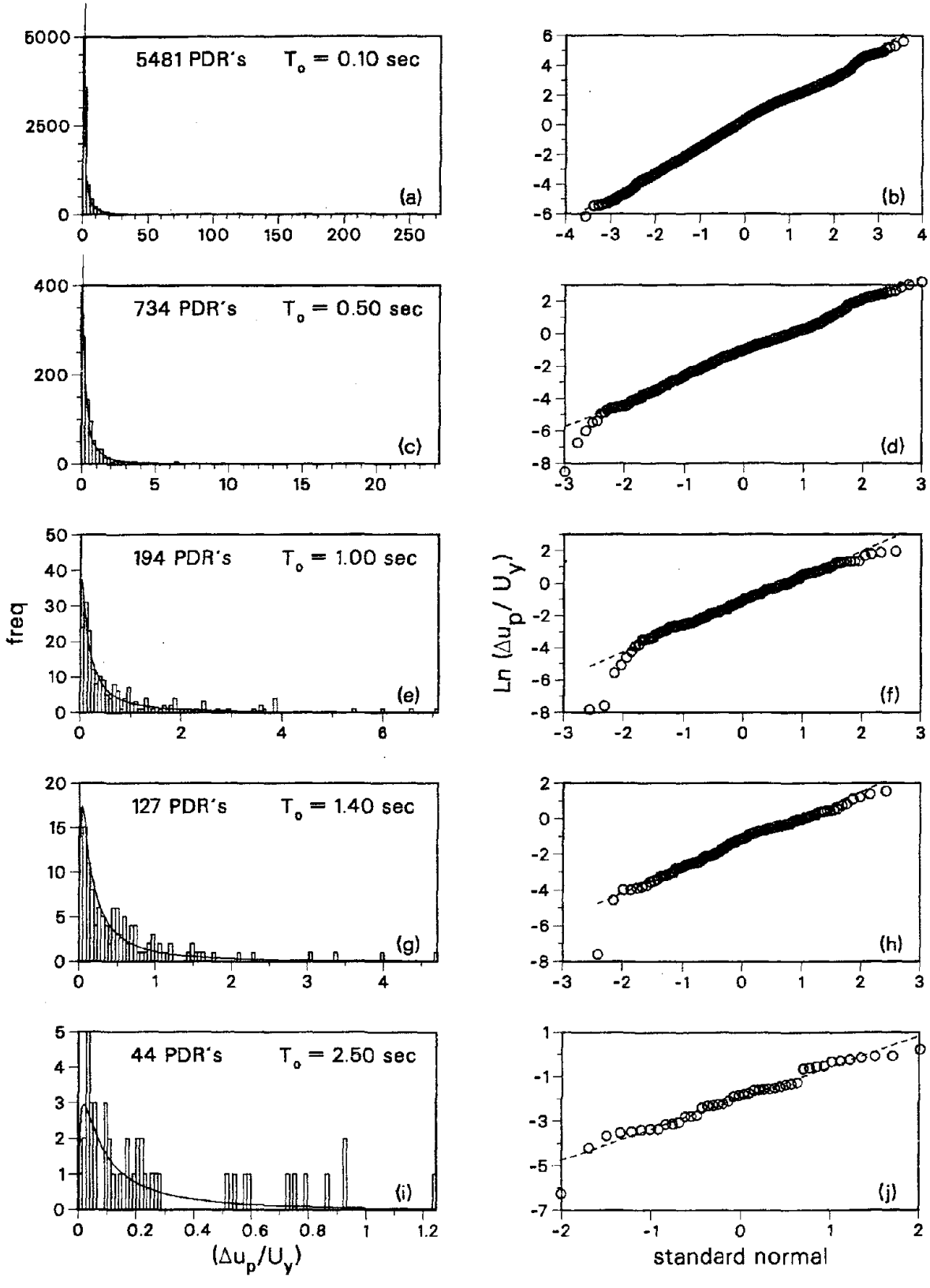

Fig. 8.30 Probability Distribution of Normalized Plastic Deformation Ranges (ARMA(4,2) Simulation of E02NS and Bilinear Inelastic Structural Model with ξ = 0.05, η = 0.05 and α = 0.00)

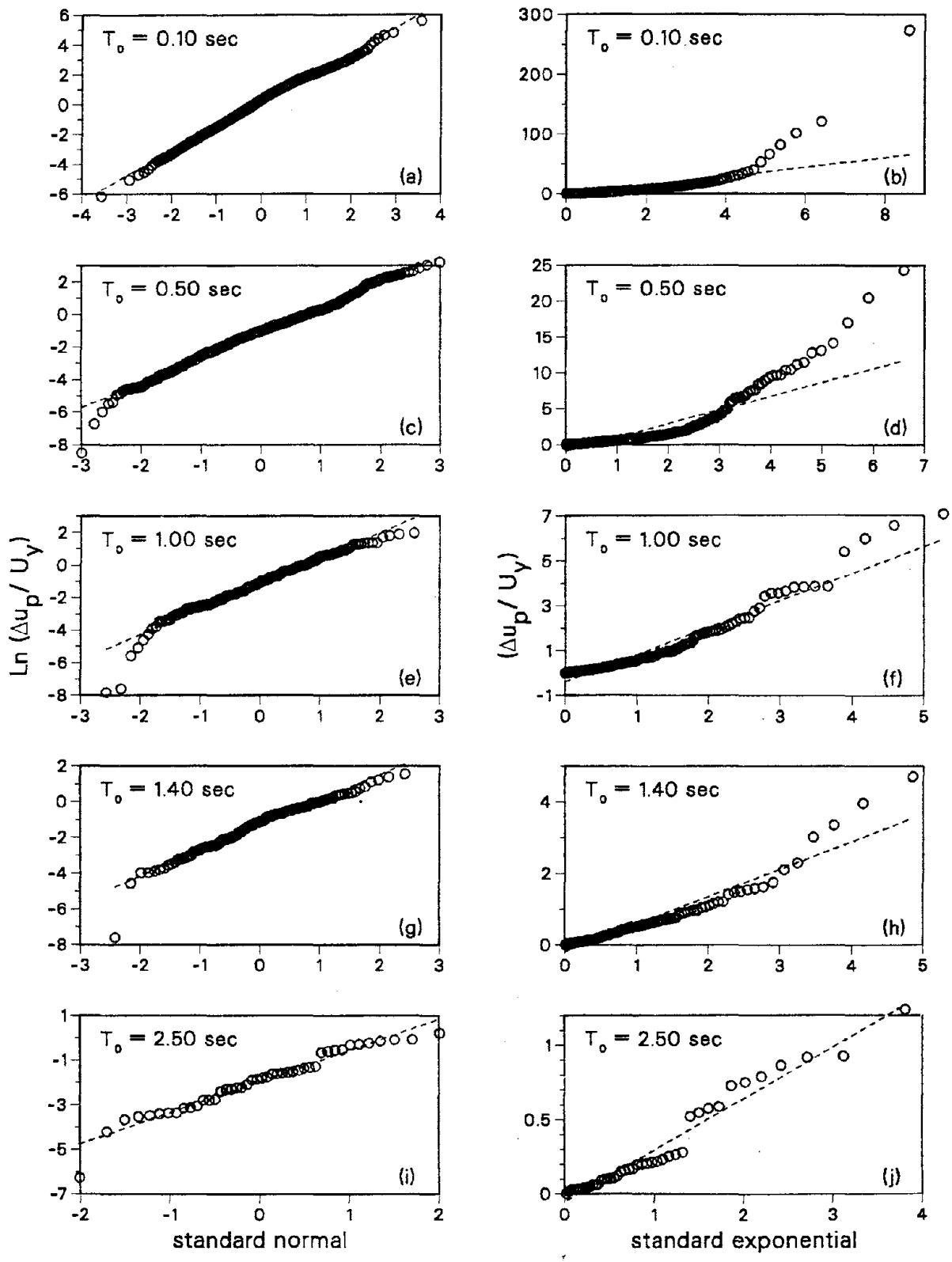

Fig. 8.31 Comparison of Lognormal and Shifted Exponential Probability Distribution Fits (ARMA(4,2) Simulation of E02NS and Bilinear Inelastic Structural Model with $\xi = 0.05$, $\eta = 0.05$ and $\alpha = 0.00$)

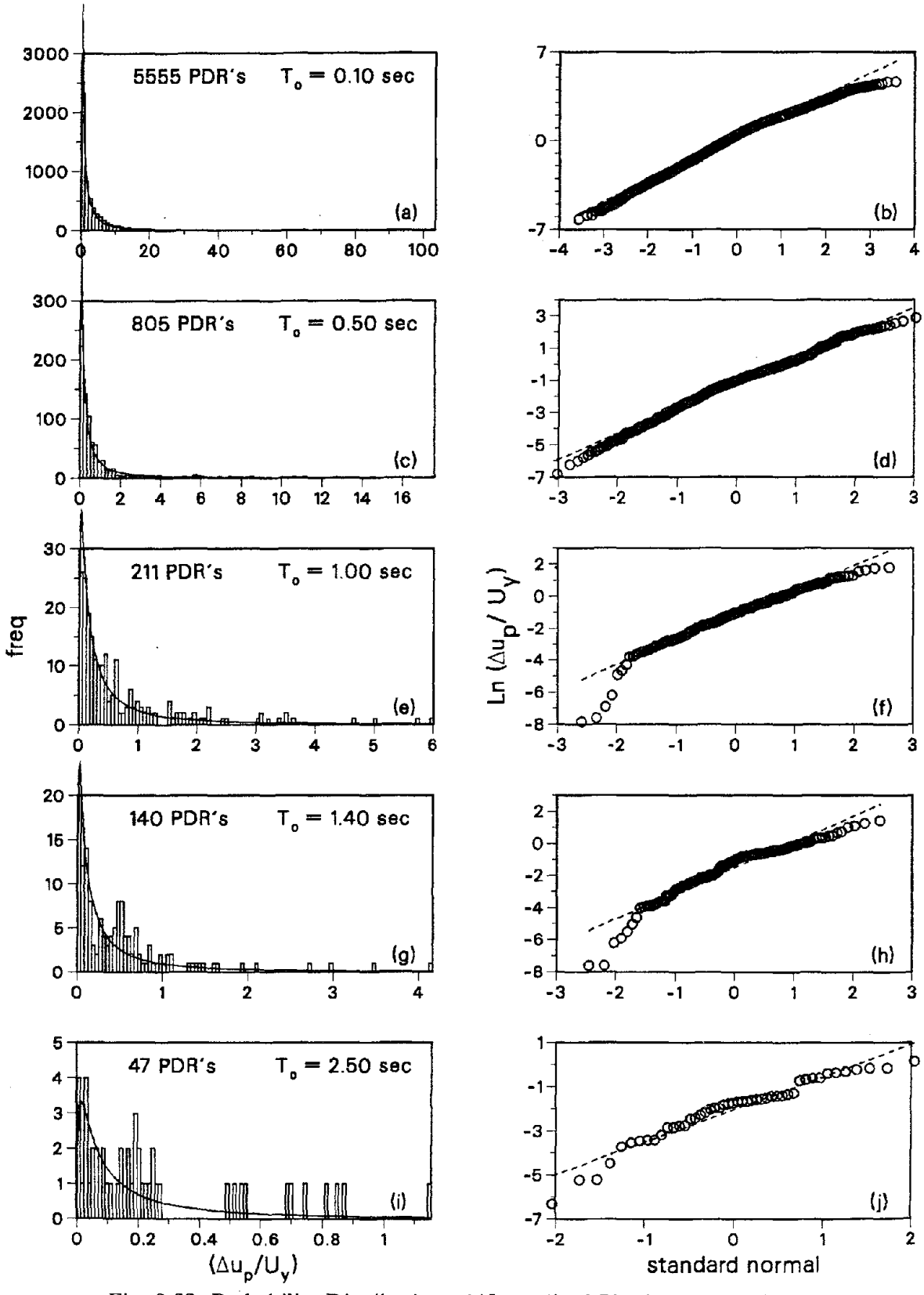

Fig. 8.32 Probability Distribution of Normalized Plastic Deformation Ranges (ARMA(4,2) Simulation of E02NS and Bilinear Inelastic Structural Model with ξ = 0.05, η = 0.05 and α = 0.05)

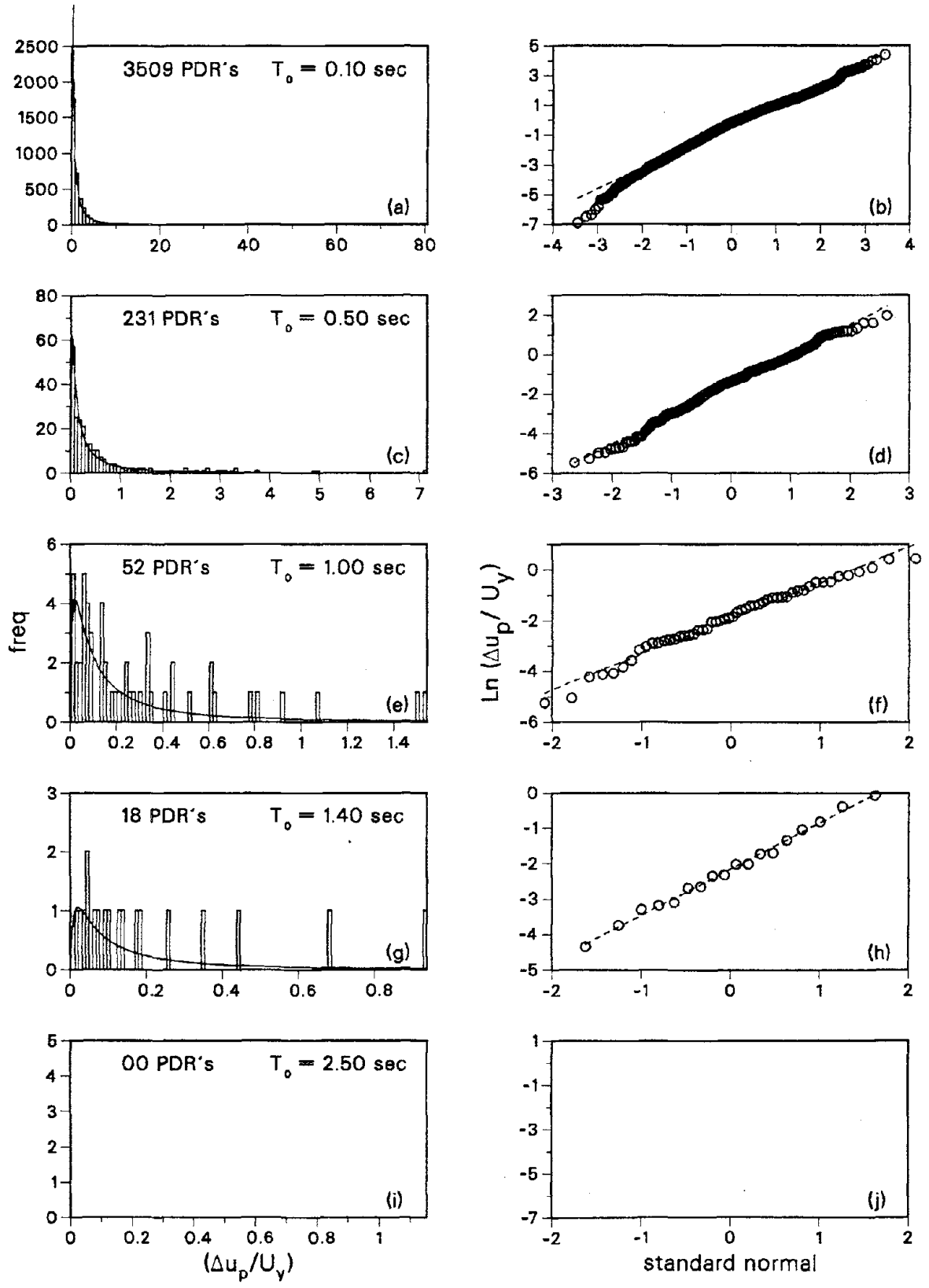

Fig. 8.33 Probability Distribution of Normalized Plastic Deformation Ranges (ARMA(4,2) Simulation of E02NS and Bilinear Inelastic Structural Model with $\xi = 0.05$, $\eta = 0.10$ and $\alpha = 0.00$)

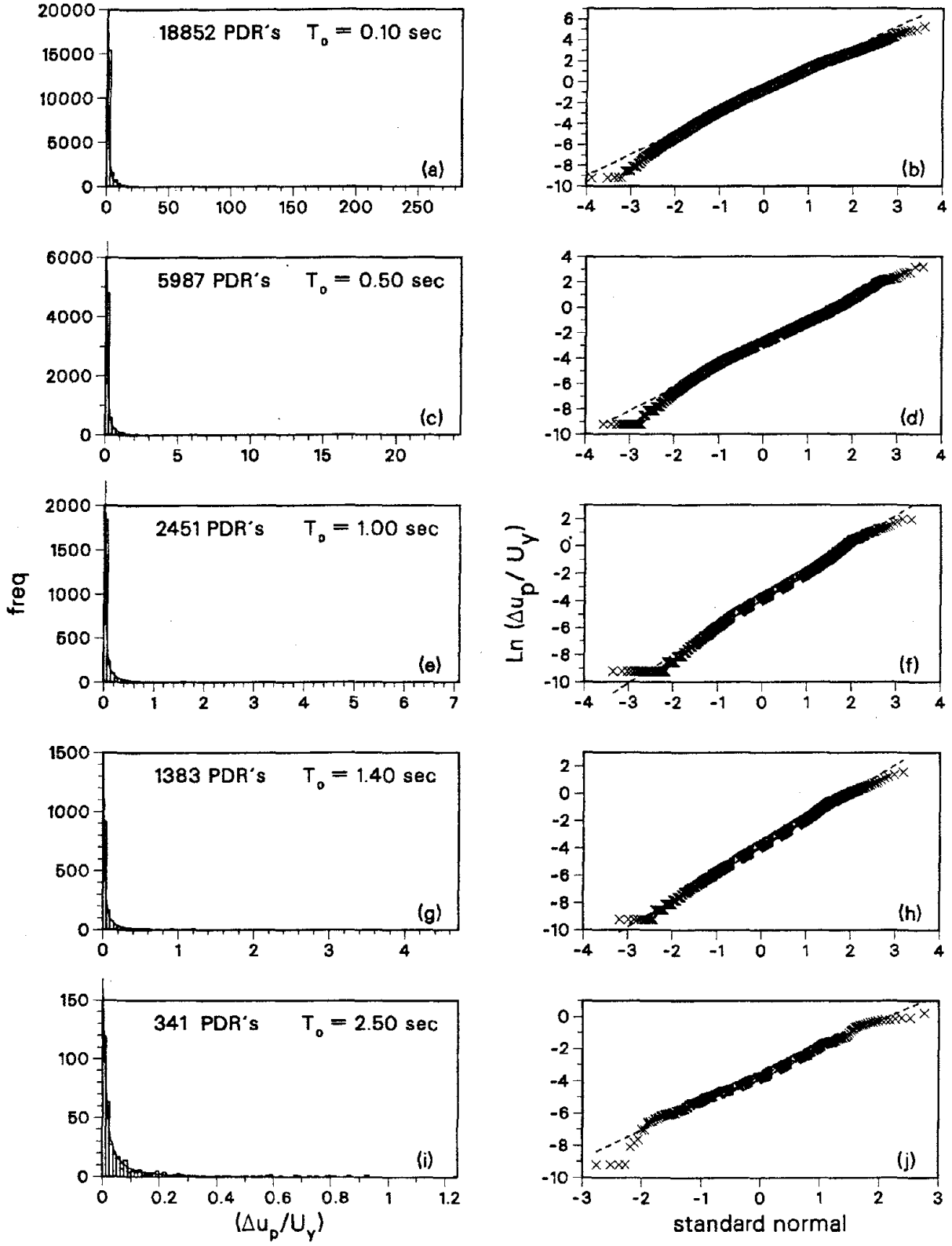

Fig. 8.34 Probability Distribution of Normalized Plastic Deformation Ranges (ARMA(4,2) Simulation of E02NS and Modified Clough's Structural Model with ξ = 0.05, η = 0.05 and α = 0.00)

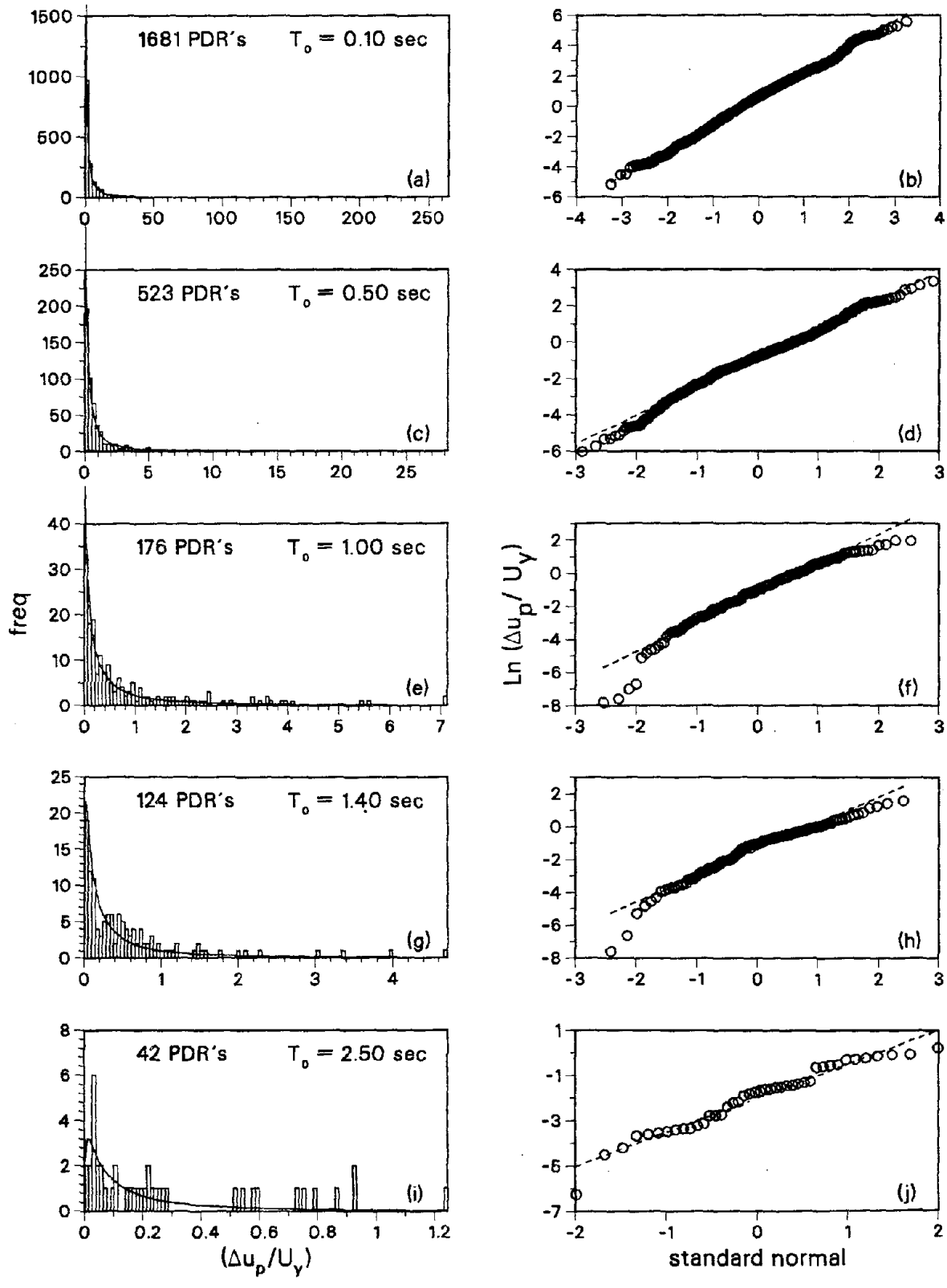

Fig. 8.35 Probability Distribution of Normalized Plastic Deformation Ranges (ARMA(4,2) Simulation of E02NS and Slip Structural Model with ξ = 0.05, η = 0.05 and α = 0.00)

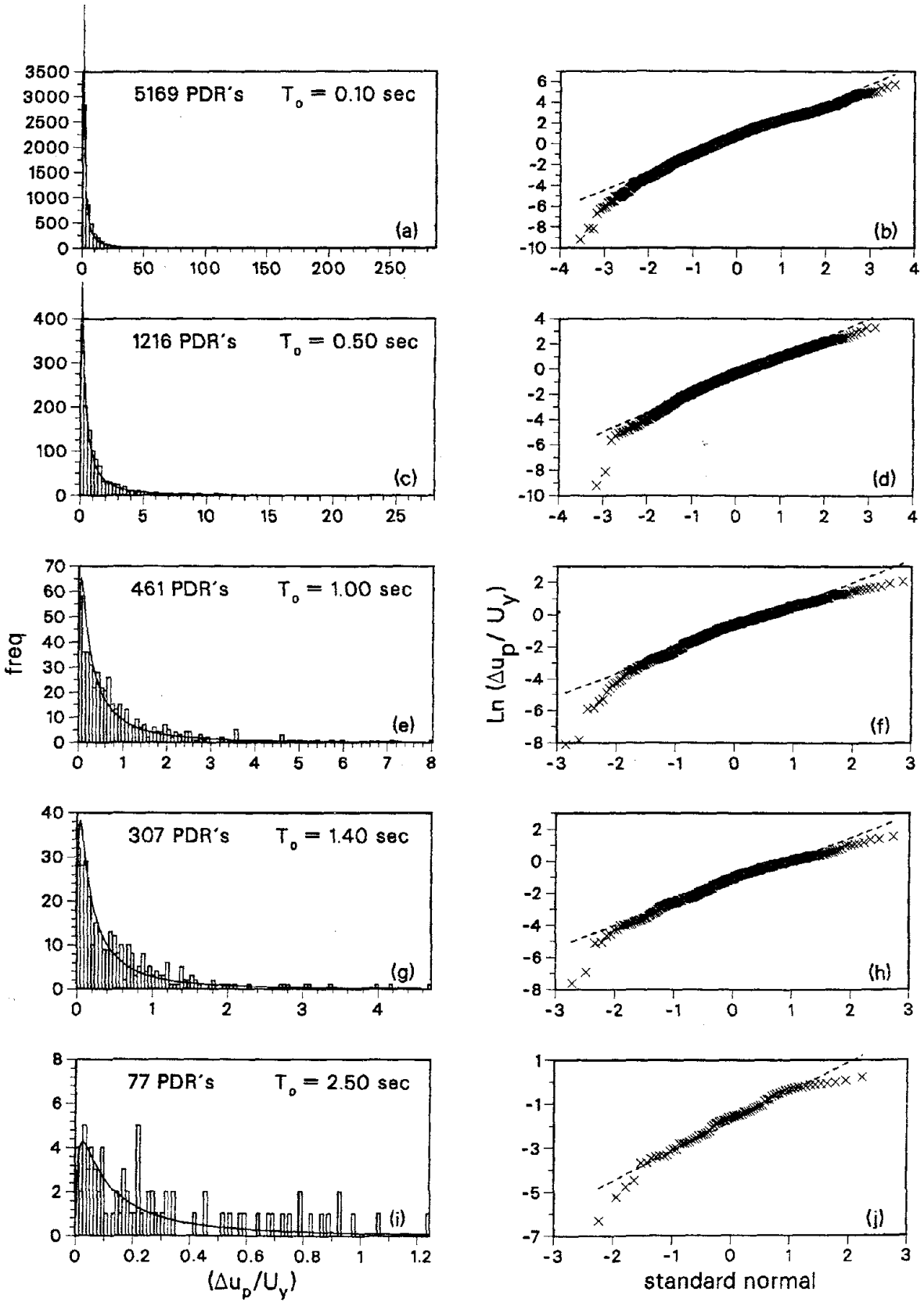

Fig. 8.36 Probability Distribution of Normalized Plastic Deformation Ranges (ARMA(4,2) Simulation of E02NS and Bilinear Elastic Structural Model with $\xi = 0.05$, $\eta = 0.05$ and $\alpha = 0.00$)

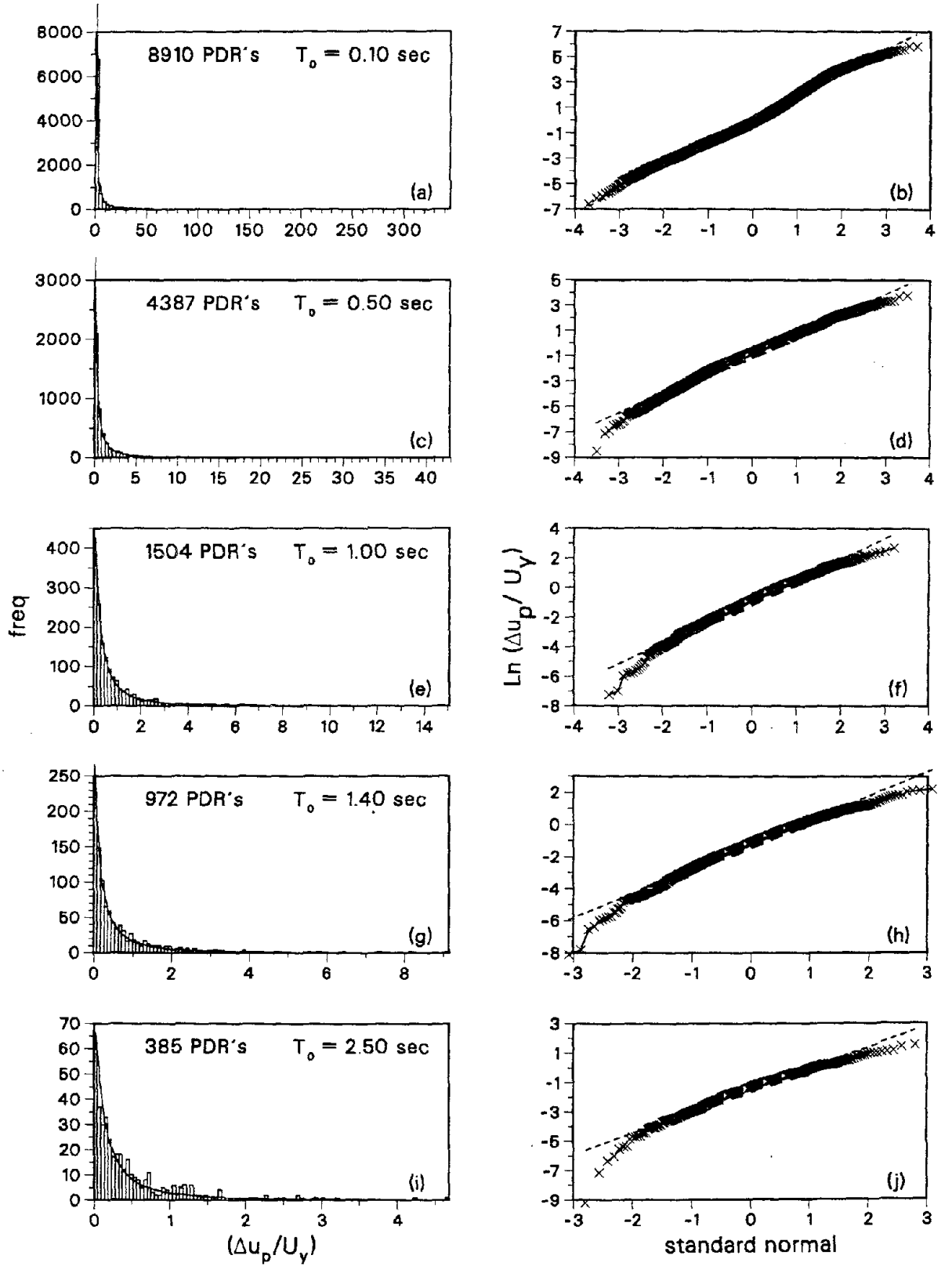

Fig. 8.37 Probability Distribution of Normalized Plastic Deformation Ranges (ARMA(2,1) Simulation of El Centro 1940 and Bilinear Inelastic Structural Model with ξ = 0.05, η = 0.10 and α = 0.00)

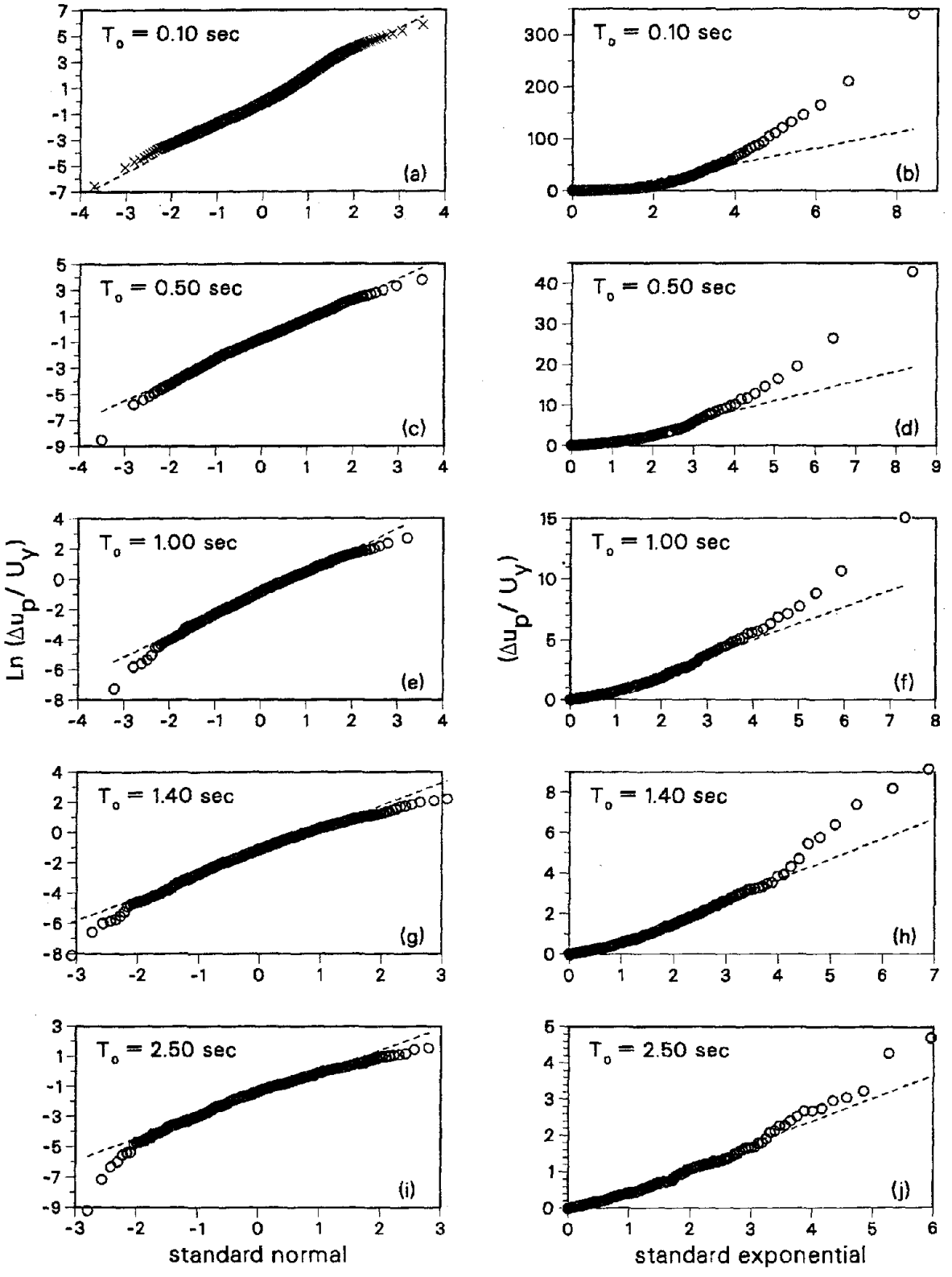

Fig. 8.38 Comparison of Lognormal and Shifted Exponential Probability Distribution Fits (ARMA(2,1) Simulation of El Centro 1940 and Bilinear Inelastic Structural Model with $\xi = 0.05$, $\eta = 0.10$ and $\alpha = 0.00$)

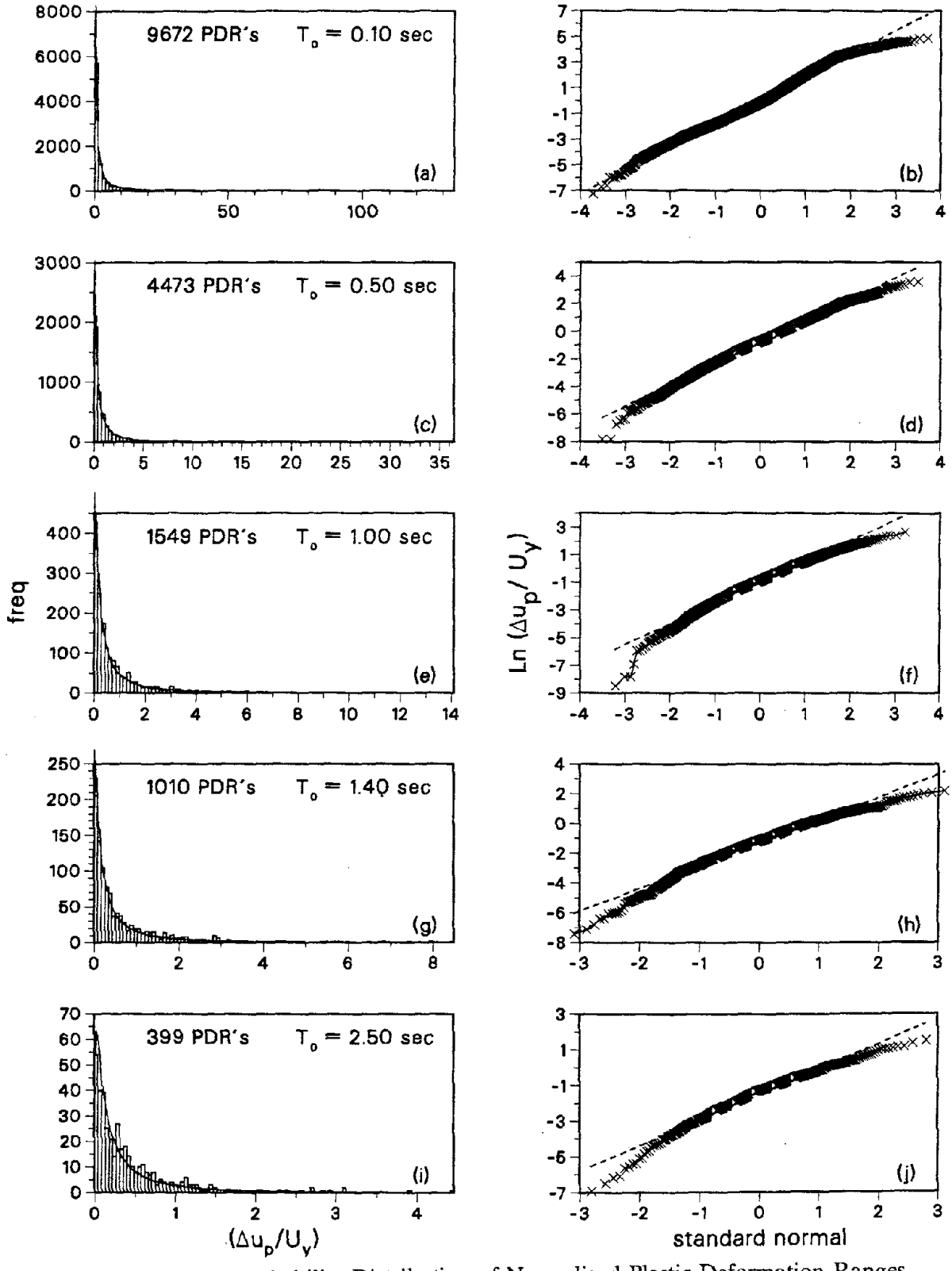

Fig. 8.39 Probability Distribution of Normalized Plastic Deformation Ranges (ARMA(2,1) Simulation of El Centro 1940 and Bilinear Inelastic Structural Model with ξ = 0.05, η = 0.10 and α = 0.05)

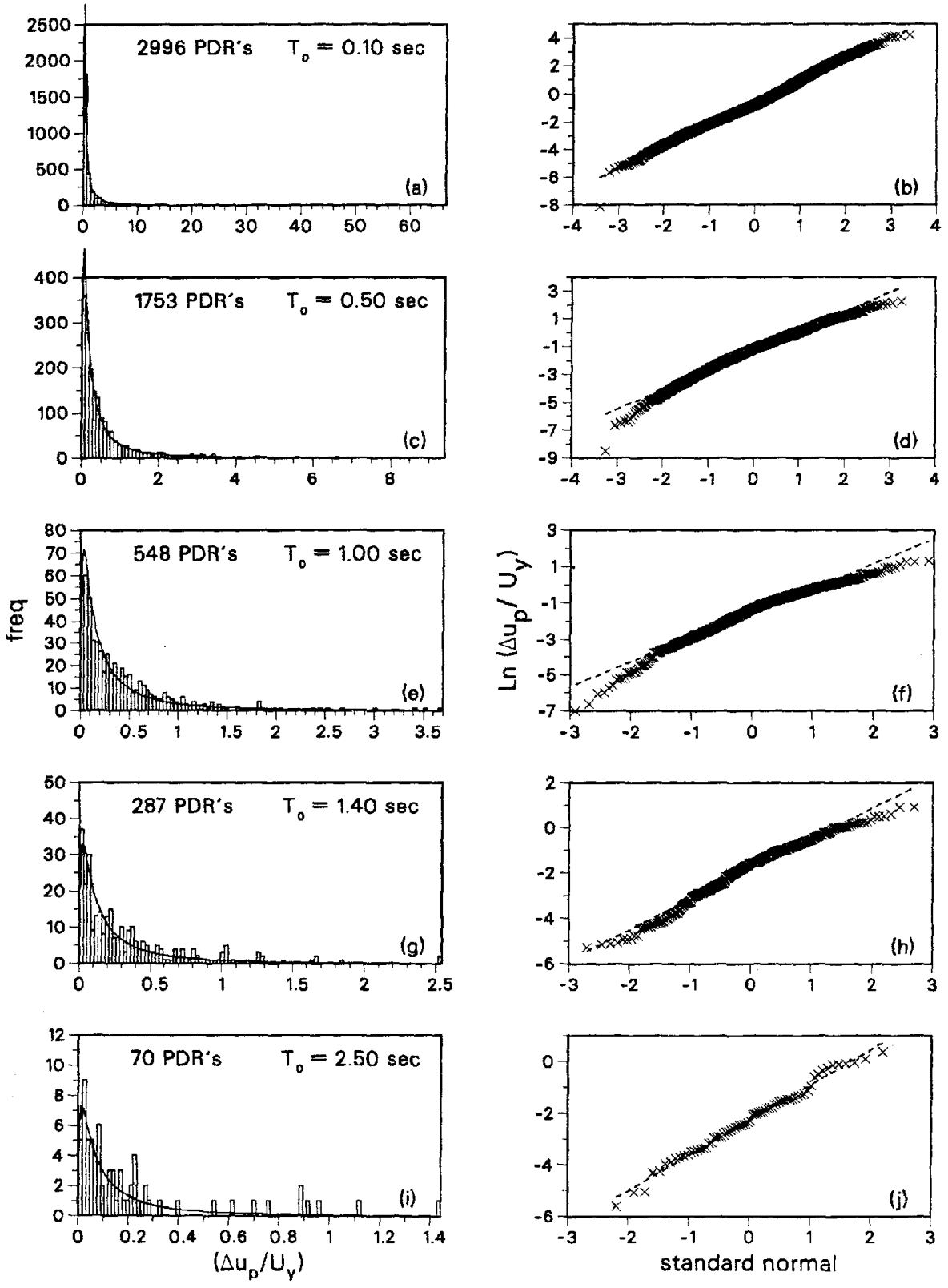

Fig. 8.40 Probability Distribution of Normalized Plastic Deformation Ranges (ARMA(2,1) Simulation of El Centro 1940 and Bilinear Inelastic Structural Model with ξ = 0.05, η = 0.20 and α = 0.00)

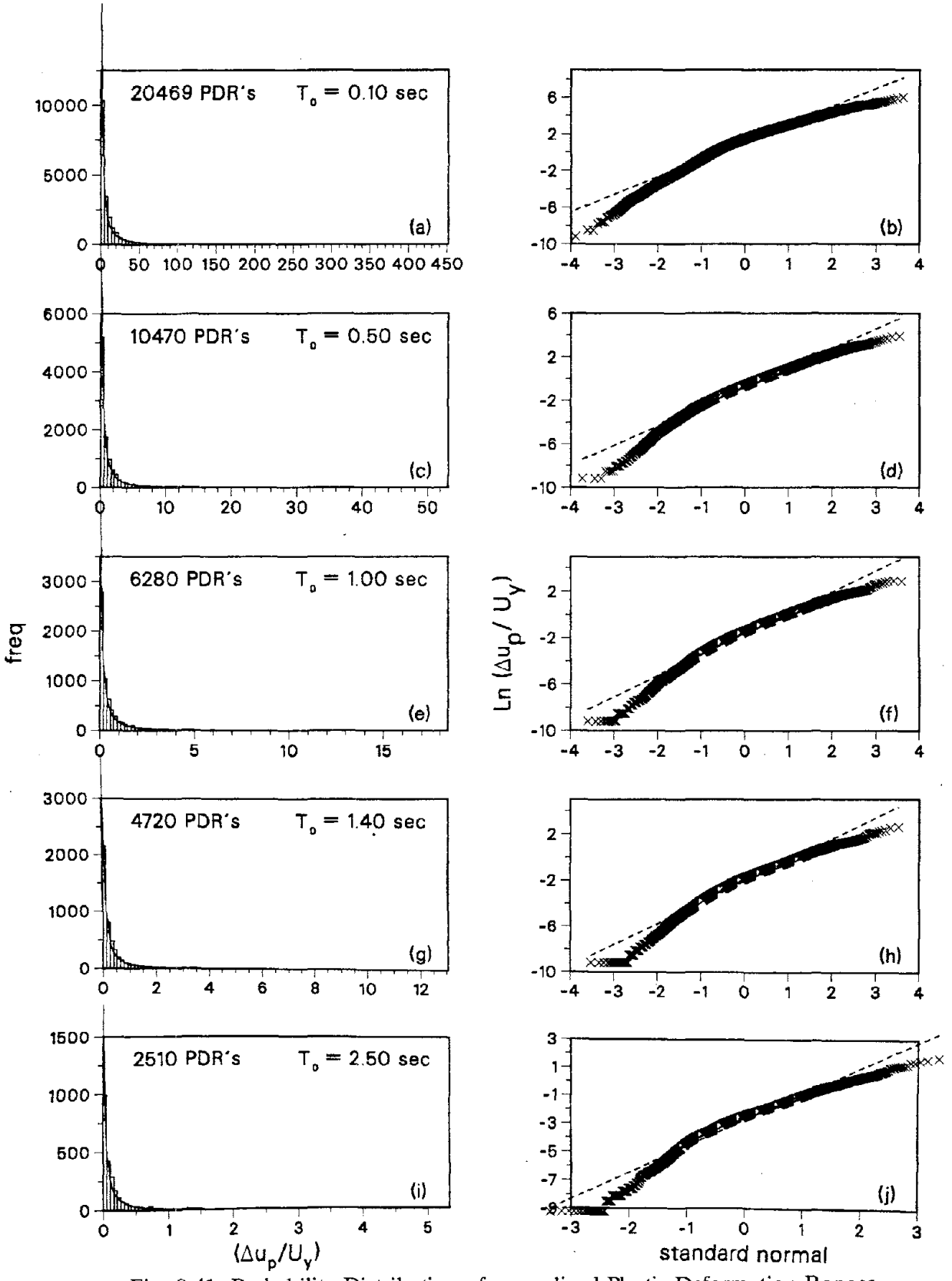

Fig. 8.41 Probability Distribution of normalized Plastic Deformation Ranges (ARMA(2,1) Simulation of El Centro 1940 and Modified Clough's Structural Model with ξ = 0.05, η = 0.10 and α = 0.00)

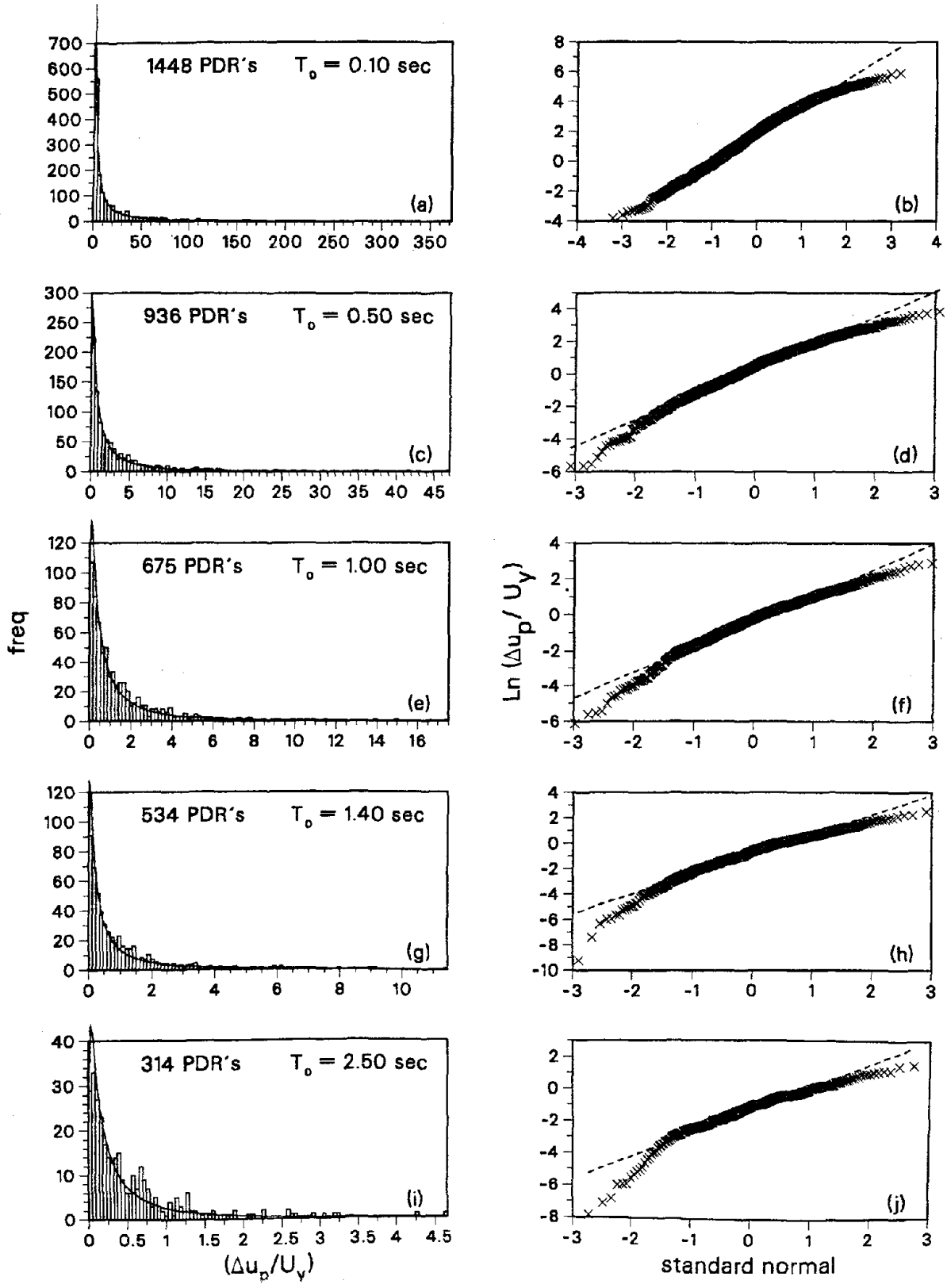

Fig. 8.42 Probability Distribution of Normalized Plastic Deformation Ranges (ARMA(2,1) Simulation of El Centro 1940 and Slip Structural Model with ξ = 0.05, η = 0.10 and α = 0.00)

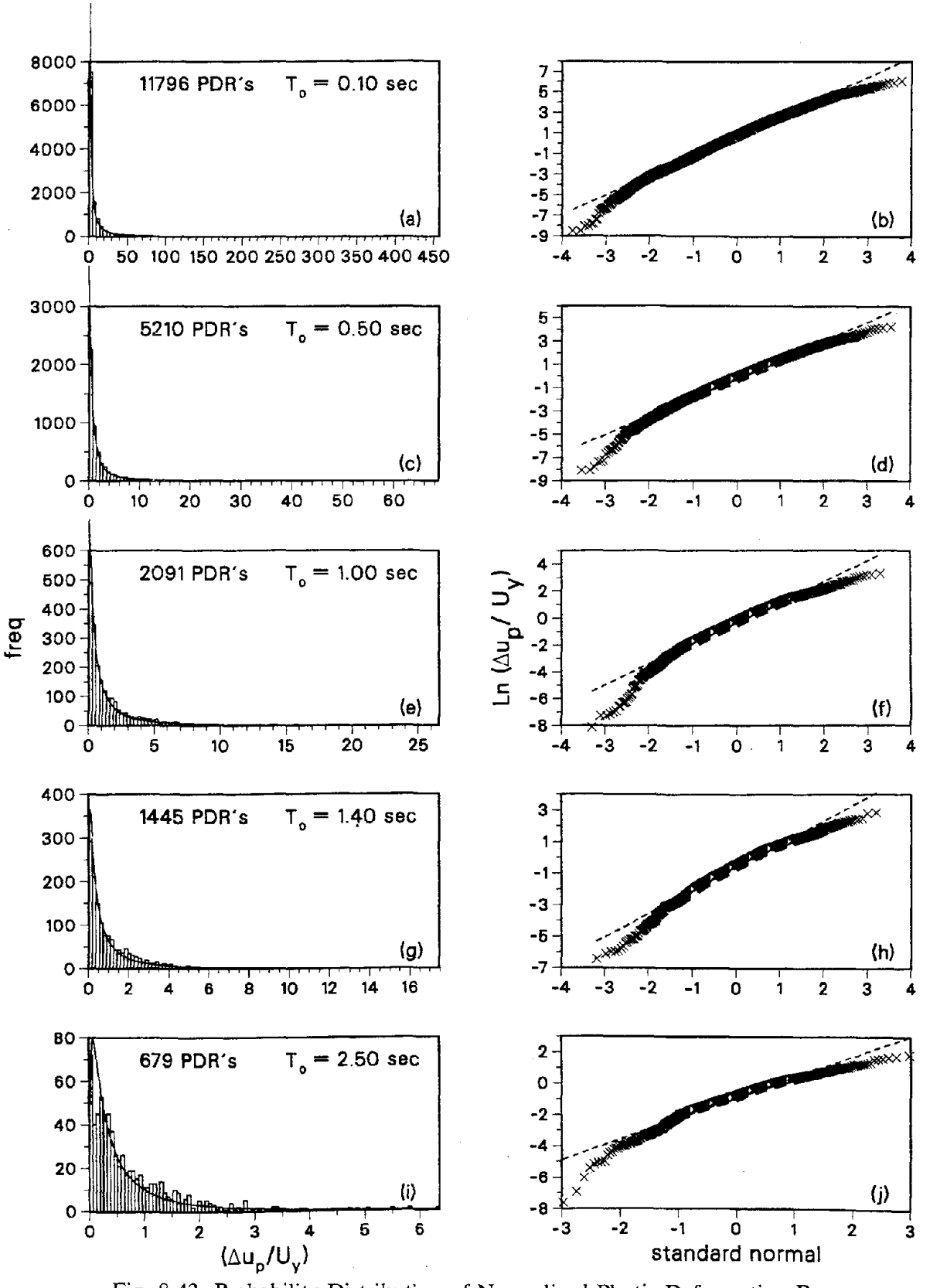

Fig. 8.43 Probability Distribution of Normalized Plastic Deformation Ranges (ARMA(2,1) Simulation of El Centro 1940 and Bilinear Elastic Structural Model with $\xi = 0.05$, $\eta = 0.10$ and $\alpha = 0.00$)

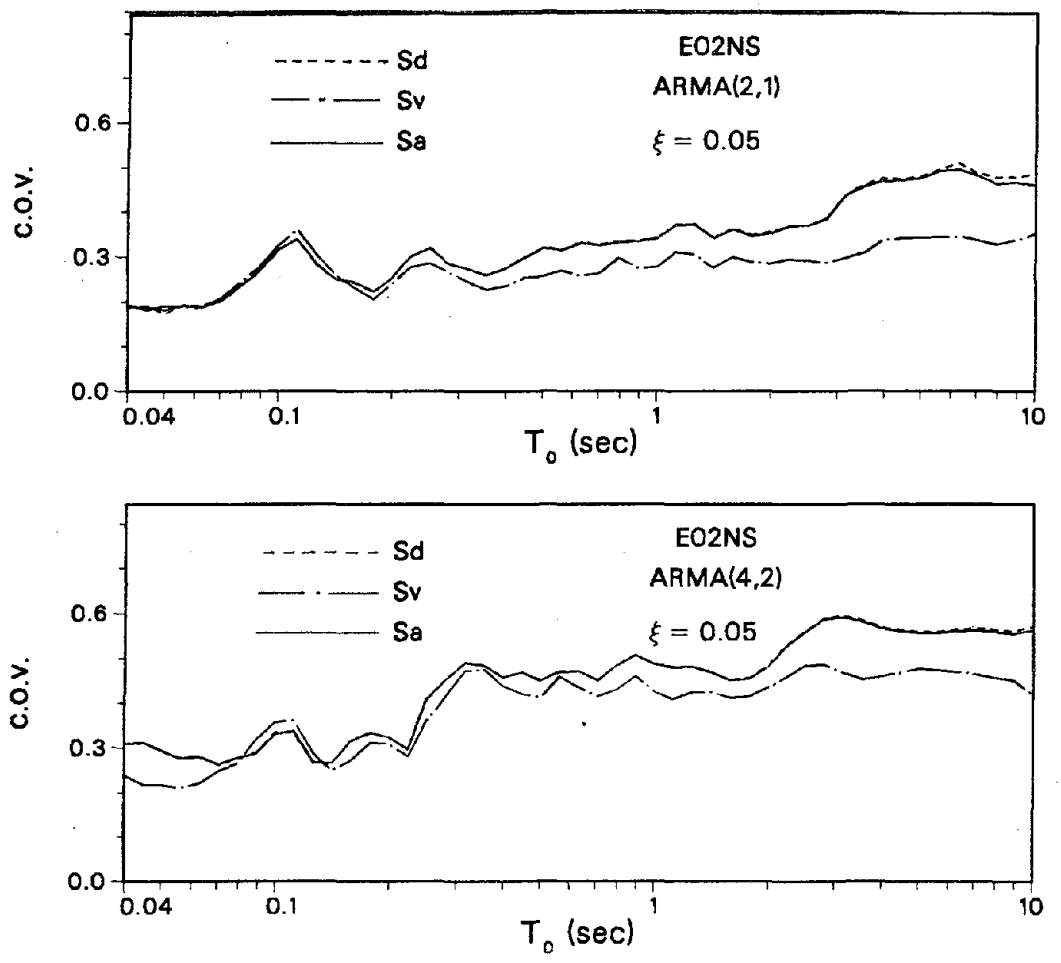

Fig. 8.44 C.O.V. of Linear Elastic Response Spectra for E02NS

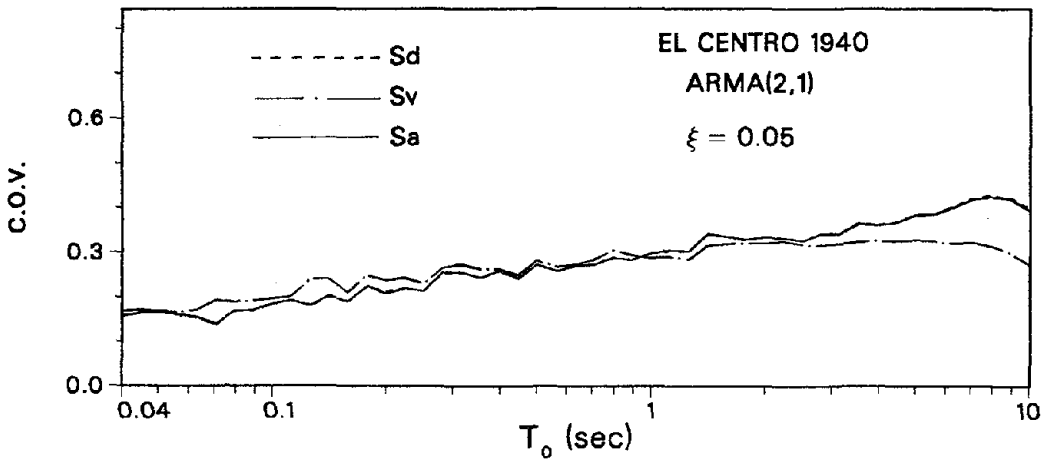

Fig. 8.45 C.O.V. of Linear Elastic Response Spectra for El Centro 1940

APPENDIX A

BI - LATERAL BUTTERWORTH FILTER

The square amplitude spectrum of the Nth-order Butterworth low-pass filter is given by the following rational function [36]:

$$|H(f_n)|^2 = \frac{1}{1 + (w/w_c)^{2N}}, \qquad -\frac{1}{2} \le f_n \le \frac{1}{2} \tag{A.1}$$

where $w = \tan \pi f_n$, Δt = sampling period, $f_n = f\Delta t$ and w_c = corner frequency. This function has the simple features of high tangency at both the origin and at infinity (in the w variable) and smoothness elsewhere. Based on Fig. A.1, the design parameters, N (number of poles) and w_c, can be obtained using the two conditions that arise at the edges of the transition band:

$$\frac{1}{1+\epsilon^2} = \frac{1}{1 + (w_p/w_c)^{2N}} \tag{A.2}$$

$$\frac{1}{A^2} = \frac{1}{1 + (w_s/w_c)^{2N}} \tag{A.3}$$

where w_p and w_s are the "pass" and "stop" frequencies, respectively.

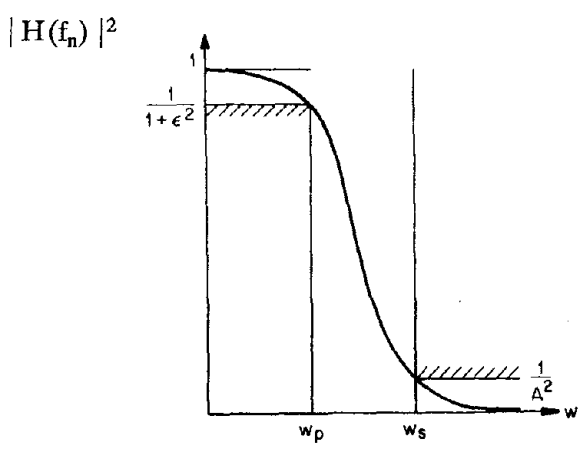

Fig. A.1 Butterworth Filter

Solving Eqs. (A.2-3) for N and w_c gives the following filter design formula:

$$N = \frac{\log(\epsilon / \sqrt{A^2 - 1})}{\log(w_p / w_s)} \tag{A.4}$$

$$w_c = \frac{w_p}{(\epsilon)^{1/N}} \tag{A.5}$$

The pure amplitude high-pass filter (zero phase filter) corresponding to the bi-lateral Butterworth filter is given by:

$$H(f_n) = 1 - \left(\frac{1}{1 + (w/w_c)^{2N}}\right)^{1/2}, \qquad -\frac{1}{2} \le f_n \le \frac{1}{2} \tag{A.6}$$

APPENDIX B

ANALYTICAL INTEGRATION OF EQUATION OF MOTION

B.1 Introduction

In this Section, analytical expressions are derived for the dynamic response of a generic nonlinear SDOF system represented in Fig. B.1. The nonlinear force-deformation behavior of the SDOF system is assumed to be piecewise linear. The class of restoring force models considered here contains, for example, the bilinear model, hysteretic or elastic, shown in Figs. B.2(a) and (d), Clough's degrading stiffness model in Fig. B.2(b) and the slip model in Fig. B.2(c). The input forcing function (earthquake ground acceleration) is also assumed to be linear between the discrete time values. An analytical integration scheme eliminates truncation errors and stability problems associated with numerical integration schemes. The response quantities derived in the next Sections concern the time histories of the SDOF deformation, restoring force, energy balance equation and power balance equation.

B.2 Equation of Motion

The viscously damped, piecewise linear hysteretic, SDOF system represented in Fig. B.1 is subjected to an imposed ground displacement type of loading $u_g(t)$. At any instant of time measured by a local time τ, the system's response is governed by the following equation of motion:

$$m\ddot{u}^t(\tau) + c\dot{u}(\tau) + R(\tau) = 0 \tag{B.1}$$

where m = system's mass, u(t) = SDOF relative displacement or deformation, $u^t(\tau) = u_g(\tau) + u(\tau)$ = SDOF total displacement, $u_g(\tau)$ = ground displacement, c = viscous damping coefficient, $R(\tau)$ = SDOF restoring force. At any time τ, the restoring force is given by:

$$R(\tau) = k_t u(\tau) + R_0 \tag{B.2}$$

where k_t and R_0 define the straight line segment of the force-deformation function followed at absolute time t (Fig. B.3). The viscous damping coefficient c is assumed to be constant (state independent), a typical assumption in nonlinear dynamic analysis of MDOF structures. Using the decomposition of the total displacement $u^t(\tau)$ of the structure and Eq. (B.2), Eq. (B.1) can be rewritten:

$$m\ddot{u}(\tau) + c\dot{u}(\tau) + k_t u(\tau) + R_0 = -m\ddot{u}_g(\tau) \tag{B.3}$$

During forced vibration of the structure, the straight line of Eq. (B.2) characterizing the force-deformation behavior changes. This change, occurring at every yielding, unloading or load reversal point, is called a state event. At every discrete ground acceleration point, called a load event, the straight line characterizing the forcing function $\ddot{u}_g(t)$ also changes. Therefore, it is necessary to introduce a local time variable τ, which is reinitialized at every load or state event. The solution of the equation of motion can have different forms, depending on the position and slope of the force-deformation relationship (k_t and R_0). The key idea in integrating the equation of motion over the duration of the earthquake is to use the end conditions (displacement and velocity) when the system leaves a state as the initial conditions for entering the new state. The only source of error occurs at the time localization of state events (yield level crossings or zero velocity crossings), but this error can be made arbitrarily small by successive iteration using the secant method, for example.

Homogeneous Solution

The characteristic roots of the homogeneous part of Eq. (B.3) are given by:

$$r_{1,2} = \frac{1}{2m}\left[-c \pm \sqrt{c^2 - 4k_t m}\right] \tag{B.4}$$

The cases (i) $0 < c < 2\sqrt{k_t m}$, (ii) $c = 2\sqrt{k_t m}$ and (iii) $c > 2\sqrt{k_t m}$ correspond to the well-known (i) underdamped, (ii) critically damped and (iii) overdamped cases,

respectively. The homogeneous solution of the equation of motion, which gives the free vibration part of the response can be expressed as:

$$u_H(\tau) = C_1 e^{r_1\tau} + C_2 e^{r_2\tau} \tag{B.5}$$

or

$$u_H(\tau) = C_1 e^{r\tau} + C_2 \tau e^{r\tau} \tag{B.6}$$

in the critically damped case ($r_1 = r_2 = r$). Table B.1 summarizes the characteristic roots r_1 and r_2 for all cases. The homogeneous solutions $u_H(\tau)$ are summarized in Table B.2a for all cases.

Particular Solution

To obtain the general solution for the equation of motion, Eq. (B.3), a particular solution $u_P(\tau)$ is needed for the linear forcing function:

$$\ddot{u}_g(\tau) = a + b\tau \tag{B.7}$$

$$\text{where} \quad a = \ddot{u}_{gi}^* \quad \text{and} \quad b = \frac{\ddot{u}_{ge} - \ddot{u}_{gi}}{\Delta t} \tag{B.8}$$

according to Fig. B.4. The ground acceleration value $\ddot{u}_{gi}^*$ corresponds to the time of the last state event, t^*, within the current time step $\Delta t = [t_i, t_{i+1}]$. If there is no state event in the current time step, $t^* = t_i$ and $\ddot{u}_{gi}^* = \ddot{u}_{gi}$. The particular solutions corresponding to all cases ($k_t > 0$, $k_t = 0$, $k_t < 0$, $c \neq 0$, $c = 0$) are summarized in Table B.2a.

General Solution

Finally, the general solution of the equation of motion, Eq. (B.3), is obtained by adding the homogeneous and the particular solutions:

$$u(t) = u_H(t) + u_P(t) \tag{B.9}$$

The two constants of integration A_1 and A_2 attached to the homogeneous solution (see Table B.2a) are derived from the system's local initial conditions (the system's state at last

load or state event):

$$u(\tau = 0) = u(t^*) \tag{B.10}$$

$$\dot{u}(\tau = 0) = \dot{u}(t^*) \tag{B.11}$$

The values of A_1 and A_2 for the different cases are also shown in Table B.2a. For completeness, the first and second time derivatives of the deformation time history $\dot{u}(t)$ and $\ddot{u}(t)$ are summarized in Table B.2b.

B.3 Energy Balance Equation

The energy balance equation is obtained by integrating the equation of motion, Eq. (B.3), with respect to the relative displacement u:

$$\int_0^t m\,\ddot{u}(\tau)\,du + \int_0^t c\,\dot{u}(\tau)\,du + \int_0^t (k_t\,u(\tau) + R_0)\,du = -\int_0^t m\,\ddot{u}_g(\tau)\,du \tag{B.12}$$

Using the relation $du = \frac{du}{d\tau}\,d\tau = \dot{u}\,d\tau$, the above equation can be rewritten

$$\int_0^t m\,\ddot{u}(\tau)\,\dot{u}(\tau)\,d\tau + \int_0^t c\,\dot{u}^2(\tau)\,d\tau + \int_0^t (k_t\,u(\tau) + R_0)\,\dot{u}(\tau)\,d\tau = -\int_0^t m\,\ddot{u}_g(\tau)\,\dot{u}(\tau)\,d\tau \tag{B.13}$$

or, more succinctly:

$$E_K(t) + E_D(t) + E_S(t) = E_I(t) \tag{B.14}$$

where $E_K(t)$ = kinetic energy, $E_D(t)$ = energy dissipated by viscous damping (or damping energy) up to time t, $E_S(t)$ = total energy absorbed by the spring (or total spring energy), which is composed of recoverable elastic strain energy $E_E(t)$ and irrecoverable hysteretic energy $E_H(t)$, and $E_I(t)$ = earthquake input energy. The kinetic energy and spring energy terms can be developed further:

$$E_K(t) = \int_0^t m\,\dot{u}(\tau)\,\ddot{u}(\tau)\,d\tau = \left[\frac{1}{2}\,m\,\dot{u}^2(\tau)\right]_0^t = \frac{1}{2}\,m\,\dot{u}^2(t) - \frac{1}{2}\,m\,\dot{u}^2(0) \tag{B.15}$$

$$
\begin{aligned}
E_S(t) &= \int_0^t k_t u(\tau)\,\dot{u}(\tau)\,d\tau + \int_0^t R_0\,\dot{u}(\tau)\,d\tau \\
&= \left[\frac{1}{2} k_t u^2(\tau)\right]_0^t + \left[R_0 u(\tau)\right]_0^t \\
&= \frac{1}{2} k_t u^2(t) - \frac{1}{2} k_t u^2(0) + R_0 u(t) - R_0 u(0)
\end{aligned}
\tag{B.16}
$$

A graphical representation of Eq. (B.16) for the spring energy is given in Fig. B.5. The recoverable elastic strain energy $E_E(t)$ is simply expressed as:

$$
E_E(t) = \frac{1}{2}\frac{R^2(t)}{k_0} \tag{B.17}
$$

where k_0 denotes the initial elastic stiffness. Using Eq. (B.17), the hysteretic energy $E_H(t)$ can be directly obtained:

$$
E_H(t) = = E_S(t) - E_E(t) = E_S(t) - \frac{1}{2}\frac{R^2(t)}{k_0} \tag{B.18}
$$

The integration over time to compute the energy terms has to be broken into as many time segments as there are time intervals with constant linear force-deformation behavior and constant linear loading. Thus, if $\{\tau_1, \tau_2, \cdots, \tau_n\}$ represents the sequence of all state and load events up to time t, a typical integral expression from the beginning of the dynamic response of the structure up to time t is computed as:

$$
\int_0^t (\,)\,d\tau = \int_0^{\tau_1} (\,)\,d\tau + \int_{\tau_1}^{\tau_2} (\,)\,d\tau + \cdots + \int_{\tau_{n-1}}^{\tau_n} (\,)\,d\tau + \int_{\tau_n}^{t} (\,)\,d\tau \tag{B.19}
$$

The analytical expressions for $u(\tau)$, $\dot{u}(\tau)$, $\ddot{u}(\tau)$ and $\ddot{u}_g(\tau)$ are found in Tables B.1a-B.2a and Eq. (B.7). They can be substituted in Eqs. (B.13-16) and closed form solutions for the various energy terms are then obtained by simple integrations.

The kinetic energy mentioned above is a "relative" kinetic energy, because it is calculated from the relative velocity $\dot{u}$. Therefore, the corresponding input energy is also relative. It does not represent the work done by the total base shear V_B at the foundation moving through the foundation displacement, which is:

$$W_B(t) = \int_0^t V_B(\tau)\, du_g = \int_0^t [-c\,\dot{u}(\tau) - R(u)]\, du_g$$
$$= \int_0^t m\,\ddot{u}^t(\tau)\, du_g = \int_0^t m\,(\ddot{u}(\tau) + \ddot{u}_g(\tau))\,\dot{u}_g(\tau)\, d\tau \tag{B.20}$$

Using integration by parts, Eq. (B.20) can be reduced to:

$$W_B(t) = -\int_0^t m\,\ddot{u}_g(\tau)\,\dot{u}(\tau)\, d\tau + [\frac{1}{2}\, m\,\dot{u}_g(\tau)]_0^t + [m\,\dot{u}(\tau)\,\dot{u}_g(\tau)]_0^t \tag{B.21}$$

where the first term of the right hand side is the earthquake input energy defined in Eqs. (B.13-B.14); the second and third terms represent the difference, δE_K, between the absolute kinetic energy and the relative kinetic energy:

$$\delta E_K(t) = [\frac{1}{2}\, m\,(\dot{u}(\tau) + \dot{u}_g(\tau))^2]_0^t - [\frac{1}{2}\, m\,\dot{u}^2(\tau)]_0^t \tag{B.22}$$

B.4 Power Balance Equation

The power balance equation is simply obtained by differentiating the energy balance equation, Eq. (B.14), with respect to time:

$$\frac{dE_K(t)}{dt} + \frac{dE_D(t)}{dt} + \frac{dE_S(t)}{dt} = \frac{dE_I(t)}{dt} \tag{B.23}$$

The various power (or rate of energy) terms are derived using the energy terms of the previous Section:

$$\frac{dE_K(t)}{dt} = m\,\dot{u}(t)\,\ddot{u}(t) \tag{B.24}$$

$$\frac{dE_D(t)}{dt} = c\,\dot{u}^2(t) \tag{B.25}$$

$$\frac{dE_S(t)}{dt} = k_t\, u(t)\,\dot{u}(t) + R_0\,\dot{u}(t) \tag{B.26}$$

The rate of the elastic strain energy, $dE_E(t)/dt$, and the rate of the hysteretic energy, $dE_H(t)/dt$, follow directly from Eqs. (B.17-18):

$$\frac{dE_E(t)}{dt} = \frac{R(t)\, k_t\,\dot{u}(t)}{k_0} \tag{B.27}$$

$$\frac{dE_H(t)}{dt} = \frac{dE_S(t)}{dt} - \frac{dE_E(t)}{dt}$$

$$= (1 - \frac{k_t}{k_0})\, k_t\, u(t)\, \dot{u}(t) + (1 - \frac{k_t}{k_0})\, R_0\, \dot{u}(t) \tag{B.28}$$

If the restoring force of the structure follows an elastic branch (i.e., $k_t = k_0$), Eq. (B.28) indicates that the rate of hysteretic energy is zero, as expected.

TABLE B.1

Characteristic Roots of Homogeneous Equation of Motion

k_t	Underdamped $0 \le c < 2\sqrt{k_t m}$ or $(\xi_t < 1)$	Critically Damped $c = 2\sqrt{k_t m}$ or $(\xi_t = 1)$	Overdamped $c > 2\sqrt{k_t m}$ or $(\xi_t > 1)$
$k_t > 0$	$r_{1,2} = -\xi_t \omega_t \pm i\omega_{D,t}$ $\omega_t = \sqrt{k_t/m}$; $2\xi_t \omega_t = c/m$ $\omega_{D,t} = \omega_t \sqrt{1-\xi_t^2}$ if $c = 0$: $\xi_t = 0$ and $\omega_{D,t} = \omega_t$	$r_{1,2} = -c/2m$	$r_{1,2} = 1/2m[-c \pm \sqrt{c^2 - 4k_t m}]$ $r_1 < 0$ $r_2 < 0$ $\lvert r_1 \rvert < \lvert r_2 \rvert$
$k_t = 0$	$r_1 = 0$ $r_2 = -c/m$		
$k_t < 0$	$r_{1,2} = 1/2m[-c \pm \sqrt{c^2 - 4k_t m}]$ $r_1 > 0$ $r_2 < 0$ $\lvert r_1 \rvert < \lvert r_2 \rvert$		

TABLE B.2a

Complete Solution of Equation of Motion (Part A)

	Undamped $c = 0$	Underdamped $0 < c < 2\sqrt{k_t m}$ (or $\xi_t < 1$)	Overdamped $c > 2\sqrt{k_t m}$ (or $\xi_t > 1$)
$k_t > 0$	$u_H(\tau) = e^{-\xi_t \omega_t \tau}[A_1 \cos \omega_{D,t}\tau + A_2 \sin \omega_{D,t}\tau]$ $u_P(\tau) = B_1 + B_2\tau$ $A_1 = u(t^*) - B_1$ $A_2 = [\dot{u}(t^*) + A_1 \xi_t \omega_t - B_2]/\omega_{D,t}$		$u_H(\tau) = A_1 e^{r_1 \tau} + A_2 e^{r_2 \tau}$ $u_P(\tau) = B_1 + B_2\tau$ $A_1 = [\dot{u}(t^*) - u(t^*) r_2 + B_1 r_2 - B_2]/(r_1 - r_2)$ $A_2 = u(t^*) - A_1 - B_1$
	$a = \ddot{u}_{gi}^* = \ddot{u}_g(\tau = 0)$ $b = (\ddot{u}_{ge} - \ddot{u}_{gi})/\Delta t$	(see Fig. B.4)	$B_2 = -mb/k_t$ $B_1 = -(ma + cB_2 + R_0)/k_t$
$k_t = 0$	$u_H(\tau) = A_1 + A_2\tau$ $u_P(\tau) = B_1\tau^2 + B_2\tau^3$ $A_1 = u(t^*)$ $A_2 = \dot{u}(t^*)$ $B_1 = -(ma \pm R_y)/2m$ $B_2 = -b/6$	$u_H(\tau) = A_1 + A_2 e^{-\frac{c}{m}\tau}$ $u_P(\tau) = B_1\tau + B_2\tau^2$ $B_2 = -mb/2c$ $B_1 = -(ma + 2mB_2 \pm R_y)/c$ $A_2 = m(B_1 - \dot{u}(t^*))/c$ $A_1 = u(t^*) - A_2$	+ positive yielding - negative yielding
$k_t < 0$	(same as overdamped case with $k_t > 0$)		

TABLE B.2b

Complete Solution of Equation of Motion (Part B)

	Undamped $c = 0$	Underdamped $0 < c < 2\sqrt{k_t m}$ (or $\xi_t < 1$)	Overdamped $c > 2\sqrt{k_t m}$ (or $\xi_t > 1$)
$k_t > 0$	$\dot{u}_H(\tau) = e^{-\xi_t \omega_t \tau}[(-A_1 \xi_t \omega_t + A_2 \omega_{D,t}) \cos \omega_{D,t} \tau + (-A_2 \xi_t \omega_t - A_1 \omega_{D,t}) \sin \omega_{D,t} \tau]$ $\ddot{u}_H(\tau) = e^{-\xi_t \omega_t \tau}[(-\xi_t \omega_t(-A_1 \xi_t \omega_t + A_2 \omega_{D,t}) + \omega_{D,t}(-A_2 \xi_t \omega_t - A_1 \omega_{D,t})) \cos \omega_{D,t} \tau + (-\xi_t \omega_t(-A_2 \xi_t \omega_t - A_1 \omega_{D,t}) - \omega_{D,t}(-A_1 \xi_t \omega_t + A_2 \omega_{D,t})) \sin \omega_{D,t} \tau]$		$\dot{u}_H(\tau) = A_1 r_1 e^{r_1 \tau} + A_2 r_2 e^{r_2 \tau}$ $\ddot{u}_H(\tau) = A_1 r_1^2 e^{r_1 \tau} + A_2 r_2^2 e^{r_2 \tau}$
	$\dot{u}_P(\tau) = B_2$ $\ddot{u}_P(\tau) = 0$		
$k_t = 0$	$\dot{u}_H(\tau) = A_2$ $\ddot{u}_H(\tau) = 0$ $\dot{u}_P(\tau) = 2B_1 \tau + 3B_2 \tau^2$ $\ddot{u}_P(\tau) = 2B_1 + 6B_2 \tau$	$\dot{u}_H(\tau) = -\frac{c}{m} A_2 e^{-\frac{c}{m}\tau}$ $\ddot{u}_H(\tau) = (\frac{c}{m})^2 A_2 e^{-\frac{c}{m}\tau}$ $\dot{u}_P(\tau) = B_1 + 2B_2 \tau$ $\ddot{u}_P(\tau) = 2B_2$	
$k_t < 0$	(same as overdamped case with $k_t > 0$)		

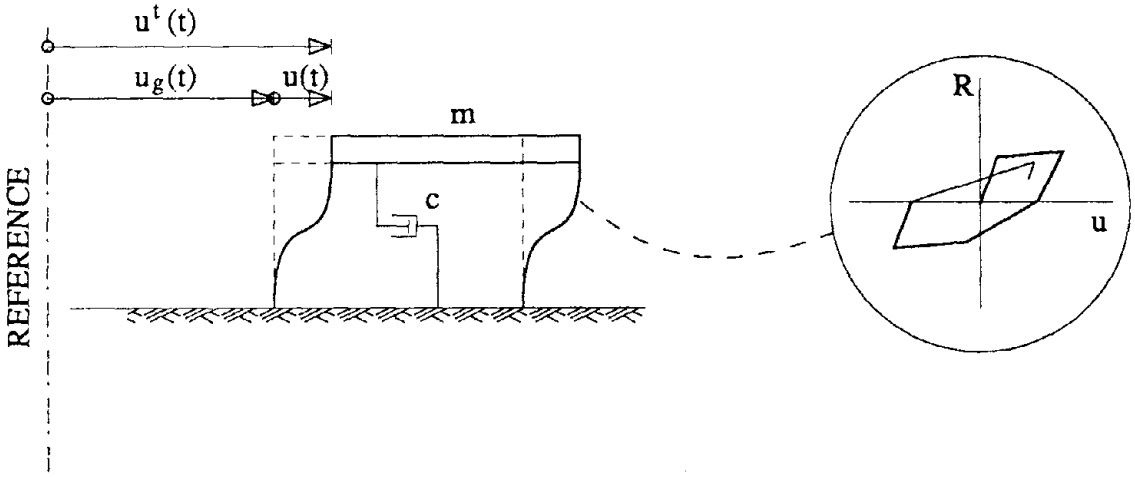

Fig. B.1 Nonlinear SDOF System

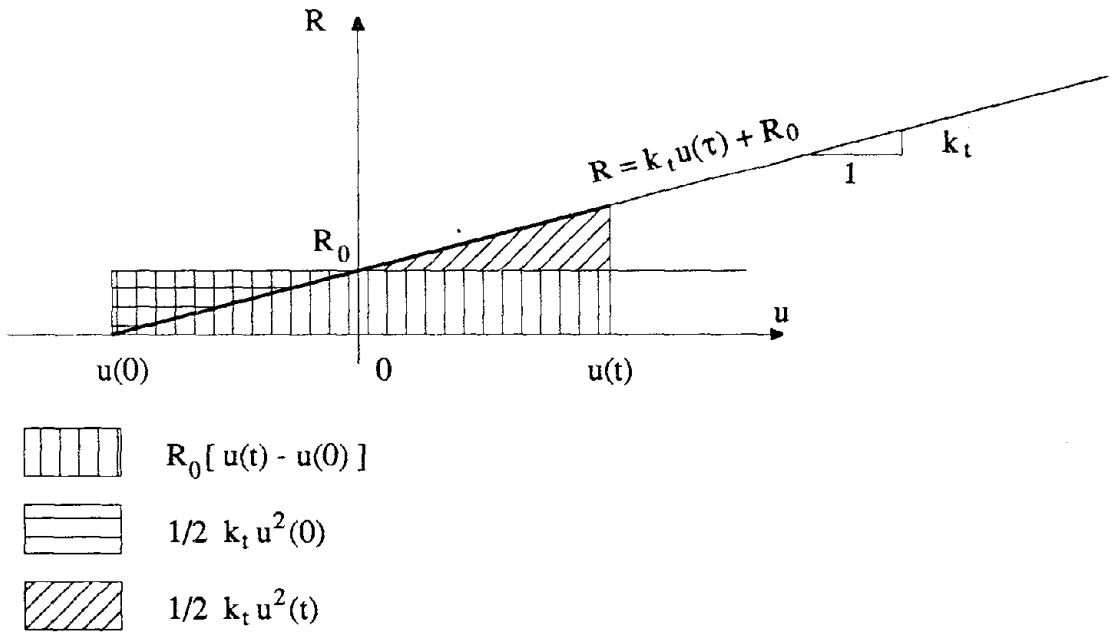

Fig. B.5 Total Spring Energy $E_s(t)$

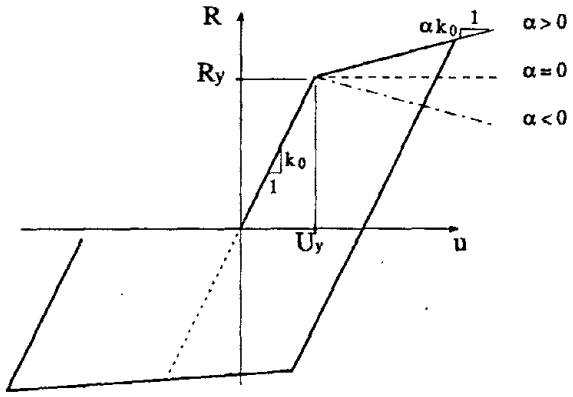

(a) Bilinear Hysteretic Model

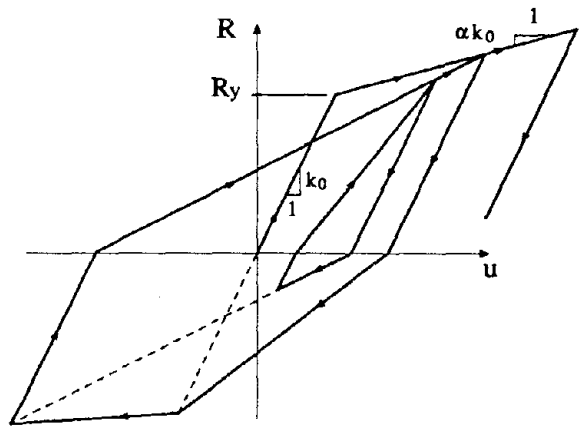

(b) Clough's Stiffness Degrading Model

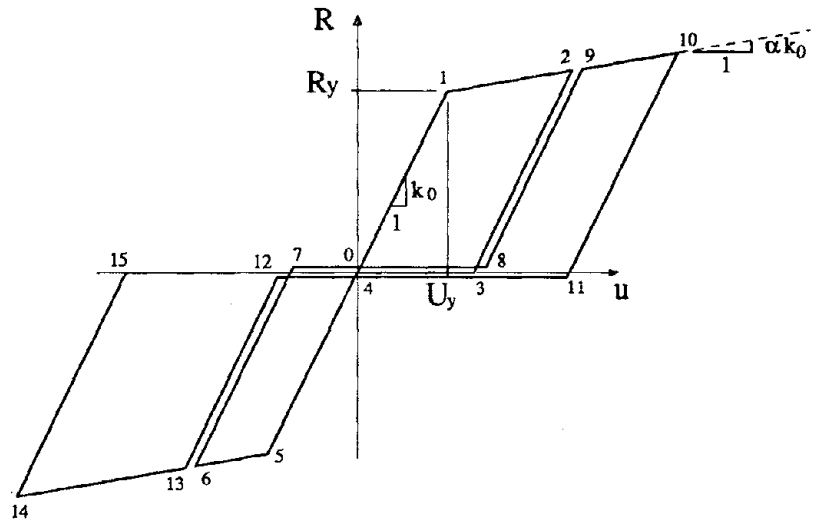

(c) Slip Model

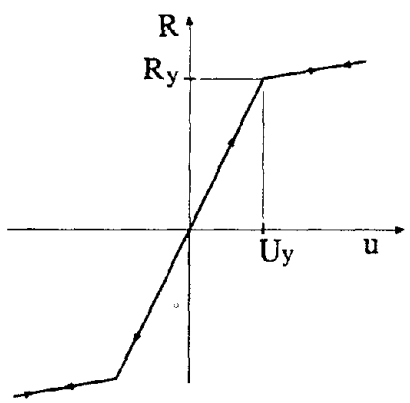

(d) Bilinear Elastic Model

Fig. B.2 Examples of Piecewise Linear Force-Deformation Behavior

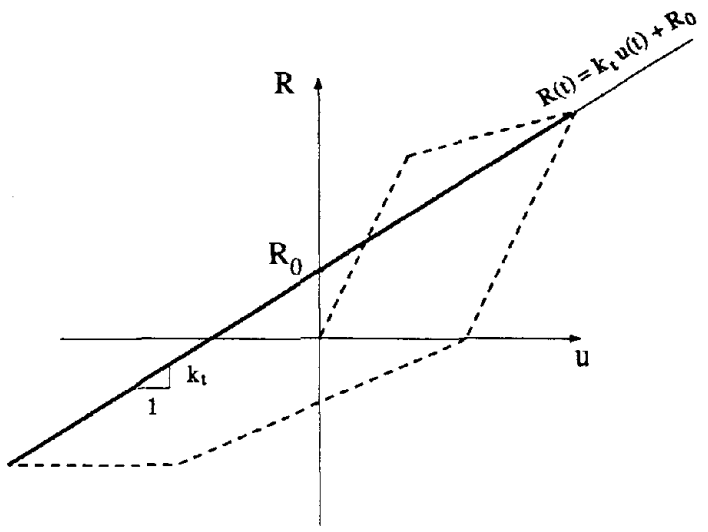

Fig. B.3 Piecewise Linear Restoring Force

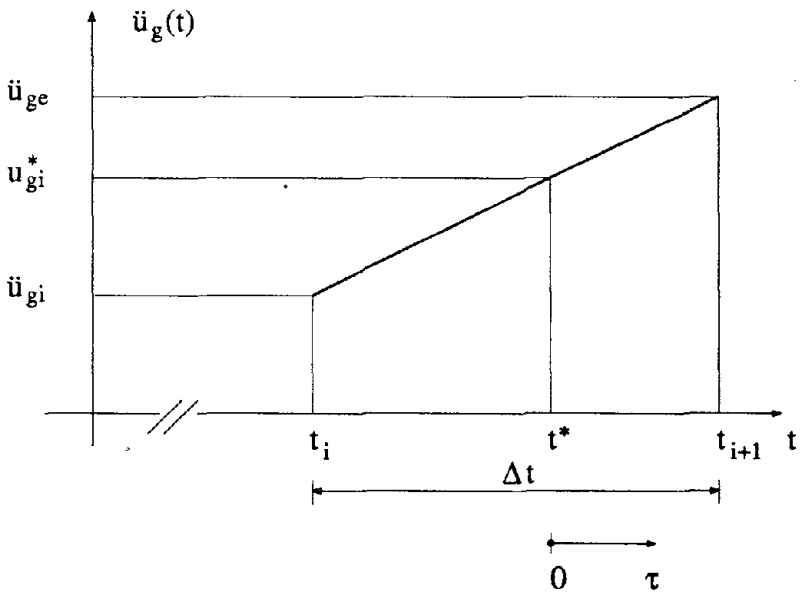

Fig. B.4 Piecewise Linear Forcing Function

EARTHQUAKE ENGINEERING RESEARCH CENTER REPORT SERIES

EERC reports are available from the National Information Service for Earthquake Engineering(NISEE) and from the National Technical Information Service(NTIS). Numbers in parentheses are Accession Numbers assigned by the National Technical Information Service; these are followed by a price code. Contact NTIS, 5285 Port Royal Road, Springfield Virginia, 22161 for more information. Reports without Accession Numbers were not available from NTIS at the time of printing. For a current complete list of EERC reports (from EERC 67-1) and availablity information, please contact University of California, EERC, NISEE, 1301 South 46th Street, Richmond, California 94804.

UCB/EERC-80/01 "Earthquake Response of Concrete Gravity Dams Including Hydrodynamic and Foundation Interaction Effects," by Chopra, A.K., Chakrabarti, P. and Gupta, S., January 1980, (AD-A087297)A10.

UCB/EERC-80/02 "Rocking Response of Rigid Blocks to Earthquakes," by Yim, C.S., Chopra, A.K. and Penzien, J., January 1980, (PB80 166 002)A04.

UCB/EERC-80/03 "Optimum Inelastic Design of Seismic-Resistant Reinforced Concrete Frame Structures," by Zagajeski, S.W. and Bertero, V.V., January 1980, (PB80 164 635)A06.

UCB/EERC-80/04 "Effects of Amount and Arrangement of Wall-Panel Reinforcement on Hysteretic Behavior of Reinforced Concrete Walls," by Iliya, R. and Bertero, V.V., February 1980, (PB81 122 525)A09.

UCB/EERC-80/05 "Shaking Table Research on Concrete Dam Models," by Niwa, A. and Clough, R.W., September 1980, (PB81 122 368)A06.

UCB/EERC-80/06 "The Design of Steel Energy-Absorbing Restrainers and their Incorporation into Nuclear Power Plants for Enhanced Safety (Vol 1a): Piping with Energy Absorbing Restrainers: Parameter Study on Small Systems," by Powell, G.H., Oughourlian, C. and Simons, J., June 1980.

UCB/EERC-80/07 "Inelastic Torsional Response of Structures Subjected to Earthquake Ground Motions," by Yamazaki, Y., April 1980, (PB81 122 327)A08.

UCB/EERC-80/08 "Study of X-Braced Steel Frame Structures under Earthquake Simulation," by Ghanaat, Y., April 1980, (PB81 122 335)A11.

UCB/EERC-80/09 "Hybrid Modelling of Soil-Structure Interaction," by Gupta, S., Lin, T.W. and Penzien, J., May 1980, (PB81 122 319)A07.

UCB/EERC-80/10 "General Applicability of a Nonlinear Model of a One Story Steel Frame," by Sveinsson, B.I. and McNiven, H.D., May 1980, (PB81 124 877)A06.

UCB/EERC-80/11 "A Green-Function Method for Wave Interaction with a Submerged Body," by Kioka, W., April 1980, (PB81 122 269)A07.

UCB/EERC-80/12 "Hydrodynamic Pressure and Added Mass for Axisymmetric Bodies.," by Nilrat, F., May 1980, (PB81 122 343)A08.

UCB/EERC-80/13 "Treatment of Non-Linear Drag Forces Acting on Offshore Platforms," by Dao, B.V. and Penzien, J., May 1980, (PB81 153 413)A07.

UCB/EERC-80/14 "2D Plane/Axisymmetric Solid Element (Type 3-Elastic or Elastic-Perfectly Plastic)for the ANSR-II Program," by Mondkar, D.P. and Powell, G.H., July 1980, (PB81 122 350)A03.

UCB/EERC-80/15 "A Response Spectrum Method for Random Vibrations," by Der Kiureghian, A., June 1981, (PB81 122 301)A03.

UCB/EERC-80/16 "Cyclic Inelastic Buckling of Tubular Steel Braces," by Zayas, V.A., Popov, E.P. and Mahin, S.A., June 1981, (PB81 124 885)A10.

UCB/EERC-80/17 "Dynamic Response of Simple Arch Dams Including Hydrodynamic Interaction," by Porter, C.S. and Chopra, A.K., July 1981, (PB81 124 000)A13.

UCB/EERC-80/18 "Experimental Testing of a Friction Damped Aseismic Base Isolation System with Fail-Safe Characteristics," by Kelly, J.M., Beucke, K.E. and Skinner, M.S., July 1980, (PB81 148 595)A04.

UCB/EERC-80/19 "The Design of Steel Energy-Absorbing Restrainers and their Incorporation into Nuclear Power Plants for Enhanced Safety (Vol.1B): Stochastic Seismic Analyses of Nuclear Power Plant Structures and Piping Systems Subjected to Multiple Supported Excitations," by Lee, M.C. and Penzien, J., June 1980, (PB82 201 872)A08.

UCB/EERC-80/20 "The Design of Steel Energy-Absorbing Restrainers and their Incorporation into Nuclear Power Plants for Enhanced Safety (Vol 1C): Numerical Method for Dynamic Substructure Analysis," by Dickens, J.M. and Wilson, E.L., June 1980.

UCB/EERC-80/21 "The Design of Steel Energy-Absorbing Restrainers and their Incorporation into Nuclear Power Plants for Enhanced Safety (Vol 2): Development and Testing of Restraints for Nuclear Piping Systems," by Kelly, J.M. and Skinner, M.S., June 1980.

UCB/EERC-80/22 "3D Solid Element (Type 4-Elastic or Elastic-Perfectly-Plastic) for the ANSR-II Program," by Mondkar, D.P. and Powell, G.H., July 1980, (PB81 123 242)A03.

UCB/EERC-80/23 "Gap-Friction Element (Type 5) for the Ansr-II Program," by Mondkar, D.P. and Powell, G.H., July 1980, (PB81 122 285)A03.

UCB/EERC-80/24 "U-Bar Restraint Element (Type 11) for the ANSR-II Program," by Oughourlian, C. and Powell, G.H., July 1980, (PB81 122 293)A03.

UCB/EERC-80/25 "Testing of a Natural Rubber Base Isolation System by an Explosively Simulated Earthquake," by Kelly, J.M., August 1980, (PB81 201 360)A04.

UCB/EERC-80/26 "Input Identification from Structural Vibrational Response," by Hu, Y., August 1980, (PB81 152 308)A05.

UCB/EERC-80/27 "Cyclic Inelastic Behavior of Steel Offshore Structures," by Zayas, V.A., Mahin, S.A. and Popov, E.P., August 1980, (PB81 196 180)A15.

UCB/EERC-80/28 "Shaking Table Testing of a Reinforced Concrete Frame with Biaxial Response," by Oliva, M.G., October 1980, (PB81 154 304)A10.

UCB/EERC-80/29 "Dynamic Properties of a Twelve-Story Prefabricated Panel Building," by Bouwkamp, J.G., Kollegger, J.P. and Stephen, R.M., October 1980, (PB82 138 777)A07.

UCB/EERC-80/30 "Dynamic Properties of an Eight-Story Prefabricated Panel Building," by Bouwkamp, J.G., Kollegger, J.P. and Stephen, R.M., October 1980, (PB81 200 313)A05.

UCB/EERC-80/31 "Predictive Dynamic Response of Panel Type Structures under Earthquakes," by Kollegger, J.P. and Bouwkamp, J.G., October 1980, (PB81 152 316)A04.

UCB/EERC-80/32 "The Design of Steel Energy-Absorbing Restrainers and their Incorporation into Nuclear Power Plants for Enhanced Safety (Vol 3): Testing of Commercial Steels in Low-Cycle Torsional Fatigue," by Spanner, P., Parker, E.R., Jongewaard, E. and Dory, M., 1980.

UCB/EERC-80/33 "The Design of Steel Energy-Absorbing Restrainers and their Incorporation into Nuclear Power Plants for Enhanced Safety (Vol 4): Shaking Table Tests of Piping Systems with Energy-Absorbing Restrainers," by Stiemer, S.F. and Godden, W.G., September 1980, (PB82 201 880)A05.

UCB/EERC-80/34 "The Design of Steel Energy-Absorbing Restrainers and their Incorporation into Nuclear Power Plants for Enhanced Safety (Vol 5): Summary Report," by Spencer, P., 1980.

UCB/EERC-80/35 "Experimental Testing of an Energy-Absorbing Base Isolation System," by Kelly, J.M., Skinner, M.S. and Beucke, K.E., October 1980, (PB81 154 072)A04.

UCB/EERC-80/36 "Simulating and Analyzing Artificial Non-Stationary Earth Ground Motions," by Nau, R.F., Oliver, R.M. and Pister, K.S., October 1980, (PB81 153 397)A04.

UCB/EERC-80/37 "Earthquake Engineering at Berkeley - 1980," by , September 1980, (PB81 205 674)A09.

UCB/EERC-80/38 "Inelastic Seismic Analysis of Large Panel Buildings," by Schricker, V. and Powell, G.H., September 1980, (PB81 154 338)A13.

UCB/EERC-80/39 "Dynamic Response of Embankment, Concrete-Gavity and Arch Dams Including Hydrodynamic Interation," by Hall, J.F. and Chopra, A.K., October 1980, (PB81 152 324)A11.

UCB/EERC-80/40 "Inelastic Buckling of Steel Struts under Cyclic Load Reversal.," by Black, R.G., Wenger, W.A. and Popov, E.P., October 1980, (PB81 154 312)A08.

UCB/EERC-80/41 "Influence of Site Characteristics on Buildings Damage during the October 3,1974 Lima Earthquake," by Repetto, P., Arango, I. and Seed, H.B., September 1980, (PB81 161 739)A05.

UCB/EERC-80/42 "Evaluation of a Shaking Table Test Program on Response Behavior of a Two Story Reinforced Concrete Frame," by Blondet, J.M., Clough, R.W. and Mahin, S.A., December 1980, (PB82 196 544)A11.

UCB/EERC-80/43 "Modelling of Soil-Structure Interaction by Finite and Infinite Elements," by Medina, F., December 1980, (PB81 229 270)A04.

UCB/EERC-81/01 "Control of Seismic Response of Piping Systems and Other Structures by Base Isolation," by Kelly, J.M., January 1981, (PB81 200 735)A05.

UCB/EERC-81/02 "OPTNSR- An Interactive Software System for Optimal Design of Statically and Dynamically Loaded Structures with Nonlinear Response," by Bhatti, M.A., Ciampi, V. and Pister, K.S., January 1981, (PB81 218 851)A09.

UCB/EERC-81/03 "Analysis of Local Variations in Free Field Seismic Ground Motions," by Chen, J.-C., Lysmer, J. and Seed, H.B., January 1981, (AD-A099508)A13.

UCB/EERC-81/04 "Inelastic Structural Modeling of Braced Offshore Platforms for Seismic Loading," by Zayas, V.A., Shing, P.-S.B., Mahin, S.A. and Popov, E.P., January 1981, (PB82 138 777)A07.

UCB/EERC-81/05 "Dynamic Response of Light Equipment in Structures," by Der Kiureghian, A., Sackman, J.L. and Nour-Omid, B., April 1981, (PB81 218 497)A04.

UCB/EERC-81/06 "Preliminary Experimental Investigation of a Broad Base Liquid Storage Tank," by Bouwkamp, J.G., Kollegger, J.P. and Stephen, R.M., May 1981, (PB82 140 385)A03.

UCB/EERC-81/07 "The Seismic Resistant Design of Reinforced Concrete Coupled Structural Walls," by Aktan, A.E. and Bertero, V.V., June 1981, (PB82 113 358)A11.

UCB/EERC-81/08 "Unassigned," by Unassigned, 1981.

UCB/EERC-81/09 "Experimental Behavior of a Spatial Piping System with Steel Energy Absorbers Subjected to a Simulated Differential Seismic Input," by Stiemer, S.F., Godden, W.G. and Kelly, J.M., July 1981, (PB82 201 898)A04.

UCB/EERC-81/10 "Evaluation of Seismic Design Provisions for Masonry in the United States," by Sveinsson, B.I., Mayes, R.L. and McNiven, H.D., August 1981, (PB82 166 075)A08.

UCB/EERC-81/11 "Two-Dimensional Hybrid Modelling of Soil-Structure Interaction," by Tzong, T.-J., Gupta, S. and Penzien, J., August 1981, (PB82 142 118)A04.

UCB/EERC-81/12 "Studies on Effects of Infills in Seismic Resistant R/C Construction," by Brokken, S. and Bertero, V.V., October 1981, (PB82 166 190)A09.

UCB/EERC-81/13 "Linear Models to Predict the Nonlinear Seismic Behavior of a One-Story Steel Frame," by Valdimarsson, H., Shah, A.H. and McNiven, H.D., September 1981, (PB82 138 793)A07.

UCB/EERC-81/14 "TLUSH: A Computer Program for the Three-Dimensional Dynamic Analysis of Earth Dams," by Kagawa, T., Mejia, L.H., Seed, H.B. and Lysmer, J., September 1981, (PB82 139 940)A06.

UCB/EERC-81/15 "Three Dimensional Dynamic Response Analysis of Earth Dams," by Mejia, L.H. and Seed, H.B., September 1981, (PB82 137 274)A12.

UCB/EERC-81/16 "Experimental Study of Lead and Elastomeric Dampers for Base Isolation Systems," by Kelly, J.M. and Hodder, S.B., October 1981, (PB82 166 182)A05.

UCB/EERC-81/17 "The Influence of Base Isolation on the Seismic Response of Light Secondary Equipment," by Kelly, J.M., April 1981, (PB82 255 266)A04.

UCB/EERC-81/18 "Studies on Evaluation of Shaking Table Response Analysis Procedures," by Blondet, J. M., November 1981, (PB82 197 278)A10.

UCB/EERC-81/19 "DELIGHT.STRUCT: A Computer-Aided Design Environment for Structural Engineering," by Balling, R.J., Pister, K.S. and Polak, E., December 1981, (PB82 218 496)A07.

UCB/EERC-81/20 "Optimal Design of Seismic-Resistant Planar Steel Frames," by Balling, R.J., Ciampi, V. and Pister, K.S., December 1981, (PB82 220 179)A07.

UCB/EERC-82/01 "Dynamic Behavior of Ground for Seismic Analysis of Lifeline Systems," by Sato, T. and Der Kiureghian, A., January 1982, (PB82 218 926)A05.

UCB/EERC-82/02 "Shaking Table Tests of a Tubular Steel Frame Model," by Ghanaat, Y. and Clough, R.W., January 1982, (PB82 220 161)A07.

UCB/EERC-82/03 "Behavior of a Piping System under Seismic Excitation: Experimental Investigations of a Spatial Piping System supported by Mechanical Shock Arrestors," by Schneider, S., Lee, H.-M. and Godden, W. G., May 1982, (PB83 172 544)A09.

UCB/EERC-82/04 "New Approaches for the Dynamic Analysis of Large Structural Systems," by Wilson, E.L., June 1982, (PB83 148 080)A05.

UCB/EERC-82/05 "Model Study of Effects of Damage on the Vibration Properties of Steel Offshore Platforms," by Shahrivar, F. and Bouwkamp, J.G., June 1982, (PB83 148 742)A10.

UCB/EERC-82/06 "States of the Art and Pratice in the Optimum Seismic Design and Analytical Response Prediction of R/C Frame Wall Structures," by Aktan, A.E. and Bertero, V.V., July 1982, (PB83 147 736)A05.

UCB/EERC-82/07 "Further Study of the Earthquake Response of a Broad Cylindrical Liquid-Storage Tank Model," by Manos, G.C. and Clough, R.W., July 1982, (PB83 147 744)A11.

UCB/EERC-82/08 "An Evaluation of the Design and Analytical Seismic Response of a Seven Story Reinforced Concrete Frame," by Charney, F.A. and Bertero, V.V., July 1982, (PB83 157 628)A09.

UCB/EERC-82/09 "Fluid-Structure Interactions: Added Mass Computations for Incompressible Fluid," by Kuo, J.S.-H., August 1982, (PB83 156 281)A07.

UCB/EERC-82/10 "Joint-Opening Nonlinear Mechanism: Interface Smeared Crack Model," by Kuo, J.S.-H., August 1982, (PB83 149 195)A05.

UCB/EERC-82/11 "Dynamic Response Analysis of Techi Dam," by Clough, R.W., Stephen, R.M. and Kuo, J.S.-H., August 1982, (PB83 147 496)A06.

UCB/EERC-82/12 "Prediction of the Seismic Response of R/C Frame-Coupled Wall Structures," by Aktan, A.E., Bertero, V.V. and Piazzo, M., August 1982, (PB83 149 203)A09.

UCB/EERC-82/13 "Preliminary Report on the Smart 1 Strong Motion Array in Taiwan," by Bolt, B.A., Loh, C.H., Penzien, J. and Tsai, Y.B., August 1982, (PB83 159 400)A10.

UCB/EERC-82/14 "Shaking-Table Studies of an Eccentrically X-Braced Steel Structure," by Yang, M.S., September 1982, (PB83 260 778)A12.

UCB/EERC-82/15 "The Performance of Stairways in Earthquakes," by Roha, C., Axley, J.W. and Bertero, V.V., September 1982, (PB83 157 693)A07.

UCB/EERC-82/16 "The Behavior of Submerged Multiple Bodies in Earthquakes," by Liao, W.-G., September 1982, (PB83 158 709)A07.

UCB/EERC-82/17 "Effects of Concrete Types and Loading Conditions on Local Bond-Slip Relationships," by Cowell, A.D., Popov, E.P. and Bertero, V.V., September 1982, (PB83 153 577)A04.

UCB/EERC-82/18 "Mechanical Behavior of Shear Wall Vertical Boundary Members: An Experimental Investigation," by Wagner, M.T. and Bertero, V.V., October 1982, (PB83 159 764)A05.

UCB/EERC-82/19 "Experimental Studies of Multi-support Seismic Loading on Piping Systems," by Kelly, J.M. and Cowell, A.D., November 1982.

UCB/EERC-82/20 "Generalized Plastic Hinge Concepts for 3D Beam-Column Elements," by Chen, P. F.-S. and Powell, G.H., November 1982, (PB83 247 981)A13.

UCB/EERC-82/21 "ANSR-II: General Computer Program for Nonlinear Structural Analysis," by Oughourlian, C.V. and Powell, G.H., November 1982, (PB83 251 330)A12.

UCB/EERC-82/22 "Solution Strategies for Statically Loaded Nonlinear Structures," by Simons, J.W. and Powell, G.H., November 1982, (PB83 197 970)A06.

UCB/EERC-82/23 "Analytical Model of Deformed Bar Anchorages under Generalized Excitations," by Ciampi, V., Eligehausen, R., Bertero, V.V. and Popov, E.P., November 1982, (PB83 169 532)A06.

UCB/EERC-82/24 "A Mathematical Model for the Response of Masonry Walls to Dynamic Excitations," by Sucuoglu, H., Mengi, Y. and McNiven, H.D., November 1982, (PB83 169 011)A07.

UCB/EERC-82/25 "Earthquake Response Considerations of Broad Liquid Storage Tanks," by Cambra, F.J., November 1982, (PB83 251 215)A09.

UCB/EERC-82/26 "Computational Models for Cyclic Plasticity, Rate Dependence and Creep," by Mosaddad, B. and Powell, G.H., November 1982, (PB83 245 829)A08.

UCB/EERC-82/27 "Inelastic Analysis of Piping and Tubular Structures," by Mahasuverachai, M. and Powell, G.H., November 1982, (PB83 249 987)A07.

UCB/EERC-83/01 "The Economic Feasibility of Seismic Rehabilitation of Buildings by Base Isolation," by Kelly, J.M., January 1983, (PB83 197 988)A05.

UCB/EERC-83/02 "Seismic Moment Connections for Moment-Resisting Steel Frames.," by Popov, E.P., January 1983, (PB83 195 412)A04.

UCB/EERC-83/03 "Design of Links and Beam-to-Column Connections for Eccentrically Braced Steel Frames," by Popov, E.P. and Malley, J.O., January 1983, (PB83 194 811)A04.

UCB/EERC-83/04 "Numerical Techniques for the Evaluation of Soil-Structure Interaction Effects in the Time Domain," by Bayo, E. and Wilson, E.L., February 1983, (PB83 245 605)A09.

UCB/EERC-83/05 "A Transducer for Measuring the Internal Forces in the Columns of a Frame-Wall Reinforced Concrete Structure," by Sause, R. and Bertero, V.V., May 1983, (PB84 119 494)A06.

UCB/EERC-83/06 "Dynamic Interactions Between Floating Ice and Offshore Structures," by Croteau, P., May 1983, (PB84 119 486)A16.

UCB/EERC-83/07 "Dynamic Analysis of Multiply Tuned and Arbitrarily Supported Secondary Systems," by Igusa, T. and Der Kiureghian, A., July 1983, (PB84 118 272)A11.

UCB/EERC-83/08 "A Laboratory Study of Submerged Multi-body Systems in Earthquakes," by Ansari, G.R., June 1983, (PB83 261 842)A17.

UCB/EERC-83/09 "Effects of Transient Foundation Uplift on Earthquake Response of Structures," by Yim, C.-S. and Chopra, A.K., June 1983, (PB83 261 396)A07.

UCB/EERC-83/10 "Optimal Design of Friction-Braced Frames under Seismic Loading," by Austin, M.A. and Pister, K.S., June 1983, (PB84 119 288)A06.

UCB/EERC-83/11 "Shaking Table Study of Single-Story Masonry Houses: Dynamic Performance under Three Component Seismic Input and Recommendations," by Manos, G.C., Clough, R.W. and Mayes, R.L., July 1983, (UCB/EERC-83/11)A08.

UCB/EERC-83/12 "Experimental Error Propagation in Pseudodynamic Testing," by Shiing, P.B. and Mahin, S.A., June 1983, (PB84 119 270)A09.

UCB/EERC-83/13 "Experimental and Analytical Predictions of the Mechanical Characteristics of a 1/5-scale Model of a 7-story R/C Frame-Wall Building Structure," by Aktan, A.E., Bertero, V.V., Chowdhury, A.A. and Nagashima, T., June 1983, (PB84 119 213)A07.

UCB/EERC-83/14 "Shaking Table Tests of Large-Panel Precast Concrete Building System Assemblages," by Oliva, M.G. and Clough, R.W., June 1983, (PB86 110 210/AS)A11.

UCB/EERC-83/15 "Seismic Behavior of Active Beam Links in Eccentrically Braced Frames," by Hjelmstad, K.D. and Popov, E.P., July 1983, (PB84 119 676)A09.

UCB/EERC-83/16 "System Identification of Structures with Joint Rotation," by Dimsdale, J.S., July 1983, (PB84 192 210)A06.

UCB/EERC-83/17 "Construction of Inelastic Response Spectra for Single-Degree-of-Freedom Systems," by Mahin, S. and Lin, J., June 1983, (PB84 208 834)A05.

UCB/EERC-83/18 "Interactive Computer Analysis Methods for Predicting the Inelastic Cyclic Behaviour of Structural Sections," by Kaba, S. and Mahin, S., July 1983, (PB84 192 012)A06.

UCB/EERC-83/19 "Effects of Bond Deterioration on Hysteretic Behavior of Reinforced Concrete Joints," by Filippou, F.C., Popov, E.P. and Bertero, V.V., August 1983, (PB84 192 020)A10.

UCB/EERC-83/20 "Correlation of Analytical and Experimental Responses of Large-Panel Precast Building Systems," by Oliva, M.G., Clough, R.W., Velkov, M. and Gavrilovic, P., May 1988.

UCB/EERC-83/21 "Mechanical Characteristics of Materials Used in a 1/5 Scale Model of a 7-Story Reinforced Concrete Test Structure," by Bertero, V.V., Aktan, A.E., Harris, H.G. and Chowdhury, A.A., October 1983, (PB84 193 697)A05.

UCB/EERC-83/22 "Hybrid Modelling of Soil-Structure Interaction in Layered Media," by Tzong, T.-J. and Penzien, J., October 1983, (PB84 192 178)A08.

UCB/EERC-83/23 "Local Bond Stress-Slip Relationships of Deformed Bars under Generalized Excitations," by Eligehausen, R., Popov, E.P. and Bertero, V.V., October 1983, (PB84 192 848)A09.

UCB/EERC-83/24 "Design Considerations for Shear Links in Eccentrically Braced Frames," by Malley, J.O. and Popov, E.P., November 1983, (PB84 192 186)A07.

UCB/EERC-84/01 "Pseudodynamic Test Method for Seismic Performance Evaluation: Theory and Implementation," by Shing, P.-S.B. and Mahin, S.A., January 1984, (PB84 190 644)A08.

UCB/EERC-84/02 "Dynamic Response Behavior of Kiang Hong Dian Dam," by Clough, R.W., Chang, K.-T., Chen, H.-Q. and Stephen, R.M., April 1984, (PB84 209 402)A08.

UCB/EERC-84/03 "Refined Modelling of Reinforced Concrete Columns for Seismic Analysis," by Kaba, S.A. and Mahin, S.A., April 1984, (PB84 234 384)A06.

UCB/EERC-84/04 "A New Floor Response Spectrum Method for Seismic Analysis of Multiply Supported Secondary Systems," by Asfura, A. and Der Kiureghian, A., June 1984, (PB84 239 417)A06.

UCB/EERC-84/05 "Earthquake Simulation Tests and Associated Studies of a 1/5th-scale Model of a 7-Story R/C Frame-Wall Test Structure," by Bertero, V.V., Aktan, A.E., Charney, F.A. and Sause, R., June 1984, (PB84 239 409)A09.

UCB/EERC-84/06 "R/C Structural Walls: Seismic Design for Shear," by Aktan, A.E. and Bertero, V.V., 1984.

UCB/EERC-84/07 "Behavior of Interior and Exterior Flat-Plate Connections subjected to Inelastic Load Reversals," by Zee, H.L. and Moehle, J.P., August 1984, (PB86 117 629/AS)A07.

UCB/EERC-84/08 "Experimental Study of the Seismic Behavior of a Two-Story Flat-Plate Structure," by Moehle, J.P. and Diebold, J.W., August 1984, (PB86 122 553/AS)A12.

UCB/EERC-84/09 "Phenomenological Modeling of Steel Braces under Cyclic Loading," by Ikeda, K., Mahin, S.A. and Dermitzakis, S.N., May 1984, (PB86 132 198/AS)A08.

UCB/EERC-84/10 "Earthquake Analysis and Response of Concrete Gravity Dams," by Fenves, G. and Chopra, A.K., August 1984, (PB85 193 902/AS)A11.

UCB/EERC-84/11 "EAGD-84: A Computer Program for Earthquake Analysis of Concrete Gravity Dams," by Fenves, G. and Chopra, A.K., August 1984, (PB85 193 613/AS)A05.

UCB/EERC-84/12 "A Refined Physical Theory Model for Predicting the Seismic Behavior of Braced Steel Frames," by Ikeda, K. and Mahin, S.A., July 1984, (PB85 191 450/AS)A09.

UCB/EERC-84/13 "Earthquake Engineering Research at Berkeley - 1984," by , August 1984, (PB85 197 341/AS)A10.

UCB/EERC-84/14 "Moduli and Damping Factors for Dynamic Analyses of Cohesionless Soils," by Seed, H.B., Wong, R.T., Idriss, I.M. and Tokimatsu, K., September 1984, (PB85 191 468/AS)A04.

UCB/EERC-84/15 "The Influence of SPT Procedures in Soil Liquefaction Resistance Evaluations," by Seed, H.B., Tokimatsu, K., Harder, L.F. and Chung, R.M., October 1984, (PB85 191 732/AS)A04.

UCB/EERC-84/16 "Simplified Procedures for the Evaluation of Settlements in Sands Due to Earthquake Shaking," by Tokimatsu, K. and Seed, H.B., October 1984, (PB85 197 887/AS)A03.

UCB/EERC-84/17 "Evaluation of Energy Absorption Characteristics of Highway Bridges Under Seismic Conditions - Volume I and Volume II (Appendices)," by Imbsen, R.A. and Penzien, J., September 1986.

UCB/EERC-84/18 "Structure-Foundation Interactions under Dynamic Loads," by Liu, W.D. and Penzien, J., November 1984, (PB87 124 889/AS)A11.

UCB/EERC-84/19 "Seismic Modelling of Deep Foundations," by Chen, C.-H. and Penzien, J., November 1984, (PB87 124 798/AS)A07.

UCB/EERC-84/20 "Dynamic Response Behavior of Quan Shui Dam," by Clough, R.W., Chang, K.-T., Chen, H.-Q., Stephen, R.M., Ghanaat, Y. and Qi, J.-H., November 1984, (PB86 115177/AS)A07.

UCB/EERC-85/01 "Simplified Methods of Analysis for Earthquake Resistant Design of Buildings," by Cruz, E.F. and Chopra, A.K., February 1985, (PB86 112299/AS)A12.

UCB/EERC-85/02 "Estimation of Seismic Wave Coherency and Rupture Velocity using the SMART 1 Strong-Motion Array Recordings," by Abrahamson, N.A., March 1985, (PB86 214 343)A07.

UCB/EERC-85/03 "Dynamic Properties of a Thirty Story Condominium Tower Building," by Stephen, R.M., Wilson, E.L. and Stander, N., April 1985, (PB86 118965/AS)A06.

UCB/EERC-85/04 "Development of Substructuring Techniques for On-Line Computer Controlled Seismic Performance Testing," by Dermitzakis, S. and Mahin, S., February 1985, (PB86 132941/AS)A08.

UCB/EERC-85/05 "A Simple Model for Reinforcing Bar Anchorages under Cyclic Excitations," by Filippou, F.C., March 1985, (PB86 112 919/AS)A05.

UCB/EERC-85/06 "Racking Behavior of Wood-framed Gypsum Panels under Dynamic Load," by Oliva, M.G., June 1985.

UCB/EERC-85/07 "Earthquake Analysis and Response of Concrete Arch Dams," by Fok, K.-L. and Chopra, A.K., June 1985, (PB86 139672/AS)A10.

UCB/EERC-85/08 "Effect of Inelastic Behavior on the Analysis and Design of Earthquake Resistant Structures," by Lin, J.P. and Mahin, S.A., June 1985, (PB86 135340/AS)A08.

UCB/EERC-85/09 "Earthquake Simulator Testing of a Base-Isolated Bridge Deck," by Kelly, J.M., Buckle, I.G. and Tsai, H.-C., January 1986, (PB87 124 152/AS)A06.

UCB/EERC-85/10 "Simplified Analysis for Earthquake Resistant Design of Concrete Gravity Dams," by Fenves, G. and Chopra, A.K., June 1986, (PB87 124 160/AS)A08.

UCB/EERC-85/11 "Dynamic Interaction Effects in Arch Dams," by Clough, R.W., Chang, K.-T., Chen, H.-Q. and Ghanaat, Y., October 1985, (PB86 135027/AS)A05.

UCB/EERC-85/12 "Dynamic Response of Long Valley Dam in the Mammoth Lake Earthquake Series of May 25-27, 1980," by Lai, S. and Seed, H.B., November 1985, (PB86 142304/AS)A05.

UCB/EERC-85/13 "A Methodology for Computer-Aided Design of Earthquake-Resistant Steel Structures," by Austin, M.A., Pister, K.S. and Mahin, S.A., December 1985, (PB86 159480/AS)A10 .

UCB/EERC-85/14 "Response of Tension-Leg Platforms to Vertical Seismic Excitations," by Liou, G.-S., Penzien, J. and Yeung, R.W., December 1985, (PB87 124 871/AS)A08.

UCB/EERC-85/15 "Cyclic Loading Tests of Masonry Single Piers: Volume 4 - Additional Tests with Height to Width Ratio of 1," by Sveinsson, B., McNiven, H.D. and Sucuoglu, H., December 1985.

UCB/EERC-85/16 "An Experimental Program for Studying the Dynamic Response of a Steel Frame with a Variety of Infill Partitions," by Yanev, B. and McNiven, H.D., December 1985.

UCB/EERC-86/01 "A Study of Seismically Resistant Eccentrically Braced Steel Frame Systems," by Kasai, K. and Popov, E.P., January 1986, (PB87 124 178/AS)A14.

UCB/EERC-86/02 "Design Problems in Soil Liquefaction," by Seed, H.B., February 1986, (PB87 124 186/AS)A03.

UCB/EERC-86/03 "Implications of Recent Earthquakes and Research on Earthquake-Resistant Design and Construction of Buildings," by Bertero, V.V., March 1986, (PB87 124 194/AS)A05.

UCB/EERC-86/04 "The Use of Load Dependent Vectors for Dynamic and Earthquake Analyses," by Leger, P., Wilson, E.L. and Clough, R.W., March 1986, (PB87 124 202/AS)A12.

UCB/EERC-86/05 "Two Beam-To-Column Web Connections," by Tsai, K.-C. and Popov, E.P., April 1986, (PB87 124 301/AS)A04.

UCB/EERC-86/06 "Determination of Penetration Resistance for Coarse-Grained Soils using the Becker Hammer Drill," by Harder, L.F. and Seed, H.B., May 1986, (PB87 124 210/AS)A07.

UCB/EERC-86/07 "A Mathematical Model for Predicting the Nonlinear Response of Unreinforced Masonry Walls to In-Plane Earthquake Excitations," by Mengi, Y. and McNiven, H.D., May 1986, (PB87 124 780/AS)A06.

UCB/EERC-86/08 "The 19 September 1985 Mexico Earthquake: Building Behavior," by Bertero, V.V., July 1986.

UCB/EERC-86/09 "EACD-3D: A Computer Program for Three-Dimensional Earthquake Analysis of Concrete Dams," by Fok, K.-L., Hall, J.F. and Chopra, A.K., July 1986, (PB87 124 228/AS)A08.

UCB/EERC-86/10 "Earthquake Simulation Tests and Associated Studies of a 0.3-Scale Model of a Six-Story Concentrically Braced Steel Structure," by Uang, C.-M. and Bertero, V.V., December 1986, (PB87 163 564/AS)A17.

UCB/EERC-86/11 "Mechanical Characteristics of Base Isolation Bearings for a Bridge Deck Model Test," by Kelly, J.M., Buckle, I.G. and Koh, C.-G., November 1987.

UCB/EERC-86/12 "Effects of Axial Load on Elastomeric Isolation Bearings," by Koh, C.-G. and Kelly, J.M., November 1987.

UCB/EERC-87/01 "The FPS Earthquake Resisting System: Experimental Report," by Zayas, V.A., Low, S.S. and Mahin, S.A., June 1987.

UCB/EERC-87/02 "Earthquake Simulator Tests and Associated Studies of a 0.3-Scale Model of a Six-Story Eccentrically Braced Steel Structure," by Whittaker, A., Uang, C.-M. and Bertero, V.V., July 1987.

UCB/EERC-87/03 "A Displacement Control and Uplift Restraint Device for Base-Isolated Structures," by Kelly, J.M., Griffith, M.C. and Aiken, I.D., April 1987.

UCB/EERC-87/04 "Earthquake Simulator Testing of a Combined Sliding Bearing and Rubber Bearing Isolation System," by Kelly, J.M. and Chalhoub, M.S., 1987.

UCB/EERC-87/05 "Three-Dimensional Inelastic Analysis of Reinforced Concrete Frame-Wall Structures," by Moazzami, S. and Bertero, V.V., May 1987.

UCB/EERC-87/06 "Experiments on Eccentrically Braced Frames with Composite Floors," by Ricles, J. and Popov, E., June 1987.

UCB/EERC-87/07 "Dynamic Analysis of Seismically Resistant Eccentrically Braced Frames," by Ricles, J. and Popov, E., June 1987.

UCB/EERC-87/08 "Undrained Cyclic Triaxial Testing of Gravels-The Effect of Membrane Compliance," by Evans, M.D. and Seed, H.B., July 1987.

UCB/EERC-87/09 "Hybrid Solution Techniques for Generalized Pseudo-Dynamic Testing," by Thewalt, C. and Mahin, S.A., July 1987.

UCB/EERC-87/10 "Ultimate Behavior of Butt Welded Splices in Heavy Rolled Steel Sections," by Bruneau, M., Mahin, S.A. and Popov, E.P., July 1987.

UCB/EERC-87/11 "Residual Strength of Sand from Dam Failures in the Chilean Earthquake of March 3, 1985," by De Alba, P., Seed, H.B., Retamal, E. and Seed, R.B., September 1987.

UCB/EERC-87/12 "Inelastic Seismic Response of Structures with Mass or Stiffness Eccentricities in Plan," by Bruneau, M. and Mahin, S.A., September 1987.

UCB/EERC-87/13 "CSTRUCT: An Interactive Computer Environment for the Design and Analysis of Earthquake Resistant Steel Structures," by Austin, M.A., Mahin, S.A. and Pister, K.S., September 1987.

UCB/EERC-87/14 "Experimental Study of Reinforced Concrete Columns Subjected to Multi-Axial Loading," by Low, S.S. and Moehle, J.P., September 1987.

UCB/EERC-87/15 "Relationships between Soil Conditions and Earthquake Ground Motions in Mexico City in the Earthquake of Sept. 19, 1985," by Seed, H.B., Romo, M.P., Sun, J., Jaime, A. and Lysmer, J., October 1987.

UCB/EERC-87/16 "Experimental Study of Seismic Response of R. C. Setback Buildings," by Shahrooz, B.M. and Moehle, J.P., October 1987.

UCB/EERC-87/17 "The Effect of Slabs on the Flexural Behavior of Beams," by Pantazopoulou, S.J. and Moehle, J.P., October 1987.

UCB/EERC-87/18 "Design Procedure for R-FBI Bearings," by Mostaghel, N. and Kelly, J.M., November 1987.

UCB/EERC-87/19 "Analytical Models for Predicting the Lateral Response of R C Shear Walls: Evaluation of their Reliability," by Vulcano, A. and Bertero, V.V., November 1987.

UCB/EERC-87/20 "Earthquake Response of Torsionally-Coupled Buildings," by Hejal, R. and Chopra, A.K., December 1987.

UCB/EERC-87/21 "Dynamic Reservoir Interaction with Monticello Dam," by Clough, R.W., Ghanaat, Y. and Qiu, X-F., December 1987.

UCB/EERC-87/22 "Strength Evaluation of Coarse-Grained Soils," by Siddiqi, F.H., Seed, R.B., Chan, C.K., Seed, H.B. and Pyke, R.M., December 1987.

UCB/EERC-88/01 "Seismic Behavior of Concentrically Braced Steel Frames," by Khatib, I., Mahin, S.A. and Pister, K.S., January 1988.

UCB/EERC-88/02 "Experimental Evaluation of Seismic Isolation of Medium-Rise Structures Subject to Uplift," by Griffith, M.C., Kelly, J.M., Coveney, V.A. and Koh, C.G., January 1988.

UCB/EERC-88/03 "Cyclic Behavior of Steel Double Angle Connections," by Astaneh-Asl, A. and Nader, M.N., January 1988.

UCB/EERC-88/04 "Re-evaluation of the Slide in the Lower San Fernando Dam in the Earthquake of Feb. 9, 1971," by Seed, H.B., Seed, R.B., Harder, L.F. and Jong, H.-L., April 1988.

UCB/EERC-88/05 "Experimental Evaluation of Seismic Isolation of a Nine-Story Braced Steel Frame Subject to Uplift," by Griffith, M.C., Kelly, J.M. and Aiken, I.D., May 1988.

UCB/EERC-88/06 "DRAIN-2DX User Guide.," by Allahabadi, R. and Powell, G.H., March 1988.

UCB/EERC-88/07 "Cylindrical Fluid Containers in Base-Isolated Structures," by Chalhoub, M.S. and Kelly, J.M. , April 1988.

UCB/EERC-88/08 "Analysis of Near-Source Waves: Separation of Wave Types using Strong Motion Array Recordings," by Darragh, R.B., June 1988.

UCB/EERC-88/09 "Alternatives to Standard Mode Superposition for Analysis of Non-Classically Damped Systems," by Kusainov, A.A. and Clough, R.W., June 1988.

UCB/EERC-88/10 "The Landslide at the Port of Nice on October 16, 1979," by Seed, H.B., Seed, R.B., Schlosser, F., Blondeau, F. and Juran, I., June 1988.

UCB/EERC-88/11 "Liquefaction Potential of Sand Deposits Under Low Levels of Excitation," by Carter, D.P. and Seed, H.B., August 1988.

UCB/EERC-88/12 "Nonlinear Analysis of Reinforced Concrete Frames Under Cyclic Load Reversals," by Filippou, F.C. and Issa, A., September 1988.

UCB/EERC-88/13 "Implications of Recorded Earthquake Ground Motions on Seismic Design of Building Structures," by Uang, C.-M. and Bertero, V.V., November 1988.

UCB/EERC-88/14 "An Experimental Study of the Behavior of Dual Steel Systems," by Whittaker, A.S. , Uang, C.-M. and Bertero, V.V., September 1988.

UCB/EERC-88/15 "Dynamic Moduli and Damping Ratios for Cohesive Soils," by Sun, J.I., Golesorkhi, R. and Seed, H.B., August 1988.

UCB/EERC-88/16 "Reinforced Concrete Flat Plates Under Lateral Load: An Experimental Study Including Biaxial Effects," by Pan, A. and Moehle, J., October 1988.

UCB/EERC-88/17 "Earthquake Engineering Research at Berkeley - 1988," by EERC, November 1988.

UCB/EERC-88/18 "Use of Energy as a Design Criterion in Earthquake-Resistant Design," by Uang, C.-M. and Bertero, V.V., November 1988.

UCB/EERC-88/19 "Steel Beam-Column Joints in Seismic Moment Resisting Frames," by Tsai, K.-C. and Popov, E.P., November 1988.

UCB/EERC-88/20 "Base Isolation in Japan, 1988," by Kelly, J.M., December 1988.

UCB/EERC-89/01 "Behavior of Long Links in Eccentrically Braced Frames," by Engelhardt, M.D. and Popov, E.P., January 1989.

UCB/EERC-89/02 "Earthquake Simulator Testing of Steel Plate Added Damping and Stiffness Elements," by Whittaker, A., Bertero, V.V., Alonso, J. and Thompson, C., January 1989.

UCB/EERC-89/03 "Implications of Site Effects in the Mexico City Earthquake of Sept. 19, 1985 for Earthquake-Resistant Design Criteria in the San Francisco Bay Area of California," by Seed, H.B. and Sun, J.I., March 1989.

UCB/EERC-89/04 "Earthquake Analysis and Response of Intake-Outlet Towers," by Goyal, A. and Chopra, A.K., July 1989.

UCB/EERC-89/05 "The 1985 Chile Earthquake: An Evaluation of Structural Requirements for Bearing Wall Buildings," by Wallace, J.W. and Moehle, J.P., July 1989.

UCB/EERC-89/06 "Effects of Spatial Variation of Ground Motions on Large Multiply-Supported Structures," by Hao, H., July 1989.

UCB/EERC-89/07 "EADAP - Enhanced Arch Dam Analysis Program: User's Manual," by Ghanaat, Y. and Clough, R.W., August 1989.

UCB/EERC-89/08 "Seismic Performance of Steel Moment Frames Plastically Designed by Least Squares Stress Fields," by Ohi, K. and Mahin, S.A., August 1989.

UCB/EERC-89/09 "Feasibility and Performance Studies on Improving the Earthquake Resistance of New and Existing Buildings Using the Friction Pendulum System," by Zayas, V., Low, S., Mahin, S.A. and Bozzo, L., July 1989.

UCB/EERC-89/10 "Measurement and Elimination of Membrane Compliance Effects in Undrained Triaxial Testing," by Nicholson, P.G., Seed, R.B. and Anwar, H., September 1989.

UCB/EERC-89/11 "Static Tilt Behavior of Unanchored Cylindrical Tanks," by Lau, D.T. and Clough, R.W., September 1989.

UCB/EERC-89/12 "ADAP-88: A Computer Program for Nonlinear Earthquake Analysis of Concrete Arch Dams," by Fenves, G.L., Mojtahedi, S. and Reimer, R.B., September 1989.

UCB/EERC-89/13 "Mechanics of Low Shape Factor Elastomeric Seismic Isolation Bearings," by Aiken, I.D., Kelly, J.M. and Tajirian, F., December 1989.

UCB/EERC-89/14 "Preliminary Report on the Seismological and Engineering Aspects of the October 17, 1989 Santa Cruz (Loma Prieta) Earthquake," by EERC, October 1989.

UCB/EERC-89/15 "Experimental Studies of a Single Story Steel Structure Tested with Fixed, Semi-Rigid and Flexible Connections," by Nader, M.N. and Astaneh-Asl, A., August 1989.

UCB/EERC-89/16 "Collapse of the Cypress Street Viaduct as a Result of the Loma Prieta Earthquake," by Nims, D.K., Miranda, E., Aiken, I.D., Whittaker, A.S. and Bertero, V.V., November 1989.

UCB/EERC-90/01 "Mechanics of High-Shape Factor Elastomeric Seismic Isolation Bearings," by Kelly, J.M., Aiken, I.D. and Tajirian, F.F., March 1990.

UCB/EERC-90/02 "Javid's Paradox: The Influence of Preform on the Modes of Vibrating Beams," by Kelly, J.M., Sackman, J.L. and Javid, A., May 1990.

UCB/EERC-90/03 "Earthquake Simulator Tests of Viscoelastic Dampers for Medium Rise Structures," by Kelly, J.M. and Aiken, I.D., May 1990.

UCB/EERC-90/04 "Damage to the San Francisco-Oakland Bay Bridge During the October 17, 1989 Earthquake," by Astaneh, A., June 1990.

UCB/EERC-90/05 "Preliminary Report on the Principal Geotechnical Aspects of the October 17, 1989 Loma Prieta Earthquake," by Seed, R.B., Dickenson, S.E., Riemer, M.F., Bray, J.D., Sitar, N., Mitchell, J.K., Idriss, I.M., Kayen, R.E., Kroop, A., Harder, L.F., Jr. and Power, M.S., April 1990.

UCB/EERC-90/06 "Models of Critical Regions in Reinforced Concrete Frames Under Seismic Excitations," by Zulfiqar, N. and Filippou, F., May 1990.

UCB/EERC-90/07 "A Unified Earthquake-Resistant Design Method for Steel Frames Using ARMA Models," by Takewaki, I., Conte, J.P., Mahin, S.A. and Pister, K.S., June 1990.

UCB/EERC-90/08 "Soil Conditions and Earthquake Hazard Mitigation in the Marina District of San Francisco," by Mitchell, J.K., Masood, T., Kayen, R.E. and Seed, R.B., May 1990.

UCB/EERC-90/09 "Influence of the Earthquake Ground Motion Process and Structural Properties on Response Characteristics of Simple Structures," by Conte, J.P., Pister, K.S. and Mahin, S.A., July 1990.